VOLCANIC LAKE DYNAMICS AND RELATED HAZARDS

EDITED BY: Dmitri Rouwet, Franco Tassi, Agnes Mazot and Corentin Caudron

PUBLISHED IN: Frontiers in Earth Science

frontiers Research Topics

ISSN 1664-8714
ISBN 978-2-88976-400-6
DOI 10.3389/978-2-88976-400-6

About Frontiers

Frontiers is more than just an open-access publisher of scholarly articles: it is a pioneering approach to the world of academia, radically improving the way scholarly research is managed. The grand vision of Frontiers is a world where all people have an equal opportunity to seek, share and generate knowledge. Frontiers provides immediate and permanent online open access to all its publications, but this alone is not enough to realize our grand goals.

Frontiers Journal Series

The Frontiers Journal Series is a multi-tier and interdisciplinary set of open-access, online journals, promising a paradigm shift from the current review, selection and dissemination processes in academic publishing. All Frontiers journals are driven by researchers for researchers; therefore, they constitute a service to the scholarly community. At the same time, the Frontiers Journal Series operates on a revolutionary invention, the tiered publishing system, initially addressing specific communities of scholars, and gradually climbing up to broader public understanding, thus serving the interests of the lay society, too.

Dedication to Quality

Each Frontiers article is a landmark of the highest quality, thanks to genuinely collaborative interactions between authors and review editors, who include some of the world's best academicians. Research must be certified by peers before entering a stream of knowledge that may eventually reach the public - and shape society; therefore, Frontiers only applies the most rigorous and unbiased reviews.
Frontiers revolutionizes research publishing by freely delivering the most outstanding research, evaluated with no bias from both the academic and social point of view. By applying the most advanced information technologies, Frontiers is catapulting scholarly publishing into a new generation.

What are Frontiers Research Topics?

Frontiers Research Topics are very popular trademarks of the Frontiers Journals Series: they are collections of at least ten articles, all centered on a particular subject. With their unique mix of varied contributions from Original Research to Review Articles, Frontiers Research Topics unify the most influential researchers, the latest key findings and historical advances in a hot research area! Find out more on how to host your own Frontiers Research Topic or contribute to one as an author by contacting the Frontiers Editorial Office: frontiersin.org/about/contact

VOLCANIC LAKE DYNAMICS AND RELATED HAZARDS

Topic Editors:
Dmitri Rouwet, Istituto Nazionale di Geofisica e Vulcanologia, sezione di Bologna, Italy
Franco Tassi, University of Florence, Italy
Agnes Mazot, GNS Science, New Zealand
Corentin Caudron, Université libre de Bruxelles, Belgium

Citation: Rouwet, D., Tassi, F., Mazot, A., Caudron, C., eds. (2022). Volcanic Lake Dynamics and Related Hazards. Lausanne: Frontiers Media SA.
doi: 10.3389/978-2-88976-400-6

Table of Contents

frontiers in Earth Science

ORIGINAL RESEARCH
published: 28 July 2021
doi: 10.3389/feart.2021.645011

Carbon Dioxide in Lake Nyos, Cameroon, Estimated Quantitatively From Sound Speed Measurements

Bertram Boehrer[1], Kazuto Saiki[2], Takeshi Ohba[3], Greg Tanyileke[4], Dmitri Rouwet[5] and Minoru Kusakabe[6]*

[1]Helmholtz-Centre for Environmental Research – UFZ, Magdeburg, Germany, [2]Graduate School of Science, Osaka University, Osaka, Japan, [3]School of Science, Tokai University, Hiratsuka, Japan, [4]Institute for Geological and Mining Res. (IRGM), Yaounde, Cameroon, [5]Istituto Nazionale di Geofisica e Vulcanologia, Sezione di Bologna, Bologna, Italy, [6]University of Toyama, Toyama, Japan

Gases dissolved in the deep water of lakes can pose a hazard when extreme concentrations are reached. A sudden release of large amounts of gas can cost the lives of humans living in the neighbourhood, as happened at Lake Nyos in 1986. Since 2001, the gas risk at Lake Nyos has been mitigated by induced degassing, but the lake continues to be supplied by CO_2, and a regular survey needs to be implemented to guarantee safe conditions. Frequent sampling of this remote lake requires an enormous effort, and many analytical techniques are very difficult to run at the lake site. In this contribution, we combined a commercially available sound speed sensor with a CTD (electrical conductivity, temperature, depth) probe to obtain an indirect but quantitative estimate of carbon dioxide concentrations with fine depth resolution (decimetre scale). Dissolved carbon dioxide increases sound speed but does not contribute to electrical conductivity. Hence the difference between measured and calculated (on the base of electrical conductivity, temperature and pressure) sound speed gives a quantitative indication of dissolved carbon dioxide. We infer the vertical distribution of dissolved CO_2 and hence continue the survey of the progress of the intended degassing. In conclusion, we present an easy to implement method for very high CO_2 concentrations in deep lakes, and we highly recommend the implementation of the sound speed-CTD probe combination at Lake Nyos and at other gas-laden volcanic lakes, as such an approach could safeguard the people living in the area with acceptable cost and effort for the operators. In this manner, alarming CO_2 concentrations in deep parts of lakes can be detected in a timely fashion.

Keywords: gas, gas pressure, lake Nyos, limnic eruption, remediation, sound speed

OPEN ACCESS

Edited by:
John Stix,
McGill University, Canada

Reviewed by:
Pingping Luo,
Chang'an University, China
Ahmed Kenawy,
Mansoura University, Egypt

****Correspondence:***
Bertram Boehrer
Bertram.Boehrer@ufz.de

Specialty section:
This article was submitted to Volcanology, a section of the journal Frontiers in Earth Science

Received: *04 March 2021*
Accepted: *01 July 2021*
Published: *28 July 2021*

Citation:
Boehrer B, Saiki K, Ohba T, Tanyileke G, Rouwet D and Kusakabe M (2021) Carbon Dioxide in Lake Nyos, Cameroon, Estimated Quantitatively From Sound Speed Measurements. Front. Earth Sci. 9:645011. doi: 10.3389/feart.2021.645011

INTRODUCTION

Extreme concentrations of dissolved gases in deep waters of lakes can pose a threat to the local population. Sudden limnic overturns can liberate large volumes of gas, which can asphyxiate humans and livestock, as happened at Lake Monoun in 1984 and at Lake Nyos in 1986 (Kling et al., 1987; Sigurdsson et al., 1987). More than 1700 humans perished in these natural disasters. Also at other places, extreme gas pressures have been detected and assessed for their danger to the local population (Lake Kivu: Lorke et al., 2004; Schmid et al., 2005; Guadiana Pit Lake: Sánchez España et al., 2014;

Boehrer et al., 2016; Lake Vollert-Sued: Horn et al., 2017; Lago Monticchio Piccolo: Caracausi et al., 2009; Cabassi et al., 2013). All these lakes are meromictic, and accumulation of solutes in the deep water can occur over long periods (e.g., Boehrer et al., 2013; Boehrer et al., 2021). In some cases, artificial degassing is considered necessary to reduce risk around the lakes (Nyos, Monoun, Guadiana Pit Lake; Sánchez España et al., 2020).

Even after removal of the gas, some of the lakes still maintain their connection to the gas source, allowing for gas recharge, as seen in Lake Monoun (Kusakabe, 2017). Other lakes, such as Lago Albano, can be recharged with gas in a sudden manner by seismic activity (Chiodini et al., 2012; Rouwet et al., 2019; Rouwet et al., 2021; Rouwet, 2021). To avoid dangerous levels of gas accumulation, gas concentrations need to be surveyed regularly. Reliable measurements of high gas concentrations are difficult, as intensive efforts on Lake Kivu have shown (Boehrer et al., 2019; Bärenbold et al., 2020, and references therein). Especially in remote localities such as Lake Nyos, measurements with sophisticated equipment and complex procedures require an enormous logistical effort. Simple, portable equipment would be most practicable for such surveys. Sanemasa et al. (2017) provided measurements of sound speed which were affected by high concentrations of carbon dioxide; they indicated that sound speed measurements could be used to quantify carbon dioxide in Lake Nyos. Saiki et al. (2017) presented measurements of sound speed with a Minos X (AML Oceanographic) used for calibrating a multibeam sonar. They correlated measured CO_2 concentrations with measured sound speeds, and demonstrated that such measurements are feasible and provide a good quantitative estimate of the carbon dioxide dissolved in the lake water.

In March 2016, 30 years after the disaster of the Nyos limnic eruption, a conference was held in Yaounde (Cameroon) to reflect upon the work so far that dealt with managing the danger of limnic eruptions at Lake Nyos and Lake Monoun. The goal was to understand the underlying volcanic connections and to examine lessons learnt from the Nyos and Monoun remediation efforts (Tanyileke et al., 2019). Artificial degassing had been induced beginning in 2001 when the first degassing tube went into operation. Degassing was enhanced in 2011 with two additional degassing tubes. The scientific meeting, the 9th Workshop of the International Association of Volcanology and Chemistry of the Earth's Interior (IAVCEI) Commission on Volcanic Lakes, was complemented by a short field campaign to document the situation in 2016, i.e., at a time when the forced degassing had removed most of the gas from the deep layer of Lake Nyos (Kusakabe, 2017; Kusakabe et al., 2019; Tanyileke et al., 2019; Halbwachs et al., 2020).

The aim of this study was the field deployment of commercially available equipment (i.e., a conductivity-density-depth probe with a sound speed sensor) to yield a profile of dissolved inorganic carbon (DIC hereafter) concentrations based on the excess sound speed in comparison to calculated sound speed. The well studied Lake Nyos itself was arguably the best suited natural laboratory to develop and verify our approach. However, in addition to the studies by Saiki et al. (2017) and Sanemasa et al. (2017), we included conductivity in the calculations and considerations of sound speed to correlate actual CO_2 (instead of DIC) with sound speed. We present a pH and site independent (background salinity) approach; hence this method has the potential to be applied to other highly CO_2-laden lakes.

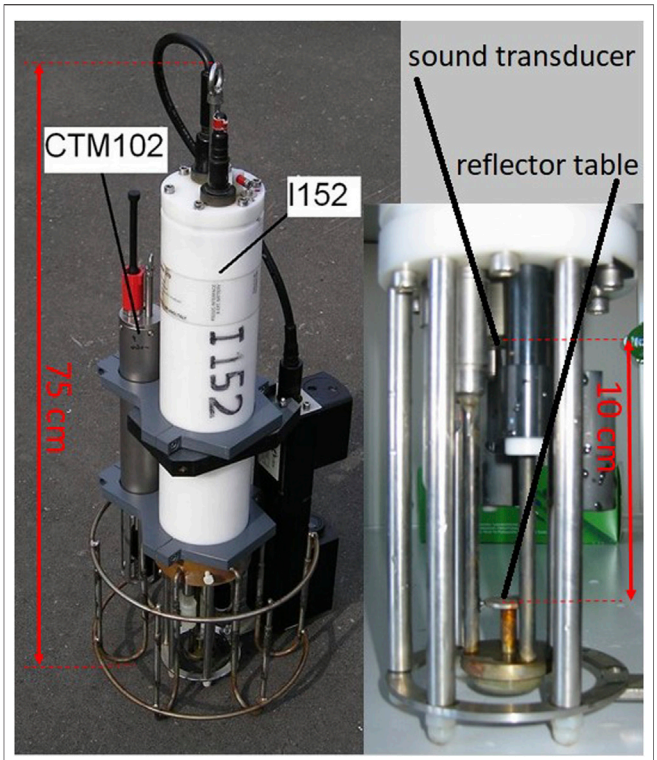

FIGURE 1 | The deployed multiparameter probe Idronaut Ocean Seven 316 "I152" with the VALEPORT sound speed sensor mounted together with a faster CTD probe "CTM102" (Sea and Sun Technology, Germany).

MEASUREMENTS

Lake Nyos is located in the Cameroon Volcanic Line in the western part of Cameroon (06°26′ N, 10°17′ E) at an altitude of 1,091 m asl. Its maximum depth reaches 210 m with a surface area of 1.58 km^2 compared to the catchment area of about 8 km^2 and a lake volume of 1.6×10^8 m^3 (Tanyileke et al., 2019). The lake has been meromictic and is known for its high carbon dioxide concentrations in the deep water, which caused a limnic eruption in 1986 costing the lives of 1,746 people.

We took part in the Nyos field campaign in 2016. We lowered our custom-built oceanographic multiparameter probe by hand from the surface to the maximum depth on a rope to document the stratification of temperature and electrical conductivity (EC hereafter) at the time. The probe was also equipped with an oxygen sensor and a pH sensor. In addition, it carried a sound speed sensor for direct measurements. Both the probe ("i152", Ocean Seven 316, Idronaut, Italy) and the sound speed sensor (VALEPORT, United Kingdom) were commercially available, and the probe manufacturer customized the sound speed sensor

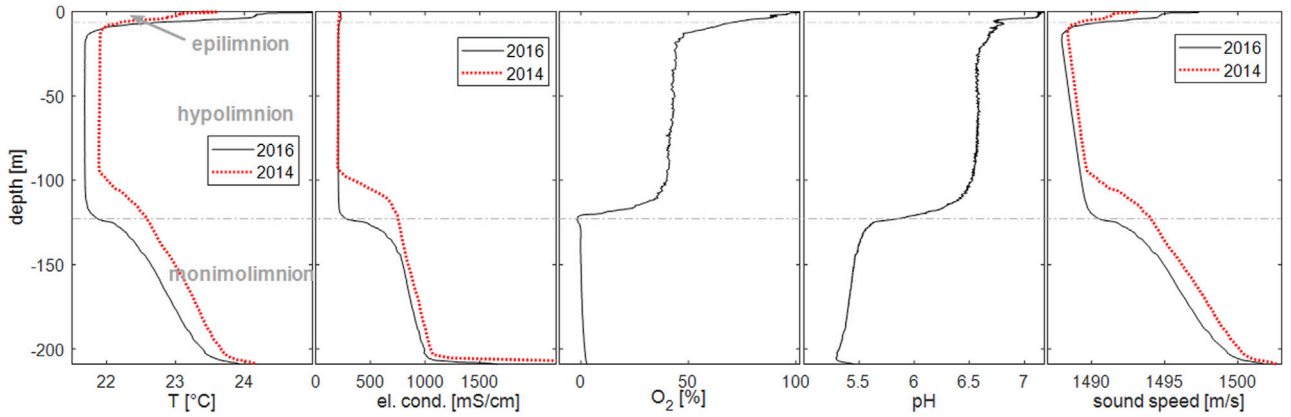

FIGURE 2 | Profiles of temperature, electrical conductivity at 25°C, oxygen saturation (calibrated on local conditions), pH and sound speed measured in Lake Nyos on 2016-03-19 in comparison with measurements in 2014 [2014 data from Saiki et al. (2017): broken red lines]. The broken horizontal line indicates the depth of the major chemical gradient, the so-called chemocline.

in the probe (see **Figure 1**). The sound speed sensor provided a direct time of flight measurement over 10 cm from a transducer to a reflector table and back. As a backup, we also mounted a CTD probe "CTM102" (Sea and Sun Technology, Trappenkamp Germany; data were for backup but not used in this publication). The full instrument weighted 9.9 kg; it was easy to handle and could be carried in a case on an airplane.

Measurements of EC showed the removal of the deep water from the monimolimnion (120–209 m depth) by syphoning water from close to the lake bed to the surface. As a consequence, the upper water body of constant salinity grew in thickness from ca. 100 m in 2014 to 120 m in 2016 (**Figure 2**). The rates of the gradient lowering agreed well with the expected value from the discharge through the degassing pipes (see Ohba et al., 2020). The higher salinity water at the surface induced mixing and created the water body of constant EC.

The temperature profile showed a shallow epilimnion of about 10 m thickness, below which we found an isothermal hypolimnion (**Figure 2**, see also Boehrer and Schultze 2008; Boehrer et al., 2013). Below 120 m depth, i.e., in the monimolimnion, temperature increased along with EC. The difference from 2014 could be explained by the continued drawdown by siphoning deeper water (Ohba et al., 2020). Temperatures in the hypolimnion had changed considerably from 2014. The deep recirculation before the measurements in March 2016 occurred at lower temperatures than in 2014, reaching the upper limit of the monimolimnion. This difference could explain the maintenance of the sharp temperature and EC gradients at the upper edge of the monimolimnion by erosive effects on the stratification (e.g., Boehrer et al., 2014).

Oxygen reached equilibrium with the atmosphere at the surface, but saturation values fell through the thermocline to remain relatively constant around 50% throughout the hypolimnion. The monimolimnion did not contain any dissolved oxygen. The pH was 6.5 in the hypolimnion, slightly higher in the epilimnion, while the monimolimnion pH showed acidic values around 5.5. The higher acidity was related to the presence of elevated concentrations of carbon dioxide, which dissociated in part into bicarbonate and hydronium ions.

Sound speed (time of flight measurements) followed the temperature through the thermocline above 10 m. In the relatively homogeneous hypolimnetic water, sound speed increased at a quite constant rate to greater depth due to increasing hydrostatic pressure to finally increase even faster through the monimolimnion. There was a small but clearly visible difference between the profiles of 2016 and 2014. In the monimolimnion, this could be attributed to the drawdown (Ohba et al., 2020), including the effects of higher pressure at the deeper location in 2016, but in the hypolimnion the difference was mainly attributed to higher temperatures in 2014.

NEW APPROACH

The profiles of temperature, EC, and pressure (depth) facilitated the calculation of sound speed v_{UNESCO} by implementation of the UNESCO formula. We followed the Saiki et al. (2017) convention and called the difference to measured sound speed v_{meas} the "excess sound speed":

$$\Delta v = v_{meas} - v_{UNESCO} \quad (1)$$

Carbon dioxide is the only dissolved substance present at high concentrations that does not contribute to EC. However, as dissolved carbon dioxide affects both density and adiabatic compressibility of water, it increases the sound speed as shown by Sanemasa et al. (2017). Hence we assumed that it is a measure for carbon dioxide. We first used the conversion factor $k_1 = 0.0323 - 0.000523 \cdot T$ (with T in °C) from Sanemasa et al. (2017) to calculate:

$$c_{CO2} = \Delta v / k_1 \quad (2)$$

In a second step, the pH information was used to calculate bicarbonate concentration from

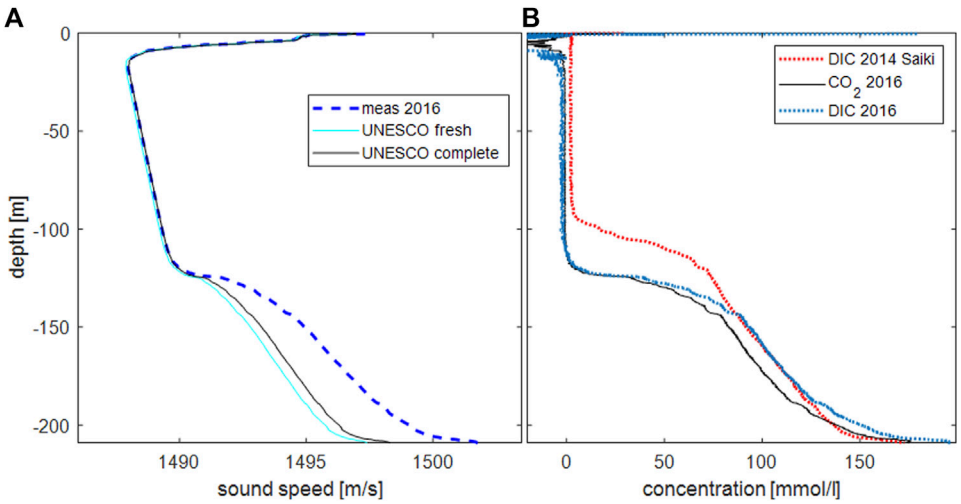

FIGURE 3 | (A): Sound speed as measured and calculated from temperature, electrical conductivity (either using measured values "UNESCO complete" or setting electrical conductivity to zero "UNESCO fresh") and pressure following UNESCO (Fofonoff, 1986). **(B)**: profile of calculated carbon dioxide concentrations as derived from the sound speed excess.

TABLE 1 | Concentrations of solutes in Lake Nyos as reported by Kusakabe et al. (2008) (K) listed in Sanemasa et al. (2017) and by Anazawa et al. (2019) (A); n.a. = not available.

	Na^+	K^+	NH_4^+	Mg^{2+}	Ca^{2+}	Fe^{2+}	Mn^{2+}	SiO_2	Cl^-	NO_3^-	SO_4^{2-}	HCO_3^-	Origin
2006/-195m	0.94	0.15	0.60	3.78	1.58	2.37	0.036	1.29	0.028	0.035	0.028	17.1	mmol/kg (K)
2015/-207m	0.81	0.18	n.a.	2.6	0.92	1.07	0.02	n.a.	n.a.	n.a.	n.a.	n.a.	mmol/l (A)
2016/-160m	0.76	0.20	0.49	1.29	0.88	1.58	0.03	0.41	0.01	0.0	0.0	10.0	mmol/l (new data)

$$c_{HCO3-} = K_s \frac{c_{CO2}}{c_{H+}} = 10^{pH-pKs} \cdot c_{CO2} \quad (3)$$

where pKs = 6.36 (Worch, 2015), pH was taken from the multiparameter profile and c_{CO2} from the calculation above (**Eq. 2**). The sum represented dissolved inorganic carbon (DIC):

$$c_{DIC} = c_{HCO3-} + c_{CO2} = \left(1 + 10^{pH-pKs}\right) \cdot c_{CO2} \quad (4)$$

RESULTS

A comparison of the resulting DIC profile with the DIC profile published by Saiki et al. (2017) for 2014 showed the vertical shift due to the drawdown, but also the considerably higher concentrations (**Figure 3B** "2014 Saiki").

Stability is controlled by density. Similar to sound speed, we capture the contribution of ionically dissolved substances by their contribution to EC. For quantification, we use the lambda-approach by Moreira et al. (2016) and Boehrer et al. (2010), who added the density contributions of solutes to the (potential) density of pure water. As in Schmid et al. (2003), we added the contribution of CO_2 in a separate term:

$$\rho(T, C_{25}) = \rho_W(T) + C_{25} \cdot (\lambda_0 + \lambda_1 \cdot (T - 25°C)) + \gamma \cdot G \cdot c_{CO2} \quad (5)$$

with fractional density contribution $\gamma = 0.212$ of CO_2 from Dietz et al. (2012), and molar mass G = 44.01 g/mol of CO_2. The coefficients λ_0 = 0.77 kg/m^3/(mS/cm) (±0.014) und λ_1 = −0.0015 kg/m^3/K/(mS/cm) (±0.00005) were obtained from the Moreira et al. (2016) density calculator, by inserting the salt composition measured in 2016 at 160 m depth (**Table 1**).

To check the variability with composition, we also inserted the salt composition measured by Kusakabe et al. (2008) at a depth of 195 m as reported by Sanemasa et al. (2017) and Anazawa et al. (2019), where we closed the charge balance with bicarbonate. The results for λ_0 and λ_1 agreed for all three solute compositions within the given narrow bounds. As a consequence, the density formula for Lake Nyos can be considered quite robust and valid for the time period covered by observations. The value for λ_0 is large, i.e., formulae based on ocean water conditions would greatly under-estimate the density effect of solutes affecting EC. Inserting the measured and calculated values into **Eq. 5** yielded the (potential) density profile (**Figure 4**), where we also showed the contribution of CO_2 separately.

Gas pressure profiles are essential to judge the proximity to spontaneous gas exsolution (Kusakabe, 2017). Hence we calculated the gas pressure induced by carbon dioxide using

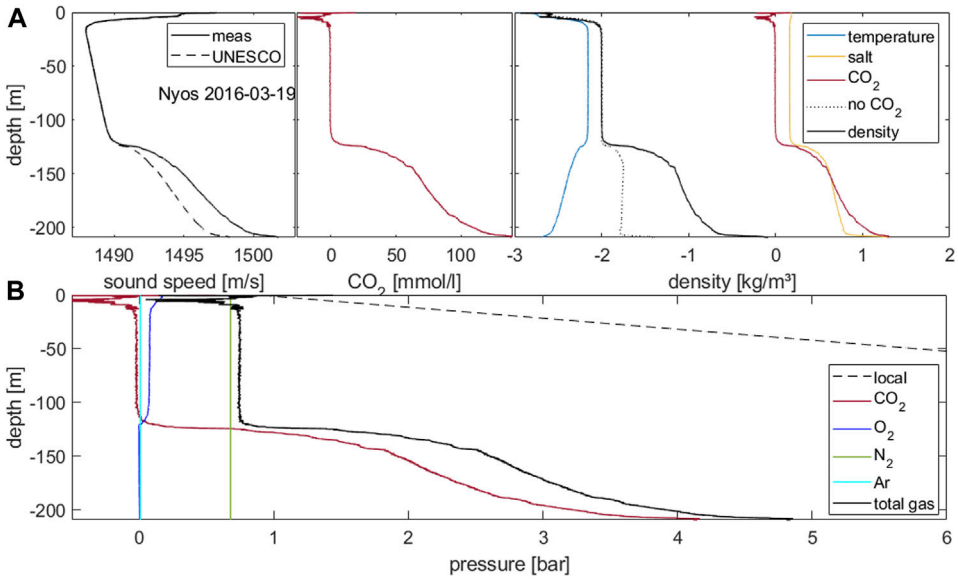

FIGURE 4 | (A): Sound speed as measured and calculated from temperature, electrical conductivity and pressure following UNESCO formula. Middle panel: profile of calculated carbon dioxide concentrations as derived from the sound speed excess. Right panel: (potential) density (−1,000 kg/m^3) as calculated from measured temperature, EC and carbon dioxide concentration and the single contributions. **(B)**: profiles of gas pressure calculated for the major contributing gases and total gas pressure as the sum in comparison to local pressure.

Henry's law and the temperature-dependent Henry coefficient. The values lie between 2 and 3 bars through the monimolimnion and rise approaching 4 bars close to the lake bed (**Figure 4**). In addition, we converted oxygen saturation into oxygen gas pressure, which started at about 0.2 bar at the surface (low atmospheric pressure at the altitude of 1,100 m a.s.l.), about 0.1 bar (50% saturation of atmospheric pressure at 1,100 m a.s.l.) throughout the hypolimnion and zero in the monimolimnion. Gas pressure for nitrogen was assumed to be in equilibrium with atmospheric N_2 partial pressure at the altitude of Lake Nyos, i.e., 0.68 bar. A similar procedure was implemented for argon (Ar) to yield 0.0087 bar. The contribution of vapour pressure reached less than 0.025 bar at temperatures measured in Lake Nyos (22–24°C, **Figure 2**).

DISCUSSION

Our goal was to test whether commercially available equipment was suited for estimating dissolved carbon dioxide on the basis of the sound speed. We used the complete UNESCO equation (Fofonoff, 1986, including the temperature scale change in 1990) for sound speed from temperature, salinity (i.e., EC), and pressure. This formula connects physical quantities, such as density and sound speed, to accurately measurable quantities of electrical conductivity, temperature and pressure. The conversion is valid for the salt composition of ocean water and applicable to limnic waters with some loss of accuracy. Most oceanographic CTD probes supply this UNESCO sound speed as a derived quantity. We compared the calculated sound speed with the sound speed from directly measured time-of-flight to find the excess sound speed for estimating carbon dioxide concentration (**Eqs 1**, **2**).

The inclusion of the salinity term in the UNESCO equation resulted in very good agreement between measured and calculated sound speeds at depths, where we did not expect high concentrations of CO_2, i.e., in the hypolimnion between 10 and 120 m depth. In the temperature-stratified top layer, larger deviations in the range of a few m/s were visible, which could be identified as artefacts and attributed to the different measuring volumes of sound speed (10 cm), temperature (as well as EC; more in the range of 2 cm; see **Figure 1**) and the high vertical temperature gradients that pronounced this feature. Below 120 m depth, the differences between calculated and measured sound speed were indicative of increasing carbon dioxide concentrations up to about 150 mmol/l at the lake bed, in good agreement with expectations from earlier measurements.

In comparison with the 2014 data, the drawdown effect became clearly visible. The steep gradient of carbon dioxide was moved downward by about 20 m due to the degassing facility removing deep water from close to the lake bed. At depths between 140 and 180 m, DIC concentrations in 2016 were marginally higher than in 2014; at depths below 180 m, the difference was larger. This indicated additional DIC, which should be the case very close to the lake bed, but probably not in the depth range from 140 to 200 m. It is more likely that this difference arose from the different approaches and different types of equipment that were implemented by the various research groups. We used the original coefficient k_1 form the laboratory measurement by Sanemasa et al. (2017), as the data from 2014 indicated a reasonably good agreement. In contrast, Saiki et al. (2017) saw evidence from samples that the correlation between

DIC and sound speed excess required corrections, which they mainly attributed to the presence of bicarbonate. The measurements by Sanemasa et al. (2017) were done at smaller outside (hydrostatic) pressures, hence may not exactly reflect the situation at great depth in Lake Nyos. We did not have the capabilities to resolve this disagreement. A closer investigation of the correlation between dissolved carbon dioxide (as well as other dissolved substances) and sound speed would be desirable. This may be possible by additional laboratory experiments or application of this method to other gas-charged lakes.

We calculated dissolved bicarbonate from the dissociation product of carbonic acid. At a pH about 1 unit smaller than the pKs of 6.36, bicarbonate contributed about 10% to DIC; hence even a considerable error in the pH measurement would not heavily bias the DIC. In comparison to the calculated values from Saiki et al. (2017) approach, very small but visible differences appeared between 10 and 120 m depth (hypolimnion). The commercial probe showed good agreement between calculated and measured values (i.e., no CO_2 in **Figure 3B**), most likely due to the inclusion of salinity in the calculation.

We implemented **Eq. 5** to calculate a density profile. We used the formula by Tanaka et al. (2001) for density of pure water. We evaluated the density contribution of dissolved ions on the basis of the measured EC profile, and finally added the density contribution of the dissolved CO_2. The increasing temperatures in the monimolimnion resulted in a density contribution which counteracted the stability, providing the potential for double diffusive convection (Schmid et al., 2004; Hirslund 2019). This was outbalanced by the dissolved solids, which contributed a density difference of about 0.5 kg/m^3, tantamount to the density effect of a 2°C temperature difference that the mixolimnion would need to be colder than the monimolimnion to overcome the density of the monimolimnion. The density contribution of the dissolved CO_2 was considerably larger, i.e. about 0.7 kg/m^3. In conclusion, the major contribution that maintained the stable stratification came from the dissolved CO_2. Together, all terms indicated a density difference of 1 kg/m^3 between waters above and below the major chemocline at 120 m depth. However as this mainly relied on the contribution of the volatile CO_2, this could not be considered safe, and the degassing of the lake had to be completed until the remaining CO_2 would not pose a danger.

From our results, gas pressures could be calculated by solving Henry's law. The contributions of CO_2 (from sound speed), oxygen from sensor measurements, and vapour pressure from temperature could be calculated in a straightforward manner. For nitrogen and argon, we assumed equilibrium with the atmospheric pressure at the altitude of the surface of Lake Nyos. These calculations yielded a total gas pressure profile as the sum of these single terms. As shown in the paper by Bärenbold et al. (2019) for the extreme case of Lake Kivu, non-linearities were expected to be small (in the range of few percent). The total gas pressure is considerably smaller than the absolute (local) pressure. Hence spontaneous exsolution of CO_2 would require that water be lifted from a depth of 140 m to about 15 m depth. This could only happen if the entire water column lost its stability, as described in the paragraph above on density.

CONCLUSION

The CTD and sound speed measurements in March 2016 at Lake Nyos, Cameroon, provided a data set that correlated very well with the CO_2 concentrations observed along a vertical depth profile from earlier measurements. A commercial sound speed sensor attached to a high accuracy CTD probe was successfully tested for its suitability to survey carbon dioxide in Lake Nyos. The instrumentation can be easily transported to remote areas, such as Lake Nyos, to acquire vertical profiles at regular time intervals. Although this approach was not a direct measurement, the accumulation of carbon dioxide is manifested in detectable, increasing sound speed values, i.e., sound speed excess with respect to calculated sound speed based on EC, temperature and depth following the UNESCO formula. As a mitigation strategy, once sound speed measurements indicate carbon dioxide concentrations of concern, direct gas measurements and dissolved gas sampling campaigns could be implemented rapidly in order to confirm the elevated gas concentrations.

Finally, the measurements of CTD and sound speed relied only on physical quantities that could be measured at high accuracy, frequency and reproducibility. Although possibly more difficult to assess in terms of absolute accuracy, this method is particularly well-suited for documenting temporal evolution and quantifying changes much more rapidly and frequently compared to direct CO_2 measurements. Profiles at high vertical resolution (decimetres) could be accomplished which guarantee that no layers remain undetected. In addition, vertical displacement, such as drawdown through siphoning, might be detectable on the base of the profile shape. Our measurements extend the documentation of the degassing progress by a further two years. We recommend frequent surveys using this approach for the timely detection of dangerous dissolved CO_2 concentrations at Lake Nyos, as well as at other similarly hazardous lakes.

Extending the work of Saiki et al. (2017), we separated the effect of CO_2 on sound speed from the bicarbonate contribution. This made the correlation factors independent of pH and background salinity. This was a step towards using the approach at other lakes with high CO_2 (e.g., the episodically recharged Lago Albano, Italy). A further investigation of the quantitative connection between solutes and sound speed remains desirable.

DATA AVAILABILITY STATEMENT

The original contributions presented in the study are included in the article, further inquiries can be directed to the corresponding author.

AUTHOR CONTRIBUTIONS

BB was responsible for the measurements 2016, and he was the lead author of this contribution. KS and TO provided the 2014 data and the detailed numerical approach of 2014. GT, DR, and MK provided information on the geological setting, comparison with other volcanic lakes and the information about the degassing history. All authors were present at the 2016 meeting and/or field measurements in 2016. All were involved in writing this paper.

REFERENCES

Anazawa, K., Fantong, W. Y., Ueda, A., Ozawa, A., Kusakabe, M., Yoshida, Y., et al. (2019). Environmental Modifications of Lake Nyos Surface Water by Artificial Degassing. *J. Afr. Earth Sci.* 152, 115–121. doi:10.1016/j.jafrearsci.2019.02.009

Bärenbold, F., Boehrer, B., Grilli, R., Mugisha, A., von Tümpling, W., Umutoni, A., et al. (2020). No Increasing Risk of a Limnic Eruption at Lake Kivu: Intercomparison Study Reveals Gas Concentrations Close to Steady State. *PLoS ONE* 15 (8), e0237836. doi:10.1371/journal.pone.0237836

Boehrer, B., Yusta, I., Magin, K., and Sanchez-España, J. (2016). Quantifying, Assessing and Removing the Extreme Gas Load from Meromictic Guadiana Pit lake, Southwest Spain. *Sci. Total Environ.* 563-564, 468–477. doi:10.1016/j.scitotenv.2016.04.12410.1016/j.scitotenv.2016.04.118

Boehrer, B., Herzsprung, P., Schultze, M., and Millero, F. J. (2010). Calculating Density of Water in Geochemical lake Stratification Models. *Limnol. Oceanogr. Methods* 8 (11), 567–574. doi:10.4319/lom.2010.8.0567

Boehrer, B., Jordan, S., Leng, P., Waldemer, C., Schwenk, C., Hupfer, M., et al. (2021). Gas Pressure Dynamics in Small to Mid-Size Lakes. *Water* 13 (13), 1824. doi:10.3390/w13131824

Boehrer, B., Kiwel, U., Rahn, K., and Schultze, M. (2014). Chemocline Erosion and its Conservation by Freshwater Introduction to Meromictic Salt Lakes. *Limnologica* 44, þ 81–89. doi:10.1016/j.limno.2013.08.003

Boehrer, B., and Schultze, M. (2008). Stratification of Lakes. *Rev. Geophys.* 46 (2), RG2005. doi:10.1029/2006rg000210

Boehrer, B., von Rohden, C., and Schultze, M. (2013). "Physical Features of Meromictic Lakes: Stratification and Circulation," in *Ecology of Meromictic Lakes*. Editors R. D. Gulati, E. S. Zadereev, and A. G. Demergendzhi (Heidelberg: Springer), 61–86.

Boehrer, B., von Tümpling, W., Mugisha, A., Rogemont, C., and Umutoni, A. (2019). Reliable Reference for the Methane Concentrations in Lake Kivu at the Beginning of Industrial Exploitation. *Hydrol. Earth Syst. Sci.* 23, 4707–4716. doi:10.5194/hess-23-4707-2019

Cabassi, J., Tassi, F., Vaselli, O., Fiebig, J., Nocentini, M., Capecchiacci, F., et al. (2013). Biogeochemical Processes Involving Dissolved CO_2 and CH_4 at Albano, Averno, and Monticchio Meromictic Volcanic Lakes (Central–Southern Italy). *Bull. Volcanol.* 75, 683. doi:10.1007/s00445-012-0683-0

Caracausi, A., Nuccio, P. M., Favara, R., Nicolosi, M., and Paternoster, M. (2009). Gas hazard Assessment at the Monticchio Crater Lakes of Mt. Vulture, a Volcano in Southern Italy. *Terra Nova* 21, 83–87. doi:10.1111/j.1365-3121.2008.00858.x

Chiodini, G., Tassi, F., Caliro, S., Chiarabba, C., Vaselli, O., and Rouwet, D. (2012). Time-dependent CO2 Variations in Lake Albano Associated with Seismic Activity. *Bull. Volcanol.* 74, 861–871. doi:10.1007/s00445-011-0573-x

Dietz, S., Lessmann, D., and Boehrer, B. (2012). Contribution of Solutes to Density Stratification in a Meromictic lake (Waldsee/Germany). *Mine Water Environ.* 31 (2), 129–137. doi:10.1007/s10230-012-0179-3

Fofonoff, N. P. (1986). Physical Properties of Seawater: A New Salinity Scale and Equation of State for Seawater. *J. Geophys. Res.* 90 (C2), 3332–3342.

Halbwachs, M., Sabroux, J.-C., and Kayser, G. (2020). Final Step of the 32-year Lake Nyos Degassing Adventure: Natural CO2 Recharge Is to Be Balanced by Discharge through the Degassing Pipes. *J. Afr. Earth Sci.* 167, 103575. doi:10.1016/j.jafrearsci.2019.103575

Hirslund, F. (2019). Dynamics of Diffusive Layering and Chemocline Formation in Lake Kivu and Brine Pools. *J. Afr. Earth Sci.* 159, 103520. doi:10.1016/j.jafrearsci.2019.103520

Horn, C., Metzler, P., Ullrich, K., Koschorreck, M., and Boehrer, B. (2017). Methane Storage and Ebullition in Monimolimnetic Waters of Polluted Mine Pit lake Vollert-Sued, Germany. *Sci. Total Environ.* 584–585, 1–10. doi:10.1016/j.scitotenv.2017.01.151

Kling, G. W., Clark, M. A., Wagner, G. N., Compton, H. R., Humphrey, A. M., Devine, J. D., et al. (1987). The 1986 Lake Nyos Gas Disaster in Cameroon, West Africa. *Science* 236 (4798), 169–175. doi:10.1126/science.236.4798.169

Kusakabe, M. (2017). Lakes Nyos and Monoun Gas Disasters (Cameroon)-Limnic Eruptions Caused by Excessive Accumulation of Magmatic CO2 in Crater Lakes. *Geochem. Monogr. Ser.* 1 (1), 1–50. doi:10.5047/gems.2017.00101.0001

Kusakabe, M., Ohba, T., Issa, Y., Yoshida, H., Ohizumi, T., Evans, W. C., et al. (2008). Evolution of CO2 in Lakes Monoun and Nyos, Cameroon, before and during Controlled Degassing. *Geochem. J.* 42, 93–118. doi:10.2343/geochemj.42.93

Kusakabe, M., Tiodjio, R. E., Christenson, B., Saiki, K., Ohba, T., and Yaguchi, M. (2019). Enrichment of Ferrous Iron in the Bottom Water of Lake Nyos. *J. Afric Earth Sci.* 37-46. doi:10.1016/j.jafrearsci.2018.10.014

Lorke, A., Tietze, K., Halbwachs, M., and Wüest, A. (2004). Response of Lake Kivu Stratification to Lava Inflow and Climate Warming. *Limnol. Oceanogr.* 49 (3), 778–783. doi:10.4319/lo.2004.49.3.0778

Moreira, S., Schultze, M., Rahn, K., and Boehrer, B. (2016). A Practical Approach to lake Water Density from Electrical Conductivity and Temperature. *Hydrol.* Earth Syst. Sci. 20, 2975–2986. doi:10.5194/hess-20-2975-2016

Ohba, T., Ooki, S., Oginuma, Y., Yoshida, H., Ntchantcho, R., Ako, A., et al. (2020). Temperature and Electrical Conductivity of Water in Lake Nyos Transmitted by an Automatic Observation Buoy. *J. Afr. Earth Sci.* 172, 103976. doi:10.1016/j.jafrearsci.2020.103976

Rouwet, D., Chiodini, G., Ciuccarelli, C., Comastri, A., and Costa, A. (2019). Lago Albano, the "Anti-nyos-type" lake: The Past as a Key for the Future. *J. Afr. Earth Sci.* 150, 425–440. doi:10.1016/j.jafrearsci.2018.09.019

Rouwet, D., Tamburello, G., Chiodini, G., Pecoraino, G., Procesi, M., Ricci, T., et al. (2021). New Insights into the Degassing Dynamics of Lago Albano (Colli Albani Volcano, Rome, Italy) during the Last Three Decades (1989-2019). *Ijg* 140 (1), 29–41. doi:10.3301/IJG.2020.19

Rouwet, D. (2021). "Volcanic lake Dynamics and Related Hazards," in *Forecasting and Planning for Volcanic Hazards, Risks and Disasters*, 439–471. doi:10.1016/b978-0-12-818082-2.00011-1

Saiki, K., Kaneko, K., Ohba, T., Sanemasa, M., Kusakabe, M., Ntchantcho, R., et al. (2017). "Vertical Distribution of Dissolved CO2 in Lakes Nyos and Monoun (Cameroon) as Estimated by Sound Speed in Water," in *Geochemistry and Geophysics of Active Volcanic Lakes*. Editors T. Ohba, B. Capaccioni, and C. Caudron (London: Geological Society), 437, 185–192. Special Publications. doi:10.1144/sp437.10

Sánchez-España, J., Boehrer, B., and Yusta, I. (2014). Extreme Carbon Dioxide Concentrations in Acidic Pit Lakes Provoked by Water/rock Interaction. *Environ. Sci. Technol.* 48 (8), 4273–4281. doi:10.1021/es5006797

Sánchez-España, J., Yusta, I., and Boehrer, B. (2020). Degassing Pit Lakes: Technical Issues and Lessons Learnt from the HERCO2 Project in the Guadiana Open Pit (Herrerías Mine, SW Spain). *Mine Water Environ.* 39, 517–534. doi:10.1007/s10230-020-00654-1

Sanemasa, M., SaikiKaneko, K. K., Kaneko, K., Ohba, T., Kusakabe, M., Ntchantcho, R., et al. (2017). "A New Method to Determine Dissolved CO2 Concentration of Lakes Nyos and Monoun Using the Sound Speed and Electrical Conductivity of lake Water," in *Geochemistry and Geophysics of Active Volcanic Lakes*. Editors T. Ohba, B. Capaccioni, and C. Caudron (London: Geological Society), 437, 193–203. Special Publications. doi:10.1144/SP437.5

Schmid, M., Halbwachs, M., Wehrli, B., and Wüest, A. (2005). Weak Mixing in Lake Kivu: New Insights Indicate Increasing Risk of Uncontrolled Gas Eruption. *Geochem. Geophys. Geosyst.* 6, a–n. doi:10.1029/2004GC000892

Schmid, M., Lorke, A., Dinkel, C., Tanyileke, G., and Wüest, A. (2004). Double-diffusive Convection in Lake Nyos, Cameroon. *Deep Sea Res. Oceanographic Res. Pap.* 51, 1097–1111. doi:10.1016/j.dsr.2004.02.010

Schmid, M., Lorke, A., Wüest, A., Halbwachs, M., and Tanyileke, G. (2003). Development and Sensitivity Analysis of a Model for Assessing Stratification and Safety of Lake Nyos during Artificial Degassing. *Ocean Dyn.* 53, 288–301. doi:10.1007/s10236-003-0032-0

Sigurdsson, H., Devine, J. D., Tchoua, F. M., Presser, T. S., Pringle, M. K. W., and Evans, W. C. (1987). Origin of the Lethal Gas Burst from Lake Monoun. Cameroun. *J. Volcanol. Geotherm. Res.* 31 (1–2), 1–16. doi:10.1016/0377-0273(87)90002-3

Tanyileke, G., Ntchantcho, R., Fantong, W. Y., Aka, F. T., and Hell, J. V. (2019). 30 Years of the Lakes Nyos and Monoun Gas Disasters: A Scientific, Technological, Institutional and Social Adventure. *J. Afr. Earth Sci.* 150, 415–424. doi:10.1016/j.jafrearsci.2018.11.022

Worch, E. (2015). *Hydrochemistry*. Berlin/Boston: deGruyter.

Conflict of Interest: The authors declare that the research was conducted in the absence of any commercial or financial relationships that could be construed as a potential conflict of interest.

Publisher's Note: All claims expressed in this article are solely those of the authors and do not necessarily represent those of their affiliated organizations, or those of the publisher, the editors and the reviewers. Any product that may be evaluated in this article, or claim that may be made by its manufacturer, is not guaranteed or endorsed by the publisher.

frontiers in Earth Science

REVIEW
published: 28 September 2021
doi: 10.3389/feart.2021.717798

Volcanic Lakes in Africa: The VOLADA_Africa 2.0 Database, and Implications for Volcanic Hazard

Dmitri Rouwet[1]*, *Karoly Németh*[2,3], *Giancarlo Tamburello*[1], *Sergio Calabrese*[4,5] and *Issa*[6]

[1]Istituto Nazionale di Geofisica e Vulcanologia, Sezione di Bologna, Bologna, Italy, [2]School of Agriculture and Environment, Massey University, Palmerston North, New Zealand, [3]Institute of Earth Physics and Space Sciences, Sopron, Hungary, [4]Dipartimento di Scienze della Terra e del Mare (DiSTeM), Università degli Studi di Palermo, Palermo, Italy, [5]Istituto Nazionale di Geofisica e Vulcanologia, Sezione di Palermo, Palermo, Italy, [6]Cameroun-Banque Mondiale, Projet de Lutte Contre les Inondations (PULCI), Yagoua, Cameroon

Volcanic lakes pose specific hazards inherent to the presence of water: phreatic and phreatomagmatic eruptions, lahars, limnic gas bursts and dispersion of brines in the hydrological network. Here we introduce the updated, interactive and open-access database for African volcanic lakes, country by country. The previous database VOLADA (VOlcanic LAke DAta Base, Rouwet et al., Journal of Volcanology and Geothermal Research, 2014, 272, 78–97) reported 96 volcanic lakes for Africa. This number is now revised and established at 220, converting VOLADA_Africa 2.0 in the most comprehensive resource for African volcanic lakes: 81 in Uganda, 37 in Kenya, 33 in Cameroon, 28 in Madagascar, 19 in Ethiopia, 6 in Tanzania, 2 in Rwanda, 2 in Sudan, 2 in D.R. Congo, 1 in Libya, and 9 on the minor islands around Africa. We present the current state-of-the-art of arguably all the African volcanic lakes that the global experts and regional research teams are aware of, and provide hints for future research directions, with a special focus on the volcanic hazard assessment. All lakes in the updated database are classified for their genetic origin and their physical and chemical characteristics, and level of study. The predominant rift-related volcanism in Africa favors basaltic eruptive products, leading to volcanoes with highly permeable edifices, and hence less-developed hydrothermal systems. Basal aquifers accumulate under large volcanoes and in rift depressions providing a potential scenario for phreatomagmatic volcanism. This hypothesis, based on a morphometric analysis and volcanological research from literature, conveys the predominance of maar lakes in large monogenetic fields in Africa (e.g. Uganda, Cameroon, Ethiopia), and the absence of peak-activity crater lakes, generally found at polygenetic arc-volcanoes. Considering the large number of maar lakes in Africa (172), within similar geotectonic settings and meteoric conditions as in Cameroon, it is somewhat surprising that "only" from Lake Monoun and Lake Nyos fatal CO_2 bursts have been recorded. Explaining why other maars did *not* experience limnic gas bursts is a question that can only be answered by enhancing insights into physical limnology and fluid geochemistry of the so far poorly studied lakes. From a hazard perspective, there is an urgent need to tackle this task as a community.

Keywords: Africa, volcanic lakes, maar, Lake Nyos, database, hazard assessment

OPEN ACCESS

Edited by:
Roberto Sulpizio,
University of Bari Aldo Moro, Italy

Reviewed by:
Dario Pedrazzi,
Instituto de Ciencias de la Tierra Jaume Almera (ICTJA), Spain
Mark Thomas,
University of Leeds, United Kingdom

****Correspondence:***
Dmitri Rouwet
dmitri.rouwet@ingv.it

Specialty section:
This article was submitted to Volcanology, a section of the journal Frontiers in Earth Science

Received: *31 May 2021*
Accepted: *09 September 2021*
Published: *28 September 2021*

Citation:
Rouwet D, Németh K, Tamburello G, Calabrese S, Issa (2021) Volcanic Lakes in Africa: The VOLADA_Africa 2.0 Database, and Implications for Volcanic Hazard. Front. Earth Sci. 9:717798. doi: 10.3389/feart.2021.717798

INTRODUCTION

The Cameroonian "killer lakes" Nyos and Monoun (Western Africa, **Figure 1**) are reputable for having induced the boom in volcanic lake studies since the late 1980s (e.g. Kling et al., 1989; Giggenbach, 1990; Giggenbach et al., 1991; Freeth, 1992; Evans et al., 1993, 1994; Freeth, 1994; Martini et al., 1994; Zhang, 1996, 1998; Viollier et al., 1995, 1997; Aeschbach-Hertig et al., 1996, 1999), to such a degree to have introduced a "Nyos bias" – for the good and the bad – on how to cope with lakes in volcanic craters in terms of hazard assessment and risk mitigation strategies (Rouwet et al., 2015a, 2019; Rouwet, 2021). A major question that arose from most of these Nyos-biased studies was whether any other lakes were capable of bursting CO_2 in a sudden manner as Lakes Monoun and Nyos did in 1984 and 1986, respectively. Despite three decades of post-Nyos research, this question still remains unanswered for too many lakes (Rouwet, 2021).

The Nyos bias expresses an ambiguity. On the one hand, dynamics at other lakes, in Africa and other continents, are often over-interpreted as if they should be Nyos-type lakes (i.e. volcanic lakes affected by cyclical, explosive gas release due to gas pressure build up in deep waters) when CO_2 degassing occurs in those lake areas; this view might be most prudent, in case of doubt, although it turns out to be unrealistic in some cases (e.g. Rouwet et al., 2019). On the other hand, the only way to discover whether CO_2, or other gas species, are accumulated up to critical pressure conditions in deep lake strata is to lower Conductivity-Temperature-Depth/Pressure (CTD) probes, sample lake water and measure dissolved gases along vertical profiles. This direct investigation has been applied only to a few lakes in order to have a complete picture of how volcanic lake degassing works. Nevertheless, it is a fact that, especially, the 1986 Lake Nyos gas burst has increased the general awareness of the potential danger this type of volcanic lakes poses (e.g. Giggenbach et al., 1991; Martini et al., 1994; Aeschbach-Hertig et al., 1996, 1999; Caliro et al., 2008; Carapezza et al., 2008; Chiodini et al., 2012; Cabassi et al., 2013, 2014; Rouwet et al., 2019, 2020; Rouwet, 2021).

Rouwet et al. (2014) introduced the first, incomplete version of the community-based, interactive, and open-source (https://vhub.org/resources/2437) VOlcanic LAkes DAta base (VOLADA). Out of respect for Lake Nyos, "the mother of volcanic lakes," here we first provide an update on the post-Pliocene (i.e. contemporaneous) volcanic lakes located on the African continent, Madagascar and minor islands (Annobon, Bioko, Tristan da Cunha, Karthala, Mohéli Island and Mayotte, **Figure 1**), presented as VOLADA_Africa 2.0. This version aims to *1*) supply an updated list of the geo-referenced volcanic lakes, *2*) shed light on the type of each lake, following classical (Pasternack and Varekamp, 1997; Varekamp et al., 2000) and novel (Christenson et al., 2015) classification schemes, *3*) show a realistic picture on the level of study of each volcanic lake in Africa, regarding volcanological research *sensu lato*, and *4*) provide a hazard assessment related to volcanic lakes in Africa. As volcanological literature revealed the maar nature of many of the catalogued lakes, an analysis of morphometric parameters for maar *craters* (Graettinger, 2018) for the entire database leads to a conceptual model that corroborates why African volcanic lakes actually are predominantly maar lakes. Consequently, we suggest strategies for future research and monitoring setups for those lakes we deem as potentially hazardous, or as peculiar for other reasons from a volcanological point of view.

THE VOLCANIC LAKE CATALOGUE FOR AFRICA

VOLADA "1.0"

VOLADA was introduced by Rouwet et al. (2014) with the aim to review and update the number of volcanic lakes reported in earlier studies (e.g. Delmelle and Bernard, 2000; Pérez et al., 2011; Lockwood and Kusakabe, 2018) and to better locate them on the globe. VOLADA aimed at being an interactive and open-access tool, perennially open for discussion, additions and corrections by the entire scientific community. In 2014, VOLADA listed 474 volcanic lakes, with 86 lakes in Europe (30 in the Azores), 97 in Africa (20 in Cameroon), 51 in North America (21 in Mexico), 58 in Central America (27 in Costa Rica), 28 in South America (18 in Chile-Argentina), 111 in Asia (33 in Indonesia), and 43 in Oceania (27 in New Zealand). If sufficient information was available, the lakes were classified following the physical (a scale from 1 to 10, based on the state of activity of the hosting volcano; Pasternack and Varekamp, 1997), and chemical properties of the lake water ("gas-dominated" versus "rock-dominated" lake waters, G versus R, Varekamp et al., 2000). The level of study of each lake was reported as a numerical scale from 1 to 5, from "well studied" (1) to "poorly or not studied" (5).

VOLADA_Africa 2.0: Revised Methodology

Subsequently, Christenson et al. (2015) proposed (by KN) an alternative classification scheme, based on the genetic process behind the lake basin formation, regardless of the current state of activity of the lakes, or the chemical-physical properties of the lake water. The latter information appeared to be often unavailable, as a consequence of the general poor level of study of most lakes.

The genetic classification scheme by Christenson et al. (2015) follows some basic rules, and results in alphanumerical codes (G0-1_R0-1_T0-1_L0-1), as:

(1) The ***geotectonic assessment*** in which the lake is located (G) can be related to monogenetic (0), or polygenetic (1) volcanism;
(2) The ***relationship*** between the volcanism and the eventual lake formation (R) is weak (0), or strong (1);
(3) The ***timing of lake formation*** in relation with the volcanism (T) can be long (0) or shortly (1) after the volcanic activity;
(4) The ***location*** of the volcanic lake in relation to the volcanic centre (L) can be off (0) or over (1) the vent.

A major accomplishment of this genetic classification scheme is to eliminate the ambiguity that existed in naming "volcanic lakes," as each alphanumerical code points to a specific type of

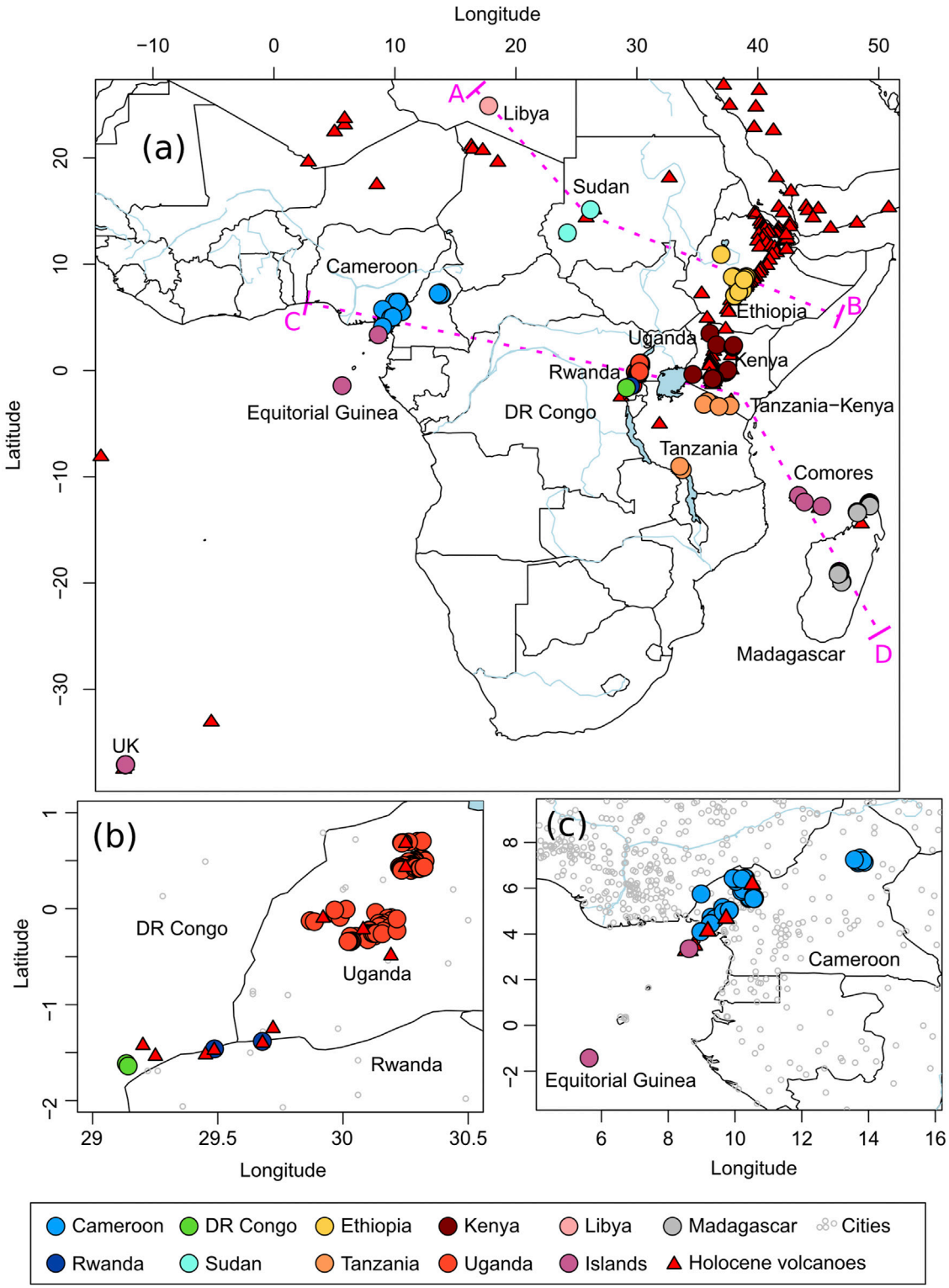

FIGURE 1 | (A) Location map of the African volcanic lakes, color-coded per country. The zoomed area mainly shows the lakes in Bunyaruguru, Ndali-Kasenda and Fort Portal volcanic fields in Uganda **(B)**, and the Cameroon Volcanic Line **(C)**. Holocene active volcanoes are exported from the Global Volcanism Program-Smithsonian database (https://volcano.si.edu/).

TABLE 1 | The VOLADA_Africa 2.0 database, mentioning the lake number (#), the number of lakes in the same country (#/country), the lake name, the volcano the depends on, the country, GVP number (Global Volcanism Program number https://volcano.si.edu/search_volcano.cfm), volcano type, the latitude and longitude (Lat. and Long. in decimal coordinates), the elevation above sea level (m a.s.l.), level of study (1–5, *see* text for details), genetic class (*see* text for details), lake type, physical and chemical classification, length of major and minor lake axes (Dmajor and Dminor, respectively, in m), lake surface area (A, in m^2), lake perimeter (in meter), Aspect Ratio (AR, **Eq. 1**), Elongation (EL, **Eq. 2**), Isoperimetric Circularity (IC, **Eq. 3**).

#	#/Country	Lake	Volcano	Country	GVP number	Volcano type	Lat.	Long.	Elevation (m asl)	Level of study	Genetic class	Lake type	Phys. Class	Chem. Class	D major (m)	D minor (m)	A (m^2)	Perimeter (m)	AR	EL	IC
1	1	Baleng	Oku volcanic field	Cameroon	224030	stratovolcano	5.550199	10.420998	1,390	3	G0R1T1L1	maar	6	R	390	245	7.87E+04	1,120	0.628	0.659	0.788
2	2	Banefo	Oku volcanic field	Cameroon	224030	stratovolcano	5.586977	10.442195	1,116	3	G0R1T1L1	maar	6	R	380	175	4.79E+04	960	0.461	0.422	0.653
3	3	Bambuluuwe	Oku volcanic field	Cameroon	224030	stratovolcano	5.861728	10.197675	2,088	3	G0R1T1L1	maar	6	R	530	445	1.82E+05	1,630	0.840	0.825	0.861
4	4	Bambili	Oku volcanic field	Cameroon	224030	stratovolcano	5.935203	10.243734	2,268	3	G0R1T1L1	maar	6	R	590	325	1.78E+05	1,615	0.551	0.651	0.858
5	5	Benakuma	Oku volcanic field	Cameroon	224030	stratovolcano	6.431842	9.945516	604	3	G0R1T1L1	maar	6	R	1,590	1,365	1.60E+06	5,900	0.858	0.806	0.578
5	5	Elum	Oku volcanic field	Cameroon	224030	stratovolcano	6.339768	10.036545	968	3	G0R1T1L1	maar	6	R	635	600	2.66E+05	1,885	0.945	0.840	0.941
6	6	Enep/Nfou	Oku volcanic field	Cameroon	224030	stratovolcano	6.298281	10.036264	725	3	G0R1T1L1	maar	6	R	690	510	2.99E+05	2,195	0.739	0.800	0.780
7	7	Mfouet	Oku volcanic field	Cameroon	224030	stratovolcano	5.537339	10.57993	1,076	3	G0R1T1L1	maar	6	R	345	275	5.76E+04	1,110	0.797	0.616	0.587
8	8	Monoun	Oku volcanic field	Cameroon	224030	stratovolcano	5.579649	10.586533	1,081	1	G0R1T1L1	maar	5b2	R	1,280	215	5.96E+05	5,545	0.168	0.463	0.244
9	9	Nchout	Oku volcanic field	Cameroon	224030	stratovolcano	5.612168	10.556276	1,095	3	G0R1T1L1	maar	6	R	615	435	1.60E+05	2,005	0.707	0.539	0.500
10	10	Nyi	Oku volcanic field	Cameroon	224030	stratovolcano	6.445293	10.314747	1,026	3	G0R1T1L1	maar	6	R	665	220	1.64E+05	2,380	0.331	0.472	0.364
11	11	Nyos	Oku volcanic field	Cameroon	224030	stratovolcano	6.439224	10.298051	1,103	1	G0R1T1L1	maar	5b2	R	1,655	1,005	1.56E+06	6,565	0.607	0.725	0.455
12	12	Negop Baghang	Oku volcanic field	Cameroon	224030	stratovolcano	5.545605	10.560219	1,098	3	G0R1T1L1	maar	6	R	330	225	5.93E+04	995	0.682	0.693	0.753
13	13	Oku	Oku volcanic field	Cameroon	224030	stratovolcano	6.189813	10.452087	2,239	3	G0R1T1L1	maar	6	R	2,010	1,285	2.26E+06	6,075	0.639	0.713	0.771
14	14	Kuk	Oku volcanic field	Cameroon	224030	stratovolcano	6.408605	10.205016	1,325	3	G0R1T1L1	maar	6	R	810	625	3.90E+05	2,425	0.772	0.757	0.833
15	15	Wum	Oku volcanic field	Cameroon	224030	stratovolcano	6.407756	10.055327	1,081	3	G0R1T1L1	maar	6	R	755	595	3.14E+05	2,310	0.788	0.701	0.739
16	16	Dissoni	Tombel Graben	Cameroon	224011	pyroclastic cones	4.730564	9.282076	462	3	G0R1T1L1	maar	6	R	1,480	1,395	1.51E+06	5,195	0.943	0.878	0.703
17	17	Barombi Mbo	Tombel Graben	Cameroon	224011	pyroclastic cones	4.660476	9.40197	314	2	G0R1T1L1	maar	6	R	2,560	2,250	4.09E+06	7,775	0.879	0.795	0.850
18	18	Barombi Koto	Tombel Graben	Cameroon	224011	pyroclastic cones	4.468989	9.259588	102	3	G0R1T1L1	maar	6	R	1,470	1,140	1.23E+06	5,110	0.776	0.725	0.592
19	19	Mboandong	Tombel Graben	Cameroon	nd	nd	4.450808	9.268923	150	3	G0R1T1L1	maar	6	R	535	440	1.53E+05	1,555	0.822	0.681	0.795
20	20	Beme	Cameroon volcanic line	Cameroon	nd	nd	5.158609	9.634794	473	3	G0R1T1L1	maar	6	R	670	610	3.35E+05	2,315	0.910	0.950	0.785
21	21	Ejagham/Idjagham	Cameroon volcanic line	Cameroon	nd	nd	5.749801	8.986962	141	3	G0R1T1L1	maar	6	R	1,015	715	5.15E+05	2,960	0.704	0.636	0.739
22	22	Edib	Cameroon volcanic line	Cameroon	nd	nd	4.957423	9.65178	1,269	3	G0R1T1L1	maar	6	R	510	430	1.85E+05	1,560	0.843	0.906	0.955
23	23	Manengouba-F	Mt Manengouba	Cameroon	nd	stratovolcano	5.035733	9.831024	1,914	3	G1R1T1L1	crater	6	R	735	620	3.62E+05	2,610	0.844	0.853	0.668
24	24	Manengouba-M	Mt Manengouba	Cameroon	nd	stratovolcano	5.032399	9.826107	1,932	3	G1R1T1L1	crater	6	R	260	175	3.40E+04	840	0.673	0.640	0.606
25	25	Debundsha Big	Mt Cameroon	Cameroon	224010	stratovolcano	4.104048	8.980358	64	3	G1R1T1L0	maar	6	R	335	255	7.29E+04	1,140	0.761	0.827	0.705
26	26	Debundsha Small	Mt Cameroon	Cameroon	224010	stratovolcano	4.09697	8.979062	32	3	G1R1T1L0	maar	6	R	80	55	2.00E+00	250	0.688	0.000	0.000
27	27	Baledjam Marbuwi	Volcanic plateau of Adamawa	Cameroon	nd	nd	7.13493	13.870481	1,256	3	G0R1T1L1	maar	6	R	575	510	1.86E+05	1,760	0.887	0.716	0.755
28	28	Ngaoundaba	Volcanic plateau of Adamawa	Cameroon	nd	nd	7.130619	13.693898	1,163	3	G0R1T1L1	maar	6	R	495	200	8.62E+04	1,820	0.404	0.448	0.327
29	29	Gegouba	Volcanic plateau of Adamawa	Cameroon	nd	nd	7.108046	13.689856	1,182	3	G0R1T1L1	maar	6	R	415	395	1.20E+05	1,450	0.952	0.887	0.717
30	30	unnamed	Volcanic plateau of Adamawa	Cameroon	nd	nd	7.181089	13.689974	1,200	3	G0R1T1L1	maar	6	R	390	275	8.73E+04	1,165	0.705	0.731	0.808
31	31	Mbalang	Volcanic plateau of Adamawa	Cameroon	nd	nd	7.324499	13.738696	1,105	3	G0R1T1L1	maar	6	R	1,065	485	4.18E+05	2,785	0.455	0.469	0.677
32	32	Fonjak	Volcanic plateau of Adamawa	Cameroon	nd	nd	7.198734	13.825379	1,072	3	G0R1T1L1	maar	6	R	595	490	2.60E+05	1,980	0.824	0.934	0.833
33	33	Tisong	Volcanic plateau of Adamawa	Cameroon	nd	nd	7.253456	13.577037	1,152	3	G0R1T1L1	maar	6	R	305	210	6.25E+04	1,060	0.689	0.855	0.699
34	1	Lac Vert	between Nyiragongo and Lake Kivu	DR Congo	nd	tuff cone	−1.613553	29.135044	1,471	4	G0R1T1L1	tuff cone	6	R	680	340	1.93E+05	1,805	0.500	0.531	0.744
35	2	Kirunga	between Nyiragongo and Lake Kivu	DR Congo	nd	tuff cone	−1.638970	29.142168	1,470	4	G0R1T1L2	tuff cone	6	R	160	95	1.09E+04	415	0.594	0.544	0.798
36	1	Ara Shetan	Butajiri Silti Field	Ethiopia	221260	fissure vents	8.044047	38.351203	2,041	5	G0R1T1L1	maar	6	R	510	460	1.82E+05	1,620	0.902	0.891	0.871
37	2	Budameda	Bilate River Field	Ethiopia	221291	monogenetic volcanic field	7.09532	38.091476	1,555	5	G0R1T1L1	maar	6	R	1,280	1,010	1.02E+06	3,750	0.789	0.793	0.911
38	3	Tilo	Bilate River Field	Ethiopia	221291	monogenetic volcanic field	7.063846	38.095431	1,555	5	G0R1T1L1	maar	6	R	1,110	730	6.09E+05	3,125	0.658	0.629	0.784
39	4	Mechaferra	Bilate River Field	Ethiopia	221291	monogenetic volcanic field	7.040021	38.086103	1,545	5	G0R1T1L1	maar	6	R	1,030	775	5.98E+05	3,385	0.752	0.718	0.656
40	5	Bishoftu Guda	Bishoftu Volcanic Field	Ethiopia	221220	fissure vents	8.787252	38.993312	1,880	3	G0R1T1L1	maar	6	R	1,075	895	7.40E+05	3,145	0.833	0.815	0.940
41	6	Kiroftu	Bishoftu Volcanic Field	Ethiopia	221220	fissure vents	8.778577	39.000554	1,880	3	G0R1T1L1	maar	6	R	480	425	1.80E+05	1,560	0.885	0.995	0.929
42	7	Hora	Bishoftu Volcanic Field	Ethiopia	221220	fissure vents	8.761578	38.992982	1,870	3	G0R1T1L1	maar	6	R	1,730	1,065	1.15E+06	4,650	0.616	0.489	0.668
43	8	Bishoftu	Bishoftu Volcanic Field	Ethiopia	221220	fissure vents	8.741218	38.982556	1,865	3	G0R1T1L1	maar	6	R	1,405	1,005	9.86E+05	3,810	0.715	0.636	0.854
44	9	K'oftu	Bishoftu Volcanic Field	Ethiopia	221220	fissure vents	8.832824	39.049267	1,935	3	G0R1T1L1	maar	6	R	2,060	1,325	1.73E+06	5,515	0.643	0.519	0.715
45	10	Ora Kilole	Bishoftu Volcanic Field	Ethiopia	221220	fissure vents	8.802948	39.083407	1,890	3	G0R1T1L1	maar	6	R	1,130	1,120	8.86E+05	3,500	0.991	0.883	0.909
46	11	Green Lake	Bishoftu Volcanic Field	Ethiopia	221220	fissure vents	8.702293	38.975288	2,020	4	G0R1T1L1	maar	6	R	945	785	5.94E+05	2,895	0.831	0.847	0.891
47	12	Dendi	Dendi Volcano	Ethiopia	nd	stratovolcano	8.838066	38.018077	2,836	5	G1R1T1L1	crater	6	R	2,415	2,005	3.84E+06	7,370	0.830	0.838	0.888
48	13	Wonchi	Wonchi Volcano	Ethiopia	nd	stratovolcano	8.792317	37.894222	2,881	5	G1R1T1L1	crater	6	R	3,010	2,025	4.23E+06	19,485	0.673	0.594	0.140
49	14	Abijatta	O'a Caldera/Shala Caldera	Ethiopia	221280	caldera	7.610656	38.602238	1,581	5	G1R1T0L1	caldera	6	R	12,110	7,040	7.45E+07	36,580	0.581	0.647	0.700
50	15	Shala	O'a Caldera/Shala Caldera	Ethiopia	221281	caldera	7.455807	38.530774	1,559	5	G1R1T0L1	caldera	6	R	24,885	14,765	3.01E+08	96,535	0.593	0.619	0.406
51	16	Langano	O'a Caldera/Shala Caldera	Ethiopia	221282	caldera	7.6015	38.750534	1,587	5	G1R1T0L1	caldera	6	R	21,385	14,150	2.31E+08	85,760	0.662	0.643	0.395
52	17	Chitu	O'a Caldera/Shala Caldera	Ethiopia	221283	monogenetic volcanic field	7.403362	38.420227	1,563	5	G0R1T0L1	maar	6	R	1,225	635	7.19E+05	3,470	0.518	0.610	0.750

(Continued on following page)

TABLE 1 | (*Continued*) The VOLADA_Africa 2.0 database, mentioning the lake number (#), the number of lakes in the same country (#/country), the lake name, the volcano the depends on, the country, GVP number (Global Volcanism Program number https://volcano.si.edu/search_volcano.cfm), volcano type, the latitude and longitude (Lat. and Long. in decimal coordinates), the elevation above sea level (m a.s.l.), level of study (1–5, *see* text for details), genetic class (*see* text for details), lake type, physical and chemical classification, length of major and minor lake axes (Dmajor and Dminor, respectively, in m), lake surface area (A, in m^2), lake perimeter (in meter), Aspect Ratio (AR, Eq. 1), Elongation (EL, Eq. 2), Isoperimetric Circularity (IC, Eq. 3).

#	#/Country	Lake	Volcano	Country	GVP number	Volcano type	Lat.	Long.	Elevation (m asl)	Level of study	Genetic class	Lake type	Phys. Class	Chem. Class	D major (m)	D minor (m)	A (m^2)	Perimeter (m)	AR	EL	IC
53	18	Zengena	nd	Ethiopia	nd	monogenetic volcanic field	10.913149	36.966771	2,515	5	G0R1T1L1	maar	6	R	840	710	4.55E+05	2,575	0.845	0.821	0.862
54	19	Dembel	Mt Zuquala	Ethiopia	nd	stratovolcano	8.542033	38.855155	2,835	5	G1R1T1L1	crater	6	R	570	370	1.65E+05	1,675	0.649	0.647	0.739
55	1	Rutundu	Mount Kenya	Kenya	nd	stratovolcano	–0.042483	37.463922	3,082	5	G1R1T0L1	crater	6	R	460	220	9.58E+04	1,220	0.478	0.576	0.809
56	2	Hohnel	Mount Kenya	Kenya	nd	stratovolcano	–0.181993	37.289730	4,215	5	G0R0T0L0	glacial lakes in volcanic environment	6	R	455	165	7.19E+04	1,195	0.363	0.442	0.633
57	3	Hidden Tarn	Mount Kenya	Kenya	nd	stratovolcano	–0.180470	37.315102	4,248	5	G0R0T0L0	glacial lakes in volcanic environment	6	R	235	175	3.32E+04	690	0.745	0.765	0.876
58	4	Carr Lakes (2)	Mount Kenya	Kenya	nd	stratovolcano	–0.180857	37.345558	3,965	5	G0R0T0L0	glacial lakes in volcanic environment	6	R	340	215	5.35E+04	1,050	0.632	0.589	0.610
59	5	Enchanted Lake	Mount Kenya	Kenya	nd	stratovolcano	–0.171586	37.335677	4,251	5	G0R0T0L0	glacial lakes in volcanic environment	6	R	290	175	4.21E+04	865	0.603	0.637	0.707
60	6	Thompson's Tarn (2)	Mount Kenya	Kenya	nd	stratovolcano	–0.168623	37.320388	4,324	5	G0R0T0L0	glacial lakes in volcanic environment	6	R	175	125	1.39E+04	530	0.714	0.578	0.622
61	7	Gallery Tarn	Mount Kenya	Kenya	nd	stratovolcano	–0.163570	37.324651	4,462	5	G0R0T0L0	glacial lakes in volcanic environment	6	R	190	65	1.03E+04	490	0.342	0.363	0.539
62	8	Teleki Tarn	Mount Kenya	Kenya	nd	stratovolcano	–0.168669	37.305970	4,296	5	G0R0T0L0	glacial lakes in volcanic environment	6	R	275	180	3.52E+04	845	0.655	0.593	0.619
63	9	Lewis Tarn	Mount Kenya	Kenya	nd	stratovolcano	–0.161640	37.310524	4,587	5	G0R0T0L0	glacial lakes in volcanic environment	6	R	135	90	1.05E+04	495	0.667	0.734	0.538
64	10	Tyndall Tarn	Mount Kenya	Kenya	nd	stratovolcano	–0.156321	37.304172	4,472	5	G0R0T0L0	glacial lakes in volcanic environment	6	R	125	60	5.18E+03	345	0.480	0.422	0.547
65	11	Two Tarn	Mount Kenya	Kenya	nd	stratovolcano	–0.156825	37.299391	4,500	5	G0R0T0L0	glacial lakes in volcanic environment	6	R	220	110	1.95E+04	650	0.500	0.513	0.580
66	12	Nanyuki Tarn	Mount Kenya	Kenya	nd	stratovolcano	–0.155001	37.297260	4,489	5	G0R0T0L0	glacial lakes in volcanic environment	6	R	105	65	6.90E+03	445	0.619	0.797	0.438
67	13	Emerald Tarn	Mount Kenya	Kenya	nd	stratovolcano	–0.152130	37.294431	4,346	5	G0R0T0L0	glacial lakes in volcanic environment	6	R	160	125	1.26E+04	475	0.781	0.627	0.702
68	14	Curling Pond	Mount Kenya	Kenya	nd	stratovolcano	–0.158445	37.314575	4,784	5	G0R0T0L0	glacial lakes in volcanic environment	6	R	40	20	5.00E+02	100	0.500	0.398	0.628
69	15	Square Tarn	Mount Kenya	Kenya	nd	stratovolcano	–0.153876	37.323172	4,656	5	G0R0T0L0	glacial lakes in volcanic environment	6	R	45	25	1.01E+03	125	0.556	0.635	0.812
70	16	Harris Tarn	Mount Kenya	Kenya	nd	stratovolcano	–0.151465	37.319496	4,760	5	G0R0T0L0	glacial lakes in volcanic environment	6	R	70	50	2.74E+03	195	0.714	0.712	0.905
71	17	Simba Tarn	Mount Kenya	Kenya	nd	stratovolcano	–0.148504	37.322257	4,601	5	G0R0T0L0	glacial lakes in volcanic environment	6	R	60	40	1.71E+03	195	0.667	0.605	0.565
72	18	Lower Simba Tarn	Mount Kenya	Kenya	nd	stratovolcano	–0.144637	37.319092	4,412	5	G0R0T0L0	glacial lakes in volcanic environment	6	R	65	20	9.69E+02	165	0.308	0.292	0.447
73	19	Kami Tarn	Mount Kenya	Kenya	nd	stratovolcano	–0.144204	37.310072	4,457	5	G0R0T0L0	glacial lakes in volcanic environment	6	R	45	35	1.05E+03	165	0.778	0.660	0.485
74	20	Oblong Tarn	Mount Kenya	Kenya	nd	stratovolcano	–0.145151	37.301596	4,368	5	G0R0T0L0	glacial lakes in volcanic environment	6	R	190	85	1.58E+04	540	0.447	0.557	0.681
75	21	Hausberg Tarn	Mount Kenya	Kenya	nd	stratovolcano	–0.144125	37.300256	4,364	5	G0R0T0L0	glacial lakes in volcanic environment	6	R	195	60	1.06E+04	500	0.308	0.355	0.533
76	22	Polish Man's Tarn	Mount Kenya	Kenya	nd	stratovolcano	–0.137082	37.295502	4,433	5	G0R0T0L0	glacial lakes in volcanic environment	6	R	70	60	3.66E+03	240	0.857	0.951	0.798
77	23	Hanging Tarn	Mount Kenya	Kenya	nd	stratovolcano	–0.155306	37.332563	4,443	5	G0R0T0L0	glacial lakes in volcanic environment	6	R	130	100	1.06E+04	420	0.769	0.799	0.755
78	24	Michaelson	Mount Kenya	Kenya	nd	stratovolcano	–0.146236	37.351426	3,958	5	G0R0T0L0	glacial lakes in volcanic environment	6	R	425	325	1.18E+05	1,370	0.765	0.832	0.790
79	25	Hall Tarns (5)	Mount Kenya	Kenya	nd	stratovolcano	–0.143371	37.345343	4,288	5	G0R0T0L0	glacial lakes in volcanic environment	6	R	250	100	1.61E+04	820	0.400	0.328	0.301
80	26	Ellis	Mount Kenya	Kenya	nd	stratovolcano	–0.123114	37.400612	3,461	5	G0R0T0L0	glacial lakes in volcanic environment	6	R	795	195	1.14E+05	1,835	0.245	0.230	0.425
81	27	Alice	Mount Kenya	Kenya	nd	stratovolcano	–0.075265	37.464472	3,557	5	G1R1T0L1	crater	6	R	725	280	1.98E+05	1,890	0.386	0.480	0.697
82	28	Sacred Lake	Mount Kenya	Kenya	nd	stratovolcano	0.047764	37.527992	2,350	5	G0R1T1L1	maar (ephemeral)	6	R	950	755	5.55E+05	2,975	0.795	0.783	0.788
83	29	Tilapia Lake (3)	Central Island	Kenya	222010	tuff cones	3.488834	36.042356	363	5	G0R1T1L1	maar	6	R	295	220	5.69E+04	935	0.746	0.833	0.818
84	30	unnamed	S Shore Lake Turkana	Kenya	nd	tuff cone?	2.415791	36.594737	364	5	G0R1T1L1	maar	6	R	265	255	5.19E+04	850	0.962	0.941	0.903
85	31	Lake Paradise	Marsabit	Kenya	222021	shield volcano	2.205042	37.931401	848	5	G0R1T1L1	maar	6	R	690	440	2.36E+05	2,560	0.638	0.631	0.453
86	32	Crater Pan	Marsabit	Kenya	222021	shield volcano	2.309932	37.969263	1,481	5	G0R1T1L1	maar	6	R	360	290	8.81E+04	1,110	0.806	0.866	0.899
87	33	Marsabit County	Marsabit	Kenya	222021	shield volcano	2.359822	37.999918	1,309	5	G0R1T1L1	maar	6	R	400	270	6.63E+04	1,140	0.675	0.528	0.641
88	34	Crescent Island crater	Lake Naivasha	Kenya		nd	–0.767585	36.408114	1,885	5	G0R1T1L1	maar	6	R	15,805	11,885	1.45E+08	77,460	0.752	0.739	0.304
89	35	Sonachi	W of Lake Naivasha	Kenya	nd	nd	–0.811956	36.278151	1,885	3	G0R1T1L1	maar	5	R	2,945	2,135	5.44E+06	9,840	0.725	0.799	0.706
90	36	Crater Lake	nd (NW of Lake Sonachi)	Kenya	nd	nd	–0.782813	36.262700	1,896	5	G0R1T1L1	maar	6	R	660	310	1.45E+05	1,860	0.470	0.424	0.527
91	37	Simbi	S of Nyanza Gulf. Lake Victoria	Kenya		nd	–0.3673	34.629500	1,145	5	G0R1T1L1	maar	6	R	800	525	3.30E+05	2,245	0.656	0.657	0.823

(Continued on following page)

TABLE 1 | (*Continued*) The VOLADA_Africa 2.0 database, mentioning the lake number (#), the number of lakes in the same country (#/country), the lake name, the volcano the depends on, the country, GVP number (Global Volcanism Program number https://volcano.si.edu/search_volcano.cfm), volcano type, the latitude and longitude (Lat. and Long. in decimal coordinates), the elevation above sea level (m a.s.l.), level of study (1–5, *see* text for details), genetic class (*see* text for details), lake type, physical and chemical classification, length of major and minor lake axes (Dmajor and Dminor, respectively, in m), lake surface area (A, in m^2), lake perimeter (in meter), Aspect Ratio (AR, Eq. 1), Elongation (EL, Eq. 2), Isoperimetric Circularity (IC, Eq. 3).

#	#/Country	Lake	Volcano	Country	GVP number	Volcano type	Lat.	Long.	Elevation (m asl)	Level of study	Genetic class	Lake type	Phys. Class	Chem. Class	D major (m)	D minor (m)	A (m^2)	Perimeter (m)	AR	EL	IC
92	1	Waw an Namus lake	SE of Al Haruj Volcanic Field	Libya	nd	nd	24.907923	17.75182	366	5	G1R1T1L1	crater	6	R	600	260	1.24E+05	1,815	0.433	0.439	0.473
93	1	Farihy Mahery	Ambre Bobaomby	Madagascar	233011	monogenetic volcanic field	−12.44058	49.244097	365	5	G0R1T1L1	maar	6	R	554	420	1.73E+05	2,295	0.758	0.718	0.413
94	2	Maharasika	Ambre Bobaomby	Madagascar	233011	monogenetic volcanic field	−12.534767	49.177112	1,062	5	G0R1T1L1	maar	6	R	255	240	3.87E+04	805	0.941	0.758	0.750
95	3	Matsabory Taranta	Ambre Bobaomby	Madagascar	233011	monogenetic volcanic field	−12.584105	49.149962	1,252	5	G0R1T1L1	maar	6	R	690	515	3.41E+05	2,285	0.746	0.912	0.821
96	4	Matsabory Malio	Ambre Bobaomby	Madagascar	233011	monogenetic volcanic field	−12.597774	49.16064	1,335	5	G0R1T1L1	maar	6	R	385	285	8.53E+04	1,090	0.740	0.733	0.902
97	5	Matsabory Manonja	Ambre Bobaomby	Madagascar	233011	monogenetic volcanic field	−12.625977	49.177434	1,035	5	G0R1T1L1	maar	6	R	620	600	2.51E+05	2,145	0.968	0.831	0.686
98	6	Matsabory Ampatan' Ambohitra	Ambre Bobaomby	Madagascar	233011	monogenetic volcanic field	−12.696976	49.167929	811	5	G0R1T1L1	maar	6	R	800	680	3.96E+05	2,505	0.850	0.788	0.793
99	7	Farihy Antanavo +1	Farihy Antanavo	Madagascar	nd	nd	−12.750169	49.25451	368	5	G0R1T1L1	maar	6	R	1,650	1,280	1.58E+06	4,865	0.776	0.739	0.839
100	8	Farihy Andjavibe	Nosy Be Island	Madagascar	233012	pyroclastic cones	−13.295901	48.22352	19	5	G0R1T1L1	maar	6	R	745	555	3.30E+05	2,685	0.745	0.757	0.575
101	9	3 unnamed	Nosy Be Island	Madagascar	233012	pyroclastic cones	−13.30949	48.238826	155	5	G0R1T1L1	maar	6	R							
102	10	Farihy Bemapaza	Nosy Be Island	Madagascar	233012	pyroclastic cones	−13.317878	48.237747	236	5	G0R1T1L1	maar	6	R	520	510	1.86E+05	1,770	0.981	0.876	0.746
103	11	Farihy Maintimasoa	Nosy Be Island	Madagascar	233012	pyroclastic cones	−13.313355	48.222779	89	5	G0R1T1L1	maar	6	R	595	495	2.31E+05	2,125	0.832	0.831	0.643
104	12	Farihy Amparihibe	Nosy Be Island	Madagascar	233012	pyroclastic cones	−13.32023	48.211217	71	5	G0R1T1L1	maar	6	R	1,645	1,210	1.64E+06	5,755	0.736	0.772	0.622
105	13	Farihy Antisidihy	Nosy Be Island	Madagascar	233012	pyroclastic cones	−13.328442	48.219704	94	5	G0R1T1L1	maar	6	R	725	610	3.27E+05	2,680	0.841	0.792	0.572
106	14	Farihy Antasahamanavaka	Nosy Be Island	Madagascar	233012	pyroclastic cones	−13.327408	48.243759	214	5	G0R1T1L1	maar	6	R	895	635	4.55E+05	2,790	0.709	0.723	0.735
107	15	Farihy Djabala	Nosy Be Island	Madagascar	233012	pyroclastic cones	−13.38642	48.242435	44	5	G0R1T1L1	maar	6	R	435	315	1.01E+05	1,560	0.724	0.680	0.522
108	16	Farihy Ampombilava	Nosy Be Island	Madagascar	233012	pyroclastic cones	−13.394032	48.244096	25	5	G0R1T1L1	maar	6	R	555	415	1.89E+05	1,985	0.748	0.781	0.603
109	17	Andraikiba	Tritrivakely/ Vakinankaratra	Madagascar	233015	pyroclastic cones	−19.874453	46.969582	1,517	5	G0R1T1L1	maar	6	R	1,090	820	9.19E+05	4,005	0.752	0.985	0.720
110	18	Tritriva	Tritrivakely/ Vakinankaratra	Madagascar	233015	pyroclastic cones	−19.929119	46.924657	1,730	5	G0R1T1L1	maar	6	R	335	105	2.49E+04	785	0.313	0.283	0.508
111	19	Itasy	Itasy Volcanic Field	Madagascar	233014	pyroclastic cones	−19.065851	46.785701	1,221	5	G0R1T1L1	maar	6	R	7,450	7,005	3.22E+07	55,335	0.940	0.739	0.132
112	20	unnamed	Itasy Volcanic Field	Madagascar	233014	pyroclastic cones	−18.920348	46.716762	1,192	5	G0R1T1L1	maar	6	R	425	255	9.46E+04	1,335	0.600	0.667	0.667
113	21	unnamed	Itasy Volcanic Field	Madagascar	233014	pyroclastic cones	−18.923107	46.726122	1,224	5	G0R1T1L1	maar	6	R	370	95	5.94E+04	1,335	0.257	0.552	0.419
114	22	Andranotoraha	Itasy Volcanic Field	Madagascar	233014	pyroclastic cones	−18.949398	46.742226	1,292	5	G0R1T1L1	maar	6	R	415	345	1.18E+05	1,395	0.831	0.872	0.762
115	23	unnamed	Itasy Volcanic Field	Madagascar	233014	pyroclastic cones	−18.999815	46.72934	1,224	5	G0R1T1L1	maar	6	R	320	170	4.91E+04	900	0.531	0.611	0.762
116	24	unnamed	Itasy Volcanic Field	Madagascar	233014	pyroclastic cones	−19.010321	46.735777	1,239	5	G0R1T1L1	maar	6	R	200	170	2.62E+04	605	0.850	0.834	0.899
117	25	unnamed	Itasy Volcanic Field	Madagascar	233014	pyroclastic cones	−19.015673	46.752733	1,232	5	G0R1T1L1	maar	6	R	635	500	2.53E+05	2,085	0.787	0.799	0.731
118	26	unnamed	Itasy Volcanic Field	Madagascar	233014	pyroclastic cones	−19.017943	46.728016	1,232	5	G0R1T1L1	maar	6	R	630	390	2.17E+05	2,215	0.619	0.696	0.556
119	27	unnamed	Itasy Volcanic Field	Madagascar	233014	pyroclastic cones	−19.131751	46.644018	1,176	5	G0R1T1L1	maar	6	R	340	280	7.32E+04	1,170	0.824	0.806	0.672
120	28	unnamed	Itasy Volcanic Field	Madagascar	233014	pyroclastic cones	−19.184869	46.646128	1,159	5	G0R1T1L1	maar	6	R	190	125	1.67E+04	555	0.658	0.589	0.681
121	1	Bisoke	Bisoke	Rwanda	223050	Stratovolcano	−1.460855	29.486841	3,600	4	G1R1T1L1	crater	6	R	305	290	6.97E+04	1,055	0.951	0.954	0.787
122	2	Muhavura	Muhavura	Rwanda-Uganda	223060	Stratovolcano	−1.382938	29.677872	4,101	5	G1R1T1L1	crater	6	R	28	27	5.60E+02	90	0.964	0.909	0.869
123	1	Deriba (2 lakes)	Caldera of Jebel Marra	Sudan	225030	volcanic field	12.950006	24.258121	2,195	5	G1R1T1L1	crater	6	R	1,150	805	7.71E+05	3,590	0.700	0.742	0.752
124	2	Malha	Meidob Volcanic Field	Sudan	225050	volcanic field	15.131185	26.171321	816	3	G1R1T1L1	maar	6	R	180	170	2.43E+04	575	0.944	0.955	0.924
125	1	Empakaai	Ngorongoro District	Tanzania	nd	caldera	−2.911639	35.839853	2,224	5	G1R1T1L1	crater	6	R	3,195	2,695	7.60E+06	10,460	0.844	0.948	0.873
126	2	Magadi	Ngorongoro District	Tanzania	nd	caldera	−3.183485	35.531512	1,732	5	G1R1T0L1	crater	6	R	3,840	2,280	6.86E+06	14,140	0.594	0.592	0.431
127	4	Masoko (6 lakes)	Rungwe Volcanic Province	Tanzania	222170	volcanic field	−9.334192	33.755974	861	5	G0R1T1L1	maar	6	R	700	675	3.73E+05	2,335	0.964	0.969	0.860
128	5	Ngozi	Ngozi	Tanzania	222164	caldera	−9.007995	33.553284	2,073	5	G1R1T1L1	crater	3	G-R	2,585	1770	3.22E+06	10,910	0.685	0.614	0.340
129	6	Chala	Chala	Tanzania-Kenya	nd	caldera	−3.318714	37.699070	879	5	G1R1T0L1	caldera	6	R	2,685	1955	4.24E+06	9,635	0.728	0.749	0.574
130	6	Duluti	S of Mt Meru	Tanzania	nd	nd	−3.386342	36.788415	1,276	3	G0R1T1L1	maar	6	R	1,110	740	5.77E+05	3,210	0.667	0.596	0.704
131	1	Kitagata	Katwe-Kikorongo	Uganda	223003	monogenetic volcanic field	−0.063042	29.97496	919	3	G0R1T1L1	maar	6	R	1,020	940	7.10E+05	3,095	0.922	0.869	0.931
132	2	Murumuli/Murumuu	Katwe-Kikorongo	Uganda	223003	monogenetic volcanic field	−0.074275	29.990778	915	3	G0R1T1L1	maar	6	R	575	510	2.37E+05	2,065	0.887	0.913	0.698
133	3	Nyamanyuka	Katwe-Kikorongo	Uganda	223003	monogenetic volcanic field	−0.090866	29.98787	905	3	G0R1T1L1	maar	6	R	1,065	950	8.04E+05	3,255	0.892	0.903	0.954
134	4	Bunyampaka	Katwe-Kikorongo	Uganda	223003	monogenetic volcanic field	−0.040083	30.130152	879	3	G0R1T1L1	maar	6	R	460	425	1.55E+05	1,430	0.924	0.933	0.952
135	5	Katwe	Katwe-Kikorongo	Uganda	223003	monogenetic volcanic field	−0.126605	29.868967	882	3	G0R1T1L1	maar	6	R	2,550	940	2.55E+06	8,595	0.369	0.499	0.434
136	6	Kikorongo/Queens Pavilion	Katwe-Kikorongo	Uganda	223003	monogenetic volcanic field	−0.007435	30.012397	914	3	G0R1T1L1	maar	6	R	1,975	1,165	1.58E+06	5,765	0.590	0.516	0.597
137	7	Mahega	Katwe-Kikorongo	Uganda	223003	monogenetic volcanic field	−0.014307	29.96674	918	3	G0R1T1L1	maar	6	R	495	415	1.63E+05	1,580	0.838	0.847	0.820
138	8	Munyanyange	Katwe-Kikorongo	Uganda	223003	monogenetic volcanic field	−0.135756	29.885665	912	3	G0R1T1L1	maar	6	R	650	465	2.92E+05	2,040	0.715	0.880	0.882
139	9	Maseche	Bunyaruguru	Uganda	223004	monogenetic volcanic field	−0.094429	30.192868	910	3	G0R1T1L1	maar	6	R	655	535	3.30E+05	2,945	0.817	0.979	0.478
140	10	Bagusa	Bunyaruguru	Uganda	223004	monogenetic volcanic field	−0.100193	30.178101	910	3	G0R1T1L1	maar	6	R	885	700	4.57E+05	2,620	0.791	0.743	0.837
141	11	Kyambura	Bunyaruguru	Uganda	223004	monogenetic volcanic field	−0.11037	30.213959	923	3	G0R1T1L1	maar	6	R	890	770	4.71E+05	2,655	0.865	0.757	0.840
142	12	unnamed1.2.3	Bunyaruguru	Uganda	223004	monogenetic volcanic field	−0.125192	30.191811	922	3	G0R1T1L1	maar (ephemeral)	6	R	255	105	2.52E+04	700	0.412	0.493	0.646
143	13	Nshenyi	Bunyaruguru	Uganda	223004	monogenetic volcanic field	−0.150209	30.159715	953	3	G0R1T1L1	maar	6	R	1,120	710	5.90E+05	3,710	0.634	0.599	0.539
144	14	Chibwera	Bunyaruguru	Uganda	223004	monogenetic volcanic field	−0.153153	30.142931	977	3	G0R1T1L1	maar	6	R	1,115	960	8.17E+05	3,465	0.861	0.837	0.855
145	15	Mbugo	Bunyaruguru	Uganda	223004	monogenetic volcanic field	−0.174004	30.156157	980	3	G0R1T1L1	maar	6	R	770	645	3.70E+05	2,445	0.838	0.795	0.778
146	16	Kyamwiga	Bunyaruguru	Uganda	223004	monogenetic volcanic field	−0.18637	30.145129	1,024	3	G0R1T1L1	maar	6	R	2,320	1,370	3.13E+06	8,925	0.591	0.740	0.494
147	17	Bugwagi	Bunyaruguru	Uganda	223004	monogenetic volcanic field	−0.1941	30.188127	1,058	3	G0R1T1L1	maar	6	R	1,095	750	6.26E+05	3,085	0.685	0.665	0.827

(Continued on following page)

TABLE 1 | (*Continued*) The VOLADA_Africa 2.0 database, mentioning the lake number (#), the number of lakes in the same country (#/country), the lake name, the volcano the depends on, the country, GVP number (Global Volcanism Program number https://volcano.si.edu/search_volcano.cfm), volcano type, the latitude and longitude (Lat. and Long. in decimal coordinates), the elevation above sea level (m a.s.l.), level of study (1–5, *see* text for details), genetic class (*see* text for details), lake type, physical and chemical classification, length of major and minor lake axes (Dmajor and Dminor, respectively, in m), lake surface area (A, in m^2), lake perimeter (in meter), Aspect Ratio (AR, Eq. 1), Elongation (EL, Eq. 2), Isoperimetric Circularity (IC, Eq. 3).

#	#/Country	Lake	Volcano	Country	GVP number	Volcano type	Lat.	Long.	Elevation (m asl)	Level of study	Genetic class	Lake type	Phys. Class	Chem. Class	D major (m)	D minor (m)	A (m^2)	Perimeter (m)	AR	EL	IC
148	18	Katinda	Bunyaruguru	Uganda	223004	monogenetic volcanic field	−0.222514	30.105217	1,042	3	G0R1T1L1	maar	6	R	840	690	4.44E+05	2,635	0.821	0.801	0.804
149	19	Mirambi	Bunyaruguru	Uganda	223004	monogenetic volcanic field	−0.2289	30.106164	1,085	3	G0R1T1L1	maar	6	R	925	820	5.75E+05	2,960	0.886	0.856	0.825
150	20	Kariya	Bunyaruguru	Uganda	223004	monogenetic volcanic field	−0.232341	30.160604	1,253	3	G0R1T1L1	maar	6	R	1,325	645	8.53E+05	4,535	0.487	0.619	0.521
151	21	Nyungu	Bunyaruguru	Uganda	223004	monogenetic volcanic field	−0.258352	30.094193	1,186	3	G0R1T1L1	maar	5b2?	R	655	345	2.04E+05	1,940	0.527	0.605	0.681
152	22	Mafuro	Bunyaruguru	Uganda	223004	monogenetic volcanic field	−0.266708	30.102212	1,275	3	G0R1T1L1	maar	6	R	525	495	1.90E+05	1,700	0.943	0.878	0.826
153	23	Luijono	Bunyaruguru	Uganda	223004	monogenetic volcanic field	−0.272808	30.085096	1,268	3	G0R1T1L1	maar	6	R	1,120	685	5.57E+05	3,110	0.612	0.565	0.724
154	24	Kyasanduka	Bunyaruguru	Uganda	223004	monogenetic volcanic field	−0.289252	30.051001	1,013	3	G0R1T1L1	maar	6	R	980	595	5.29E+05	3,045	0.607	0.701	0.717
155	25	Nyamusingire	Bunyaruguru	Uganda	223004	monogenetic volcanic field	−0.288466	30.028927	984	3	G0R1T1L1	maar	6	R	3,470	1745	4.09E+06	12,425	0.503	0.433	0.333
156	26	Kigezi	Bunyaruguru	Uganda	223004	monogenetic volcanic field	−0.287449	30.109972	1,313	3	G0R1T1L1	maar	6	R	445	315	1.03E+05	1,340	0.708	0.662	0.721
157	27	Mugogo	Bunyaruguru	Uganda	223004	monogenetic volcanic field	−0.285688	30.125189	1,322	3	G0R1T1L1	maar	6	R	1875	475	1.22E+06	7,715	0.253	0.442	0.258
158	28	Kako	Bunyaruguru	Uganda	223004	monogenetic volcanic field	−0.307614	30.097811	1,411	3	G0R1T1L1	maar	6	R	600	365	1.97E+05	1,770	0.608	0.697	0.790
159	29	Nkugute	Bunyaruguru	Uganda	223004	monogenetic volcanic field	−0.324301	30.098871	1,411	3	G0R1T1L1	maar	6	R	1,355	720	9.54E+05	5,545	0.531	0.662	0.390
160	30	Murabio	Bunyaruguru	Uganda	223004	monogenetic volcanic field	−0.33551	30.036281	1,116	3	G0R1T1L1	maar	6	R	715	395	2.77E+05	2,285	0.552	0.690	0.667
161	31	Kacuba	Bunyaruguru	Uganda	223004	monogenetic volcanic field	−0.344124	30.030834	1,132	3	G0R1T1L1	maar	6	R	355	270	6.82E+04	1,140	0.761	0.689	0.659
162	32	Karolero	Bunyaruguru	Uganda	223004	monogenetic volcanic field	−0.342163	30.024982	1,116	3	G0R1T1L1	maar	6	R	960	735	5.80E+05	3,040	0.766	0.801	0.789
163	33	Kyogo	Bunyaruguru	Uganda	223004	monogenetic volcanic field	−0.341566	30.019982	1,126	3	G0R1T1L1	maar	6	R	185	180	2.30E+04	660	0.973	0.856	0.663
164	34	Chema	Bunyaruguru	Uganda	223004	monogenetic volcanic field	−0.256705	30.117617	1,271	3	G0R1T1L1	maar	6	R	1,060	900	7.26E+05	3,400	0.849	0.823	0.789
165	35	Kamweru	Bunyaruguru	Uganda	223004	monogenetic volcanic field	−0.259025	30.124511	1,282	3	G0R1T1L1	maar	6	R	680	410	2.40E+05	1,970	0.603	0.661	0.777
166	36	Kasirya	Bunyaruguru	Uganda	223004	monogenetic volcanic field	−0.25905	30.131988	1,296	3	G0R1T1L1	maar	6	R	475	265	1.20E+05	1,525	0.558	0.677	0.648
167	37	Kamunzuka	Bunyaruguru	Uganda	223004	monogenetic volcanic field	−0.262087	30.156326	1,287	3	G0R1T1L1	maar	6	R	575	525	2.44E+05	2,070	0.913	0.940	0.716
168	38	Kabarogi	Bunyaruguru	Uganda	223004	monogenetic volcanic field	−0.229048	30.21549	1,363	3	G0R1T1L1	maar	6	R	725	575	2.91E+05	2,355	0.793	0.705	0.659
169	39	Nyamirina	Ndali-Kasenda	Uganda	223001	monogenetic volcanic field	0.519526	30.318823	1,505	3	G0R1T1L1	maar	6	R	590	435	1.86E+05	2,015	0.737	0.680	0.576
170	40	Nyinabulitwa	Ndali-Kasenda	Uganda	223001	monogenetic volcanic field	0.510415	30.322963	1,427	3	G0R1T1L1	maar	6	R	950	465	3.81E+05	2,930	0.489	0.538	0.558
171	41	Nkuruba	Ndali-Kasenda	Uganda	223001	monogenetic volcanic field	0.5171	30.302842	1,518	3	G0R1T1L1	maar	6	R	285	130	2.51E+04	1,185	0.456	0.393	0.225
172	42	Nyabikere	Ndali-Kasenda	Uganda	223001	monogenetic volcanic field	0.496664	30.32771	1,384	3	G0R1T1L1	maar	6	R	940	520	4.43E+05	3,495	0.553	0.638	0.456
173	43	Nyanswiga	Ndali-Kasenda	Uganda	223001	monogenetic volcanic field	0.506321	30.287665	1,478	3	G0R1T1L1	maar	6	R	260	125	3.12E+04	1,190	0.481	0.588	0.277
174	44	Nyahira	Ndali-Kasenda	Uganda	223001	monogenetic volcanic field	0.498907	30.286612	1,455	3	G0R1T1L1	maar	6	R	225	145	2.81E+04	870	0.644	0.707	0.467
175	45	Lyantonde	Ndali-Kasenda	Uganda	223001	monogenetic volcanic field	0.489147	30.280036	1,407	3	G0R1T1L1	maar	6	R	475	385	1.40E+05	1,745	0.811	0.790	0.578
176	46	Nyinambuga	Ndali-Kasenda	Uganda	223001	monogenetic volcanic field	0.479359	30.289753	1,366	3	G0R1T1L1	maar	6	R	1,360	485	5.82E+05	4,215	0.357	0.401	0.412
177	47	Rukwanzi	Ndali-Kasenda	Uganda	223001	monogenetic volcanic field	0.47683	30.278245	1,341	3	G0R1T1L1	maar	6	R	385	300	9.22E+04	1,380	0.779	0.792	0.608
178	48	Katanda	Ndali-Kasenda	Uganda	223001	monogenetic volcanic field	0.48065	30.262707	1,345	3	G0R1T1L1	maar	6	R	780	655	3.93E+05	2,755	0.840	0.822	0.651
179	49	Mwegenyi	Ndali-Kasenda	Uganda	223001	monogenetic volcanic field	0.489331	30.262118	1,401	3	G0R1T1L1	maar	6	R	975	665	3.33E+05	3,235	0.682	0.446	0.400
180	50	Mwamba	Ndali-Kasenda	Uganda	223001	monogenetic volcanic field	0.462061	30.274514	1,304	3	G0R1T1L1	maar	6	R	1,060	440	4.19E+05	4,620	0.415	0.475	0.247
181	51	Mbajo	Ndali-Kasenda	Uganda	223001	monogenetic volcanic field	0.449373	30.274308	1,265	3	G0R1T1L1	maar	6	R	500	360	1.60E+05	1,935	0.720	0.815	0.537
182	52	Lugembe	Ndali-Kasenda	Uganda	223001	monogenetic volcanic field	0.448728	30.281302	1,295	3	G0R1T1L1	maar	6	R	420	290	8.75E+04	1,310	0.690	0.632	0.641
183	53	Ndicho	Ndali-Kasenda	Uganda	223001	monogenetic volcanic field	0.446313	30.269921	1,269	3	G0R1T1L1	maar	6	R	385	300	9.61E+04	1,400	0.779	0.826	0.616
184	54	Rwenjuba	Ndali-Kasenda	Uganda	223001	monogenetic volcanic field	0.441383	30.266734	1,254	3	G0R1T1L1	maar	6	R	665	465	2.15E+05	2,275	0.699	0.619	0.522
185	55	Mubiro	Ndali-Kasenda	Uganda	223001	monogenetic volcanic field	0.439453	30.253723	1,214	3	G0R1T1L1	maar	6	R	650	405	1.87E+05	2,030	0.623	0.564	0.570
186	56	Nyarayabana	Ndali-Kasenda	Uganda	223001	monogenetic volcanic field	0.429438	30.249043	1,192	3	G0R1T1L1	maar	6	R	455	390	1.12E+05	1,455	0.857	0.689	0.665
187	57	Nyamugoro	Ndali-Kasenda	Uganda	223001	monogenetic volcanic field	0.449911	30.241177	1,281	3	G0R1T1L1	maar	6	R	405	365	1.11E+05	1,540	0.901	0.862	0.588
188	58	Nyamiteza	Ndali-Kasenda	Uganda	223001	monogenetic volcanic field	0.435937	30.225592	1,263	3	G0R1T1L1	maar	6	R	730	620	3.00E+05	2,440	0.849	0.717	0.633
189	59	Nyamugosani	Ndali-Kasenda	Uganda	223001	monogenetic volcanic field	0.424384	30.229734	1,228	3	G0R1T1L1	maar	6	R	415	335	1.01E+05	1,255	0.807	0.747	0.806
190	60	Wankenzi	Ndali-Kasenda	Uganda	223001	monogenetic volcanic field	0.420011	30.26604	1,168	3	G0R1T1L1	maar	6	R	665	400	1.94E+05	2,485	0.602	0.559	0.395
191	61	Wandakara	Ndali-Kasenda	Uganda	223001	monogenetic volcanic field	0.417167	30.270892	1,169	3	G0R1T1L1	maar	6	R	310	125	3.63E+04	845	0.403	0.481	0.639
192	62	Kitere	Ndali-Kasenda	Uganda	223001	monogenetic volcanic field	0.398254	30.27139	1,142	3	G0R1T1L1	maar	6	R	540	160	1.12E+05	1,590	0.296	0.489	0.557
193	63	Ntambi	Ndali-Kasenda	Uganda	223001	monogenetic volcanic field	0.410681	30.230353	1,169	3	G0R1T1L1	maar	6	R	685	620	3.19E+05	2,560	0.905	0.866	0.612
194	64	Kanyamukali	Ndali-Kasenda	Uganda	223001	monogenetic volcanic field	0.400376	30.234127	1,162	3	G0R1T1L1	maar	6	R	510	295	1.20E+05	1,530	0.578	0.587	0.644
195	65	Kyanga	Ndali-Kasenda	Uganda	223001	monogenetic volcanic field	0.400234	30.234193	1,163	3	G0R1T1L1	maar	6	R	510	295	1.20E+05	1,530	0.578	0.587	0.644
196	66	Murigamire	Ndali-Kasenda	Uganda	223001	monogenetic volcanic field	0.42051	30.286289	1,201	3	G0R1T1L1	maar	6	R	685	665	2.78E+05	2,335	0.971	0.754	0.641
197	67	Kanyabutetere	Ndali-Kasenda	Uganda	223001	monogenetic volcanic field	0.415455	30.288305	1,200	3	G0R1T1L1	maar	6	R	130	125	1.22E+04	435	0.962	0.919	0.810
198	68	Murusi	Ndali-Kasenda	Uganda	223001	monogenetic volcanic field	0.42729	30.292303	1,226	3	G0R1T1L1	maar	6	R	540	490	2.23E+05	1,895	0.907	0.974	0.780
199	69	Kasenda	Ndali-Kasenda	Uganda	223001	monogenetic volcanic field	0.431837	30.290425	1,247	3	G0R1T1L1	maar	6	R	335	280	6.99E+04	1,035	0.836	0.793	0.820
200	70	Kanyamansira	Ndali-Kasenda	Uganda	223001	monogenetic volcanic field	0.416434	30.305052	1,198	3	G0R1T1L1	maar	6	R	315	160	4.00E+04	960	0.508	0.513	0.545
201	71	Kerere	Ndali-Kasenda	Uganda	223001	monogenetic volcanic field	0.419421	30.309173	1,205	3	G0R1T1L1	maar	6	R	760	590	3.13E+05	2,615	0.776	0.690	0.575
202	72	Kyerbwato	Ndali-Kasenda	Uganda	223001	monogenetic volcanic field	0.431286	30.323265	1,231	3	G0R1T1L1	maar	6	R	575	225	1.20E+05	1,775	0.391	0.462	0.479
203	73	Kanyanchu	Ndali-Kasenda	Uganda	223001	monogenetic volcanic field	0.433931	30.323854	1,249	3	G0R1T1L1	maar	6	R	170	125	1.87E+04	525	0.735	0.824	0.853
204	74	Kyaninga	Fort Portal	Uganda	223001	monogenetic volcanic field	0.700409	30.297701	1,540	3	G0R1T1L1	maar	5b1	R	895	265	2.98E+05	3,630	0.296	0.474	0.284
205	75	Ekikoto	Fort Portal	Uganda	223001	monogenetic volcanic field	0.701051	30.314185	1,544	3	G0R1T1L1	maar	6	R	195	150	2.02E+04	910	0.769	0.676	0.307
206	76	Kayihara	Fort Portal	Uganda	223001	monogenetic volcanic field	0.702266	30.316305	1,549	3	G0R1T1L1	maar	6	R	100	80	5.66E+03	465	0.800	0.721	0.329
207	77	Kaitabarago	Fort Portal	Uganda	223001	monogenetic volcanic field	0.693624	30.262095	1,558	3	G0R1T1L1	maar	6	R	220	120	2.52E+04	800	0.545	0.663	0.495
208	78	Saka	Fort Portal	Uganda	223001	monogenetic volcanic field	0.689259	30.240581	1,567	3	G0R1T1L1	maar	6	R	1,350	420	5.61E+05	6,430	0.311	0.392	0.171
209	79	Nyabikora	Fort Portal	Uganda	223001	monogenetic volcanic field	0.687741	30.233634	1,575	3	G0R1T1L1	maar	6	R	350	290	7.80E+04	1,120	0.829	0.811	0.781
210	80	Kyegere	Fort Portal	Uganda	223001	monogenetic volcanic field	0.681489	30.235666	1,569	3	G0R1T1L1	maar	6	R	510	350	1.24E+05	1,740	0.686	0.607	0.515
211	81	Kibengo	Lake George	Uganda	nd	monogenetic volcanic field	−0.107156	30.215242	925	5	G0R1T1L1	maar	6	R	895	735	4.70E+05	2,975	0.821	0.747	0.667
212	1	A Pot/Mazafim	Annobon Island	Equitorial Guinea	nd	shield. caldera. pyroclastic cones	−1.425709	5.632444	258	5	G1R1T1L1	crater	6	R	770	660	4.15E+05	2,650	0.857	0.891	0.743

(Continued on following page)

TABLE 1 | (*Continued*) The VOLADA_Africa 2.0 database, mentioning the lake number (#), the number of lakes in the same country (#/country), the lake name, the volcano the depends on, the country, GVP number (Global Volcanism Program number https://volcano.si.edu/search_volcano.cfm), volcano type, the latitude and longitude (Lat. and Long. in decimal coordinates), the elevation above sea level (m a.s.l.), level of study (1–5, see text for details), genetic class (see text for details), lake type, physical and chemical classification, length of major and minor lake axes (Dmajor and Dminor, respectively, in m), lake surface area (A, in m^2), lake perimeter (in meter), Aspect Ratio (AR, Eq. 1), Elongation (EL, Eq. 2), Isoperimetric Circularity (IC, Eq. 3).

#	#/Country	Lake	Volcano	Country	GVP number	Volcano type	Lat.	Long.	Elevation (m asl)	Level of study	Genetic class	Lake type	Phys. Class	Chem. Class	D major (m)	D minor (m)	A (m^2)	Perimeter (m)	AR	EL	IC
213	2	Moca	Bioko	Equitorial Guinea	224003	shield, caldera, pyroclastic cones	3.357009	8.62453	1,818	5	G1R1T1L1	crater	6	R	895	755	5.00E+05	2,830	0.844	0.795	0.785
214	1	Queen's Mary Peak	Tristan da Cunha	United Kingdom	386010	shield, pyroclastic cones. lava domes	−37.109115	−12.288894	1,954	5	G1R1T1L1	crater	6	R	85	65	4.16E+03	285	0.765	0.733	0.644
215	2	Bottom Pond	Tristan da Cunha	United Kingdom	386010	shield, pyroclastic cones. lava domes	−37.07359	−12.262347	614	5	G0R1T1L1	maar	6	R	220	145	2.47E+04	696	0.659	0.650	0.643
216	3	Middle Pond	Tristan da Cunha	United Kingdom	386010	shield, pyroclastic cones. lava domes	−37.077374	−12.264395	616	5	G0R1T1L1	maar	6	R	240	200	3.62E+04	835	0.833	0.778	0.634
217	4	Top Pond	Tristan da Cunha	United Kingdom	386010	shield, pyroclastic cones. lava domes	−37.080559	−12.266451	733	5	G0R1T1L1	maar	6	R	165	90	1.28E+04	590	0.545	0.599	0.462
218	1	Karthala	Karthala	Comores	233010	shield volcano	−11.765959	43.365019	2,017	3	G1R1T1L1	crater (ephemeral)	6	R	260	235	4.53E+04	770	0.904	0.853	0.960
219	2	Dzani Boundouni	Mohéli Island	Comores	nd	maar	−12.378808	43.848209	20	5	G0R1T1L1	maar	6	R	700	330	2.11E+05	2,470	0.471	0.548	0.435
220	3	Dzani Dzaha	Mayotte	Comores	nd	maar	−12.770623	45.288824	6	5	G0R1T1L1	maar	6	R	675	400	2.12E+05	1,770	0.593	0.593	0.851
-	Average																		0.693	0.691	0.654
-	stdev																		0.179	0.166	0.185

lake: crater lake (G1R1T1L1), caldera lake (G1R1T0L1), maar-diatreme lake (G0R1T1L1), geothermal lake (G0-1R1T1L0-1), lake in a volcanic environment (G1R0T0L0), lake dammed by volcanic deposits (G0-1R0-1T0-1L0), volcanic lake after snow melting (G0-1R1T1L1), and the generic "volcanic lake" covering the entire range of lake types (G0-1R0-1T0-1L0-1). This "grassroots" classification scheme, especially adapted to shed light on the poorly studied lakes, will now be applied to VOLADA, starting with an update for the African lakes (VOLADA_Africa 2.0) (**Table 1**).

The chemical classification system (G-versus R-dominated, Varekamp et al., 2000) was maintained here, despite the poor knowledge on lake water chemistry of the African lakes. Gas-dominated lakes (G) are generally found in craters of (highly) active volcanoes, with low-pH and heated water bodies that result from gas and vapor input from the underlying magmatic-hydrothermal system. Rock-dominated lakes (R) host water with a purely meteoric origin that attained equilibrium through water-rock interaction with the host rock that composes the lake basin. As the gas-dominated lakes are often easily recognized by their color (turquoise, green, blue-green, white, grey, or even yellow; Christenson et al., 2015), or the presence of evaporation plumes coming off their surface, in the absence of this characteristic feature the lakes were, arguably correctly, classified as R-dominated. Apparently, Africa does not host gas-dominated, "erupting," peak-, high- and medium-activity lakes, hence, all lakes are R-dominated (**Table 1**). The physical classification system by Rouwet et al. (2014) (simplified from Pasternack and Varekamp, 1997) is adopted here: *1*) erupting (i.e. hot, hyper-saline and ultra-acidic (pH near 0) lakes breached periodically by phreatic or phreatomagmatic eruptions), *2*) peak-activity (i.e. heated, saline and acidic (pH < 2 lakes topping actively degassing magmatic systems), *3*) high activity (a and b, for higher and lower solutes contents, respectively) (i.e. saline and acidic (pH < 2) lakes showing evidence of heating and passively degassing hydrothermal systems; e.g. steam heated SO_4-rich lakes), *4*) medium activity (a and b, for higher and lower solutes contents, respectively) (i.e. lakes with low heating and input from an underlying hydrothermal system, but not composed of purely meteoric water), *5*) low activity (a and b1/b2, for higher and lower solutes contents, respectively, i.e. non-acidic lakes generally with evidence of input of CO_2-rich fluids), *6*) no activity (i.e. lakes composed of purely meteoric water without any evidence of a degassing hydrothermal system). Noteworthy, lake class "5b2" points to the potentially hazardous "Nyos-type" lakes.

The level of study (a numerical scale from 1 to 5) of volcanic lakes is revised here, following the new criteria: (1) monitored, (2) well studied in the scientific literature, (3) few scientific publications available, (4) no publications, but web-sourced information available, (5) no information available, at all.

African volcanic lakes are well studied in terms of micro- and macrobiology of the water, and palynology, microfacies analyses (climate studies), dating, stable isotopic composition, and non-terrestrial biological records of cores from lake sediments, among other topics (e.g. Gasse and Van Campo, 1998, 2001; Williamson et al., 1999; Barker et al., 2000; Rumes et al., 2005; Eggermont

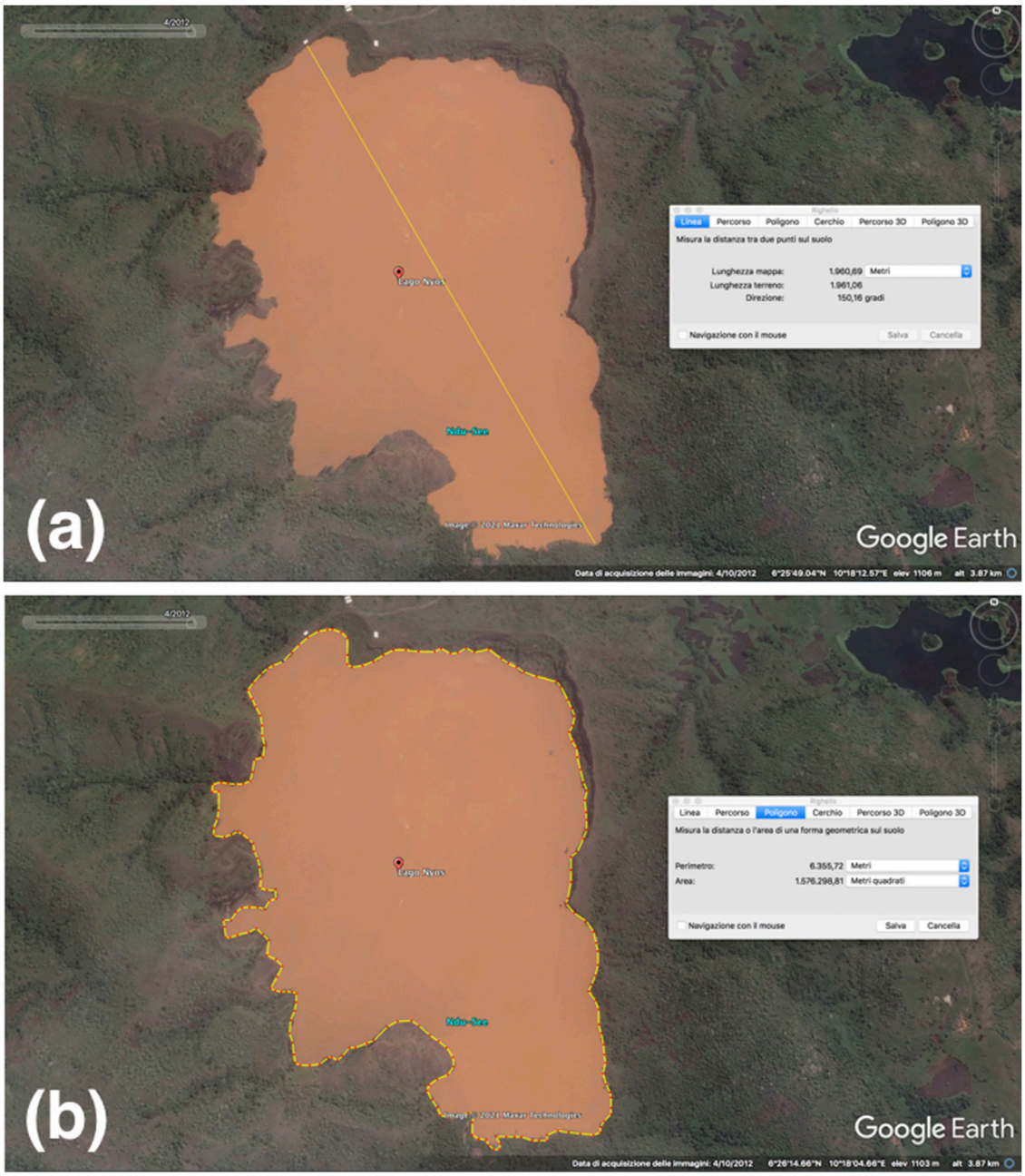

FIGURE 2 | (A) Ruler option to measure distances in GoogleEarth, **(B)** Polygone option to measure circumferences and surface areas in GoogleEarth (image© Maxar Technologies).

et al., 2006; Delalande et al., 2008; Kebede et al., 2009; Lemma, 2009; Russell et al., 2009; Cocquyt et al., 2010; Giresse and Makaya-Mvoubou, 2010; Ndebele-Murisa et al., 2010; Ryves et al., 2011; Garcin et al., 2012, 2014; Lebamba et al., 2016). These numerous studies sometimes revealed useful details, but their goals are outside the scope of the present review that aims to provide a better database on the volcanic lakes's physical limnology and volcanology, to convert VOLADA_Africa 2.0 into a useful tool to better assess future volcanic hazards related to the African volcanic lakes (Aka et al., 2017). The physical volcanology and petrogenetic aspects of some lake-hosting areas, however, have largely increased our insights in single cases (Chapman et al., 1998; Barker et al., 2000; Freeth and Rex, 2000; Anema and Fesselet 2003; Haileab et al., 2004; Deruelle et al., 2007; Aka et al., 2008, 2018; Ngwa et al., 2010; Bruhn et al., 2011; Nkouandou and Temdjim, 2011; Ngos and Giresse, 2012; Temdjim, 2012; Aka and Yokoyama, 2013; Tchamabe et al., 2013; Rufer et al., 2014; Asaah et al., 2015; Delalande-Le Mouëllic et al.,

FIGURE 3 | Panoramic view of Lake Nyos, Cameroon, showing the system of the three artificial degassing pipes near the horizon (picture by DR).

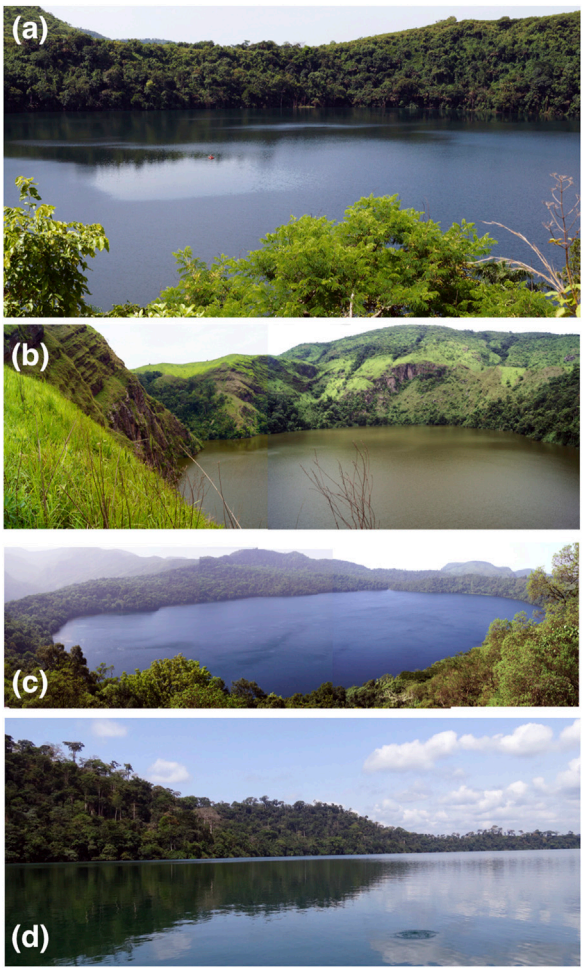

FIGURE 4 | Views of the Cameroonian maar lakes **(A)** Elum, **(B)** Enep, **(C)** Oku and **(D)** Barombi Mbo (pictures **(A–C)** by Issa, picture **(D)** by DR).

2015; Balashova et al., 2016; Pouclet et al., 2016; Jolie, 2019; Venturi et al., 2019). Nevertheless, the general number of these studies remains limited in many areas.

The African volcanic lakes were pin-pointed by decimal coordinates by scanning the Earth's surface through GoogleEarthPro (https://www.google.it/intl/it/earth/index.html) and OpenStreetMap (https://www.openstreetmap.org/) web sources (**Figure 1**), resulting in an interactive VOLADA-Africa 2.0 spreadsheet (**Table 1**), free available through VHub (https://vhub.org/groups/iavceicvl/resources). Lakes were ordered by country. Where available, the GVP number (http://volcano.si.edu/search_volcano.cfm) (Global Volcanism Program), its elevation above sea level, and the volcano and type of volcano the lake belongs to, are reported. Holocene volcanoes are exported on the map in **Figure 1** from the Global Volcanism Program; it is apparent that not all volcanic lakes coincide with Holocene active volcanoes, which implies that *1*) not all the lakes belong to Holocene active volcanoes, or *2*) the date of the last eruptions from the reported lakes is unknown.

A recent study by Graettinger (2018) deduced dimensionless morphometric parameters (ratios) to better describe maar *crater* morphology. The use of ratios provides the benefit to represent lake shape, regardless of the absolute dimensions of the craters. We here apply the same approach for the *lake* morphology of the 220 volcanic lakes in Africa, through the "ruler" and "polyogone" tools in GoogleEarthPro (**Figure 2**), with an accuracy of ± 5 m (**Table 1**; **Figure 2**). The Aspect Ratio (AR) is the ratio between the lake's minor (Dmin) and major (Dmax) diameter, with the minor diameter perpendicular to the major diameter:

$$AR = D_{min}/D_{max} \quad (1)$$

An AR closer to 1 implies an equant distance from the center of the lake.

The Elongation (EL) instead relates the area of a circle with the measured major diameter to the surface area of the lake (A). EL better describes asymmetrical morphologies compared to AR.

$$EL = A/[\pi\,(Dmax/2)^2] \quad (2)$$

The Isoperimetric Circularity (IC) compares the lake surface area with the area (A) of a circle with the same perimeter (p):

$$IC = 4\pi A/p^2 \quad (3)$$

Perfectly circu ar lake shapes have IC values near 1 or equal to 1, whereas lake shapes with a varying angle of curvature along their perimeter deviate further from 1.

A simple statistical approach (histograms) of the morphometric data for the African volcanic *lakes* is applied and compared to the data provided by Graettinger (2018) for *maar craters* in the world.

VOLADA_Africa 2.0: Country by Country

The updated database VOLADA_Africa 2.0 (**Table 1**) counts a significantly higher number (220) of volcanic lakes in Africa, compared to the 97 lakes in the original version of VOLADA (Rouwet et al., 2014). This large difference results mainly from the inclusion of numerous lakes in Uganda, Kenya, and Madagascar,

previously not counted. Volcanic lakes in Africa are often located in remote and/or low population density regions (**Figure 1**). The country with most volcanic lakes is Uganda (81), followed by Kenya (37), Cameroon (33), Madagascar (28), Ethiopia (19), Tanzania (6), the minor islands (i.e. Annobon, Bioko and Tristan da Cunha, West of the continent; and Karthala, Mohéli and Mayotte, Southeast of the continent, (9), Rwanda (2), Sudan (2), D.R. Congo (2), and Libya (1).

Cameroon

The pioneering study by Kling (1988) on the limnology of 39 Cameroonian lakes, of which 33 are of volcanic origin, forms the basis of the revised catalogue for Cameroon. Recent insights on the chemical and stable isotopic composition of 17 of the 33 Cameroonian volcanic lakes came from Issa et al. (2014), which followed the cataloguing philosophy adopted by Kling (1988), and our current study. Needless to say, Lakes Nyos (**Figure 3**) and Monoun are arguably two of the most studied volcanic lakes on Earth. Well studied aspects for Lakes Nyos and Monoun are:

(5) the degassing dynamics of the 1984 and 1986 gas bursts (Freeth and Kay, 1987; Kling et al., 1987; Sigurdsson et al., 1987; Barberi et al., 1989; Kanari, 1989; Tazieff, 1989; Freeth, 1990; Freeth, 1992; Evans et al., 1993; Freeth, 1994);
(6) the hazard assessment mainly based on the chemistry of lake water and dissolved gases (Sano et al., 1987, 1990; Tuttle et al., 1987; Kling et al., 1989; Kusakabe et al., 1989, 2000, 2008; Lockwood and Rubin, 1989; Giggenbach, 1990; Nojiri et al., 1990, 1993; Faivre Pierret et al., 1992; Kusakabe and Sano, 1992; Tietze, 1992; Evans et al., 1993, 1994; Kantha and Freeth, 1996; Tanyileke et al., 1996; Nagao et al., 2010; Yoshida et al., 2010; Issa et al., 2014; Tassi and Rouwet, 2014; Anazawa et al., 2019; Kusakabe et al., 2019);
(7) the risk mitigation through artificial degassing (since 2001, intensified since 2011 and ongoing; Halbwachs and Sabroux, 2001; Halbwachs et al., 1993, 2004, 2020; McCord and Schladow, 1998; Schmid et al., 2003, 2004, 2006; Kling et al., 2005; Ohba et al., 2017; Saiki et al., 2017; Yoshida et al., 2017);
(8) the dam stability and its recent (2014–2015) reinforcement (Lockwood et al., 1988; Freeth and Rex, 2000; Aka et al., 2008; Aka and Yokoyama, 2013; Fantong et al., 2015; Tanyileke et al., 2019);
(9) the topic of numerous projects (e.g. NyMo degassing, France-Cameroon; SATREPS, Japan-Cameroon), studies and review papers (Aka, 2015; Kling et al., 2015; Kusakabe, 2015, 2017; Tanyileke et al., 2019).

Besides Lake Nyos and Lake Monoun, the Oku Volcanic Field in NW Cameroon (**Figure 1C**) hosts 13 other maar lakes (**Table 1**). Lake Wum (Kusakabe et al., 1989), near the homonymous city (>80,000 inhabitants), and Lake Bambuluwe (Freeth, 1990) were subjected to a vertical sampling soon after the Lake Nyos gas burst, and resulted gas-free and not-heated from below. The remaining 12 lakes of the Oku Volcanic Field (i.e. Baleng, Banefo, Bambili, Benakuma, Elum – **Figure 4A**, Enep – **Figure 4B**, Mfouet, Nchout, Nyi, Negop Baghang, Oku – **Figure 4C**, and Kuk) are less studied (**Table 1**; Issa et al., 2014).

During the 9th Workshop of the IAVCEI Commission on Volcanic Lakes (March 2016), Barombi Mbo (Maley et al., 1990; Kling et al., 1991; Tchamabe et al., 2013; **Figure 4D**), the maar lake with the largest surface area in Cameroon (**Table 1**), was subjected to a pioneering physical limnological and fluid geochemical survey. Within the philosophy of the "Nyos bias," lowering CTD probes and water and dissolved gas sampling along the vertical profile of the 110 m deep lake, revealed that the gas stored in deep lake strata is far from reaching near-threshold pressures to cause a limnic gas burst. This "non-result" does have strong implications on the hazard assessment for the inhabited shores of Barombi Mbo, and the nearby city of Kumba (>125,000 inhabitants). The three remaining maar lakes in the Tombel Graben (Dissoni, the only 5 m deep Barombi Koto and Mboandang) are less studied (Kling, 1988; Issa et al., 2014).

Mt Manengouba, a 2,411 m high shield volcano overlain by a stratovolcano located in the Northern sector of the Tombel Graben, is probably the second most famous volcano in Cameroon after the active Mt Cameroon (Pouclet et al., 2014). The 3 km wide caldera hosts two "twin crater lakes," Manengouba Male and Manengouba Female (**Figure 5**). The dark colored Manengouba Female is the second deepest volcanic lake in Cameroon (168 m), after Lake Nyos, while Manengouba Male is 90 m deep and green colored inside a steep-walled crater basin. Both lakes are inactive and fed by meteoric water, hence the color difference is explained by different microbial activity (Issa et al., 2014) reported, however, a weak degassing activity of Mt Manengouba, stressing the need for a monitoring setup for these summit crater lakes.

The Debunscha lakes (big and small, 7.27×10^4 m^2 and 3.51×10^3 m^2, respectively) are small maars located a few hundred meters from the Atlantic Ocean at the foot of Mt Cameroon. The massive amounts of rainfall in the coastal area (12,000 mm of

FIGURE 5 | The Manengouba Female (left – black) and Manengouba Male (right – green) crater lakes of Mt Manengouba (Cameroon; picture by P. Hernández).

FIGURE 6 | Crater lake of Mt Bisoke (Rwanda) (November 2013; picture by SC).

rain/year; Issa et al., 2014) and strong winds change the isotopic composition of the lake water, despite being in mass balance equilibrium with the meteoric rain input (13.5 m deep, Debunscha big). Their nearness to the ocean (<50 m), and at the center of the most active sector of the Cameroon Volcanic Line (CVL hereafter; Aka et al., 2001, 2004) between Mt Cameroon and the island of Bioko, suggests that the Debunscha maar lakes were formed by phreatomagmatic eruptions from satellite vents of Mt Cameroon interacting with seawater inside the coastal aquifers (Ngwa et al., 2010, 2017).

To the Northeastern extent of the CVL seven maar lakes are located near the city of Ngaounderé (>260,000 inhabitants in 2005) in the Volcanic Plateau of Adamawa (Aka et al., 2018; and references therein). Kling (1988) put them on the map by studying their basic physical limnological characteristics, while recently Issa et al., 2014 tackled them for their stable isotopic composition of the water. Given its unique location between the Sahel and the sub-equatorial rainforest, paleoclimate during the Pleistocene-Holocene was reconstructed in recent studies (Ngos and Giresse, 2012; N'nanga et al., 2019), based on the geochemistry and mineralogy of sediments from Lake Fonjak, Mbalang and Tizong. Issa et al. (this topic collection) demonstrated a high similarity to Lakes Nyos and Monoun, and suggest that these seven lakes should become a priority in future monitoring efforts.

D.R. Congo

Lac Vert, less than 2 km north of the western sector of the Lake Kivu main basin (**Figures 1A,B**), fills up the central sector (695–385 m) of three nested craters, interpreted as a maar complex. Lake Kivu, a major rift lake of the Western branch of the East African Rift (EAR hereafter), creates an ideal hydrological and tectonic setting to create phreatomagmatic volcanism near its shores. Poppe et al. (2016) emphasized the importance of phreatomagmatic volcanism from a hazard point of view in the area between Lake Kivu and the famous, active volcanoes of the Virunga Volcanic Province: Nyamulagira and Nyiragongo. Moreover, Lac Vert is situated northeast of the Kabuno Basin, the northwestern sub-basin of Lake Kivu that is almost cut off entirely from Lake Kivu. The Kabuno Basin area is characterized by more magmatic gas signatures ($^3He/^4He$ ratios of 5.4 Ra), and the inland degassing features tend to have similar degassing sources as Nyiragongo ($^3He/^4He$ ratios of 8.7 Ra): Sake (west of Lac Vert, $^3He/^4He$ ratios of 7.7 Ra) and the CO_2-rich degassing areas (Mazukos, $^3He/^4He$ ratios of 8.4 Ra; Tedesco et al., 2010; Vaselli et al., 2015) towards Lac Vert. The depth of Lac Vert is unknown; CTD measurements and water and gas sampling along the vertical profiles still lack.

A small lake partially occupies the Kirunga tuff ring, less than 100 m from the Lake Kivu shore. Kirunga is one of the 15 eruptive centers recognized along the northern shore of Lake Kivu, here occasionally filled by a lake (Poppe et al., 2016). Besides the direct gas hazard that could originate from the lakes (Lac Vert), the occurrence of renewed phreatomagmatic volcanism due to effective magma-water interaction with Lake Kivu is not excluded in the future for the densely inhabited Goma area, home to at least 750.000 people (note: at the moment of writing, the crisis of Nyiragongo volcano is ongoing, and includes this proposed scenario as one of the related hazardous outcomes).

Ethiopia

The maar lakes in the Bishoftu Volcanic Field in Central Ethiopia (**Figure 1A**) have been studied during the early 1960s for their physical limnology (Wood et al., 1976). They were recognised to turn over in winter (December), and do not show a stable stratification. A recent biolimnological study by Lemma (2009) on Lake Hora (35 m deep) and Lake Bishoftu Guda (55 m deep) show a seasonal decrease in temperature from 22–23°C at the surface to 20–21°C at depth. Anoxic environments set in below 5–10 m depth. These physical characteristics demonstrate that the "Bishoftu lakes" are unstably stratified, solar heated and highly sensitive to seasonal, and even diurnal variations. From the hazard point of view, this implies that these lakes are inefficient in storing CO_2 in their bottom waters, regardless of the fact that this recharge effectively occurs, which does not seem to be the case. The city of Debre Zenit (approx. 100,000 inhabitants) surrounding the lakes is hence not exposed to possible Nyos-type hazards.

FIGURE 7 | Lake Empakaai (seen from the southwest), Northern Tanzania (picture by B. Fontaine). Volcanoes in the back are Oldoinyo Lengai (left) and Kerimasi (right).

The lakes in the Butajiri Silti and Bilate River Fields are unreported in the scientific literature (level of study 5). A geodynamic model for the Butajiri Silti Field was proposed by Hunt et al. (2020), however, they did not enter in detail on the existence of volcanic lakes in the area (e.g. Ara Shetan, **Table 1**).

Mt Dendi is an inactive volcano peaking at 3,260 m a.s.l. with a 4 km-wide caldera like crater. Inside this crater, a peculiar dumbbell-shaped lake filled with meteoric water is hosted. Still, in the Central highlands of Ethiopia, 13.5 km Southwest of Mt Dendi a similarly shaped volcano, Mt Wonchi (3,450 m a.s.l.) houses an irregular-shaped crater lake that fills part of the 4.5 km wide summit caldera, also host to hot springs. Nevertheless, both large edifice volcanoes are inactive, and hence their crater lakes do not seem to be a topic of interest regarding natural hazard assessment. The extinct Mt Zuqualla volcano, 40 km south of Ethiopia's capital Addis Abeba, hosts Dembel crater lake.

The strongly rift-related soda Lakes Shala, Langano, Chitu and Abijatta are arguably maar lakes (Le Turdu et al., 1999). The maar Lake Shala is approximately 87 m deep (max depth 266 m) and has a pH ranging from 9.8 to 10.2, depending on the season. No clear stratification appears, coinciding with the fact that "soda lakes" are often sensitive to external changes (Osato et al., 2016). Lake Zengena appears to be a small solitary maar lake (approx. 450 m diameter) towards the Lake Tana wetlands area in Northwestern Ethiopia.

Kenya

Of the 33 volcanic lakes in Kenya (**Figure 1A**), 27 are located on the flanks of the inactive (eruptive period between 3.1 and 2.6 Ma) large-edifice stratovolcano, Mt Kenya (5,199 m a.s.l.), the second highest mountain in Africa, after Kilimanjaro, in Tanzania. The volcano does not show a clear summit crater, and all lakes appear to be distributed in satellite vents and craters, or filled-up glacial depressions on the volcano flank (Loomis et al., 2012). No data are available on the chemical and physical properties of these lakes. Hydrothermal activity is not reported for Mt Kenya.

Three peculiar maar lakes (Tilapia lakes) are formed on the Central Island of Lake Turkana, a major rift lake in the EAR. These lakes are unstudied, but their setting and appearance suggest that they are formed by phreatomagmatic eruptions beneath Lake Turkana. Another unnamed maar-type lake is found near the southern shores of Lake Turkana.

The shield volcano Marsabit (1,707 m a.s.l.), towards Northern Kenya, is dotted by 22 maars, three of which are recognized to contain lakes. No further information is available on these maar lakes.

"Crater Lake" just East of the large freshwater (non-volcanic) Lake Naivasha fills in a third of a maar. Lake Naivasha is a large (150 km^2), shallow (17 m) basin fed by extended aquifers (wetland) (Yihdego and Becht, 2013; Fazi et al., 2018), that arguably provided an aquifer through which phreatomagmatic eruptions breached, giving origin to the "Crater Lake," or Lake Sonachi. The temperature and alkalinity increase with depth (max 7 m) at Lake Sonachi, which suggests sublacustrine input of alkaline springs. Despite its shallow depth, Lake Sonachi is permanently stratified (meromixis) at depth due to the high content of organic carbon, but mixes its upper water layers even in day-night cycles. The high pH (9.5) limits CO_2 dissolution in bottom waters, where instead a CH_4 environment reigns (Venturi et al., 2019). Lake Sonachi is an exotic, small "bio-activity" crater lake (Cabassi et al., 2014; Rouwet, 2021).

Libya

Miocene to recent intracontinental volcanic fields compose distinct landforms in Libya's Sahara region. In these volcanic fields, monogenetic volcanic bodies, such as scoria and spatter cones, are the most dominant volcano types; however, broad craters with low rims are commonly interpreted as maar volcanoes in spite that most of them are dry, or host only shallow playa lakes. In Al Haruj al Abyad broad maar-like depressions are common (Németh, 2004; Martin and Németh, 2006; Cvetkovic et al., 2010; Bardintzeff et al., 2012).

The most recently active volcano in Southern Libya, Waw an Namus (**Figure 1A**), figures as a black dot of tephra in the Quaternary yellow sediments of the Sahara Desert (Bardintzeff et al., 2012). The volcano, a broad volcanic depression, is thought to be a satellite vent of the Al Haruj Volcanic Province to the North (Bardintzeff et al., 2012; Elshaafi and Gudmundsson, 2016, 107, 2018). Inside the 4 km-wide depression, inferred to be a maar volcano, a 150 m cone rises up to 547 m a.s.l. Three shallow, warm and saline lakes flank the base of the tephra cone. Although apparently young sulfur and (probably) alunite deposits are reported (Bardintzeff et al., 2012), there is no further mention of hydrothermal activity. We interpret the salinity and temperature of the three Waw an Namus crater (or intracaldera) lakes as resulting from solar heating and consequent steady evaporation, without further implications for volcanic hazard.

Madagascar

Considering their shapes, observed from satellite images, and their geology from rare studies (Rasamimanana et al., 1998; Bardintzeff et al., 2010; Rufer et al., 2014), the volcanic lakes in Madagascar appear to be maar lakes. From North to central

Madagascar, maar lakes are located in several volcanic fields: Ambre Bobaomby (six lakes), Farihy Antanavo (one single lake), Nosy Be Island (NW Madagascar, nine lakes), Tritrivakely (two lakes; Sibree, 1891; Gasse et al., 1994; Gasse and Van Campo, 1998, 2001; Williamson et al., 1998), and Itasy (10 lakes) (**Figure 1A**). Lake Itasy is an irregularly shaped large lake (6 × 7 km approx.), clearly composed of multiple craters, ruling out its origin as a caldera basin. Lake Itasy is surrounded by many smaller (unnamed) maars. Lake Tritriva shows that maar lakes are not necessarily circular or ellipse-shaped, as recently conveyed by Graettinger (2018), pointing to a multiple-vent origin and/or erosional enlargement due to landslides along the inner crater wall. To the best of our knowledge, no data are available on water chemistry, or physical limnological characteristics of the maar lakes in Madagascar.

Rwanda

In the shadows of the infamous volcanoes Nyiragongo and Nyamulagira, Mt Bisoke stratovolcano (3,711 m a.s.l.) straddles the border between Rwanda and D.R. Congo (Barette et al., 2017) (**Figures 1A,B**). The summit contains a circular shaped crater lake (**Figure 6**), with a diameter of approximately 300 m. The lake was sampled in November 2013 and analyzed for its water chemistry (by SC and Giovanni Bruno Giuffrida), whereas its water temperature varied from 10° to 15°C, with a measured pH of 6.27. The chemistry did not show any evidence of hydrothermal activity, reflected by very low SO_4 and Cl contents (<3 and <1 mg L-1, respectively), although a local guide reports on vague memories of the smell of sulfur close to the water surface. Despite this limited data set, we argue that Mt Bisoke is in a state of quiescence after it last erupted in 1957. If the volcano reawakens in the future, the physical and chemical properties of the crater lake are suspected to show variations, possibly detectable by satellite imagery (e.g. lake disappearance upon evaporation, color changes).

The tiny crater lake (27–28 m) at the >4,100 Muhavura stratovolcano in the Virunga Volcanic Province, at the border between Rwanda and Uganda, has well preserved its pollen-record for the Holocene (McGlynn et al., 2013), but does not show evidence of volcanic activity.

Sudan

The 3,042 m high Deriba Caldera is the most spectacular feature of the Jebel Marra Volcanic Field in the Darfur region of Western Sudan (Burton and Wickers, 1966; Hammerton, 1968; Vail, 1972; Davidson and Wilson, 1989; Franz et al., 1997) (**Figure 1A**). Inside the 5 km-wide steep-walled caldera, formed 3,500 yr B.P. during voluminous pumice fall eruptions, a 700 × 1000 m-wide crater lake fills a horseshoe-shaped crater. A second lake is formed to the Northeast, at the lower rim of the caldera, probably as an affluent basin of rain falling inside the caldera capture area. To the best of our knowledge, no limnological or geochemical information is available for the two crater lakes. Nevertheless, it is worth noting that fumarolic activity has been observed inside the caldera in relatively recent times (Burton and Wickers, 1966).

One of the approximately 700 vents of the Pliocene to Holocene Meidob Volcanic field in Western Sudan, 150 km Northeast of the Deriba Caldera (**Figure 1A**), hosts a 180 m-diameter maar lake, without manifestation of any activity. The small monogenetic Bayuda Volcanic Field (BVF; 480 km^2) about 700 km NE from the Meidob Volcanic Field, comprises at least 53 cinder cones and 15 maar volcanoes in the Bayuda desert of northern Sudan of Quaternary age. The largest maar (800 m in diameter and 386 m deep) in the area is the Hosh Ea Dalam (32°35′38,32″E, 18°24′29,07″N). None of the 15 maars has a permanent lake, and are only shallow "salt pans" (Almond et al., 1969; Lenhardt et al., 2018).

Tanzania

Two renowned volcanic lakes are located in the Ngorongoro Crater Highlands in Northern Tanzania (**Figure 1A**): Lake Empakaai (or Lake Emakat, **Figure 7**) and Lake Magadi. Empakaai crater lake is 79 m-deep and well studied for its palynology and paleoclimate record from water and sediment cores (Muzuka et al., 2004; Ryner et al., 2006). The lake water chemistry reflects a high salinity (Total Dissolved Solid contents between 12,000 and 14,000 mg L-1), with Na and K as main cationic solutes (500–600 mg L-1 and 400–500 mg L-1, respectively; Muzuka et al., 2004). This composition probably originates from water-rock interaction with trachytic and phonolitic magmas (Fontijn et al., 2012), consequently enriched by enhanced evaporation by solar heating. No clear evidence of a hydrothermal system exists to hypothesize alternatively.

Northeast of Lake Empakaai (**Figures 1A**, **7**), passing the famous natro-carbonatitic volcano Oldoinyo Lengai (Keller and Zaitsev, 2012), Lake Natron fills the rift depression towards the border with Kenya. Lake Natron is not a volcanic lake, but rather a "rift lake in a volcanic environment," and we hence choose to not include it in VOLADA_Africa 2.0 despite its particular chemistry resulting from the water-rock interaction with carbonatitic country rocks: Na-HCO_3-CO_3 with a pH as high as 9.5 (*see* Pecoraino et al., 2015, for a review,; Fazi et al., 2018). Lake Magadi, Southeast of Lake Empakaai, partially fills the almost 20 km-wide Ngorongoro crater and hosts a saline brine, similar to Lake Empakaai. The exotic water chemistry of the three lakes (Empakaai, Magadi and Natron) hence results from solute enrichment by evaporation from an endorheic basin after water-rock interaction with the exceptional host rocks of the Ngorongoro area.

Lake Chala is located on the lower Eastern flanks of Mt Kilimanjaro, Africa's highest peak, at an elevation of 880 m a.s.l., and is shared with Kenya (**Figure 1A**). We here classify Lake Chala as a caldera lake. The lake is 94 m deep and has a nearly triangular shape with a main diameter of approx. 2 km. Lake Chala has been well studied in recent years in terms of palynology and limnology (Barker et al., 2013; Buckles et al., 2014, 2016; van Bree et al., 2018), although volcanology-focussed information lacks. The stratification of the lake is highly sensitive to seasonal variations (e.g. multiple rainy "seasons" per year; van Bree et al., 2018), which makes us suspect that long-term accumulation of gases in bottom waters is strongly inhibited–if gas input occurs in the first place.

The maar lakes in Southern Tanzania (Lake Masoko and five others in the Rungwe Volcanic Province; Fontijn et al., 2012), near the northern shores of Lake Malawi, are relatively well studied for their hydrology, (paleo)limnology, isotopy and palynology (Williamson et al., 1999; Barker et al., 2000; Delalande et al., 2008). The small maar lakes are sensitive to climate changes and hence ideal to reconstruct paleoclimate in the region, and to store ash records of past volcanic eruptions in the area (Fontijn et al., 2012). As the lakes in Northern Tanzania, the six "Mbaka lakes" are saline; suspicion exists on a possible hydrothermal input from beneath these lakes, which invites to future fluid geochemical surveys and hazard analyses for the area.

Lake Ngozi (83 m deep) tops one of the three major volcanoes, the 2,620 m-high homonymous volcano, in the Northwestern part of the Rungwe Volcanic Province (Fontijn et al., 2012) (**Figure 1A**). The irregular shape of the 3 km-wide collapse caldera and its crater lake is in agreement with the presumed young age of the crater and the latest magmatic eruption (<1 ka; Fontijn et al., 2010). A pioneering study on the water chemistry of Lake Ngozi (Delalande-Le Mouëllic et al., 2015) hypothesizes that the lake is affected by geothermal input (Na-Cl-rich, Mg-poor) and hydrothermal activity (pH 6.4–6.9, SO_4-rich steam heated waters), similar to the caldera lakes in El Salvador (Cabassi et al., 2019; Rouwet, 2021). Dominant CO_2 degassing (δ13C-DIC from +2.8 to +5.8‰, Delalande-Le Mouëllic et al., 2015) is probably of magmatic origin as also suggested by the high $^3He/^4He$ ratios (7–8.3 Ra, de Moor et al., 2013). The absence of any thermal and chemical stratification and the high pCO_2 along the water column results in diffuse CO_2 degassing at the lake surface (Jolie, 2019). This CO_2 degassing is structurally controlled, along E-W trending faults at the southern parts of the caldera lake, near the presumably last eruptive vent (Fontijn et al., 2010). Funnel-shaped depressions along this fault reach lake bottom temperatures up to 89°C (i.e. near boiling at the elevation of the lake, 2,060 m a.s.l.) (Jolie, 2019). These findings suggest that Lake Ngozi is topping an active volcano that could escalate into unrest in the future. A similar, though more vigorous CO_2 degassing dynamics was observed at Kelud crater lake, Indonesia, prior to the 2007 dome extrusion eruption (Caudron et al., 2012).

Moreover, we can mention that there are many maar-like dry craters in Tanzania. The genetic origin of these maars is currently under debate, as they arguably seem to be inexplicable by the general phreatomagmatic model (Mattson and Tripoli, 2011; Berghuijs and Mattson, 2013). This alternative model would imply that they could have been water filled during wet periods. Dry maars are, however, a recurrent feature in monogenetic volcanic fields, in Africa and elsewhere.

Uganda

The 81 volcanic lakes in Uganda are distributed in four volcanic fields: the Bunyaruguru (30 lakes) and Katwe-Kikorongo (eight lakes) Volcanic Fields in the South, near the EAR rift lakes George and Edward, and Ndale-Kasenda (36 lakes) and Fort Portal (seven lakes) Volcanic Fields in the North (Rumes et al., 2005; Stoppa and Schiazza, 2013) (**Figures 1A,B**). All the 81 lakes are classified as maar lakes (Melack, 1978). An early study by Mungoma (1990) revealed that the lake water chemistry of eight lakes in the Katwe-Kikorongo (Kikorongo, Nyamunyuka, Katwe, Bunyampaka and Kitagata; Lowenstein and Russell, 2011) and Bunyaruguru (Maseshe, Bagusa, Mahega) are highly saline (Conductivity 16.3 to 455 mS cm-1) and alkaline (pH 9–10.5), caused by water-rock interaction and enhanced evaporation of the generally small and shallow maar lakes. Solar heating results in mesothermal stratification of the studied lakes, shown by inverted vertical temperature profiles. Three water types are distinguished: carbonate-chloride- and chloride-type lakes in the Katwe-Kikorongo, and carbonate-sulfate-type lakes in Bunyaruguru.

In their turn, the deeper lakes in Uganda (e.g. Lake Kyaninga, 220 m deep, the largest lake in the Fort Portal Volcanic Field) seem to be geothermally heated, as shown by heated bottom waters. Lake Kyaninga is arguably meromictic (i.e. permanently stratified) below 100 m depth (Cocquyt et al., 2010). The particular chemistry, with high Cl, HCO_3 and SO_4 concentrations (up to 149, 108 and 64 mg L-1, respectively), rises curiosity on generic processes behind their formation and the need for renewed hypotheses and conceptual models, regarding natural hazard assessment. A recent study by De Crop and Verschuren (2019) on 11 maar lakes in Uganda stressed that high-frequency monitoring of physical-chemical parameters along water columns in tropical lakes is a must to better understand water mixing at various time scales (days to decades). The limnological control on water mixing can have implications on hazard, especially when gas or heat enters lake bottoms.

African Minor Islands

Peculiarly, some of the minor islands around the African continent host volcanic lakes. The islands of Bioko and Annobon (Equitorial Guinea) are shield volcanoes along the ocean-ward side of the CVL (Aka et al., 2001, 2004) (**Figures 1A,C**), topped by crater lakes Moca and Pot, respectively. Bioko, together with Mt Cameroon, is considered the most active centre of the CVL (Aka et al., 2004).

In the summit crater of Queen's Mary Peak (2,060 m a.s.l.), on the remote island of Tristan da Cunha (a British Overseas Territory, South Atlantic) (**Figure 1A**), a heart-shaped shallow lake filled with meteoric water is present (**Figure 8A**), whereas three aligned maar lakes (**Figure 8B**) –called "the ponds" by the locals (1, 2, 3 in **Figure 8C**)– are found on the Northeastern lower flank of the stratovolcano. The peculiar setting might teach us that maar volcanoes can form on top of composite polygenetic volcanoes, if the environment (e.g. ground-water and/or surface water availability) is favorable to produce explosive magma-water interaction (Kereszturi et al., 2011, 2014; Smith and Németh, 2017; Geshi et al., 2019). In the case of Tristan da Cunha, the maar lakes could have been formed by magma interacting with the incursion of marine water into the near-coastal aquifer (Németh and Cronin, 2009, 2011). The last eruptive activity that occurred in 1961–1962 did not originate from the summit crater, but on a coastal plateau near the northern shores of the island (Baker et al., 1964).

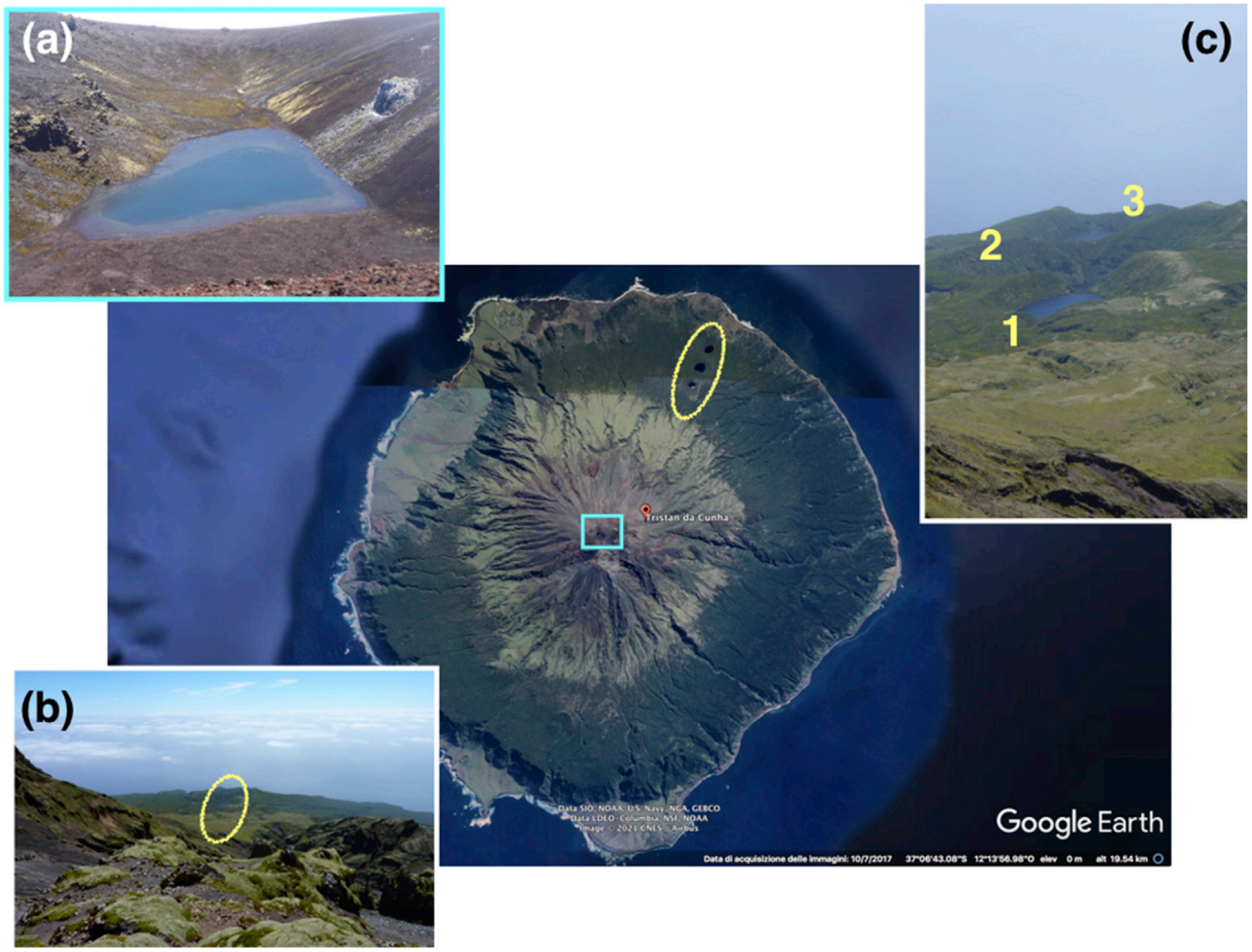

FIGURE 8 | (A) The heart-shaped crater lake of the St. Mary's Peak of Tristan da Cunha, Southern Atlantic Ocean (turquoise square in inset map); **(B)** location of the aligned maars at northern flank of Tristan da Cunha island (yellow ellipse in inset map); **(C)** the three maar lakes, called "the ponds." Note: the yellow patches to the right of "pond 1" are lichens, not sulphur remnants of extinct fumaroles (pictures by A. Hicks).

Southeast of Africa, in the Comores Archipelago, the crater of the Karthala shield volcano was filled by a green lake prior to the 2005 eruption (Pons, 2006) (**Figure 1A**). The lake is ephemeral as the open-conduit volcano is often a heat emitter too high for the lake to sustain. The Dziani Boundouni lake on Mohéli Island (Comores, **Figure 1A**) is a maar lake with, arguably, at least two nested craters. Lake Dziani Dzaha, a shallow (5 m deep) maar lake on a minor island east of Mayotte (Comores, **Figure 1A**) is located only 240 m from the Indian Ocean, and its chemistry is hence affected by seawater. The lake is studied for its microbialites (i.e. sediment aggregates formed by microbial activity) and microbial productivity (Fouilland et al., 2014; Dupuy et al., 2016). Volcanic hazard assessment remains an untouched topic, despite the manifestations of minor CO_2 degassing, probably of volcanic origin (https://www.youtube.com/watch?v=XsgoWl728hM).

All nine "off-shore" volcanic lakes in Africa are poorly studied, and probably mainly fed by meteoric water.

MORPHOMETRIC ANALYSIS

From the 220 volcanic lakes in Africa, 172 are classified as maar lakes, based on their volcanic setting (*see* **section 2**) and morphological aspects (**Table 1**). Whereas approximately 54% of the maars (i.e. craters) in the MaarVLS database by Graettinger (2018) are located at elevations below 750 m a.s.l., about 86% of the African volcanic lakes are located above 800 m a.s.l., despite being predominantly maar lakes (**Figure 9A**). In fact, the maar lakes in Kenya, Tanzania and Uganda are located in volcanic fields in the highlands created by the horst-graben structure of the EAR, in Cameroon in the CVL, and in the central highlands of Madagascar. Crater lakes on the stratovolcanoes Dendi, Wonchi and Zuquala in Ethiopia, Mt Kenya in Kenya and Bisoke and Muhavura in Rwanda are hosted in craters or glacial depressions above 2,800 m a.s.l. Lakes at low elevations (0–300 m a.s.l.) are found on the islands (Nosy Be Island in Madagascar and off-continent islands), near the Atlantic Ocean in Cameroon, or in the Sahara Desert in Libya.

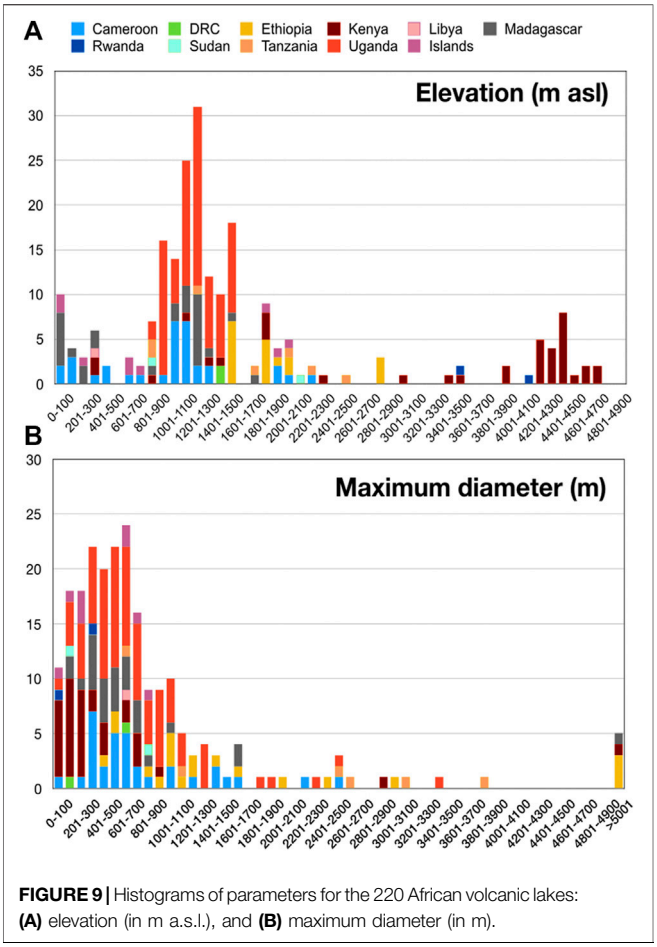

FIGURE 9 | Histograms of parameters for the 220 African volcanic lakes: **(A)** elevation (in m a.s.l.), and **(B)** maximum diameter (in m).

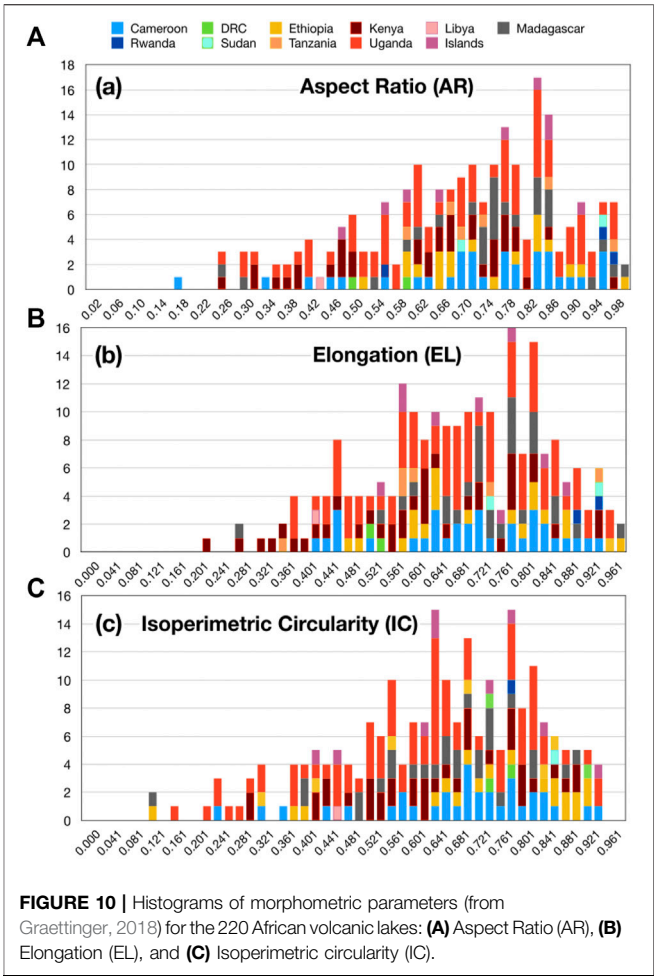

FIGURE 10 | Histograms of morphometric parameters (from Graettinger, 2018) for the 220 African volcanic lakes: **(A)** Aspect Ratio (AR), **(B)** Elongation (EL), and **(C)** Isoperimetric circularity (IC).

Excluding the four caldera lakes and one composite maar (Lake Itasy, Madagascar), the distribution of the maximum diameter of African volcanic lakes peak between 400 and 800 m, similar as for maar lakes worldwide (Graettinger, 2018) (**Figure 9B**). In conclusion, the African volcanic lakes are hence merely maar lakes, but are clearly located at higher elevations, if compared with maars worldwide (Graettinger, 2018).

The average Aspect Ratio (AR, i.e. a measure of the distance from the centre of the lake for minor and major axis) for the African volcanic *lakes* of 0.69 (±0.18 STDEV) is lower than for maar *craters* worldwide (0.81, Graettinger, 2018), also reflected in **Figure 10A** as a more smeared out distribution towards lower AR values. The AR peaks at 0.82–0.86, with a secondary peak at 0.74–0.80 (**Figure 10A**). Only 4% of the AR ratios are above 0.96, whereas 17% are below 0.5. The irregularly shaped Lake Monoun has the lowest AR (0.17), despite being a maar lake. Its river flow-through nature can explain its irregular shape, stressing a dynamic sedimentary regime for Lake Monoun. Indeed, Graettinger, 2018 suggested that maars with anomalous shapes should become a focus for future research to better understand the interaction between local hydrology and its volcanic creation; multiple overlapping maar craters corroborate polygenetic maar formations.

The Elongation (EL, i.e. a measure of the asymmetry of the lake shapes) of African volcanic lakes averages 0.69 (±0.16 STDEV), again lower than the EL values for maar *craters* (0.80 ± 0.12; Graettinger, 2018). 93% of EL values are below 0.92 (versus 85% for maar *craters*); 16% are below 0.5 (versus 5% for maar *craters*; Graettinger, 2018) (**Table 1**). EL peaks at 0.76–0.82 (**Figure 10B**). Although the lakes on the flanks of Mt Kenya weigh in this distribution, caldera and crater lakes do not deviate more from El = 1 than maar lakes do, hence suggesting that maar lakes in Africa appear more elongated with respect to maar craters worldwide. This observation can be explained by a structural control on the morphology of maar lakes and volcanism of the East African Rift system (e.g. Hunt et al., 2020), or more in general, that the maars are located in an extensional rift axis where hydrogeology also plays a role as they are low, longitudinal valleys.

Figure 10C represents a similar distribution of Isoperimetric Circularity (IC, i.e. a measure of the circularity of the lake shape) as for AR and EL. The average IC for African volcanic lakes is 0.66 (±0.18 STDEV), clearly lower than for maar *craters* worldwide (0.9 ± 0.08; Graettinger, 2018). IC values of 0.62–0.64 and 0.76–0.78 are the most common (**Figure 10C**). Contrary to the statistical

distribution for maar *craters*, only 6% of volcanic lakes in Africa have an IC value above 0.9 (versus 65% for maar *craters* worldwide), whereas 76% have an IC value below 0.8 (versus 9% for maar *craters* worldwide; Graettinger, 2018). For maar *craters*, IC values below 0.9 were explained to reflect a compound shape. Caution is needed to avoid over interpretation of the IC trends for African volcanic *lakes*, in the light of Graettinger, 2018 correct hypothesis for maar *craters*: *1*) lakes do not necessarily fill up entire circular-shaped craters, but can present with a more exotic, less circular morphology, and *2*) islands and peninsula in the larger lakes, considered in the calculation of A and p (**Eq. 3**) of the volcanic lakes, can drastically decrease the IC values. Nevertheless, the lower IC values resulting from (2) can be an additional argument in favor of polygenetic phreatomagmatic volcanism leading to irregular craters and lakes.

CONCEPTUAL MODEL: WHY ARE MAAR LAKES SO DOMINANT IN AFRICA?

Besides Lakes Nyos and Monoun, none of the African volcanic lakes are (well) studied regarding volcanic hazard assessment. Pioneering work on paleo-, bio- and physical limnology and hydroclimatology for lakes in Cameroon, Uganda, Kenya, Tanzania and Ethiopia (Kling, 1988; Eggermont et al., 2006; Kebede et al., 2009; Lemma, 2009; Russell et al., 2009; Giresse and Makaya-Mvoubou, 2010; Ryves et al., 2011; Garcin et al., 2012; Loomis et al., 2012; Garcin et al., 2014; Lebamba et al., 2016; De Crop and Verschuren, 2019) should guide volcanologists to shed light on the many poorly studied lakes in Africa (predominantly quoted "5" in VOLADA_Africa 2.0, **Table 1**) with the scope to better assess future natural hazards.

Besides the 26 glacial volcanic lakes of Mt Kenya (Loomis et al., 2012), about 89% (172) of volcanic lakes reported for Africa are maar lakes (**Table 1**). Africa does not host any peak activity lakes (i.e. acidic crater lakes overlying degassing magmatic-hydrothermal systems, often subjected to phreatic and phreatomagmatic eruptions; Rouwet, 2021), peculiar for such a large continent with active volcanoes (Global Volcanism Program, 2013). However, the continent does not manifest "classical" arc-type volcanism, but evidently hosts intraplate polygenetic volcanoes with a different chemical affinity than arc volcanoes. Hydrothermal activity is abundant, but is mainly related to the gradual break-up of the thick continental crust (e.g. EAR, **Figure 11**), and to mafic magmas.

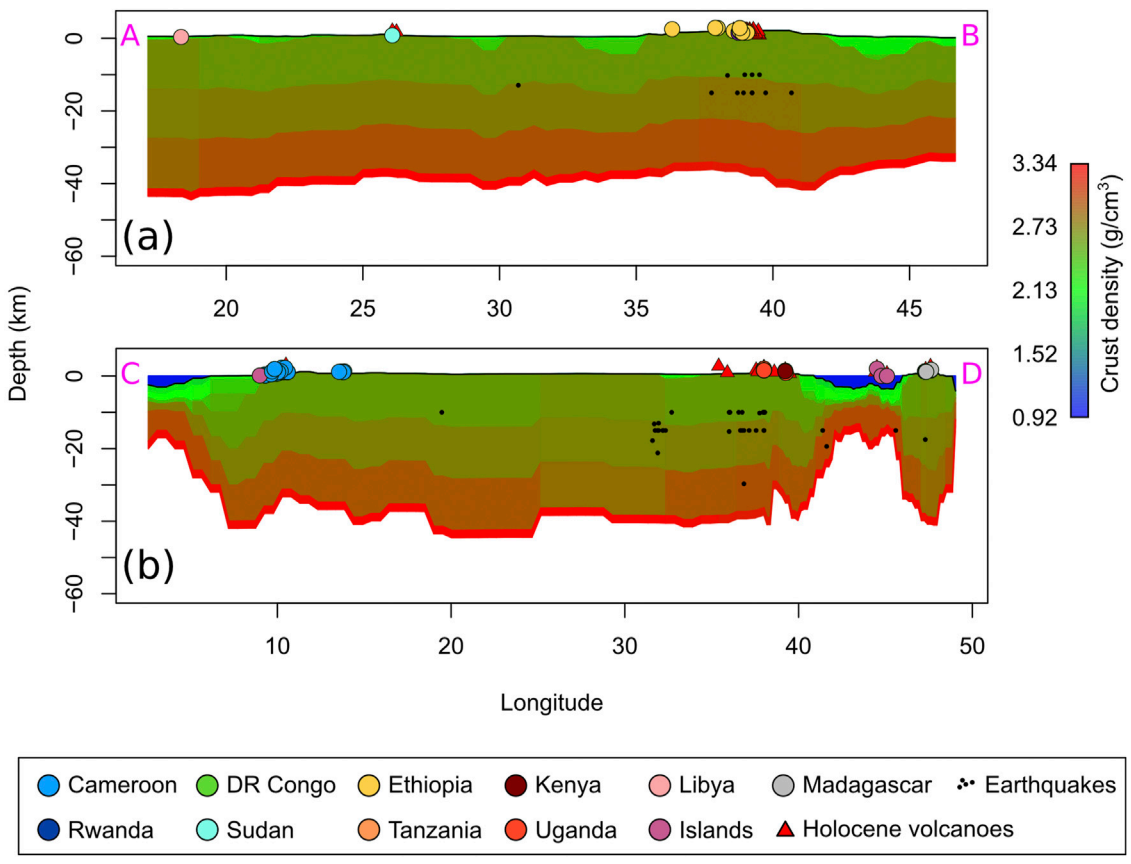

FIGURE 11 | Conceptual model to explain the abundant maar volcanism of the EAR and CVL, through a vertical section of the first 40–50 km through the Earth's crust (Laske et al., 2013). The transects A-B and C-D are traced in **Figure 1**. Holocene active volcanoes are exported from the Global Volcanism Program-Smithsonian database (https://volcano.si.edu/).

Stratovolcanoes or (dome) complex volcanoes with well-developed hydrothermal systems that provide the prototype settings to develop crater lakes on volcano summits (wet volcanoes; Caudron et al., 2015; Rouwet et al., 2015b), are relatively scarce in Africa. The EAR volcanism is MORB- or OIB-type leading to predominantly basaltic (Mt Cameroon; Mbassa et al., 2012; Kervyn et al., 2014; Adams et al., 2015; Nyamulagira, Nyiragongo; Pouclet et al., 2016; Karthala, outside the EAR; Class et al., 2009; Pelleter et al., 2014), or sporadically carbonatitic volcanism (Oldoinyo Lengai; Kervyn et al., 2014; Keller and Zaitsev, 2012; Weidendorfer et al., 2017). Despite the tropical climate and abundant rainfall in subsaharan Africa, insufficient constraints are met to sustain crater lake presence at the active volcanoes (Pasternack and Varekamp, 1997), for example: *1*) a too high heat flux from open-conduit volcanoes (i.e., lava lakes instead of "water lakes" in most extreme cases, e.g. Nyiragonogo, Nyamulagira, and Erta Ale; Giggenbach and Le Guern, 1976), and *2*) a too high permeability of the volcanic edifice, flushing out meteoric water from the summit areas of volcanoes. Instead, aquifers arguably accumulate at the base of volcanoes, or in rift depressions, hence creating an ideal hydrogeological architecture for magma-water interaction to take place at lower elevations (**Figure 11**), resulting in phreatomagmatic eruptions and consequent maar formation, a common phenomenon observed in monogenetic volcanic fields (e.g. Cas et al., 2017; Kereszturi et al., 2017). The many maar fields in Africa (e.g. Uganda, in the EAR, and Cameroon, in the CVL) probably reflect this large-scale and tectonically driven process. In fact, active seismicity occurs along the EAR (International Seismological Centre, 2020), as well as Holocene active volcanism does (Global Volcanism Program, 2013) (**Figures 1**, **11**). Unsurprisingly, seismicity, volcanism and volcanic lakes occur where the Earth crusts thins due to rifting, as shown in the two transects A-B and C-D in **Figures 11A,B**, respectively. The CVL is often interpreted as resulting from failed rifting following continental break up starting 120 Ma ago (Fitton, 1983; Aka et al., 2004); volcanism in Cameroon and the southern islands hence occur along this aulacogen (**Figure 11A**).

Within this maar-rich setting, combined with regional scale CO_2-rich degassing along the EAR and CVL, the deepest lakes in Africa might be able to store dissolved CO_2 in their bottom waters. The absence of a high gradient in yearly atmospheric temperature, and thus lake surface water temperature, favors meromixsy (e.g. Lake Nyos); instead, possible geothermal heating in deep rift lakes (e.g. Lake Kyaninga) inhibits a stable thermal stratification. The latter process provides a hypothesis for the observation that no other maar lake along the EAR or CVL has bursted in a fatal way like Lake Monoun and Lake Nyos did in 1984 and 1986, respectively. Moreover, possible diurnal cycles in the stratification, especially in the epilimnion of high-altitude lakes in Uganda, Kenya, Ethiopia, Tanzania and Cameroon, however, favors daily partial mixing and, hence, possible degassing if the lakes are fed by gas-rich fluids from below. Needless to say that further research in physical limnology, hydrogeology and fluid geochemistry of single lakes is highly recommendable in order to better assess future volcanic hazard for the 172 African maar lakes.

FINAL REMARKS AND STRATEGIES FOR FUTURE RESEARCH

VOLADA_Africa 2.0 compiles arguably the complete number of volcanic lakes on the African continent (220), Madagascar and the minor islands. Volcanic lakes are pin-pointed, country by country, through decimal coordinates, made available to the community (https://vhub.org/resources/). All lakes are classified for their genetic origin (Christenson et al., 2015), and physical and chemical characteristics (Rouwet et al., 2014, and references therein). The classification results as follows:

(1) 18 lakes are crater lakes (Manengouba Lakes, Cameroon; crater lakes of Zuquala, Dendi and Wonchi volcanoes, Ethiopia; Rutundu and Alice on Mt Kenya, Kenya; Waw an Namus in Libya; Mt Bisoke's and Mt Muhavura crater lakes, Rwanda; Deriba crater lakes, Sudan; Empakaai, Magadi and Ngozi crater lakes in Tanzania; crater lakes on the islands of Annobon, Bioko, Tristan da Cunha and Karthala);
(2) 4 are caldera lakes (3 in the O'a Caldera, Ethiopia; Lake Chala in Tanzania);
(3) 26 are lakes filling glacial depressions on the flanks of Mt Kenya (Kenya);
(4) The remaining 172 volcanic lakes are maar/tuff cone lakes.

Africa does not host peak-activity or high-activity lakes in active volcano craters. The renowned "killer lakes" Nyos and Monoun are "5b2-type" lakes (i.e. gas storing Nyos-type lake); Lake Nyungu and Lake Kyaninga, two of the 81 maar lakes in Uganda, are suspected to be "Nyos-type lakes." Arguably all lake waters have a purely meteoric origin, that attained a chemical equilibrium upon water-rock interaction with the host rock of the lake basin (i.e. rock-dominated lakes), and evaporation, in more or less extent. We proposed a conceptual model on why Africa provides the ideal tectonic and volcanic settings for maar lakes to form, and why peak activity crater lakes, "windows" into "wet volcanoes" are absent, in spite of the often ideal climatic conditions for such lakes to form. The dominance of intraplate volcanism and the absence of arc-type volcanism appear to be key factors.

The uniqueness to accomplish the necessary conditions for a gas burst to occur has been extensively studied during the past 30+ years. As we presumably know why the two fatal gas bursts *did* occur, the question for the remaining 172 African maar lakes seems to be "why do gas bursts *not* occur?" (by assuming they did not), as climatic, limnological and volcanic constraints are very similar than those for the Cameroonian "killer" lakes. Non-volcanological explanations that haze our insights into possible other "Nyos-type" events in the past lie in the facts that *1*) written history is reported only since the late 19th century for most of the African continent, and *2*) volcanic lakes are often located in remote and poorly inhabited regions. The recurrence time of geological phenomena is longer (e.g. 100–10,000's of years for dyke intrusions, maar formation, and "Nyos-type" gas bursts), and hence not synchronized with written history. Nevertheless, clues on suspicious "Nyos-type" behavior could be found in the study of oral traditions and legends that trace further back in the past. Future historiographical research should hence aim at explaining if "only" two lethal gas bursts occurred (Monoun-1984, Nyos-1986), as

reported in the documented history (Westerman, 2013). Moreover, the database on volcanic lakes in Africa presented here can be a useful resource to apply to other continents as a future aim of the International Association of Volcanology and Chemistry of the Earth's Interior (IAVCEI) Commission on Volcanic Lakes.

AUTHOR CONTRIBUTIONS

DR Development idea, MS writing, DB compilation, elaboration data KN Development idea, MS writing GT MS writing, DB compilation, elaboration data SC MS writing, field work, elaboration data I MS writing, field work.

ACKNOWLEDGMENTS

Research funding for DR during this research came from CALAPA-FISR 2016 (INGV, 2018). We thank Anna Hicks for providing comments on and the picture of the remote Tristan da Cunha crater lake. Pedro Hernández and Bernard Fontaine are grateful for sharing the pictures in **Figures 5**, **7**, respectively.

REFERENCES

Adams, A. N., Wiens, D. A., Nyblade, A. A., Euler, G. G., Shore, P. J., and Tibi, R. (2015). Lithospheric Instability and the Source of the Cameroon Volcanic Line: Evidence from Rayleigh Wave Phase Velocity Tomography. *J. Geophys. Res. Solid Earth.* 120 (3), 1708–1727. doi:10.1002/2014jb011580

Aeschbach-Hertig, W., Hofer, M., Kipfer, R., Imboden, D. M., and Wieler, R. (1999). Accumulation of Mantle Gases in a Permanently Stratified Volcanic lake (Lac Pavin, France). *Geochim. Cosmochim. Acta.* 63 (19/20), 3357–3372. doi:10.1016/s0016-7037(99)00257-4

Aeschbach-Hertig, W., Kipfer, R., Hofer, M., Imboden, D. M., Wieler, R., and Signer, P. (1996). Quantification of Gas Fluxes from the Subcontinental Mantle: The Example of Laacher See, a Maar lake in Germany. *Geochimica et Cosmochimica Acta.* 60, 31–41. doi:10.1016/0016-7037(95)00370-3

Aka, F. T., Buh, G. W., Fantong, W. Y., Issa, I. T., Zouh, S. L. B., Ghogomu, R. T., et al. (2017). Disaster Prevention, Disaster Preparedness and Local Community Resilience within the Context of Disaster Risk Management in Cameroon. *Nat. Hazards.* 86 (1), 57–88. doi:10.1007/s11069-016-2674-5

Aka, F. T. (2015). "Depth of Melt Segregation Below the Nyos Maar-Diatreme Volcano (Cameroon, West Africa): Major-Trace Element Evidence and Their Bearing on the Origin of CO_2 in Lake Nyos," in *Volcanic Lakes*. Editors D. Rouwet, B. Christenson, F. Tassi, and J. Vandemeulebrouck (Heidelberg: Springer), 467–488. doi:10.1007/978-3-642-36833-2_21

Aka, F. T., Hasegawa, T., Nche, L. A., Asaah, A. N. E., Mimba, M. E., Teitchou, I., et al. (2018). Upper Triassic Mafic Dykes of Lake Nyos, Cameroon (West Africa) I: K-Ar Age Evidence within the Context of Cameroon Line Magmatism, and the Tectonic Significance. *J. Afr. Earth Sci.* 141, 49–59. doi:10.1016/j.jafrearsci.2018.02.001

Aka, F. T., Kusakabe, M., Nagao, K., and Tanyileke, G. (2001). Noble Gas Isotopic Compositions and Water/gas Chemistry of soda springs from the Islands of Bioko, São Tomé and Annobon, along with Cameroon Volcanic Line, West Africa. *Appl. Geochem.* 16, 323–338. doi:10.1016/s0883-2927(00)00037-8

Aka, F. T., Nagao, K., Kusakabe, M., Sumino, H., Tanyileke, G., Ateba, B., et al. (2004). Symmetrical Helium Isotope Distribution on the Cameroon Volcanic Line, West Africa. *Chem. Geology.* 203, 205–223. doi:10.1016/j.chemgeo.2003.10.003

Aka, F. T., and Yokoyama, T. (2013). Current Status of the Debate about the Age of Lake Nyos Dam (Cameroon) and its Bearing on Potential Flood Hazards. *Nat. Hazards.* 65, 875–885. doi:10.1007/s11069-012-0401-4

Aka, F. T., Yokoyama, T., Kusakabe, M., Nakamura, E., Tanyileke, G., Ateba, B., et al. (2008). U-series Dating of Lake Nyos Maar Basalts, Cameroon (West Africa): Implications for Potential Hazards on the Lake Nyos Dam. *J. Volcanology Geothermal Res.* 176, 212–224. doi:10.1016/j.jvolgeores.2008.04.009

Alexandrine, N. n., Simon, N., III, and Gabriel, N. (2019). The Late Pleistocene - Holocene Paleoclimate Reconstruction in the Adamawa Plateau (Central Cameroon) Inferred from the Geochemistry and Mineralogy of the Lake Fonjak Sediments. *J. Afr. Earth Sci.* 150, 23–36. doi:10.1016/j.jafrearsci.2018.09.024

Almond, D. C., Ahmed, F., and Khalil, B. E. (1969). An Excursion to the Bayuda Volcanic Field of Northern Sudan. *Bull. Volcanol.* 33, 549–565. doi:10.1007/BF02596524

Anazawa, K., Fantong, W. Y., Ueda, A., Ozawa, A., Kusakabe, M., Yoshida, Y., et al. (2019). Environmental Modifications of Lake Nyos Surface Water by Artificial Degassing. *J. Afr. Earth Sci.* 152, 115–121. doi:10.1016/j.jafrearsci.2019.02.009

Anema, A., and Fesselet, J.-F. (2003). A Volcanic Issue - Lessons Learned in Goma. *Waterlines.* 21 (4), 9–11. doi:10.3362/0262-8104.2003.019

Asaah, A. N. E., Yokoyama, T., Aka, F. T., Usui, T., Kuritani, T., Wirmvem, M. J., et al. (2015). Geochemistry of Lavas from Maar-Bearing Volcanoes in the Oku Volcanic Group of the Cameroon Volcanic Line. *Chem. Geology.* 406, 55–69. doi:10.1016/j.chemgeo.2015.03.030

Baker, P. E., Gass, I. G., Harris, P. G., and le Maitre, R. W. (1964). The Volcanological Report of the Royal Society Expedition to Tristan da Cunha, 1962. *Phil. Trans. R. Soc. Lond. A.* 256, 439–575. doi:10.1098/rsta.1964.0011

Balashova, A., Mattsson, H. B., Hirt, A. M., and Almqvist, B. S. G. (2016). The Lake Natron Footprint Tuff (Northern Tanzania): Volcanic Source, Depositional Processes and Age Constraints from Field Relations. *J. Quat. Sci.* 31 (5), 526–537. doi:10.1002/jqs.2876

Barberi, F., Chelini, W., Marinelli, G., and Martini, M. (1989). The Gas Cloud of Lake Nyos (Cameroon, 1986): Results of the Italian Technical mission. *J. Volcanology Geothermal Res.* 39, 125–134. doi:10.1016/0377-0273(89)90053-x

Bardintzeff, J.-M., Deniel, C., Guillou, H., Platevoet, B., Télouk, P., and Oun, K. M. (2012). Miocene to Recent Alkaline Volcanism Between Al Haruj and Waw an Namous (Southern Libya). *Int. J. Earth Sci. (Geol Rundsch).* 101, 1047–1063. doi:10.1007/s00531-011-0708-5

Bardintzeff, J.-M., Liégeois, J.-P., Bonin, B., Bellon, H., and Rasamimanana, G. (2010). Madagascar Volcanic Provinces Linked to the Gondwana Break-Up: Geochemical and Isotopic Evidences for Contrasting Mantle Sources. *Gondwana Res.* 18, 295–314. doi:10.1016/j.gr.2009.11.010

Barette, F., Poppe, S., Smets, B., Benbakkar, M., and Kervyn, M. (2017). Spatial Variation of Volcanic Rock Geochemistry in the Virunga Volcanic Province: Statistical Analysis of an Integrated Database. *J. Afr. Earth Sci.* 134, 888–903. doi:10.1016/j.jafrearsci.2016.09.018

Barker, P. A., Hurrell, E. R., Leng, M. J., Plessen, B., Wolff, C., Conley, D. J., et al. (2013). Carbon Cycling within an East African lake Revealed by the Carbon Isotope Composition of Diatom Silica: A 25-ka Record from Lake Challa, Mt. Kilimanjaro. *Quat. Sci. Rev.* 66, 55–63. doi:10.1016/j.quascirev.2012.07.016

Barker, P., Telford, R., Merdaci, O., Williamson, D., Taieb, M., Vincens, A., et al. (2000). The Sensitivity of a Tanzanian Crater lake to Catastrophic Tephra Input and Four Millennia of Climate Change. *The Holocene.* 10 (3), 303–310. doi:10.1191/095968300672848582

Berghuijs, J. F., and Mattsson, H. B. (2013). Magma Ascent, Fragmentation and Depositional Characteristics of "Dry" Maar Volcanoes: Similarities with Vent-Facies Kimberlite Deposits. *J. Volcanology Geothermal Res.* 252, 53–72. doi:10.1016/j.jvolgeores.2012.11.005

Bruhn, R. L., Brown, F. H., Gathogo, P. N., and Haileab, B. (2011). Pliocene Volcano-Tectonics and Paleogeography of the Turkana Basin, Kenya and Ethiopia. *J. Afric. Earth Sci.* 59 (2-3), 295–312. doi:10.1016/j.jafrearsci.2010.12.002

Buckles, L. K., Verschuren, D., Weijers, J. W. H., Cocquyt, C., Blaauw, M., and Sinninghe Damsté, J. S. (2016). Interannual and (Multi-)decadal Variability in the Sedimentary BIT Index of Lake Challa, East Africa, Over the Past

2200 years: Assessment of the Precipitation Proxy. *Clim. Past.* 12, 1243–1262. doi:10.5194/cp-12-1243-2016

Buckles, L. K., Weijers, J. W. H., Verschuren, D., and Sinninghe Damsté, J. S. (2014). Sources of Core and Intact Branched Tetraether Membrane Lipids in the Lacustrine Environment: Anatomy of Lake Challa and its Catchment, Equatorial East Africa. *Geochimica et Cosmochimica Acta.* 140, 106–126. doi:10.1016/j.gca.2014.04.042

Burton, A. N., and Wickens, G. E. (1966). Jebel Marra Volcano, Sudan. *Nature* 210, 1146–1147. doi:10.1038/2101146a0

Cabassi, J., Capecchiacci, F., Magi, F., Vaselli, O., Tassi, F., Montalvo, F., et al. (2019). Water and Dissolved Gas Geochemistry at Coatepeque, Ilopango and Chanmico Volcanic Lakes (El Salvador, Central America). *J. Volcanology Geothermal Res.* 378, 1–15. doi:10.1016/j.jvolgeores.2019.04.009

Cabassi, J., Tassi, F., Mapelli, F., Borin, S., Calabrese, S., Rouwet, D., et al. (2014). Geosphere-Biosphere Interactions in Bio-Activity Volcanic Lakes: Evidences from Hule and Rio Cuarto (Costa Rica). *PLoS ONE.* 9 (7), e102456. doi:10.1371/journal.pone.0102456

Cabassi, J., Tassi, F., Vaselli, O., Fiebig, J., Nocentini, M., Capecchiacci, F., et al. (2013). Biogeochemical Processes Involving Dissolved CO_2 and CH_4 at Albano, Averno, and Monticchio Meromictic Volcanic Lakes (Central-Southern Italy). *Bull. Volcanol.* 75, 683. doi:10.1007/s00445-012-0683-0

Caliro, S., Chiodini, G., Izzo, G., Minopoli, C., Signorini, A., Avino, R., et al. (2008). Geochemical and Biochemical Evidence of lake Overturn and Fish Kill at Lake Averno, Italy. *J. Volcanology Geothermal Res.* 178 (2), 305–316. doi:10.1016/j.jvolgeores.2008.06.023

Carapezza, M. L., Lelli, M., and Tarchini, L. (2008). Geochemistry of the Albano and Nemi Crater Lakes in the Volcanic District of Alban Hills (Rome, Italy). *J. Volcanology Geothermal Res.* 178, 297–304. doi:10.1016/j.jvolgeores.2008.06.031

Cas, R., van Otterloo, J. B. T., and van den Hove, J. (2017). "The Dynamics of a Very Large Intra-plate Continental Basaltic Volcanic Province, the Newer Volcanics Province, South-Eastern Australia, and Implications for Other Provinces," in *Monogenetic Volcanism*. Editors K. Németh, G. Carrasco-Nuñez, J. J. Aranda-Gomez, and I. E. M. Smith (Bath, UK: The Geological Society Publishing House).

Caudron, C., Lecocq, T., Syahbana, D. K., McCausland, W., Watlet, A., Camelbeeck, T., et al. (2015). Stress and Mass Changes at a "Wet" Volcano: Example During the 2011-2012 Volcanic Unrest at Kawah Ijen Volcano (Indonesia). *J. Geophys. Res. Solid Earth.* 120, 5117–5134. doi:10.1002/2014JB011590

Caudron, C., Mazot, A., and Bernard, A. (2012). Carbon Dioxide Dynamics in Kelud Volcanic Lake. *J. Geophys. Res.* 117, B05102. doi:10.1029/2011JB008806

Chapman, L. J., Chapman, C. A., Crisman, T. L., and Nordlie, F. G. (1998). Dissolved Oxygen and Thermal Regimes of a Ugandan Crater lake. *Hydrobiologia.* 385, 201–211. doi:10.1023/a:1003527016384

Chiodini, G., Tassi, F., Caliro, S., Chiarabba, C., Vaselli, O., and Rouwet, D. (2012). Time-dependent CO_2 Variations in Lake Albano Associated with Seismic Activity. *Bull. Volcanol.* 74, 861–871. doi:10.1007/s00445-011-0573-x

Christenson, B., Németh, K., Rouwet, D., Tassi, F., Vandemeulebrouck, J., and Varekamp, J. C. (2015). "Volcanic Lakes," in *Volcanic Lakes*. Editors D. Rouwet, B. Christenson, F. Tassi, and J. Vandemeulebrouck (Heidelberg: Springer), 1–20. doi:10.1007/978-3-642-36833-2_1

Class, C., Goldstein, S. L., and Shirey, S. B. (2009). Osmium Isotopes in Grande Comore Lavas: A New Extreme Among a Spectrum of EM-type Mantle Endmembers. *Earth Planet. Sci. Lett.* 284 (1-2), 219–227. doi:10.1016/j.epsl.2009.04.031

Cocquyt, C., Plisnier, P.-D., Gelorini, V., Rumes, B., and Verschuren, D. (2010). Observations on the Limnology and Phytoplankton Community of Crater Lake Kyaninga (Uganda), with Special Attention to its Diatom flora. *Plecevo.* 143 (3), 365–377. doi:10.5091/plecevo.2010.420

Cvetkovic, V., Toljic, M., Ammar, N. A., Rundic, L., and Trish, K. B. (2010). Petrogenesis of the Eastern Part of the Al Haruj Basalts (Libya). *J. Afric. Earth Sci.* 58 (1), 37–50. doi:10.1016/j.jafrearsci.2010.01.006

Davidson, J. P., and Wilson, I. R. (1989). Evolution of an Alkali basalt-trachyte Suite from Jebel Marra Volcano, Sudan, Through Assimilation and Fractional Crystallization. *Earth Planet. Sci. Lett.* 95, 141–160. doi:10.1016/0012-821x(89)90173-8

De Crop, W., and Verschuren, D. (2019). Determining Patterns of Stratification and Mixing in Tropical Crater Lakes Through Intermittent Water-Column Profiling: A Case Study in Western Uganda. *J. Afr. Earth Sci.* 153, 17–30. doi:10.1016/j.jafrearsci.2019.02.019

Delalande, M., Bergonzini, L., Branchu, P., Filly, A., and Williamson, D. (2008). Hydroclimatic and Geothermal Controls on the Salinity of Mbaka Lakes (SW Tanzania): Limnological and Paleolimnological Implications. *J. Hydrol.* 359 (3-4), 274–286. doi:10.1016/j.jhydrol.2008.07.007

Delalande-Le Mouëllic, M., Gherardi, F., Williamson, D., Kajula, S., Kraml, M., Noret, A., et al. (2015). Hydrogeochemical Features of Lake Ngozi (SW Tanzania). *J. Afr. Earth Sci.* 103, 153–167. doi:10.1016/j.jafrearsci.2014.11.004

Delmelle, P., and Bernard, A. (2000). "Volcanic Lakes," in *Encyclopedia of Volcanoes*. Editors H. Sigurdsson, B. Houghton, S. McNutt, H. Rymer, and J. Stix (San Diego, CA: Academic Press), 877–895.

de Moor, J. M., Fischer, T. P., King, P. L., Botcharnikov, R. E., Hervig, R. L., Hilton, D. R., et al. (2013). Volatile-Ricj Solicate Melts From Oldoinyo Lengai Volcano (Tanzania): Implications for Carbinatite Genesis and Eruptive Behavior. *Earth Planet. Sci. Lett.* 361, 379–390. doi:10.1016/j.epsl.2012.11.006

Déruelle, B., Ngounouno, I., and Demaiffe, D. (2007). The 'Cameroon Hot Line' (CHL): A Unique Example of Active Alkaline Intraplate Structure in Both Oceanic and Continental Lithospheres. *Comptes Rendus Geosci.* 339 (9), 589–600. doi:10.1016/j.crte.2007.07.007

Dupuy, C., Pagano, M., Got, P., Domaizon, I., Chappuis, A., Marchessaux, G., et al. (2016). Trophic Relationships Between Metazooplankton Communities and Their Plankton Food Sources in the Iles Eparses (Western Indian Ocean). *Mar. Environ. Res.* 116, 18–31. doi:10.1016/j.marenvres.2016.02.011

Ebinger, C. J. (1989). Geometric and Kinematic Development of Border Faults and Accommodation Zones, Kivu-Rusizi Rift, Africa. *Tectonics.* 8 (1), 117–133. doi:10.1029/tc008i001p00117

Eggermont, H., Heiri, O., and Verschuren, D. (2006). Fossil Chironomidae (Insecta: Diptera) as Quantitative Indicators of Past Salinity in African Lakes. *Quat. Sci. Rev.* 25, 1966–1994. doi:10.1016/j.quascirev.2005.04.011

Elshaafi, A., and Gudmundsson, A. (2017). Distribution and Size of Lava Shields on the Al Haruj Al Aswad and the Al Haruj Al Abyad Volcanic Systems, Central Libya. *J. Volcanology Geothermal Res.* 338, 46–62. doi:10.1016/j.jvolgeores.2017.03.012

Elshaafi, A., and Gudmundsson, A. (2018). Mechanical Interaction Between Volcanic Systems in Libya. *Tectonophysics.* 722, 549–565. doi:10.1016/j.tecto.2017.11.031

Elshaafi, A., and Gudmundsson, A. (2016). Volcano-tectonics of the Al Haruj Volcanic Province, Central Libya. *J. Volcanology Geothermal Res.* 325, 189–202. doi:10.1016/j.jvolgeores.2016.06.025

Evans, W. C., Kling, G. W., Tuttle, M. L., Tanyileke, G., and White, L. D. (1993). Gas Buildup in Lake Nyos, Cameroon: The Recharge Process and its Consequences. *Appl. Geochem.* 8, 207–221. doi:10.1016/0883-2927(93)90036-g

Evans, W. C., White, L. D., Tuttle, M. L., Kling, G. W., Tanyileke, G., and Michel, R. L. (1994). Six Years of Change at Lake Nyos, Cameroon, Yield Clues to the Past and Cautions for the Future. *Geochem. J.* 28, 139–162. doi:10.2343/geochemj.28.139

Faivre Pierret, R. X., Berne, P., Roussel, C., and Le Guern, F. (1992). The Lake Nyos Disaster: Model Calculations for the Flow of Carbon Dioxide. *J. Volcanology Geothermal Res.* 51, 161–170. doi:10.1016/0377-0273(92)90066-m

Fantong, W. Y., Kamtchueng, B. T., Yamaguchi, K., Ueda, A., Issa, R., Wirmvem, M. J., et al. (2015). Characteristics of Chemical Weathering and Water-Rock Interaction in Lake Nyos Dam (Cameroon): Implications for Vulnerability to Failure and Re-enforcement. *J. Afr. Earth Sci.* 101, 42–55. doi:10.1016/j.jafrearsci.2014.08.011

Fazi, S., Butturini, A., Tassi, F., Amalfitano, S., Venturi, S., Vázquez, E., et al. (2018). Biogeochemistry and Biodiversity in a Network of Saline-alkaline Lakes: Implications of Ecohydrological Connectivity in the Kenyan Rift Valley. *Ecohydrology & Hydrobiology.* 18, 96–106. doi:10.1016/j.ecohyd.2017.09.003

Fontijn, K., Ernst, G. G. J., Elburg, M. A., Williamson, D., Abdallah, E., Kwelwa, S., et al. (2010). Holocene Explosive Eruptions in the Rungwe Volcanic Province, Tanzania. *J. Volcanology Geothermal Res.* 196, 91–110. doi:10.1016/j.jvolgeores.2010.07.021

Fontijn, K., Williamson, D., Mbede, E., and Ernst, G. G. J. (2012). The Rungwe Volcanic Province, Tanzania - A Volcanological Review. *J. Afr. Earth Sci.* 63, 12–31. doi:10.1016/j.jafrearsci.2011.11.005

Fouilland, E., Vasseur, C., Leboulanger, C., Le Floc'h, E., Carré, C., Marty, B., et al. (2014). Coupling Algal Biomass Production and Anaerobic Digestion: Production Assessment of Some Native Temperate and Tropical Microalgae. *Biomass and Bioenergy*. 70, 564–569. doi:10.1016/j.biombioe.2014.08.027

Franz, G., Breitkreuz, C., Coyle, D. A., El Hur, B., Heinrich, W., Paulick, H., et al. (1997). The Alkaline Meidob Volcanic Field (Late Cenozoic, Northwest Sudan). *J. Afr. Earth Sci.* 25 (2), 263–291. doi:10.1016/s0899-5362(97)00103-6

Freeth, S. J., and Kay, R. L. F. (1987). The Lake Nyos Gas Disaster. *Nature.* 325, 104–105. doi:10.1038/325104a0

Freeth, S. J., Kling, G. W., Kusakabe, M., Maley, J., Tchoua, F. M., and Tietze, K. (1990). Conclusions from Lake Nyos Disaster. *Nature.* 348, 201. doi:10.1038/348201a0

Freeth, S. J. (1994). Lake Nyos: Can Another Disaster Be Avoided? *Geochem. J.* 28, 163–172. doi:10.2343/geochemj.28.163

Freeth, S. J., and Rex, D. C. (2000). Constraints on the Age of Lake Nyos, Cameroon. *J. Volcanol. Geotherm. Res.* 97 (1-4), 261–269. doi:10.1016/s0377-0273(99)00172-9

Freeth, S. J. (1990). The Anecdotal Evidence, Did it Help or Hinder Investigation of the Lake Nyos Gas Disaster? *J. Volcanology Geothermal Res.* 42, 373–380. doi:10.1016/0377-0273(90)90033-c

Freeth, S. J. (1992). "The Lake Nyos Gas Disaster," in *Natural Hazards in West and Central Africa*. Editors S. J. Freeth, C. O. Ofoegbu, and K. M. Onuoha (Braunschweig: Vieweg), 63–82. doi:10.1007/978-3-663-05239-5_8

Garcin, Y., Schefuß, E., Schwab, V. F., Garreta, V., Gleixner, G., Vincens, A., et al. (2014). Reconstructing C_3 and C_4 Vegetation Cover Using N -alkane Carbon Isotope Ratios in Recent Lake Sediments from Cameroon, Western Central Africa. *Geochimica et Cosmochimica Acta.* 142, 482–500. doi:10.1016/j.gca.2014.07.004

Garcin, Y., Schwab, V. F., Gleixner, G., Kahmen, A., Todou, G., Séné, O., et al. (2012). Hydrogen Isotope Ratios of Lacustrine Sedimentary N-Alkanes as Proxies of Tropical African Hydrology: Insights from a Calibration Transect across Cameroon. *Geochimica et Cosmochimica Acta.* 79, 106–126. doi:10.1016/j.gca.2011.11.039

Gasse, F., Cortijo, E., Disnar, J. R., Ferry, L., Gibert, E., Kissel, C., et al. (1994). A 36-ka Environmental Record in the Southern Tropics—Lake Tritrivakely (Madagascar). *Comptes Rendus de L'academie des Sciences—Serie II.* 318, 1513–1519.

Gasse, F., and Van Campo, E. (1998). A 40,000-yr Pollen and Diatom Record from Lake Tritrivakely, Madagascar, in the Southern Tropics. *Quat. Res.* 49, 299–311. doi:10.1006/qres.1998.1967

Gasse, F., and Van Campo, E. (2001). Late Quaternary Environmental Changes from a Pollen and Diatom Record in the Southern Tropics (Lake Tritrivakely, Madagascar). *Palaeogeogr. Palaeoclimatol. Palaeoecol.* 167, 287–308. doi:10.1016/s0031-0182(00)00242-x

Geshi, N., Németh, K., Noguchi, R., and Oikawa, T. (2019). Shift from Magmatic to Phreatomagmatic Explosions Controlled by the Lateral Evolution of a Feeder dike in the Suoana-Kazahaya Eruption, Miyakejima Volcano, Japan. *Earth Planet. Sci. Lett.* 511, 177–189. doi:10.1016/j.epsl.2019.01.038

Giggenbach, W. F., and Guern, F. L. (1976). The Chemistry of Magmatic Gases from Erta'Ale, Ethiopia. *Geochimica et Cosmochimica Acta.* 40, 25–30. doi:10.1016/0016-7037(76)90190-3

Giggenbach, W. F., Sano, Y., and Schmincke, H. U. (1991). CO_2-rich Gases from Lakes Nyos and Monoun, Cameroon; Laacher See, Germany; Dieng, Indonesia, and Mt. Gambier, Australia-variations on a Common Theme. *J. Volcanology Geothermal Res.* 45, 311–323. doi:10.1016/0377-0273(91)90065-8

Giggenbach, W. F. (1990). Water and Gas Chemistry of Lake Nyos and its Bearing on the Eruptive Process. *J. Volcanology Geothermal Res.* 42, 337–362. doi:10.1016/0377-0273(90)90031-a

Giresse, P., and Makaya-Mvoubou (2010). Sediment and Particulate Organic Carbon Fluxes in Various Lacustrine Basins of Tropical Africa and in the Gulf of Guinea. *Glob. Planet. Change.* 72, 341–355. doi:10.1016/j.gloplacha.2010.01.010

Global Volcanism Program (2013). "Volcanoes of the World (VOTW) Database Information," in *Volcanoes of the World*. Editors E. Venzke (Washington, DC: Smithsonian Institution). doi:10.5479/si.GVP.VOTW4-2013

Godfrey Fitton, J. (1983). Active Versus Passive continental Rifting: Evidence from the West African Rift System. *Tectonophysics.* 94, 473–481. doi:10.1016/0040-1951(83)90030-6

Graettinger, A. H. (2018). Trends in Maar Crater Size and Shape Using the Global Maar Volcano Location and Shape (MaarVLS) Database. *J. Volcanology Geothermal Res.* 357, 1–13. doi:10.1016/j.jvolgeores.2018.04.002

Haileab, B., Brown, F. H., McDougall, I., and Gathogo, P. N. (2004). Gombe Group Basalts and Initiation of Pliocene Deposition in the Turkana Depression, Northern Kenya and Southern Ethiopia. *Geol. Mag.* 141 (1), 41–53. doi:10.1017/s001675680300815x

Halbwachs, M., and Sabroux, J. C. (2001). Removing CO_2 from Lake Nyos in Cameroon. *Science.* 292, 438. doi:10.1126/science.292.5516.438a

Halbwachs, M., Grangeon, J., Sabroux, J. -C., and Villevielle, A. (1993). Purge par auto-siphon du gaz carbonique dissous dans le lac Monoun (Cameroun): premiers resultants experimentaux. *C. R. Acad. Sci. Paris.* 316, 483–489.

Halbwachs, M., Sabroux, J.-C., Grangeon, J., Kayser, G., Tochon-Danguy, J.-C., Felix, A., et al. (2004). Degassing the "Killer Lakes" Nyos and Monoun, Cameroon. *Eos Trans. AGU.* 85, 281–285. doi:10.1029/2004eo300001

Halbwachs, M., Sabroux, J.-C., and Kayser, G. (2020). Final Step of the 32-year Lake Nyos Degassing Adventure: Natural CO_2 Recharge Is to Be Balanced by Discharge Through the Degassing Pipes. *J. Afr. Earth Sci.* 167, 103575. doi:10.1016/j.jafrearsci.2019.103575

Hammerton, D. (1968). "Recent Discoveries in the Caldera of Jebel Marra," in *Sudan Notes and Records* (Khartoum: University of Khartoum), 136–148.

Hunt, J. A., Mather, T. A., and Pyle, D. M. (2020). Morphological Comparison of Distributed Volcanic fields in the Main Ethiopian Rift Using High-Resolution Digital Elevation Models. *J. Volcanology Geothermal Res.* 393, 106732. doi:10.1016/j.jvolgeores.2019.106732

Issa, Aka Tongwa, F., Mouliom, A. G., Rouwet, D., Fantong, W. Y., Chako Tchamabé, B., et al. (2014). $\delta^{18}O$ and δD Variations in Some Volcanic Lakes on the Cameroon Volcanic Line (West-Africa): Generating Isotopic Baseline Data for Volcano Monitoring and Surveillance in Cameroon. *J. Limnol.* 73 (1), 95–113. doi:10.4081/jlimnol.2014.966

International Seismological Centre (2020). *ISC-GEM Earthquake Catalogue*. Thatcham, United Kingdom: International Seismological Centre. doi:10.31905/d808b825

Jolie, E. (2019). Detecting Gas-Rich Hydrothermal Vents in Ngozi Crater Lake Using Integrated Exploration Tools. *Sci. Rep.* 9, 12164. doi:10.1038/s41598-019-48576-5

Kanari, S.-I. (1989). An Inference on the Process of Gas Outburst from Lake Nyos, Cameroon. *J. Volcanology Geothermal Res.* 39, 135–149. doi:10.1016/0377-0273(89)90054-1

Kantha, L. H., and Freeth, S. J. (1996). A Numerical Simulation of the Evolution of Temperature and CO_2 stratification in Lake Nyos Since the 1986 Disaster. *J. Geophys. Res.* 101 (B4), 8187–8203. doi:10.1029/96jb00324

Kebede, S., Travi, Y., and Rozanski, K. (2009). The $\delta^{18}O$ and δ2H Enrichment of Ethiopian Lakes. *J. Hydrol.* 365, 173–182. doi:10.1016/j.jhydrol.2008.11.027

Keller, J., and Zaitsev, A. N. (2012). Geochemistry and Petrogenetic Significance of Natrocarbonatites at Oldoinyo Lengai, Tanzania: Composition of Lavas from 1988 to 2007. *Lithos.* 148, 45–53. doi:10.1016/j.lithos.2012.05.022

Kereszturi, G., Bebbington, M., and Németh, K. (2017). Forecasting Transitions in Monogenetic Eruptions Using the Geologic Record. *Geology.* 45 (3), 283–286. doi:10.1130/g38596.1

Kereszturi, G., Németh, K., Cronin, S. J., Procter, J., and Agustín-Flores, J. (2014). Influences on the Variability of Eruption Sequences and Style Transitions in the Auckland Volcanic Field, New Zealand. *J. Volcanology Geothermal Res.* 286, 101–115. doi:10.1016/j.jvolgeores.2014.09.002

Kereszturi, G., Németh, K., Csillag, G., Balogh, K., and Kovacs, J. (2011). The Role of External Environmental Factors in Changing Eruption Styles of Monogenetic Volcanoes in a Mio/Pleistocene continental Volcanic Field in Western Hungary. *J. Volcanol. Geotherm. Res.* 201 (1-4), 227–240. doi:10.1016/j.jvolgeores.2010.08.018

Kervyn, M., van Wyk de Vries, B., Walter, T. R., Njome, M. S., Suh, C. E., and Ernst, G. G. J. (2014). Directional Flank Spreading at Mount Cameroon Volcano: Evidence from Analogue Modeling. *J. Geophys. Res. Solid Earth.* 119 (10), 7542–7563. doi:10.1002/2014jb011330

Kling, G. W., Clark, M. A., Wagner, G. N., Compton, H. R., Humphrey, A. M., Devine, J. D., et al. (1987). The 1986 lake Nyos Gas Disaster in Cameroon, West Africa. *Science.* 236, 169–175. doi:10.1126/science.236.4798.169

Kling, G. W., Clark, M. A., Wagner, G. N., Compton, H. R., Humphrey, A. M., Devine, J. D., et al. (1987). The 1986 Lake Nyos Gas Disaster in Cameroon, West Africa. *Science.* 236, 169–175. doi:10.1126/science.236.4798.169

Kling, G. W. (1988). Comparative Transparency, Depth of Mixing, and Stability of Stratification in Lakes of Cameroon, West Africa1. *Limnol. Oceanogr.* 33 (1), 27–40. doi:10.4319/lo.1988.33.1.0027

Kling, G. W., Evans, W. C., Tanyileke, G., Kusakabe, M., Ohba, T., Yoshida, Y., et al. (2005). From the Cover: Degassing Lakes Nyos and Monoun: Defusing Certain Disaster. *Proc. Natl. Acad. Sci.* 102 (40), 14185–14190. doi:10.1073/pnas.050337410210.1073/pnas.0502274102

Kling, G. W., Evans, W. C., and Tanyileke, G. Z. (2015). "The Comparative Limnology of Lakes Nyos and Monoun, Cameroon," in *Volcanic Lakes*. Editors D. Rouwet, B. Christenson, F. Tassi, and J. Vandemeulebrouck (Heidelberg: Springer), 401–425. doi:10.1007/978-3-642-36833-2_18

Kling, G. W., Evans, W. C., and Tuttle, M. L. (1991). A Comparative View of Lakes Nyos and Monoun, Cameroon, West Africa. *SIL Proc. 1922-2010.* 24, 1102–1105. doi:10.1080/03680770.1989.11898921

Kling, G. W., Tuttle, M. L., and Evans, W. C. (1989). The Evolution of Thermal Structure and Water Chemistry in Lake Nyos. *J. Volcanology Geothermal Res.* 39, 151–165. doi:10.1016/0377-0273(89)90055-3

Kusakabe, M. (2015). "Evolution of CO_2 Content in Lakes Nyos and Monoun, and Sub-lacustrine CO_2-recharge System at Lake Nyos as Envisaged from $CO_2/^3$He Ratios and Noble Gas Signatures," in *Volcanic Lakes*. Editors D. Rouwet, B. Christenson, F. Tassi, and J. Vandemeulebrouck (Heidelberg: Springer). 427–450. doi:10.1007/978-3-642-36833-2_19

Kusakabe, M. (2017). Lakes Nyos and Monoun Gas Disasters (Cameroon)-Limnic Eruptions Caused by Excessive Accumulation of Magmatic CO_2 in Crater Lakes. *Geochem. Monogr. Ser.* 1 (1), 1–50. doi:10.5047/gems.2017.00101.0001

Kusakabe, M., Ohba, T., Issa, Y., Yoshida, H., Ohizumi, T., Evans, W. C., et al. (2008). Evolution of CO_2 in Lakes Monoun and Nyos, Cameroon, Before and During Controlled Degassing. *Geochem. J.* 42, 93–118. doi:10.2343/geochemj.42.93

Kusakabe, M., Ohsumi, T., and Aramaki, S. (1989). The Lake Nyos Gas Disaster: Chemical and Isotopic Evidence in Waters and Dissolved Gases from Three Cameroonian Crater Lakes, Nyos, Monoun and Wum. *J. Volcanology Geothermal Res.* 39, 167–185. doi:10.1016/0377-0273(89)90056-5

Kusakabe, M., and Sano, Y. (1992). "The Origin of Gases in Lake Nyos, Cameroon," in *International Monograph Series On Interdisciplinary Earth Science Research And Applications*. Editors S. J. Freeth, C. O. Ofoegb, and K. M. Onohua (Braunschweig, Wiesbaden: Friedrich Vieweg & SohnVerlag), 83–95. doi:10.1007/978-3-663-05239-5_9

Kusakabe, M., Tanyileke, G. Z., McCord, S. A., and Schladow, S. G. (2000). Recent pH and CO_2 Profiles at Lakes Nyos and Monoun, Cameroon: Implications for the Degassing Strategy and its Numerical Simulation. *J. Volcanology Geothermal Res.* 97, 241–260. doi:10.1016/s0377-0273(99)00170-5

Kusakabe, M., Tiodjio, R. E., Christenson, B., Saiki, K., Ohba, T., and Yaguchi, M. (2019). Enrichment of Ferrous Iron in the Bottom Water of Lake Nyos. *J. Afr. Earth Sci.* 150, 37–46. doi:10.1016/j.jafrearsci.2018.10.014

Laske, G., Masters, G., Ma, Z., and Pasyanos, M. (2013). Update on CRUST1.0 - A 1-degree Global Model of Earth's Crust. *Geophys. Res. Abstr.* 15, 2013–2658.

Le Turdu, C., Tiercelin, J.-J., Gibert, E., Travi, Y., Lezzar, K.-E., Richert, J.-P., et al. (1999). The Ziway-Shala Lake Basin System, Main Ethiopian Rift: Influence of Volcanism, Tectonics, and Climatic Forcing on Basin Formation and Sedimentation. *Palaeogeogr. Palaeoclimatol. Palaeoecol.* 150, 135–177. doi:10.1016/s0031-0182(98)00220-x

Lebamba, J., Vincens, A., Lézine, A.-M., Marchant, R., and Buchet, G. (2016). Forest-savannah Dynamics on the Adamawa Plateau (Central Cameroon) during the "African Humid Period" Termination: A New High-Resolution Pollen Record from Lake Tizong. *Rev. Palaeobotany Palynology.* 235, 129–139. doi:10.1016/j.revpalbo.2016.10.001

Lemma, B. (2009). Observations on the Relations of Some Physico-Chemical Features and DVM of Paradiaptomus Africanus in Lakes Bishoftu-Guda and Hora-Arsedi, Bishoftu, Ethiopia. *Limnologica.* 39, 230–243. doi:10.1016/j.limno.2008.06.007

Lenhardt, N., Borah, S. B., Lenhardt, S. Z., Bumby, A. J., Ibinoof, M. A., and Salih, S. A. (2018). The Monogenetic Bayuda Volcanic Field, Sudan - New Insights into Geology and Volcanic Morphology. *J. Volcanology Geothermal Res.* 356, 211–224. doi:10.1016/j.jvolgeores.2018.03.010

Lockwood, J., and Kusakabe, M. (2018). IWGCL Newsletters. Available at: https://iavceicvl.files.wordpress.com/2018/07/iwgcl-cvl-newsletters.pdf.

Lockwood, J. P., Costa, J. E., Tuttle, M. L., Nni, J., and Tebor, S. G. (1988). The Potential for Catastrophic Dam Failure at Lake Nyos Maar, Cameroon. *Bull. Volcanol.* 50, 340–349. doi:10.1007/bf01073590

Lockwood, J. P., and Rubin, M. (1989). Origin and Age of the Lake Nyos Maar, Cameroon. *J. Volcanology Geothermal Res.* 39, 117–124. doi:10.1016/0377-0273(89)90052-8

Loomis, S. E., Russell, J. M., Ladd, B., Street-Perrott, F. A., and Sinninghe Damsté, J. S. (2012). Calibration and Application of the Branched GDGT Temperature Proxy on East African Lake Sediments. *Earth Planet. Sci. Lett.* 357-358, 277–288. doi:10.1016/j.epsl.2012.09.031

Lowenstein, T. K., and Russell, J. M. (2011). A Brine Evolution Model and Mineralogy of Chemical Sediments in a Volcanic Crater, Lake Kitagata, Uganda. *Aquat. Geochem.* 17 (2), 129–140. doi:10.1007/s10498-010-9108-x

Maley, J., Livingstone, D. A., Giresse, P., Thouveny, N., Brenac, P., Kelts, K., et al. (1990). Lithostratigraphy, Volcanism, Paleomagnetism and Palynology of Quaternary Lacustrine Deposits From Barombi Mbo (West Cameroon): Preliminary Results. *J. Volcanol. Geotherm. Res.* 42, 319–335. doi:10.1016/s0031-0182(98)00220-x

Martin, U., and Németh, K. (2006). How Strombolian Is a "Strombolian" Scoria Cone? Some Irregularities in Scoria Cone Architecture from the Transmexican Volcanic Belt, Near Volcan Ceboruco, (Mexico) and Al Haruj (Libya). *J. Volcanol. Geotherm. Res.* 155 (1-2), 104–118. doi:10.1016/j.jvolgeores.2006.02.012

Martini, M., Giannini, L., Prati, F., Tassi, F., Capaccioni, B., and Iozzelli, P. (1994). Chemical Characters of Crater Lakes in the Azores and Italy: The Anomaly of Lake Albano. *Geochem. J.* 28 (3), 173–184. doi:10.2343/geochemj.28.173

Mattson, H. B., and Tripoli, B. A. (2011). Depositional Characteristics and Volcanic Landforms in the Lake Natron-Engaruka Monogenetic Field, Northern Tanzania. *J. Volcanol. Geotherm. Res.* 203 (1-2), 23–34. doi:10.1016/j.jvolgeores.2011.04.010

Mbassa, B. J., Njonfang, E., Benoit, M., Kamgang, P., Gregoire, M., Duchene, S., et al. (2012). Mineralogy, Geochemistry and Petrogenesis of the Recent Magmatic Formations from Mbengwi, a Continental Sector of the Cameroon Volcanic Line (CVL), Central Africa. *Mineralogy Pet.* 106 (3-4), 217–242. doi:10.1007/s00710-012-0227-5

McCord, S. A., and Schladow, S. G. (1998). Numerical Simulations of Degassing Scenarios for CO_2-rich Lake Nyos, Cameroon. *J. Geophys. Res.* 103, 12355–12364. doi:10.1029/98jb00393

McGlynn, G., Mooney, S., and Taylor, D. (2013). Palaeoecological Evidence for Holocene Environmental Change from the Virunga Volcanoes in the Albertine Rift, Central Africa. *Quat. Sci. Rev.* 61, 32–46. doi:10.1016/j.quascirev.2012.11.008

Mungoma, S. (1990). The Alkaline, Saline Lakes of Uganda – A Review. *Hydrobiologia.* 208 (1-2), 75–80. doi:10.1007/bf00008445

Muzuka, A. N. N., Ryner, M., and Holmgren, K. (2004). 12,000-Year, Preliminary Results of the Stable Nitrogen and Carbon Isotope Record from the Empakai Crater Lake Sediments, Northern Tanzania. *J. Afr. Earth Sci.* 40 (5), 293–303. doi:10.1016/j.jafrearsci.2004.12.005

Nagao, K., Kusakabe, M., Yoshida, Y., and Tanyileke, G. (2010). Noble Gases in Lakes Nyos and Monoun, Cameroon. *Geochem. J.* 44, 519–543. doi:10.2343/geochemj.1.0101

Ndebele-Murisa, M. R., Musil, C. F., and Raitt, L. (2010). A Review of Phytoplankton Dynamics in Tropical African Lakes. *S. Afric. J. Sci.* 106 (1-2), 13–18. doi:10.4102/sajs.v106i1/2.64

Németh, K., and Cronin, S. J. (2011). Drivers of Explosivity and Elevated Hazard in Basaltic Fissure Eruptions: The 1913 Eruption of Ambrym Volcano, Vanuatu (SW-Pacific). *J. Volcanol. Geotherm. Res.* 201 (1-4), 194–209. doi:10.1016/j.jvolgeores.2010.12.007

Németh, K., and Cronin, S. J. (2009). Phreatomagmatic Volcanic Hazards Where Rift-Systems Meet the Sea, a Study from Ambae Island, Vanuatu. *J. Volcanol. Geotherm. Res.* 180 (2-4), 246–258. doi:10.1016/j.jvolgeores.2008.08.011

Németh, K. (2004). The Morphology and Origin of Wide Craters at Al Haruj Al Abyad, Libya: Maars and Phreatomagmatism in a Large Intracontinental Flood Lava Field? *zfg.* 48 (4), 417–439. doi:10.1127/zfg/48/2004/417

Ngos, S., III, and Giresse, P. (2012). The Holocene Sedimentary and Pyroclastic Accumulations of Two Crater Lakes (Mbalang,Tizong) of the Volcanic Plateau of Adamawa (Cameroon): Palaeoenvironmental Reconstruction. *The Holocene.* 22 (1), 31–42. doi:10.1177/0959683611409779

Ngwa, C. N., Hansteen, T. H., Devey, C. W., van der Zwan, F. M., and Suh, C. E. (2017). Origin and Evolution of Primitive Melts from the Debunscha Maar, Cameroon: Consequences for Mantle Source Heterogeneity Within the Cameroon Volcanic Line. *Lithos.* 288-289, 326–337. doi:10.1016/j.lithos.2017.06.028

Ngwa, C. N., Suh, C. E., and Devey, C. W. (2010). Phreatomagmatic Deposits and Stratigraphic Reconstruction at Debunscha Maar (Mt Cameroon Volcano). *J. Volcanol. Geotherm. Res.* 192 (3-4), 201–211. doi:10.1016/j.jvolgeores.2010.02.012

Nkouandou, O. F., and Temdjim, R. (2011). Petrology of Spinel Lherzolite Xenoliths and Host Basaltic Lava from Ngao Voglar Volcano, Adamawa Massif (Cameroon Volcanic Line, West Africa): Equilibrium Conditions and Mantle Characteristics. *J. Geosci.* 56 (4), 375–387.

Nojiri, Y., Kusakabe, M., Hirabatashi, J.-I., Sato, H., Sano, Y., Shinohara, H., et al. (1990). Gas Discharge at Lake Nyos. *Nature.* 346, 322–323. doi:10.1038/346322a0

Nojiri, Y., Kusakabe, M., Tietze, K., Hirabayashi, J.-i., Sato, H., Sano, Y., et al. (1993). An Estimate of CO_2 Flux in Lake Nyos, Cameroon. *Limnol. Oceanogr.* 38, 739–752. doi:10.4319/lo.1993.38.4.0739

Ogato, T., Kifle, D., and Lemma, B. (2016). Spatio-temporal Variations in Underwater Light Climate, Thermal and Chemical Characteristics of the Tropical Soda Lake, Lake Shala, Ethiopia. *Limnology.* 17, 59–69. doi:10.1007/s10201-015-0462-7

Ohba, T., Ooki, S., Oginuma, Y., Kusakabe, M., Yoshida, Y., Ueda, A., et al. (2017). Decreasing Removal Rate of the Dissolved CO_2 in Lake Nyos, Cameroon, After the Installation of Additional Degassing Pipes, *Geol. Soc. Lond. Spec. Publications.* 437, 177–184. doi:10.1144/SP437.6

Pasternack, G. B., and Varekamp, J. C. (1997). Volcanic lake Systematics I. Physical Constraints. *Bull. Volcanology.* 58, 528–538. doi:10.1007/s004450050160

Pecoraino, G., D'Alessandro, W., and Inguaggiato, S. (2015). "The Other Side of the Coin: Geochemistry of Alkaline Lakes in Volcanic Areas," in *Volcanic Lakes*. Editors D. Rouwet, B. Christenson, F. Tassi, and J. Vandemeulebrouck (Heidelberg: Springer), 219–237. doi:10.1007/978-3-642-36833-2_9

Pelleter, A.-A., Caroff, M., Cordier, C., Bachelery, P., Nehlig, P., Debeuf, D., et al. (2014). Melilite-bearing Lavas in Mayotte (France): An Insight into the Mantle Source Below the Comores. *Lithos.* 208-209, 281–297. doi:10.1016/j.lithos.2014.09.012

Pérez, N. M., Hernández, P. A., Padilla, G., Nolasco, D., Barrancos, J., Melían, G., et al. (2011). Global CO_2 Emission from Volcanic Lakes. *Geology.* 39, 235–238. doi:10.1130/g31586.1

Pons, E. (2006). *Le Karthala, Un Volcan Méconnu? Scientific Documentary, DVD Footage*. Le Centre Multimédia de l'Université de La Réunion.

Poppe, S., Smets, B., Fontijn, K., Rukeza, M. B., De Marie Fikiri Migabo, A., Milungu, A. K., et al. (2016). Holocene Phreatomagmatic Eruptions Alongside the Densely Populated Northern Shoreline of Lake Kivu, East African Rift: Timing and Hazard Implications. *Bull. Volcanol.* 78, 82. doi:10.1007/s00445-016-1074-8

Pouclet, A., Bellon, H., and Bram, K. (2016). The Cenozoic Volcanism in the Kivu Rift: Assessment of the Tectonic Setting, Geochemistry, and Geochronology of the Volcanic Activity in the South-Kivu and Virunga Regions. *J. Afr. Earth Sci.* 121, 219–246. doi:10.1016/j.jafrearsci.2016.05.026

Pouclet, A., Kagou Dongmo, A., Bardintzeff, J.-M., Wandji, P., Chakam Tagheu, P., Nkouathio, D., et al. (2014). The Mount Manengouba, A Complex Volcano of the Cameroon Line: Volcanic History, Petrological and Geochemical Features. *J. Afr. Earth Sci.* 97, 297–321. doi:10.1016/j.jafrearsci.2014.04.023

Rasamimanana, G., Bardintzeff, J.-M., Rasendrasoa, J., Bellon, H., Thouin, C., Gioan, P., et al. (1998). Les épisodes magmatiques du Sud-Ouest de Madagascar (bassin de Morondava), marqueurs des phénomènes de rifting crétacé et néogène. *Comptes Rendus de l'Académie des Sci. - Ser. IIA - Earth Planet. Sci.* 326, 685–691. doi:10.1016/s1251-8050(98)80179-1

Rouwet, D., Chiodini, G., Ciuccarelli, C., Comastri, A., and Costa, A. (2019). Lago Albano, The "Anti-nyos-type" lake: The Past as a Key for the Future. *J. Afr. Earth Sci.* 150, 425–440. doi:10.1016/j.jafrearsci.2018.09.019

Rouwet, D., Christenson, B., Tassi, F., and Vandemeulebrouck, J. (2015a). "Volcanic Lakes," in *Volcanic Lakes*. Editors D. Rouwet, B. Christenson, F. Tassi, and J. Vandemeulebrouck (Heidelberg: Springer), 533.

Rouwet, D., Tamburello, G., Chiodini, G., Pecoraino, G., Procesi, M., Ricci, T., et al. (2021). New Insights into the Degassing Dynamics of Lago Albano (Colli Albani Volcano, Rome, Italy) During the Last Three Decades (1989-2019). *Ijg.* 140 (1), 29–41. doi:10.3301/IJG.2020.19

Rouwet, D., Taran, Y., and Inguaggiato, S. (2015b). Fluid Geochemistry of Tacaná Volcano-Hydrothermal System," in *Active Volcanoes of Chiapas (Mexico): El Chichón and Tacaná*. Editors J. L. Macías and T. Scolamacchia (Heidelberg: Springer), 139–154. doi:10.1007/978-3-642-25890-9_7

Rouwet, D., Tassi, F., Mora-Amador, R., Sandri, L., and Chiarini, V. (2014). Past, Present and Future of Volcanic lake Monitoring. *J. Volcanology Geothermal Res.* 272, 78–97. doi:10.1016/j.jvolgeores.2013.12.009

Rouwet, D. (2021). "Volcanic lake Dynamics and Related Hazards," in *Forecasting and Planning for Volcanic Hazards, Risks and Disasters*. Editor P Papale, 439–471. doi:10.1016/B978-0-12-818082-210.1016/b978-0-12-818082-2.00011-1

Rufer, D., Preusser, F., Schreurs, G., Gnos, E., and Berger, A. (2014). Late Quaternary History of the Vakinankaratra Volcanic Field (Central Madagascar): Insights from Luminescence Dating of Phreatomagmatic Eruption Deposits. *Bull. Volcanol.* 76 (5), 817. doi:10.1007/s00445-014-0817-7

Rumes, B., Eggermont, H., and Verschuren, D. (2005). Representation of Aquatic Invertebrate Communities in Subfossil Death Assemblages Sampled Along a Salinity Gradient of Western Uganda Crater Lakes. *Hydrobiologia.* 542, 297–314. doi:10.1007/s10750-004-1873-3

Russell, J. M., McCoy, S. J., Verschuren, D., Bessems, I., and Huang, Y. (2009). Human Impacts, Climate Change, and Aquatic Ecosystem Response During the Past 2000 Yr at Lake Wandakara, Uganda. *Quat. Res.* 72, 315–324. doi:10.1016/j.yqres.2009.06.008

Ryner, M., Bonnefille, R., Holmgren, K., and Muzuka, A. (2006). Vegetation Changes in Empakaai Crater, Northern Tanzania, at 14,800-9300 Cal Yr BP. *Rev. Palaeobot. Palynol.* 140 (3-4), 163–174. doi:10.1016/j.revpalbo.2006.03.006

Ryves, D. B., Mills, K., Bennike, O., Brodersen, K. P., Lamb, A. L., Leng, M. J., et al. (2011). Environmental Change over the Last Millennium Recorded in Two Contrasting Crater Lakes in Western Uganda, Eastern Africa (Lakes Kasenda and Wandakara). *Quat. Sci. Rev.* 30, 555–569. doi:10.1016/j.quascirev.2010.11.011

Saiki, K., Kaneko, K., Ohba, T., Sanemasa, M., Kusakabe, M., Ntchantcho, R., et al. (2017). Vertical Distribution of Dissolved CO_2 in Lakes Nyos and Monoun (Cameroon) as Estimated by Sound Speed in Water. *Geol. Soc. Lond. Spec. Publications.* 437, 185–192. doi:10.1144/SP437.10

Sano, Y., Kusakabe, M., Hirabayashi, J.-i., Nojiri, Y., Shinohara, H., Njine, T., et al. (1990). Helium and Carbon Fluxes in Lake Nyos, Cameroon: Constraint on Next Gas Burst. *Earth Planet. Sci. Lett.* 99, 303–314. doi:10.1016/0012-821x(90)90136-l

Sano, Y., Wakita, H., Ohsumi, T., and Kusakabe, M. (1987). Helium Isotope Evidence for Magmatic Gases in Lake Nyos, Cameroon. *Geophys. Res. Lett.* 14, 1039–1041. doi:10.1029/gl014i010p01039

Schmid, M., Halbwachs, M., and Wüest, A. (2006). Simulation of CO_2 concentrations, Temperature, and Stratification in Lake Nyos for Different Degassing Scenarios. *Geochem. Geophys. Geosyst.* 7. doi:10.1029/2005GC001164

Schmid, M., Lorke, A., Dinkel, C., Tanyileke, G., and Wüest, A. (2004). Double-diffusive Convection in Lake Nyos, Cameroon. *Deep Sea Res. Oceanographic Res. Pap.* 51, 1097–1111. doi:10.1016/j.dsr.2004.02.010

Schmid, M., Lorke, A., Wuest, A., Halbwachs, M., and Tanyileke, G. (2003). Development and Sensitivity Analysis of a Model for Assessing Stratification and Safety of Lake Nyos During Artificial Degassing. *Ocean Dyn.* 53, 288–301. doi:10.1007/s10236-003-0032-0

Sibree, J. (1891). The Volcanic Lake of Tritriva, Central Madagascar. *Proc. R. Geographical Soc. Monthly Rec. Geogr.* 13, 477–483. doi:10.2307/1801202

Sigurdsson, H., Devine, J. D., Tchua, F. M., Presser, F. M., Pringle, M. K. W., and Evans, W. C. (1987). Origin of the Lethal Gas Burst from Lake Monoun, Cameroun. *J. Volcanology Geothermal Res.* 31, 1–16. doi:10.1016/0377-0273(87)90002-3

Smith, I. E. M., and Németh, K. (2017). "Source to Surface Model of Monogenetic Volcanism: A Critical Review," in *Monogenetic Volcanism*. Editors K. Németh, G. Carrasco-Nuñez, J. J. Aranda-Gomez, and I. E. M. Smith (Bath, United Kingdom: The Geological Society Publishing House). doi:10.1144/sp446.14

Stoppa, F., and Schiazza, M. (2013). An Overview of Monogenetic Carbonatitic Magmatism from Uganda, Italy, China and Spain: Volcanologic and Geochemical Features. *J. South Am. Earth Sci.* 41, 140–159. doi:10.1016/j.jsames.2012.10.004

Tanyileke, G., Ntchantcho, R., Fantong, W. Y., Aka, F. T., and Hell, J. V. (2019). 30 Years of the Lakes Nyos and Monoun Gas Disasters: A Scientific, Technological, Institutional and Social Adventure. *J. Afr. Earth Sci.* 150, 415–424. doi:10.1016/j.jafrearsci.2018.11.022

Tanyileke, G. Z., Kusakabe, M., and Evans, W. C. (1996). Chemical and Isotopic Characteristics of Fluids Along the Cameroon Volcanic Line, Cameroon. *J. Afr. Earth Sci.* 22, 433–441. doi:10.1016/0899-5362(96)00025-5

Tassi, F., and Rouwet, D. (2014). An Overview of the Structure, Hazards, and Methods of Investigation of Nyos-type Lakes from the Geochemical Perspective. *J. Limnol.* 73 (1), 55–70. doi:10.4081/jlimnol.2014.836

Tazieff, H. (1989). Mechanisms of the Nyos Carbon Dioxide Disaster and of So-Called Phreatic Steam Eruptions. *J. Volcanology Geothermal Res.* 39, 109–116. doi:10.1016/0377-0273(89)90051-6

Tchamabe, B. C., Youmen, D., Owona, S., Issa, T., Németh, K., Ngapna, M. N., et al. (2013). Eruptive History of the Barombi Mbo Maar, Cameroon Volcanic Line, Central Africa: Constraints from Volcanic Facies Analysis. *Cent. Europ. J. Geosci.* 5 (4), 480–496. doi:10.2478/s13533-012-0147-2

Tedesco, D., Tassi, F., Vaselli, O., Poreda, R. J., Darrah, T., Cuoco, E., et al. (2010). Gas Isotopic Signatures (He, C, and Ar) in the Lake Kivu Region (Western Branch of the East African Rift System): Geodynamic and Volcanological Implications. *J. Geophys. Res.* 115, B01205. doi:10.1029/2008JB006227

Temdjim, R. (2012). Ultramafic Xenoliths from Lake Nyos Area, Cameroon Volcanic Line, West-central Africa: Petrography, mineral Chemistry, Equilibration Conditions and Metasomatic Features. *Geochemistry.* 72 (1), 39–60. doi:10.1016/j.chemer.2011.07.002

Tietze, K. (1992). "Cyclic Gas Bursts: Are They a 'usual' Feature of Lake Nyos and Other Gas-Bearing Lakes?," in *Natural Hazards in West and Central Africa*. Editors S. J. Freeth, C. O. Ofoegbu, and K. M. Onuoha (Braunschweig: Vieweg), 97–107. doi:10.1007/978-3-663-05239-5_10

Vail, J. R. (1972). Jebel Marra, A Dormant Volcano in Darfur Province, Western Sudan. *Bull. Volcanol.* 36, 251–265. doi:10.1007/BF02596994

van Bree, L. G. J., Peterse, F., van der Meer, M. T. J., Middelburg, J. J., Negash, A. M. D., De Crop, W., et al. (2018). Seasonal Variability in the Abundance and Stable Carbon-Isotopic Composition of Lipid Biomarkers in Suspended Particulate Matter from a Stratified Equatorial Lake (Lake Chala, Kenya/Tanzania): Implications for the Sedimentary Record. *Quat. Sci. Rev.* 192, 208–224. doi:10.1016/j.quascirev.2018.05.023

Varekamp, J. C., Pasternack, G. B., and Rowe, G. L. (2000). Volcanic lake Systematics II. Chemical Constraints. *J. Volcanology Geothermal Res.* 97, 161–179. doi:10.1016/s0377-0273(99)00182-1

Vaselli, O., Tedesco, D., Cuoco, E., and Tassi, F. (2015). "Are Limnic Eruptions in the CO_2-CH_4-Rich Gas Reservoir of Lake Kivu (Democratic Republic of the Congo and Rwanda) Possible? Insights from Physico-Chemical and Isotopic Data," in *Volcanic Lakes*. Editors D. Rouwet, B. Christenson, F. Tassi, and J. Vandemeulebrouck (Heidelberg: Springer), 489–505. doi:10.1007/978-3-642-36833-2_22

Venturi, S., Cabassi, J., Butturini, A., Vázquez, E., Pacini, N., Tassi, F., et al. (2019). *Biogeochemical Processes in a Small Kenyan Rift Valley Soda lake (Lake Sonachi): Implications for Methane Emissions*. Taupo, New Zealand, 45.

Viollier, E., Jézéquel, D., Michard, G., Pèpe, M., Sarazin, G., and Albéric, P. (1995). Geochernical Study of a Crater lake (Pavin Lake, France): Trace-Element Behaviour in the Monimolimnion. *Chem. Geology.* 125, 61–72. doi:10.1016/0009-2541(95)00059-u

Viollier, E., Michard, G., Jézéquel, D., Pèpe, M., and Sarazin, G. (1997). Geochemical study of a Crater lake: Lake Pavin, Puy de Dôme, France. Constraints Afforded by the Particulate Matter Distribution in the Element Cycling Within the Lake. *Chem. Geology.* 142, 225–241. doi:10.1016/s0009-2541(97)00093-4

Weidendorfer, D., Schmidt, M. W., and Mattsson, H. B. (2017). A Common Origin of Carbonatite Magmas. *Geology.* 45 (6), 507–510. doi:10.1130/g38801.1

Westerman, F. (2013). *Stikvallei*. Amsterdam: De Bezige Bij, 317.

Williamson, D., Jackson, M. J., Banerjee, S. K., Marvin, J., Merdaci, O., Thouveny, N., et al. (1999). Magnetic Signatures of Hydrological Change in a Tropical Maar-lake (Lake Massoko, Tanzania): Preliminary Results. *Phys. Chem. Earth, A: Solid Earth Geodesy.* 24 (9), 799–803. doi:10.1016/s1464-1895(99)00117-9

Williamson, D., Jelinowska, A., Kissel, C., Tucholka, P., Gibert, E., Gasse, F., et al. (1998). Mineral-magnetic Proxies of Erosion/oxidation Cycles in Tropical Maar-lake Sediments (Lake Tritrivakely, Madagascar): Paleoenvironmental Implications. *Earth Planet. Sci. Lett.* 155, 205–219. doi:10.1016/s0012-821x(97)00217-3

Wood, R. B., Prosser, M. V., and Baxter, R. M. (1976). The Seasonal Pattern of Thermal Characteristics of Four of the Bishoftu Crater Lakes, Ethiopia. *Freshw. Biol.* 6, 519–530. doi:10.1111/j.1365-2427.1976.tb01643.x

Yihdego, Y., and Becht, R. (2013). Simulation of Lake-aquifer Interaction at Lake Naivasha, Kenya Using a Three-Dimensional Flow Model with the High Conductivity Technique and a DEM with Bathymetry. *J. Hydrol.* 503, 111–122. doi:10.1016/j.jhydrol.2013.08.034

Yoshida, Y., Issa, M., Kusakabe, H., and Ohba, T. (2010). An Efficient Method for Measuring CO_2 Concentration in Gassy Lakes: Application to Lakes Nyos and Monoun, Cameroon. *Geochem. J.* 44, 441–448. doi:10.2343/geochemj.1.0078

Yoshida, Y., Kusakabe, M., Issa, T., Ohba, G., and Hell, J. V. (2017). Decreasing Capability of the Degassing Systems at Lakes Nyos and Monoun (Cameroon): A New Gas Removal System Applied to Lake Monoun to Prevent a Future Limnic Eruption. *Geol. Soc. Lond. Spec. Publications.* 437, 205–212. doi:10.1144/SP437.3

Zhang, Y. (1996). Dynamics of CO_2-driven lake Eruptions. *Nature.* 379, 57–59. doi:10.1038/379057a0

Zhang, Y. (1998). Experimental Simulations of Gas-Driven Eruptions: Kinetics of Bubble Growth and Effect of Geometry. *Bull. Volcanology.* 59, 281–290. doi:10.1007/s004450050192

Conflict of Interest: The authors declare that the research was conducted in the absence of any commercial or financial relationships that could be construed as a potential conflict of interest.

Publisher's Note: All claims expressed in this article are solely those of the authors and do not necessarily represent those of their affiliated organizations, or those of the publisher, the editors and the reviewers. Any product that may be evaluated in this article, or claim that may be made by its manufacturer, is not guaranteed or endorsed by the publisher.

frontiers in Earth Science

ORIGINAL RESEARCH
published: 28 October 2021
doi: 10.3389/feart.2021.722056

The Evolution of Peteroa Volcano (Chile–Argentina) Crater Lakes Between 1984 and 2020 Based on Landsat and Planet Labs Imagery Analysis

Felipe Aguilera[1,2,3]*, *Javiera Caro*[1,2] *and Susana Layana*[1,2,3]

[1]Núcleo de Investigación en Riesgo Volcánico-Ckelar Volcanes, Universidad Católica del Norte, Antofagasta, Chile, [2]Departamento de Ciencias Geológicas, Universidad Católica del Norte, Antofagasta, Chile, [3]Centro de Investigación para la Gestión Integrada del Riesgo de Desastres (CIGIDEN), Santiago, Chile

OPEN ACCESS

Edited by:
Dmitri Rouwet,
Istituto Nazionale di Geofisica e Vulcanologia, sezione di Bologna, Italy

Reviewed by:
Akihiko Terada,
Tokyo Institute of Technology, Japan
Clive Oppenheimer,
University of Cambridge, United Kingdom

***Correspondence:**
Felipe Aguilera
feaguilera@ucn.cl

Specialty section:
This article was submitted to Volcanology, a section of the journal Frontiers in Earth Science

Received: *08 June 2021*
Accepted: *23 September 2021*
Published: *28 October 2021*

Citation:
Aguilera F, Caro J and Layana S (2021) The Evolution of Peteroa Volcano (Chile–Argentina) Crater Lakes Between 1984 and 2020 Based on Landsat and Planet Labs Imagery Analysis. Front. Earth Sci. 9:722056. doi: 10.3389/feart.2021.722056

One of the major challenges in the understanding of the crater lakes dynamics and their connection with magmatic/hydrothermal processes is the continuous tracking of the physical behavior of lakes, especially in cases of remote and poorly accessible volcanoes. Peteroa volcano (Chile–Argentina border) is part of the Planchón–Peteroa–Azufre Volcanic Complex, one of the three volcanoes in the Southern Volcanic Zone of the Andes with crater lakes. Peteroa volcano is formed by a ~5 km diameter caldera-type crater, which hosts four crater lakes and several fumarolic fields. Peteroa volcano has a large history of eruptive activity including phreatic-and-phreatomagmatic explosions and several episodes of strong degassing from its crater lakes. Here, we used TIR and SWIR bands from Landsat TM, ETM+, and OLI images available from October 1984 to December 2020 to obtain thermal parameters such as thermal radiance, brightness temperature, and heat fluxes, and Planet Labs Inc. images (RapidEye and PlanetScope) available between May 2009 and December 2020 to obtain physical parameters such as area, color, and state (liquid or frozen) of the crater lakes. We reviewed the historical eruptive activity and compared it with thermal and physical data obtained from satellite images. We determined the occurrence of two eruptive/thermal cycles: 1) Cycle 1 includes the formation of a new fumarolic field and two active craters during a short eruptive period, which includes thermal activity in three of the four crater lakes, and a strong degassing process between October 1998 and February 2001, coincident with a peak of volcanic heat flux (Q_{volc}) in two craters. The cycle finished with an eruptive episode (September 2010–July 2011). 2) Cycle 2 is represented by the thermal reactivation of two crater lakes, formation and detection of thermal activity in a new nested crater, and occurrence of a new eruptive episode (October 2018–April 2019). We observed a migration of the thermal and eruptive activity between the crater lakes and the interconnection of the pathways that feed the lakes, in both cases, partially related to the presence of two deep magma bodies. The Q_{volc} in Peteroa volcano crater lakes is primarily controlled by volcanic activity, and seasonal effects affect it at short-term, whilst at long-term, seasonal effects do not show clear influences in the volcanic heat fluxes. The maximum Q_{volc} measured between all crater lakes during quiescent periods

was 59 MW, whereas during unrest episodes Q_{volc} in single crater lakes varied from 7.1 to 38 MW, with Peteroa volcano being classified as a low volcanic heat flux system. The detection of new thermal activity and increase of Q_{volc} in Peteroa volcano previous to explosive unrest can be considered as a good example of how thermal information from satellite images can be used to detect possible precursors to eruptive activity in volcanoes which host crater lakes.

Keywords: Southern Volcanic Zone of the Andes, eruptive activity, RapidEye, PlanetScope, VIPS, VOLCANOMS, energy balance

INTRODUCTION

A crater lake is one of the several superficial expressions of volcanic activity which consist of a water body confined in a crater. Crater lakes are a consequence of a complex interaction between deep/shallow volcanic, hydrothermal, and degassing processes, superficial factors like climate conditions, and morphological elements such as crater geometry (Pasternack and Varekamp, 1997; Christenson et al., 2015). Several disciplines and methods have been applied to understand the processes involved in the formation and evolution of crater lakes, including fluid geochemistry (Dmitri Rouwet and Franco Tassi, 2011; Rouwet et al., 2017), geophysics (Caudron et al., 2012), hydrogeology (Mazza et al., 2015), biology (Mapelli et al., 2015), and limnology (Kling et al., 2015), among others. In the case of some high latitude and high altitude volcanoes, the applicability and frequency of the field methods is restricted to the dry season, impeding the study of the characteristics and dynamics of their crater lakes in a continuous manner. One technique that allows the study of crater lakes independently of seasonal restrictions is the use of satellite images, which have been widely used to monitor changes in lake temperature (Oppenheimer, 1993; Trunk and Bernard, 2008), determine heat fluxes and heat budget (Oppenheimer, 1996; Oppenheimer, 1997a; Lewicki et al., 2016), detect changes in the crater lake color (Oppenheimer, 1997b; Murphy et al., 2018), and investigate the thermal evolution of volcanic lakes through time (Candela-Becerra et al., 2020), among other applications. The combination of satellite images with accurate *in situ* and/or other remote measurements, such as lake temperature, air temperature, humidity, windspeed, and others, has allowed us to improve the calculations of energy balance and to better understand the dynamics of crater lakes (Lewicki et al., 2016). Additionally, the availability of improved satellite technology provides new tools and more accurate data, which have been recently incorporated into volcanological research. One example is the use of satellite data provided by Planet Labs Inc., a constellation of CubeSats with high temporal (<1–72 h) and spatial (from 0.8 to 5 m) resolutions, which have been recently used to map ash clouds, pyroclastic density currents (PDCs), lava flows, to track ash plumes, and to identify morphological changes in eruptive craters (Aldeghi et al., 2019; Romero et al., 2020).

Along the Southern Volcanic Zone of the Andes, where at least 60 volcanes have been considered as active/potentially active (Stern, 2004), only three volcanes host volcanic lakes on their craters, corresponding from north to south to Tupungatito, Peteroa, and Copahue volcanoes (**Figure 1**). Tupungatito hosts one lake and has sporadic low magnitude historical eruptive activity (Benavente et al., 2013), whereas Copahue and Peteroa volcanoes host one and four volcanic lakes, respectively, in both cases with frequent records of low-to-moderate eruptive activity (Naranjo and Polanco, 2004; Caselli et al., 2016; Aguilera et al., 2016; Romero et al., 2020).

Peteroa volcano (35.240°S, 70.570°W, 3,603 m a. s. l.) is a composite stratovolcano located in the Transitional Southern Volcanic Zone (TSVZ; López-Escobar et al., 1995; Sellés et al., 2004), on the border between Chile and Argentina, and it is formed by a ~5 km diameter caldera-type crater, which includes four nested craters (150–500 m diameter; all hosting lakes) and a scoria cone (**Figure 1**). Fumarolic activity is present in Craters 1, 2, and 3, and in the zone between Craters 2 and 4 (**Figure 1**). Several glaciers are located in the caldera area and in the highest parts of the flank valleys. Peteroa volcano is part of a major north-to-south trending volcanic complex named the Planchón–Peteroa–Azufre Volcanic Complex. It constitutes three overlapping volcanic edifices, which have formed from basaltic andesites to rhyodacitic lava and pyroclastic flows and lahars. The Planchón–Peteroa–Azufre Volcanic Complex evolved in at least four eruptive stages, Azufre (<219 ± 14 ka), Planchón I (~72 ± 11 to ~11 ka), Planchón II (~11–~7 ka), and Peteroa (<7 ka) (Tormey et al., 1989; Tormey et al., 1995; Naranjo et al., 1999; Naranjo and Haller, 2002; Tormey, 2010; Klug et al., 2018). A total of 18 eruptions have been recorded at Peteroa volcano during the period between 1660 and 2020, mostly corresponding to phreatic-to-phreatomagmatic eruptions (VEI ≤ 2), although some major eruptions (VEI = 4) have been also recorded (Haller et al., 1994; Gonzalez-Ferrán, 1995; Naranjo et al., 1999; Haller and Risso, 2011). The greatest historical eruption occurred in 1762 (VEI = 4), when the explosive and effusive activity was followed by the partial collapse of the volcanic edifice, producing debris, avalanches, and lahars, and damming the Río Teno for several days (González-Ferrán, 1995; Haller and Risso, 2011). Explosive and/or effusive activity was recorded in 1660, 1835, 1837, 1860, 1869, 1878, 1889 (lasting 5 years), 1937 (a scoria cone was formed, and a short lava flow was emitted; **Figure 1**), 1938, 1959, 1960, 1962, 1967, 1991, 1998, 2010–2011, and 2018–2020.

In this article, we present a temporal analysis of Peteroa volcano crater lakes, by using two large databases based on Landsat imagery (1984–2020) including Landsat TM, ETM+, and OLI-TIRS and Planet Labs Inc. imagery (2009–2020)

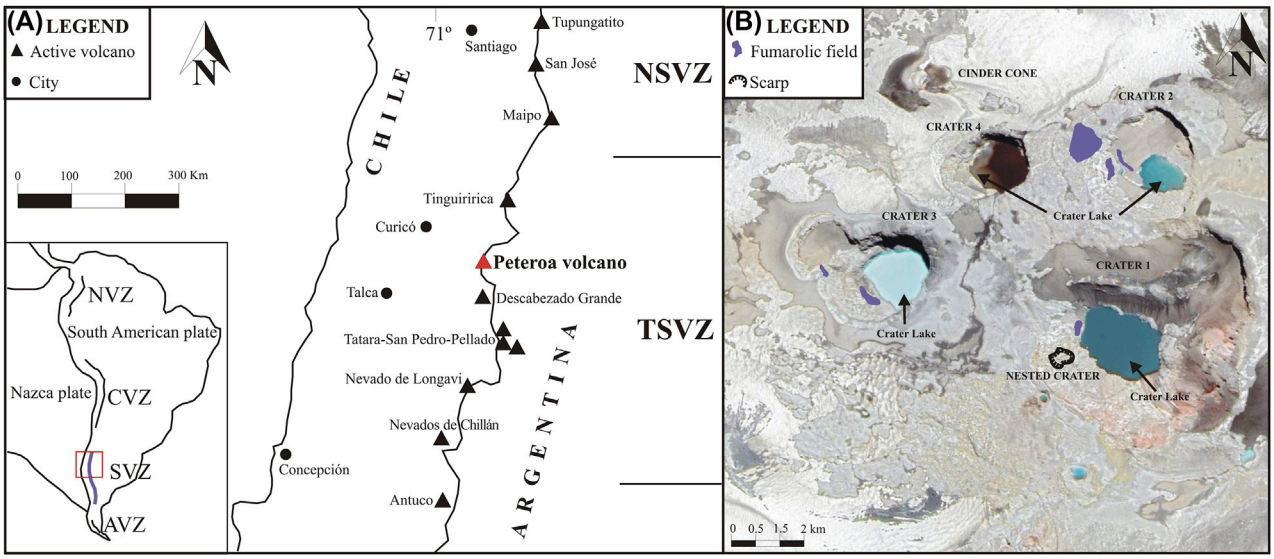

FIGURE 1 | (A) Location map of Peteroa volcano. NSVZ: Northern Southern Volcanic Zone of the Andes; TSVZ: Transitional Southern Volcanic Zone of the Andes. **(B)** PlanetScope image (natural color) showing the location of the crater lakes and fumarolic fields of Peteroa volcano. The location of the new nested crater is also indicated.

including RapidEye and PlanetScope images, with the objectives 1) to determine the temporal evolution of the Peteroa volcano crater lakes, 2) to assess the energy balance of those lakes, and 3) to correlate the temporal evolution of the lakes with the seasonal variations of the climate and eruptive activity. We have selected Peteroa volcano as a priority to be studied using a long-term remote-based monitoring system between the three volcanoes with crater lakes due to its extent and frequent eruptive historical record, which includes a VEI 4 eruption, partial flank collapse, lahars, and creation of new craters. Additionally, Peteroa has been categorized as the second most hazardous volcano for Argentina, and 23rd for Chile, being a priority for volcanic monitoring in both countries.

HISTORICAL ERUPTIVE ACTIVITY IN THE PERIOD 1984–2020

In the period 1984–1990 Peteroa volcano was still in a quiescence state, although in January 1987 a new fumarolic field was reported close to the 1937 cinder cone, covering an area of ~100 m^2 (Global Volcanism Program, 1987; **Figure 2**). On February 9, 1991, a new eruptive period started, characterized by the occurrence of phreatomagmatic explosions and emitting eruptive columns of 400–700 m over the main caldera, and occasionally over 1,000 m (Gardeweg, 1991; Global Volcanism Program, 1991). The eruption lasted until February 15, 1991, and generated two new craters, both hosting volcanic lakes, corresponding to Craters 3 and 4 (**Figures 1**, **3**; Gardeweg, 1991; Global Volcanism Program, 1991). After 7 years of quiescence period, a short unrest occurred between October and November 1998, when steam and tephra plumes were produced and transported up to 8 km NW from the volcano (Global Volcanism Program, 1999). Increases in gas emissions were reported during February–March 1999 and December 2000–February 2001, producing a gas plume up to 500 m over the caldera and transported up to 1 km to the east (Global Volcanism Program, 2001). No eruptive activity was recorded between March 2001 and December 2009. The February 1991 eruptive period was characterized by the presence of juvenile eruptive products and by the low magnitude of the eruptions (VEI 1; Naranjo et al., 1999), whereas the later eruptions emitted exclusively non-juvenile products.

On January 4, 2010, an increase in degassing activity started in Crater 3, producing frequent and rhythmical phreatic explosions, and generating a 200 m high gas plume over the crater rim, which lasted up to August 7, 2010 (Aguilera et al., 2016). On 8th August, scarce ash was observed in the gas plume (Aguilera et al., 2016). On September 4, 2010 a new eruptive activity started in Crater 3, characterized by the occurrence of phreatic explosions and the emission of tephra plumes (up to 3 km height over the crater rim; Aguilera et al., 2016). Between November 2, 2010, and February 16, 2011, only gas/steam plumes were emitted (up to 1.5 km height over the crater rim), and at least during November 2010 no lake was present in Crater 3, which was completely vaporized after previous eruptive activity (Aguilera et al., 2016). New eruptive activity was observed during 17th February–20th May 2011 and 17th June–13th July 2011, characterized by the emission of tephra plumes with maximum heights of 1.5 and 0.5 km over the crater rim, respectively (Aguilera et al., 2016). Since July 14, 2011, and at least in March 2012, the activity was restricted to the emission of low altitude gas plume (50–100 m; Aguilera et al., 2016). This eruptive period was characterized by the absence of juvenile eruptive products and by the low magnitude of the eruptions (VEI 0-2; Aguilera et al., 2016).

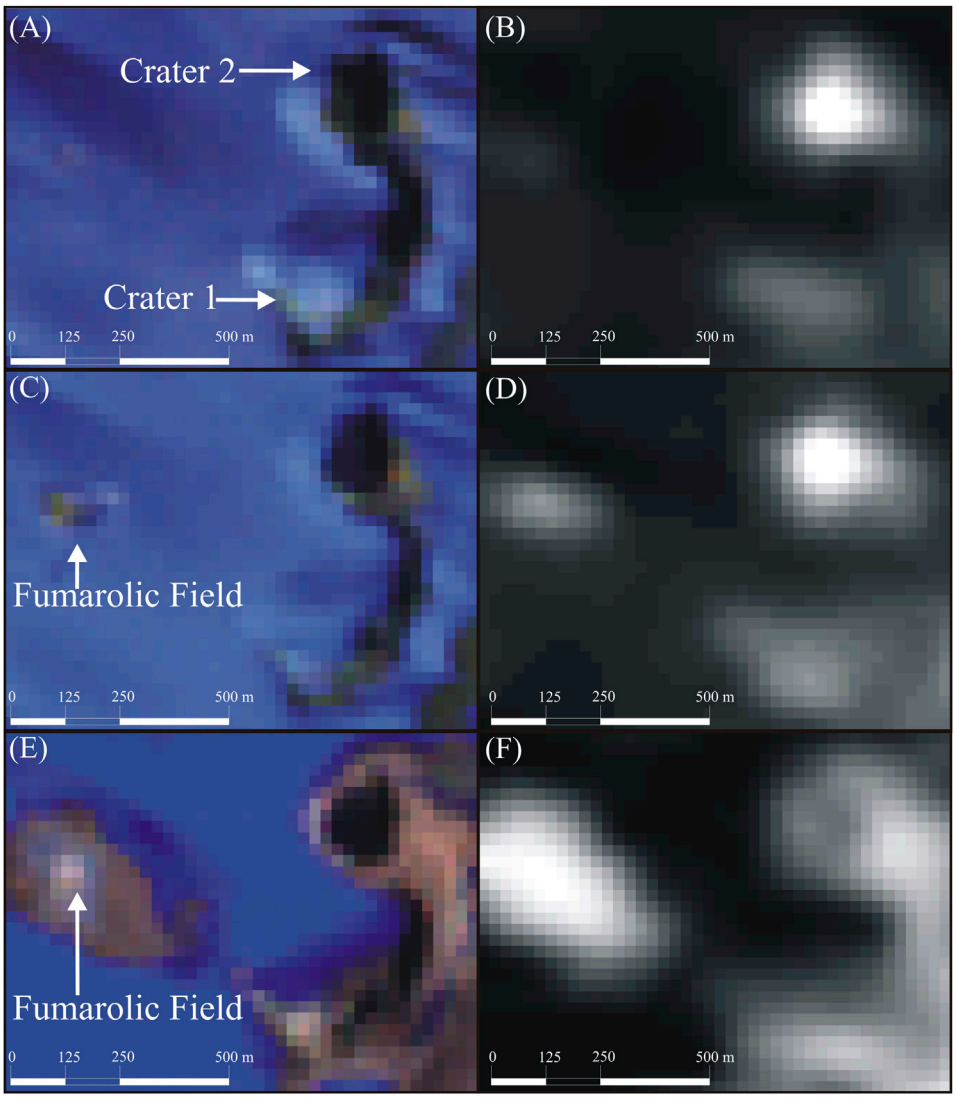

FIGURE 2 | (A) Landsat TM (combination 754 in RGB) showing Crater Lakes 1 and 2 (August 17, 1986). **(B)** Landsat TM (TIR band) showing Crater Lakes 1 and 2 (August 17, 1986). **(C)** Landsat TM (combination 754 in RGB) showing the new fumarolic field, Crater Lakes 1 and 2 (August 18, 1986). **(D)** Landsat TM (TIR band) showing the new fumarolic field, Crater Lakes 1 and 2 (September 18, 1986). **(E)** Landsat TM (combination 754 in RGB) showing an extended fumarolic field, Crater Lakes 1 and 2 (January 10, 1991). **(F)** Landsat TM (TIR band) showing an extended fumarolic field, Crater Lakes 1 and 2 (January 10, 1991).

The last eruptive cycle started probably in January 2018, when a crater with a small lake was formed in the southwestern wall of Crater 1, accompanied with very diffuse degassing in the upper part of the wall. In March 2018, the degassing activity in the main lake of Crater 1 increased substantially. By May 2018, the nested crater increased its size and fumarolic activity. On October 13, 2018, tephra started to be emitted from the nested crater, followed by almost 7 months of intermittent emission of tephra and gas plumes, varying from 0.6 to 2 km over the crater rim (Global Volcanism Program, 2019; Romero et al., 2020). By the end of this eruptive cycle, the nested crater grew up to ~75 m diameter. This eruptive period was characterized by the presence of abundant juvenile eruptive products (Romero et al., 2020) and by the low magnitude of the eruptions (VEI 0-2).

METHODOLOGIES

Landsat TM, ETM+, and OLI Imagery Acquisition and Processing

We used 1,208 Landsat images available from the period 1984–2020, corresponding to TM (600 images), ETM+ (302 images), and OLI-TIRS (306 images) sensors. Landsat TM sensor was mounted on two satellites (Landsat 4 and 5), whereas Landsat ETM+ and OLI-TIRS on one satellite each (Landsat 7 and 8, respectively). Landsat satellites include 7, 8, and 11 bands (TM, ETM+, and OLI-TIRS, respectively) between blue and thermal infrared, spatial resolution variable between 15 and 120 m, and the revisit time is 16 days for each satellite. The images were downloaded in a GeoTIFF format from the site http://

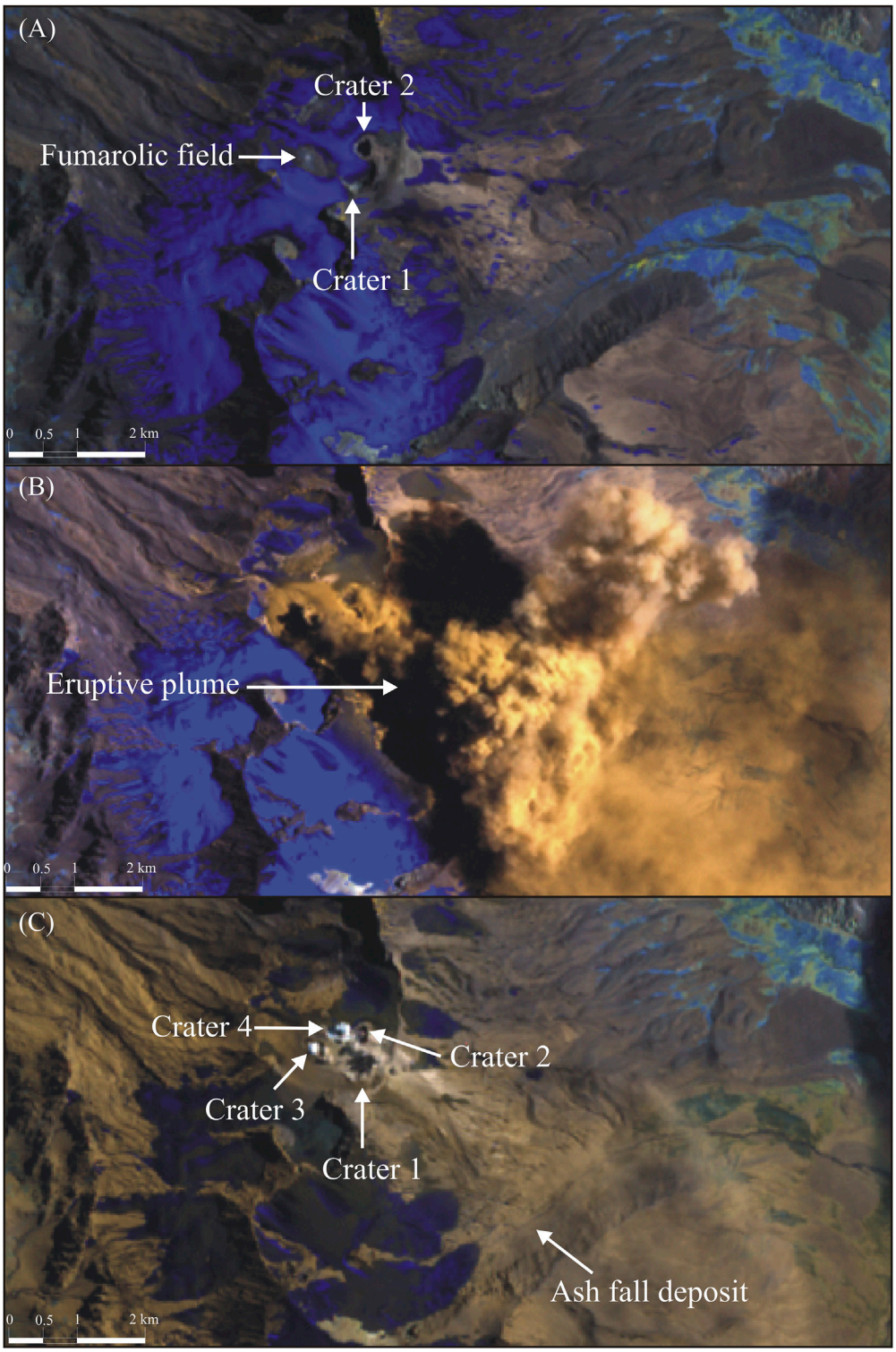

FIGURE 3 | (A) Landsat TM (combination 754 in RGB) showing Crater Lakes 1 and 2 (February 4, 1991). **(B)** Landsat TM (combination 754 in RGB) showing the eruptive plume (February 11, 1991). **(C)** Landsat TM (combination 754 in RGB) showing Crater Lakes 1, 2, and the new Craters 3 and 4. Ash fall deposit is also shown (February 27, 1991).

earthexplorer.usgs.gov, and visually revised using natural color combination in RGB, with the objective to separate pixels corresponding exclusively to crater lakes, fumaroles, and the surrounding area. Additionally, the images were visually revised using natural color combination with the objective to determine the presence or absence of crater lakes. Thermal bands (TIR) were processed using the VIPS software included in the VOLCANOMS platform (Layana et al., 2020) to obtain the thermal radiance, brightness temperature, and radiant heat flux from the crater lakes and fumarolic fields separately. Short wave infrared bands (SWIR) were also processed to obtain thermal radiance from fumarolic fields. 400 images were discarded because of the presence of clouds covering the four craters; three images were discarded due to tephra plumes covering the four craters, and 113 images were partially processed due to the presence of black stripes (caused by the failure of the ETM + sensor), which covered between Craters 1 and 3.

PlanetScope Imagery Acquisition and Processing

A total of 551 RapidEye and PlanetScope images were acquired from the Planet Labs Inc. site (www.planet.com) for the period between May 27, 2009, and December 31, 2020. RapidEye is a constellation of five satellites which collected five bands (between blue and near infrared) images characterized by a spatial resolution of 5 m and a temporal resolution variable from 5.5 days to daily, being available between 2009 and 2020 (www.planet.com). PlanetScope is a constellation of ~120 CubeSat (called doves) which collected four bands (between blue and near infrared) images with a 3–4 m pixel size and a daily or several images per day revisit time (www.planet.com). We acquired 117 RapidEye and 434 PlanetScope images, which were downloaded in the GeoTIFF format, and processed to obtain physical parameters including area, color, and state (liquid or frozen) of the crater lakes, presence or absence of crater lakes, and presence of clouds, gas/steam plumes, or tephra plumes.

Areas of lakes were calculated using a GIS-based analysis, with the lakes being mapped individually and their areas then obtained. The color and state of the crater lakes were obtained by a visual inspection, using natural color combination in RGB. Subsequently, color and the state of the crater lakes (liquid, frozen, liquid + ice, and no lake) classifications were done, with both parameters being expressed as frequency.

Heat Flux Calculations

According to Pasternack and Varekamp, (1997), the energy balance of a crater lake can be expressed as follows (**Figure 4**):

$$Q_{sun} + Q_{atm} + Q_{volc-cond} + Q_{volc} = Q_{rad} + Q_{evap} + Q_{cond} + Q_{rain}, \quad (1)$$

where Q expresses the heat flux from the sun (Q_{sun}), atmosphere (Q_{atm}), conductive heat from a shallow magma body ($Q_{volc\text{-}cond}$), and volcanic/hydrothermal contribution from the bottom of the lake (Q_{volc}). Heat fluxes related to a crater lake correspond to radiative (Q_{rad}), evaporative (Q_{evap}), conductive (Q_{cond}), and rain water input (Q_{rain}).

According to Linacre (1992), heat fluxes from the sun (Q_{sun} in MW) and atmosphere (Q_{atm} in MW) are calculated as follows:

$$Q_{sun} = \left(185 + 5.9\varnothing - 0.22\varnothing^2 + 0.00267\varnothing^3\right)A, \quad (2)$$

$$Q_{atm} = (208 + 6T_a)\left(1 + 0.0034C^2\right)A, \quad (3)$$

where $\varnothing$ is the latitude in decimal degrees, A is the area of the lake (in m^2), T_a the atmospheric temperature (in °C), and C (average cloud cover) is calculated as follows:

$$C = 5.1946 - 0.23227\varnothing + 6.7727 \times 10^{-3}\varnothing^2 - 4.9495 \times 10^{-5}\varnothing^3. \quad (4)$$

The atmospheric temperature was obtained for each month from Liaudat et al., 2014, corresponding to the atmospheric temperature at the Peteroa volcano caldera rim. Conductive heat flux has been considered negligible as the shallow magma source is located at depth > 1 km (Lewicki et al., 2016), whereas Q_{volc} is the parameter to be calculated. Radiative heat flux has been calculated using the procedure proposed by Layana et al. (2020), where the thermal radiance ($R_{TIR,\ thermal}$) is initially calculated as follows:

$$R_{TIR,\ thermal} = \left(R_{TIR} - R_{TIR,U}\right)/(\varepsilon\tau), \quad (5)$$

where $R_{TIR,U}$ is the upwelling radiance, τ the transmissivity, and ε the emissivity. In order to isolate the thermal anomaly from non-thermal pixels, we used a digital number threshold ($DN_{threshold}$) which can be calculated using the mean ($\mu_{non\ thermal}$) and standard deviation (σ) from non-thermal pixels using the following equation:

$$DN_{threshold} = \mu_{non\ thermal} + 2\sigma_{non\ thermal}. \quad (6)$$

Before applying **Eq. 6**, thermal and non-thermal pixels are separated by visual inspection of the satellite image, where thermal pixels are recognized by their higher brightness (high DN) than non-thermal pixels (very low brightness and DN). Brightness temperature (T), which is directly dependent of the spectral radiance (L_λ), and consequently, dependent on the wavelength (λ), can be calculated after thermal pixels are isolated using the following equation:

$$T = \frac{K_2}{ln\left(\frac{K_1}{L_\lambda} + 1\right)}, \quad (7)$$

where K_1 and K_2 are the thermal conversion constants (or calibration constants) 607.76 $W/m^2\mu msr$ and 1,260.56 K, respectively. Radiative heat flux (Q_{rad} in W/pixel) is calculated from each thermal pixel as follows:

$$Q_{rad} = \sigma\varepsilon \sum_i T_i^4 A_i, \quad (8)$$

where σ is the Stefan–Boltzmann constant (5.67×10^{-8} W/m^2K^4), ε is emissivity (emissivity for the lake surface was variable depending on the seasons, being 0.94 for summer, 0.93 for winter and spring, and 0.95 for autumn, whereas for the ground surface was 0.98 for all season), T is brightness temperature at each pixel i (K), and A_i is the pixel area (m^2/pixel). In order to obtain a radiative heat flux attributable

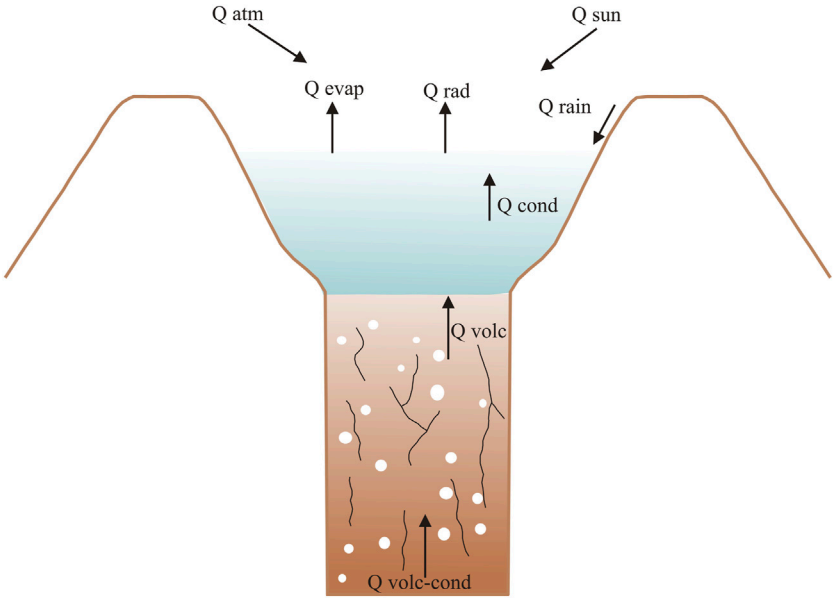

FIGURE 4 | Heat fluxes involved in the energy balance of a crater lake. Heat flux from the sun (Q_{sun}), atmosphere (Q_{atm}), radiative (Q_{rad}), evaporative (Q_{evap}), conductive (Q_{cond}), rain water input (Q_{rain}), conductive heat from a shallow magma body ($Q_{volc\text{-}cond}$), and volcanic/hydrothermal contribution from the bottom of the lake (Q_{volc}).

only to the crater lake, the average of non-thermal heat flux is subtracted from Q_{rad} (background correction). Considering that other thermal features can coexist with crater lakes (e.g., fumarolic fields), those features can be thermally correlated and compared with crater lakes by using Q_{rad}, where T can be calculated directly from the pixel DN and/or field measurements of the temperature (e.g., fumaroles temperature) and the area from the pixel size. Evaporative heat flux (Q_{evap} in MW) was obtained by the following (Ryan et al., 1974):

$$Q_{evap} = \left[2.7\,(T_{wv} - T_{av})^{\frac{1}{3}} + 3.2v\right](e_w - e_a)\sum_i A_i, \tag{9}$$

where A_i is the pixel area (m^2/pixel), and v is the wind speed (ms^{-1}), which was obtained from the National Oceanic and Atmospheric Administration (NOAA) atmospheric models for an altitude of 3,460 m a.s.l, corresponding to the average altitude of the Peteroa caldera, where the four crater lakes are hosted. An average value (8 ms^{-1}) was used after a revision of data from 1984 to 2020. The parameter e can be calculated using an absolute temperature (T in K) as follows (Haar et al., 1984):

$$e = 9.667 \times 10^{-6}T^4 - 1.091 \times 10^{-2}T^3 + 4.648 \times T^2 - 8.856 \times 10^2 T + 6.360. \tag{10}$$

The parameters e_w and e_a (mbar) correspond to saturated water and atmospheric vapor pressures at the temperature of water from the lake (T_w) and air temperature (T_a), respectively. In our case, we used T_w as the brightness temperature for each single thermal pixel in every crater lake, whereas T_a is the same used for the **Eq. 3**. T_{wv} (K) and T_{av} (K) correspond to the virtual air temperatures derived from T_w and T_a, respectively. Using an absolute temperature (T in K) and vapor pressure (e), the virtual temperature T_v can be calculated as follows (Pasternack and Varekamp, 1997):

$$T_v = \frac{T}{1 - \frac{0.378}{P_a}}, \tag{11}$$

where P_a is the atmospheric pressure in mbar. We calculated the P_a (670 mbar) from the NOAA atmospheric models for an altitude of 3,460 m a.s.l. T_{wv} and T_{av} were calculated using T_w and T_a, respectively. Conductive heat flux (Q_{cond} in MW) can be calculated by the following (Brown et al., 1991):

$$Q_{cond} = 0.61\,[\,(T_w - T_a)/(e_w - e_a)]Q_{evap}. \tag{12}$$

The rain water input heat flux (Q_{rain} in MW) is calculated as follows (Pasternack and Varekamp, 1997):

$$Q_{rain} = f A_c I (T_w - T_r) C p_{water}, \tag{13}$$

where f is a conversion factor (55,555.6 mol/m^3), A_c is the catchment area (m^2), I is the precipitation rate (md^{-1}), T_r is the rain temperature (K), and Cp_{water} is the average heat capacity of water (75.42 J/molK; Robie et al., 1979). In our case, we used a standard T_r of 283 K, whereas the average precipitation rate used was 0.0029 md^{-1}, calculated on the basis of the NOAA data available for the period 1981 and 2010, for an altitude of 3,460 m a.s.l. The catchment area for each crater was calculated considering the highest points (the highest-level curve) around each crater rim, which are mostly located tens of meters from the

crater border. The catchment areas calculated correspond to 262,000, 110,000, 76,000, and 91000 m^2 for Craters 1, 2, 3, and 4, respectively.

Uncertainties Related to Atmospheric Parameters

Uncertainties linked to atmospheric parameters are related to the estimation of wind speed, atmospheric pressure, precipitation rate, and atmospheric temperature. The wind speed can vary largely if measurements are carried out 1) in free air conditions (tens/hundreds of meters over the surface) or 2) close to the surface. In the last case, some small variations could be related to topographic effects. In order to reduce the uncertainties related to wind speed, we used atmospheric models considering the closest altitude to the Peteroa caldera floor (3,460 m a.s.l.), which has small topographic variations. Although wind speed variability in the period 1984–2020 was reduced, we used a fixed average in order to avoid uncertainties related to wind speed variations possibly linked to seasonal effects. The relative "high" wind speed average (8 ms^{-1}) used in this study is a consequence of the high latitude and high altitude where Peteroa volcano is located. Similarly, atmospheric pressure (assuming 100% of relative humidity) and precipitation rates were obtained at the same altitude of wind speed, in order to reduce the uncertainties due to variabilities in the atmospheric conditions. The use of fixed atmospheric pressure and precipitation rate removes strong variations of those parameters related to seasonal effects. The atmospheric temperature obtained from Liaudat et al., 2014 was measured in the inner rim of the caldera, at similar altitudes to other atmospheric parameters, with small uncertainties expected.

Uncertainties Related to Satellite Images

Uncertainties related to catchment and lake areas have a direct relation to the pixel size of RapidEye and PlanetScope images, with the uncertainties of the calculated area variable from ±2 to ±6 m^2. In the case of Landsat imagery, one of the most critical uncertainties corresponds to the lake surface temperature. Lake temperature measured remotely has a strong dependence on the temperature distribution through the lake water body. This non-uniform distribution of the temperature can also affect the temperature calculation in a single pixel. Based on *in situ* measurements, we have estimated discrepancies of ±1 and ±4 K between satellite-based and *in situ* temperatures. These discrepancies can be attributed to several processes including differential absorption of thermal radiation by vapor and liquid phases present over the lake surface, especially in cases when intense evaporation occurs. Additionally, discrepancies can occur due to the location of *in situ* measurements, where differences can be observed between near and offshore measurements. However, the observed discrepancies imply small differences in the radiative heat flux if we consider only a single pixel (after background correction), varying between 0.003 and 0.006 MW. Average temperature difference between thermal and non-thermal pixels for our database was 8 K, whereas minimum difference was only 2 K. If we consider the minimum difference between thermal temperature threshold and non-thermal temperature (2 K), the minimum thermal radiative heat flux able to be measure in a single pixel, after background correction, is 0.007 MW.

RESULTS

General Results From the Landsat and PlanetScope Imagery Database

The results from Landsat images are presented in detail in the **Supplementary Table S1**. The measured maximum radiative heat fluxes (Q_{rad}) measured were 1.2, 1.5, 2.3, and 1.4 MW for Crater Lake 1, 2, 3, and 4, respectively, whereas the measured maximum volcanic heat fluxes (Q_{volc}) measured were 7.1, 38, 31, and 23 MW, respectively (**Figure 5**). The highest brightness temperature measured in each crater lake was 323, 328, 334, and 326 K for Lake 1, 2, 3, and 4, respectively, corresponding to the value of the single pixel with the highest temperature. The fumarolic fields detectable by TIR bands from Landsat images were those located in the western side of the Crater 1 (**Figure 1**), and the fumarolic field emerged previous to the formation of the Crater 3 during the eruptive process in February 1991. The maximum thermal radiance and radiative heat flux (Q_{rad}) measured in the fumarolic field of Crater 1 were 13.3 W/$m^2\mu$msr and 1.1 MW, respectively, and in the case of fumarolic field pre-Crater 3 maximum thermal radiance and Q_{rad} were 12.1 W/$m^2\mu$msr and 2.1 MW, respectively (**Figure 5**). Thermal anomalies in SWIR bands were observed exclusively in the nested Crater 1, being detected for the first time on December 6, 2018, exclusively in band 7 (Landsat OLI), with a thermal radiance of 0.4 W/$m^2\mu$msr (**Table 2**). On August 22, 2020, the maximum thermal radiance (17.4 W/$m^2\mu$msr) was recorded in band 7 (for Landsat ETM+ and OLI), whilst, simultaneously, for the first time an anomaly was recorded in band 5 (Landsat ETM+), with a radiance of 7.3 W/$m^2\mu$msr (**Table 1**). Thermal anomaly in band 5/6 (for Landsat ETM+/OLI, respectively) was newly detected on 14th September and November 1, 2020, with thermal radiance of 1 and 3.2 W/$m^2\mu$msr, respectively (**Table 1**).

The results from Planet Lab Inc. images are presented in detail in the **Supplementary Table S2**, and the summary of the most relevant data is presented in **Table 2**. The maximum area measured of Crater Lakes 1, 2, 3, and 4 corresponds to 31,514, 10,575, 20,344, and 15171 m^2, respectively (**Figure 6**). In all craters the lakes changed from liquid to frozen, and occasionally a transition corresponding to a liquid lake with ice patches (**Figure 7**). Craters 1, 2, and 4 present similar behaviors, dominated by presence of liquid water (between 47 and 67% of the total images processed), and frozen lakes between 24 and 35%. In the case of Crater Lake 3, liquid water appears in 78% of the images, whereas frozen lakes only in 3% of the images. Liquid water + ice was observed only between 1 and 7% of the images in all craters. Absence of crater lakes was observed in all cases, varying between 2% in the case of Crater 4 and 23% of the images in Crater 1. A wide range of colors were observed between all crater lakes, including turquoise, blue, brown-to-dark brown, green-to-dark green, and white, with

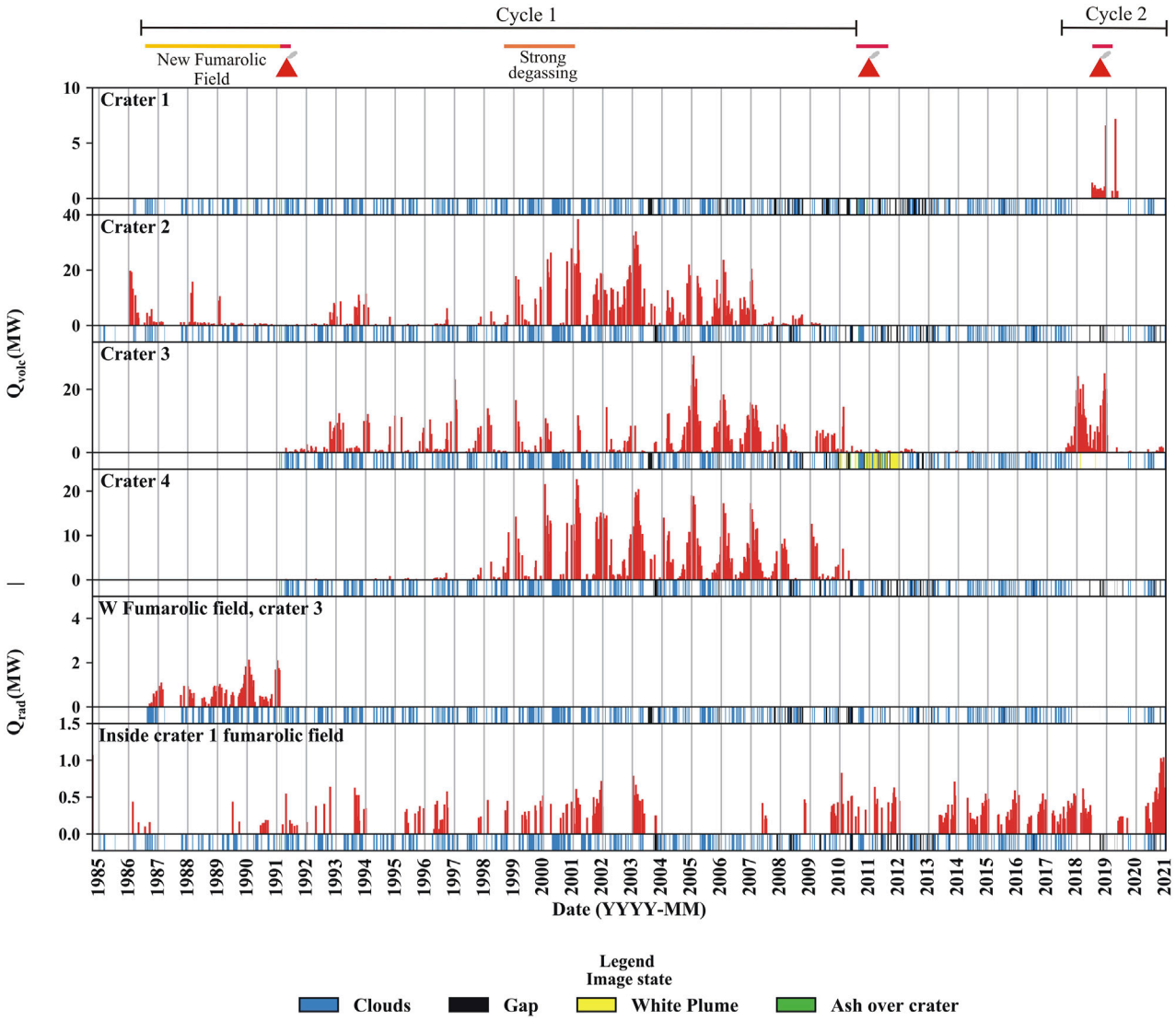

FIGURE 5 | Q_{volc} and Q_{rad} in MW vs. date (YYYY-MM) is shown for Crater Lakes 1, 2, 3, and 4, and for the new fumarolic field in the current position of Crater 3 and Crater 1 fumarolic field, respectively. The major evolutive cycles and eruptive activity are shown in the upper part. Red lines accompanied by red volcano indicate volcanic unrest periods, yellow line the presence of a new fumarolic field, and orange line the strong degassing process. The secondary graphics at the base of Q_{volc} and Q_{rad} graphics showed the state of the satellite images, corresponding to free clouds images (white area), presence of clouds (light blue area), gas plume (yellow area), and ash (green area) over crater lakes. Vertical grey lines correspond to an annual timescale.

Crater Lake 1 displaying the most variability of colors. The turquoise color is dominant in the case of Crater 2 and 3 (65 and 68%, respectively), blue in Crater 1 (72%), and brown in Crater 4 (68%).

Thermal and Temporal Evolution of Crater Lakes and Their Relation With Unrest Episodes

October 1984–January 1991

In late 1984, Peteroa volcano was in a long period of quiescence period since at least 1968 (González-Ferrán, 1995; Haller and Risso, 2011), with only two active craters (Crater 1 and 2; **Figures 1**, **2**), both hosting lakes and fumarolic activity. Particularly in the case of Crater 1, the fumarolic activity was located in the western side of the crater (**Figure 1**). In the first image available from Landsat satellite (October 14, 1984; Landsat TM), a thermal anomaly was observed only in the Crater 1 fumarolic field, the lake in Crater 1 was absent, and the lake in Crater 2 produced no thermal anomaly. Up to September 1986, thermal activity was observed intermittently in the Crater 1 fumarolic field (Q_{rad} 0.09–0.44 MW) and continuously in the lake of Crater 2 at least since January 1986, with Q_{volc} between 0.71 and 19 MW. On September 18, 1986, for the first time a thermal anomaly was observed in the same position as where Crater 3 is currently located, with a Q_{rad} of 0.12 MW (**Figures 2**, **5**). According to the

TABLE 1 | Date, image type, and thermal radiance of SWIR bands 1 (band 5 and 6 for Landsat ETM+ and OLI, respectively) and 2 (band 7 for Landsat ETM+ and OLI) in W/m^2μmsr for the nested crater of Peteroa volcano.

Date	Image type	SWIR 2	SWIR 1
06_12_2018	OLI	0.4	0
07_12_2018	ETM+	2.2	0
21_08_2020	OLI	6	0
22_08_2020	ETM+	17.4	7.3
30_08_2020	OLI	1.8	0
06_09_2020	OLI	2.9	0
07_09_2020	ETM+	3.9	0
14_09_2020	ETM+	5.3	1
22_09_2020	OLI	5.2	0
08_10_2020	OLI	0.7	0
24_10_2020	OLI	0	0
01_11_2020	ETM+	6.8	3.2
09_11_2020	OLI	0.8	0
18_11_2020	OLI	0	0
25_11_2020	OLI	0	0
04_12_2020	OLI	0.9	0
11_12_2020	OLI	0	0
20_12_2020	OLI	0	0

Global Volcanism Program (1987), a new fumarolic field was created in the current position of Crater 3, constituted by 40–50 vents, covering an area of ~100 m^2, and producing a small plume (up to 300 m over the Peteroa caldera rim). The thermal activity related to the fumarolic field was continuous for 4 years and 5 months, being relatively stable for almost 3 years with Q_{rad} between 0.1 and 1.1 MW (**Figure 5**). However, since October 1989 the Q_{rad} began to increase up to 2.1 MW on February 1, 1990, returning to the normal values in April 1990 until November 1990, and increased between January and February 1991, with a peak of 2.1 MW on January 19, 1991 (**Figure 5**). In the period October 1986–January 1991, the thermal anomaly in the Crater 1 fumarolic field appeared very sporadically with relatively low Q_{rad} (0.11–0.44 MW), whereas the Q_{volc} related to the Crater Lake 2 decreased quickly down to zero in December 1990, despite the occurrence of two peaks of thermal activity on February 28, 1988, and January 29, 1989 (10 and 15 MW, respectively; **Figure 5**).

February 1991–August 2010

Eruptive activity was recorded between 9th and February 15, 1991, when Craters 3 and 4 were formed (**Figure 3**; Gardeweg, 1991; Global Volcanism Program, 1991). No thermal anomalies were observed immediately after the end of the eruption in Crater lakes 1, 3, and 4, whereas in Crater Lake 2, the Q_{volc} measured was 0.3 MW. On April 25, 1991, thermal anomalies were detected for the first-time in Lakes 3 and 4, with Q_{volc} reaching up to 1.5 and 0.2 MW, respectively (**Figure 5**). After 1.5 years with very low Q_{volc} in Lakes 2, 3, and 4, the thermal activity of the Crater Lakes 2 and 3 started to increase on October 20, 1992 (Q_{volc} 4.5 and 9.5 MW, respectively; **Figure 5**), remaining relatively high in Crater Lake 3, whereas in the case of Lake 2, the thermal activity returned to a very low values after February 3, 1994 (Q_{volc} 6.6 MW). The lake in Crater 4 remained without detectable thermal activity up to May 3, 1994, when Q_{volc} measured was 0.12 MW (**Figure 5**).

In the following years, the activity of Crater Lake 3 remained relatively high, whilst in the case of lake 4, the thermal activity increased since December 1, 1997 (Q_{volc} 2.7 MW), and the Crater Lake 2 from January 25, 1999 (Q_{volc} 18 MW; **Figure 5**). The highest Q_{volc} for lakes 2 and 4 was detected on March 2, 2001, corresponding to 38 and 23 MW, respectively. The increase in the thermal activity in lakes 2 and 4 was coincident with the gas and tephra emissions between October and November 1998, and the

TABLE 2 | Color and state of crater lakes of Peteroa Volcano. The frequency and percentage (%) of color and state of the lake is indicated. Maximum area (m^2) of the lakes is also indicated.

	Frequency				Percentage (%)			
Color	**Crater 1**	**Crater 2**	**Crater 3**	**Crater 4**	**Crater 1**	**Crater 2**	**Crater 3**	**Crater 4**
Turquoise	17	170	223	42	7	65	68	12
Blue	186	16	62	74	72	6	19	21
Brown	13	67	0	243	5	26	0	68
Dark brown	37	0	0	0	14	0	0	0
Green	0	9	0	0	0	3	0	0
Dark green	3	0	0	0	1	0	0	0
White	4	0	43	0	2	0	13	0
Total	260	262	328	359	100	100	100	100
STATUS								
No Lake	111	84	46	11	23	16	12	2
Liquid	252	250	300	332	52	47	78	67
Frozen	114	183	12	130	24	35	3	26
Liquid + ice	7	12	25	26	1	2	7	5
Total	484	529	383	499	100	100	100	100
Maximum area (m^2)	31,514	10,575	20,344	15,171				

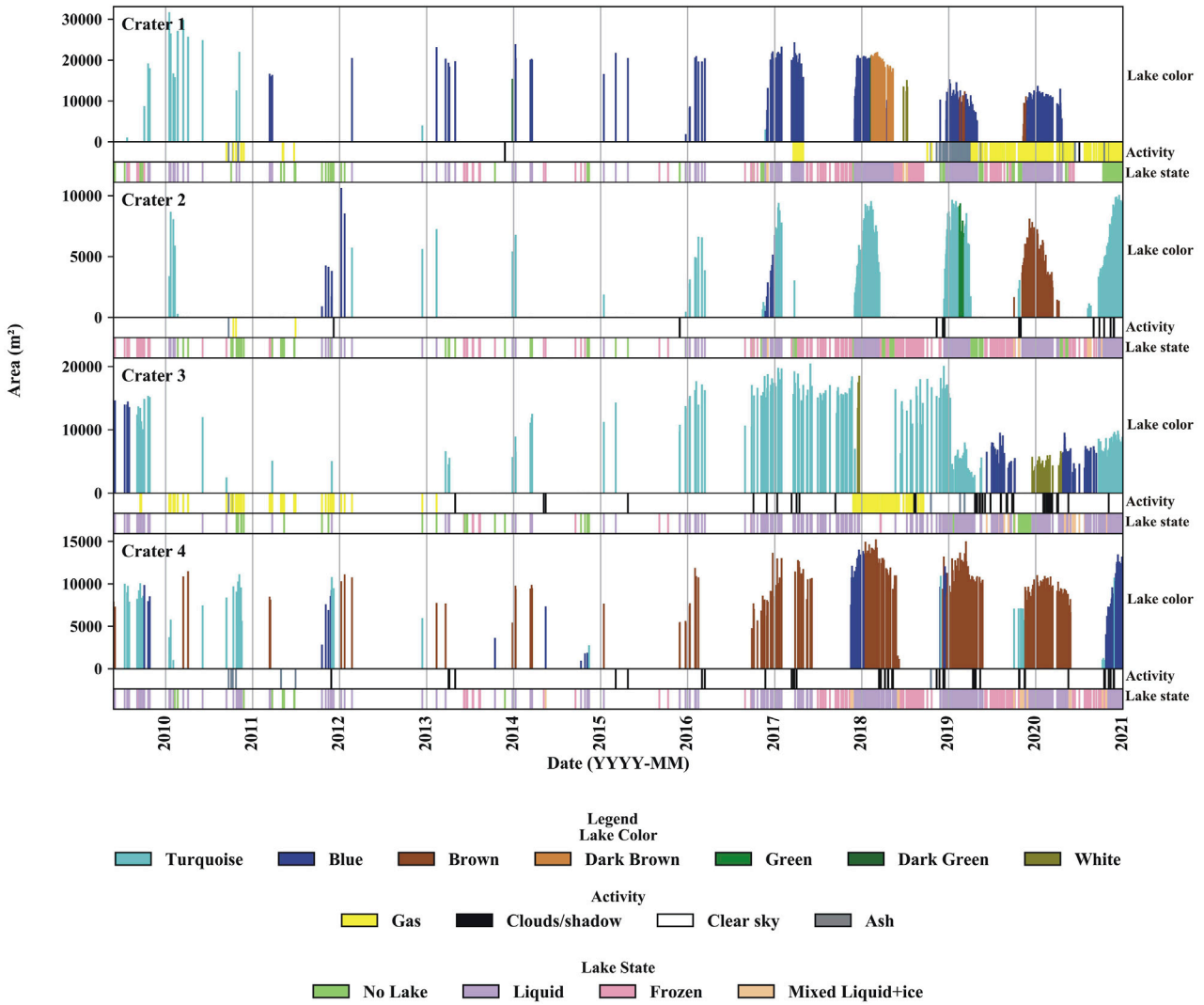

FIGURE 6 | Area in m^2 vs. date (YYYY-MM) is shown for Crater Lakes 1, 2, 3, and 4. The secondary graphics at the base of main graphics showed the lake color, superficial atmospheric/volcanic activity over the crater lakes (presence of gas, clouds or shadow, and ash over crater; white areas correspond to clear sky), and lake state (liquid, frozen, or mixed liquid + ice).

increase in the gas emission in February–March 1999 and December 2000–February 2001 (**Figure 5**; Global Volcanism Program, 1999; Global Volcanism Program, 2001).

After February 2001, the thermal activity in Crater Lakes 2 and 4 remained relatively high, although a progressive decreasing was observed in both lakes, with the last thermal anomaly being recorded on April 26, 2009 (Q_{volc} 0.49 MW), and on August 2, 2010 (Q_{volc} 0.14 MW), for Crater 2 and 4, respectively (**Figure 5**). In the case of Crater Lake 3, a high and stable thermal activity was measured, and the highest Q_{volc} was detected on February 10, 2005 (31 MW; **Figure 5**). Subsequently, a decreasing thermal activity was observed, especially after March 2010, when Q_{volc} regularly was > 2 MW, with the lowest Q_{volc} detected on July 17, 2010 (0.28 MW; **Figure 5**). Since January 2010, an increase in the gas emission was observed in Crater Lake 3, with emissions continuing for several months up to August 8, 2010, when ash emission was observed for the first time (Aguilera et al., 2016).

In the case of Crater Lake 1, no thermal anomaly was observed in this period, whilst in the Crater 1 fumarolic field, the thermal anomaly was detected frequently, with a Q_{rad} variable between 0.07 and 0.83 MW (**Figure 5**).

September 2010–December 2017

On September 4, 2010, a new eruptive cycle started in Crater 3, when several tephra explosions were observed, accompanied by an almost permanent strong degassing and the intermittent total evaporation of the lake, which caused its temporary absence (**Figure 8**). Despite the eruptive activity, Craters 1, 2, and 4 showed no thermal activity during the eruptive period (September 2010–July 2011), whereas Crater 3 presented low Q_{volc} values between 0.32 and 1.1 MW (**Figures 5**, **8**). According to Aguilera et al. (2016), the temperatures during March 2011 in Lakes 1, 2, and 4 were 7.4, 43, and 19°C, respectively, which is consistent with the absence of a thermal anomaly in the case of Craters 1 and 4 due to their low

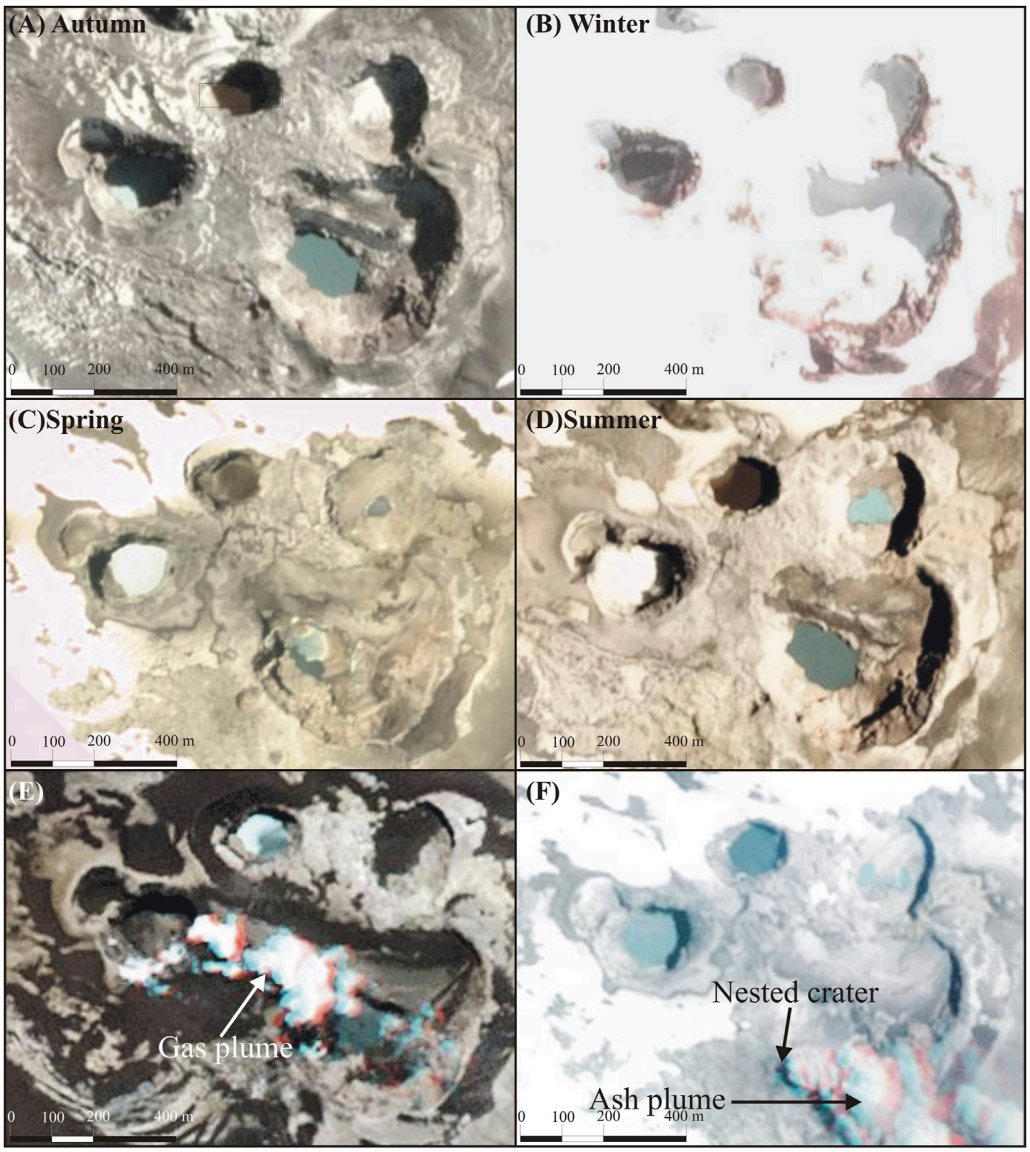

FIGURE 7 | A sequence of PlanetScope images in natural color showing the Peteroa volcano crater lakes during autumn **(A)**, winter **(B)**, spring **(C)**, and summer **(D)** seasons. Additionally, PlanetScope images in natural color show strong degassing and eruptive plume on October 25, 2010 **(E)** and December 14, 2018 **(F)**, respectively.

temperatures, whereas in the case of Crater 2, the absence of thermal anomaly could be related to the very small size of lake at the moment of the measurement. After the eruptive cycle, in the period August 2011–December 2017, no anomalies were detected in Craters 1, 2, and 4, whilst in Crater 3, very sporadic anomalies were measured, with Q_{volc} variable from 0.13 to 1 MW up to May 2017 (**Figure 5**). Between June and December 2017, a fast increase in Q_{volc} was observed, starting with 0.34 MW (18th June) up to 20 MW (28th December; **Figure 5**). During the September 2010–December 2017 period, the Crater 1 fumarolic field maintained its behavior, producing sporadic thermal anomalies with Q_{rad} variable between 0.12 and 0.7 MW (**Figure 5**).

January 2018–December 2020

On July 8, 2018, the first thermal anomaly was identified in Crater Lake 1 (Q_{volc} 1.4 MW; **Figure 5**), which occurred during the autumn–winter seasons, when the lake is typically frozen. The presence of the thermal anomaly is coincident with a short-lived (16 days) defrosting of the lake. In the following months, the crater was characterized by the presence of snow patches in the crater bottom and several fumarolic vents, the last producing thermal anomalies with Q_{volc} variable between 0.42 and 1.2 MW (**Figure 5**). In October 2018, the nested crater in the southwestern flank of the Crater 1, which started to be formed in January 2018 (*Historical Eruptive*

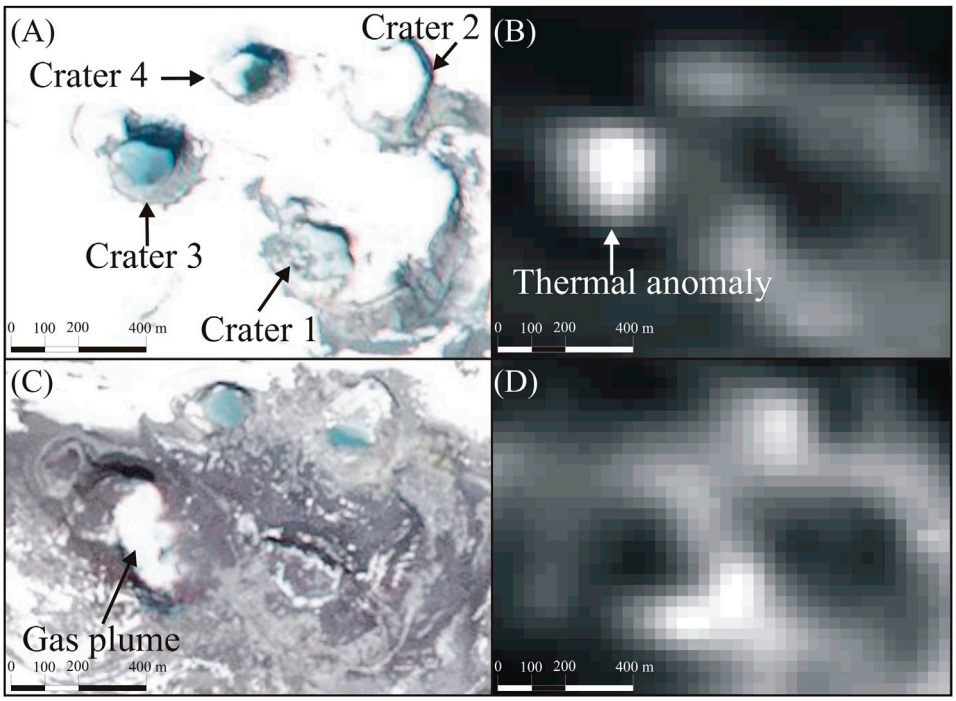

FIGURE 8 | (A) RapidEye image (natural color) showing the crater lakes on October 3, 2009. **(B)** Landsat TM Thermal Infrared Band (TIR) showing the thermal anomaly on Crater Lake 3 (October 3, 2009). **(C)** RapidEye image (natural color) showing the crater lakes on November 15, 2011. A gas plume emitted from Crater 3 is also shown. **(D)** Landsat TM Thermal Infrared Band (TIR) showing no thermal anomalies (November 17, 2011).

Activity in the Period 1984–2020), began to emit gas and tephra plumes (**Figure 9**). Between November 2018 and May 2019, although the lake was present, it was smaller in comparison with the previous years in the same seasons and was completely absent for short periods. This period is coincident with the maximum Q_{volc} recorded on December 22, 2018 (6.6 MW), and April 21, 2019 (7.1 MW; **Figure 5**). On 6th and 7th December 2018, for the first time thermal anomalies were recorded in the nested crater using Landsat SWIR bands (**Figure 9**; **Table 2**). After May 2019 and up to early November 2019, no lake was observed (only snow patches between June and early August, and a few days in September), no thermal anomalies were recorded, and gas plumes were constantly emitted from the nested crater. From November 2019 up to December 2020, Crater 1 was characterized initially by the presence of a lake (November 2019–April 2020) and subsequently, by its total absence (snow patches were observed during late May–early June 2020). The activity in the nested crater for the same period was characterized by a constant emission of gas plumes, with very sporadic tephra explosions, and since August 2020 thermal anomalies were recorded by the Landsat SWIR bands (thermal radiance between 0.7 and 17 $W/m^2\mu msr$; **Figure 9** and **Table 2**). Along the eruptive activity of the nested crater, the Crater 1 fumarolic field (**Figure 1**) showed similar behavior (intermittent thermal anomalies) and heat fluxes (0.12–0.16 MW) than previous periods (**Figure 5**). However, a sustained increase of the heat fluxes was observed since May 2020, with a peak of 1 MW on December 11, 2020.

Between January 2018 and January 2019, a renewed and strong thermal activity was recorded in Crater Lake 3, following the increased thermal activity observed in the previous period (started on June 18, 2017), measuring several peaks of Q_{volc} on 20th January, 21st February, 25th March, 29th November, and December 31, 2018 (24, 20, 22, 20, and 20 MW, respectively; **Figure 5**). The increase of the thermal activity is partially coincident with the increase in the eruptive and thermal activity in Crater Lake 1. However, in the next 2 years (2019–2020), very low Q_{volc} were measured due to the decreasing activity.

According to the Planet Labs Inc. images, in the period reviewed here (January 2018–December 2020), Crater Lakes 1, 2, and 4 showed a regular behavior considering area of the lakes and their states, being liquid and having their bigger areas during summer, whereas frozen lakes were present during winter and partially in spring and autumn. The only exception occurred in Crater 1 during spring and the beginning of summer 2020–2021 (December 2020) when the lake was completely absent, probably due to the intense thermal activity of both the nested crater and Crater 1 fumarolic field. The color of the lakes was relatively regular in the Craters 1, 2, and 4. Lake 1 was mostly blue, although in some periods it appeared in brown, dark brown, and green colors. Lake 2 was permanently turquoise, although in the summer of 2019 and 2020 it changed to green and brown color, respectively. Lake 4 is mostly brown, but at the beginning of summer season changed to blue or turquoise colors (**Figure 6**).

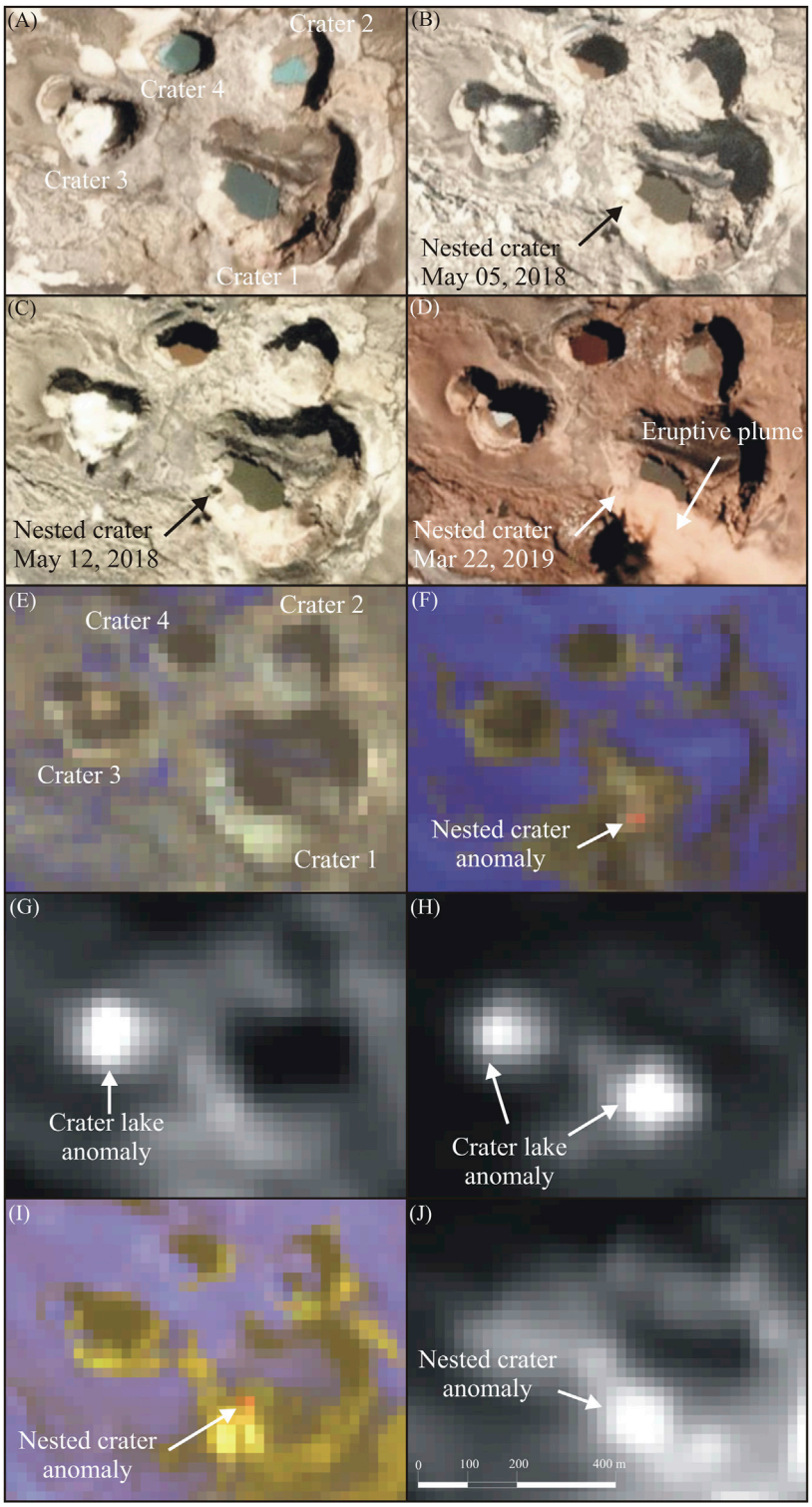

FIGURE 9 | A sequence of PlanetScope images (natural color) showing the evolution of the nested crater in Crater 1 on January 12, 2018 **(A)**, May 5, 2018 **(B)**, May 12, 2018 **(C)**, and March 22, 2019 **(D)**. Landsat OLI images (combination 765 in RGB) showing the nested crater without [May 5, 2018; **(E)**] and with thermal anomaly [December 6, 2018; **(F)**]. Landsat OLI images (TIR bands) showing the thermal anomaly in Crater Lake 3 [May 5, 2018; **(G)**], and Crater Lakes 1 and 3 [November 4, 2018; **(H)**]. Landsat OLI image showing the nested crater with thermal anomaly on August 21, 2018, combination 765 in RGB **(I)** and TIR band **(J)**.

At the beginning of the period, between January and September 2018, intense evaporation was observed from Crater Lake 3, which produced a permanent gas/steam plume. This activity correlates with the high Q_{volc} measured in the same period. In the following months, the behavior of Crater Lake 3 had no correlation with the meteorological seasons, being mostly in liquid state (78% of the images reviewed), whereas frozen and mixed liquid + ice lakes appear in 11% of the images, and 11% absence of lake. Since January 2019, the Crater Lake 3 area has decreased to 56% of the average area in the last 9 years, whilst the color of the lake underwent changes from the regular turquoise color to blue and white.

DISCUSSION

Cyclic Thermal Activity

Thermal Cycle 1 (September 1986–July 2011)

The thermal activity of Peteroa volcano has varied through time in concordance to the eruptive activity. Since October 1984, thermal activity was recorded exclusively in the Crater 1 fumarolic field, whilst Crater Lake 2 started with a continuous, but decreasing, thermal activity since January 1986 (**Figure 5**). We interpret the decreasing thermal activity in Crater Lake 2 as a remnant heat related to the unrest activity between 1959 and 1967, which occurred in that crater (González-Ferrán, 1995).

In September 1986, the appearance of a new fumarolic field in the current position of Crater 3 can be cataloged as a precursor activity previous to the eruptive cycle recorded in February 1991, which finished with the creation of Craters 3 and 4. Complementary, the sustained increase of Q_{rad} in the fumarolic field since September 1986 up to the eruption in February 1991 (**Figure 5**) supports our interpretation.

After the eruptive period in February 1991, and for the next ~20 years, the thermal activity was continuous in Crater Lakes 2, 3, and 4. In the case of Crater Lakes 2 and 4, both lakes showed very similar thermal behavior, correlating very well with the increase in degassing between October 1998 and February 2001, when an increase in Q_{volc} was observed, reaching a peak in March 2001, and then a progressive descending after February 2001, in coincidence with the absence of superficial activity up to December 2009. In the case of Crater 3, it seems that the thermal activity in the lake was initially not completely coupled with Craters 2 and 4, especially during the increased degassing in the period October 1998–February 2001. In fact, the highest Q_{volc} was measured in February 2005. However, after February 2005 its decreasing thermal activity is coincident with the decrease of Q_{volc} in Craters 2 and 4, suggesting that thermal activity between the three craters is linked. At the end of the ~20 years of continuous thermal activity in the three crater lakes, the thermal activity disappeared in Crater Lakes 2 and 4, whereas in Crater 3 Q_{volc} remained with minimum values since April 1991.

In January 2010, eruptive activity was detected in Crater 3, characterized by phreatic explosions. This was followed by an eruptive episode that started in September 2010 and lasted 10 months (up to July 2011). We suggest that this eruptive activity is the last event related to thermal cycle 1 of Peteroa volcano.

Transitional Period (August 2011–May 2017)

This period was characterized by occurrence of thermal activity exclusively in Crater Lake 3, with sporadic presence of thermal anomalies (Q_{volc} <1 MW; **Figure 5**). We interpret that this transitional period corresponds to a residual heat after the intense thermal activity related to cycle 1.

Thermal Cycle 2 (June 2017–December 2020)

During June 2017, the thermal activity in Crater Lake 3 increased, and in July 2018, a thermal anomaly was recorded for the first time in Crater Lake 1. These anomalies are coincident with the formation of a new nested crater in the southwestern flank of Crater 1, and an eruptive episode between October 2018 and April 2019. Similarly to thermal cycle 1, we suggest that the previously described thermal activity in Crater Lakes 1 and 3 is precursor of the eruptive activity recorded since October 2018. Since December 2018, thermal activity has also been recorded in the nested crater, being detected in SWIR bands (for first time along the studied period), and the Crater 1 fumarolic field showed an increase in Q_{rad} from May 2020, after decades of intermittent and irregular thermal activity not correlating to previous eruptive activity and thermal cycles. No thermal activity was observed in Crater Lakes 2 and 4 (**Figure 5**).

In this period all craters presented a regular behavior, with a liquid lake during summer and partially during late spring and early spring, whereas frozen and liquid + ice lakes occurred during winter, late autumn, and early spring. The only exception corresponds to Crater Lake 3, especially during 2017, where the lake was present in liquid state also during autumn, winter, and spring. Since March 2018, the lake area in Crater 1 decreased progressively, disappearing completely in April 2020, whereas Crater Lake 3 decreased in area since January 2019 from ~15,000 to ~5,000 m^2 (**Figure 6**).

The 1) detection of thermal anomalies in Crater Lake 1 and the nested crater, 2) decreasing of the area in the Crater Lakes 1 and 3, 3) increase of thermal activity in the Crater 1 fumarolic field and Crater 3, and 4) previous of eruptive activity in the period December 2018–April 2019 all suggest a second thermal cycle. In this cycle, Crater Lakes 1 and 3, Crater 1 fumarolic field, and the nested crater are involved and directly linked.

Relationships Between Migration of Thermal/Eruptive Activity, Fluid Pathways, and Magma Sources

The migration of eruptive and thermal activity has been clearly observed in Peteroa volcano. Eruptive activity during the 20th century was concentrated mainly in Crater 2 (González-Ferrán, 1995). In fact, the first thermal activity detected with Landsat imagery in Peteroa volcano was in Crater 2 (**Figure 5**). However, at the beginning of thermal cycle 1, the activity migrated to the new fumarolic field located in the current position of Crater 3, and after the eruptive activity of February 1991, when Crater 3 and 4 were formed, the thermal activity was concentrated in the Craters 2, 3, and 4. At the end of thermal cycle 1, the thermal and eruptive activity were concentrated exclusively in Crater 3. Subsequently, in thermal cycle 2 the thermal activity was still active in Crater 3, with

the thermal and eruptive activity concentrated in Crater 1. The migration has been accompanied by simultaneous thermal activity in at least two craters, which suggests an interconnection between the fluid pathways that feed the crater lakes. In fact, the formation of Craters 3 and 4 during the eruptive activity of February 1991 evidences that fluid pathways are related and/or connected to each other. Additionally, we suggest that Crater 2 was partially connected with Craters 3 and 4, considering the simultaneous thermal activity early in thermal cycle 1 with the fumarolic field, and subsequently, the coincident thermal activity of Crater Lakes 2, 3, and 4. Similarly, early in thermal cycle 2, the coincident thermal activity of Crater Lakes 1 and 3, including the precursory activity of October 2018–April 2019 unrest, could be a consequence of an interconnection of fluid pathways between these crater lakes.

The migration of eruptive/thermal activity, and the possible interconnection of crater lakes, could be partially explained by the presence of more than one magmatic source. Romero et al. (2020) showed that eruptive products related to the activities of the scoria cone in 1937, February 1991, and October 2018–April 2019, had basaltic andesite, andesitic-to-dacitic, and andesitic compositions, respectively. These three eruptions involved juvenile products, whereas eruptive products from September 2010–July 2011 were constituted only by lithics fragments, without juvenile products, and a wide range of compositions, including from basaltic andesites to rhyolites. Similarly, Tassi et al. (2016) showed that fumarolic gases from Crater 2 varied their compositions in the period between February 2010 and March 2015. Fumarolic fluids emitted between 2010 and 2011 were sourced from a basaltic magma body, fumarolic fluids released during 2012 had compositions related to a more degassed dacitic body, whereas gases sampled in 2014 and 2015 showed compositions compatible with a mixing of fluids from both sources. Consequently, both gas and rock geochemistry data show evidence of the existence of at least two magmatic sources. We suggest that those magmatic sources are feeding and connecting the crater lakes, and sourcing the fluids released and the eruptive products, individually and/or mixed, in different periods of time. Probably the location of the magmatic sources, and how these sources are connected to the craters that host the acid lakes, dictate the migration of the thermal/eruptive activity.

Energy Balance of Peteroa Volcano Crater Lakes

According to our data (**Supplementary Table S1**), and the previously exposed relation between Q_{volc} and eruptive activity, the energy balance of four crater lakes in Peteroa volcano is primarily controlled by volcanic activity, and partially affected by seasonal effects. In fact, the variations of Q_{volc}, Q_{rad}, Q_{evap}, and Q_{cond} were directly controlled by the eruptive activity, the increase/decrease of degassing (in both fumarolic fields and lakes), and the activity of the crater lakes. Q_{volc} from crater lakes and Q_{rad} both from crater lakes and fumarolic fields showed a close relation with the occurrence of eruptive activity, changes in the crater lakes, and degassing processes, especially in the cases previous to February 1991 eruption, with increasing degassing in the period October 1998–February 2001, and before, during, and after the eruptive process between January 2018 and May 2019. On the contrary, before and during the eruptive activity for the period September 2010–July 2011, a fast decrease in Q_{volc} and Q_{rad} was recorded, lasting for several years after this unrest period. Q_{cond} and Q_{evap} showed similar behavior, although they are partially influenced by seasonal effects, as it is reflected in the oscillatory behavior of Q_{volc} (**Figure 5**). The oscillation is caused by the decrease in evaporation and conduction during the winter season (partially in spring and autumn), when the crater lakes are totally or partially frozen. Despite this, we reduced the seasonal effects by use of fixed atmospheric parameters such as wind speed, atmospheric pressure, and precipitation rate, which could be strongly dependent on seasonal effects (*Uncertainties Related to Atmospheric Parameters*). Q_{evap}, and consequently Q_{cond}, are dependent on the lake area, which is partially controlled by seasonal effects. However, it has been observed that the variation of lake areas is strongly influenced by the eruptive activity, especially in the cases of Crater Lakes 1 and 3 (e.g., 2010–2011, and 2018–2020 unrest activity; Aguilera et al., 2016; Romero et al., 2020). Additionally, it is noteworthy that the oscillatory behavior of Q_{volc} is strongly controlled by the absence or limited data due to total or partial cloud coverage over crater lakes, producing an underestimation of Q_{volc}, especially in cases when total cloud coverage occurs, where $Q_{volc} = 0$ (**Figure 5**). Although seasonal effects do not totally mask the primary volcanic activity in a long-term assessment of the Q_{volc}, they must be taken into account when short periods of time are considered, since some climate factors (e.g., evaporation) can cause under or overestimation of Q_{volc}, during winter and summer seasons, respectively. In the case of Q_{sun} and Q_{atm}, they showed a very limited influence on Q_{volc}, whilst $Q_{cond\text{-}volc}$ is negligible as was indicated previously in the *Heat Flux Calculations*.

The highest Q_{volc} recorded on Peteroa volcano was reached during a quiescence period, specifically in January 2006, corresponding to 59 MW, when three craters were thermally active (Craters 2, 3, and 4). Individually, the peak of Crater Lake 1 occurred at the end of October 2018–April 2019 eruptive activity (April 2019, 7.1 MW), and in Crater Lakes 2 and 4 immediately after the increase in degassing period between October 1998 and February 2001 finished (March 2001, 38 and 23 MW, respectively), and the peak of Crater Lake 3 occurred during a quiescence period (January 2005, 31 MW). According to those Q_{volc}, Peteroa volcano can be considered at a global scale as a low volcanic heat flux system. Similar Q_{volc} has been found during quiescence periods in Copahue (Chile–Argentina) (7–45 MW; Varekamp et al., 2001), Ruapehu (New Zealand) (50 MW; Hurst et al., 2012), Ebeko (Kuril Islands, Russia), and Quilotoa (Ecuador) volcanoes (69 and 72 MW; Pasternack and Varekamp, 1997), whereas moderate-to-high Q_{volc} have been measured at 68–111 Kawah Ijen (Indonesia) (Lewicki et al., 2016) and Poás (Costa Rica) volcanoes ~200–600 (Rowe et al., 1992). As a comparison, volcanoes during unrest periods could reach high Q_{volc} like the cases of Ruapehu volcano (265 MW; Hurst et al., 2012) and Kawah Ijen volcano

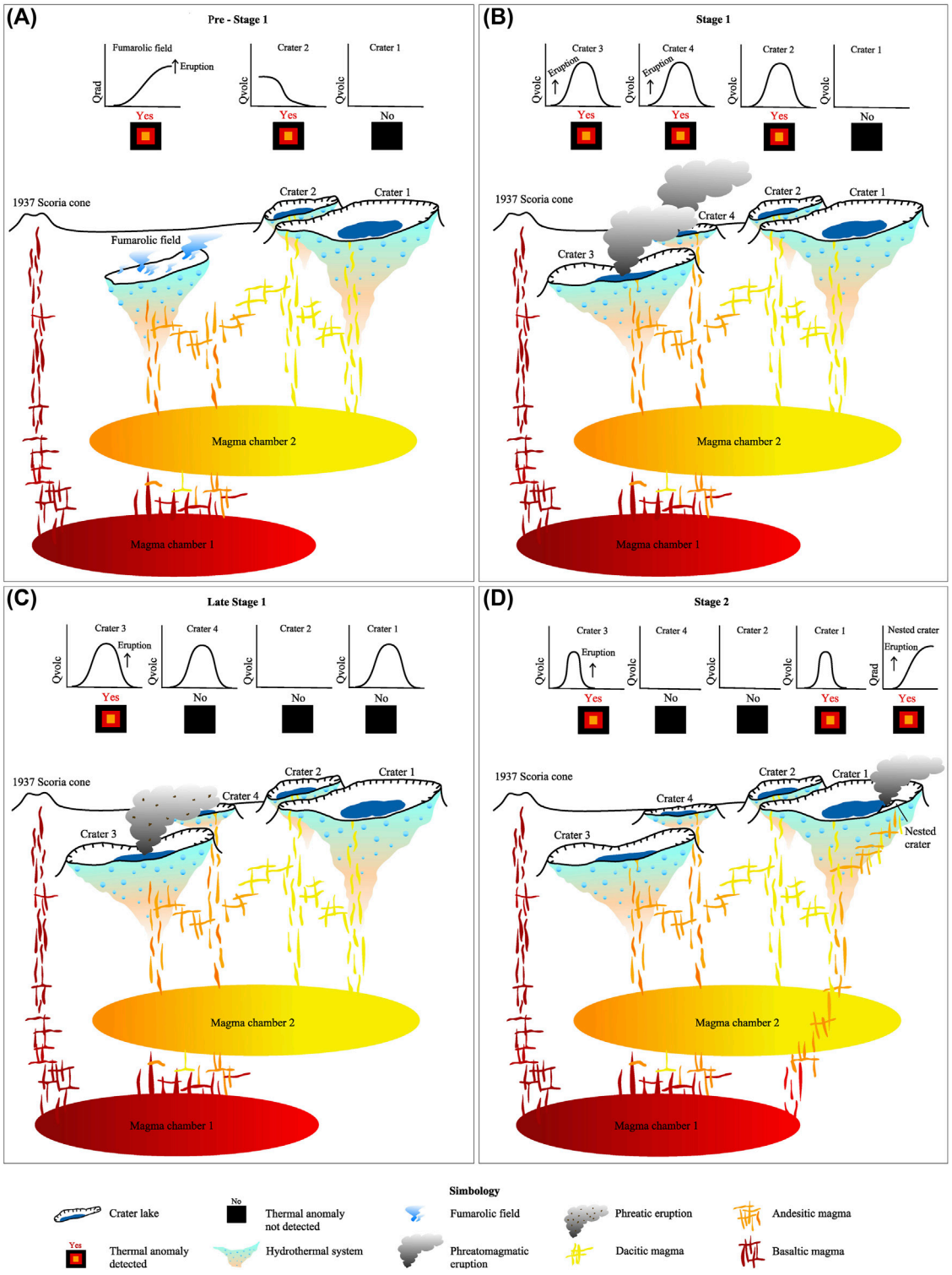

FIGURE 10 | Conceptual model of Peteroa volcano evolution between 1984 and 2020. **(A)** Pre-Stage 1 (1984-January 1991). **(B)** Early Stage 1 (February 1991–August 2010). **(C)** Late Stage 1 (September 2010–July 2011). **(D)** Stage 2 (June 2017–December 2020). Presence/absence of thermal anomalies and behavior of Q_{volc} and Q_{rad} are also shown. Model not to scale.

(289–430 MW; Lewicki et al., 2016). The low volcanic heat flux emitted from Peteroa volcano can be explained by the small size of the crater lakes, and probably by the limited contributions from magmatic sources to the lakes (Aguilera et al., 2016), which prevent higher volcanic heat fluxes. This behavior is very similar to that observed on Copahue volcano, previous to the eruptive activity of 2012 (Caselli et al., 2016). Consequently, despite the frequent eruptive activity on Peteroa volcano, the scarce magmatic inputs produce low Q_{volc} during unrest periods. This is clearly observed in its thermal precursory activity, which starts when thermal activity is very low or absent. Consequently, the occurrence of medium-to-high Q_{volc} in Peteroa volcano could be considered as an increase of the magmatic inputs, and a precursor of major future eruptive activity.

CONCLUSION

We conclude that only two major eruptive/thermal cycles have occurred at Peteroa volcano in the period 1984–2020; the first one represented by the formation of a new fumarolic field and Craters 3 and 4, followed by the thermal activity of Crater Lakes 2, 3, and 4, which were directly related to strong degassing process occurring between October 1998 and February 2001 (**Figures 5**, **10**). This process finished with the September 2010–July 2011 eruptive episode. The second cycle is represented by the reactivation of Crater Lake 3, detection of the thermal activity in Crater Lake 1, formation of the nested crater in Crater 1, occurrence of the eruptive episode between October 2018 and April 2019, and an increase of the thermal activity in the Crater 1 fumarolic field and the nested crater (**Figures 5**, **10**). The increase of thermal activity in the new fumarolic field located in the current site where Crater 3 is present (early thermal cycle 1) and the increase of Q_{volc} in Crater Lakes 1 and 3 (early thermal cycle 2) can be considered as good examples of how thermal information from satellite images can be used to detect possible precursors to eruptive activity, even in volcanoes with low volcanic heat fluxes, like the case of Peteroa volcano.

One of the most important findings is that we have observed the migration of the thermal/eruptive activity, and the interconnection of fluid pathways that feed the crater lakes (**Figure 10**). Both processes seem to be partially related to the existence of at least two deep magmatic sources, which are feeding the craters that host the acid lakes.

The Q_{volc} in the four crater lakes are primarily controlled by volcanic activity, whereas seasonal effects can affect the Q_{volc} at short-term, whilst at long-term the seasonal effects do not show major influence. The highest Q_{volc} on Peteroa volcano was measured during a quiescence period (59 MW), which included thermal activity in three crater lakes (lakes 2, 3, and 4). During unrest periods, Q_{volc} in single crater lakes varied from 7.1 to 38 MW, which still corresponds to low volcanic heat flux. Consequently, we expect that future medium-to-high Q_{volc} could be considered as a possible precursor to major magmatic-dominated eruptive activity.

DATA AVAILABILITY STATEMENT

The original contributions presented in the study are included in the article/**Supplementary Material**; further inquiries can be directed to the corresponding author.

AUTHOR CONTRIBUTIONS

FA and SL made the conceptualization and wrote the heat fluxes routines; FA wrote and reviewed the original draft; JC downloaded and processed the satellite images database and reviewed the original draft; SL reviewed the original draft and drew the figures.

FUNDING

This work has been partially funded by Antofagasta Regional Government, FIC-R project, code BIP N°30488832-0 and by Research Center for Integrated Disaster Risk Management (CIGIDEN), ANID/FONDAP/15110017. SL is funded by CONICYT-PCHA Doctorado Nacional 2016-21160276 fellowship.

ACKNOWLEDGMENTS

Our acknowledgements to Planet Labs Education and Research Standard Program for providing us the PlanetScope and RapidEye imagery. We are warmly grateful of Dr. Thomas Wilkes (The University of Sheffield, United Kingdom) for his English revision of the last version of the manuscript. Alfredo Esquivel (Universidad Católica del Norte, Chile) to provide data related to atmospheric parameters, and to Felipe Rojas (Universidad Católica del Norte, Chile) for his very valuable help in the drawing of some graphics. Our acknowledgments to two reviewers and the editors (Dr. Valerio Acocella and Dr. Dmitri Rouwet) by their comments, which helped to improve the original version of the manuscript.

SUPPLEMENTARY MATERIAL

The Supplementary Material for this article can be found online at: https://www.frontiersin.org/articles/10.3389/feart.2021.722056/full#supplementary-material

REFERENCES

Aguilera, F., Benavente, O., Gutiérrez, F., Romero, J., Saltori, O., González, R., et al. (2016). Eruptive Activity of Planchón-Peteroa Volcano for Period 2010-2011, Southern Andean Volcanic Zone, Chile. *andgeo* 43 (1), 20–46. doi:10.5027/andgeoV43n1-a02

Aldeghi, A., Carn, S., Escobar-Wolf, R., and Groppelli, G. (2019). Volcano Monitoring from Space Using High-Cadence Planet CubeSat Images Applied to Fuego Volcano, Guatemala. *Remote Sensing* 11, 2151. doi:10.3390/rs11182151

Benavente, O., Tassi, F., Gutiérrez, F., Vaselli, O., Aguilera, F., and Reich, M. (2013). Origin of Fumarolic Fluids from Tupungatito Volcano (Central Chile): Interplay between Magmatic, Hydrothermal, and Shallow Meteoric Sources. *Bull. Volcanol* 75, 746. doi:10.1007/s00445-013-0746-x

Brown, G. C., Rymer, H., and Stevenson, D. (1991). Volcano Monitoring by Microgravity and Energy Budget Analysis. *J. Geol. Soc.* 148, 585–593. doi:10.1144/gsjgs.148.3.0585

Candela-Becerra, L. J., Toyos, G., Suárez-Herrera, C. A., Castro-Godoy, S., and Agusto, M. (2020). Thermal Evolution of the Crater lake of Copahue Volcano with ASTER during the Last Quiescence Period between 2000 and 2012 Eruptions. *J. Volcanology Geothermal Res.* 392, 106752. doi:10.1016/j.jvolgeores.2019.106752

Caselli, A., Agusto, M., Velez, M. L., Forte, P., Bengoa, C., Daga, R., et al. (2016). "The 2012 Eruption," in *Copahue Volcano*. Editors F. Tassi, O. Vaselli, and A. Caselli (Berlin Heidenberg: Springer-Verlag), 61–77. doi:10.1007/978-3-662-48005-2_4

Caudron, C., Mazot, A., and Bernard, A. (2012). Carbon Dioxide Dynamics in Kelud Volcanic lake. *J. Geophys. Res.* 117, a–n. doi:10.1029/2011JB008806

Christenson, B., Németh, K., Rouwet, D., Tassi, F., Vandemeulebrouck, J., and Varekamp, J. C. (2015). "Volcanic Lakes," in *Volcanic Lakes*. Editors D. Rouwet, B. Christenson, F. Tassi, and J. Vandemeulebrouk (Berlin Heidenberg: Springer-Verlag), 1–20. doi:10.1007/978-3-642-36833-2_1

Dmitri Rouwet, D., and Franco Tassi, F. (2011). Geochemical Monitoring of Volcanic Lakes. A Generalized Box Model for Active Crater Lakes. *Ann. Geophys.* 54, 2. doi:10.4401/ag-5035

Gardeweg, M. (1991). *Erupción 1991 Volcán Planchón-Peteroa (Informe N°1)*. Santiago, Chile: SERNAGEOMIN.

Global Volcanism Program (1987). "Report on Planchon-Peteroa (Chile)," in *Scientific Event Alert Network Bulletin*. Editor L. McClelland (Smithsonian Institution), 12, 3. doi:10.5479/si.GVP.SEAN198703-357040

Global Volcanism Program (1991). "Report on Planchon-Peteroa (Chile)," in *Bulletin of the Global Volcanism Network*. Editor L. McClelland (Smithsonian Institution), 16, 1. doi:10.5479/si.GVP.BGVN199101-357040

Global Volcanism Program (2019). "Report on Planchon-Peteroa (Chile)," in *Bulletin of the Global Volcanism Network*. Editors D. B. Krippner, and E. Venzke (Smithsonian Institution), 44, 6. doi:10.5479/si.GVP.BGVN201906-357040

Global Volcanism Program (1999). "Report on Planchon-Peteroa (Chile)," in *Bulletin of the Global Volcanism Network*. Editor R. Wunderman (Smithsonian Institution), 24, 3. doi:10.5479/si.GVP.BGVN199903-357040

Global Volcanism Program (2001). "Report on Planchon-Peteroa (Chile)," in *Bulletin of the Global Volcanism Network*. Editor R. Wunderman (Smithsonian Institution), 26, 3. doi:10.5479/si.GVP.BGVN200103-357040

González-Ferrán, O. (1995). *Volcanes de Chile*. Santiago, Chile: Instituto Geográfico militar, 640.

Haar, L. Gallagher, J. S., and Kelt, G. S. (1984). *NBS/NRC Steam Tables*. New York: Hemisphere, 320. doi:10.1002/cite.330570931

Haller, M. J. Ostera, H. A. Pesce, A. H. Gardini, M., and Folguera, A. (1994). *Vulcanoestratigrafía reciente y eruptividad del Volcán Peteroa*. Actas: 7° Congreso Geológico Chileno, 319–323. (Concepción).

Haller, M. J. and Risso, C. (2011). La erupción del volcán Peteroa (35°15'S, 70°18'o) del 4 de septiembre de 2010. *Rev. Asoc. Geol. Argent.* 68 (2), 295–305.

Hurst, T., Christenson, B., and Cole-Baker, J. (2012). Use of a Weather Buoy to Derive Improved Heat and Mass Balance Parameters for Ruapehu Crater Lake. *J. Volcanology Geothermal Res.* 235-236, 23–28. doi:10.1016/j.jvolgeores.2012.05.004

Kling, G. W., Evans, W. C., and Tanyileke, G. Z. (2015). "The Comparative Limnology of Lakes Nyos and Monoun, Cameroon," in *Volcanic Lakes*. Editors D. Rouwet, B. Christenson, F. Tassi, and J. Vandemeulebrouk (Berlin Heidenberg: Springer-Verlag), 401–425. doi:10.1007/978-3-642-36833-2_18

Klug, J., Singer, B., Jicha, B., Ramirez, A., and Sruoga, P. (2018). "40Ar/39Ar Geochronology and Geochemical Evolution of Planchon-Peteroa Volcanic Complex," in GSA Annual Meeting in Indianapolis, Indiana, USA – 2018, January 2018 (Boulder, CO: Geological Society of America Abstracts with Programs), 270–277. doi:10.1130/abs/2018am-322292

Layana, S., Aguilera, F., Rojo, G., Vergara, Á., Salazar, P., Quispe, J., et al. (2020). Volcanic Anomalies Monitoring System (VOLCANOMS), a Low-Cost Volcanic Monitoring System Based on Landsat Images. *Remote Sensing* 12, 1589. doi:10.3390/rs12101589

Lewicki, J. L., Caudron, C., van Hinsberg, V. J., and Hilley, G. E. (2016). High Spatio-Temporal Resolution Observations of Crater lake Temperatures at Kawah Ijen Volcano, East Java, Indonesia. *Bull. Volcanol* 78, 53. doi:10.1007/s00445-016-1049-9

Liaudat, D. T., Penas, P., and Aloy, G. (2014). Impact of Volcanic Processes on the Cryospheric System of the Peteroa Volcano, Andes of Southern Mendoza, Argentina. *Geomorphology* 208, 74–87. doi:10.1016/j.geomorph.2013.11.016

Linacre, E. (1992). *Climate Data and Resources. A Reference and Guide*. London: Routledge.

López-Escobar, L., Cembrano, J., and Moreno, H. (1995). Geochemistry and Tectonics of the Chilean Southern Andes Basaltic Quaternary Volcanism (37-46°S). *Rev. Geol. Chile* 22 (2), 219–234. doi:10.5027/andgeoV22n2-a06

Mapelli, F., Marasco, R., Rolli, E., Daffonchio, D., Donachie, S., and Borin, S. (2015). "Microbial Life in Volcanic Lakes," in *Volcanic Lakes*. Editors D. Rouwet, B. Christenson, F. Tassi, and J. Vandemeulebrouk (Berlin Heidenberg: Springer-Verlag), 507–522. doi:10.1007/978-3-642-36833-2_23

Mazza, R., Taviani, S., Capelli, G., De Benedetti, A. A., and Giordano, G. (2015). "Quantitative Hydrogeology of Volcanic Lakes: Examples from the Central Italy Volcanic Lake District," in *Volcanic Lakes*. Editors D. Rouwet, B. Christenson, F. Tassi, and J. Vandemeulebrouk (Berlin Heidenberg: Springer-Verlag), 355–377. doi:10.1007/978-3-642-36833-2_16

Murphy, S., Wright, R., and Rouwet, D. (2018). Color and Temperature of the Crater Lakes at Kelimutu Volcano through Time. *Bull. Volcanol* 80, 2. doi:10.1007/s00445-017-1172-2

Naranjo, J. A., and Haller, M. J. (2002). Erupciones holocenas principalmente explosivas del volcán Planchón, Andes del sur (35°15'S). *Rev. Geol. Chile* 29 (1), 93–113. doi:10.4067/S0716-02082002000100006

Naranjo, J. A., Haller, M. J., Ostera, H. A., Pesce, A. H., and Sruoga, P. (1999). Geología y peligros del Complejo Volcánico Planchón-Peteroa, Andes del Sur (35°15'S), Región del Maule, Chile-Provincia de Mendoza, Argentina. *Boletín* 52, 55.

Naranjo, J. A., and Polanco, E. (2004). The 2000 AD Eruption of Copahue Volcano, Southern Andes. *Rev. Geol. Chile* 31 (2), 279–292. doi:10.4067/S0716-02082004000200007

Oppenheimer, C. (1996). Crater lake Heat Losses Estimated by Remote Sensing. *Geophys. Res. Lett.* 23 (14), 1793–1796. doi:10.1029/96GL01591

Oppenheimer, C. (1993). Infrared Surveillance of Crater Lakes Using Satellite Data. *J. Volcanology Geothermal Res.* 55, 117–128. doi:10.1016/0377-0273(93)90093-7

Oppenheimer, C. (1997a). Ramifications of the Skin Effect for Crater lake Heat Budget Analysis. *J. Volcanology Geothermal Res.* 75, 159–165. doi:10.1016/S0377-0273(96)00037-6

Oppenheimer, C. (1997b). Remote Sensing of the Colour and Temperature of Volcanic Lakes. *Int. J. Remote Sensing* 18, 5–37. doi:10.1080/014311697219259

Pasternack, G. B., and Varekamp, J. C. (1997). Volcanic Lake Systematics I. Physical Constraints. *Bull. Volcanology* 58, 528–538. doi:10.1007/s004450050160

Robie, R. A., Hemingway, B. S., and Fisher, J. (1978). Thermodynamic Properties of Minerals and Related Substances at 298.15 K and 1 Bar (105 Pascals) Pressure and at Higher Temperatures. *US Geol. Surv. Bull.* 1452, 456. doi:10.3133/b1452

Romero, J. E., Aguilera, F., Delgado, F., Guzmán, D., Van Eaton, A. R., Luengo, N., et al. (2020). Combining Ash Analyses with Remote Sensing to Identify Juvenile Magma Involvement and Fragmentation Mechanisms during the 2018/19 Small Eruption of Peteroa Volcano (Southern Andes). *J. Volcanology Geothermal Res.* 402, 106984. doi:10.1016/j.jvolgeores.2020.106984

Rouwet, D., Mora-Amador, R., Ramírez-Umaña, C. J., González, G., and Inguaggiato, S. (2017). "Dynamic Fluid Recycling at Laguna Caliente (Poás, Costa Rica) before and during the 2006-ongoing Phreatic Eruption Cycle (2005-10),". *Geochemistry and Geophysics of Active Volcanic Lakes*. Editors

T. Ohba, B. Capaccioni, and C. Caudron (London: Geological Society), 437, 73–96. doi:10.1144/SP437.11

Rowe, G. L., Brantley, S. L., Fernandez, M., Fernandez, J. F., Borgia, A., and Barquero, J. (1992). Fluid-volcano Interaction in an Active Stratovolcano: the Crater lake System of Poás Volcano, Costa Rica. *J. Volcanology Geothermal Res.* 49, 23–51. doi:10.1016/0377-0273(92)90003-V

Ryan, P. J., Harleman, D. R. F., and Stolzenbach, K. D. (1974). Surface Heat Loss from Cooling Ponds. *Water Resour. Res.* 10, 930–938. doi:10.1029/WR010i005p00930

Sellés, D., Rodríguez, A. C., Dungan, M. A., Naranjo, J. A., and Gardeweg, M. (2004). Geochemistry of Nevado de Longaví Volcano (36.2°S): a compositionally atypical arc volcano in the Southern Volcanic Zone of the Andes. *Rev. Geol. Chile* 31 (2), 293–315. doi:10.4067/S0716-02082004000200008

Stern, C. R. (2004). Active Andean Volcanism: Its Geologic and Tectonic Setting. *Rev. Geol. Chile* 31, 161–206. doi:10.5027/andgeoV31n2-a01

Tassi, F., Aguilera, F., Benavente, O., Paonita, A., Chiodini, G., Caliro, S., et al. (2016). Geochemistry of Fluid Discharges from Peteroa Volcano (Argentina-Chile) in 2010-2015: Insights into Compositional Changes Related to the Fluid Source Region(s). *Chem. Geology.* 432, 41–53. doi:10.1016/j.chemgeo.2016.04.007

Tormey, D., Frey, F., and López-Escobar, L. (1989). Geologic History of the Active Azufre-Planchón-Peteroa Volcanic Center (35°15'S, Southern Andes) with Implications for the Development of Compositional Gaps. *Rev. Asoc Geol. Argent* 44 (1–4), 420–430.

Tormey, D. (2010). Managing the Effects of Accelerated Glacial Melting on Volcanic Collapse and Debris Flows: Planchon-Peteroa Volcano, Southern Andes. *Glob. Planet. Change* 74 (2), 82–90. doi:10.1016/j.gloplacha.2010.08.003

Tormey, D. R., Frey, F. A., and Lopez-Escobar, L. (1995). Geochemistry of the Active Azufre--Planchon--Peteroa Volcanic Complex, Chile (35 15'S): Evidence for Multiple Sources and Processes in a Cordilleran Arc Magmatic System. *J. Pet.* 36 (2), 265–298. doi:10.1093/petrology/36.2.265

Trunk, L., and Bernard, A. (2008). Investigating crater lake warming using ASTER thermal imagery: Case studies at Ruapehu, Poás, Kawah Ijen, and Copahué Volcanoes. *J. Volcanology Geothermal Res.* 178, 259–270. doi:10.1016/j.jvolgeores.2008.06.020

Varekamp, J. C., Ouimette, A. P., Herman, S. W., Bermudez, A., and Delpino, D. (2008). Hydrothermal element fluxes from Copahue, Argentina: A 鋪beehive鋪 volcano in turmoil. *Geology* 29, 1059–1062. doi:10.1130/0091-7613(2001)029

Conflict of Interest: The authors declare that the research was conducted in the absence of any commercial or financial relationships that could be construed as a potential conflict of interest.

Publisher's Note: All claims expressed in this article are solely those of the authors and do not necessarily represent those of their affiliated organizations, or those of the publisher, the editors, and the reviewers. Any product that may be evaluated in this article, or claim that may be made by its manufacturer, is not guaranteed or endorsed by the publisher.

frontiers in Earth Science

ORIGINAL RESEARCH
published: 02 November 2021
doi: 10.3389/feart.2021.764087

Gypsum Precipitating From Volcanic Effluent as an Archive of Volcanic Activity

Vincent J. van Hinsberg[1]*, *Kim Berlo*[1], *Daniele L. Pinti*[2] and *Bassam Ghaleb*[2]

[1]GEOTOP Research Center, Department of Earth and Planetary Sciences, McGill University, Montreal, QC, Canada, [2]GEOTOP Research Center, Département des Sciences de la Terre et de l'atmosphère, Université de Québec à Montréal, Montreal, QC, Canada

Records of volcanic activity are a key resource in volcano monitoring and hazard mitigation. The time period for which such records are available and the level of detail vary widely among volcanic centers and there is, therefore, a need for supplementary sources of this information. Here, we use growth-zoned gypsum as a mineral archive of the activity of Kawah Ijen volcano in East-Java, Indonesia. Gypsum precipitates where water seeps from the crater lake and hydrothermal system, and it has formed a 100 m long cascading plateau. A 19 cm plateau cross-section was analysed for minor and trace elements using laser-ablation ICP-MS. Absolute ages were assigned to this transect based on ^{210}Pb dating. This ^{210}Pb age model was corrected for variations in the $^{210}Pb_0$ resulting from fluctuations in the volcanic radon flux by using $^{84}Kr/^{36}Ar$ and $^{132}Xe/^{36}Ar$. The age model indicates that the transect covers a period from 1919 ± 12 to 2008 ± 0.2. Gypsum-fluid partition coefficients (D) permit the gypsum compositions to be converted to the concentrations in the fluid from which each growth zone grew. The D-values also show the compatibility of the elements in the gypsum structure, and identify the LREE, Sr, Pb, Tl, Ni, Co, Cu, Zn, Cd, Sb, Th, and Mo as least susceptible to contamination from rock fragment and mineral inclusions, and therefore as most reliable elements of the gypsum record. Compositional variability in the timeseries correlates with known element behavior in the Kawah Ijen system and shows three element groups: the LREE, Sr, and Pb that represent rock-leaching; Cu, Zn, and Cd, which have previously been linked to immiscible sulfide destabilization in a deep-seated basalt; and Sb, Tl, and As which point to a contribution from the shallow system and evolved magma. Moreover, the gypsum record shows that episodes of unrest and quiescence have a distinct compositional signature in Kawah Ijen seepage fluids, and can be distinguished. Thus, we show that gypsum is a sensitive recorder of volcanic activity and can provide detailed information on the state of the magmatic-hydrothermal system in the past.

Keywords: gypsum, Kawah Ijen, crater lake, magmatic-hydrothermal system, volcano monitoring, element partitioning, historical record., trace elements

OPEN ACCESS

Edited by:
Franco Tassi,
University of Florence, Italy

Reviewed by:
Yuri Taran,
National Autonomous University of Mexico, Mexico
Pierpaolo Zuddas,
Sorbonne Universités, France

***Correspondence:**
Vincent J. van Hinsberg
V.J.vanHinsberg@gmx.net

Specialty section:
This article was submitted to Geochemistry, a section of the journal Frontiers in Earth Science

Received: *25 August 2021*
Accepted: *18 October 2021*
Published: *02 November 2021*

Citation:
van Hinsberg VJ, Berlo K, Pinti DL and Ghaleb B (2021) Gypsum Precipitating From Volcanic Effluent as an Archive of Volcanic Activity. Front. Earth Sci. 9:764087. doi: 10.3389/feart.2021.764087

INTRODUCTION

Growth-zoned mineral precipitates are powerful archives of the conditions and compositions of their growth environment, and the changes therein over time. Stalactites and stalagmites of carbonates and sulfates provide information on past climate (e.g., Goede and Vogel 1991; Gazquez et al., 2020). Similarly, precipitates formed in volcanic settings can provide information on element fluxes and their variability, e.g., travertine as a recorder of volcanic CO_2 emissions (Capezzuoli et al., 2014), and gypsum stalactites have been shown to preserve an archive of physical disturbances in a volcanic setting, i.e., volcanic seismicity (Utami et al., 2019). The main benefit of these mineral archives is their ability to provide information on time periods well before historical records are available.

Minerals precipitating under equilibrium conditions incorporate minor and trace elements following their equilibrium mineral-fluid element partition coefficients, which in turn are controlled by the mineral crystal structure (cf. (Blundy and Wood, 2003; van Hinsberg et al., 2010a). This mineral-lattice control is diminished for disequilibrium growth, but as long as precipitation takes place under constant conditions, the element distribution between mineral and fluid can remain constant as well. A constant element distribution between mineral and fluid permits for the composition of the fluid to be recorded by the mineral in a predictable fashion. Where the process or parameter of interest has a characteristic compositional signature, the variability in this variable can be reconstructed by later interrogation of the mineral record (assuming compositional preservation of the precipitate). Moreover, multiple variables can be investigated at the same time when each has its own isotopic or elemental fingerprint.

Here, we investigate the use of growth-zoned gypsum, precipitated from fluids seeping from the Kawah Ijen volcano in Indonesia, as an archive of the volcanic activity of this system. In this approach, we build upon our earlier work for a Kawah Ijen gypsum stalactite reported in Utami et al. (2019), in which it was shown that gypsum composition is sensitive to fluctuations in its formation fluid. These compositional variations could in turn be linked to changes in the activity of the Kawah Ijen system, in particular an input of rock-derived elements linked to increased rockfalls and landslides as a result of physical disturbances in the system (e.g., seismicity). Utami et al. (2019) also showed that gypsum linked to the 1817 phreatomagmatic eruption of Kawah Ijen has a markedly different composition, with a strong magmatic signature. In this contribution, we aim to extend the timeseries further back in time and bridge the gap between the stalactite record (1970–2009) and the 1817 gypsum, and to improve our understanding of element partitioning between gypsum and fluid to ground-truth its use as a compositional monitor of volcanic activity.

This approach is particularly pertinent for Kawah Ijen because the historical record of its activity is incomplete and consists of only punctuated reports with variable levels of detail. Mineral archives can provide the ability to verify the available historical record, permit comparing the reports of unrest to establish a consistent and leveled record of activity, and extend the record to beyond the time period for which historical accounts are available.

GEOLOGICAL SETTING

Kawah Ijen Volcano

Kawah Ijen volcano is a passively degassing stratovolcano located within the Ijen caldera complex of East Java (**Figure 1**). It is positioned on the inner flank of the Merapi caldera rim volcano and it is the only currently active center in the caldera complex (Kemmerling, 1921; Caudron et al., 2015b). Kawah Ijen has erupted magmatic products of basaltic to dacitic bulk compositions (Handley et al., 2007; Kemmerling, 1921; Lowenstern et al., 2018; Sitorus, 1990; van Hinsberg et al., 2010b; 2017), including lavaflows, scoria and ash fall deposits, and pyroclastic flow deposits that extend in age to >21 kyr BP (Sitorus, 1990). The most recent magmatic eruption of Kawah Ijen volcano took place in 1817 (Oudgast, 1820; Bosch, 1858), but phreatic eruptions and steam explosions are common (Caudron et al., 2015a; 2015b), and fumaroles on the western lake shore emit ~200 ton/day of SO_2 in passive degassing (Vigouroux, 2011; Gunawan et al., 2016; van Hinsberg et al., 2017).

The summit crater of the volcano is occupied by a large lake (27 million m^3—Caudron et al., 2015b). The lake waters are warm hyperacidic SO_4-Cl brines with a pH ~ 0, T = 40 ± 10°C and TDS = 100 g/kg (Delmelle and Bernard, 1994; Takano et al., 2000; Caudron et al., 2015b; van Hinsberg et al., 2017). A lake has occupied the crater since at least 1796 (de la Tour, 1805; Oudgast, 1820), although it was expelled in the 1817 eruption (Bosch, 1858). The lake water composition reflects inputs from the magmatic-hydrothermal system, rainwater, and rock alteration, with mineral precipitation, evaporation and seepage as the main output fluxes (van Hinsberg et al., 2017).

In the late 19th century, a dam was built to control lake outflow (Hengeveld, 1920), with the most recent iteration of this dam still in place today. Up to the 1980s, water was periodically released from the lake to lower its level and avoid detrimental effects where the lake effluent reached irrigation systems in the Asambagus plain (see Hengeveld, 1920; van Rotterdam-Los et al., 2008; Yudiantoro et al., 2020). Since then, the level of the lake has dropped significantly, and now stands well below the level of the dam (Caudron et al., 2015b).

The compositions of melt inclusions and gas and fluid emissions from Kawah Ijen indicates the presence of two magma bodies: A deep-seated mafic magma that contributes CO_2 and a metal signature related to sulfide-liquid breakdown, and; A shallow, evolved magma characterized by elevated concentrations of semi-metals (Berlo et al., 2014). These magmatic sources are modified by interaction with the hydrothermal system and resultant element scrubbing (cf. Symonds et al., 2001), and transient mineral precipitation (van Hinsberg et al., 2017; Berlo et al., 2020).

Gypsum Deposits at Kawah Ijen

Acidic waters emerge on the western flanks of the volcano in a series of springs along the Banyu Pait river valley (**Figure 1**). The

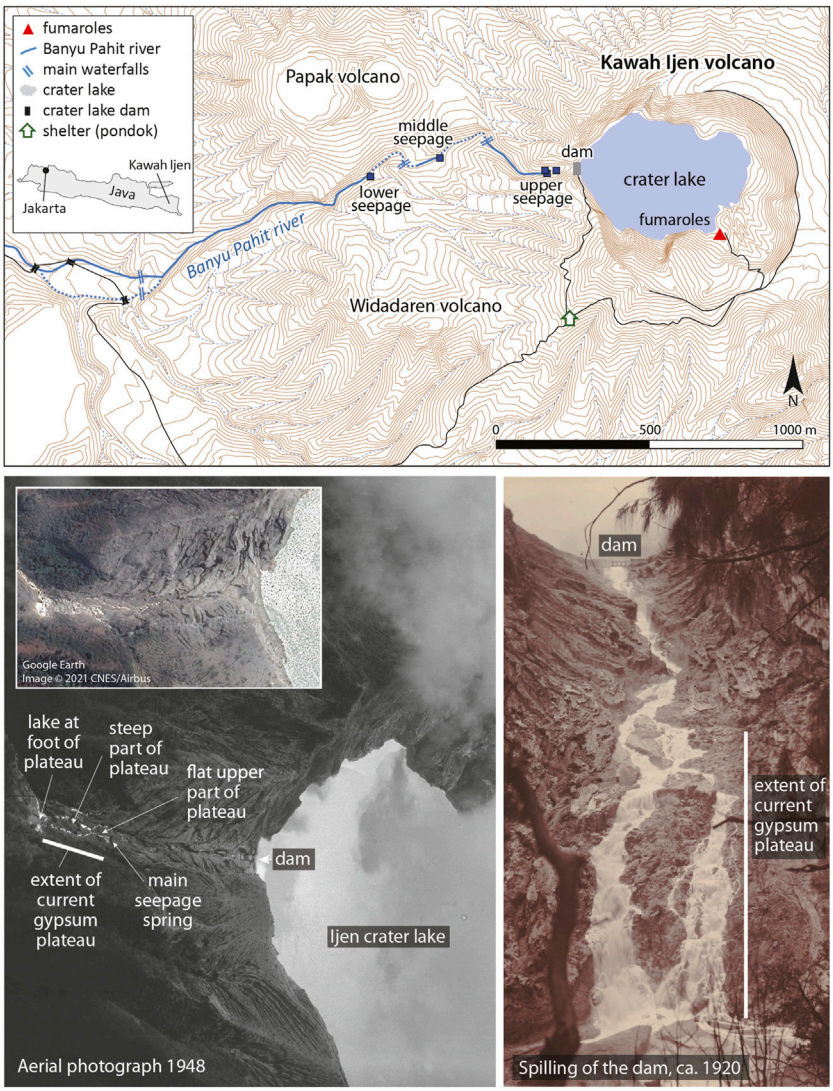

FIGURE 1 | (A). Topographic map showing the crater lake and upper Banyu Pait river valley of Kawah Ijen volcano, and its location in East Java. **(B)**. Aerial photograph showing the upper Banyu Pait river valley and the position of the gypsum plateau within it. The two main water channels on the plateau are also visible and are still present today as shown in the inset satellite image from March 2014 **(C)**. Photograph showing the upper Banyu Pait valley up to the dam during an episode of spilling around 1920. No gypsum is evident in this photograph, suggesting the plateau formed post-1920. The photographs shown in b and c are from the KITLV image library hosted by Leiden University.

uppermost springs are dominantly lake seepage, with an increasing contribution of effluent from the hydrothermal system in springs further downstream (Palmer, 2009). The lower seepage springs are the main source of the Banyu Pait River, and river flow is continuous from this seepage area. Gypsum precipitates are found at all springs, and along the riverbed of the Banyu Pait River up to the 3rd set of springs. Gypsum precipitation is most extensive at the uppermost springs with a 100 m long cascading plateau ending in a gypsum-covered lake (**Figure 2**).

The gypsum plateau consists of a more or less flat area at the top with water flowing onto this from several small springs at the upper plateau edge (**Figures 2C,F**, **3A**), and a spring with larger discharge that emerges upstream of the plateau (**Figures 2C,D**). Gypsum covered steps descend from this flat area with a thin film of water flowing over these. The main flow shifts from the center of the plateau to the left (north) on this steep section, with most of the discharged water descending a lavaflow at the edge of the plateau in a series of small ponds rimmed by gypsum (**Figure 2B**). This lavaflow appears to continue underneath the gypsum adjacent, and may be the cause for the steep valley topography. An additional seepage spring is present on the southern edge (**Figure 2B**) with water flow initially in a channel on scoria before creating the southern gypsum plateau extension and discharging onto the gypsum-covered lake at the foot of the plateau. This lake cover is a thick crust of gypsum, although the extent of this cover downstream varied between 2007 and 2015. Two small seepage springs are present upstream

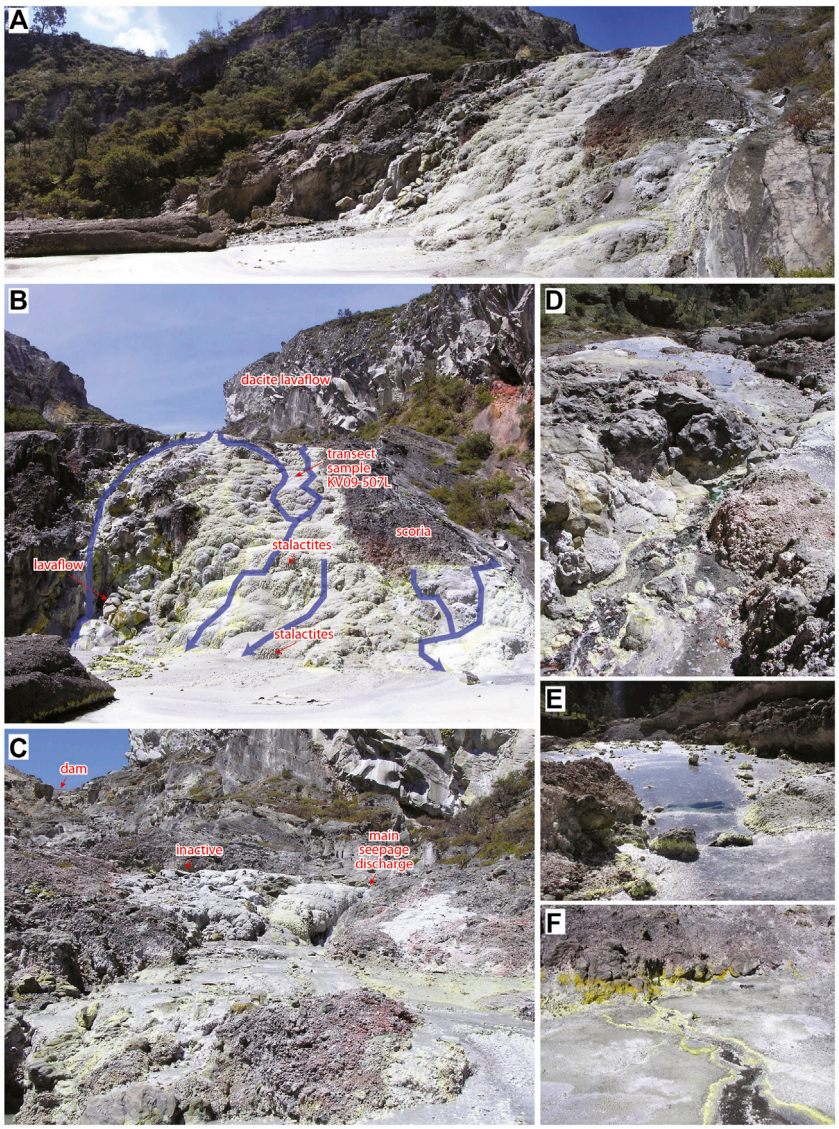

FIGURE 2 | Overview photographs of the gypsum plateau. **(A,B)**. View of the plateau looking approximately north-east and east, respectively, showing its stepped cascade shape. Gypsum stalactites grow from the overhangs of the steps. The main flow over the plateau is on the left, along the exposed lavaflow, the right center, over the sample site, and from a spring on the right that has produced the gypsum starting about two-thirds down the face on the right. **(C)**. View of the uppermost section of the plateau (not visible in a,b). The main seepage spring is on the right in this image and forms a channel with subsequent spreading out of water over the flat section of gypsum in the foreground. The white, fractured crusts of gypsum on the left represent an inactive section of the plateau. **(D)**. View towards the west from the main seepage spring above the plateau. Only small amounts of gypsum precipitate at the seepage outlets and the water flows on sediment instead. **(E)**. View of the top, flat part of the gypsum plateau looking west showing the thin film of water that covers the gypsum. **(F)**. Channel of seepage water with yellow (Na,K)-alum precipitates on either side, resulting from evaporation of spray.

of the plateau, and have gypsum and (Na,K)-alum precipitates, but water flow does not continue to the main plateau. Water outflow from the various plateau seepage springs has a temperature of 30–37°C (measured August 5th, 2009 with an ambient air temperature of 17°C).

The seepage fluids are not saturated in gypsum where they emerge, but reach saturation by cooling and evaporative concentration (Delmelle and Bernard, 2000; Utami et al., 2019). This is evidenced in the field by gypsum-free channels at the seepage outlets and initial flow on a streambed of (altered) volcaniclastic material (**Figure 2D**). Flow is, moreover, channelized on the uppermost part of the plateau, with gypsum growing as "cauliflower" domes above the fluid level from spray (**Figures 2F**, **3A**). Where gypsum saturation is reached, the fluid spreads out into a thin sheet that covers a flat, but rough surface of gypsum laths, both on the horizontal parts of the plateau and on the steps (**Figures 2E,F**, **3A,C,D**). The laths mostly grow vertically and are dominantly 1 to 2 mm in diameter. Larger gypsum laths are found on the sides of channels and ponds growing inward (**Figure 3B**). Radial growth of gypsum

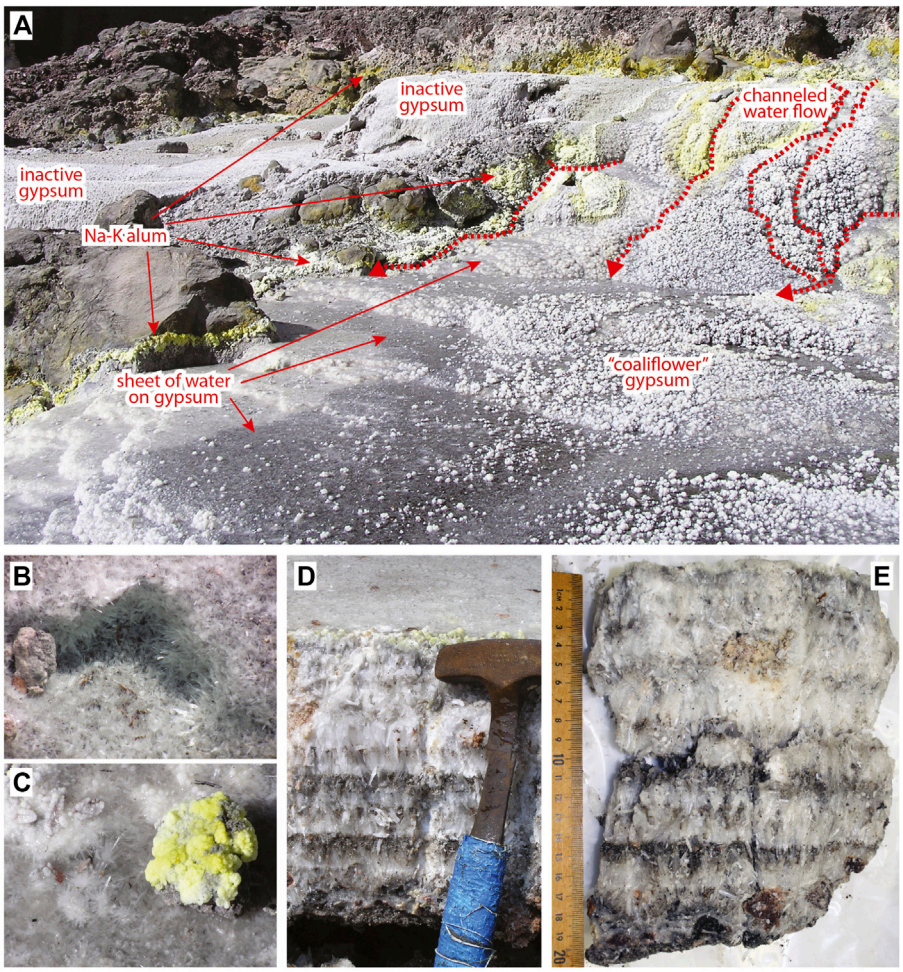

FIGURE 3 | (A–C) Types of gypsum found in the uppermost part of the plateau. Initial water flow is channelized and flows on sediment, with gypsum precipitation limited to a "cauliflower" type that extends above the water. The seepage water subsequently spreads out into a film on a sheet of flat-lying gypsum with mm-sized gypsum laths protruding upward into the fluid. Locally, ponds are present, with gypsum laths growing inward. Precipitation of yellow (Na-K)-alum is limited to the margins of the flow, and areas above the water level. **(D)**. View of the gypsum section (sample KV09-507L) before extraction, showing growth zoning outlined by dark debris horizons. The surface gypsum is covered with a film of water. **(E)**. The gypsum section as sampled.

is common on detritus including rock fragments and pieces of wood. Open caverns are present under a number of the steps. No water can be seen dripping from their gypsum roof, indicating that there is no permeability in the gypsum.

Cross-sections through the gypsum plateau show growth zoning (**Figures 3D,E**), outlined by both small color variations in the gypsum, and by horizons of detritus (mostly wood fragments, leaves, charcoal and variably altered rock fragments). These detritus horizons will reflect mud and debris flows onto the gypsum plateau. Growth zones are mostly horizontal and parallel to the upper gypsum surface, except where detritus is present and gypsum growth becomes radial (**Figure 3E**). Growth zones are remarkably regular, can be traced from one section to another, and are of near-constant thickness along a section. This suggests a spatially constant rate of growth.

Gypsum stalactites form on the overhangs of the steps (**Figure 2B** and Utami et al., 2019; Utami et al., 2020). These stalactites have a conical shape, and where actively growing, they terminate in a transparent, idiomorphic gypsum lath that can be up to several cm in length. These laths were removed on a number of actively growing stalactites in 2008, and had completely regrown in 2009, indicating that they form rapidly. In cross-section, the stalactites show growth zoning, similarly outlined by gypsum color variations and detritus horizons (Utami et al., 2019).

The streamlets that feed the plateau are not fixed in location, nor is the water flow over the plateau itself. As a result, water meanders over the plateau and the water feed to a section of the plateau can shift from one spring to another. There are also sections of the plateau that are inactive (**Figure 2C**). The gypsum in these inactive parts is brittle and milky white to grey in color.

Gypsum is also found as fragments and grains in phreatic and phreato-magmatic deposits in the Banyu Pait river valley and on the outer flanks of the volcano, as gypsum needles cementing the

1817 base fall deposit (Utami et al., 2019), and as a surface coating on phreatic deposits around the crater. The latter appear to form from remobilization of SO_4 from the phreatic deposits, or from SO_4 formed in the oxidation of native sulfur contained within these deposits.

Gypsum precipitates are a long-lived feature of the Kawah Ijen system as evidenced by the presence of gypsum fragments in phreatic and phreato-magmatic deposits. Gypsum stalactites are mentioned in a report of an expedition to the crater lake and Banyu Pait River that took place in 1789 (Oudgast, 1820). A layer of gypsum just above the level of the lake is reported by Kemmerling (1921). However, neither author mentions the gypsum plateau, despite the fact that "Oudgast" (i.e., old-timer) descended along the river. Other authors describing the Kawah Ijen—Banyu Pait system in the late 19th and early 20th centuries also make no mention of the plateau, including Hengeveld (1920) who surveyed the upper river valley for the construction of a new dam and did observe the seepage springs that currently feed the plateau. Moreover, a photograph taken of the upper Banyu Pait river valley that shows the dam down to the plateau location during a spilling event around 1920 does not appear to show the gypsum plateau, although it is partly covered by water (**Figure 1C**). Combined, this suggests that a gypsum plateau was not yet present in the early 1920s, or at least not as significant as it is now.

Other precipitate phases found associated with the spring and river water include (Na,K)-alum, barite, syngenite, amorphous silica, and jarosite (Delmelle and Bernard, 2000; van Hinsberg et al., 2017; Utami et al., 2019).

METHODS AND MATERIALS

Layered gypsum was investigated as a timeseries of changes in the composition of the crater lake and hydrothermal effluent from which it formed, and thereby a proxy record for changes in volcanic input and activity. Absolute time was assigned to this record using noble gas corrected ^{210}Pb radionuclide dating. The gypsum record was converted to a fluid compositional record by use of partition coefficients.

Samples

Samples of the gypsum plateau were collected in 2009 from the central part of the plateau where active fluid flow occurs (**Figure 2B**). A 19 cm gypsum cross-section was cut that extends from the substrate to the actively growing surface (Sample KV09-507L). The surface of the gypsum consists of idiomorphic gypsum laths terminating on the fluid surface (**Figure 3D**). The gypsum cross-section consists of layered gypsum growing from a substrate of altered rock fragments (**Figures 3D,E**). Individual gypsum crystals can be recognized in the growth bands and consist of upward growing and broadening crystals that are transparent to milky white in color. Three distinct horizons of variably altered rock fragments are found in the cross-section, as well as isolated fragments of fresh and altered rocks, and organic material (twigs, leaves and charcoal). Radiating gypsum growth is present where these foreign objects occur. Most of the layers are dense, but the gypsum immediately below the rock fragment horizons has porosity and is similar in texture to that of the actively growing surface, suggesting that it represents an active growth surface rapidly buried by influx of rock fragments.

A more detailed inspection of polished gypsum sub-samples from the transect sample was conducted by back-scattered electron microscopy and EDS semi-quantitative analysis using a PhenomXL SEM with CeB_6 electron source operating at 10 kV and Si-drift EDX detector. This imaging confirmed that the inclusions consist of variably altered magmatic rock fragments (containing glass, plagioclase, clino-pyroxene, Ti-magnetite and their altered equivalents—see Lowenstern et al., 2018; van Hinsberg et al., 2020) and organic debris, as well as euhedral to subhedral grains of barite, syngenite and (Na,K)-alum. The rock fragments and organic debris vary in size from *ca.* 100 μm to 3 cm, and are readily identifiable in the gypsum from their dark color. Barite, alum and syngenite range from submicron to minor larger grains of ~200 μm, with most approximately 2–10 μm. Whereas barite and syngenite are homogenously distributed, alum is commonly concentrated in bands.

To convert the gypsum composition to that of the fluid from which it formed requires knowledge of the partitioning of the elements between gypsum and fluid. To determine this, gypsum laths actively growing on gypsum stalactites were collected, as was the fluid from which these laths were growing. These laths had been broken off the year before sampling, so the laths that were sampled represent 1 year of growth. Three pairs of gypsum (KV08-407, KV09-505, KV09-303) and fluid (SP2008-L, KV09-506, KV09-304) were collected.

Gypsum and Fluid Compositional Analyses

The composition of gypsum was determined *in-situ* along a point transect using laser-ablation ICP-MS, and in bulk samples by wet ashing followed by solution ICP-MS. Bulk analyses were conducted on select growth bands in the gypsum cross-section that were further analyzed for ^{210}Pb and noble gases. Bulk analyses were also conducted on actively growing gypsum laths that were combined with fluid analyses to obtain partition coefficients. The growth bands represent clearly defined growth zones of sufficient width to yield the sample amounts needed for the combined analyses. The extracted gypsum growth zones were coarse crushed in an agate pestle and mortar, washed in ethanol to remove dust, and clear, inclusion-free crystals hand-picked with the help of a binocular microscope. An aliquot of *ca.* 250 mg was then finely ground in an agate mortar under ethanol and dissolved in 25 ml 10% trace element grade HNO_3 solution at 40°C under constant stirring. The resulting solutions were clear and devoid of precipitate/residue. Solutions were analyzed by ICP-QMS at GeoLabs (Sudbury, Canada). A sample of the outermost growth surface of the gypsum transect, consisting of mm-sized laths of gypsum that protrude from the surface and were submerged in the acid water when the sample was taken, was similarly crushed, washed in distilled water and ethanol to remove soluble co-precipitates (e.g., alum and syngenite) and dust, and finely ground in an agate mortar. The resulting powder

was pressed into a 13 mm diameter pellet without additives and analyzed by laser-ablation ICP-MS.

Laser-ablation ICP-MS analyses were conducted using a NewWave 213 nm Nd:YAG laser system coupled to a Thermo Finnigan iCAP Qc quadrupole ICP-MS in the trace-element laboratory of McGill University. The laser was operated at 10 Hz repetition rate, a 120 µm crater size and with a fluence of 5.5 J/cm^2 for the *in-situ* transect analyses. The pellet was sampled in troughs of ~10 mm length using a 20 Hz repetition rate, 80 µm crater diameter and fluence of 5 J/cm^2. In both types of analyses, the surface was cleaned prior to the analyses using a 140 µm crater. The ablated material was transported to the ICP-MS in an 800 ml/min He flow that was mixed with 1 L/min of Ar prior to injection into the ICP-MS plasma. NIST SRM 610 was used as the primary standard to correct for drift, and bracketed the gypsum analyses. Reference glasses BCR-2G, BIR-1G, KL2, and T1 were used as secondary standards to determine accuracy. Certified values for all SRM were the preferred values taken from the GEOREM database (Jochum et al., 2005). Calcium was used as the internal reference element to correct for variations in ablation behavior between gypsum and glasses, assuming a stoichiometric content of Ca in the gypsum. Data were processed using the Iolite version 2.5 software package (Paton et al., 2011). Each analysis spot was integrated in full (the full dataset) and integrated while excluding any obvious inclusions (the inclusion-filtered dataset). Inclusions were identified by inspecting the Ca-divided element signals, in particular Ba/Ca (barite), Al/Ca (alum), Mg/Ca (syngenite), and Si/Ca (silicates). The *in-situ* transect samples consisted of 2 cm long, polished sub-samples cut from the gypsum transect, and cover the full transect from base to top, except for some of the detritus horizons (**Supplementary Figure S1**). The laser ablation transect followed upward growing crystals and targeted the densest parts of the samples, and the transect is therefore kinked and discontinuous in places. The spacing between craters was varied, with the highest density, and hence resolution, for the most recent part of the transect. Analysis craters were located afterwards in optical microscopy (**Supplementary Figure S1**) and their position relative to the surface determined by projecting these positions onto the vertical.

The samples of the water from which the stalactite tips were growing were analyzed by ICP-OES for major elements and ICP-QMS for trace elements at GeoLabs (Sudbury, Canada). The digested samples were diluted 8 times in a trace element grade nitric acid solution for ICP-OES and 145 times for ICP-MS. Detection limits and reproducibility of reference materials for these methods are given in **Supplementary Table S1**.

^{210}Pb and Noble Gas Analyses

A *ca.* 1 g aliquot of the handpicked gypsum was ground under ethanol in an agate pestle and mortar and prepared for alpha spectrometry in the radionuclide laboratory at UQAM. The gypsum samples were dissolved in HCl spiked with a known mass of ^{209}Po tracer, plated onto silver discs, and the discs counted for Po isotopes using an EG&G Ortec 576 alpha spectrometer. Analyses followed the protocol of Utami et al. (2019) and more details on the analytical method can be found there.

Noble gas He, Ne, Ar, Kr, and Xe concentrations and ^{40}Ar/^{36}Ar, ^{86}Kr/^{84}Kr, and ^{129}Xe/^{132}Xe ratios were determined at the Geotop GRAM laboratory at UQAM, by noble gas mass spectrometry (NGMS). Between 0.25 and 0.45 g of the material was hand-picked and placed in a stainless-steel vessel with a iron ball and pumped to vacuum overnight using a primary pump. Any washing, both in water and in ethanol/acetone was avoided, because previous essays showed that humidity is impossible to remove by pumping, likely because of the porosity and typology of the gypsum crystals. After a vacuum of less than 5×10^{-4} mbar was reached (measured on a Pirani gauge), the iron ball was agitated 200 times using an external magnet to crush the gypsum and release the noble gases for analysis. The reactive gases were removed using two Ti getters at 600°C for 15 min followed by 10 min at ambient temperature and one Zr-V-Fe SAES® ST-707 getter at 100°C for 15 min followed by 10 min at ambient temperature. Gases were then adsorbed onto an Advanced Research System® cryogenic trap containing activated charcoal at 11 K and released sequentially at 35 K (He), 110 K (Ne), 210 K (Ar), and 310 (Kr and Xe). Noble gas isotopes were measured using a Thermo® HELIX-MC using the axial Faraday detector in peak jumping mode. Signals were calibrated against a known aliquot of standard air. Typical air standard isotopic measurement reproducibility is 1.5–2%, while uncertainties on noble gas isotopic concentration analyses are between 0.1 and 0.01%.

The gypsum-fluid pair KV09-505 and KV09-506 was also analyzed for ^{210}Pb. The gypsum sample was treated as the transect gypsum growth zone samples described above. Approximately 20 g of the brine was accurately weighed into a glass beaker that contained a known mass of ^{209}Po yield tracer. The fluid was evaporated to dry and re-dissolved in 80 ml of 0.6 M HCl. Polonium isotopes were spontaneously deposited from this solution overnight onto silver disks and their activities counted in an EG&G Ortec 576 alpha spectrometer running the Maestro software. The gypsum and brine samples were measured 750 days after sampling to ensure equilibrium between ^{210}Po and ^{210}Pb.

RESULTS

Gypsum and Fluid Compositions

Table 1 presents the median and 1st and 3rd quartile gypsum compositions for the gypsum transect (full and inclusion-filtered integration windows for *in-situ* analyses and the GeoLabs bulk analyses) and the compositions of the gypsum-fluid pairs that were analyzed to obtain partition coefficients. The full datasets are given in **Supplementary Table S1**. Compared to the seepage waters, gypsum is particularly enriched in Sr, the LREE, Ni, Cu, Pb, and Mo, and depleted in the alkali elements, Be, Mg, Mn, Al, and the HFSE. The transect shows largest relative compositional variability in Zr, Ba, Tl, U, Sb, Ti, V, Mn, Nb, and Al.

The compositions of bulk-digested gypsum are equivalent to those measured *in-situ* (**Table 1**). There is more variability for the

TABLE 1 | Compositions of gypsum and fluid samples.

Sample	KV09-507L			KV09-507L			KV09-507L			KV09-303	KV09-304	KV09-505	KV09-506	KV08-407	SP08-L	KV09-507L	KV09-507L
Material	Gypsum			Gypsum			Gypsum			Gypsum	Fluid	Gypsum	Fluid	Gypsum	Fluid	Gypsum	Gypsum
Comment	Transect–full			Transect–inclusion filtered			Bulk digested samples			Stalactite tip	New spring	Stalactite tip	Main spring	Stalactite tip	Main spring	Top–pellet	Top–*in-situ*
	median	P25	P75	median	P25	P75	median	P25	P75								
Li	0.03	0.02	0.05	0.02	0.01	0.04	0.07	0.06	0.09	0.07	0.99	0.05	1.20	n.d.	0.59	0.25	0.07
Be	n.a.	n.a.	n.a.	n.a.	n.a.	n.a.	n.a.	n.a.	n.a.	n.d.	0.08	n.d.	0.09	n.d.	0.06	0.008	0.005
B	1.1	0.6	1.9	0.8	0.5	1.3	3.7	2.8	4.6	4.4	34.0	3.3	34.0	n.a.	n.d.	n.a.	n.a.
Na	62	31	104	40	20	76	92	84	112	79	1,025	123	1,130	n.a.	916	336	79
Mg	18	12	33	13	9	22	19	15	22	20	709	23	756	n.a.	567	43	19
Al	66	27	158	38	15	93	50	38	62	62	5,624	90	6,233	n.a.	4,772	329	1,572
Si	4,423	2,186	7,857	n.d.	n.d.	n.d.	8	6	10	n.a.	n.a.	n.a.	n.a.	n.a.	n.a.	n.a.	n.a.
K	27	13	54	18	7	35	55	44	59	52	1,206	56	1,354	n.a.	1,027	291	23
Ca	fixed	fixed	fixed	fixed	fixed	fixed	230,076	222,355	233,914	220,245	823	225,505	1,051	225,000	697	232,834	232,834
Sc	0.3	0.2	0.5	0.2	0.2	0.4	0.4	0.4	0.5	0.6	1.3	1.2	1.4	n.d.	1.1	1.0	0.4
Ti	1.5	0.6	4.1	0.8	0.4	2.1	0.9	0.8	1.0	1.0	36.5	1.0	25.9	12.9	20.3	34.0	3.6
V	0.15	0.07	0.35	0.08	0.04	0.21	0.09	0.07	0.11	0.14	12.32	0.18	13.38	0.13	10.78	2.36	0.84
Cr	n.a.	n.a.	n.a.	n.a.	n.a.	n.a.	0.11	0.09	0.12	0.13	0.82	0.08	0.44	0.01	0.28	0.34	0.35
Mn	0.7	0.3	1.6	0.4	0.2	0.9	0.4	0.3	0.4	0.5	48.1	0.6	51.1	0.6	42.2	7.2	1.0
Fe	n.a.	n.a.	n.a.	n.a.	n.a.	n.a.	18	15	26	32	2,567	37	2,617	n.a.	2,432	n.a.	n.a.
Co	0.11	0.09	0.12	0.10	0.09	0.12	0.81	0.76	0.85	0.81	0.59	0.91	0.61	0.34	0.61	0.27	0.19
Ni	1.4	1.3	1.4	1.3	1.3	1.4	0.7	0.6	1.1	0.8	0.2	1.0	0.2	n.a.	0.3	0.9	1.0
Cu	0.11	0.08	0.17	0.09	0.07	0.13	2.0	1.8	2.7	2.2	0.4	1.6	0.2	n.a.	0.1	1.5	0.2
Zn	0.3	0.2	0.5	0.2	0.1	0.4	14	4	63	2.8	6.1	26.9	6.2	6.0	n.d.	0.9	0.6
Ga	0.02	0.01	0.05	0.01	0.01	0.03	0.32	0.30	0.33	0.38	1.11	0.55	1.22	0.01	1.14	0.30	0.38
As	0.3	0.2	0.4	0.2	0.1	0.2	0.2	0.2	0.2	0.3	n.d.	0.3	n.d.	n.d.	n.d.	11.8	0.3
Rb	0.14	0.05	0.26	0.08	0.03	0.18	0.17	0.14	0.18	0.13	3.42	0.16	4.21	0.10	3.25	0.93	0.10
Sr	785	708	849	775	697	852	803	759	833	821	15	1,058	18	n.a.	14	888	852
Y	2.2	1.8	2.9	2.0	1.6	2.7	2.5	2.4	2.7	3.2	0.8	4.2	1.0	2.8	0.9	4.0	3.3
Zr	0.08	0.03	0.27	0.04	0.02	0.14	0.19	0.16	0.31	0.15	1.91	0.12	2.19	0.05	1.82	1.87	0.09
Nb	0.0012	0.0004	0.0038	0.0014	0.0007	0.0037	0.0016	0.0014	0.0019	0.0019	0.0019	n.d.	n.d.	n.d.	0.0008	0.058	0.0010
Mo	0.005	0.003	0.010	0.005	0.003	0.010	0.035	0.029	0.043	0.035	0.008	0.021	0.007	n.d.	n.d.	0.042	0.029
Cd	0.002	0.001	0.004	0.002	0.001	0.004	0.015	0.013	0.017	n.d.	0.036	n.d.	0.056	0.004	0.044	0.015	0.006
Sn	n.a.	n.a.	n.a.	n.a.	n.a.	n.a.	0.03	0.02	0.04	0.03	0.37	0.02	0.38	0.01	0.21	10.59	21.41
Sb	0.018	0.008	0.045	0.010	0.003	0.028	0.024	0.016	0.036	0.021	0.035	0.019	0.070	0.001	0.053	0.467	0.014
Cs	0.005	0.003	0.008	0.003	0.001	0.005	0.019	0.011	0.042	0.047	0.094	0.012	0.112	0.007	0.105	0.044	0.005
Ba	0.09	0.04	0.42	0.06	0.02	0.21	0.46	0.39	0.74	0.16	0.05	0.13	0.06	0.07	0.04	5.41	0.13
La	12	9	16	11	7	16	11	11	12	14	0.56	24	0.67	19	0.60	16	16
Ce	42	30	53	39	25	51	45	41	47	50	1.31	74	1.52	53	1.33	59	57
Pr	n.a.	n.a.	n.a.	n.a.	n.a.	n.a.	6.8	6.2	7.1	7	0.18	10	0.20	7	n.d.	8	8
Nd	28	19	35	26	18	35	29	27	30	32	0.76	40	0.87	31	0.73	36	38
Sm	4.6	3.4	5.7	4.4	3.0	5.6	4.9	4.6	5.1	5.5	0.18	6.8	0.20	4.9	0.16	6.4	6.6
Eu	1.0	0.8	1.2	0.9	0.7	1.2	1.0	0.9	1.0	1.2	0.05	1.4	0.06	1.0	0.05	1.5	1.3
Gd	2.0	1.6	2.4	1.9	1.5	2.4	2.2	2.1	2.3	2.7	0.17	3.4	0.19	3.9	0.17	3.0	2.8
Tb	n.a.	n.a.	n.a.	n.a.	n.a.	n.a.	0.23	0.22	0.23	0.3	0.03	0.4	0.03	0.3	0.03	0.4	0.3
Dy	n.a.	n.a.	n.a.	n.a.	n.a.	n.a.	0.99	0.96	1.02	1.3	0.16	1.6	0.18	1.0	0.15	1.5	1.3
Ho	n.a.	n.a.	n.a.	n.a.	n.a.	n.a.	0.13	0.13	0.14	0.2	0.03	0.2	0.04	0.1	0.03	0.2	0.2
Er	0.28	0.22	0.35	0.26	0.21	0.33	0.28	0.27	0.30	0.35	0.10	0.47	0.11	0.48	0.09	0.48	0.38

(Continued on following page)

TABLE 1 | (*Continued*) Compositions of gypsum and fluid samples.

Sample	KV09-507L			KV09-507L			KV09-507L			KV09-303	KV09-304	KV09-505	KV09-506	KV08-407	SP08-L	KV09-507L	KV09-507L
Material	Gypsum			Gypsum			Gypsum			Gypsum	Fluid	Gypsum	Fluid	Gypsum	Fluid	Gypsum	Gypsum
Comment	Transect–full			Transect–inclusion filtered			Bulk digested samples			Stalactite tip	New spring	Stalactite tip	Main spring	Stalactite tip	Main spring	Top–pellet	Top–*in-situ*
	median	P25	P75	median	P25	P75	median	P25	P75								
Tm	n.a.	n.a.	n.a.	n.a.	n.a.	n.a.	0.03	0.03	0.03	0.03	0.01	0.04	0.02	n.a.	n.d.	0.06	0.03
Yb	0.13	0.10	0.16	0.12	0.09	0.15	0.12	0.12	0.13	0.15	0.09	0.20	0.10	0.19	0.09	0.27	0.17
Lu	n.a.	n.a.	n.a.	n.a.	n.a.	n.a.	0.01	0.01	0.01	0.02	0.01	0.02	0.02	0.02	0.01	0.05	0.02
Hf	n.a.	n.a.	n.a.	n.a.	n.a.	n.a.	0.01	0.01	0.01	0.011	0.037	0.015	0.043	0.010	0.036	0.059	0.001
Ta	0.0002	0.0001	0.0004	0.0003	0.0001	0.0005	0.0008	0.0006	0.0010	0.0004	n.d.	0.0005	n.d.	n.a.	0.0001	0.0051	0.0001
W	0.004	0.002	0.008	0.003	0.001	0.006	0.016	0.012	0.020	0.020	n.d.	0.014	0.002	0.009	n.a.	0.249	0.123
Tl	0.054	0.038	0.077	0.015	0.006	0.042	0.042	0.035	0.045	0.031	0.635	0.043	0.721	0.058	0.702	0.186	0.053
Pb	17.2	14.2	19.3	15.8	12.2	18.5	16.3	15.3	17.5	16.4	3.4	24.0	4.1	24.2	3.9	19.0	15.9
Bi	0.19	0.11	0.27	0.18	0.08	0.25	0.19	0.16	0.21	0.31	0.62	0.20	0.66	n.a.	0.71	0.43	0.13
Th	0.25	0.16	0.36	0.22	0.14	0.32	0.28	0.27	0.30	0.39	0.25	0.71	0.28	0.45	0.25	0.88	0.50
U	0.0017	0.0007	0.0044	0.0010	0.0004	0.0028	0.0014	0.0010	0.0022	0.002	0.055	0.002	0.061	0.004	0.051	0.091	0.022

Concentrations for the gypsum transect (both the full and inclusion-filtered integration windows), and bulk digested gypsum are given as the median and 1st and 3rd quartile. The full dataset of in-situ gypsum analyses is given in ***Supplementary Table S1****. All values are given in mg/kg.*

in-situ analyses, which is to be expected as the bulk analyses represent a larger growth interval and will therefore average out the variability. The Cu, Co, and Zn contents of the bulk-digested samples are consistently higher. It is unclear what causes this as no inclusion phase with these specific elements was identified in electron imaging. The equivalence in composition between *in-situ* and bulk analyses indicates that the bulk analyses are representative of gypsum, as there is no evidence for a significant presence of inclusions in the bulk-digested samples. For example, the median Al content of the bulk-digested gypsum is 50^{+12}_{-12} mg/kg and it is 38^{+55}_{-23} mg/kg for the *in-situ*, inclusion-filtered analyses, which rules out a significant presence of alum. Similarly, Si contents are low at a median of only 8 ± 2 mg/kg. This means that the ^{210}Pb activities and noble gas data determined from bulk samples are representative for gypsum.

Noble Gas and ^{210}Pb Data

The noble gas data are given in **Table 2**, and the ^{210}Pb activities for these same growth horizons in **Table 3**. The ^{210}Pb data for the gypsum-fluid pairs are given in **Table 4**.

The gypsum samples contain minor amounts of ^{4}He and ^{22}Ne (a few fA signal on the Faradays axial cup of the HELIX-MC mass spectrometer), which precluded the precise measurement of their isotopic composition (i.e., ^{3}He/^{4}He, ^{20}Ne/^{22}Ne, and ^{21}Ne/^{22}Ne), whereas Ar, Kr, and Xe concentrations were high, which enabled us to obtain precise isotopic ratios (100–1,000 fA signal on axial Faraday' cup). The abundance ratios ^{4}He/^{36}Ar, ^{20}Ne/^{36}Ar, ^{87}Kr/^{36}Ar, and ^{132}Xe/^{36}Ar, normalized to the same ratios in the atmosphere for simplicity (the so-called F-values: $(^{i}X/^{36}Ar)_{sample}/(^{i}X/^{36}Ar)_{air}$) show values from near atmospheric for Ne/Ar (0.97–4.79), to ratios of 90–2000 for Kr/Ar and Xe/Ar indicating a contemporary enrichment for the lighter and heavier noble gases compared to the atmosphere in the gypsum. A similar observation was reported for gypsum by Utami et al. (2019).

The observed enrichments are not unique in geological materials and have been observed in several environments, with F-Xe enrichments ranging from 10 to 10,000 (e.g., Torgersen et al., 2004). Enrichments are reported for sedimentary rocks (oceanic sediments—Matsuda and Nagao 1986; Pitre and Pinti 2010 and shales—Fanale and Cannon 1971; Bernatowicz et al., 1984); tephra (Pinti et al., 1999); and hydrothermal deposits (geothermal amorphous silica—Matsubara and Matsuda 1988 and hydrothermal quartz—Fairmaid et al., 2011). F-values measured in the Kawah Ijen gypsum overlap with shales and amorphous silica (**Supplementary Figure S2**) and there is a near perfect match for F-Kr and F-Xe with amorphous silica precipitated in geothermal areas, which represent the closest depositional environment to that where Kawah Ijen gypsum precipitated.

The ^{40}Ar/^{36}Ar ratios range from a likely atmospheric but mass-fractionated value of 290.0 ± 0.9 (air = 295.5; Ozima and Podosek, 1983) up to a value of 316.1 ± 1.1 (**Table 2**). The ^{86}Kr/^{84}Kr ratios range from 0.2974 ± 0.0022 to 0.31255 ± 0.00042, close to the atmospheric value of 0.30524 (Ozima and Podosek, 1983) with some mass-fractionation. The ^{129}Xe/^{132}Xe ratios vary between 0.9193 ± 0.0029 and 1.0245 ± 0.0054, with the

TABLE 2 | Noble gas data for growth horizons in the gypsum section (KV09-507) and the 1-year gypsum growth (KV09-503).

Sample no.	^{4}He	1s	^{22}Ne	1s	^{36}Ar	1s	^{84}Kr	1s	^{132}Xe	1s
	• 10^{-8}		• 10^{-9}		• 10^{-8}		• 10^{-9}		• 10^{-10}	
KV09-507L-C	1.578	0.001	2.27	0.02	2.89	0.01	1.34	0.03	5.1	0.1
KV09-507L-D	0.570	0.001	1.54	0.01	1.817	0.008	5.0	0.2	52	1
KV09-507L-E1	0.321	0.005	0.63	0.02	0.354	0.001	0.339	0.002	0.80	0.02
KV09-507L-E2	0.5303	0.0005	1.4	0.2	2.43	0.02	2.7	0.1	5.9	0.2
KV09-507L-F	1.157	0.002	1.87	0.02	0.730	0.004	13.7	0.2	39.1	0.8
KV09-507L-G1	0.307	0.001	0.70	0.02	0.329	0.003	4.80	0.09	20.0	0.4
KV09-507L-G2	0.4888	0.0004	0.59	0.01	0.290	0.001	0.8	0.1	8.4	0.1
KV09-507L-H1	0.2450	0.0004	0.51	0.01	0.884	0.008	3.70	0.07	5.6	0.2
KV09-507L-H2	0.413	0.008	0.42	0.02	0.316	0.001	1.93	0.05	48.2	0.8
KV09-503	6.963	0.004	0.36	0.01	0.685	0.007	3.2	0.1	10.70	0.02
Sample no.	^{40}Ar/^{36}Ar	1s	^{86}Kr/^{84}Kr	1s	^{129}Xe/^{132}Xe	1s				
KV09-507L-C	290.0	0.9	0.3096	0.0006	0.928	0.017				
KV09-507L-D	304.9	0.9	0.3111	0.0003	0.919	0.003				
KV09-507L-E1	295.1	0.7	0.297	0.002	0.99	0.04				
KV09-507L-E2	297.1	0.8	0.3131	0.0004	0.974	0.008				
KV09-507L-F	304	1	0.2998	0.0007	0.983	0.006				
KV09-507L-G1	315	1	0.3083	0.0004	1.017	0.007				
KV09-507L-G2	308	1	0.3150	0.0005	0.960	0.004				
KV09-507L-H1	315	1	0.3049	0.0007	0.98	0.02				
KV09-507L-H2	304.7	0.8	0.3117	0.0007	0.981	0.005				
KV09-503	316	1	0.3126	0.0004	1.025	0.005				

Growth zone C is stratigraphically the youngest, and H2 the oldest. Concentrations are reported as ccSTP/g and their 1 standard deviation uncertainty.

TABLE 3 | ^{210}Pb data for growth horizons in the gypsum section (KV09-507) and the 1-year growth (KV09-503), and the noble gas corrected apparent ages for these samples. Not analysed—n.a.

Sample no.	^{84}Kr/^{36}Ar	1s	^{132}Xe/^{36}Ar	1s	k Kr	k Xe	Wt. k	^{210}Pb	1s	Age	1s
507L-C	0.046	0.001	0.018	0.001	0.10	0.11	0.10	0.59	0.02	-49	4
507L-D	0.27	0.01	0.285	0.006	0.59	1.83	1.04	0.63	0.02	24	2
507L-E1	0.096	0.001	0.023	0.001	0.21	0.15	0.17	0.36	0.01	-16	1
507L-E2	0.113	0.004	0.024	0.001	0.24	0.15	0.23	0.34	0.00	-4.6	0.4
507L-F	1.88	0.03	0.54	0.01	4.02	3.43	3.85	0.47	0.02	77	6
507L-G1	1.46	0.03	0.61	0.01	3.13	3.89	3.38	n.a.	-		
507L-G2	0.27	0.05	0.290	0.005	0.58	1.86	0.70	0.53	0.02	17	3
507L-H1	0.419	0.009	0.064	0.003	0.90	0.41	0.78	0.52	0.02	21	2
507L-H2	0.61	0.02	1.52	0.03	1.31	9.75	6.40	0.46	0.02	94	7
KV09-503	0.47	0.02	0.156	0.002	1	1	1	0.91	0.03	11	-

Uncertainties are reported as 1 standard deviation and ^{210}Pb values are given in decays per minute per Gram of gypsum (dpm/g).

atmospheric value being 0.9832 (Ozima and Podosek, 1983). Interestingly there is no relationship between ^{86}Kr/^{84}Kr and ^{40}Ar/^{36}Ar ratios, indicating that high ^{40}Ar/^{36}Ar values are not caused by mass-fractionated atmospheric Ar diffusing from the sample, as observed in some tephra (Pinti et al., 1999), but rather reflects addition of terrigenic (crustal and/or mantle) ^{40}Ar*. Given the very young age of the samples, their low K content (a few tens of ppm; **Table 1**) and the absence of detrital components in the crushed crystals, ^{40}Ar/^{36}Ar ratios higher than the atmosphere cannot be related to *in situ* production of radiogenic ^{40}Ar*, but only associated with the addition of mantle Ar. Interestingly, there is a positive trend between ^{40}Ar/^{36}Ar and ^{129}Xe/^{132}Xe (not shown here), possibly suggesting a small anomaly in mantle ^{129}Xe (Staudacher and Allègre, 1982), to be confirmed by further analyses.

TABLE 4 | ^{210}Pb data for gypsum—fluid pairs and the tip laths of stalactites.

Sample no.	Type	^{210}Pb	1s
KV09-505	Stalactite tip	1.50	0.05
KV09-506	Fluid	0.247	0.009
KV09-501	Stalactite tip	1.33	0.05
KV09-503new	Stalactite tip	1.28	0.05
KV08-407	Stalactite tip	1.16	0.09

Values are given in dpm/g with their 1 s uncertainty and have been recalculated for their ^{210}Pb activity at the time of sampling.

Gypsum-Fluid Element Partition Coefficients

Partition coefficients for the natural gypsum-fluid pairs are shown in **Figure 4A** where $D_i = C_i^{gypsum}/C_i^{fluid}$, and i is the

element of interest and *C* is its concentration in mg/kg. Results for the different pairs are consistent in inter-element trends, but do show a spread in absolute values of, commonly, up to 1 log unit. In part, this spread results from analytical uncertainty, in particular where the element is close to the detection limit in one of the sample materials (e.g., Rb in gypsum), but for others, it may reflect the presence of micro-inclusions in the gypsum (e.g., Ba, Hf, and Al). The median value for each element was chosen as the representative partition coefficient, and is shown with an emphasized symbol in **Figure 4A**.

Strontium, Ni, Cu, Ba, Pb, Mo, and the REE are compatible in gypsum, whereas the alkalis, Tl, Mg, Zn, Mn, Cd, B, Al, and the HFSE are incompatible. This element association agrees with that which would be expected from the charge and size of the cation site in the gypsum structure. The REE + Sc + Y illustrate this particularly well when their D values are plotted against their ionic radii (Shannon, 1976) in an Onuma diagram (Onuma et al., 1968). A Lattice-Strain Theory fit (Blundy and Wood, 1994) through these data (**Figure 4B**) provides an estimate of 1.118 Å (111.8 pm) for the ideal radius, which is equivalent to that of Ca^{2+} in cubic coordination (1.12 Å, 112 pm).

The partition coefficients reported here are apparent partition coefficients, because it is not known whether gypsum grew in full equilibrium with the fluid. Gypsum precipitates because the fluid reaches gypsum supersaturation by evaporation and cooling (Delmelle and Bernard, 2000; Utami et al., 2019) and non-equilibrium element partitioning can develop under such conditions. In general, elements do not reach the equilibrium and maximum fractionation between mineral and fluid under non-equilibrium conditions, resulting in D-values that are closer to unity than at equilibrium. There are no experimentally-determined D-values for gypsum, as far as we are aware, and the gypsum-fluid D-values reported by Inguaggiato et al. (2020) for gypsum precipitated from vials containing Kawah Ijen lake waters represent bulk solids that include co-precipitated barite, Al-sulfates as well as a silicate (likely amorphous silica). The major element composition of these bulk solids, in particular their high Na and K contents (**Table 3** of Inguaggiato et al., 2020), suggests that these co-precipitated phases contribute significantly to the bulk composition. The REE are not expected to be compatible in these co-precipitated phases (*cf.* the D_{REE} for alum in **Figure 4B**), and the bulk digestion method would thus dilute the overall REE content, leading to lower apparent gypsum D_{REE}. The trend in the D_{REE} is, however, consistent with what we observe.

Assuming that the present-day formation conditions for gypsum are equivalent to those in the recent past, the apparent partition coefficients determined here can be applied to reconstruct fluid concentrations along the plateau transect. It can, nonetheless, not be excluded that some of the variability observed results from changes in D-values.

The partition coefficient for ^{210}Pb is the same as that of Pb within their respective 1s uncertainties (5.88 ± 0.24 for Pb and 6.07 ± 0.22 for ^{210}Pb). This indicates that ^{210}Pb is incorporated into gypsum as Pb, and is not the ingrowth product from incorporation of parent isotope Rn. Lead is also compatible in (Na,K)-alum and, especially in barite (**Figure 4A**). Assuming that ^{210}Pb is similarly incorporated as Pb in these phases, a significant fraction of the ^{210}Pb could potentially be hosted by these inclusion phases. However, the low Al content of the bulk-digested samples shows that alum can only be a minor component in the bulk digestion solution that was analyzed for ^{210}Pb, and the use of a 40°C HCl digestion solution in preparing the samples for ^{210}Pb analysis should have prevented barite from dissolving. There is therefore no evidence that the ^{210}Pb contents are affected by barite, alum or other possible inclusion phases.

^{210}Pb Timeseries and Mass Balance

The ^{210}Pb activity timeseries does not show a progressive decrease in ^{210}Pb with stratigraphic position (i.e., time), which would be expected if decay were the only variable controlling the ^{210}Pb activity (**Figure 5**; cf. Ali et al., 2008). This behavior can reflect diffusional mobility of Pb in gypsum, a non-constant initial ^{210}Pb activity, or variable ingrowth because of differences in the parent-isotope concentrations. The latter can be discounted, because the activity of ^{226}Ra, the main parent isotope of sufficient longevity, is negligible (*ca.* 0.003 dpm/g as determined from preliminary γ-counting on Kawah Ijen gypsum samples). There appear to be no data on volume diffusion of elements in gypsum, but rapid variations in Li content along the transect (**Supplementary Figure S4**) suggest diffusion to be slow, given that Li is one of the fastest diffusing elements in minerals owing to its small ionic radius and 1 + charge (cf. Brady and Cherniak 2010). Variations among the growth zones in the starting ^{210}Pb content at time of formation is therefore the likely cause for the irregular ^{210}Pb *vs.* time. This cause was also argued by Utami et al. (2019) for gypsum stalactites at Kawah Ijen, and tied to variations in the volcanic flux of parent isotope ^{222}Rn.

Seepage water ^{210}Pb has two main sources: **1.** Rock leaching, which is the principal source of cations to the lake; and 2. Volcanic gas, which predominantly contributes anions and volatile (semi-)metals (van Hinsberg et al., 2017). Rock leaching is thought to involve mostly material falling into the lake in rock falls and slides, which are common, and therefore primarily includes magmatic deposits exposed in the crater walls (van Hinsberg et al., 2010b, 2017). These are predominantly basalts and basaltic-andesites, with lesser andesite and dacite. The ^{210}Pb in these magmatic deposits ultimately derives from the decay of ^{238}U, along a series of intermediate isotopes with variable half-lifes. In a first approximation, we assume the U decay series to be in secular equilibrium, in which case the activities of all isotopes of the decay series are equal. This permits calculating the ^{210}Pb content from the U concentration of the bulk rocks. Using the mean U contents of Kawah Ijen basalt, andesite and dacite (0.67, 2.3, and 3.5 mg/kg, respectively–van Hinsberg et al., 2010b), the ^{210}Pb activity of these rocks is 0.5, 1.7, and 2.6 dpm/g of rock. Kawah Ijen lake water reflects 42 ± 2 g of rock leaching per kg of water (van Hinsberg et al., 2010b), meaning that leaching would contribute between 0.02 (basalt) and 0.11 (dacite) dpm of ^{210}Pb per g of lake water. This is significantly lower than the measured ^{210}Pb activity in seepage waters of 0.25 dpm/g water (**Table 4**). Moreover, common Pb is retained during leaching by incorporation into the secondary

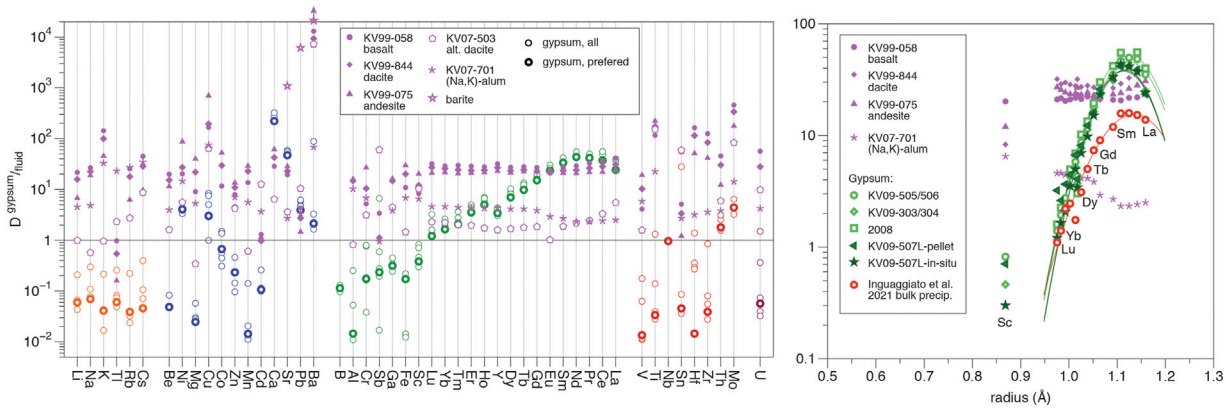

FIGURE 4 | (A). Gypsum-fluid element partition coefficients as determined from co-sampled pairs of actively growing gypsum and the fluid from which it was growing. Element are ordered by charge and then increasing radius. The apparent fluid partition coefficients for Kawah Ijen magmatic deposits, their altered equivalent (Na,K)-alum and barite are shown for comparison. The LREE and Sr are strongly compatible in gypsum, whereas the alkalis and HFSE are incompatible. **(B)**. Onuma diagram for the 3 + elements and Lattice-Strain Theory (LST) fits through these data for gypsum (solid lines). Adherence to LST indicates that element incorporation is controlled by the crystallography of the gypsum mineral structure. The ideal radius derived from the LST fit (1.118 Å) corresponds to that of Ca^{2+} in cubic coordination (1.12 Å), showing that the REE reside in the Ca site. The gypsum D-values presented here are higher than those of Inguaggiato et al. (2020), likely because of dilution of the gypsum REE content by the presence of other phases in the bulk-digested precipitate.

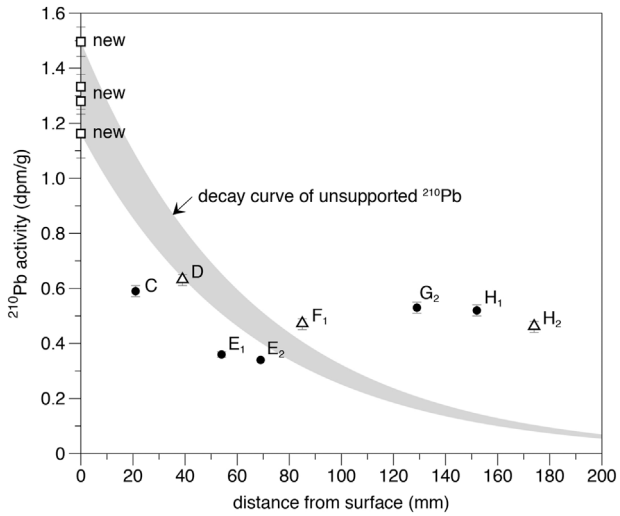

FIGURE 5 | Activity of ^{210}Pb for the growth zones versus their stratigraphic position in the transect. A simple unsupported ^{210}Pb decay curve cannot explain the observed trend as ^{210}Pb activity does not consistently decrease with distance. The uncertainty shown is 1 standard deviation.

phase barite, with a 10-fold reduction in the Pb leaching flux (van Hinsberg et al., 2010b). All isotopes of Pb should show equivalent behavior, and the total ^{210}Pb contribution from leaching can thus be expected to be only 0.002 to 0.011 dpm/g fluid. This dissolved element load of the lake has built up progressively, and concurrent ^{210}Pb decay must therefore be taken into account. Using the lake water total dissolved solids timeseries (**Figure 5** in van Hinsberg et al., 2017) as the leaching flux, we calculate a maximum rock contribution of 0.002 dpm/g at ~1900, with decay exceeding input of ^{210}Pb thereafter. This indicates that rock leaching can only be a minor contributor to the ^{210}Pb activity of the seepage waters and volcanic gas must be the main source.

Volcanic gas is an important source for "excess" ^{210}Pb in volcanic systems, because parent isotope ^{222}Rn is a gas, and is mobilized in volcanic degassing (see Berlo and Turner 2010 for a review). Vigorous gas injection into the lake was observed by Takano et al. (2004) in echo-soundings of the lake, and is further evident from bubbling of lake waters at the dam and fumaroles. Measurements of volcanic gas Rn activity show it to be high; 1.2—2.3 • 10^5 dpm/m^3 for Etna fumaroles (Giammanco et al., 2007) and 2.4—9.0 • 10^5 dpm/m^3 for 500°C Merapi fumaroles (Zimmer and Erzinger 2003). Volcanic gas is thus a viable source for the ^{210}Pb in the lake waters, and fluctuations in this volcanic flux (Merapi fumaroles varied from 2.4 to 8.4 • 10^5 dpm/m^3 within a single day—Zimmer and Erzinger 2003) will lead to variations in the $^{210}Pb_0$ in the seepage waters from which the gypsum grew.

Absolute Age Assignment

The half-life of Rn is only 3.8 days and variations in the Rn-flux are only preserved in Rn activity for a few weeks. A different recorder of variations in Rn-flux is thus required to correct for the resulting changes in $^{210}Pb_0$. Concentrations of Rn are insufficient for it to form its own gas phase. Rather, it partition into any gas phase formed by the major volatiles CO_2 and H_2O, as do other minor volatile components including the other noble gases. We previously proposed a correction method based on the content of the stable isotopes of the noble gases Kr and Xe in gypsum as a proxy for the volcanic gas flux (Utami et al., 2019). We chose Kr and Xe, because, as noble gases, their elemental behavior will be similar to Rn, and their isotopic composition allows for source identification. The noble gases are assumed to be dominantly present in fluid inclusions in the gypsum, trapped at time of growth, and therefore to reflect the noble gas composition of the formation fluid.

Noble gases in the gypsum formation waters are dominantly sourced from atmosphere, either directly or via an air-saturated groundwater intermediary, and from the magmatic-hydrothermal system. The noble gas contribution from rock leaching can be expected to be negligible. The elemental ratios of the noble gases measured in the gypsum samples are elevated compared to the atmosphere, with large anomalies in the F-values of Kr and Xe (**Supplementary Figure S2**). The mass dependence in the F-values for gypsum is common and has also been reported for sedimentary, volcanic, and hydrothermal deposits (e.g., Fanale and Cannon 1971; Bernatowicz et al., 1984; Matsuda and Nagao 1986; Matsubara and Matsuda 1988; Pinti et al., 1999; Pitre and Pinti 2010; Fairmaid et al., 2011). The current consensus hypothesis (Torgersen et al., 2004) is that this predominantly reflects diffusion-control, with retention of the heavier, larger-size Kr and Xe compared to Ar, Ne, and He. The gypsum noble gas composition could thus result from atmospheric noble gases diffusing in and out of the sample at different rates. However, when this process is modeled in F(^{84}Kr) vs the ^{40}Ar/^{36}Ar space for single step mass-dependent fractionation in a closed system (see e.g. Kaneoka 1994), or for an open-system diffusion-controlled Rayleigh distillation, the gypsum data do not follow the resulting trends (**Figure 6**). Rather, the gypsum samples define a trend from the atmospheric reservoir (Air Saturated Water) to a component with magmatic ^{40}Ar* excesses and high Kr/Ar and Xe/Ar ratios, which we interpret to be the magmatic-hydrothermal system. The preservation of magmatic Ar in a volcano-sedimentary deposit such as gypsum could appear odd, but Cogliati et al. (2021) have recently shown mantle ^{40}Ar* excess preserved in even more fragile volcanic eruptive products such as Pele's hairs and tears, indicating that magmatic Ar can be retained in a variety of volcanic products that were previously not considered as a reliable magmatic record, due to their propensity for being contaminated by air.

Having established that the noble gas signature of gypsum reflects binary mixing of atmosphere and a volcanic component, we can quantify the variations in the relative volcanic contribution, which we equate to variations in the volcanic Rn-flux. We use ^{84}Kr and ^{132}Xe as two independent measures of the volcanic contribution, normalized to ^{36}Ar to correct for differences in the absolute amount of noble gas recovered from each sample. The weighted mean of ^{84}Kr/^{36}Ar and ^{132}Xe/^{36}Ar is then normalized to these same ratios for a gypsum sample of known age as the time anchor point. For ^{84}Kr/^{36}Ar, following Utami et al. (2019):

$$^{84}Kr/^{36}Ar\ (Gypsum) = x \cdot {}^{84}Kr/^{36}Ar\,(Atmosphere) + (1-x) \cdot {}^{84}Kr/^{36}Ar\ (Volcanic\ gas)$$

A higher mass fraction of volcanic gas would reflect a higher ^{222}Rn flux, and hence a higher ^{210}Pb$_0$, and we assume that this relationship is linear in a first approximation. This allows us to calculate the ^{210}Pb$_0$ for the various growth zones relative to the ^{210}Pb$_0$ for the sample of known age (where the ^{210}Pb initial for the known-age sample can be calculated from the measured ^{210}Pb and its age at time of measurement): $^{210}Pb_0^{growth\ zone} = {}^{210}Pb_0^{growth\ zone} k$, where k is the uncertainty-weighted mean of k_{Kr} and k_{Xe} and

$$k_{Kr} = \frac{^{84}Kr}{^{36}Ar}(growth\ zone)/\frac{^{84}Kr}{^{36}Ar}(known\ age),$$
$$k_{Xe} = \frac{^{132}Xe}{^{36}Ar}(growth\ zone)/\frac{^{132}Xe}{^{36}Ar}(known\ age)$$

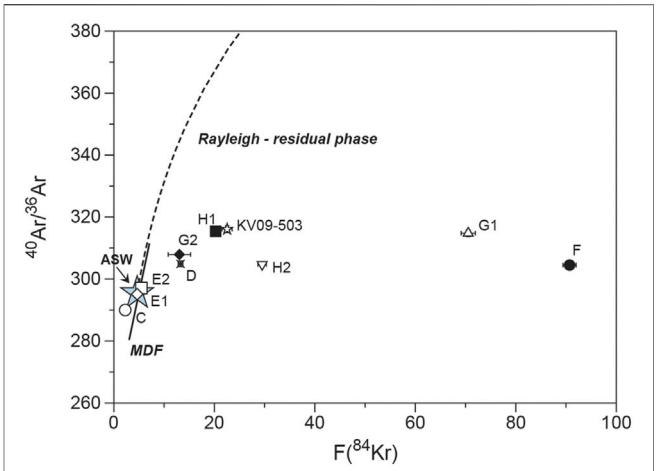

FIGURE 6 | The F(^{84}Kr) versus ^{40}Ar/^{36}Ar ratio measured in the different gypsum layers. The blue star indicates the composition of Air Saturated Water (^{40}Ar/^{36}Ar = 295.5 and F(^{84}Kr) ranging between 1.835 at 20°C and 1.47 at 100°C—Smith and Kennedy 1983). The straight line labeled "MDF" represents the closed-system isotopic and elemental fractionation of Kr and Ar for a single step mass-dependent fractionation by diffusion. The dashed curve represents a diffusion-controlled Rayleigh distillation.

The sample of known age in these calculations is sample KV09-503 (this is a different sample than that used by Utami et al., 2019, and was a tip growing on a stalactite in close proximity to the gypsum plateau sample site from the same water flow).

Variations in the volcanic gas flux are potentially also recorded by other elements, in particular the volatile metals, which are enriched in the gas emissions at Kawah Ijen (van Hinsberg et al., 2017). This would permit a higher resolution age determination, as less sample material is required for elemental than noble gas analyses. We therefore compared the noble gas compositions for the investigated samples to the concentrations of all elements determined for these same samples by bulk-digested ICP-OES and ICP-MS, but found no statistically significant correlations with any of the elements. Similarly, dividing the ^{210}Pb activities by the volatile (semi-)metals does not produce a stratigraphy-consistent ^{210}Pb decay pattern. This indicates that the elemental compositions can, unfortunately, not be used to correct for variations in volcanic gas flux, not even those elements that are enriched in the fumarole emissions. This is probably because these elements are still derived from multiple sources, and although they are enriched in the gaseous emissions, they are not sufficiently exclusive to the gas to be used as a monitor of volcanic gas flux. The measurements of ^{40}Ar/^{36}Ar higher than the atmospheric value (**Table 2**), a first in

hydrothermal gypsum, corroborate that noble gases are recording the active volcanic flux through the Kawah Ijen system.

The noble gas corrected ^{210}Pb data define two parallel, age-consistent trends in a plot versus stratigraphic distance (**Figure 7**), both trends defining a growth rate of 2 mm/year. The offset between these two linear trends is best explained by the sample of known age not reflecting the source fluid for the full duration of growth of the plateau. The gypsum plateau is fed by a number of seepage springs, some of which coalesce, whereas others feed only a restricted part of the plateau (**Figures 2**, **3**), and flow patterns have likely changed over time. The various springs differ in their composition, although elemental ratios are similar, suggesting that the variations are mainly the result of different degrees of dilution by circumneutral groundwater. The ^{210}Pb activity of gypsum needles grown from various streamlets also varies (**Tables 3**, **4**), confirming that the fluid $^{210}Pb_0$ activity is variable. The two trends are thus interpreted to reflect growth from two distinct fluid sources with variable $^{210}Pb_0$ and/or noble gas contents, but both define a common, and constant upwards gypsum growth rate of 2 mm/year. This constant growth rate suggests that a dynamic equilibrium has established itself between the residence time of seepage fluids on the plateau surfaces and saturation of these fluids in gypsum by cooling and evaporation. This is supported by the apparent spatially constant growth rate as evidenced by growth layers of constant thickness along plateau cross-sections (see also 2.2). The 2 mm/year rate has been used to assign absolute ages to the growth zones in the plateau transect.

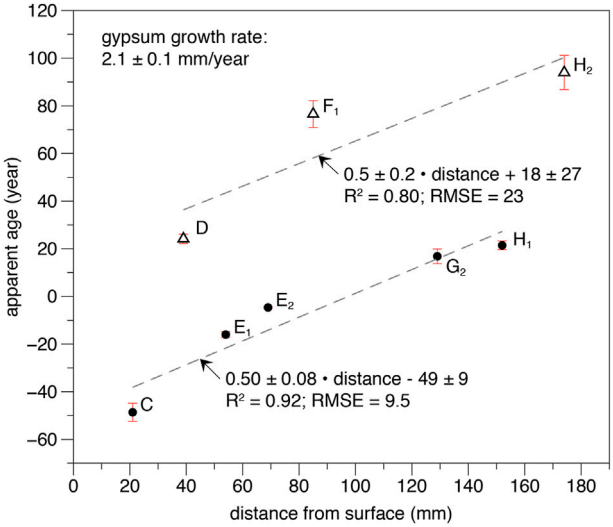

FIGURE 7 | Apparent ages for the gypsum growth zones based on ^{210}Pb activities corrected for variations in volcanic Rn-flux with noble gases. The ages define two parallel trends with equivalent slopes of 2 mm of gypsum growth per year. The two trends are interpreted to represent growth from two seepage flows. Uncertainties are 1 standard deviation.

DISCUSSION

The integrity of the gypsum record depends on gypsum capturing a characteristic and reproducible fingerprint of the fluid composition, and for this fingerprint to be preserved. This requires constant partition coefficients for elements between gypsum and fluid, continuity in growth, and a lack of post-formation element mobility. Given that the seepage fluids are not saturated in gypsum where they emerge, and reach saturation only by cooling and evaporative concentration, gypsum formation is likely affected by weather conditions, with most precipitation expected when evaporation is most pronounced. As a result, growth is unlikely to be continuous throughout the year, and biased towards the dry season. Moreover, fluid dilution by rainfall would lead to undersaturation, and potential dissolution of gypsum. Indeed, a full day of undersaturation would be predicted to dissolve 0.2 mm of gypsum as calculated from the experimentally-determined dissolution rate data of Zaier et al. (2020) for low-porosity, crystalline gypsum. With 176 rainy days per year and a total precipitation of 2,416 mm/year at the nearby city of Banyuwangi (data from www.climate-data.org), dissolution should be an important process. Indeed, the surface layer of the crater lake is strongly diluted during the rainy season (Sumarti, 1998). Nonetheless, the very presence of the plateau, and its persistent growth as identified from visible growth zoning and quantified in the age model, indicate that growth exceeds dissolution, or that dissolution is kinetically limited.

Repeated mineral precipitation and dissolution can lead to a progressive increase in compatible elements, and removal of incompatible elements (*cf.* zone refining (Pfann, 1962). A negative correlation between compatible and incompatible elements would in this case develop, assuming variable precipitation-dissolution throughout the gypsum transect. Plotting Ce/Sr versus Ti/Sr or Sc/Sr, where Ce is compatible and Ti and Sc are incompatible, does not show the expected negative correlation (**Supplementary Figure S3**), indicating that zone refining is unlikely to significantly contribute to the gypsum composition, which in turn suggests limited precipitation-dissolution cycling. This is also in agreement with optical and electron microscopy, which does not show dissolution surfaces, but rather continuous growth of gypsum laths with idiomorphic growth surfaces preserved within individual gypsum crystals. There is, therefore, no evidence for gypsum dissolution, which is surprising given the abundance of rain and the resulting effect of dilution on the saturation state of the seepage fluids, and the gypsum dissolution rates determined by Zaier et al. (2020). This strongly suggests that dissolution is hindered. Still, even if pre-existing gypsum does not dissolve, no gypsum will precipitate when the fluids are undersaturated, and the gypsum record will therefore reflect only part of the year. The continuous growth model applied to the transect to obtain absolute ages can therefore only be interpreted up to a yearly resolution.

Equilibrium partition coefficients depend on physical conditions (e.g., P and T) and the major element compositions of the mineral and fluid (see van Hinsberg et al., 2010a and references therein). Under disequilibrium conditions, element partitioning will moreover depend on kinetic factors, including growth rate. There is no evidence to assume that seepage outflow temperatures changed significantly, with 1993–1996

temperatures reported by Delmelle and Bernard (2000) the same as our 1999 and 2007–2009 measurements. The major element composition of gypsum does not change along the transect, and the noble-gas corrected ^{210}Pb ages suggest a steady growth rate throughout. Measured variability in major element composition of the fluid results from variable dilution with only minor variability superimposed on top of this. Given that gypsum only precipitates once evaporation concentrates the fluid to gypsum saturation, variable dilution is likely inherently cancelled out. In conclusion, constant D-values can be assumed, and, hence, a constant and predictable incorporation of the fluid compositional fingerprint by gypsum. Together with the apparent lack of reworking, this makes gypsum a reliable archive of the seepage water composition.

Gypsum Transect Time Period

The oldest growth zone for the gypsum transect formed in 1919 ± 12 years as estimated from the 2 mm/yr growth rate determined from the noble gas corrected ^{210}Pb age model. This age is similar to the maximum age determined from visit reports and photographs from the 1920s, and would suggest the sampled section represents the full history of the plateau. It is unclear what changed in the 1920s to lead to formation of the plateau. Gypsum precipitates have been reported from the lake and Banyu Pait river valley as early as 1789 (Oudgast, 1820), and are mentioned by Stöhr in 1858 (Stohr, 1862), but the plateau appears to be more recent. Construction of a dam in the 1920s involved significant movement of material in the uppermost section of the Banyu Pait valley, just below the dam, and it is conceivable that this changed the seepage patterns. Whereas seepage was reported just below the dam for the earliest dam iterations leading to undercutting (see Hengeveld, 1920), this appears not to have been the case for later dams, where seepage moved further downstream.

Compositional History

The fluid compositional record can be reconstructed from approximately 1920–2008 by combining the element partition coefficients with the gypsum transect analyses. This record reflects two fluid sources as identified from the parallel trends in noble gas corrected ^{210}Pb (**Figure 7**). Moreover, absolute concentrations in the fluid will have varied with the degree of evaporative concentration of the fluid, or their dilution by ground and rainwater. The latter effect can be removed by dividing by a conservative element, and Sr has been chosen here for this purpose. Comparing the Sr-normalized compositions for the intervals representing the two fluid sources as identified by ^{210}Pb shows that there is no statistically significant difference between these fluids at the 5% confidence level (Mann-Whitney test of equality of medians), indicating that the two fluid sources dominantly differed in their absolute concentrations and that this difference is removed by dividing by Sr. This allows for the Sr-divided transect data to be interpreted as a single record.

Figure 8 shows the timeseries for a range of elements next to photographs of the gypsum transect. The most prominent features are the higher values for most elements around 1950, 1997, 2003, and 2006. The excursion around 1997 is particularly pronounced, for example in Cu/Sr. The 1997 and 2003 excursions are of similar magnitude in Rb and Mg, whereas the 1997 excursion is larger for Cu and the 2003 one for Sb and As. This suggests that different processes controlled these excursions. Not all elements show these excursions; Pb and the LREE do not and form a separate compositional group. The overall trend among the LREE and Pb is similar, although the trough in Pb/Sr around 2003 is not observed for the LREE. Sr-normalized LREE and Pb are, in general, higher where visible inclusion bands are present in the gypsum (e.g., in 1959, 1982, 1993, 2007; **Figure 8**), but this is not a perfect correlation (e.g., in 1940). The other elements do not show a correlation with inclusion bands for these inclusions-filtered gypsum analyses, but a correlation is present for the data derived from the full integration windows.

The gypsum-fluid partition coefficients can be used to determine the susceptibility of the elements to compositional overprinting by inclusions. Inclusions are predominantly variably-altered rock fragments, plant debris and minerals including syngenite, barite and (Na,K)-alum. Solid/fluid D-values for Kawah Ijen basalt, andesite, dacite, strongly altered dacite, and (Na,K)-alum are shown in **Figure 4A**, as well as D-values for Ba, Sr and Pb for barite (data for solid and fluid phases from van Hinsberg et al. (2010b); van Hinsberg et al. (2010c); van Hinsberg et al. (2017), no trace element data are available for syngenite or plant debris). Rock fragments in the gypsum are mostly variably altered dacite, with subordinate basalt and andesite. Analyses for elements that are incompatible in gypsum, and that have a high concentration in the inclusion phases (represented by a D-value significantly higher than the D-value of gypsum) are most susceptible to modification. These elements therefore need to be interpreted with caution, and include the alkalis, Mg, Mn, and Ba. The HREE are more susceptible than the LREE, and co-variation of Ba, Sr and Pb would be indicative of barite contamination. Overall, the LREE, Sr, Pb, Tl, Ni, Co, Cu, Zn, Cd, Sb, Th, and Mo are least susceptible to inclusions, and therefore provide the best record of the fluid compositions from which the gypsum grew. We will restrict our interpretation to these elements in the following.

Controls on Seepage Water Compositions

The seepage spring waters are predominantly derived from the crater lake as evidenced by their near-identical conservative element ratios (Palmer, 2009). However, Utami et al. (2019) show that the rapid variability observed in the gypsum record can only be explained if an additional source of fluid is present locally, because the long residence time of elements in this large volume of brine means that it takes considerable time for compositional disturbances to be visible in the overall lake water composition (cf. Rouwet and Tassi, 2011). Gas bubbling is observed in the lake just in front of the dam, and the conservative element ratios in the various seepage springs suggest a 5% contribution from a different source than the lake (Palmer, 2009). Local groundwater is unable to change elemental ratios as it is too dilute, which suggests that this contribution is derived from the magmatic-hydrothermal system.

Of the most robust elements, LREE, Sr, and Pb are predominantly present in the Kawah Ijen acidic fluids as a

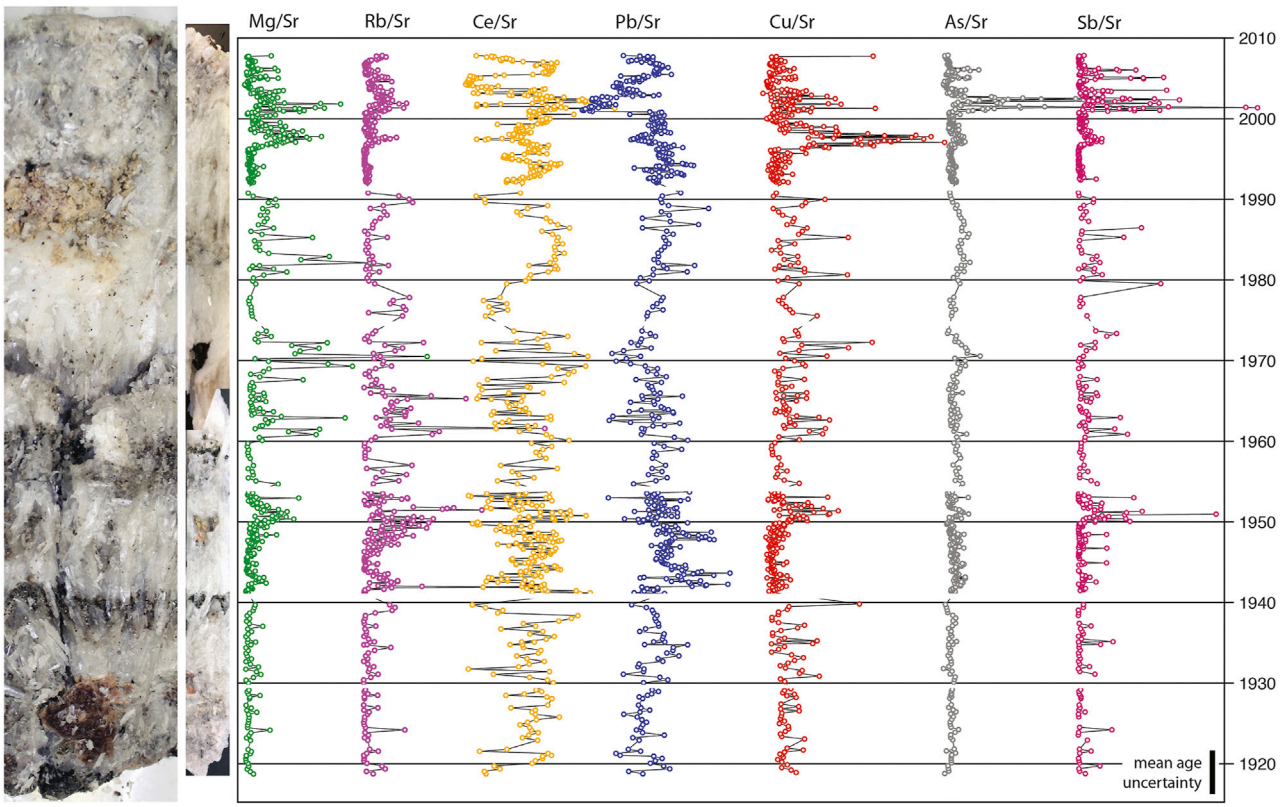

FIGURE 8 | Compositional timeseries for selected elements along the gypsum section shown on the **left**.

result of rock leaching, whereas Sb, Tl, and Cu are relatively enriched in its gaseous emissions (van Hinsberg et al., 2010b; van Hinsberg et al., 2017). Within the gaseous emissions themselves, Cu has been linked to destabilization of immiscible sulfide liquid in a deep-seated basaltic magma (together with Cd and Zn), whereas Sb and Tl, as well as, are associated with a shallower dacitic magma (Berlo et al., 2014). The behavior of Cu in the Kawah Ijen hydrothermal system is also affected by intermittent stability of a Cu-sulfide, as seen in monitoring of the Banyu Pait river water (Berlo et al., 2020). The behavior of the other (base) metals is not significantly impacted by this sulfide phase.

The gypsum timeseries shows covariation of the LREE and Pb, defining one compositional group, and covariation of Cu, Sb, Tl, As, Cd, and Zn in a second group (**Figure 8** and **Supplementary Figure S4**). This suggests a first-order signature in the timeseries that is related to rock-leaching and volcanic emissions, with little temporal overlap between these two processes. Within the metal group, Cu, Zn, and Cd show a more pronounced excursion in 1997 than in 2003, whereas Sb, Tl, and As show the reverse. This elemental grouping corresponds to that observed in melt inclusions and gas emissions by Berlo et al. (2014), which would indicate that the gypsum is recording varying contributions from the basaltic and dacitic magma bodies. It also matches the main difference in metal signature between modern and 1817 gypsum (Utami et al., 2019). Although the magnitude of Cu variation exceeds that of Zn and Cd, there is strong co-variation among these elements, which suggests that intermittent Cu-sulfide stability does not contribute to the behavior of Cu at these uppermost seepage springs, possibly related to the absence of H_2S (see Berlo et al., 2014).

Utami et al. (2019) observed a similar grouping of the LREE + Pb, and the metals for their timeseries reconstructed from a Kawah Ijen gypsum stalactite. Separation within the metals is less clear in this timeseries. However, the foremost compositional signature in this stalactite is a bimodality in element variability, with low variance up to 1980, and high variance thereafter. Utami et al. (2019) interpreted this to represent an increase in particulates in the seepage fluids, and hence inclusions in the gypsum, as a result of the physical disturbances to the system as activity increased post-1980 (e.g., rock falls and lake sediment re-suspension). We do not observe the same bimodality in the plateau transect, although the most variability in composition is observed for the post-1990 period (**Figure 8**). This difference could reflect the different formation setting and conditions for the stalactites compared to the plateau. Whereas the plateau gypsum grows upward in pools, the stalactites form from water that flows over them and cools and evaporates as it does so.

Correlations With Volcanic Activity

Comprehensive monitoring of Kawah Ijen volcano has only commenced following unrest in 2010. The historical record of volcanic activity up to this point is incomplete and varies

TABLE 5 | Summary of volcanic unrest reported for Kawah Ijen volcano, dominated by phreatic explosions and gas upwelling.

Year	Month	Main observations	Spilling	Event severity
1917	Feb-Mar	Temperature fluctuations; water thrown over dam	yes	medium
1921	Feb	Gas upwelling + "boiling"; Temperature rise	yes	low
1923	Mar	Temperature rise	?	low
1933	Apr	Temperature rise; gas upwelling	?	low
1934		Gas upwelling; Temperature rise	yes	low
1935		Temperature rise	?	low
1936	May	Temperature rise, gas upwelling	?	low
1936	Nov	Gas upwelling; Water fountains; Lake level fluctuations	?	medium
1938	Jan–Mar	Lake level fluctuations, Gas upwellingg, Temperature rise, Lake color white	?	medium
1939	Feb–Apr	Temperature rise; gas upwelling	?	low
1939	Apr	Temperature rise; gas upwelling	yes	low
1940	Feb-Mar	Temperature rise; gas upwelling	?	low
1941	Apr	Temperature rise; gas upwelling	yes	low
1952	Apr	Explosion and a 1 km tall plume	?	high
1957	Aug	Temperature rise; gas upwelling	?	low
1962	Apr	Gas slug explosions; Gas upwelling	?	medium
Lack of reports for the 1970s and 1980s				
1991	Mar-Apr	Gas explosions	no	medium
1993	Jul–Nov	Gas explosions and plume to 500 m	no	high
1994	Feb	Gas explosion	no	medium
1997	Jun-Dec	Seismicity	no	low
1999	Apr–Jun	Seismicity; Gas explosions	no	medium
2000	Jun–Sep	Plume to 25 m	no	medium
2001	Feb–Sep	Seismicity	no	low
2002	May–Aug	Seismicity; Small plumes	no	medium
2003	Oct	Seismicity	no	low
2004	May–Dec	Seismicity; Gas upwelling	no	high
Lull in activity from 2004 to 2010				
2011–2012		Seismicity, Temperature fluctuations, Gas upwelling	no	high

In a number of cases, the activity accompanied lowering of the lake level during intentional dam spilling, and was likely triggered by this. A spilling trigger was no longer present in the 1990s and 2000s because the water level was below that of the dam and no spilling took place. The assigned severity of unrest is relative, and no major events took place within the time period covered by the gypsum transect. Data from Caudron et al. (2015b) and references therein. Activity records for Kawah Ijen are incomplete and reporting strongly varies in detail.

significantly in the level of detail of reporting (Caudron et al., 2015b). This complicates developing an accurate record of volcanic activity at Kawah Ijen, and hinders comparing reported activity and establishing the significance of events. Small phreatic events appear to take place every year, and are reported as early as the 1900s (Kemmerling, 1921). They may result from lake overturn following development of stratification during the rainy season (Caudron et al., 2017). These smaller events include steam explosions, bubbling, rapid temperature and lake level variations and small phreatic plumes (see the overview in Caudron et al. (2015b). In part, lowering of the lake level during dam spilling periods triggered these events. Tourism and sulfur mining in the crater ensure that these events are witnessed at present, but given that these events are generally restricted to the lake and crater, could have easily gone unreported in the past. Overall, the most significant events since the start of the 20th century appear to have been phreatic unrest in 1952 in which a plume rose to 1 km height, phreatic steam explosions and a 500 m plume in 1993, unrest in 2004 with gas upwelling and increased seismicity and the seismicity crisis of 2011–2012 (**Table 5**, Caudron et al., 2015b). No reports are available for the 1970s and 1980s and this time period is therefore commonly regarded as a period of relative quiescence, but it is unclear to what extent this rather owes to a lack of available reports. The Ijen volcano observer, who has worked at the Ijen observatory since the 1980s regards the unrest of 1993 and 2004 as the most significant (Caudron et al., 2015b).

Figure 9 shows the episodes of volcanic unrest overlain on the compositional transect. The period of unrest in the late 1930s appears to correlate with a layer of debris in the gypsum, and this is also the case for the 1952 activity and that in the 2000s when some leeway in positioning is taken into account owing to the uncertainty in the absolute age assignment. The debris horizons around 1970 and 1985 do not correspond to known activity. The debris consists of variably altered rock fragments and organic material and is the same as material that is locally present on the slopes of the Banyu Pait valley. We therefore interpret it to represent local mobilization of material that is deposited onto the gypsum plateau. Volcanic activity resulted in material transfer over the dam in the past, although there is no mention of this after 1917. More likely, correlations with unrest result from rock falls and slides that accompanied the volcanic seismicity. Major rainstorms could have achieved the same, which can explain the presence of debris horizons where no activity was recorded. Indeed, it is known that severe rainstorms are common, and if anything, it is surprising that there are not more such horizons. The present-day plateau surface is mostly free of rock-fragments (**Figures 2**, **3**), despite the presence of loose material right next to the gypsum (e.g., **Figure 2C**). Perhaps, rainstorms, and dam spilling flush the plateau clean of debris, and it is only when rapid growth consolidates this debris that it is preserved. This could be verified in a visit during the rainy season. Such a visit would also be highly desirably to understand the apparent lack of gypsum

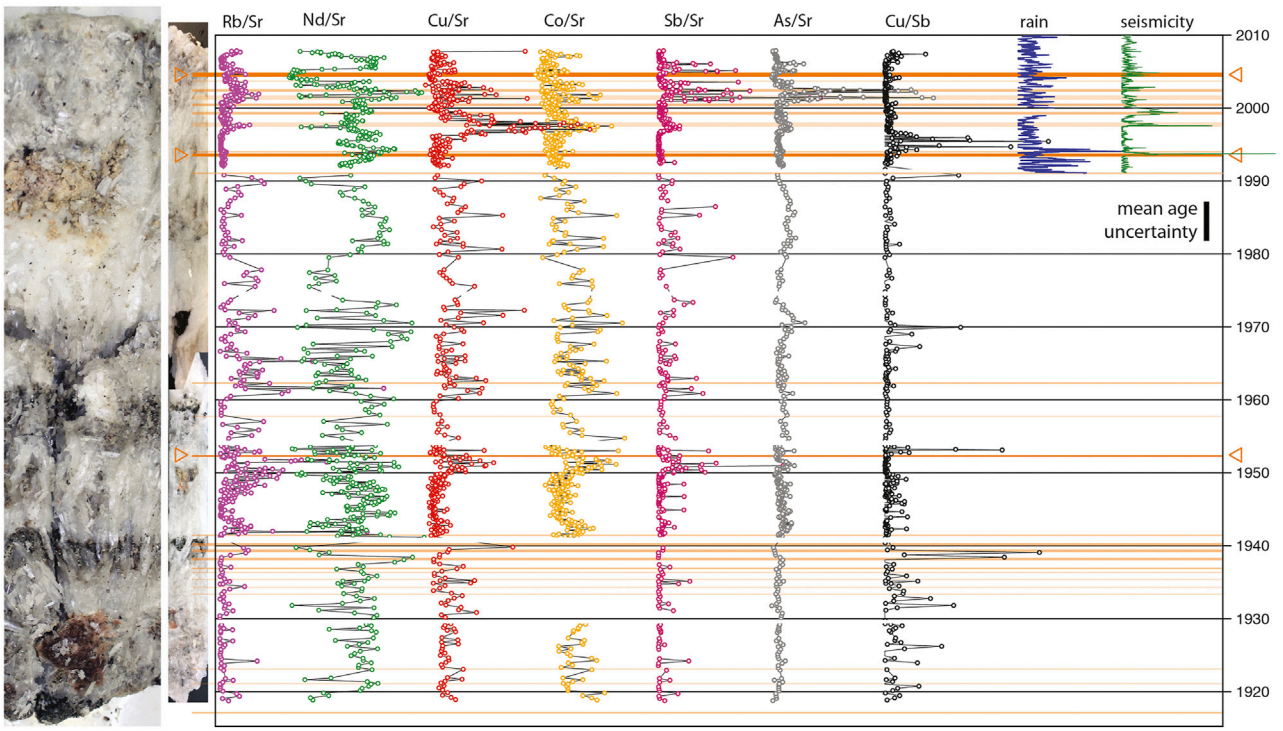

FIGURE 9 | Timeseries for selected elements along the gypsum transect with known periods of unrest overlain. The main volcanic unrest within this time period took place in 1952, 1993 and 2004 (marked with a triangle). Events that involved explosions or columns of water are shaded a darker hue that those that only involved gas upwelling and/or temperature fluctuations. Precipitation and the sum of seismic events from Caudron et al. (2015b) are shown for comparison.

dissolution during times of rain-diluted undersaturation of the seepage fluids.

Comparing the activity record to the timeseries for the elements that are least susceptible to overprinting shows correlations between the records (**Figure 9**). The large 1952 event corresponds to a peak in Sr-normalized Cu, Co, Sb, and As, and these same elements are high for the activity in the 1990s and 2000s. However, the large 1993 event does not appear to be present in the record and the largest excursion in Cu matches with what is only regarded as a minor event. This mismatch could be the result of the uncertainty in the absolute age assignment, and the 1993 event matches the Cu excursion within age uncertainty.

To determine whether there is a statistically significant signature of volcanic activity in the gypsum record, we conducted a PLS-DA analysis on the timeseries. Given the uncertainty in the absolute ages, the timeseries was smoothed with a 5-years moving average and each period of volcanic activity compared at intervals of 5 years (e.g. 1945 ± 2.5 years as a quiet period and 1950 ± 2.5 years as a period of unrest). The period from 1970 to 1980 was not included as it is unclear if no activity took place, or it was not reported. The PLS-DA analysis indicates that periods of activity can be separated from those of quiescence, with the LREE and then Zn the most important variables in this separation. The LREE are lower for periods of activity, whereas Zn is higher (**Figure 10**). Only one time period is assigned wrongly, 1960. We classified this as a period of activity given the gas slug explosions reported for April 1962, but the PLS-DA groups it with the quiescent time periods. Given that the smoothing and binning removes most of the detail in the timeseries, this is a surprisingly clear result, and a strong indicator that active periods do have a distinct compositional signature that is recorded, and identifiable in the gypsum. When the resulting model is applied to the 1970s and 1980s, unrest is strongly predicted for the 1975 bin (the assignment has a score of 1.9 ± 1.1 with the cutoff between unrest and quiescence at 0). This suggests that there may have been an episode of unreported unrest in this time period.

A record of seismicity, lake temperature and precipitation is available from 1991 onward (Caudron et al., 2015b). To compare this dataset to the timeseries, we converted both to common time interval using linear interpolation, and the timeseries data were smoothed with a 5-years moving average window to account for the uncertainty in the absolute ages. No statistically significant correlations were found, and a visible inspection of the data confirms this (**Figure 9**). Rather than a lack of correlation, this may result from the uncertainty in the absolute age assignment.

Gypsum as a Recorder of Volcanic Activity at Kawah Ijen

The plateau gypsum timeseries provides a high-resolution record of volcanic activity at Kawah Ijen volcano. The element grouping observed corresponds to known element behavior at Kawah Ijen, and links to both rock leaching and volcanic contributions (*cf.* Berlo et al., 2014; Delmelle and Bernard, 1994; Takano et al., 2004; van Hinsberg et al., 2010b; van Hinsberg et al., 2017). Episodes of activity

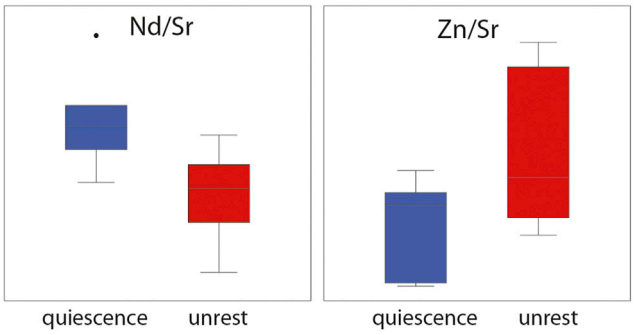

FIGURE 10 | Boxplots showing a characteristic and statistically significant (at α = 5%) difference in Nd/Sr and Zn/Sr between active and quiet periods. The data were smoothed and binned in 5-years intervals to account for the uncertainty in absolute age assignment.

display a higher metal content in the gypsum, and, therefore, a higher content in the seepage waters (assuming constant partition coefficients). This metal enrichment is either dominated by Cu, Zn, and Cd, or by Sb, As, and Tl, suggesting two sources, whose contribution varies among events. The Cu, Zn, and Cd suite of elements has previously been linked to the deep-seated mafic magma at Kawah Ijen, whereas Sb, As, and Tl are characteristic of a shallower dacitic magma (Berlo et al., 2014). We therefore tentatively assign the Sb-As-Tl characterized events to the shallow magmatic-hydrothermal system, whereas Cu-Zn-Cd excursions would indicate involvement of a deeper source. Unfortunately, the uncertainty in absolute age assignment does not permit determining whether the larger events have a distinct signature, and a stronger contribution from either source. However, Utami et al. (2019) show that gypsum from the 1817 phreato-magmatic eruption of Kawah Ijen has a metal signature that fits the Cu-Zn-Cd suite, and for this eruption, involvement of the deeper reservoir is therefore likely. The cause for the strong negative correlation between activity and the LREE is unclear at present. The LREE derive predominantly from rock leaching, and Utami et al. (2019) show a positive correlation between activity and rock derived material, linked to increased rock falls and re-suspension of lake sediments as a result of physical disturbances of the system (i.e., seismicity). Takano et al. (2004) similarly suggest a positive correlation between REE contents and activity. Partition coefficients are particularly high for the LREE between gypsum and fluid. Possibly, the decrease in LREE content results from faster gypsum growth or higher water temperatures, both of which would lower partition coefficients.

CONCLUSION

- Gypsum provides a record of Kawah Ijen volcanic effluent from 1919 to 2008.
- Gypsum-fluid element partitioning indicates that the LREE, Sr, Pb, Ni, Co, Cu, Sb, Mo, and Th are least susceptible to overprinting by mineral and rock fragment inclusions, and are therefore the most robust indicators of changes in seepage fluid composition.
- Compositional variability correlates with known elemental sources and can be grouped in three elemental sets: LREE + Sr + Pb which represents a rock-leaching signature; Cu, Zn, Cd which suggests a source linked to deep-seated immiscible sulfide destabilization; and Sb, Tl, and As which point to a contribution from shallow evolved rocks.
- A distinct signature of volcanic unrest can be recognized in the gypsum composition, allowing for episodes of unrest and quiescence to be identified.
- Unambiguous linking of the compositional timeseries with existing records of volcanic unrest and seismicity are unfortunately hindered by uncertainty in the absolute age assignment, and a higher resolution age model is desired.
- Growth zoned gypsum is a reliable and robust recorder of fluid composition, and has the potential to provide a high-resolution record of volcanic activity. The Kawah Ijen compositional variability that it records also informs what elements are best suited to monitoring efforts.
- Gypsum is a common precipitate phase from volcanic brines (e.g., Poás volcano—Rodriguez and van Bergen 2017; Copahue Volcano—RodriguezVarekamp et al., 2016; Popocatépetl—Armienta et al., 2000; and Mount Ruapehu—Kilgour et al., 2010), and thus holds great promise as an archive of past volcanic activity where compositional preservation can be shown.

DATA AVAILABILITY STATEMENT

The original contributions presented in the study are included in the article/**Supplementary Material**, further inquiries can be directed to the corresponding author.

AUTHOR CONTRIBUTIONS

The study was conceived jointly by the authors. VvH and KB conducted fieldwork and collected samples. VvH prepared the samples and VvH and KB conducted the laser ablation ICP-MS analyses; BG conducted the ^{210}Pb analyses; and DP the noble gas isotope analyses. All authors contributed to data interpretation, figure and table preparation, and writing of the article.

FUNDING

The research was funded by an Osisko Research stipend to VvH, NSERC Discovery Grant funding to KB (no. RGPIN-2014-03882) and VvH (no. RGPIN-2020-04173), and a GEOTOP collaborative research grant.

ACKNOWLEDGMENTS

We thank Romain Lauzeral, Sri Budhi Utami, Philipson Bani, Corentin Caudron, Bruce Christenson, Peter Kelly, Jennifer

Lewicki, Maria Martínez-Cruz, Wendy McCausland, John Pallister, Sofyan Primulyana, Dmitri Rouwet, Ugan Saing, Heather Wright, and the other participants of the Cities on Volcanoes 8 Wet Volcanoes workshop for discussions on the Kawah Ijen system and a fruitful exchange of ideas on establishing records of volcanic activity at wet volcanoes. We also thank Pak Heri and Pak Parjan for their invaluable help in the field, and we acknowledge the generous logistical support by CVGHM. We warmly thank Marcus Burnham (GeoLabs) for help with analyzing these non-standard samples, and Yuri Taran for insightful comments that improved the final article.

SUPPLEMENTARY MATERIAL

The Supplementary Material for this article can be found online at: https://www.frontiersin.org/articles/10.3389/feart.2021.764087/full#supplementary-material

REFERENCES

Armienta, M. A., De la Cruz-Reyna, S., Macı´as, J. L., and Macias, J. (2000). Chemical characteristics of the crater lakes of Popocatetetl, El Chichon, and Nevado de Toluca volcanoes, Mexico. *J. Volcanology Geothermal Res.* 97, 105–125. doi:10.1016/s0377-0273(99)00157-2

Berlo, K., and Turner, S. (2010). 210Pb-226Ra Disequilibria in Volcanic Rocks. *Earth Planet. Sci. Lett.* 296, 155–164. doi:10.1016/j.epsl.2010.05.023

Berlo, K., van Hinsberg, V. J., Vigouroux, N., Gagnon, J. E., and Williams-Jones, A. E. (2014). Sulfide Breakdown Controls Metal Signature in Volcanic Gas at Kawah Ijen Volcano, Indonesia. *Chem. Geology.* 371, 115–127. doi:10.1016/j.chemgeo.2014.02.009

Berlo, K., van Hinsberg, V., SuparjanPurwanto, B. H., Purwanto, B. H., and Gunawan, H. (2020). Using the Composition of Fluid Seepage from the Magmatic-Hydrothermal System of Kawah Ijen Volcano, Indonesia, as a Monitoring Tool. *J. Volcanology Geothermal Res.* 399, 106899. doi:10.1016/j.jvolgeores.2020.106899

Bernatowicz, T. J., Podosek, F. A., Honda, M., and Kramer, F. E. (1984). The Atmospheric Inventory of Xenon and noble Gases in Shales: The Plastic Bag experiment. *J. Geophys. Res.* 89, 4597–4611. doi:10.1029/jb089ib06p04597

Blundy, J., and Wood, B. (2003). Partitioning of Trace Elements between Crystals and Melts. *Earth Planet. Sci. Lett.* 210, 383–397. doi:10.1016/s0012-821x(03)00129-8

Blundy, J., and Wood, B. (1994). Prediction of crystal-melt Partition Coefficients from Elastic Moduli. *Nature* 372, 452–454. doi:10.1038/372452a0

Bosch, C. J. (1858). Uitbarstingen der vulkanen Idjin en Raun (Banjoewangi). *Tijdschr. Ind. Taal-, Land- en Volkenkunde VII*, 265–286.

Brady, J. B., and Cherniak, D. J. (2010). 20. Diffusion in Minerals: An Overview of Published Experimental Diffusion Data. *Rev. Mineral. Geochem.* 72, 899–920. doi:10.1515/9781501508394-021

Capezzuoli, E., Gandin, A., and Pedley, M. (2014). Decoding Tufa and Travertine (Fresh Water Carbonates) in the Sedimentary Record: The State of the Art. *Sedimentology* 61, 1–21. doi:10.1111/sed.12075

Caudron, C., Campion, R., Rouwet, D., Lecocq, T., Capaccioni, B., Syahbana, D., et al. (2017). Stratification at the Earth's Largest Hyperacidic lake and its Consequences. *Earth Planet. Sci. Lett.* 459, 28–35. doi:10.1016/j.epsl.2016.11.002

Caudron, C., Lecocq, T., Syahbana, D. K., McCausland, W., Watlet, A., Camelbeeck, T., et al. (2015a). Stress and Mass Changes at a "wet" Volcano: Example during the 2011-2012 Volcanic Unrest at Kawah Ijen Volcano (Indonesia). *J. Geophys. Res. Solid Earth* 120, 5117–5134. doi:10.1002/2014jb011590

Caudron, C., Syahbana, D. K., Lecocq, T., van Hinsberg, V., McCausland, W., Triantafyllou, A., et al. (2015b). Kawah Ijen Volcanic Activity: a Review. *Bull. Volcanol* 77, 16. doi:10.1007/s00445-014-0885-8

Cogliati, S., Sherlock, S., Halton, A., Reid, K., Rymer, H., and Kelley, S. (2021). Tracking the Behaviour of Persistently Degassing Volcanoes Using noble Gas Analysis of Pele's Hairs and Tears: A Case Study of the Masaya Volcano (Nicaragua). *J. Volcanology Geothermal Res.* 414, 107212. doi:10.1016/j.jvolgeores.2021.107212

de la Tour, L. (1805). Notice sur un lac d'acide sulfurique qui se trouve au fond d'un volcan du Mont-Idienne, situe dans la province de Bagnia-Vangni, côte de l'ile de Java. *Ann. Mus. Hist. Nat.* 18, 425–446.

Delmelle, P., and Bernard, A. (2000). Downstream Composition Changes of Acidic Volcanic Waters Discharged into the Banyupahit Stream, Ijen Caldera, Indonesia. *J. Volcanology Geothermal Res.* 97, 55–75. doi:10.1016/s0377-0273(99)00159-6

Delmelle, P., and Bernard, A. (1994). Geochemistry, Mineralogy, and Chemical Modeling of the Acid Crater lake of Kawah Ijen Volcano, Indonesia. *Geochimica et Cosmochimica Acta* 58, 2445–2460. doi:10.1016/0016-7037(94)90023-x

Fairmaid, A. M., Kendrick, M. A., Phillips, D., and Fu, B. (2011). The Origin and Evolution of Mineralizing Fluids in a Sediment-Hosted Orogenic-Gold Deposit, Ballarat East, Southeastern Australia. *Econ. Geology.* 106, 653–666. doi:10.2113/econgeo.106.4.653

Fanale, F. P., and Cannon, W. A. (1971). Physical Adsorption of Rare Gas on Terrigenous Sediments. *Earth Planet. Sci. Lett.* 11, 362–368. doi:10.1016/0012-821x(71)90195-6

Gázquez, F., Bauska, T. K., Comas-Bru, L., Ghaleb, B., Calaforra, J.-M., and Hodell, D. A. (2020). The Potential of gypsum Speleothems for Paleoclimatology: Application to the Iberian Roman Humid Period. *Sci. Rep.* 10, 14705. doi:10.1038/s41598-020-71679-3

Giammanco, S., Sims, K. W. W., and Neri, M. (2007). Measurements of Rn-220 and Rn-222 and CO_2 Emissions in Soil and Fumarole Gases on Mt. Etna Volcano (Italy): Implications for Gas Transport and Shallow Ground Fracture. *Geochem. Geophys. Geosys* 8, Q10001. doi:10.1029/2007gc001644

Goede, A., and Vogel, J. C. (1991). Trace Element Variations and Dating of a Late Pleistocene Tasmanian Speleothem. *Palaeogeogr. Palaeoclimatol. Palaeoecol.* 88, 121–131. doi:10.1016/0031-0182(91)90018-m

Gunawan, H., Caudron, C., Pallister, J., Primulyana, S., Christenson, B., McCausland, W., et al. (2016). New Insights into Kawah Ijen's Volcanic System from the Wet Volcano Workshop experiment. *Geol. Soc. Lond. Sp Pub* 437, 1–22. doi:10.1144/sp437.7

Handley, H. K., Macpherson, C. G., Davidson, J. P., Berlo, K., and Lowry, D. (2007). Constraining Fluid and Sediment Contributions to Subduction-Related Magmatism in Indonesia: Ijen Volcanic Complex. *J. Petrol.* 48, 1155–1183. doi:10.1093/petrology/egm013

Hengeveld, G. J. N. (1920). De mogelijkheid en de plaats van den bouw van een nieuwe sluis bij het kratermeer Kawah Idjen. *Geologische onderzoekingen ten behoeve van 's lands waterstaat-, gewestelijke- en gemeentewerken in Nederlandsch Indie* 93–118.

Inguaggiato, C., Pappaterra, S., Peiffer, L., Apollaro, C., Brusca, L., De Rosa, R., et al. (2020). Mobility of REE from a Hyperacid Brine to Secondary Minerals Precipitated in a Volcanic Hydrothermal System: Kawah Ijen Crater lake (Java, Indonesia). *Sci. Total Environ.* 740, 140133. doi:10.1016/j.scitotenv.2020.140133

Jochum, K. P., Nohl, U., Herwig, K., Lammel, E., Stoll, B., and Hofmann, A. W. (2005). GeoReM: A New Geochemical Database for Reference Materials and Isotopic Standards. *Geostand Geoanalyt Res.* 29, 333–338. doi:10.1111/j.1751-908x.2005.tb00904.x

Kaneoka, I. (1994). "The Effect of Water on noble Gas Signatures of Volcanic Materials," in *Noble Gas Geochemistry*. Editor J. Matsuda (Tokyo: TERRAPUB), 205–215.

Kemmerling, G. L. L. (1921). *Het Idjen Hoogland. De geologie en geomorphologie van den Idjen. Koninklijke Natuurkundige Vereeniging Monografie II, Weltevreden-Batavia*. Batavia - Weltevreden: G. Kolff & Co, 134.

Kilgour, G., V. Manville, V., Pasqua, F. D., A. Graettinger, A., Hodgson, K. A., and Jolly, G. E. (2010). The 25 September 2007 Eruption of Mount Ruapehu, New Zealand: Directed Ballistics, Surtseyan Jets, and Ice-Slurry Lahars. *J. Volcanology Geothermal Res.* 191, 1–14. doi:10.1016/j.jvolgeores.2009.10.015

Lowenstern, J. B., van Hinsberg, V., Berlo, K., Liesegang, M., Iacovino, K., Bindeman, I. N., et al. (2018). Opal-a in Glassy Pumice, Acid Alteration,

and the 1817 Phreatomagmatic Eruption at Kawah Ijen (Java), Indonesia. *Front. Earth Sci.* 6, 475. doi:10.3389/feart.2018.00011

Matsubara, K., Matsuda, J.-i., Nagao, K., Kita, I., and Taguchi, S. (1988). Xe in Amorphous Silica: a New Thermometer in Geothermal Systems. *Geophys. Res. Lett.* 15, 657–660. doi:10.1029/gl015i007p00657

Matsuda, J.-i., and Nagao, K. (1986). Noble Gas Abundances in a Deep-Sea Sediment Core from Eastern Equatorial Pacific. *Geochem. J.* 20, 71–80. doi:10.2343/geochemj.20.71

Onuma, N., Higuchi, H., Wakita, H., and Nagasawa, H. (1968). Trace Element Partition between Two Pyroxenes and the Host Lava. *Earth Planet. Sci. Lett.* 5, 47–51. doi:10.1016/s0012-821x(68)80010-x

Oudgast (1820). *Mengelingen*, 7. Batavia: Bataviasche Courant.

Ozima, M., and Podosek, F. A. (1983). *Noble Gas Geochemistry*. Cambridge: Cambridge University Press, 367.

Palmer, S. (2009). *Hydrogeochemistry of the Upper Banyu Pahit River valley, Kawah Ijen Volcano, Indonesia.* Montreal, Canada: MSc thesis, McGill University, 114.

Paton, C., Hellstrom, J., Paul, B., Woodhead, J., and Hergt, J. (2011). Iolite: Freeware for the Visualisation and Processing of Mass Spectrometric Data. *J. Anal. Spectrom.* 26, 2508–2518. doi:10.1039/c1ja10172b

Pfann, W. G. (1962). Zone Melting. *Science* 135, 1101–1109. doi:10.1126/science.135.3509.1101

Pinti, D. L., Wada, N., and Matsuda, J.-i. (1999). Neon Excess in Pumice: Volcanological Implications. *J. Volcanology Geothermal Res.* 88, 279–289. doi:10.1016/s0377-0273(99)00006-2

Pitre, F., and Pinti, D. L. (2010). Noble Gas Enrichments in Porewater of Estuarine Sediments and Their Effect on the Estimation of Net Denitrification Rates. *Geochimica et Cosmochimica Acta* 74, 531–539. doi:10.1016/j.gca.2009.10.004

Rodríguez, A., and van Bergen, M. J. (2017). Superficial Alteration Mineralogy in Active Volcanic Systems: An Example of Poás Volcano, Costa Rica. *J. Volcanology Geothermal Res.* 346, 54–80. doi:10.1016/j.jvolgeores.2017.04.006

Rodríguez, A., Varekamp, J. C., van Bergen, M. J., Kading, T. J., Oonk, P., Gammons, C. H., et al. (2016). "Acid Rivers and Lakes at Caviahue-Copahue Volcano as Potential Terrestrial Analogues for Aqueous Paleo-Environments on Mars," in *Copahue Volcano. Active Volcanoes of the World*. Editors F. Tassi, O. Vaselli, and A. Caselli (Berlin, Heidelberg: Springer). doi:10.1007/978-3-662-48005-2_7

Rouwet, D., and Tassi, F. (2011). Geochemical Monitoring of Volcanic Lakes. A Generalized Box Model for Active Crater Lakes. *Ann. Geophys.* 54, 161–173. doi:10.4401/ag-5035

Shannon, R. D. (1976). Revised Effective Ionic Radii and Systematic Studies of Interatomic Distances in Halides and Chalcogenides. *Acta Cryst. Sect A.* 32, 751–767. doi:10.1107/s0567739476001551

Sitorus, K. (1990). *Volcanic Stratigraphy and Geochemistry of the Idjen Caldera Complex, Indonesia*. Wellington, New Zealand: MSc thesis, University of Wellington, 148.

Smith, S. P., and Kennedy, B. M. (1983). The Solubility of noble Gases in Water and in NaCl Brine. *Geochimica et Cosmochimica Acta* 47, 503–515. doi:10.1016/0016-7037(83)90273-9

Staudacher, T., and Allègre, C. J. (1982). Terrestrial Xenology. *Earth Planet. Sci. Lett.* 60, 389–406. doi:10.1016/0012-821x(82)90075-9

Stöhr, E. (1862). Der Vulkan Idjen in Ost-Java. *Verhandelingen van het Koninklijk Bataviaasch Genootschap der Kunsten en Wetenschappen* 7, 30–47.

Sumarti, S. (1998). *Volcanic Pollutants in Hyperacid River Water Discharged from Ijen Crater lake, East Java, Indonesia*. Utrecht, Netherlands: MSc thesis. Utrecht University.

Symonds, R. B., Gerlach, T. M., and Reed, M. H. (2001). Magmatic Gas Scrubbing: Implications for Volcano Monitoring. *J. Volcanology Geothermal Res.* 108, 303–341. doi:10.1016/s0377-0273(00)00292-4

Takano, B., Fazlullin, S. M., and Delmelle, P. (2000). Analytical Laboratory Comparison of Major and Minor Constituents in an Active Crater lake. *J. Volcanology Geothermal Res.* 97, 497–508. doi:10.1016/s0377-0273(99)00171-7

Takano, B., Suzuki, K., Sugimori, K., Ohba, T., Fazlullin, S. M., Bernard, A., et al. (2004). Bathymetric and Geochemical Investigation of Kawah Ijen Crater lake, East Java, Indonesia. *J. Volcanology Geothermal Res.* 135, 299–329. doi:10.1016/j.jvolgeores.2004.03.008

Torgersen, T., Kennedy, B. M., and van Soest, M. C. (2004). Diffusive Separation of noble Gases and noble Gas Abundance Patterns in Sedimentary Rocks. *Earth Planet. Sci. Lett.* 226, 477–489. doi:10.1016/j.epsl.2004.07.030

Utami, S. B., van Hinsberg, V. J., Ghaleb, B., and Pinti, D. L. (2019). Growth-zoned gypsum Stalactite from the Kawah Ijen Volcanic lake, Indonesia, Records a >40-year Record of Volcanic Activity. *Bull. Volcanol* 81, 52. doi:10.1007/s00445-019-1314-9

Utami, S. B., van Hinsberg, V. J., Ghaleb, B., and van Dijk, A. E. (2020). Oxygen Isotope Fractionation between gypsum and its Formation Waters: Implications for Past Chemistry of the Kawah Ijen Volcanic lake, Indonesia. *Am. Mineral.* 105, 756–763. doi:10.2138/am-2020-7298

van Hinsberg, V., Berlo, K., and Lowenstern, J. (2020). An Experimental Investigation of Interaction between Andesite and Hyperacidic Volcanic Lake Water. *Minerals* 10, 96. doi:10.3390/min10020096

van Hinsberg, V., Berlo, K., Sumarti, S., van Bergen, M., and Williams-Jones, A. (2010b). Extreme Alteration by Hyperacidic Brines at Kawah Ijen Volcano, East Java, Indonesia: II. *J. Volcanology Geothermal Res.* 196, 169–184. doi:10.1016/j.jvolgeores.2010.07.004

van Hinsberg, V., Berlo, K., van Bergen, M., and Williams-Jones, A. (2010c). Extreme Alteration by Hyperacidic Brines at Kawah Ijen Volcano, East Java, Indonesia: I. Textural and Mineralogical Imprint. *J. Volcanology Geothermal Res.* 198, 253–263. doi:10.1016/j.jvolgeores.2010.09.002

van Hinsberg, V. J., Migdisov, A. A., and Williams-Jones, A. E. (2010a). Reading the mineral Record of Fluid Composition from Element Partitioning. *Geol* 38, 847–850. doi:10.1130/g31112.1

van Hinsberg, V., Vigouroux, N., Palmer, S., Berlo, K., Mauri, G., Williams-Jones, A., et al. (2017). "Element Flux to the Environment of the Passively Degassing Crater lake-hosting Kawah Ijen Volcano, Indonesia, and Implications for Estimates of the Global Volcanic Flux," in *Geochemistry and Geophysics of Active Volcanic Lakes*. Editors T. Ohba, B. Capaccioni, and C. Capaccioni (London: Geological Society, Special Publications), 437, 9–34.

van Rotterdam-Los, A. M. D., Vriend, S. P., van Bergen, M. J., and van Gaans, P. F. M. (2008). The Effect of Naturally Acidified Irrigation Water on Agricultural Volcanic Soils. The Case of Asembagus, Java, Indonesia. *J. Geochemical Exploration* 96, 53–68. doi:10.1016/j.gexplo.2007.07.003

Vigouroux, N. (2011). *Tracking the Evolution of Magmatic Volatiles from the Mantle to the Atmosphere Using Integrative Geochemical and Geophysical Methods*. Vancouver, Canada: PhD thesis Simon Fraser University, 265.

Yudiantoro, D. F., Irawan, B. A., Haty, I. P., Sayudi, D. S., Suproboriniaru, A., Sekarwati, B., et al. (2020). Geochemistry Acidic Water of Banyupait River Effect Seepage of Crater Water Ijen Volcano, Asembagus, Situbondo, East Java, Indonesia. *Preprints*. doi:10.20944/preprints202008.0344.v1

Zaier, I., Billiotte, J., Charmoille, A., and Laouafa, F. (2020). The Dissolution Kinetics of Natural gypsum: a Case Study of Eocene Facies in the north-eastern Suburbs of Paris. *Env Earth Sci.* 80, 1–16. doi:10.1007/s12665-020-09275-x

Zimmer, M., and Erzinger, J. (2003). Continuous H2O, CO2, 222Rn and Temperature Measurements on Merapi Volcano, Indonesia. *J. Volcanology Geothermal Res.* 125, 25–38. doi:10.1016/s0377-0273(03)00087-8

Conflict of Interest: The authors declare that the research was conducted in the absence of any commercial or financial relationships that could be construed as a potential conflict of interest.

frontiers in Earth Science

ORIGINAL RESEARCH
published: 03 December 2021
doi: 10.3389/feart.2021.741742

Groundwater Interacting at Depth With Hot Plastic Magma Triggers Phreatic Eruptions at Yugama Crater Lake of Kusatsu-Shirane Volcano (Japan)

Muga Yaguchi[1]*, *Takeshi Ohba*[2] and *Akihiko Terada*[3]

[1]Department of Volcanology Research, Meteorological Research Institute, Japan Meteorological Agency, Tsukuba, Japan, [2]Department of Chemistry, School of Science, Tokai University, Hiratsuka, Japan, [3]Volcanic Fluid Research Center, School of Science, Tokyo Institute of Technology, Meguro, Japan

OPEN ACCESS

Edited by:
Dmitri Rouwet, Istituto Nazionale di Geofisica e Vulcanologia, sezione di Bologna, Italy

Reviewed by:
Yuri Taran, National Autonomous University of Mexico, Mexico
María Martínez Cruz, Costa Rica Volcanological and Seismological Observatory (OVSICORI), Costa Rica

***Correspondence:**
Muga Yaguchi
myaguchi@mri-jma.go.jp

Specialty section:
This article was submitted to Volcanology, a section of the journal Frontiers in Earth Science

Received: *15 July 2021*
Accepted: *21 October 2021*
Published: *03 December 2021*

Citation:
Yaguchi M, Ohba T and Terada A (2021) Groundwater Interacting at Depth With Hot Plastic Magma Triggers Phreatic Eruptions at Yugama Crater Lake of Kusatsu-Shirane Volcano (Japan). Front. Earth Sci. 9:741742. doi: 10.3389/feart.2021.741742

Interpreting the triggering mechanisms for phreatic eruptions is a key to improving the hazard assessment of crater lakes. Yugama Crater Lake at Kusatsu-Shirane volcano, Japan, is the site of frequent phreatic eruptions with the recent eruptions in 1982–83, 1989, and 1996, as well as volcanic unrest, including earthquake swarms in 2014 and 2018. To understand the magma–hydrothermal interaction beneath Yugama Crater Lake, we analyzed lake waters from November 2005 to May 2021. From 2005 to 2012, Cl and SO_4 concentrations decreased slowly, suggesting the development of a self-sealing zone surrounding the crystallizing magma. We focused on Ca, Al, and Si concentrations as representatives of the breach and dissolution of minerals comprising the self-sealing zone and the Mg/Cl ratio as an indicator for enhanced interaction between groundwater and hot plastic rock within the self-sealing zone. In 2006–2007, the Ca, Al, Si concentrations and the Mg/Cl ratio increased. No Cl and SO_4 increase during this period suggests the self-sealing zone was leached by deep circulating groundwater rather than by magmatic fluids injection. After the 2014 earthquakes, Ca, Al, and Si increased again but were associated with a significant Cl increase and a pH decrease. We believe that the HCl-rich magmatic fluids breached the self-sealing zone, leading to fluids injection from the crystallizing magma to the Yugama crater. During this period, the Mg/Cl ratio did not increase, meaning that magmatic fluids ascending from the breached area of the self-sealing zone inhibited deep intrusion of groundwater into the hot plastic rock region. In 2018, magmatic fluids ascended through the self-sealing zone again with less intensity than in 2014. All eruptions since 1982 have been accompanied by a Mg/Cl ratio increase and a Cl decrease, whereas, when a significant HCl input occurs, as in 2014, no eruptions and no Mg/Cl ratio increase occurred. This demonstrates that the groundwater–hot plastic rock interaction, rather than the magmatic fluids input, played an essential role in triggering phreatic eruptions; i.e., phreatic eruptions can potentially occur without clear signs of fresh magma intrusions.

Keywords: crater lake, phreatic eruption, hydrothermal system, Kusatsu-Shirane volcano, self-sealing zone, crystallizing magma, Mg/Cl ratio, geochemical monitoring

INTRODUCTION

Phreatic eruptions do not expel juvenile magma and are typically small in scale. For "wet volcanoes" they can be the dominant type of volcanic eruption that sometimes causes hazardous damage (e.g., Caudron et al., 2015; Yamaoka et al., 2016; Mannen et al., 2019). Although understanding the mechanism and forecast of phreatic eruptions are still challenging, previous studies have shown that various processes in magma–hydrothermal systems, such as rapid pressurization of fluids due to contact between groundwater and hot rocks, increased release of magmatic gases, rapid vaporization of superheated water due to decompression, and sealing by precipitation of hydrothermal minerals, play an important role in triggering this type of eruption (e.g., Hedenquist and Henley, 1985; Barberi et al., 1992; Mastin, 1995; Browne and Lawless, 2001; Stix and de Moor, 2018; Ohba et al., 2019a). An active crater lake connected to a magma–hydrothermal system is a suitable site for studying magma–hydrothermal activity. For example, in Ruapehu (New Zealand), Poás (Costa Rica), and Kelut (Indonesia), chemical analyses of crater lakes were applied as a means of volcanic surveillance (e.g., Giggenbach and Glover, 1975; Rowe et al., 1992; Badrudin, 1994; Bernard and Mazot, 2004; Martínez et al., 2000, 2019; Martínez, 2008; Christenson et al., 2010; Rouwet et al., 2017, 2019).

Yugama Crater Lake at Kusatsu-Shirane volcano on Honshu Island, Japan (**Figures 1A–C**), is known as a frequent phreatic eruption site (e.g., Ohba et al., 2008a; Terada, 2018) despite there is no clear evidence of recent fresh magma intrusion at shallow depths and actively degassing. Yugama Crater Lake is also an important resource for tourism and economic activities. Interpreting the triggering mechanisms for phreatic eruptions, which occur at such crater lakes as Yugama, is essential to improve how to assess the hazard of phreatic activity at crater

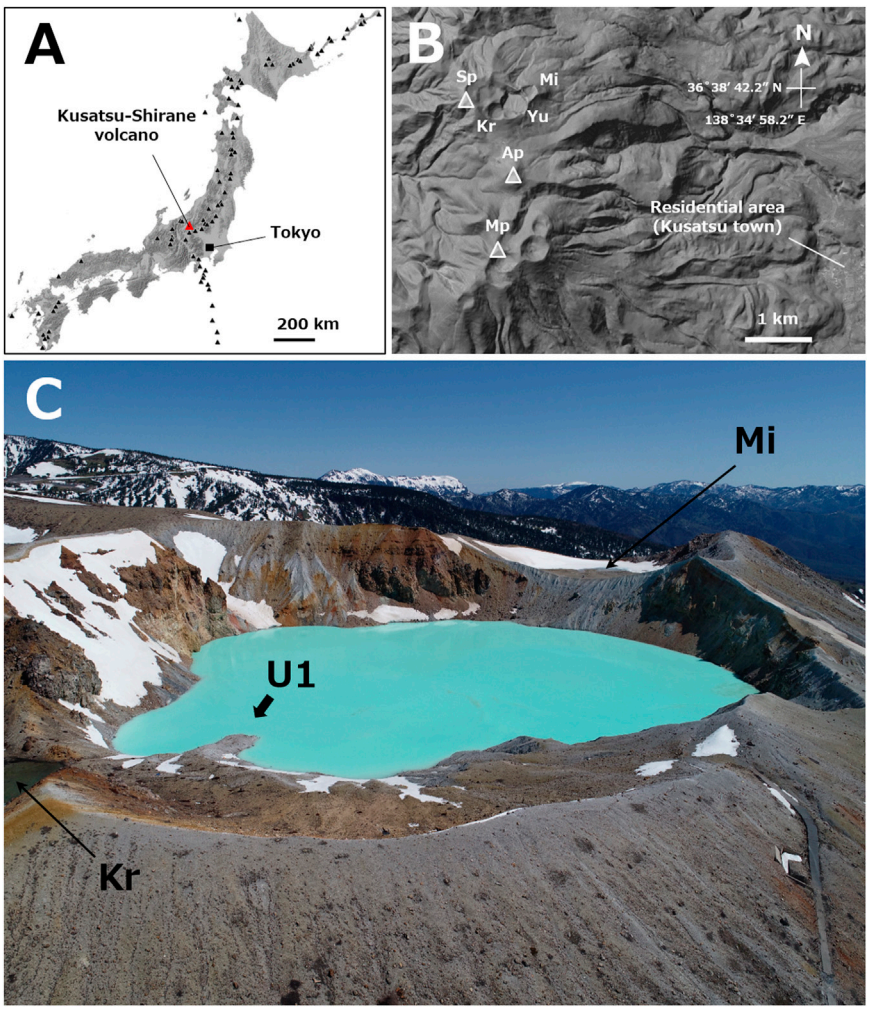

FIGURE 1 | Index map of Kusatsu-Shirane volcano and Yugama crater. **(A)** Location map of Kusatsu-Shirane volcano (Source of the base map; the Geographical Survey Institute of Japan). Solid triangles indicate an active volcano. **(B)** Shaded-relief image overlapping the aerial photograph around Kusatsu-Shirane volcano (Source of the base map; the Geographical Survey Institute of Japan). Sp, the peak of Mt. Shirane; Ap, the peak of Mt. Ainomine; Mp, the peak of Mt. Motoshirane; Yu, Yugama crater; Mi, Mizugama crater; and Kr, Karegama. **(C)** Yugama crater (photograph taken by AT using a drone on May 8, 2020). U1, regular sampling point.

lake-bearing volcanoes. Accordingly, the correspondence between changes in the chemical composition of lake water and eruptive activity has been investigated at the Yugama crater (e.g., Ohba et al., 1994, 2000, 2008a). For example, in the last 50 years, a phreatic eruption occurred within the Mizugama crater adjacent to the Yugama crater in 1976, and phreatic eruptions occurred within and surrounding the Yugama crater in 1982–83, 1989, and 1996 (Ida et al., 1989; Kusatsu-Shirane Volcano Observatory, Tokyo Institute of Technology, 1996, 1997; Terada, 2018). No eruption has occurred at the Yugama crater since then, but there were earthquake swarms beneath the Yugama crater in 1989–91, followed by a pH drop in the lake water (Ohba et al., 1994, 2000). For this series of activities, Ohba et al. (2008a) proposed the following model, based on the chemical analysis of lake water at crater Yugama. The 1982–83 eruption was triggered by vapor expansion following the interaction between groundwater and the hot plastic rock region inside the self-sealing zone. The 1989–91 earthquakes and subsequent pH drops were caused by the groundwater that intruded within the self-sealing zone, extracting HCl-rich fluids from the hot plastic rock region and supplying it to the Yugama crater.

If development and breach of the self-sealing zone play key roles in the magma–hydrothermal activity beneath the Yugama crater, this cycle may continue until the underlying magma cools and loses its volatiles. As expected, earthquake swarms reoccurred around the Yugama crater from March 2014 and in April 2018. Ohba et al. (2019b) estimated that the earthquake swarms in 2014 and 2018 were triggered by the increased pressure in the hydrothermal reservoir due to the injection of magmatic gas, a model based on the analytical results of the chemical and stable isotopic compositions of the fumarolic gases near the Yugama crater. This result made us expect that magma–hydrothermal interaction can be inferred through the chemical composition of Yugama Crater Lake because magmatic gas contains many water-soluble components. In this study, we present the chemical composition of water at Yugama Crater Lake, which was sampled almost every month from November 2005 to May 2021 except for the volcanic unrest period and snow season, and based on this, we investigate the magma–hydrothermal interaction beneath Yugama Crater Lake during this period and propose a key mechanism for the recent eruptions at this crater.

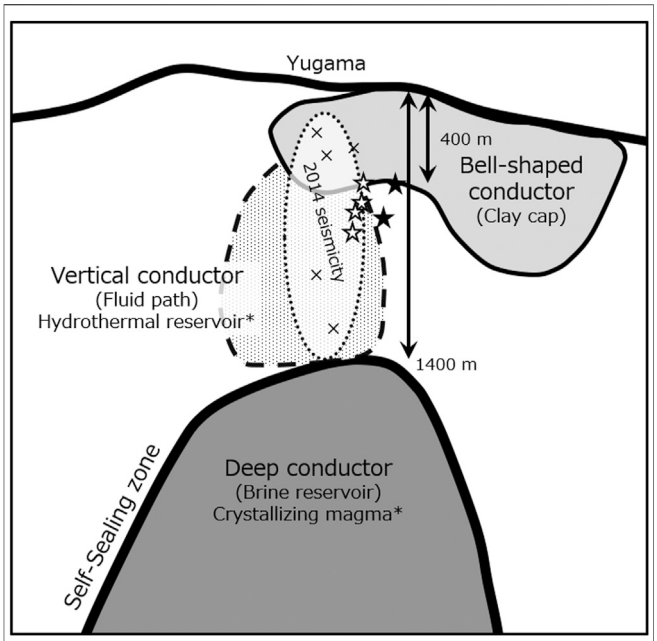

FIGURE 2 | Major structures beneath the Yugama crater inferred by the magnetotellurics survey simplified from Tseng et al. (2020). Cross marks indicate simplified earthquake locations. Open and solid stars indicate approximate locations of magnetizations and demagnetizations corresponding to the volcanic events in 1982–2012 (Takahashi and Fujii, 2014), respectively. *The deep conductor and vertical conductor correspond to crystallizing magma and a hydrothermal reservoir (Ohba et al., 2008a; Ohba et al., 2019b).

STUDY AREA

Kusatsu-Shirane Volcano and Hydrothermal Systems Beneath the Yugama Crater

Kusatsu-Shirane volcano is an active volcano consisting of the pyroclastic cones of Shirane, Ainomine, and Motoshirane (**Figure 1B**). The eruption stages of this volcano are distinguished into the following: 0.6–0.5 Ma, 0.5–0.3 Ma, and 16 ka-present (Hayakawa and Yui, 1989; Kaneko et al., 1991; Takahashi et al., 2010). Three pyroclastic cones were formed since 16 ka, and recent studies have shown that the Mt. Motoshirane and Mt. Shirane experienced magmatic eruptions at approximately 1.5 and 1.4 ka, respectively (Ishizaki et al., 2020; Kametani et al., 2021). The Yugama crater is located near the summit of Mt. Shirane (**Figure 1B**). All recorded (since 1805) eruptions were phreatic, and almost all occurred in and around the Yugama crater, except for the phreatic eruption at Mt. Motoshirane on January 23, 2018 (e.g., Uto et al., 1983; Japan Meteorological Agency, 2013; Terada, 2018). The last eruption at the Yugama crater was in 1996, but turbulence on the lake surface, such as a dome-shaped water bulge in 1997 and a water jet in 2004, have been observed (Kusatsu-Shirane Volcano Observatory, Tokyo Institute of Technology, 1996, 1997; Volcanic Fluid Research Center, Tokyo Institute of Technology, 2004).

The hydrothermal structure beneath Kusatsu-Shirane volcano has been investigated mainly by magnetotelluric (MT) or audio-frequency magnetotellurics (AMT) methods (Nurhasan et al., 2006; Matsunaga et al., 2020; Tseng et al., 2020). Among these, Tseng et al. (2020) investigated the electrical conductivity structure specifically focused on just beneath the Yugama crater and pointed out three major conductors: a bell-shaped conductor from near the surface to about 400 m below the surface (m.b.s.), interpreted as the smectite-rich layer; a deep conductor at >1,500 m.b.s., interpreted as the brine reservoir; and a vertical conductor connecting the deep conductor and the shallow

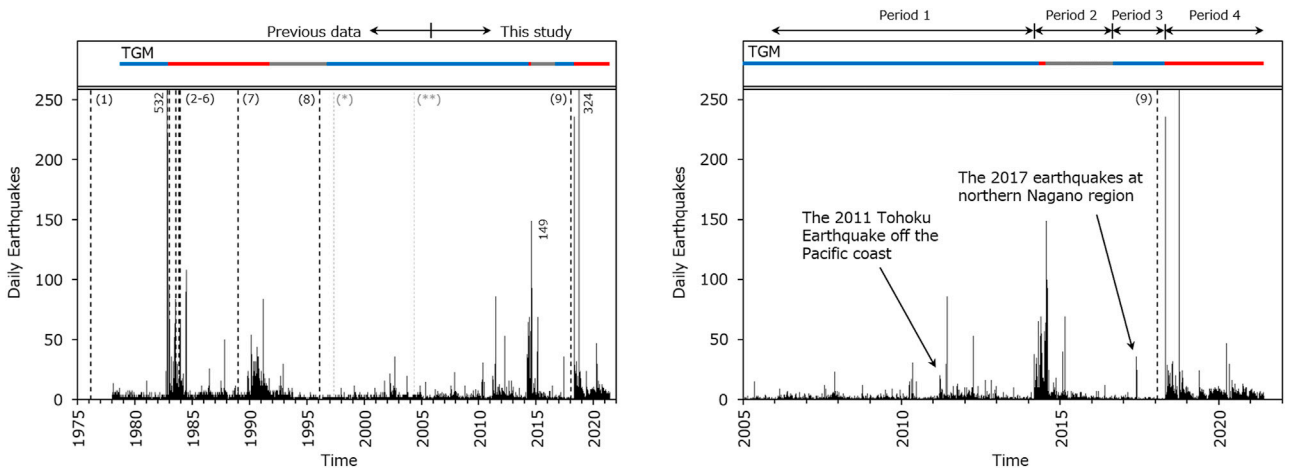

FIGURE 3 | Seismicity and thermal activity around the Yugama crater. The number of earthquakes from January 1978 to May 2017 are earthquakes that occurred in the Kusatsu-Shirane volcano, and earthquakes after June 2017 are earthquakes that occurred near the Yugama crater. The 2011 off the Pacific coast of Tohoku Earthquake and the 2017 earthquakes in northern Nagano region are not earthquakes that occurred near the Yugama crater. TGM; Thermal activity beneath the Yugama crater inferred from geomagnetic measurements. Blue periods indicate a magnetizing trend (cooling periods); red periods indicate a demagnetizing trend (heating periods); and gray periods indicate an unclear or stagnant period. Vertical dashed lines indicate eruptive events: (1), the eruption at Mizugama crater in 1976; (2–6), eruptions at the Yugama and the Karegama crater in 1982–1983; (7), a small eruption at the Yugama crater in 1989; (8), a small eruption at the Yugama crater in 1996; and (9), an eruption at Mt. Motoshirane peak in 2018. Vertical thin dashed lines indicate the turbulence on the lake surface: (*), water dome in 1997; and (**), water jet in 2004.

conductor (**Figure 2**). Such hydrothermal structures have also been suggested by geochemical studies of lake water in the Yugama crater and volcanic gases around the Yugama crater (Ohba et al., 2000; Ohba et al., 2008a; Ohba et al., 2019b). Considering this information, a deep conductor corresponds to magma and the surrounding hot plastic rock region, and a vertical conductor corresponds to a two-phase hydrothermal reservoir of liquid and vapor. Flushing of magmatic fluids from deep conductors is thought to be controlled by self-sealing due to mineral deposition.

Volcanic earthquakes have occurred at mainly 1,000 m beneath the Yugama crater (Japan Meteorological Agency, 2019; Terada et al., 2021). Source locations of thermal magnetization and demagnetization are estimated to be about 400–700 m beneath the Mizugama crater (Takahashi and Fujii, 2014). The seismicity and thermal activity indicate a magmatic fluids injection into the hydrothermal reservoir due to a breach of the self-sealing zone (Ohba et al., 1994, 2008a, 2019b; Tseng et al., 2020).

Overview of Recent Activities of Kusatsu-Shirane Volcano

Seismic and Thermal Activity

As phreatic eruptions have occurred mainly at Mt. Shirane in the last 200 years, geodetic, seismic, and geomagnetic observations have been carried out around the Yugama crater since the 1970s (Ohchi, 1987; Japan Meteorological Agency, 2013). In this study, to discuss the lake water chemistry, we identified the periods of volcanic activity into Periods 1–4 based on the seismic and the geomagnetic observations (**Figure 3**). Thermal activity in **Figure 3** shows the results of geomagnetic observations simplified into demagnetization (heating), magnetization (cooling), and stagnation.

Period 1 (November 2005–February 2014)

Although seismic activity, such as after the 2011 Tohoku Earthquake off the Pacific coast (about 420 km northeast of Kusatsu-Shirane volcano) has been observed, the seismicity from November 2005 to February 2014 was essentially less active (**Figure 3**). The low seismic activity was consistent with the geomagnetic observations, indicating cooling beneath the Yugama crater during this period (Takahashi and Fujii, 2014; Kakioka Magnetic Observatory, 2016).

Period 2 (March 2014–August 2016)

Earthquake swarms occurred at Mt. Shirane from March to August 2014, followed by minor seismic activity until March 2018 (the end of Period 3; **Figure 3**). The thermal demagnetization was observed beneath the Yugama crater from May to June 2014. The thermal demagnetization appeared to stop after July 2014 (Kakioka Magnetic Observatory, 2019).

Period 3 (September 2016–March 2018)

Minor seismicity at Mt. Shirane was still observed during this period. Although many earthquakes were observed in May 2017 (**Figure 3**), these earthquakes corresponded to the seismicity at the northern part of Nagano Prefecture, more than 5 km north of Kusatsu-Shirane volcano (Japan Meteorological Agency, 2018). A magnetized trend was observed from summer in 2016 to March 2018. We consider that the beginning of the magnetization was from September 2016, the same as Period 2 (Kakioka Magnetic Observatory, JMA, 2019).

On January 23, 2018, a phreatic eruption occurred at Mt. Motoshirane, 2 km south of the Yugama crater. No precursors, such as changes in seismicity, ground deformations, and thermal demagnetizations, were observed at the Kusatsu-Shirane volcano preceding this eruption (Ogawa et al., 2018; Terada et al., 2021).

Period 4 (April 2018–May 2021)

Three months after the eruption of Mt. Motoshirane, an earthquake swarm started in late April 2018 at Mt. Shirane (Terada et al., 2021). Seismic activity remained high until May 2021; especially, many earthquakes occurred in May 2019 and March 2020 (**Figure 3**). A demagnetized trend during this period suggests that a temperature increase in the subsurface of the crater continued from April 2018 to May 2021 (Kakioka Magnetic Observatory, 2019; Japan Meteorological Agency, 2021).

Crustal Deformation

Crustal deformations have been observed at the Kusatsu-Shirane volcano using tiltmeters and GNSSs. According to tiltmeter observations, the shallow inflation of 1.2×10^5 m^3 beneath the Yugama crater (about 1,000 m.b.s.) was observed from March 2014 to approximately October 2016 (Terada et al., 2021). Such inflation has been detected intermittently also from April 2018, but its inflated volume is one-third of the one of 2014–2016 (Kusatsu-Shirane Volcano Observatory, Tokyo Institute of Technology, 2021).

Preceding the earthquake swarms in 2014 and 2018, the deep pressure source at about 2 km northwest of the Yugama crater, at a depth of about 6.3 km below the lake surface, was inflated (Munekane, 2021). The inflated volumes from late-2013 to mid-2015 and from late-2017 to mid-2020 are estimated at 5×10^6 m^3 and 2.5×10^6 m^3, respectively. We consider that the deep inflation source affected the earthquake swarms in 2014 and 2018.

MATERIALS AND METHODS

This study presents the chemical composition of lake water within the Yugama crater from November 2005 to May 2021. The sampling frequency is usually at least once a month, but samples from December to March were usually unavailable because snow inhibits access to the sampling site. The lake water was basically collected using a plastic cup with a long handle on the southwest coast (U1; **Figure 1C**) of Yugama Crater Lake, but since 2017, remote sampling using a drone, as in Terada et al. (2018), was also applied. The analyses of lake water collected from November 2005 to August 2009 were conducted at Tokyo Institute of Technology, as in Ohba et al. (2008a), and samples collected after this period were analyzed at the Meteorological Research Institute (MRI). At the MRI, the pH and electrical conductivity were measured using a handheld pH/EC meter (Horiba, D-74) equipped with a glass electrode (Horiba, 9615S-10D) calibrated with pH 1.68 and 4.00 buffer solutions and a platinum–platinum black electrode (Horiba, 3552-10D), respectively. The lake waters were filtered with 0.45-μm membrane filters and diluted with ultra-pure water using the appropriate dilution factor to bring the concentrations of the analytes to within the calibration ranges and limit of detections (LOD; **Table 1**), and then subjected to ion chromatography (Thermo Scientific, Dionex Integrion HPIC) to determine Cl and SO_4 concentrations, and microwave plasma atomic emission spectrometer (Agilent, 4210 MP-AES) to determine Na, K, Ca, Mg, Fe, Al, Mn, and Si (expressed as SiO_2 in **Table 2**) concentrations. The relative standard deviations (RSD) of IC and MP-AES analyses were better than 3% (**Table 1**). Stable isotope ratios (δD and δ^{18}O) of lake waters sampled after 2012 were analyzed by using a cavity ring-down spectrometer (Picarro, L2140-i) and expressed in per mil (‰) relative to VSMOW. Analytical precisions tested were within ±0.4‰ for δD and ±0.05‰ for δ^{18}O. The analytical results are listed in **Table 2**.

RESULTS

Period 1 (November 2005–February 2014)

The lake water's pH is approximately 1.2–1.3, and no significant change was observed (**Table 2** and **Figure 4**). The concentrations of anions, Cl and SO_4, showed a gradual decreasing trend throughout the period with short-term fluctuations (**Figure 5A**). The concentrations of Na, K, Fe, and Mn did not change significantly, but Si and certain cations, such as Al, Ca, and Mg, increased temporarily from September 2006 to November 2007 (**Figure 5B**).

Period 2 (March 2014–August 2016)

The pH decreased sharply (**Figure 4**), and almost all concentrations of anions, cations, and SiO_2 increased (**Figure 5**). Among these, the decrease in pH and increase in Cl concentrations reach values of pH = 0.91 and Cl = 5,180 mg/L on August 7, 2016, respectively, which is the lowest and highest compared to past observations (Ohba et al., 2008a and references therein), respectively. At the same date, δD = −39.4‰ and δ^{18}O = −1.7‰ (**Table 2**) were observed, which are the highest values ever observed.

Period 3 (September 2016–March 2018)

The concentrations of dissolved components that increased in Period 2 maintained high values, with fluctuations, until October 2016. Thereafter, the pH increased until the end of this period, and the concentrations of various constituents decreased in general, with fluctuations (**Figures 4**, **5**).

Period 4 (April 2018–May 2021)

The overall trend in this period was a persistent decrease in Cl and SO_4 concentrations, which started in August–October 2016. However, after the earthquake swarms (e.g., in April–September 2018, May 2019, and April 2020), an increase in Cl and SO_4 concentration (or stagnation of concentration decrease) occurred. The acceleration in speed of such increases in Cl and SO_4 concentrations after the earthquake swarms were accompanied by increases in Ca, Al, Fe, and Si concentrations (**Figure 5**).

TABLE 1 | Analytical performance of anions, cations and Si analyzed at the MRI.

Analyte	Technique	Dilution factor	Calibration range mg/L	LOD mg/L	RSD %
Cl	IC	1,000 and 500	0–10	[a] 5.05×10^{-3}	0.15
SO_4	IC	100 and 50	0–40	[a] 2.04×10^{-2}	0.25
Al	MP-AES	40	0–10	[b] 4.92×10^{-4}	1.54
Ca	MP-AES	40	0–5	[b] 4.42×10^{-4}	0.45
Fe	MP-AES	40	0–5	[b] 8.19×10^{-4}	2.59
K	MP-AES	40	0–1	[b] 1.72×10^{-4}	0.87
Mg	MP-AES	40	0–1	[b] 3.97×10^{-4}	0.90
Mn	MP-AES	40	0–1	[b] 5.56×10^{-4}	1.31
Na	MP-AES	40	0–1	[b] 4.35×10^{-4}	0.69
Si	MP-AES	40	0–5	[b] 9.01×10^{-3}	2.32

[a]*LODs of IC analysis were calculated as three times the peak height to baseline noise (S/N = 3) at the standard's concentration tested (1 mg/L for Cl and 4 mg/L for SO_4).*
[b]*LODs of MP-AES analysis were calculated as LOD = $3\sigma C/(I_C - I_B)$, where σ is the standard deviation of blank's intensity, I_C is the standard's intensity, I_B is the blank's intensity, C is the standard's concentration tested (0.1 mg/L for all analytes).*

DISCUSSION

Assumptions for Discussion

In the following discussion, we assume that the magma–hydrothermal system is affected by crystallization (cooling), rather than melting magma (**Figure 6A**). The latest magmatic eruption at Mt. Shirane occurred about 1.4 ka ago. Moreover, no magma intrusions into the shallow depth have been detected since the 1990s (Munekane, 2021; Terada et al., 2021). Additionally, although a large amount of heat of over 120 MW is released during the quiescent period (Ueki and Terada, 2012), concentrations of SO_2 in fumarolic gas, as a representative of magmatic gas derived from fresh magma at shallow depth, are low (Ohba et al., 2019b). In the assumed system (**Figure 6A**), magmatic fluids are degassed through the impermeable hot plastic rock surrounding a crystallizing magma, as Giggenbach (1992a) proposed. Secondary mineral deposition as a self-sealing zone occurs at the margin of the hot plastic rock region at about 370–400°C (Fournier, 1999). The self-sealing zone corresponds to brittle to plastic transition: dominantly meteoric water circulates at hydrostatic pressure in brittle rock while dominantly magmatic fluids at lithostatic pressure accumulates in hot plastic rock. Magmatic fluids flushes into the overlying brittle region when episodic and temporary breaching of a normally self-sealed zone occurs. Such magma-hydrothermal structure has not yet been demonstrated in the Kusatsu-Shirane volcano, but a very similar structure has been observed in the deep wells drilled in the Kakkonda geothermal field located in northeast Japan. According to the deepest geothermal well (named WD-1a; total depth of 3,729 m) data, the quaternary granitic pluton, which is the heat source of this field, was encountered at 2,860 m.b.s., and the brittle-plastic transition was confirmed at 3,100 m.b.s. at about 380°C, the maximum temperature of 500–510°C was recorded at 3,700 m.b.s. (Muraoka et al., 1998). In the brittle rock region of this well, the deeper fluids have a higher salinity (Komatsu et al., 1998). Saline fluids are also recognized below the brittle-plastic transition; for example, hypersaline liquid (about 40 wt% total chloride species) has been obtained from 3,708 m.b.s. (Kasai et al., 1998). Those Cl-rich fluids were concentrated in the liquid phase during the crystallization process of the crystallizing magma. In the case of Yugama crater lake, Cl species released to the brittle rock region would be dominated by HCl. This is because, in the assumed hydrothermal system, magmatic fluids are released from the plastic rock region when the self-sealing zone is breached, i.e., under a hydrostatic pressure of about 150 bar (assuming that the depth of plastic rock is 1,500 m; Tseng et al., 2020); at such low pressure, the silicate-water interaction leads to a high HCl/NaCl ratio in the aqueous phase (Shinohara and Fujimoto, 1994).

Anionic species (e.g., Cl and SO_4) in the most active volcanic lakes mostly originate from the degassing magma, whereas rock-forming species (e.g., Na, K, Ca, Mg, Al, Mn, Fe, and Si) originate from the leaching from the rock (Ohba et al., 2008a; Rouwet et al., 2014; Varekamp, 2015). However, it is not always necessary that SO_4 in the water of Yugama Crater Lake be derived from the unique origin. This is because the sulfur components initially come to the hydrothermal system from the gas phase, but some of them are removed from the aqueous phase as elemental sulfur, and the precipitation and dissolution of secondary minerals such as sulfates and sulfides contribute to the SO_4 concentration in lake water. In addition, some of the sulfur species absorbed by the lake water are dissolved in chemical forms other than SO_4, such as polythionates (Takano and Watanuki, 1990; Ohba et al., 2008a; Takano et al., 2008).

Phreatic eruptions may form even in the case of magma crystallizing and driving the shallower hydrothermal circulation. In this case, the Mg/Cl ratio can be used as an indicator of water–hot plastic rock contact. We assume that Cl and Mg originate from the crystallizing magma. In this situation, an increase in Mg/Cl is interpreted to correspond to enhanced interaction between water and a hot plastic rock region relative to the stable HCl degassing state (Giggenbach and Glover, 1975; Giggenbach, 1996; Rouwet et al., 2014). Increases in the Mg/Cl ratio were observed before and after all eruptions at Yugama Crater Lake since 1982 (i.e., in 1982–82, 1989, and 1996) and the water bulge appearance in 1997 (Ohba et al., 2008a).

TABLE 2 | Chemical and isotopic composition of lake water in Yugama crater sampled from November 2005 to May 2021.

Sampling date	Temp. °C	pH	EC S/m	Cl mg/L	SO_4 mg/L	Al mg/L	Ca mg/L	Fe mg/L	K mg/L	Mg mg/L	Mn mg/L	Na mg/L	SiO_2 mg/L	$\delta^{18}O$ ‰	δD ‰
November 4, 2005	17.9	1.28	ND	2,840	1740	140	94.2	86.2	11.7	20.9	0.86	23.0	163	ND	ND
April 20, 2006	8.6	1.30	ND	2,570	1,460	129	85.6	70.9	11.1	20.4	0.87	20.1	139	ND	ND
May 25, 2006	18.3	1.31	ND	2,500	1,350	128	86.2	73.6	10.1	20.2	0.85	18.9	142	ND	ND
June 15, 2006	19.1	1.30	ND	2,430	1,360	125	84.4	68.5	10.4	19.9	0.84	18.9	133	ND	ND
July 20, 2006	23.7	1.31	ND	2,430	1,290	124	83.2	67.9	9.3	19.3	0.82	17.9	130	ND	ND
August 14, 2006	26.8	1.29	ND	2,470	1,390	128	85.9	71.6	9.3	19.9	0.83	18.5	134	ND	ND
September 5, 2006	26.4	1.29	ND	2,490	1,390	127	86.1	71.0	10.1	20.1	0.84	19.2	134	ND	ND
October 13, 2006	18.7	1.29	ND	2,460	1,480	132	89.6	72.3	10.3	23.8	1.04	20.5	137	ND	ND
November 18, 2006	16.1	1.25	ND	2,520	1,590	135	94.0	73.6	10.0	27.9	1.25	22.1	154	ND	ND
April 20, 2007	11.2	1.27	ND	2,640	1,580	150	97.7	63.7	12.9	30.0	1.27	20.0	164	ND	ND
May 31, 2007	17.1	1.27	ND	2,600	1,520	152	100	64.4	11.4	30.0	1.25	21.3	171	ND	ND
June 27, 2007	22.8	1.27	ND	2,590	1,500	152	100	65.3	15.3	30.3	1.28	22.1	169	ND	ND
July 19, 2007	25.5	1.27	ND	2,620	1,470	158	101	69.1	11.5	29.7	1.25	22.1	168	ND	ND
August 21, 2007	26.9	1.25	ND	2,720	1,540	166	103	70.0	12.0	30.7	1.32	23.5	187	ND	ND
September 19, 2007	24.9	1.28	ND	2,540	1,510	162	105	74.8	11.2	29.4	1.27	22.7	185	ND	ND
October 21, 2007	20.9	1.22	ND	2,630	1,620	166	108	75.6	9.7	30.4	1.24	21.2	177	ND	ND
November 14, 2007	14.8	1.23	ND	2,550	1,670	170	107	76.0	11.3	30.3	1.24	21.8	181	ND	ND
April 24, 2008	11.2	1.31	ND	2,440	1,330	142	91.0	58.0	16.5	25.1	0.80	25.1	154	ND	ND
May 13, 2008	13.6	1.29	ND	2,450	1,340	147	94.8	59.3	11.5	25.6	0.84	23.8	153	ND	ND
June 11, 2008	20.1	1.30	ND	2,360	1,290	138	94.6	58.8	11.5	24.5	0.79	22.6	149	ND	ND
July 16, 2008	25.2	1.35	ND	2,340	1,330	132	90.9	56.5	13.0	23.0	0.87	21.9	144	ND	ND
August 15, 2008	26.9	1.34	ND	2,370	1,330	135	93.5	61.5	13.8	23.1	0.88	22.6	148	ND	ND
September 2, 2008	25.5	1.33	ND	2,320	1,430	146	100	68.4	12.5	25.0	0.93	24.4	153	ND	ND
October 21, 2008	20.4	1.30	ND	2,460	1,590	144	97.1	72.3	10.2	25.3	0.75	22.7	153	ND	ND
November 7, 2008	15.3	1.28	ND	2,520	1,630	147	96.3	72.2	6.5	25.3	0.75	23.2	159	ND	ND
April 23, 2009	12.1	1.30	ND	2,540	1,410	136	89.9	57.7	11.2	23.4	0.78	22.3	142	ND	ND
May 21, 2009	19.0	1.30	ND	2,560	1,360	140	92.0	59.6	11.1	23.7	0.86	23.0	149	ND	ND
June 9, 2009	20.2	1.29	ND	2,570	1,290	140	92.8	59.0	10.2	23.8	0.94	23.4	149	ND	ND
July 16, 2009	22.4	1.28	ND	2,580	1,300	144	92.3	59.8	12.1	24.5	0.92	24.0	150	ND	ND
August 13, 2009	27.1	1.29	ND	2,570	1,300	144	94.5	61.3	11.2	24.7	0.84	24.0	151	ND	ND
June 26, 2012	21.6	1.29	2.35	2,230	1,120	132	92.0	64.3	10.2	19.5	0.66	22.3	161	−6.4	−60.2
May 19, 2014	18.8	1.24	2.76	2,630	1,100	124	85.2	68.0	10.4	19.9	0.70	21.1	162	−5.6	−58.7
August 23, 2014	ND	1.19	2.93	2,680	1,250	130	92.8	75.7	10.3	20.8	0.74	22.7	168	−5.0	−55.1
September 27, 2014	25.3	1.15	3.24	3,000	1,370	144	98.9	77.7	10.3	22.8	0.77	23.3	181	−4.2	−51.6
May 15, 2015	22.6	1.07	3.97	3,630	1,310	160	96.9	67.1	12.0	25.2	0.81	25.7	194	−4.1	−48.2
August 28, 2015	ND	1.02	4.49	4,040	1,670	179	105	82.2	13.2	28.0	0.92	29.4	208	−3.0	−44.1
October 15, 2015	21.4	1.01	4.62	4,170	1780	178	111	79.9	12.6	29.1	0.96	29.2	211	−2.7	−42.2
April 22, 2016	16.6	0.94	5.48	4,670	1890	210	120	79.9	14.8	33.9	1.11	33.0	219	−2.1	−39.5
August 7, 2016	29.8	0.91	5.79	5,180	2,220	217	129	88.7	18.0	35.4	1.18	38.3	213	−1.7	−39.4
August 25, 2016	27.5	0.91	5.76	5,180	2,230	226	132	94.1	17.0	36.5	1.21	37.0	214	−1.8	−39.5
September 6, 2016	26.5	0.91	5.71	5,000	2,200	222	133	94.3	16.8	36.1	1.19	36.2	217	−1.8	−39.5
September 29, 2016	24.9	0.94	5.42	4,900	2,140	219	131	95.0	17.1	34.4	1.22	37.4	211	−2.5	−42.6
October 17, 2016	21.9	0.92	5.55	5,080	2,230	226	132	104	17.0	36.9	1.17	37.0	215	−2.1	−41.3
October 27, 2016	17.4	0.92	5.69	5,140	2,230	236	137	102	20.0	37.5	1.26	45.7	221	−1.8	−40.0
April 25, 2017	13.8	0.96	4.97	4,370	1790	205	121	81.3	14.1	32.2	1.08	31.7	170	−3.9	−48.5
May 17, 2017	17.0	0.98	5.14	4,750	1840	200	122	81.0	13.7	31.8	1.09	33.5	176	−3.6	−47.3
July 21, 2017	26.5	0.97	5.02	4,460	1810	203	121	82.3	14.2	32.3	1.08	33.8	179	−3.6	−48.3
September 13, 2017	24.0	1.00	4.76	4,250	1780	199	118	82.2	13.5	30.3	1.03	30.9	175	−3.3	−47.0
October 5, 2017	19.3	0.98	4.79	4,300	1800	204	119	89.0	13.6	31.0	1.01	32.3	177	−3.2	−46.4
[a] October 18, 2017	ND	1.01	4.98	4,450	1830	205	120	93.4	16.7	28.4	1.31	37.5	160	−3.6	−48.5
November 10, 2017	11.7	1.00	4.75	4,200	1800	194	121	87.1	13.9	30.5	1.03	31.3	175	−3.7	−49.0
May 18, 2018	18.6	1.02	4.51	4,220	1,490	189	120	82.4	14.8	27.9	1.17	31.4	152	−4.3	−51.6
June 19, 2018	22.5	1.01	4.54	4,340	1,550	198	129	86.3	14.6	29.2	1.17	32.2	158	−4.0	−50.7
July 9, 2018	24.5	1.03	4.42	4,420	1,610	226	123	92.0	15.3	29.7	1.22	35.3	164	−4.1	−51.6
August 2, 2018	26.8	1.04	4.50	4,360	1,640	214	134	90.9	15.9	30.4	1.15	34.3	181	−3.8	−50.6
October 17, 2018	21.4	1.03	4.35	4,270	1,620	201	122	93.2	13.6	30.1	0.91	29.7	189	−3.6	−49.4
May 24, 2019	18.8	1.10	4.29	4,270	1,420	211	128	84.9	14.6	31.4	1.01	35.0	188	−3.6	−47.0
[b] July 1, 2019	ND	1.05	4.20	4,130	1,420	204	139	89.5	14.5	33.4	0.98	31.3	201	−3.7	−47.9
[c] July 1, 2019	ND	1.05	4.21	4,100	1,410	196	135	85.9	16.0	32.3	0.94	44.0	195	−3.7	−47.9
[d] July 1, 2019	ND	1.04	4.20	4,110	1,410	194	131	84.5	14.2	32.0	0.96	33.2	193	−3.4	−47.3
August 2, 2019	27.1	1.07	4.10	4,070	1,420	219	148	104	15.9	31.7	1.06	33.5	203	−3.8	−49.1
August 26, 2019	26.0	1.06	4.21	4,090	1,460	219	144	99.4	16.7	31.8	1.09	33.2	199	−3.6	−48.2
October 1, 2019	25.0	1.06	4.24	4,160	1,550	231	165	118	20.6	33.4	1.25	38.0	222	−3.0	−46.1

(Continued on following page)

TABLE 2 | (*Continued*) Chemical and isotopic composition of lake water in Yugama crater sampled from November 2005 to May 2021.

Sampling date	Temp. °C	pH	EC S/m	Cl mg/L	SO_4 mg/L	Al mg/L	Ca mg/L	Fe mg/L	K mg/L	Mg mg/L	Mn mg/L	Na mg/L	SiO_2 mg/L	$\delta^{18}O$ ‰	δD ‰
October 16, 2019	ND	1.11	3.86	3,800	1,460	230	164	120	17.7	30.8	1.23	35.9	196	−3.9	−49.7
November 9, 2019	15.4	1.07	3.90	3,850	1,470	234	171	129	17.9	32.7	1.30	38.8	204	−3.7	−49.4
December 3, 2019	ND	1.09	4.03	3,920	1,500	230	174	130	17.1	31.7	1.24	35.4	202	−3.3	−47.8
April 3, 2020	8.3	1.13	3.77	3,790	1,310	206	159	119	15.5	32.2	1.13	34.1	193	−3.8	−49.8
April 30, 2020	14.3	1.16	3.41	3,170	1,100	180	140	102	15.5	28.0	0.94	30.4	169	−4.6	−51.8
[b] May 8, 2020	ND	1.13	3.67	3,900	1,330	222	165	122	16.9	31.3	1.27	36.6	184	−3.9	−49.5
[c] May 8, 2020	ND	1.13	3.67	3,880	1,330	221	163	120	16.7	31.1	1.23	36.3	184	−3.5	−49.3
June 2, 2020	20.8	1.11	3.70	3,830	1,320	225	170	127	16.7	32.4	1.26	35.9	189	−3.7	−49.9
August 11, 2020	26.9	1.13	3.63	3,820	1,350	221	166	129	18.7	31.0	1.29	37.5	190	−3.6	−52.1
September 8, 2020	27.2	1.12	3.79	3,910	1,390	235	173	139	17.2	33.2	1.27	38.5	196	−3.3	−50.0
October 15, 2020	21.5	1.12	3.79	3,990	1,420	243	176	141	17.7	33.9	1.31	39.1	200	−3.3	−49.4
November 5, 2020	16.6	1.13	3.90	4,040	1,420	238	174	142	17.6	33.9	1.32	39.2	199	−2.8	−48.0
[b]November 14, 2020	ND	1.08	3.89	4,110	1,430	240	176	142	17.5	34.2	1.33	38.8	206	−2.9	−47.3
April 20, 2021	13.1	1.11	3.90	4,080	1,270	205	149	104	15.0	32.8	1.06	32.7	197	−3.6	−48.5
April 26, 2021	13.5	1.11	3.85	4,140	1,280	242	169	127	17.2	34.0	1.25	38.9	198	−3.5	−48.8
May 31, 2021	20.3	1.12	3.92	4,070	1,260	227	172	126	17.9	33.9	1.28	40.2	203	−3.4	−47.4

[a]*Data cited from Terada et al. (2018).*
[b]*Water sampled approximately 10 m offshore from the U1 point by using a drone.*
[c]*Water sampled near the center of the crater by using a drone.*
[d]*Water sampled from the discolored area of the crater by using a drone.*

Period 1 (November 2005–February 2014)

Development of the Self-Sealing Zone and its Breach due to Leaching by Deep Circulating Water

During this period, Cl and SO_4 concentrations decreased gradually. Considering the minor seismicity and the cooling of the hydrothermal reservoir inferred by the geomagnetic observation (Takahashi and Fujii, 2014), the supply of magmatic fluids was suppressed due to the development of the self-sealing zone. The gradual decrease in Cl and SO_4 is considered due to dominantly meteoric groundwater circulating in the hydrothermal system only mixing with the residual saline fluids in the deep part of the brittle rock region, and being washed away to the Yugama Crater Lake, with no additional magmatic fluids ascending, as shown in **Figure 6A**. Considering that the cooling of the hydrothermal reservoir in Period 1 has continued since 1996 (**Figure 3**; Kakioka Magnetic Observatory, 2016), self-sealing may have started before this study period.

Nevertheless, the Mg concentration increased from 2006 to 2007 (**Figure 5B**), resulting in an increase in the Mg/Cl ratio (circle "a" in **Figure 7**). At this time, the increase of Al, Ca, and Si was also observed (**Figure 5B**). As Al, Ca, and Si are major components of secondary mineral depositions that constitute the self-sealing zone (e.g., alunite, gypsum/anhydrite or SiO_2) and Mg originates dissolution of crystallizing magma, we believe that two processes occurred in 2006: 1) the breach (dissolution) of the self-sealing zone, and 2) the contact between groundwater and the hot plastic rock region inside the self-sealing zone. However, since the increase in Al, Ca, and Si concentrations were smaller than before and after the 1982–83 eruptive period (**Figure 5B**), the breach of the self-sealing zone in 2006 would have been smaller in scale. Moreover, the region below the brittle-plastic transition has a temperature of about >400°C with low permeability, by referring to the deep well in the Kakkonda geothermal field (Komatsu et al., 1998; Muraoka et al., 1998). The saturated vapor temperature of water at 150 bar is about 340°C; thus, the groundwater that reached the hot plastic rock from the small breached part of the self-sealing zone in 2006 could not invade deeply and abundantly as, otherwise, it would evaporate.

Direct evidence for the presence and mineral species of the self-sealing zone beneath the Yugama Crater Lake has not been revealed by direct drilling, however, ejecta from past phreatic eruptions provide important insights. The abundant phases in eruptive ejecta of Ruapehu Crater Lake (New Zealand), which has repeated phreatic eruptions, are low-temperature SiO_2 polymorphs such as cristobalite, sulfates such as gypsum/anhydrite and alunite, pyrite, and native sulfur (Christenson and Wood, 1993). Especially, native sulfur, alunite, anhydrite, and SiO_2 are considered to be readily precipitated in hydrothermal systems (Christenson et al., 2010). Alunite, gypsum/anhydrite, and SiO_2 polymorphs are also abundant in the ejecta of the 1982–83 eruptions at the Yugama Crater Lake (Ossaka et al., 1984; **Table 3**), supporting the presence of a self-sealing zone and its dissolution to enhance the increase of Al, Ca, and Si concentrations in Yugama Crater Lake. Considering no increase in Cl or SO_4 before or after the increase of the Mg/Cl ratio in 2006, it is unlikely that the injection of magmatic fluids caused the breach of the self-sealing zone at that time. Therefore, we believe that a long period of suppression of magmatic fluids, arguably also due to the presence of the self-sealing zone, allows groundwater to circulate deeply and allows groundwater to leach the mineral deposition of the self-sealing zone and intrusion into the hot plastic rock region (path "i" in **Figure 6B$_I$**). Afterward, the self-

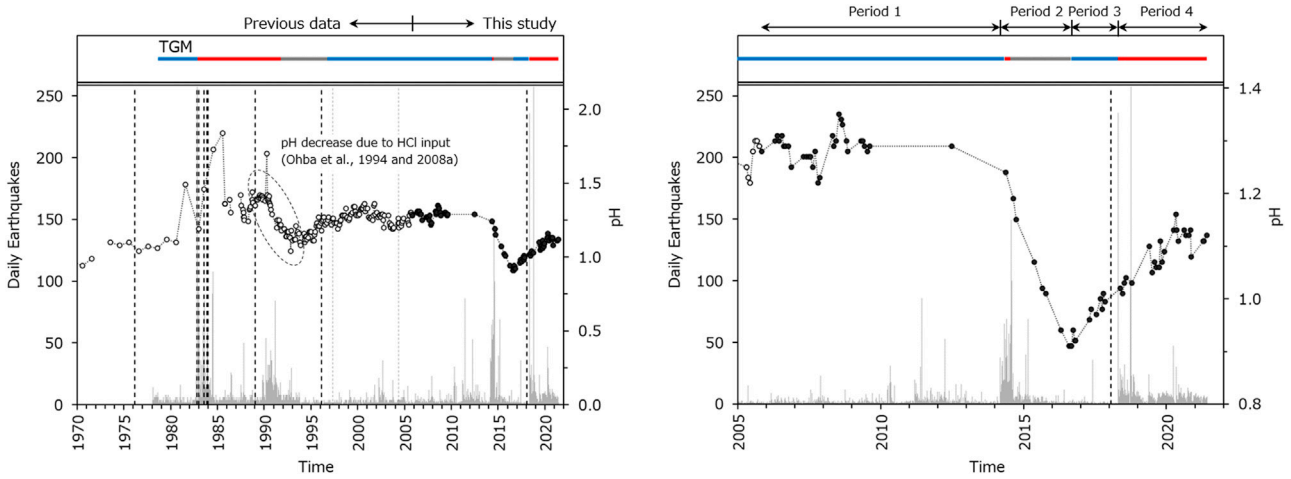

FIGURE 4 | Lake water pH values in Yugama crater. Open and solid circles indicate the previous data since the 1970s (Ohba et al., 2008a) and the present analyses, respectively. TGM and the vertical dashed line show the same as **Figure 3**.

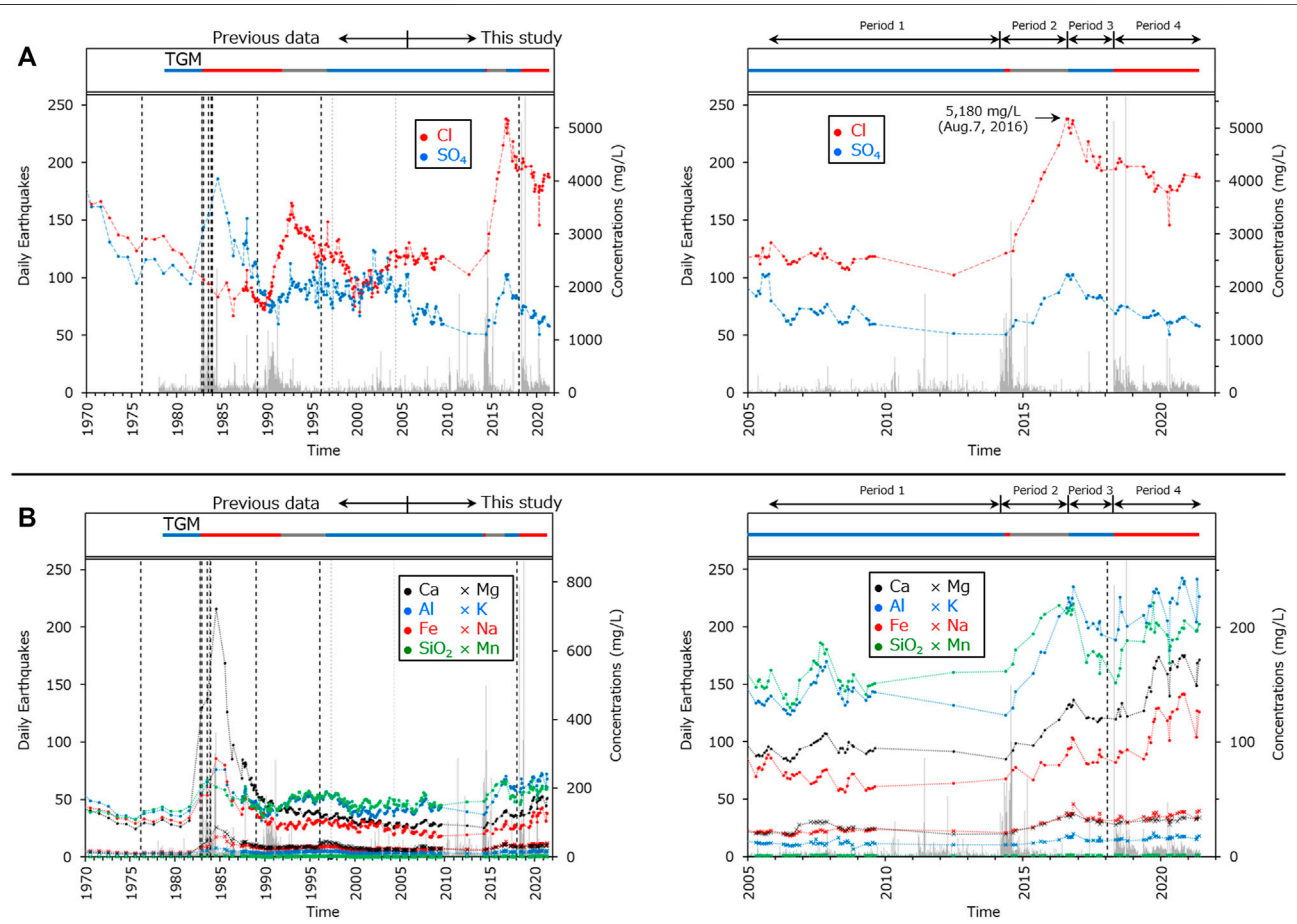

FIGURE 5 | Concentrations of anions **(A)**, cations, and silica **(B)** of lake water in Yugama crater. Data before October 2005 were cited from Ohba et al. (2008a). TGM and the vertical dashed line show the same as **Figure 3**.

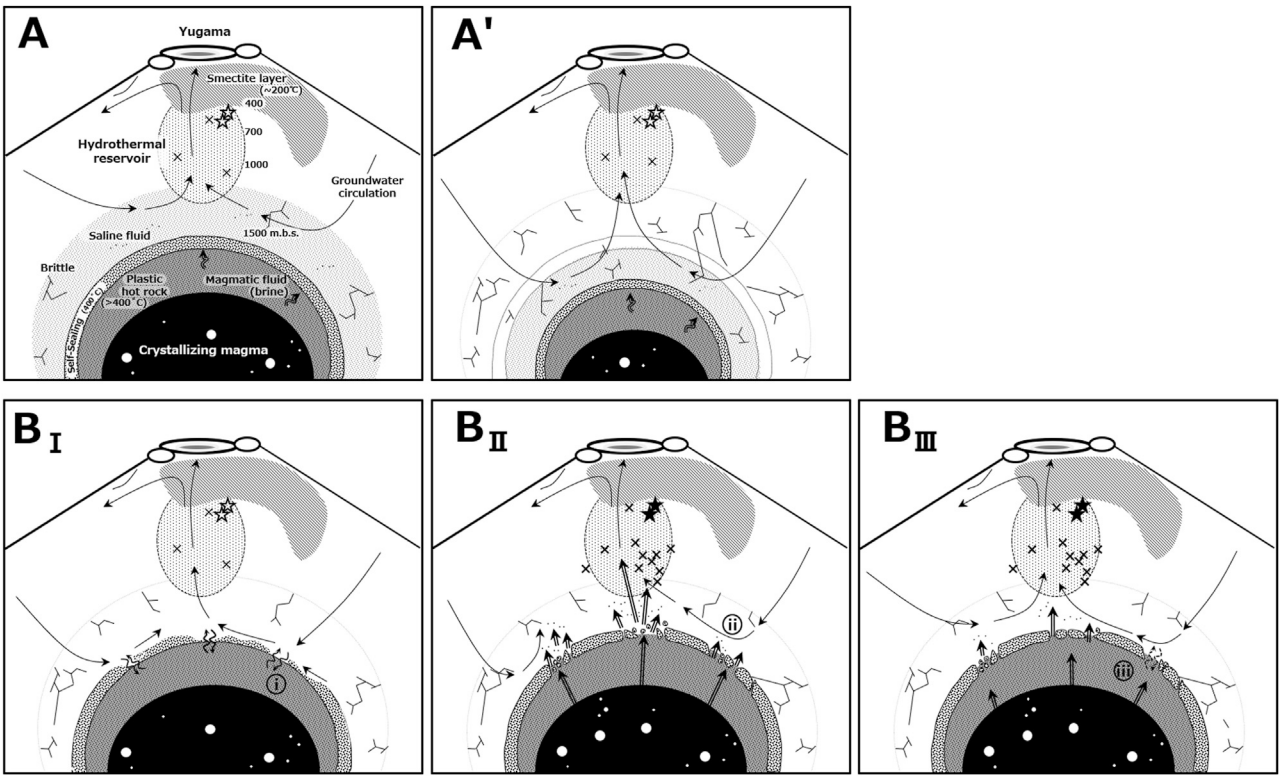

FIGURE 6 | Schematic image for the state of magma–hydrothermal system beneath Yugama Crater Lake modeled after (Giggenbach, 1992a; Fournier, 1999; Ohba et al., 2008a, 2019b). Cross marks indicate simplified earthquake locations. Open and solid stars indicate approximate locations of magnetizations and demagnetizations corresponding to the volcanic events in 1982–2012 (Takahashi and Fujii, 2014), respectively. The cooling magma is surrounded by a hot plastic rock region. A self-sealing zone composed of secondary minerals, such as silica, gypsum/anhydrite, and alunite, separate the hot plastic rock region and the brittle rock region. This boundary plays a role in the advancing front of brittle fracturing. Cl-rich saline fluid expelled from the crystallizing magma remains in the deep part of the brittle region. **(A)** Development of the self-sealing zone suppresses the ascent of magmatic fluid to the hydrothermal reservoir, resulting in the cooling of the reservoir. The groundwater circulation dilutes the remaining Cl in the deep in the brittle region and supplies them to the Yugama crater through the hydrothermal reservoir. **(B)** Breaching phase of the self-sealing zone. **(B_I)**: The groundwater circulation continues to transport Cl with heat from deep to the Yugama crater and deepens the circulation. Continuous deep groundwater circulation causes the leaching of the self-sealing zone, and contacts the hot plastic rock region (path "i"). **(B_{II})**: A significant ascent of magmatic HCl-rich fluid breaches the self-sealing zone. Contact between the groundwater and the hot plastic rock region is not enhanced because the deep circulating groundwater is inhibited by the ascending flow of magmatic fluid (path "ii"). **(B_{III})**: A less intense ascent of magmatic fluid allows groundwater to intrude slightly into the hot plastic rock region (path "iii"). **(A′)** The self-sealing zone regrows, but its location advances toward the depth through repeated breaches and regrowth. Deeper circulation is needed for the contact between groundwater and hot plastic rock.

sealing zone regrew and returned to the state shown in **Figure 6A**, until the end of this period.

Although no eruption occurred at the Yugama Crater Lake in 2006, the above mentioned invasion of groundwater into the brittle magma carapace that envelops the hot plastic rock and the self-sealing zone can trigger hydrothermal destabilization and phreatic eruptions. For example, at the hyperacid crater lake of Poás volcano in Costa Rica, the lake level dropped by about 8 m accompanied by an increase in seismic activity through 1998, followed by, between late 1998 and mid-1999, the opening of cracks in the ground and new fumaroles, and enhanced influx of heat and volatiles into the lake as indicated by the increase in lake water temperature and concentrations of solutes (Martínez, 2008). At Yugama Crater Lake, the water level was high during the eruption and decreased after the eruption in the active period of 1982–83. In particular, after the October 26, 1982 eruption, the first eruption of the 1982–83 series, the water level decreased remarkably, dropping about 7 m, followed by the subsequent eruption on December 29 (Tokyo Institute of Technology and Sophia University, 1983). The high lake level during the eruption is attributed to the discharge pressure of the volcanic fluids, while the decrease after the eruption is attributed to the deep invasion of lake water, mainly through the conduit created by the eruption (Tokyo Institute of Technology and Sophia University, 1983; Ossaka et al., 1984). The lake level rise during the eruption would be similar to that occurred about a year before the first phreatic eruption at Poás in March 2006, which is interpreted as the pushing vapor front (Rouwet et al., 2017). For the period without eruptions, i.e., when there is no open conduit to a deep hydrothermal system, the depth of groundwater invasion or percolation at Kusatsu-Shirane volcano has not yet been evaluated by geochemical or geophysical observations. On the other hand, other volcanoes and geothermal fields in Japan, such as Mt. Fuji and the

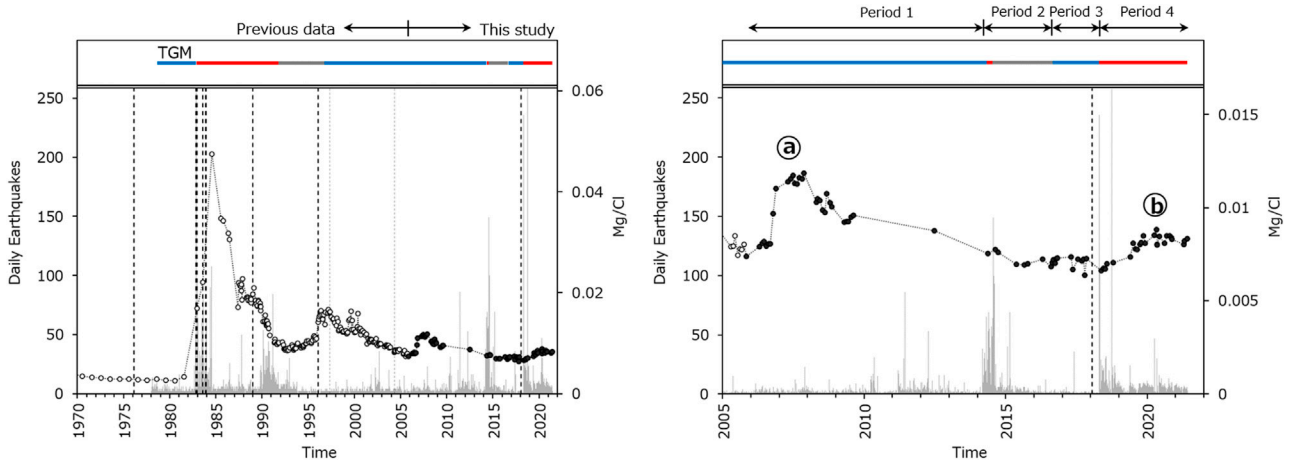

FIGURE 7 | Mg/Cl weight ratio of lake water in Yugama crater. Open and solid circles indicate the previous data since the 1970s (Ohba et al., 2008a) and the present analyses, respectively. TGM and the vertical dashed line show the same as **Figure 3**.

TABLE 3 | Constituent minerals in the ejecta of the 1982–83 eruptions at Yugama Crater Lake (data cited from Ossaka et al. (1984).

Eruption date	Qz	Cr	Tr	Fd	Gy	Ah	Al	Py	Pr	Ka	Mo
October 26, 1982	++	+	+	(+)	++	-	+	++	++	++	++
December 29, 1982	+	+	+	(+)	+++	-	+	++	++	+++	+++
December 29, 1982	++	+	++	-	++	-	+	++	+++	+++	+
December 29, 1982	-	+	+	-	-	+	++	++	++	++	-
July 26, 1983	+	-	+	(+)	++	+	++	++	++	++	+
November 13, 1983	++	+	+	-	+	-	+	++	++	++	++
November 13, 1983	++	+	+	-	+	-	+	++	++	++	++
November 13, 1983	++	+	+	-	+	-	+	++	++	++	(+)
November 13, 1983	++	+	+	-	-	-	+	-	+	++	(+)

Abundance: +++, very abundant; ++, abundant; +, present; -, absent; (+), unidentified.
Qz, Quartz; Cr, Cristobalite; Tr, Tridymite; Fd, Feldspar; Gy, Gypsum; Ah, Anhydrite; Al, Alunite; Py, Pyrite; Pr, Pyrophyllite; Ka, Kaolin; Mo Montmorillonite.

Kakkonda geothermal field, have demonstrated deep groundwater percolation reaching 1,500–3,000 m.b.s. (Saishu et al., 2014; Yaguchi et al., 2016). In the case of a hydrothermal system beneath the Yugama crater, such deep groundwater percolation corresponds to a depth below the self-sealing zone and is sufficient for the groundwater to interact with the mineral deposition of the self-sealing zone, or with the hot plastic rock region.

Period 2 (March 2014–August 2016)

HCl Input Into the Hydrothermal Reservoir

The earthquake swarm in 2014 was accompanied by a significant increase in Cl concentration and a decrease in pH, which is similar to the case of the earthquake swarm in 1990–93 (**Figure 4**) caused by the supply of HCl-rich magmatic fluids from the hot plastic rock region (Ohba et al., 2008a). The state of the magma–hydrothermal system in this period is represented in **Figure 6B$_{II}$**.

To be precise, acidic gases, such as HF, HCl, and sulfur gases likely cause decreases in pH in the crater lake. However, it is difficult to estimate the contribution of each of the acidic gases quantitatively because our analyses (ion chromatography) contain a large uncertainty in the HF concentrations due to an interference by coexisting species. Dissolved SO_4 is also not always representative of the total amount of sulfur gases supplied from magma to the crater lake, as explained above. Moreover, SO_2 is probably already released for being less soluble in magma with respect to HCl and HF. The crystallizing magma is hence relatively rich in HCl with respect to a fresh, less degassed magma (richer in SO_2). This also explains why the pH is not lower at Yugama, as for Poás, White Island or Kawah Ijen for instance. Despite the uncertainty in the contributions of HF and sulfur species, a high correlation was observed between H^+ and Cl concentrations during this study period (**Figure 8**), indicating that the increase in Cl in 2014–16 was caused by the input of HCl-rich fluids to the hydrothermal reservoir. The slope lower than 1 in the regression line (appears to be H^+ poor) is probably the result of the suppression of H^+ activity due to the high ionic strength of the lake water. This is supported by the activity coefficient of H^+ in the ionic strength of the lake water during this study period (0.09–0.17) obtained by using

the extended Debye-Hückel equation resulting in 0.81–0.83, which is very similar to the slope (0.867) of the regression line. These situations were similar to 1990–93; however, the δD and $\delta^{18}O$ of the lake water after the 2014 activity were the highest ever observed (−39.4‰ and −1.7‰ on August 7, 2016, respectively; **Table 2**). We propose that the amount of HCl-rich magmatic fluids in 2014–16 was more significant in magnitude than that in 1990–93. Incidentally, although the main water source of any crater lake is generally meteoric precipitation, Yugama Crater Lake water is more enriched in δD and $\delta^{18}O$ than the local meteoric water, and the $\delta D/\delta^{18}O$ slope is 4.7 (**Figure 9A**). This slope very much resembles the slope of about 5, which typically results from the evaporation of lake water at ambient temperature (e.g., Matsubaya and Sakai, 1978; Rowe, 1994; Balistrieri et al., 2007). According to Ohba et al. (2000), however, this isotopic enrichment mainly results from evaporation, but there is a small contribution of isotopically heavy Cl-rich fluids. This isotopically heavy fluids is a liquid phase separated by boiling of a mixture of local meteoric water and a magmatic fluids rich in Cl. The isotopic enrichment of lake water relative to local meteoric water ($\Delta\delta D$ and $\Delta\delta^{18}O$) can be obtained by subtracting the δ value of local meteoric water (δD_{lmw} = −79.3‰ and $\delta^{18}O_{lmw}$ = −11.8‰; Ohba et al., 2000) from the δ value of lake water (δD_{lake} and $\delta^{18}O_{lake}$). For example, the Δδ values on August 7, 2016, are calculated as $\Delta\delta D$ = +39.9‰ and $\Delta\delta^{18}O$ = +10.1‰. On the other hand, the isotope enrichment of lake water by the addition of isotopically heavy Cl-rich fluids ($\Delta\delta D_{Cl}$ and $\Delta\delta^{18}O_{Cl}$) can be estimated by multiplying the Cl concentration (mg/L) of the lake water by the coefficients, 2.10×10^{-3} for δD and 5.16×10^{-4} for $\delta^{18}O$ (see Ohba et al., 2000 for more details). Based on this simple calculation, it is estimated that the $\Delta\delta D_{Cl}$ = +10.9‰ and $\Delta\delta^{18}O_{Cl}$ = +2.7‰, which account for 27.3 and 26.7% of ΔD and $\Delta^{18}O$, respectively. The contributions of the addition of isotopically heavy Cl-rich fluids to total isotope enrichment calculated in this way were 21–32% (average in δD and $\delta^{18}O$) throughout the present study period, which is not significantly different from the period 1990–93 (**Figure 9B**). In other words, although there is isotope enrichment by addition of Cl-rich fluids, the heavy isotope ratio of lake water relative to local meteoric water is mainly due to evaporative enrichment even during this study period.

Self-Sealing Zone Breach due to Magmatic Fluids Ascend

In addition to Cl and SO_4, the concentrations of rock-forming species increased, especially Ca, Al, Fe, and Si (**Figure 5**). As mentioned above, these species are probably derived from the secondary mineral deposition. The increases in these components suggest that a breach (dissolution) of the self-sealing zone occurred corresponding to the earthquake swarm in 2014. However, we believe that the breaching process was different than the one in 2006.

The significant increase in Cl suggests that the breach of the self-sealing zone in 2014 was caused by an internal pressurization due to the Cl-rich fluids accumulation or injection from depth. The deep deformation source pressurized in 2013–2015 (at a depth of 6.3 km and 2 km northwest of the Yugama Crater Lake; Munekane, 2021) may not be a direct source of Cl because the HCl should remain dissolved in the magma at this depth (e.g., Christopher et al., 2015), but may have induced the supply of Cl-rich magma fluids from the crystallizing magma. During this period, there were no obvious increases in the Mg/Cl ratio despite the breach of the self-sealing zone (**Figure 7**). This implies that the ascending of the Cl-rich magmatic fluids from inside the self-sealing zone through the breached section inhibited the deep circulation of the groundwater; as a result, the groundwater could not intrude into the hot plastic rock region inside the self-sealing zone (path "ii" in **Figure 6B$_{II}$**).

All eruptions at the Yugama crater since 1982 were accompanied by an increase in the Mg/Cl ratio during a decrease in Cl concentration (**Figure 5A**). In contrast, neither eruptions nor increases in Mg/Cl ratio occurred in 1990 and 2014, when a significant HCl input occurred (**Figure 7**). This means that the contact between groundwater and the hot plastic rocks has played an important role in triggering phreatic eruptions at the Yugama crater since 1982, rather than the magmatic fluids input to the hydrothermal reservoir. In other words, fresh magma or actively degassing volcanic systems are not necessarily required to trigger phreatic eruptions. The water temperature in the Yugama Crater Lake has remained relatively cold for decades, although it once reached 55.5°C just after the eruption in 1982 (Tokyo Institute of Technology et al., 1983), compared to the hyperacid lake of Poás volcano (up to 94°C; Rowe, 1994), where magmatic or phreatomagmatic eruptions occur. This seems to support the idea that the contact between groundwater and the hot

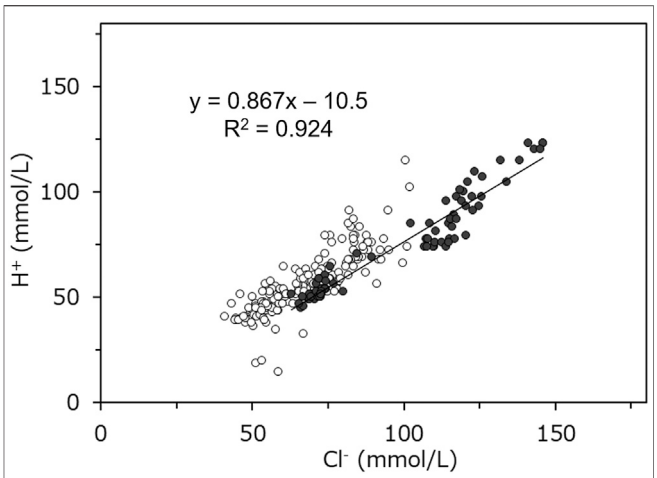

FIGURE 8 | Relationship between H^+ and Cl concentrations. H^+ concentrations were calculated as $[H^+] = 10^{-pH}$. Open and solid circles indicate the previous data since the 1970s (Ohba et al., 2008a) and the present analyses, respectively. The regression line is calculated for the lake water during this study period (November 2005 to May 2021; **Table 2**).

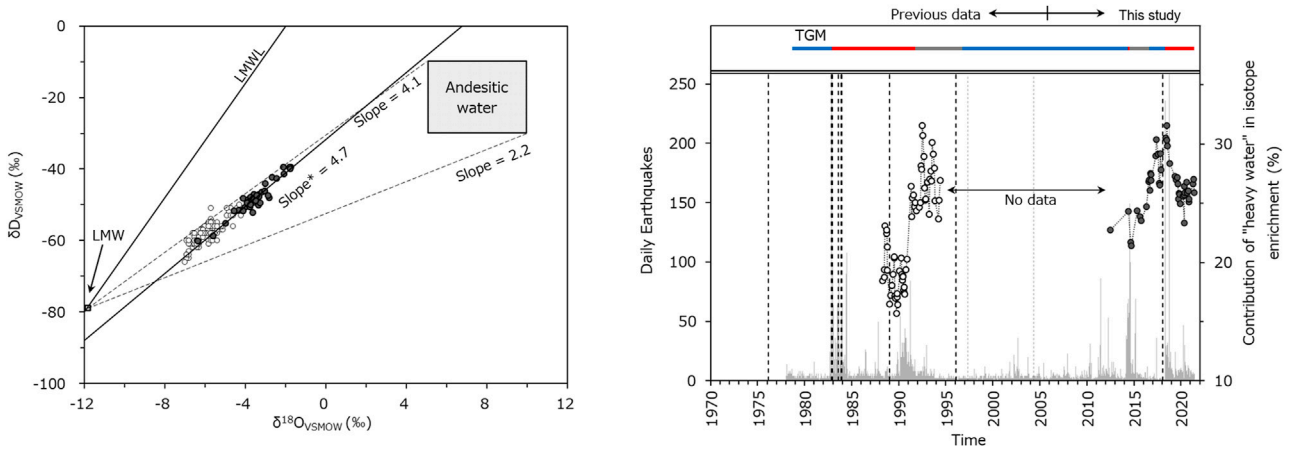

FIGURE 9 | (A) δD vs. $\delta^{18}O$ plot for lake water in Yugama crater. The "andesitic water" field (δD = −10 to −30‰, $\delta^{18}O$ = +5 to +10‰; Taran et al., 1989; Giggenbach., 1992b), local meteoric water (LMW, δD = −79‰, $\delta^{18}O$ = −11.8‰; Ohba et al., 2000), and the local meteoric water line (LMWL, δD = 8 $\delta^{18}O$ + 16; Ohwada et al., 2003) are also shown. *The δD/$\delta^{18}O$ slope (4.7) for the lake water during this study period. **(B)** The contribution of "heavy water" addition in the isotopic enrichment of lake water (average in δD and $\delta^{18}O$). Open and solid circles indicate the previous data (available from 1988 to 1996; Ohba et al., 2000) and the present analyses, respectively.

plastic rocks, which triggered the recent phreatic eruptions at Yugama Crater Lake, was not caused by magma intrusion, or magma intrusions at Yugama Crater Lake might be fairly small in volume with no critical mass to destabilize the hydrothermal system and trigger eruptions.

Period 3 (September 2016–March 2018)

Regrowth of the Self-Sealing Zone

The changes in water chemistry in the Yugama Crater Lake during this period are characterized by an increase (recovering) in pH and a general decrease in the concentrations of various components (**Figures 4**, **5**). Considering the low seismic activity and cooling in the hydrothermal reservoir suggested by the magnetizing trend, we suggest that the self-sealing zone was redeveloped during this recovery period, leading to the suppression of the ascending magmatic fluids to the Yugama crater (**Figure 6A**). According to the volcanic gas study (Ohba et al., 2019b), the redevelopment of the self-sealing zone has been suggested as the decrease in the fraction of magmatic components in the volcanic gas around the Yugama Crater Lake from April 2016 to November 2017, which is consistent with the interpretation of the present study. This situation is similar to Period 1, but because this period ended rapidly, the state of the magma–hydrothermal system did not move from the dynamics exposed in **Figures 6A–6B$_I$**, as in Period 1.

Period 4 (April 2018–May 2021)

Intermittent Breaching of the Self-Sealing Zone due to Less Intense Ascent of Magmatic Fluids

Increases in Ca, Al, Fe, Si, and Cl, an earthquake swarm, and a repressurizing of the deep source (Munekane, 2021) were observed. Based on the similarity to the event in 2014, we believe that the magmatic fluid intermittently breached the self-sealing zone, causing repeated injections of the magmatic fluid to the Yugama crater. Although the number of daily earthquakes in 2018 (324 earthquakes on September 29) is larger than that in 2014 (149 on July 24), the lake water temperature, Cl concentration, δD, and $\delta^{18}O$ values since 2018 are lower than those observed in 2014 (**Figure 5**; **Table 2**). The amount of magmatic fluids supply in 2018–21 was probably smaller than in 2014–16, which is consistent with the slight increase in the Mg/Cl ratio in 2018 (circle "b" in **Figure 7**). Because of the less intense discharge of magmatic fluids from the self-sealing zone, groundwater intruded into the hot plastic rock region inside the self-sealing zone, allowing the transport of Mg to the Yugama crater (path "iii" in **Figure 6B$_{III}$**).

Aging of Crystallizing Magma

Although we should be cautious because the total amount of S was not analyzed in this study, the long-term SO_4/Cl molar ratio fluctuates along a general decreasing trend (**Figure 10A**). Sulfur is one of the major volatiles in magma, but the magma becomes relatively S-poor, Cl-rich as degassing progresses because SO_2 is less soluble than HCl (Giggenbach, 1996). The decrease in the S/Cl ratio with progressive degassing has been demonstrated in volcanic gases. At Unzen volcano in Japan, where magmatic eruptions occurred from 1991 to 1996, the S/Cl ratio of volcanic gases collected from the cooling lava dome after the eruption (Shinohara et al., 2008) was lower than the S/Cl ratio detected during the eruption (Ohba et al., 2008b). Therefore, the long-term decrease in the S/Cl ratio in the lake water may indicate that the crystallizing magma beneath the Yugama crater is gradually becoming S-depleted due to the progress of degassing. On the other hand, the lake water analyzed in this study has a lower SO_4 concentration and a higher Cl concentration than in the previous studies (before November 2005; **Figure 10B**), indicating that the decreasing trend of the SO_4/Cl ratio of the lake water is not only due to sulfur depletion but also to the

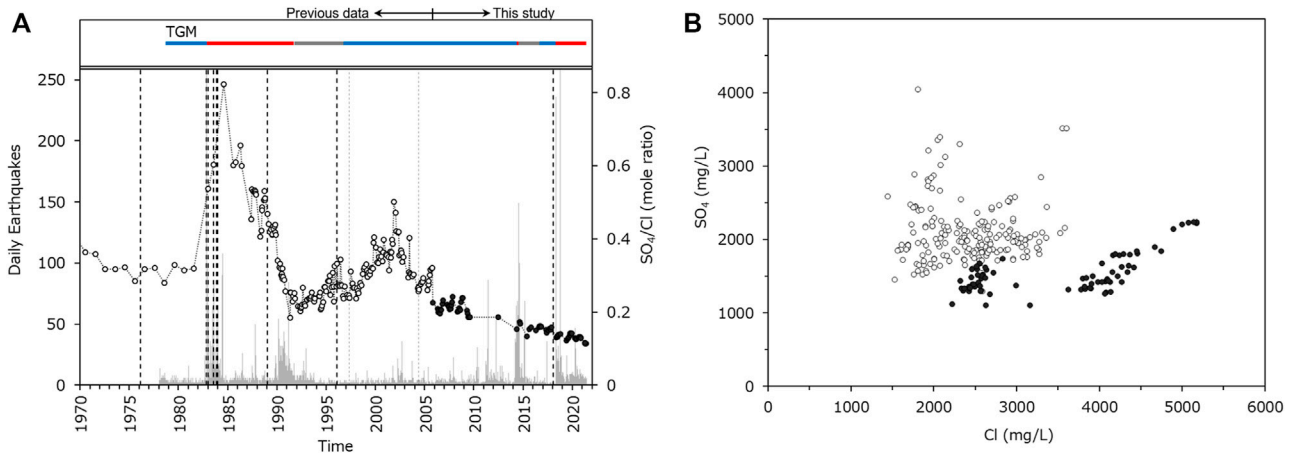

FIGURE 10 | (A) The SO_4/Cl mole ratio of lake water in Yugama crater. Data before October 2005 were cited from Ohba et al. (2008a). TGM and the vertical dashed line show the same as **Figure 3**. **(B)** SO_4 vs. Cl plot for lake water in Yugama crater. Open and solid circles indicate the previous data since the 1970s (Ohba et al., 2008a) and the present analyses, respectively.

increase in Cl concentration. According to Bodnar (1992), the salinity of brine exsolving from a magma crystallizing below 1.3 kbar is initially low, but it continues to increase as the magma crystallizes and eventually exceeds 50 wt%. That is, the increase in Cl concentration can be interpreted as being caused by the progress of magma crystallization, and this is responsible for the decrease in the SO_4/Cl ratio of the lake water along with the sulfur depletion.

In addition, it is interesting that the peak value of the Mg/Cl ratio in Yugama Crater Lake decreases with age (**Figure 7**). We believe that the hot plastic rock region may be shrinking during the repeated cycles of breach and regrowth of the self-sealing zone (**Figure 6A′**). However, this hypothesis does not guarantee that the SO_4/Cl and Mg/Cl ratios in the Yugama crater will continue to decrease in the future. If new magma intrusions, extrusions, or exposures of hot plastic rock regions occur in the future, these indicators should be refreshed. Therefore, lake water monitoring should continue. Also, phreatic eruptions triggered by other mechanisms, such as eruptions involving the self-sealing of the liquid sulfur pool at the lake bottom (Rouwet and Morrissey, 2015; Rouwet et al., 2017), should be focused on for future safety and research because a molten sulfur pool has been found at the bottom of the Yugama Crater Lake.

CONCLUSION

Water samples collected from Yugama Crater Lake at Kusatsu-Shirane volcano were analyzed from November 2005 to May 2021 to discuss the magma–hydrothermal interaction beneath this crater lake and a key mechanism for the recent eruptions at this crater. The conclusions drawn are summarized as follows.

1) The magma beneath the Yugama crater supplies HCl-rich fluid to the lake through the hydrothermal reservoir. The long-term SO_4/Cl ratio in Yugama Crater Lake is decreasing, which may reflect the chemical evolution of magmatic fluid due to the degassing process of crystallizing magma.
2) Suppression of magmatic fluids due to the development of the self-sealing zone surrounding degassing magma was estimated from 2005 to 2012 because Cl and SO_4 concentrations in lake water decreased slowly during this period. On the other hand, increases in certain rock-forming species, including Ca, Si, and Al, as well as in the Mg/Cl ratio were observed from 2006 to 2007. This is because the suppression of ascending magmatic fluids due to the developed self-sealing zone led to the deep circulation of groundwater, the chemical and arguably physical leaching of the self-sealing zone, and, eventually, the contact with the hot plastic rock region.
3) An input of magmatic fluid to the hydrothermal reservoir breaching the self-sealing zone was estimated in 2014 because a significant increase in Cl concentrations and those of certain solute metal species indicating the leaching of the self-sealing zone, such as Ca, Al, Fe, and Si, were observed in lake water. At this time, the Mg/Cl ratio of the lake water did not increase because the ascending magmatic fluid inhibited the deep intrusion of groundwater into the hot plastic rock region.
4) The input of magmatic fluid through the self-sealing zone was repeated in 2018, 2019, and 2020 on a smaller scale than after the 2014 earthquakes, shown by only slight increases in the Mg/Cl ratio, suggesting the less intense ascend of magmatic fluid, allowing deep groundwater intrusion to the hot plastic rock region.
5) The δD and $\delta^{18}O$ of the waters in the Yugama crater lake are enriched relative to the local meteoric water. This is mainly due to evaporation effects, but magmatic fluid input accounts for 21–32% (average in δD and $\delta^{18}O$) of the total isotopic

enrichment relative to local meteoric water throughout the present study period.

6) The contact between the groundwater and the hot plastic rock played an essential role in the mechanism of the eruptions that occurred at the Yugama crater after 1982, rather than the input of magmatic gas itself. This is because these eruptions were always accompanied by an increase in the Mg concentration and the Mg/Cl ratio, and they occurred during a decrease in the Cl concentration, while the Mg/Cl ratio did not increase and no eruptions occurred during the 1990 and 2014 unrest when there were significant HCl supplies to the Yugama crater.

Our study demonstrates that, in contrast to more actively degassing volcanic systems which are involved in the eruptions at hyperacid crater lakes, such as Poás and Kawah Ijen, phreatic eruptions can potentially occur without clear signs of new magma intrusions, but also during stages of cooling of relatively degassed magmas.

DATA AVAILABILITY STATEMENT

The original contributions presented in the study are included in the article/Supplementary Material, further inquiries can be directed to the corresponding author.

AUTHOR CONTRIBUTIONS

MY drafted the manuscript. MY and TO sampled lake water by using a ladle and then analyzed the samples. AT sampled lake water by using a ladle and a drone. All authors read and approved the final manuscript.

FUNDING

This study was supported by ERI JURP (2020-KOBO11, 2019-Y-volcano5, 2018-Y-volcano4, 2017-Y-volcano4) in Earthquake Research Institute, the University of Tokyo, and the Japanese Ministry of Education, Culture, Sports, Science and Technology, under grant of the Integrated Program for Next Generation Volcano Research and Human Resource Development 2016 to 2021.

ACKNOWLEDGMENTS

We wish to express our sincere appreciation to S. Matsusue of JMA for providing the information on daily earthquakes and the funders for their financial support of this study, the two reviewers (YT and MM), the handling editor (DR), and the chief editor (Valerio Acocella) for their efforts in reviewing and providing constructive comments to improve the manuscript.

REFERENCES

Badrudin, M. (1994). Kelut Volcano Monitoring: Hazards, Mitigation and Changes in Water Chemistry Prior to the 1990 Eruption. *Geochem. J.* 28, 233–241. doi:10.2343/geochemj.28.233

Balistrieri, L. I., Shanks, W. C., Cuhel, R. L., Aguilar, C., and Klump, J. V. (2007). "The Influence of Sublacustrine Hydrothermal Vent Fluids on the Geochemistry of Yellowstone Lake," in *Integrated Geoscience Studies In the Greater Yellowstone Area—Volcanic, Tectonic, and Hydrothermal Processes In the Yellowstone Geoecosystem*. Editor L. A. Morgan (Reston, Virginia: U.S. Geological Survey), 169–199.

Barberi, F., Bertagnini, A., Landi, P., and Principe, C. (1992). A Review on Phreatic Eruptions and Their Precursors. *J. Volcanology Geothermal Res.* 52, 231–246. doi:10.1016/0377-0273(92)90046-G

Bernard, A., and Mazot, A. (2004). "Geochemical Evolution of the Young Crater lake of Kelud Volcano in Indonesia," in *Water-Rock Interaction (WRI-11)*. Editors R. B. Wanty and R. R. Seal (Leiden; New York: A.A. Balkema), 87–90.

Bodnar, R. J. (1992). Can We Recognize Magmatic Fluid Inclusions in Fossil Systems Based on Room-Temperature Phase Relations and Microthermometric Behavior? *Rept. Geol. Surv. Jpn.* 279, 26–30.

Browne, P. R. L., and Lawless, J. V. (2001). Characteristics of Hydrothermal Eruptions, with Examples from New Zealand and Elsewhere. *Earth-Science Rev.* 52, 299–331. doi:10.1016/S0012-8252(00)00030-1

Caudron, C., Lecocq, T., Syahbana, D. K., McCausland, W., Watlet, A., Camelbeeck, T., et al. (2015). Stress and Mass Changes at a "wet" Volcano: Example during the 2011-2012 Volcanic Unrest at Kawah Ijen Volcano (Indonesia). *J. Geophys. Res. Solid Earth* 120, 5117–5134. doi:10.1002/2014JB011590

Christenson, B. W., Reyes, A. G., Young, R., Moebis, A., Sherburn, S., Cole-Baker, J., et al. (2010). Cyclic Processes and Factors Leading to Phreatic Eruption Events: Insights from the 25 September 2007 Eruption through Ruapehu Crater Lake, New Zealand. *J. Volcanology Geothermal Res.* 191, 15–32. doi:10.1016/j.jvolgeores.2010.01.008

Christenson, B. W., and Wood, C. P. (1993). Evolution of a Vent-Hosted Hydrothermal System beneath Ruapehu Crater Lake, New Zealand. *Bull. Volcanol.* 55, 547–565. doi:10.1007/BF00301808

Christopher, T. E., Blundy, J., Cashman, K., Cole, P., Edmonds, M., Smith, P. J., et al. (2015). Crustal-scale Degassing Due to Magma System Destabilization and Magma-Gas Decoupling at Soufrière Hills Volcano, Montserrat. *Geochem. Geophys. Geosyst.* 16, 2797–2811. doi:10.1002/2015GC005791

Fournier, R. O. (1999). Hydrothermal Processes Related to Movement of Fluid from Plastic into Brittle Rock in the Magmatic-Epithermal Environment. *Econ. Geol.* 94, 1193–1211. doi:10.2113/gsecongeo.94.8.1193

Giggenbach, W. F. (1996). "Chemical Composition of Volcanic Gases," in *Monitoring And Mitigation Of Volcano Hazards*. Editors R. Scarpa and R. I. Tilling (Berlin: Springer), 221–256. doi:10.1007/978-3-642-80087-0_7

Giggenbach, W. F., and Glover, R. B. (1975). The Use of Chemical Indicators in the Surveillance of Volcanic Activity Affecting the Crater Lake on Mt Ruapehu, New Zealand. *Bull. Volcanol.* 39, 70–81. doi:10.1007/BF02596947

Giggenbach, W. F. (1992b). Isotopic Shifts in Waters from Geothermal and Volcanic Systems along Convergent Plate Boundaries and Their Origin. *Earth Planet. Sci. Lett.* 113, 495–510. doi:10.1016/0012-821X(92)90127-H

Giggenbach, W. F. (1992a). Magma Degassing and Mineral Deposition in Hydrothermal Systems along Convergent Plate Boundaries. *Econ. Geol.* 87, 1927–1944. doi:10.5382/SP.10.01

Hayakawa, Y., and Yui, M. (1989). Eruptive History of the Kusatsu Shirane Volcano. *Daiyonki-kenkyu* 28, 1–17. doi:10.4116/jaqua.28.1

Hedenquist, J. W., and Henley, R. W. (1985). Hydrothermal Eruptions in the Waiotapu Geothermal System, New Zealand; Their Origin, Associated Breccias, and Relation to Precious Metal Mineralization. *Econ. Geol.* 80, 1640–1668. doi:10.2113/gsecongeo.80.6.1640

Ida, Y., Osada, N., Sawada, M., Koyama, E., and Kagiyama, T. (1989). Seismological Study Based on Recently Installed Permanent Stations and a Small Eruptive Event on January 6, 1989 at Kusatsu-Shirane Volcano. *Bull. Earthq. Res. Inst. Univ. Tokyo* 64, 325–345. doi:10.15083/0000032805

Ishizaki, Y., Nigorikawa, A., Kametani, N., Yoshimoto, M., and Terada, A. (2020). Geology and Eruption History of the Motoshirane Pyroclastic Cone Group, Kusatsu-Shirane Volcano, central Japan. *Jour. Geol. Soc. Jpn.* 126, 473–491. doi:10.5575/geosoc.2020.0022

Japan Meteorological Agency (2013). "Kusatsu-Shiranesan," in *National Catalogue of the Active Volcanoes in Japan*. 4th Edition (Tokyo: Japan Meteorological Agency), 44645–44672. Available at: https://www.data.jma.go.jp/svd/vois/data/tokyo/STOCK/souran_eng/volcanoes/044_kusatsu-shiranesan.pdf (Accessed July 14, 2021).

Japan Meteorological Agency (2021). Seismology and Volcanology Department, JMA. Available at: http://www.jma.go.jp/jma/press/2106/30a/yochiren210630_1.pdf (Accessed July 14, 2021).

Japan Meteorological Agency (2018). Volcanic Activity of Kusatsu-Shiranesan Volcano (January 2017–June 8, 2017). *Rep. Coord. Comm. Predict. Volcan. Eruption* 127, 53–68. (in Japanese).

Japan Meteorological Agency (2019). Volcanic Activity of Kusatsu-Shiranesan Volcano (October 2018–January 2019). *Rep. Coord. Comm. Predict. Volcan. Eruption* 132, 67–92. (in Japanese).

Kakioka Magnetic Observatory, JMA (2016). Variation of Geomagnetic Total Intensity at Kusatsu-Shirane Volcano. *Rep. Coord. Commit. Pred. Volc. Eruption* 118, 22–23. (in Japanese).

Kakioka Magnetic Observatory, JMA (2019). Variation of Geomagnetic Total Intensity at Kusatsu-Shirane Volcano. *Rep. Coord. Commit. Pred. Volc. Eruption* 132, 93–96. (in Japanese).

Kametani, N., Ishizaki, Y., Katsuoka, N., Yoshimoto, M., and Terada, A. (2021). Eruption Styles and Ages of the Shirane-Minami Crater Chain and the Yumi-Ike Maar on the Southern Foot of the Shirane Pyroclastic Cone Group, Kusatsu-Shirane Volcano, Central Japan. *Bull. Volcanol. Soc. Jpn.* 66, 1–19. doi:10.18940/kazan.66.1_1

Kaneko, T., Shimizu, S., and Itaya, T. (1991). K-ar Ages of the Quaternary Volcanoes in the Shin-Etsu highland Area, central Japan, and Their Formation History. *Bull. Earthq. Res. Inst. Univ. Tokyo* 66, 299–332. doi:10.15083/0000032764

Kasai, K., Sakagawa, Y., Komatsu, R., Sasaki, M., Akaku, K., and Uchida, T. (1998). The Origin of Hypersaline Liquid in the Quaternary Kakkonda Granite, Sampled from Well WD-1a, Kakkonda Geothermal System, Japan. *Geothermics* 27, 631–645. doi:10.1016/S0375-6505(98)00037-6

Komatsu, R., Ikeuchi, K., Doi, N., Sasaki, M., Uchida, T., and Sasada, M. (1998). Characteristics of the Quaternary Kakkonda Granite and Geothermal System Clarified by Fluid Inclusion Study of Deep Investigation Well, Kakkonda, Japan. *J. Geotherm. Res. Soc. Jpn.* 20, 209–224. doi:10.11367/grsj1979.20.209

Kusatsu-Shirane Volcano Observatory, Tokyo Institute of Technology (2021). "Crustal Deformation Around the Yugama Crater of Kusatsu Shirane Volcano*," in *The 148th Coordinating Committee for Prediction of Volcanic Eruption: Part 1–1 Kusatsu-Shirane Volcano* (Tokyo: Japan Meteorological Agency), 19–20.

Kusatsu-Shirane Volcano Observatory, Tokyo Institute of Technology (1996). The Activity on February, 1996 of Kusatsu-Shirane Volcano. *Rep. Coord. Commit. Pred. Volc. Eruption* 65, 29–32. (in Japanese).

Kusatsu-Shirane Volcano Observatory, Tokyo Institute of Technology (1997). The Occurrence of Sudden Gas Jet and Water Dome at Yugama Crater on 2nd May, 1997. *Rep. Coord. Commit. Pred. Volc. Eruption* 68, 33–34. (in Japanese).

Mannen, K., Roman, D., Leonard, G., Prejean, S., and Nakagawa, M. (2019). Special Issue "Towards Forecasting Phreatic Eruptions: Examples from Hakone Volcano and Some Global Equivalents". *Earth Planets Space* 71, 91. doi:10.1186/s40623-019-1068-9

Martínez, M., Fernández, E., Valdés, J., Barboza, V., Van derLaat, R., Duarte, E., et al. (2000). Chemical Evolution and Volcanic Activity of the Active Crater lake of Poás Volcano, Costa Rica, 1993-1997. *J. Volcanol. Geotherm. Res.* 97, 127–141. doi:10.1016/S0377-0273(99)00165-1

Martínez, M. (2008). *Geochemical Evolution of the Acid Crater lake of Poás Volcano (Costa Rica): Insights into Volcanic-Hydrothermal Processes*. Netherlands (Utrecht): Universiteit Utrecht. Ph.D. thesis.

Martínez, M., van Bergen, M. J., Takano, B., Fernández-Soto, E., and Barquero-Hernández, J. (2019). "Behaviour of Polythionates in the Acid Lake of Poás Volcano: Insights into Changes in the Magmatic-Hydrothermal Regime and Subaqueous Input of Volatiles," in *Poás Volcano, Active Volcanoes of the World*. Editors F. Tassi, O. Vaselli, and R. Mora-Amador (Cham: Springer), 155–202. doi:10.1007/978-3-319-02156-0_7

Mastin, L. G. (1995). Thermodynamics of Gas and Steam-Blast Eruptions. *Bull. Volcanol.* 57, 85–98. doi:10.1007/BF00301399

Matsubaya, O., and Sakai, H. (1978). D/H and 18O/16O Fractionation Factors in Evaporation of Water at 60 and 80.DEG.C. *Geochem. J.* 12, 121–126. doi:10.2343/geochemj.12.121

Matsunaga, Y., Kanda, W., Takakura, S., Koyama, T., Saito, Z., Seki, K., et al. (2020). Magmatic Hydrothermal System Inferred from the Resistivity Structure of Kusatsu-Shirane Volcano. *J. Volcanology Geothermal Res.* 390, 106742. doi:10.1016/j.jvolgeores.2019.106742

Munekane, H. (2021). Modeling Long-Term Volcanic Deformation at Kusatsu-Shirane and Asama Volcanoes, Japan, Using the GNSS Coordinate Time Series. *Earth Planets Space* 73, 192. doi:10.1186/s40623-021-01512-2

Muraoka, H., Uchida, T., Sasada, M., Yagi, M., Akaku, K., Sasaki, M., et al. (1998). Deep Geothermal Resources Survey Program: Igneous, Metamorphic and Hydrothermal Processes in a Well Encountering 500°C at 3729 M Depth, Kakkonda, japan. *Geothermics* 27, 507–534. doi:10.1016/S0375-6505(98)00031-5

Nurhasan, N., Ogawa, Y., Ujihara, N., Tank, S. B., Honkura, Y., Onizawa, S. y., et al. (2006). Two Electrical Conductors beneath Kusatsu-Shirane Volcano, Japan, Imaged by Audiomagnetotellurics, and Their Implications for the Hydrothermal System. *Earth Planet Space* 58, 1053–1059. doi:10.1186/BF03352610

Ogawa, Y., Aoyama, H., Yamamoto, M., Tsutsui, T., Terada, A., Ohkura, T., et al. (2018). Comprehensive Survey of 2018 Kusatsu-Shirane Eruption. *Proc. Symp. Natural Disaster Sciences* 55, 25–30. (in Japanese).

Ohba, T., Hirabayashi, J.-i., Nogami, K., Kusakabe, M., and Yoshida, M. (2008b). Magma Degassing Process during the Eruption of Mt. Unzen, Japan in 1991 to 1995: Modeling with the Chemical Composition of Volcanic Gas. *J. Volcanology Geothermal Res.* 175, 120–132. doi:10.1016/j.jvolgeores.2008.03.040

Ohba, T., Hirabayashi, J.-i., and Nogami, K. (2008a). Temporal Changes in the Chemistry of lake Water within Yugama Crater, Kusatsu-Shirane Volcano, Japan: Implications for the Evolution of the Magmatic Hydrothermal System. *J. Volcanology Geothermal Res.* 178, 131–144. doi:10.1016/j.jvolgeores.2008.06.015

Ohba, T., Hirabayashi, J.-i., and Nogami, K. (1994). Water, Heat and Chloride Budgets of the Crater lake, Yugama at Kusatsu-Shirane Volcano, Japan. *Geochem. J.* 28, 217–231. doi:10.2343/geochemj.28.217

Ohba, T., Hirabayashi, J., and Nogami, K. (2000). D/H and 18 O/16 O Ratios of Water in the Crater lake at Kusatsu-Shirane Volcano, Japan. *J. Volcanology Geothermal Res.* 97, 329–346. doi:10.1016/S0377-0273(99)00169-9

Ohba, T., Yaguchi, M., Nishino, K., Numanami, N., Daita, Y., Sukigara, C., et al. (2019a). Time Variations in the Chemical and Isotopic Composition of Fumarolic Gases at Hakone Volcano, Honshu Island, Japan, over the Earthquake Swarm and Eruption in 2015, Interpreted by Magma Sealing Model. *Earth Planets Space* 71, 48. doi:10.1186/s40623-019-1027-5

Ohba, T., Yaguchi, M., Nishino, K., Numanami, N., Tsunogai, U., Ito, M., et al. (2019b). Time Variation in the Chemical and Isotopic Composition of Fumarolic Gasses at Kusatsu-Shirane Volcano, Japan. *Front. Earth Sci.* 7, 249. doi:10.3389/feart.2019.00249

Ohchi, K. (1987). Observation of the Geomagnetic Total Force at Kusatsu-Shirane Volcano. *Mem. Kakioka Mag. Obs.* 22, 1–9.

Ohwada, M., Ohba, T., Hirabayashi, J.-i., Nogami, K., Nakamura, K., and Nagao, K. (2003). Interaction between Magmatic Fluid and Meteoric Water, Inferred from 18O/16O and 36Ar/H2O Ratios of Fumarolic Gases at the Kusatsu Shirane Volcano, Japan. *Earth Planet Space* 55, 105–110. doi:10.1186/BF03351737

Ossaka, J., Hirabayashi, J., and Ozawa, T. (1984). "The Activity of Kusatsu-Shirane Volcano in Recent Years and Geochemical Study*," in *Fundamental Research for Predicting Volcanic Eruption through Observation of Volcanic Gases*. Editor J. Ossaka (Japan: Ministry of Education), 96–112.

Rouwet, D., Mora Amador, R. A., Sandri, L., Ramírez-UmañaGonzález, C. G., González, G., Pecoraino, G., et al. (2019). "39 Years of Geochemical Monitoring of Laguna Caliente Crater Lake, Poás: Patterns from the Past as Keys for the Future," in *Poás Volcano, Active Volcanoes of the World*. Editors F. Tassi,

O. Vaselli, and R. Mora-Amador (Cham: Springer), 213–233. doi:10.1007/978-3-319-02156-0_9

Rouwet, D., Mora-Amador, R., Ramírez-Umaña, C. J., González, G., and Inguaggiato, S. (2017). Dynamic Fluid Recycling at Laguna Caliente (Poás, Costa Rica) before and during the 2006-ongoing Phreatic Eruption Cycle (2005-10). *Geol. Soc. Lond. Spec. Publications* 437, 73–96. doi:10.1144/SP437.11

Rouwet, D., and Morrissey, M. M. (2015). "Mechanisms of Crater lake Breaching Eruptions," in *Volcanic Lakes, Advances in Volcanology*. Editors D. Rouwet, B. Christenson, F. Tassi, and J. Vandemeulebrouck (Heidelberg: Springer), 73–91. doi:10.1007/978-3-642-36833-2_3

Rouwet, D., Tassi, F., Mora-Amador, R., Sandri, L., and Chiarini, V. (2014). Past, Present and Future of Volcanic lake Monitoring. *J. Volcanology Geothermal Res.* 272, 78–97. doi:10.1016/j.jvolgeores.2013.12.009

Rowe, G. L., Ohsawa, S., Takano, B., Brantley, S. L., Fernandez, J. F., and Barquero, J. (1992). Using Crater Lake Chemistry to Predict Volcanic Activity at Poás Volcano, Costa Rica. *Bull. Volcanol.* 54, 494–503. doi:10.1007/BF00301395

Rowe, Jr., G. L. (1994). Oxygen, Hydrogen, and Sulfur Isotope Systematics of the Crater lake System of Poas Volcano, Costa Rica. *Geochem. J.* 28, 263–287. doi:10.2343/geochemj.28.263

Saishu, H., Okamoto, A., and Tsuchiya, N. (2014). The Significance of Silica Precipitation on the Formation of the Permeable-Impermeable Boundary within Earth's Crust. *Terra Nova* 26, 253–259. doi:10.1111/ter.12093

Shinohara, H., and Fujimoto, K. (1994). Experimental Study in the System Albite-Andalusite-Quartz-NaCl-HCl-H2o at 600°C and 400 to 2000 Bars. *Geochimica et Cosmochimica Acta* 58, 4857–4866. doi:10.1016/0016-7037(94)90216-X

Shinohara, H., Ohba, T., Kazahaya, K., and Takahashi, H. (2008). Origin of Volcanic Gases Discharging from a Cooling Lava Dome of Unzen Volcano, Japan. *J. Volcanology Geothermal Res.* 175, 133–140. doi:10.1016/j.jvolgeores.2008.03.024

Stix, J., and de Moor, J. M. (2018). Understanding and Forecasting Phreatic Eruptions Driven by Magmatic Degassing. *Earth Planets Space* 70, 83. doi:10.1186/s40623-018-0855-z

Takahashi, K., and Fujii, I. (2014). Long-term thermal Activity Revealed by Magnetic Measurements at Kusatsu-Shirane Volcano, Japan. *J. Volcanology Geothermal Res.* 285, 180–194. doi:10.1016/j.jvolgeores.2014.08.014

Takahashi, M., Kawamata, H., Yasui, M., and Kanamaru, T. (2010). Whole Rock Major Element Chemistry for Eruptive Products of Kusatsu-Shirane Volcano, central Japan: Summary of 306 Analytical Data. *Proc. Inst. Nat. Sci. Nihon Univ.* 45, 205–254. (in Japanese).

Takano, B., Kuno, A., Ohsawa, S., and Kawakami, H. (2008). Aqueous Sulfur Speciation Possibly Linked to Sublimnic Volcanic Gas-Water Interaction during a Quiescent Period at Yugama Crater lake, Kusatsu-Shirane Volcano, Central Japan. *J. Volcanology Geothermal Res.* 178, 145–168. doi:10.1016/j.jvolgeores.2008.06.038

Takano, B., and Watanuki, K. (1990). Monitoring of Volcanic Eruptions at Yugama Crater lake by Aqueous Sulfur Oxyanions. *J. Volcanology Geothermal Res.* 40, 71–87. doi:10.1016/0377-0273(90)90107-Q

Taran, Y. A., Pokrovsky, B. G., and Doubik, M. (1989). Isotopic Composition and Origin of Water from Andesitic Magmas. *Dokl. Acad. Sci. USSR* 304, 440–443.

Terada, A., Kanda, W., Ogawa, Y., Yamada, T., Yamamoto, M., Ohkura, T., et al. (2021). The 2018 Phreatic Eruption at Mt. Motoshirane of Kusatsu-Shirane Volcano, Japan: Eruption and Intrusion of Hydrothermal Fluid Observed by a Borehole Tiltmeter Network. *Earth Planets Space* 73, 157. doi:10.1186/s40623-021-01475-4

Terada, A. (2018). Kusatsu-Shirane Volcano as a Site of Phreatic Eruptions. *Jour. Geol. Soc. Jpn.* 124, 251–270. doi:10.5575/geosoc.2017.0060

Terada, A., Morita, Y., Hashimoto, T., Mori, T., Ohba, T., Yaguchi, M., et al. (2018). Water Sampling Using a Drone at Yugama Crater lake, Kusatsu-Shirane Volcano, Japan. *Earth Planets Space* 70, 64. doi:10.1186/s40623-018-0835-3

Tokyo Institute of Technology and Sophia University (1983). The Activity of Kusatsu-Shirane Volcano in 1982 and Geochemical Study (II). *Rep. Coord. Commit. Pred. Volc. Eruption* 28, 7–18. (in Japanese).

Tokyo Institute of Technology, Sophia University, and Saitama University (1983). The Activity of Kusatsu-Shirane Volcano in October 1982 and Geochemical Study (I). *Rep. Coord. Commit. Pred. Volc. Eruption* 26, 8–19. (in Japanese).

Tseng, K. H., Ogawa, Y., Tank, S. B., Ujihara, N., Honkura, Y., Terada, A., et al. (2020). Anatomy of Active Volcanic Edifice at the Kusatsu-Shirane Volcano, Japan, by Magnetotellurics: Hydrothermal Implications for Volcanic Unrests. *Earth Planets Space* 72, 161. doi:10.1186/s40623-020-01283-2

Ueki, K., and Terada, A. (2012). Field Excursion Guide to Kusatsu-Shirane Volcano. *Bull. Volcanol. Soc. Jpn.* 57, 235–251. (in Japanese). doi:10.18940/kazan.57.4_235

Uto, K., Hayakawa, Y., Aramaki, S., and Ossaka, J. (1983). *Geological Map of Kusatsu-Shirane Volcano*. Ibaraki: Geological Survey of Japan.

Varekamp, J. C. (2015). "The Chemical Composition and Evolution of Volcanic Lakes," in *Volcanic Lakes, Advances In Volcanology*. Editors D. Rouwet, B. Christenson, F. Tassi, and J. Vandemeulebrouck (Heidelberg: Springer), 93–123. doi:10.1007/978-3-642-36833-2_4

Volcanic Fluid Research Center, Tokyo Institute of Technology (2004). Recent Activity of Kusatsu-Shirane Volcano—Water Jet from Crater lake Yugama on 17, May 2004. *Rep. Coord. Commit. Pred. Volc. Eruption* 88, 49–54. (in Japanese).

Yaguchi, M., Muramatsu, Y., Chiba, H., Okumura, F., and Ohba, T. (2016). The Origin and Hydrochemistry of Deep Well Waters from the Northern Foot of Mt. Fuji, central Japan. *Geochem. J.* 50, 227–239. doi:10.2343/geochemj.2.0409

Yamaoka, K., Geshi, N., Hashimoto, T., Ingebritsen, S. E., and Oikawa, T. (2016). Special Issue "The Phreatic Eruption of Mt. Ontake Volcano in 2014". *Earth Planets Space* 68, 175. doi:10.1186/s40623-016-0548-4

Conflict of Interest: The authors declare that the research was conducted in the absence of any commercial or financial relationships that could be construed as a potential conflict of interest.

Publisher's Note: All claims expressed in this article are solely those of the authors and do not necessarily represent those of their affiliated organizations, or those of the publisher, the editors and the reviewers. Any product that may be evaluated in this article, or claim that may be made by its manufacturer, is not guaranteed or endorsed by the publisher.

frontiers in Earth Science

ORIGINAL RESEARCH
published: 13 December 2021
doi: 10.3389/feart.2021.741528

Geochemistry of Water and Gas Emissions From Cuicocha and Quilotoa Volcanic Lakes, Ecuador

G. V. Melián[1,2], T. Toulkeridis[3], N. M. Pérez[1,2], P. A. Hernández[1,2], L. Somoza[4], E. Padrón[1,2], C. Amonte[1,2], M. Alonso[1,2], M. Asensio-Ramos[1] and M. Cordero[1]*

[1]Instituto Volcanológico de Canarias (INVOLCAN), Santa Cruz de Tenerife, Spain, [2]Instituto Tecnológico y de Energías Renovables (ITER), Granadilla de Abona, Spain, [3]Universidad de las Fuerzas Armadas ESPE, Sangolquí, Ecuador, [4]Marine Geological Resources Division, Geological Survey of Spain (IGME), Madrid, Spain

There are hundreds of volcanic lakes around the world that represent an important hazard due to the potential occurrence of phreatomagmatic or limnic eruptions. Variations in geochemical and geophysical parameters could help to identify potential risks for these events. Cuicocha and Quilota volcanic lakes, located at the North Andean Volcanic Zone of Ecuador, are geologically young, with gas emissions manifested mainly as CO_2 via bubbling gases. Both lakes present a limited monitoring record. Therefore, volcanic monitoring is a priority task due to the potential hazard they represent by the possibility of water stratification and CO_2 accumulation. During 2012-2018 period, geochemical investigation based mainly on diffuse CO_2 surveys and analyzing the chemical and isotopic composition of bubbling gases has been carried out at Cuicocha and Quilotoa lakes. Additionally, vertical profiles of water columns were conducted in both lakes to investigate the possibility of water stratification and CO_2 accumulation in the lakes. A bathymetric study was also carried out in Quilotoa in 2017, giving further information about the degasification processes and the morphology of the lake bottom. The computed diffuse CO_2 output for Cuicocha volcanic lake (3.95 km^2) showed a range from 53 to 652 t d^{-1} for the period 2006–2018, with a maximum value in 2012, coinciding with a maximum of the $^3He/^4He$ ratio measured at the bubbling gases and an increase in the seismic activity with an episode of long-period seismicity recorded in 2011–2012. For Quilotoa volcanic lake (3.50 km^2) diffuse CO_2 output was estimated between 141 and 536 t d^{-1} for the period 2014–2018. The chemical and isotopic data show that Cuicocha has a chemical composition typical of worldwide superficial shallow waters and aquifers, while Quilotoa shows a chemical composition typical of crater lakes in active volcanic systems. The distribution of the dissolved gas composition along the vertical profiles shows the existence of different water masses in both lakes, with an increase in the concentration of dissolved gases with depth. The carbon isotopic signature indicates an endogenous origin of the CO_2, with a greater contribution in the stratification zone in both lakes. This study shows methods applicable to other volcanic lakes of the world to monitor their activity and potential risks.

Keywords: geochemistry of water, volcanic gases, gas emissions, volcanic lake, Cuicocha and Quilotoa lakes, Ecuador

OPEN ACCESS

Edited by:
Agnes Mazot,
GNS Science, New Zealand

Reviewed by:
Ery Catherine Hughes,
GNS Science, New Zealand
Jennifer Lewicki,
United States Geological Survey,
United States

****Correspondence:***
G. V. Melián
gladys@iter.es

Specialty section:
This article was submitted to Volcanology, a section of the journal Frontiers in Earth Science

Received: *14 July 2021*
Accepted: *11 November 2021*
Published: *13 December 2021*

Citation:
Melián GV, Toulkeridis T, Pérez NM, Hernández PA, Somoza L, Padrón E, Amonte C, Alonso M, Asensio-Ramos M and Cordero M (2021) Geochemistry of Water and Gas Emissions From Cuicocha and Quilotoa Volcanic Lakes, Ecuador. Front. Earth Sci. 9:741528. doi: 10.3389/feart.2021.741528

INTRODUCTION

Volcanic lakes consist of accumulations of water inside a volcanic depression. The study of the physical and chemical characteristics of these water masses constitutes a powerful tool to evaluate the activity level of volcanic systems (Mazot and Taran, 2009; Rouwet et al., 2014, 2015; Andrade et al., 2016, 2019, 2021; Hernández et al., 2017). After the two well-known limnic eruptions ocurred in Camerron at Lake Monoun in 1984 and Lake Nyos in 1986, special importance has been paid to the development of CO_2 emission surveys in different volcanic lakes (Padrón et al., 2008; Mazot and Taran, 2009; Hernández et al., 2011, 2017; Pérez et al., 2011; Mazot et al., 2014; Melián et al., 2017; Sierra et al., 2021). These periodic CO_2 emission surveys in volcanic lakes are an important task for the surveillance of these systems. Although much effort has been made in the last 15 years to study the diffuse CO_2 emission rate at several volcanic lakes in the world (Mazot and Taran, 2009; Pérez et al., 2011; Melián et al., 2017), many lakes are still noninvestigated and very few have been regularly monitored to create time series (Sierra et al., 2021).

Changes in temperature and water chemistry (chemical and isotopic composition, as well as dissolved gas composition and fluxes) of volcanic lakes may also indicate processes occurring deeper in the volcanic system. Water composition is strongly influenced by the fluid inputs and changes to it may signify variations in the composition or magnitude of fluid discharges into the system (Christenson, 2000; Gunkel et al., 2008, 2009; Inguaggiato et al., 2010, 2016; Hernández et al., 2017; Rouwet et al., 2017). Bathymetry studies have been employed to identify CO_2 degassing vents (Aguilera et al., 2000; Goepel et al., 2015; Hernández et al., 2017; Melián et al., 2017), to evaluate ideal drilling sites into geothermal reservoirs (Brehme et al., 2019, 2021), and to evaluate hazards due to accumulation of CO_2 in volcanic lakes (Anzidei et al., 2008).

Cuicocha and Quilotoa are potentially hazardous volcanic lakes located in Ecuador (**Figure 1**). Despite this, these lakes have not been extensively studied and there are only a few published works. Both volcanic lakes have been investigated by Gunkel et al. (2008) to evaluate the hazard due to the occurrence of CO_2 emissions that can generate the accumulation of CO_2 in the deep-water body. In this research, they conclude that Cuicocha can give rise to phreatic-magmatic eruptions due to the small amount of sediments, mainly carbonates and organic material, such that a remobilization of the sedimentation layer can be caused by earthquakes or rock slides. On the other hand, Quilotoa is more susceptible to the occurrence of potential limnic eruptions since it presents an atypical water mixture called atelomixis that can cause the release of diffuse CO_2 during periods of calm or absence of wind in the caldera.

Gunkel et al. (2009) present a characterization of the lake water during the period 2004–2006, through the study of vertical profiles and an eco-sounder (ES) survey. The results showed that Cuicocha volcanic lake presents a monomictic stratification and during overturn an intensive gas exchange can occur. The ES survey also showed an intensive gas emission, mainly CO_2, at the western basin of the Cuicocha volcanic lake and a sediment layer of up to 10–20 cm in the deeper part of the lake. This sediment layer is not present in the zone of intense degassing. Gunkel et al. (2009) and Inguaggiato et al. (2010) studied the chemical composition of bubbling. These authors indicate that CO_2 is the predominant gas, with concentrations approximately 37–51%.V, followed by N_2 (~45%.V) and O_2 (~3.5%.V). The $^3He/^4He$ (R/R_A = 5.73) and $\delta^{13}C$–CO_2 (−3.94‰) ratios of the bubbling gases were interpreted as a consequence of a magmatic

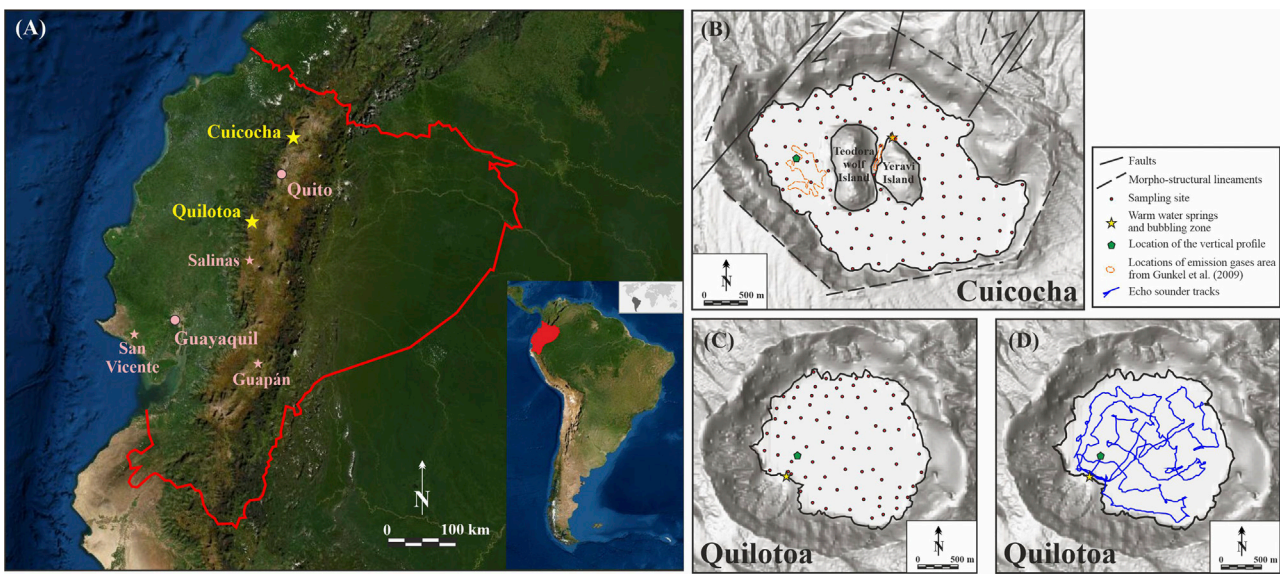

FIGURE 1 | (A) Local map of Ecuador with the geographic location of Cuicocha and Quilotoa volcano. Location of the diffuse CO_2 efflux measurements sites (red dots), vertical profiles (green pentagons), and warm water springs and bubbling sites (yellow stars) for **(B)** Cuicocha and **(C)** Quilotoa volcanic lakes. **(D)** Localization of echo-sounder track in Quilotoa volcanic lake for the 2017 survey. Orange line show.

contribution (Inguaggiato et al., 2010). The first study of diffuse CO_2 emission at Cuicocha volcanic lake was reported by Padrón et al. (2008). The authors estimated the CO_2 emission of the lake at 53 t d^{-1} using the sequential Gaussian simulation (sGs) method. More recently, Sierra et al. (2021) presented the results of long-term analysis of diffuse CO_2 emission, estimating an emission of 400 kt of CO_2 during the period 2011–2019 (8.13 years), with an average rate of ~135 t d^{-1}. Sierra et al. (2021) considered that the CO_2 emission peak registered in 2012-2013 was related to the anomalous seismicity occurred during this period due to deep origin processes that affect the hydrothermal system.

Regarding Quilotoa, most of the published studies have been focused on its volcanism and the last (800 years BP) eruption (Rosi et al., 2004; Di Muro et al., 2008; Hall and Mothes, 2008; Mothes and Hall, 2008) and only a few works have been published about the water chemistry of the lake. Based on data from water vertical profiles (pH, electrical conductivity (EC), temperature, chemical composition of water), Aguilera et al. (2000) observed two water bodies at Quilotoa volcanic lake: a thin (~14 m) oxic epilimnion overlying a thick (~200 m) anoxic hypolimnion. Inguaggiato et al. (2010) report a clearly CO_2-dominated (96%.V) chemical composition of the bubbling gases, followed by N_2 (~3%.V) and O_2 (~0.4%.V). As in the case of Cuicocha, He and N_2 composition shows two groups of samples based on the geographical limit of the active volcanic arc in Ecuador. Quilotoa is in the group of active volcanism (quaternary arc). In the case of Quilotoa, no previous works have been published on the emission of CO_2 from the volcanic lake.

We herein report the results of CO_2 efflux surveys carried out in the Cuicocha and Quilotoa volcanic lakes, with the aim of evaluating the temporal variation of CO_2 efflux from de water surface and $^3He/^4He$ ratio of bubbling gases and their relationship with volcanic activity. Additionally, vertical profiles of dissolved gases and chemical and isotopic composition of the water column were carried out in both volcanic lakes; an ES survey was conducted at the Quilotoa volcanic lake to study the stratifications of the water layers, accumulation of gases, and the possibility of future dangerous gas outburst episodes.

GEOLOGICAL BACKGROUND

The North Andean volcanic zone is part of a ~7,000 km long active continental margin on the western edge of the South American continent (Jordán et al., 1983; Garrison and Davidson, 2003). The ESE trending oceanic Nazca plate is subducting below the South American and Caribbean continental segments, which give rise to the active volcanism within Colombia and Ecuador (Gutscher et al., 1999). Here volcanism is aligned in a NNW-SSE orientation within a number of volcanic arcs, with approximately 250 volcanoes in Ecuador (Rodriquez et al., 2017; Toulkeridis and Zach, 2017). Within the western volcanic cordillera, which represents the volcanic front, the only two water-filled calderas appear, Cuicocha to the north and Quilotoa to the southeast of Ecuador's capital Quito (**Figure 1**).

The Cuicocha Volcanic System

The Cuicocha volcano is situated in the south of the older and extinct edifice of the nearby Cotacachi volcano. The oldest edifice of the Cotacachi volcano initiated approximately 160,000 years ago (Almeida Vaca, 2016). Both are located along the Otavalo—Umpalá fracture zone (Hanus, 1987). However, above the older units of the Cotacachi volcano four principal parasitic domes were emplaced, of which Cuicocha is the youngest (Sierra et al., 2021). Its collapse formed the caldera approximately 4,500 years ago, which has since been the location of intense eruptions with volcanic explosivity indexes (VEI) of 5–6, lahars, and massive pyroclastic flows through to approximately 1,300 years ago (Hillebrant, 1989). The Cuicocha volcano is truncated by an elliptical caldera with a maximum diameter of 3.2 km, and a lake within, with maximum depth of 148 m and a volume of 0.28 km^3. The surface of the lake is at an altitude of 3,072 m.a.s.l. The water in the caldera initially resulted from the melting of the Cotacachi volcano glacier and later fed by rainwater and hydrothermal vents. The last eruptive activity of Cuicocha is evidenced by the formation of four domes distributed on two islands in the center of the lake named Isla Yerovi and Wolf, and a further one in the northeast extreme on the caldera wall. All domes have an andesitic composition (Gunkel et al., 2009). Both lahars and pyroclastic flows have reached distant areas such as the towns of Quiroga (population: 3,300), Cotacachi (population: 8,800), and even the highly populated Otavalo (population: 40,000), all of them located only a few dozens of km from the caldera (Bustos-Gordón and Serrano-Abarca, 2014). Post-volcanic activity is evidenced by the emission of volcanic gases in the form of gas bubbles and dead vegetation because of the action of these gases. The most constant and noticeable of these is located on the northern shoreline of Yeravi island but they are also observed in the eastern area of the lake (**Figure 1B**; Gunkel et al., 2008; Padrón et al., 2008).

Ecuador's volcanic activity is monitored by the Ecuadorian Instituto Geofísico de la Escuela Politécnica Nacional (IG-EPN). Cuicocha volcanic lake hosts a broadband seismic station and a GPS (www.igepn.edu.ec/). The seismic activity of Cuicocha volcanic lake is characterized in general by volcano-tectonic seismicity (VT) of low-magnitude earthquakes ($M < 2$; IGEPN, 2010, 2018, 2019). Several episodes of high long-period (LP) seismicity were identified in the 2011–2012 period (Sierra et al., 2021). The available deformation data registered in Cuicocha volcanic lake (January 2018–February 2020) do not show significant variations according to IGEPN (2019). Since 2011, CO_2 diffuse flux studies were conducted by IG-EPN in Cuicocha volcanic lake with a variable periodicity.

The Quilotoa volcanic System

The collapse of a stratovolcano gave rise to the Quilotoa caldera (Aguilera et al., 2000). The caldera has an elliptical shape with a diameter of 2.4–2.8 km and a depth of up to 256 m. The surface of the lake hosted within the caldera is 3,500 m.a.s.l. and the total volume of the water is estimated at 0.35 km^3 (Aguilera et al., 2000). The water level has been continuously declining for the past 30 years, as attested by the lacustrine deposits observable on

the shore banks (Aguilera et al., 2000; Gunkel et al., 2008; Bustos-Gordón and Serrano-Abarca, 2014). The eruptive record of Quilotoa exhibits a long series of Plinian eruptions with a VEI between 4 and 6, covering a large part of the region and ash and pumice traced across the entire country (Aguilera et al., 2000; Rosi et al., 2004). In the last 2,11,000 years, there have been more than a dozen different cycles every 10,000–15,000 years (Rosi et al., 2004; Di Muro et al., 2008). The eruptions were characterized by different phases, commonly starting with phreato-magmatic explosions followed by falls rich in lapilli-size pumice, ending with pyroclastic and ash-flows of mostly dacitic composition (Rosi et al., 2004; Hall and Mothes, 2008). There are approximately 18 domes identified around the Quilotoa caldera, being of dacitic to rhyolitic composition (Panchana Guerra, 2015). These originated from the various phases of the eruptive activities beginning ~34,000 years ago. Furthermore, the Quilotoa caldera experienced 4 limnic explosions during the 18th century (Simkin and Siebert, 1994). The last violent gas escape event (February 4, 1797) originated due to an earthquake under the Tungurahua volcano, generated flames and suffocating gases in the lake, and destroyed the cattle on the slopes of Quilotoa (Lyell, 1830). It is worth noting that near the volcano, there are many settlements of native indigenous people dedicated to agriculture and tourism. Additionally, very strong gas emissions, manifest mainly as CO_2 emission via bubbling gases and hydrothermal waters, occur in the south and southwest shorelines of the lake (**Figures 1C,D**; Aguilera et al., 2000; Gunkel et al., 2008). Regarding geophysical monitoring of Quilotoa volcanic lake, a GPS station is installed in the volcanic lake, but there are not public data (www.igepn.edu.ec/).

SAMPLING PROCEDURES, ANALYTICAL METHODS, AND DATA PROCESSING

During the period 2012–2018, four and three diffuse CO_2 efflux surveys were conducted at Cuicocha and Quilotoa volcanic lakes, respectively. Bubbling gas samples were also collected from both lakes during the period 2014–2018 to study their chemical (He, O_2, N_2, and CO_2) and isotopic ($^3He/^4He$ ratio and $\delta^{13}C\text{-}CO_2$) composition. Additionally, in 2017 and 2018, vertical profiles of dissolved gases (He, H_2, O_2, N_2, CO_2, and CH_4) and chemical (Ca^{2+}, Mg^{2+}, K^+, Na^+, HCO_3^-, Cl^-, and SO_4^{2-}) and isotopic (δ^2H, $\delta^{18}O$, and $\delta^{13}C\text{-}CO_2$) composition of the water column were carried out in both volcanic lakes. All samples (water and gases) were transported from Ecuador to Tenerife (Canary Islands, Spain), where the analyses were carried out in the ITER laboratory. Water pH, temperature, and EC were measured at 30 cm depth from the water surface at each sampling site and in water samples in the vertical profiles. During the 2017 survey, an ES survey was also conducted at Quilotoa volcanic lake.

Diffuse CO_2 efflux survey was intentionally carried out in days of stable weather conditions (sunny days without wind) to minimize the effects of variable meteorological conditions on CO_2 emission. Approximately 113 (for Cuicocha) and 84 (for Quilotoa) sampling sites were selected to cover homogeneously all the surface of volcanic lakes with site spacing of about 180 m for both (**Figures 1B,C**). The GPS position of each measurement point was recorded with a resolution of ±5 m. Measurements of diffuse CO_2 efflux at the water surface of the lakes were conducted *in situ* using the accumulation chamber method (Parkinson, 1981; Chiodini et al., 1998) with the chamber placed on a flotation device (Huttunen et al., 2003; Pérez et al., 2011). These measurements were conducted by means of a portable CO_2 efflux instrument provided with a nondispersive infrared (NDIR) CO_2 analyzer LICOR-800 system (West Systems Ltd). The accuracy of the diffuse CO_2 efflux measurements for the range 10–35,000 $g{\cdot}m^{-2}{\cdot}d^{-1}$ was estimated at 10% for this study. Spatial distribution maps for Cuicocha and Quilotoa volcanic lakes were constructed using sGs (Deutsch and Journel, 1998; Cardellini et al., 2003). The final maps were constructed as an average of 100 equiprobable realizations and the differences among all simulated maps were used to compute the uncertainty in the estimation of diffuse CO_2 emission of the studied areas.

Water pH, temperature, and EC were measured by means of an Oakton Waterproof pH/CON 10 m (accuracies ±0.2, ±0.5, and ±1%, respectively), where calibration was done on site before the start of the survey.

A vertical profile of 80 m depth was studied in both 2017 and 2018, sampling every 10 m (green pentagon in **Figure 1B**), at Cuicocha volcanic lake. In the case of Quilotoa, a 140 m depth profile was conducted in 2017 and a 120 m depth profile in 2018, and water samples were collected every 30 and 20 m, respectively (green pentagon in **Figure 1C**). Water samples were collected using a 2.2 L WaterMark horizontal PVC water bottle. Total alkalinity (HCO_3^-) in the water samples was analyzed by automatic titration Metrohm 716 DMS Titrino. The concentration of Cl^- and SO_4^{2-} was analyzed by means of a Dionex ICS-2100 system, while the concentration of Ca^{2+}, Mg^{2+}, K^+, and Na^+ was determined by means of a 861 Advanced Compact IC. The cations were determined in filtered acidified samples. Each sample was analyzed in triplicate and the accuracy of the analyses was estimated at 2.5%. The quality of the geochemical data was checked in each sample by calculating the ion balance error (IBE = (sum cations–sum anions)/(sum cations + sum anions)). Only those results with IBE of ±5% were considered for processing.

The δ^2H and $\delta^{18}O$ values of water and $\delta^{13}C\text{-}CO_2$ in dissolved and bubbling gas were obtained by isotopic ratio mass spectrometry (IRMS; Thermo-Finnigan MAT 253). For $\delta^{18}O$ and δ^2H, the results are reported in δ units per mil vs Vienna Standard Mean Ocean Water (VSMOW) with experimental errors of ±0.1 and ±1‰, respectively. For $\delta^{13}C\text{-}CO_2$, the results are reported in δ units per mil vs Vienna Pee Dee Belemnite standard (VPDB) with an analytical error of ±0.01‰.

Dissolved He, H_2, O_2, N_2, CO_2, and CH_4 concentrations were analyzed following the method of Capasso and Inguaggiato (1998), with pure Ar as the host gas using a two-channel Agilent 490 micro-chromatograph with thermal conductivity detection (TDC). The instrumental precision and limit of detection was estimated as 2% and 0.3 ppm.V (parts per million in volume) for He, 2% and 0.3 ppm.V for H_2, 0.1%

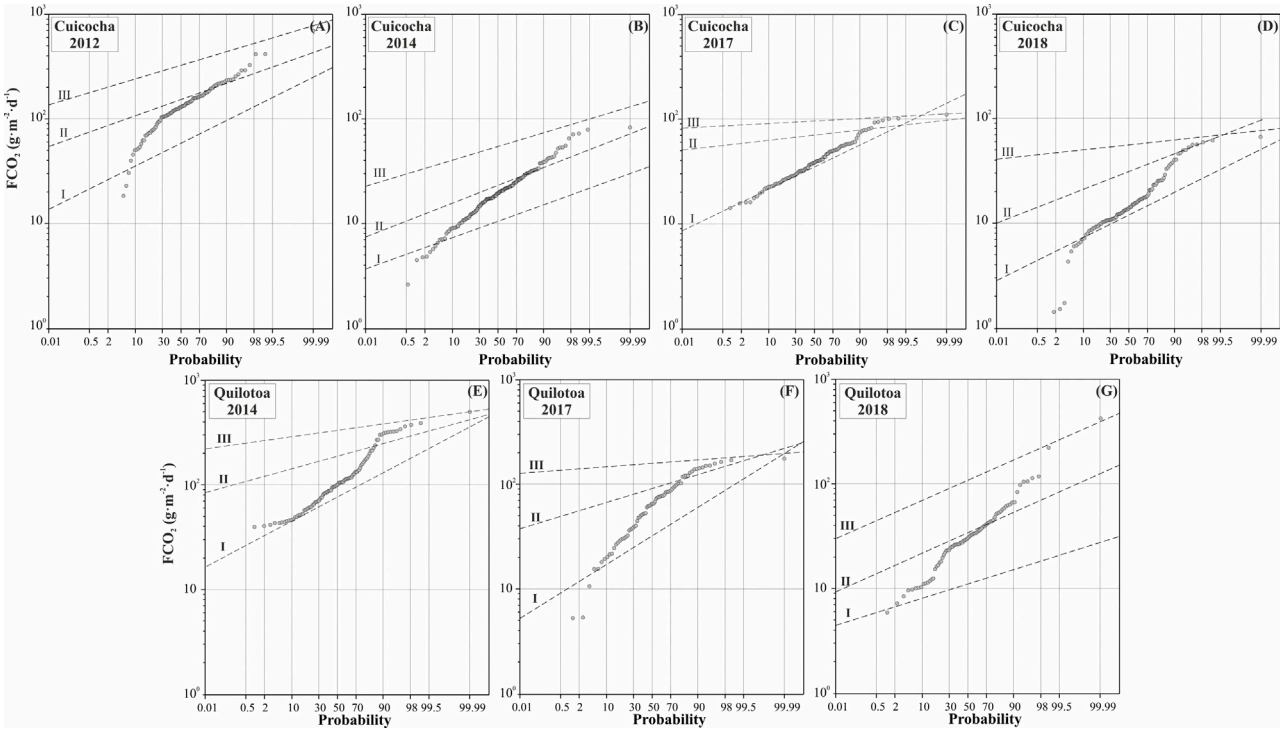

FIGURE 2 | Probability-plots of the CO_2 efflux data measured at the Cuicocha volcanic lake for **(A)** 2012, **(B)** 2014, **(C)** 2017, and **(D)** 2018; and Quilotoa volcanic lake for **(E)** 2014, **(F)** 2017, and **(G)** 2018. The black dots indicate the original data. Dashed lines indicate separated geochemical populations.

and 15 ppm.V for O_2, 0.1% and 50 ppm.V for N_2, 2% and 7 ppm.V for CO_2, and 2% and 1.6 ppm.V for CH_4.

The chemical composition of the collected bubbling gas was analyzed by quadrupole mass spectrometers (QMS), models Pfeiffer Omnistar 422 and HIDEN QGA. Analytical error was estimated as <5% and <10% for the main (O_2, N_2, and CO_2) and minor (He) gas components, respectively.

Elemental abundances of He and Ne, and He isotope composition of the gas samples were analyzed in a high-precision VG Isotech modified VG-5400 noble gas mass spectrometer. The analytical error for $^3He/^4He$ determination was <2%. Air standards were measured frequently during analyses to determine sensitivities of the mass spectrometer. The correction factor for helium isotope ratios was determined by the measurement of an inter-laboratory helium standard named HESJ with a recommended $^3He/^4He$ ratio of 20.63 ± 0.10 R_A (Matsuda et al., 2002). The measured $^3He/^4He$ ratios were corrected for the addition of air based on the $^4He/^{20}Ne$ ratios measured by mass spectrometry, assuming that Ne has an atmospheric origin (Craig and Lupton, 1976) and normalized to that in the atmosphere ($R_A = 1.384 \times 10^{-6}$; Clarke et al., 1976).

Finally, an ES survey was carried out at Quilotoa in 2017 by means of a Lowrance HDS-5 ES equipped with a dual frequency (83 and 200 kHz) transducer. Boat velocity ranged on average between 0.5 and 3 knots. ES data were processed according to the methodology used by Hernández et al. (2017) and Melián et al. (2017). The digital ES echograms were processed using Sonar Viewer 2.1.2 software. Extracted bathymetric data were converted from the Lowrance-type Mercator projection to universal Transverse Mercator (WGS1984 UTM Zone 17S) using ArcGis 10.2. Bathymetric data from the two frequencies (Primary at 200 kHz and Secondary at 83 kHz) were interpolated using the natural neighbor technique of the 3D analyst tools.

RESULTS

CO_2 Diffuse Degassing

Cuicocha Volcanic Lake

The CO_2 efflux values measured at Cuicocha volcanic lake ranged between below the detection limit of the instrument (<0.5 $g \cdot m^{-2} \cdot d^{-1}$) to 695 $g \cdot m^{-2} \cdot d^{-1}$, with an average value of 54 $g \cdot m^{-2} \cdot d^{-1}$ for the four surveys (**Supplementary Table S1** in Supplementary Material). The surface water temperature presented a range between 14.5 and 17.3°C (average of 15.9°C). The pH value of the water was slightly basic, ranging between 7.17 and 9.02 (average of 8.2) and EC ~700 µS cm^{-1}. No significant spatial variation of EC was observed at 30 cm depth. The water temperature values are ~2°C higher in the bubbling zone, while the pH is ~0.4 units lower with respect to the rest of the lake.

To check for the presence of overlapping log-normal populations of the efflux data, we applied the probability-plot technique (Sinclair, 1974) to the entire CO_2 efflux data

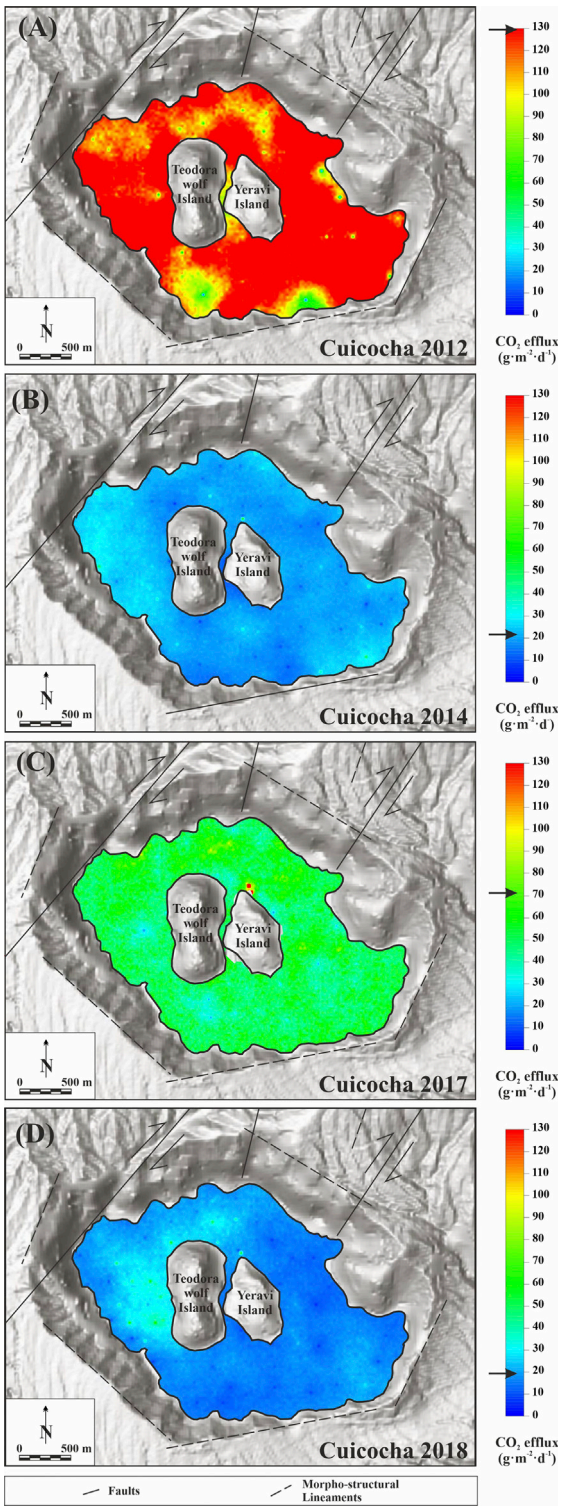

FIGURE 3 | Spatial distribution of CO_2 efflux (g m^{-2} d^{-1}) at the Cuicocha volcanic lake for **(A)** 2012, **(B)** 2014, **(C)** 2017, and **(D)** 2018. Location of the main tectonic structures according to Sierra et al. (2021) are also shown. Horizontal arrow at each color scale indicates the average value of the data used to construct the spatial distribution map.

(cumulative percentile frequencies versus class intervals). The inflection point of the curve allows the threshold value between different populations to be distinguished. The descriptive statistics summary of CO_2 efflux values partitioned populations at each survey are shown in **Supplementary Table S1** (Supplementary Material). The result of the statistical-graphic analysis of CO_2 efflux data (**Figures 2A–D**) showed different populations for each survey: population I (background) with values from 6.1 to 58.0 $g{\cdot}m^{-2}{\cdot}d^{-1}$ (average 15.9 $g{\cdot}m^{-2}{\cdot}d^{-1}$) and represented between 29.6 and 53.8% of the total data (average 54%). Population III (anomalous or peak), which presented a range from 4.8 to 9.1% (average 6.9%) of the total data, showed values between 27.4 and 326 $g{\cdot}m^{-2}{\cdot}d^{-1}$ (average 59 $g{\cdot}m^{-2}{\cdot}d^{-1}$). The rest of the cumulative probability (population II) corresponding to the mixing of two log-normal populations (background and peak) is not considered as a product of a different source or mechanism, but rather the mixture of the previous ones.

Figure 3 shows the spatial distribution maps of CO_2 efflux at the Cuicocha volcanic lake for the period 2012–2018. **Supplementary Figure 1S** in Supplementary Material shows the omnidirectional experimental variogram of CO_2 efflux normal scores from the survey conducted at the Cuicocha volcanic lake, as well as the parameters that refer to the variogram models. An inspection of CO_2 efflux distribution maps shows that background CO_2 efflux values (~16 $g{\cdot}m^{-2}{\cdot}d^{-1}$) are identified across most of the studied area, except for the 2012 survey that shows values of ~100 $g{\cdot}m^{-2}{\cdot}d^{-1}$. For all the surveys, relatively high CO_2 efflux values were observed in the bubbling gas zone located in the northern corner of Yerovi island (>40 $g{\cdot}m^{-2}{\cdot}d^{-1}$), close to CO_2 bubbling areas (temperature of 16-17°C and pH of 7–8). During the 2012 survey, the highest CO_2 degassing rate showed four areas with particularly high values (>200 $g{\cdot}m^{-2}{\cdot}d^{-1}$): 1) in the NW shores of the lake; 2) along the eastern shores of Wolf Island; 3) in the southern zone of the lake; and 4) along the SW shores (**Figure 3A**). Relatively high CO_2 efflux values (>35 $g{\cdot}m^{-2}{\cdot}d^{-1}$) were measured in 2014 at the western zone of the lake and at the eastern shores (**Figure 3B**). The spatial distribution map of the 2017 survey shows constant CO_2 efflux values (>60 $g{\cdot}m^{-2}{\cdot}d^{-1}$) over the entire surface of the lake (**Figure 3C**). Finally, the 2018 CO_2 efflux map shows a significant decrease in the magnitude of the values, with relatively high values of CO_2 efflux measured in the small area located to the W and NW of Wolf Island (**Figure 3D**).

Guided by the variogram model, sGs of diffuse CO_2 efflux data were conducted covering an area of 3.95 km^2 for each survey in the period 2012–2018. The CO_2 output estimated shows a range from 76 ± 3 to 652 ± 25 $t{\cdot}d^{-1}$ in the 2012–2018 period, with 2018 and 2012 surveys showing the lowest and maximum values, respectively (**Table 1** and **Figure 4A**). The normalized CO_2 emission value by area (3.95 km^2) ranged between 19 ± 1 $t{\cdot}d^{-1}{\cdot}km^{-2}$ (in 2018) and 165 ± 6 $t{\cdot}d^{-1}{\cdot}km^{-2}$ (in 2012; **Supplementary Table S1** in Supplementary Material).

Quilotoa volcanic Lake

CO_2 efflux values ranged from 5.2 to 542 g·m^{-2}·d^{-1}, with an average value of 83 g·m^{-2}·d^{-1}. The surface water temperature ranges between 10.7 and 15.5°C (average 13.6°C), with pH ranging between 6.60 and 8.10 (average 7.3). Similar to Cuicocha lake, no significant spatial variations of EC were observed on the water at 30 cm depth. In the bubbling gas zone water temperature is ~1–2°C higher and pH is 0.5 units lower than the rest of the lake.

The probability-plot technique applied to the diffuse CO_2 efflux values confirms the existence of two log-normal populations (**Figures 2E–G**; **Supplementary Table S1** in Supplementary Material). Population I showed values from 11 to 74 g·m^{-2}·d^{-1} (average 39 g·m^{-2}·d^{-1}), which represented between 21.9 and 73.2% of the total data (average 48.4%). Population III, which represented a range from 9.7 to 33.9% (average 18.3%) of the total data, showed values between 107 and 354 g·m^{-2}·d^{-1} (average 206 g·m^{-2}·d^{-1}).

The CO_2 efflux maps (**Figure 5**) show the highest values are located mainly in the SW shores (>450 g·m^{-2}·d^{-1}), where gas bubbles and warm water springs appear, being characterized also by a relatively high water temperature and pH (temperature of ~22°C and pH of ~6.8) (6). In 2014, other high values of the CO_2 efflux were observed in the SW shores (>450 g·m^{-2}·d^{-1}) and in the north-eastern zone of the lake (>200 g·m^{-2}·d^{-1}; **Figure 5A**). During the 2017 survey, relatively high values of CO_2 efflux were observed in the eastern zone of the lake, with values > 250 g·m^{-2}·d^{-1} (**Figure 5B**). Regarding the 2018 survey, a general decrease on the extension and magnitude of the values were registered, with the principal anomalies focused in the south-western zone (**Figure 5C**).

The diffuse CO_2 emission at Quilotoa was estimated between 141 ± 6 and 536 ± 35 t·d^{-1} (average 330 t·d^{-1}; **Table 1** and **Figure 4B**), corresponding to an area of 3.50 km^2. The normalized emission value ranged between 40 ± 2 t·d^{-1}·km^{-2} (in 2018) and 153 ± 10 t·d^{-1}·km^{-2} (in 2014; see **Supplementary Table S1** in Supplementary Material).

Lake Water Chemistry and Vertical Profiles

Table 2 and **Figure 6** present the chemical composition of the vertical profiles of water samples collected during 2017 and 2018 at Cuicocha and Quilotoa volcanic lakes (location of lake profiles is shown by green pentagon in **Figures 1B,C**). The water temperature of Cuicocha volcanic lake ranged between 14.9 and 17.8°C (**Figure 6A**). Temperature differences were observed between the surface waters and 20 m depth in both 2017 and 2018 surveys, signifying that thermal stratification at Cuicocha is likely typical. An alkaline pH along the water column (~8.2 for the 2017 survey and ~7.8 for the 2018 survey; **Figures 6A,B**) and a gradient along the water column of 0.2–0.4 pH units were recorded. Moreover, pH values were higher on the surface compared with the lake bottom. EC values were relatively low at Cuicocha volcanic lake (<700 µS·cm^{-1}; **Figure 6C**) along the water column. The water samples from Cuicocha volcanic lake showed relatively low concentration of Na^+ (64.5–68.1 ppm·m (parts per million in mass); **Figure 6D**), Ca^{2+} (41.6–57.6 ppm·m; **Figure 6D**), and Mg^{2+} (29.6–39.9 ppm·m; **Figure 6D**) and

TABLE 1 | Estimated diffuse CO_2 emission rates, chemical composition of bubbling gases, $^3He/^4He$ (R/R_A)$_{corr}$ and $^4He/^{20}Ne$ ratios in bubbling gases, $\delta^{13}C$-CO_2 and $CO_2/^3He$ ratios for Cuicocha and Quilotoa volcanic lakes during the 2006–2018 period.

		CO_2 emission (t·d^{-1})			He	O_2	N_2	CO_2	$^3He/^4He$ (R/R_A)			($^3He/^4He$)$_{corr}$ (R/R_A)			$^4He/^{20}Ne$	^4He (ppm.V)	^{20}Ne (ppm.V)	$\delta^{13}C$-CO_2 (‰ vs PDB)			$CO_2/^3He$ x10^9
Cuicocha	2004–2006	n.m.				3.04[a]	23.1[a]	5,11,000[a]	n.m.			n.m.			n.m.	n.m.	n.m.	n.m.			n.m.
	July 19, 2006	53[b]	±	2[b]	n.m.	n.m.	n.m.	n.m.	4.04	±	0.04	4.28	±	0.05	4.47	9.61	2.15				
	February 27, 2009	n.m.			n.m.	42,300[c]	592,600[c]	3,74,300[c]	5.73[c]			6.26			3.18[c]	2.66[c]	6.26[c]	–3.94[c]			17.5
	July 23, 2012	652	±	25	n.m.	n.m.	n.m.	n.m.	3.90	±	0.04	4.23	±	0.07	3.08	5.06	1.64				
	February 14, 2014	95	±	2	9.7	46,100	3,61,250	5,92,640	3.92	±	0.03	4.17	±	0.05	4.03	4.23	1.05	–6.87	±	0.01	25.4
	September 23, 2017	206	±	24	19.2	11,914	3,31,723	6,56,343	3.94	±	0.04	4.03	±	0.04	10.46	16.70	1.60	–6.65	±	0.03	7.2
	November 01, 2018	76	±	3	25.1	45,333	5,84,916	3,69,726	2.63	±	0.02	2.67	±	0.02	14.90	32.70	2.20	–6.34	±	0.07	3.0
Quilotoa	April 14, 2009	n.m.				4,200[c]	30,800[c]	9,63,300[c]	1.87[c]			2.07			1.72[c]	0.09[c]	2.07[c]	–4.94[c]			4,090
	February 20, 2014	536	±	35	6.8	63,459	3,23,745	6,11,237	2.93	±	0.17	3.12	±	0.19	3.46	0.14	0.04	–5.10	±	0.02	1,061
	September 20, 2017	314	±	20	10.7	6,863	7,279	9,85,938	1.04	±	0.30	1.04	±	0.31	7.78	1.4	0.18	–4.35	±	0.05	487
	November 05, 2018	141	±	6	9.8	22,399	1,99,939	7,76,892	0.42	±	0.01	0.42	±	0.01	29.22	27.35	0.94	–3.69	±	0.10	47.7

[a]*Data from Gubkel et al. (2009).*
[b]*Data from Padrón et al. (2008).*
[c]*Data from Inguaggiato et al. (2010).*
n.m., not measured.

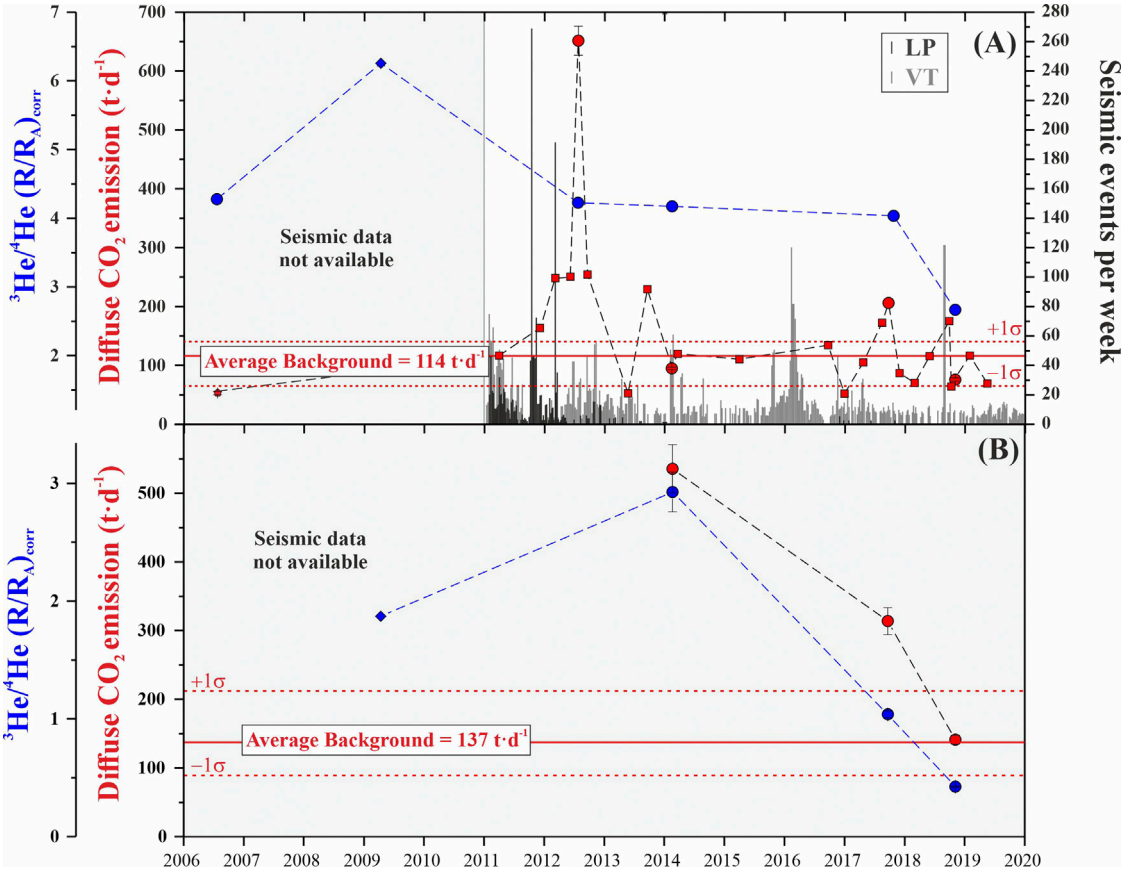

FIGURE 4 | Temporal evolution of diffuse CO_2 emission (red dots for present work data, red pentagon from Padrón et al. (2008), and red squares for sGs flux data from Sierra et al. (2021)) and $(^3He/^4He)_{corr}$ (blue dots for present work data and blue diamond for data from Inguaggiato et al. (2010)) measured in **(A)** Cuicocha and **(B)** Quilotoa volcanic lakes in the period 2006–2018. Vertical error bars in the CO_2 emission data depict 1 sigma of the 100 equiprobable sGs realizations. Uncertainties with reported $^3He/^4He$ ratios (vertical error bars) are 1 sigma, including error of the measured raw $^3He/^4He$ ratio, that of measured raw $^3He/^4He$ ratio of HESJ, and that on the recommended $^3He/^4He$ ratio of HESJ. Average background CO_2 emission (red line) with ±σ (red dash line) is also shown. The seismic event data of Cuicocha are from the IG-EPN seismic network and reported by Sierra et al. (2021): Volcanic Tectonic event (VT: gray vertical bars) and Long Period event (LP: black vertical bars).

relatively high values of HCO_3^- (314–382 ppm·m; **Figure 6E**) and lower concentration of Cl^- (73.5–64.1 ppm·m; **Figure 6E**) and SO_4^{2-} (19.6–21.4 ppm·m; **Figure 6E**).

For Quilotoa volcanic lake, the water temperature ranged between 12.5 and 15.4°C (**Figure 6A**) with neutral pH values (~7.4 and ~7.2 for 2017 and 2018 surveys, respectively; **Figure 6B**) and the gradient along the water column reached 0.2–0.4 pH units. The EC presents high values along the water column (~13,000 μS·cm^{-1}; **Figure 6C**) associated with high contents of Na^+, Cl^-, and SO_4^{2-}. The samples of Quilotoa volcanic lake showed high concentrations of Na^+ (2,369–2,485 ppm·m; **Figure 6F**) and relatively high concentrations of Mg^{2+} (625–871 ppm·m; **Figure 6F**) and Ca^{2+} (248–561 ppm·m; **Figure 6F**). The samples along the water column were rich in Cl^- (4,073–4,229 ppm·m; **Figure 6G**) and SO_4^{2-} (2,372–2,524 ppm·m; **Figure 6G**) and relatively low concentrations of HCO_3^- (686–1.399 ppm·m; **Figure 6G**).

In general, variations in the physical-chemical parameters and concentrations of K^+, Na^+, Cl^-, and SO_4^{2-} with depth are not observed at either of the lakes in this study during the 2017-2018 period. Ca^{2+}, Mg^{+2}, and HCO_3^- content present significant variations along the water column (**Figures 6D–G**) with changes also between 2017 and 2018. Despite these vertical changes in chemistry, the dissolved cationic constituents decreased in abundance in all water samples in both lakes as follows: $Na^+ > Mg^{2+} > Ca^{2+} > K^+$; regarding anionic constituents, the order was $HCO_3^- > Cl^- > SO_4^{2-}$ for Cuicocha and $Cl^- > SO_4^{2-} > HCO_3^-$ for Quilotoa.

Table 2 and **Figure 7** show the oxygen and hydrogen isotopic composition of water column. $\delta^{18}O_{VSMOW}$-H_2O values ranged from −6.2 to −5.6‰ and δ^2H_{VSMOW}-H_2O values from −47 to F02D−39‰ for Cuicocha volcanic lake. No significant variations of $\delta^{18}O_{VSMOW}$-H_2O values are observed between 2017 and 2018; however, a slight decrease in δ^2H_{VSMOW}-H_2O is observed (−41‰ for 2017 to −45‰ for 2018). For Quilotoa volcanic lake, the values ranged from −1.8 to −1.2‰ for $\delta^{18}O_{VSMOW}$-H_2O and δ^2H_{VSMOW}-H_2O values ranged from −32 to −28‰ and variations that are not considered significant were observed between 2017 and 2018.

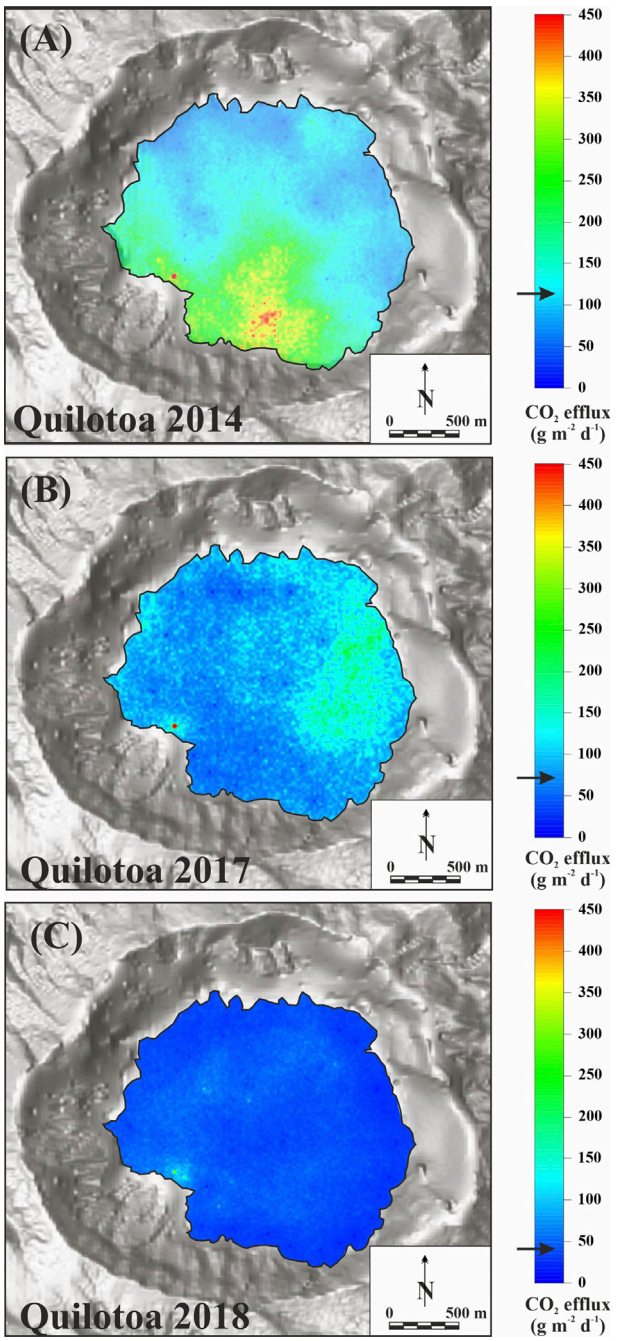

FIGURE 5 | Spatial distribution of CO_2 efflux ($g{\cdot}m^{-2}{\cdot}d^{-1}$) at Quilotoa volcanic lake for **(A)** July 2014, **(B)** 2017, and **(C)** 2018. Horizontal arrow at each color scale indicates the average value of the data used to construct the spatial distribution map.

Dissolved and Bubbling Gases

The analytical results of both dissolved and bubbling gases contents, as well as carbon isotopic composition of CO_2 and $^3He/^4He$ $(R/R_A)_{corr}$, are presented in **Tables 1**, **3** and **Figure 8**. For Cuicocha volcanic lake, the predominant chemical species in the dissolved gases in the water column was CO_2, with values ranging from 3.8 to 89.7 $cm^3{\cdot}STP{\cdot}L^{-1}$ (**Figure 8A**), followed by N_2 (~6.3 $cm^3{\cdot}STP{\cdot}L^{-1}$) and O_2 (~3.0 $cm^3{\cdot}STP{\cdot}L^{-1}$) with values of O_2/N_2 ratio of ~0.5 (**Figure 8B**). The average concentrations of H_2 (**Figure 8C**), He and CH_4 (**Figure 8D**) were ~5×10^{-3}, ~4×10^{-3}, and 1×10^{-3} $cm^3{\cdot}STP{\cdot}L^{-1}$, respectively. In the water column of Quilotoa volcanic lake the predominant chemical species in the dissolved gas was also CO_2, with values ranging from 19.3 to 190 $cm^3{\cdot}STP{\cdot}L^{-1}$ (**Figure 8F**), followed by N_2 (~6.6 $cm^3{\cdot}STP{\cdot}L^{-1}$) and O_2 (~2.2 $cm^3{\cdot}STP{\cdot}L^{-1}$) with values of O_2/N_2 ratio of ~0.4 (**Figure 8G**). The average concentrations of H_2 (**Figure 8H**), He and CH_4 (**Figure 8I**) were ~5.9×10^{-2}, ~4.5×10^{-2}, and ~1.3×10^{-4} $cm^3{\cdot}STP{\cdot}L^{-1}$, respectively. $\delta^{13}C$ values (vs. VPDB) in the dissolved CO_2 in the water columns of Cuicocha and Quilotoa volcanic lakes varied from −4.94 to −0.16‰ (**Figure 8E**) and from −3.50 to −0.17‰ (**Figure 8J**), respectively.

Table 1 shows the chemical and isotopic composition of bubbling gases from Cuicocha and Quilotoa volcanic lakes. Their chemistry shows a clearly CO_2-dominated composition (~54%.V for Cuicocha and ~79%.V for Quilotoa), followed by N_2 (~43%.V for Cuicocha and ~18%.V for Quilotoa), O_2 (~3.0%.V for both lakes), and He (~18 ppm.V for Cuicocha and ~9 ppm.V for Quilotoa). The $\delta^{13}C$-CO_2 in bubbling gases presented a range from −6.65 to −6.34‰ for Cuicocha and from −5.10 to −3.69‰ for Quilotoa.

The $(^3He/^4He)_{corr}$ in bubbling gases ranged from 2.67 to 6.26 R_A at Cuicocha volcanic lake and between 0.42 and 3.12 R_A at Quilotoa volcanic lake, while $^4He/^{20}Ne$ ratios ranged from 3.09 to 14.9 and from 1.72 to 29.2 for Cuicocha and Quilotoa volcanic lakes, respectively (**Table 1** and **Figures 4A,B**). To study the origin of the He, we used the three endmembers (magmatic, atmospheric, and crustal) model proposed by Sano and Wakita (1985). The fraction of atmospheric, magmatic, and crustal components in the sample "i" can be calculated using the following equations:

$$(^3He/^4He)_i = (^3He/^4He)_a \times A + (^3He/^4He)_m \times M + (^3He/^4He)_c \times C \quad (1)$$

$$1/(^4He/^{20}Ne)_i = A/(^4He/^{20}Ne)_a + M/(^4He/^{20}Ne)_m + C/(^4He/^{20}Ne)_c \quad (2)$$

$$A + M + C = 1 \quad (3)$$

where subscripts "a", "m", and "c" indicate atmospheric, magmatic, and crustal sources, respectively; and A, M, and C are the fraction of helium from atmospheric, magmatic, and crustal, respectively (Sano et al., 1985; Sano and Wakita, 1985). Using the following values: $(^3He/^4He)_a$ = 1 R_A, $(^4He/^{20}Ne)_a$ = 0.318, $(^3He/^4He)_m$ = 8 R_A, $(^4He/^{20}Ne)_m$ = 1,000, $(^3He/^4He)_c$ = 0.01 R_A, $(^4He/^{20}Ne)_c$ = 1,000. For Cuicocha volcanic lake, helium isotopic composition of bubbling gases samples indicated a predominant crustal and magmatic component, with values ~53 and ~41% respectively, and relatively low atmospheric contribution (~7%; **Supplementary Table S2** in Supplementary Material). For Quilotoa volcanic lake, helium isotopic composition of bubbling gases samples indicated that crustal He component is predominant (~79%), followed by

TABLE 2 | Chemical and isotopic data of the samples of Cuicocha and Quilotoa volcanic lakes water profiles, including temperature, pH, electrical conductivity (EC), and major ion compositions. The chemical composition is expressed in ppm.m and water stable isotopes are expressed in ‰ vs. VSMOW.

		Depth	T Water	pH	EC	Li^+	Na^+	K^+	Mg^{2+}	Ca^{2+}	HCO_3^-	Cl^-	SO_4^{2-}	$\delta^{18}O_{VSMOW}$-H_2O			δ^2H_{VSMOW}-H_2O		
		(m)	(^oC)		($\mu S\ cm^{-1}$)	(ppm.m)								(‰)			(‰)		
Cuicocha	September 23, 2017	0	17.8	8.36	678	0.11	65.4	5.42	32.2	46.2	338	65.8	20.5	−5.9	±	0.1	−39	±	2
		−10	15.2	8.3	645	0.12	65.9	5.48	31.4	42.4	314	65.0	19.9	−5.8	±	0.1	−40	±	1
		−20	15.3	8.18	684	0.12	66.2	5.54	33.5	47.7	333	68.3	19.9	−5.7	±	0.1	−42	±	1
		−30	15.0	8.35	674	0.12	65.6	5.47	31.5	43.6	329	66.8	19.9	−5.7	±	0.1	−41	±	1
		−40	15.0	8.37	683	0.12	65.3	5.43	29.6	41.6	335	71.6	19.6	−5.8	±	0.1	−44	±	1
		−50	14.9	8.22	686	0.12	65.3	5.48	31.4	43.5	338	66.0	19.5	−5.9	±	0.1	−40	±	2
		−60	15.0	8.24	654	0.11	65.2	5.44	31.2	44.2	332	66.0	20.1	−5.7	±	0.1	−42	±	2
		−70	15.0	8.21	789	0.12	64.6	5.37	30.8	41.9	328	65.1	19.9	−5.8	±	0.1	−41	±	1
		−80	15.3	8.08	740	0.12	65.6	5.42	31.7	43.3	382	64.1	19.5	−5.9	±	0.1	−42	±	2
	October 31, 2018	0	16.4	7.83	681	0.12	65.2	5.91	37.3	57.6	346	67.6	19.5	−6.1	±	0.1	−44	±	2
		−10	16.3	7.95	672	0.12	65.3	5.87	37.3	57.6	342	67.6	19.5	−5.6	±	0.1	−46	±	1
		−20	16.6	7.99	671	0.13	64.8	5.94	34.8	50.7	337	67.8	19.5	−5.6	±	0.1	−44	±	1
		−30	15.6	7.96	679	0.12	65.3	5.89	35.0	51.5	362	67.7	19.5	−5.9	±	0.1	−45	±	2
		−40	15.3	7.92	676	0.11	64.6	5.83	34.3	50.4	361	67.7	19.6	−5.9	±	0.1	−45	±	2
		−50	15.2	7.87	677	0.15	64.6	5.82	34.0	49.7	362	67.8	19.5	−5.6	±	0.1	−47	±	1
		−60	15.0	7.41	680	0.11	65.2	5.96	38.6	52.3	361	68.1	19.6	−6.2	±	0.1	−46	±	2
		−70	15.2	7.58	679	0.12	66.4	6.19	39.9	53.9	361	69.1	19.9	−5.7	±	0.1	−44	±	2
		−80	15.2	7.61	690	0.12	68.1	6.44	35.0	50.0	361	73.5	21.0	−6.1	±	0.1	−47	±	1
Quilotoa	September 20, 2017	0	15.0	7.57	13,890	0.73	2,485	196	685	249	707	4,073	2,524	−1.8	±	0.1	−29	±	2
		−30	12.5	7.43	13,960	0.73	2,482	192	688	356	881	4,140	2,484	−1.6	±	0.1	−32	±	1
		−60	12.8	7.43	13,800	0.79	2,436	193	672	476	708	4,125	2,474	−1.6	±	0.1	−31	±	2
		−90	13.0	7.43	13,800	0.76	2,413	189	672	484	686	4,213	2,478	−1.5	±	0.1	−31	±	2
		−140	12.8	7.42	13,730	0.76	2,434	192	624	420	704	4,109	2,471	−1.6	±	0.1	−29	±	2
	November 06, 2018	0	15.4	7.45	12,960	3.93	2,370	198	768	376	983	4,229	2,491	−1.2	±	0.1	−29	±	1
		−20	13.3	7.50	13,040	4.10	2,453	201	872	478	1,128	4,156	2,434	−1.6	±	0.1	−29	±	3
		−40	13.2	7.27	13,020	4.05	2,409	200	851	498	1,210	4,175	2,439	−1.4	±	0.1	−29	±	1
		−60	13.6	7.06	13,040	4.08	2,390	197	837	552	1,338	4,088	2,372	−1.3	±	0.1	−30	±	1
		−80	13.5	7.04	13,050	3.86	2,369	199	844	561	1,336	4,152	2,427	−1.4	±	0.1	−29	±	2
		−100	13.9	7.05	13,030	4.05	2,441	204	856	560	1,335	4,170	2,433	−1.4	±	0.1	−28	±	2
		−120	13.6	7.00	13,030	4.18	2,396	201	826	533	1,399	4,111	2,394	−1.5	±	0.1	−30	±	1

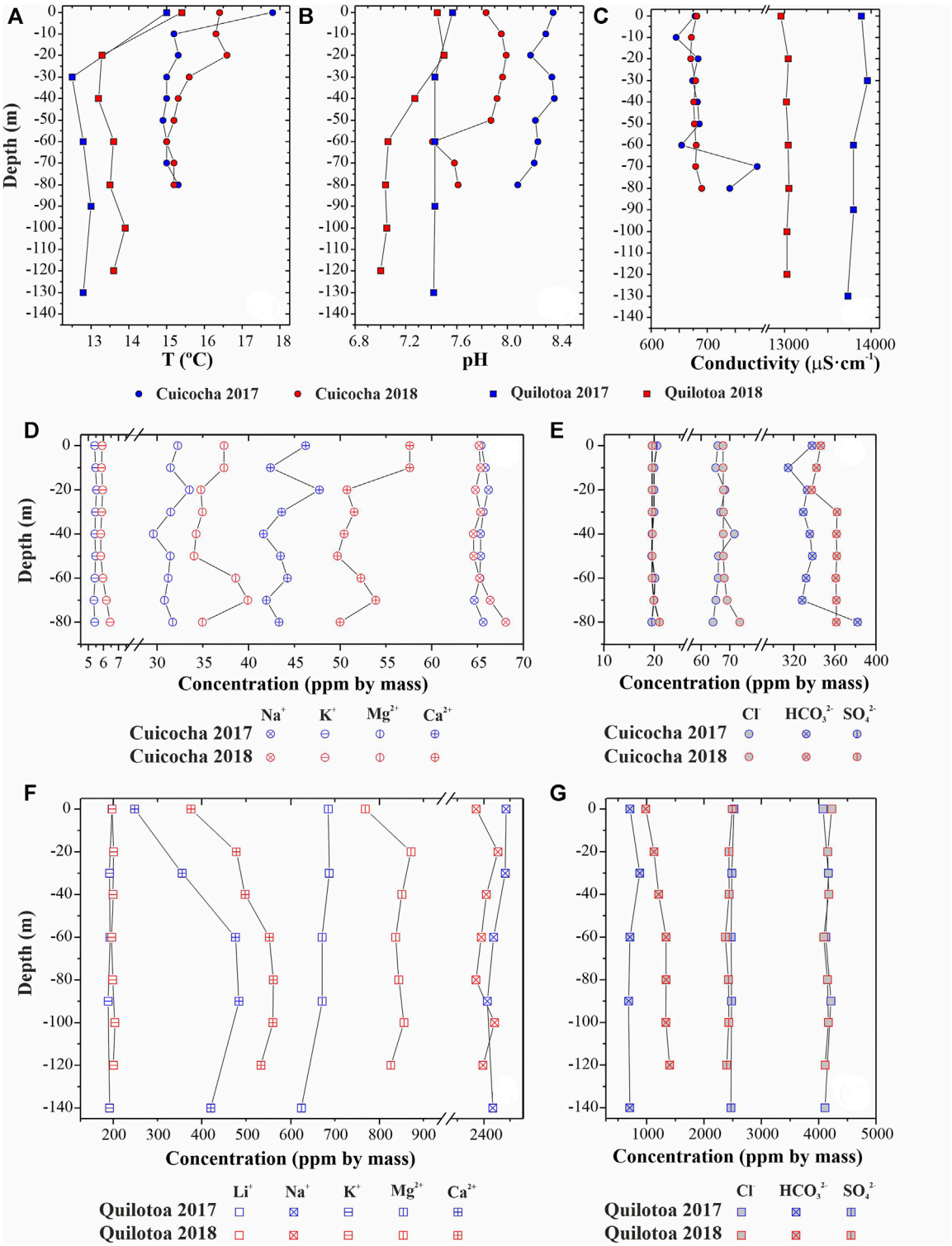

FIGURE 6 | Vertical profiles of **(A)** temperature, **(B)** pH, **(C)** electrical conductivity (EC), and major **(D,F)** cations and **(E,G)** anions in the Cuicocha and Quilotoa waters.

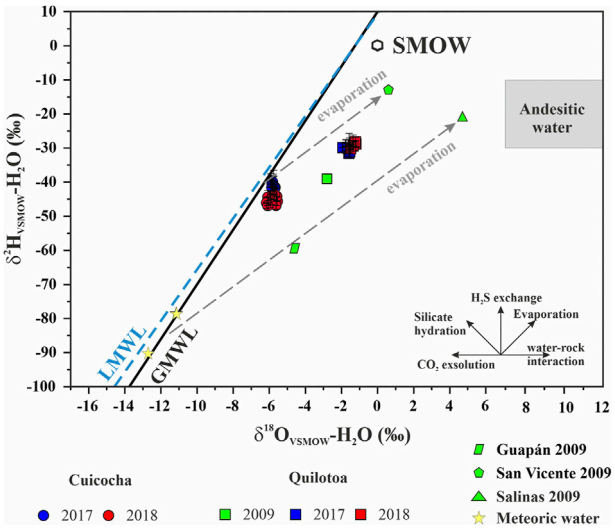

FIGURE 7 | δ^2H_{VSMOW}-H_2O vs $\delta^{18}O_{VSMOW}$-H_2O for samples along the water column at Cuicocha (dots) and Quilotoa (squares) for 2017 (blue) and 2018 (red) surveys. The Global Meteoric Water Line (GMWL; Craig, 1961) and the Local Meteoric Water Line (LMWL; Inguaggiato et al., 2010) are shown. The isotopic composition of the sea water (SMOW), magmatic waters (Giggenbach, 1992), meteoric water (start yellow; Rozanski and Araguás, 1995), and data from Inguaggiato et al. (2010; green) are also plotted. Black lines adapted from (Karolyte et al., 2017).

magmatic He contribution (~16%) and low atmospheric contribution (~5%; **Supplementary Table S2** in Supplementary Material).

Bathymetry Data and Acoustic Anomalies at Quilotoa volcanic Lake

Bathymetry data from the Quilotoa volcanic lake extend across a 2,200 m by 1,560 m oval with the major axis-oriented NW-SE, covering a total surface of 7,100 m^2 (**Figure 1D**). Two bathymetric maps have been made from data of two frequencies: primary at 200 kHz (**Figure 9A**), and secondary at 83 kHz (**Figure 9B**). The 200 kHz bathymetric map (**Figure 9A**) shows a strong anomaly (25 m water depth) surrounded by deep floor (300 m) at the NW of the crater lake. Furthermore, the 83 kHz bathymetric map shows two main anomalies in the center of the deep crater lake (**Figure 9B**). The northern anomaly (25–30 m water depth) is located at the same place as that identified with 200 kHz. However, a second anomaly is in the SW following a certain NW-SE lineament with the northern anomaly (**Figure 9A**). Both anomalies are surrounded by a deep basin reaching water depths of 330 m, while the deep floor of the lake is surrounded by a step flank and a rimmed platform at 25–50 m water depth (**Figure 9B**). Additionally, minor positive anomalies are identified within the flanks, which are also interpreted as minor degassing vents. During the period in which the bathymetric survey was conducted, the lake floor was partially masked by acoustic anomalies from a shallow high-reflective stratified plume that generated backscatter values. The bathymetry shows maximum water depths of 330 m, surrounded by a rimmed platform located between 50 and 75 m (**Figures 9A,B**).

DISCUSSION

Cuicocha Volcanic Lake

CO_2 Diffuse Degassing, Temporal Evolution of Diffuse CO_2 Emission, and $^3He/^4He$ Isotopic Composition at Cuicocha Volcanic Lake

The observed bimodal distributions reflected the existence of more than one population of CO_2 efflux (**Figure 2**), which suggests the occurrence of different sources for the CO_2, as well as the existence of different mechanisms of gas transport (Padrón et al., 2008; Cardellini et al., 2017). In this respect, during the period 2012–2018, Cuicocha volcanic lake presents background CO_2 emission values represented predominantly by the diffusion of CO_2 through the water-air interface. The mean value of the background with a confidence level of one standard deviation was used to estimate the contribution of CO_2 from population I to the CO_2 emission of Cuicocha lake, as previously described (Melián et al., 2014). Assuming an area of 3.95 km^2 for Cuicocha volcanic lake, the cutoff background emission was estimated as 114 $t{\cdot}d^{-1}$ and the standard deviation of the background emission was computed as 65 $t{\cdot}d^{-1}$ for the 16th percentile (-1σ) and 141 $t{\cdot}d^{-1}$ for the 84th percentile ($+1\sigma$). These values are similar to those considered by Sierra et al. (2021), who estimated values of cutoff background emission approximately 79–119 $t{\cdot}d^{-1}$ (20–30 $g{\cdot}m^{-2}{\cdot}d^{-1}$) based on the Graphical Statistical Approach method calculations and the model proposed by Mazot et al. (2014).

The advective mechanism represents an important contribution in population III for Cuicocha volcanic lake, not only by the direct transport to the surface, but also because bubbling contributes to the dissolved CO_2, and as such increases the CO_2 gradient between the bottom and the surface of the lake. The origin of population III is likely the CO_2 released from a magma chamber that escapes to the surface with a crustal CO_2 contribution from carbonate decomposition. Thus, the isotopic composition of dissolved gases (see *Dissolved and Bubbling Gases at Cuicocha Volcanic Lake* section) and the isotopic composition of bubbling gases evidence the existence of deep-seating magmatic degassing that in turn affects the lake.

The temporal evolution of diffuse CO_2 emission measured at the water surface is depicted in **Figure 4A** for Cuicocha volcanic lake (red dots for the present work data, red pentagon for data from Padrón et al. (2008), and red squares for the data from Sierra et al. (2021)), plotted together with the $^3He/^4He$ isotopic ratio measured in the bubbling gases collected in the lake in the period 2006–2018 (blue dots for the present work data and blue diamonds for the data from Inguaggiato et al. (2010)). The seismic event data of Cuicocha are from the IG-EPN seismic network and reported by Sierra et al. (2021). The diffuse CO_2 emission values for Cuicocha volcanic lake were similar to those reported by Padrón et al. (2008) and Sierra et al. (2021; **Figure 4**). Cuicocha is a monomictic lake, *i.e.*, it has an overturn period every year from June to August, when circulation reduces the CO_2 accumulated in the deepest water. Under these conditions, a

TABLE 3 | Chemical (cm^3·STP·L^{-1}) and isotopic (‰ vs VPDB) composition of dissolved gases in the samples of Cuicocha and Quilotoa volcanic lakes water profiles.

		Depth	He	H_2	O_2	N_2	CH_4	CO_2	$\delta^{13}C\text{-}CO_2$		
		(m)	(cm^3· SPT·L^{-1})						(‰ vs. PDB)		
Cuicocha	September 23, 2017	0	n.m.	$3.29{\cdot}10^{-3}$	3.49	6.85	$1.78{\cdot}10^{-3}$	30.4	–0.16	±	0.06
		–10	n.m.	$1.30{\cdot}10^{-3}$	2.57	4.84	$1.46{\cdot}10^{-3}$	20.2	–0.91	±	0.26
		–20	n.m.	$7.43{\cdot}10^{-4}$	2.86	6.01	$1.28{\cdot}10^{-3}$	10.0	–2.68	±	0.04
		–30	n.m.	$7.05{\cdot}10^{-3}$	5.67	12.44	$2.77{\cdot}10^{-3}$	42.5	–0.30	±	0.06
		–40	n.m.	$4.58{\cdot}10^{-3}$	2.87	6.19	$2.65{\cdot}10^{-4}$	10.7	–1.50	±	0.05
		–50	n.m.	$6.84{\cdot}10^{-3}$	2.58	4.87	$9.59{\cdot}10^{-4}$	30.3	–1.87	±	0.04
		–60	n.m.	$1.04{\cdot}10^{-2}$	3.03	6.66	$4.50{\cdot}10^{-4}$	24.7	–1.83	±	0.05
		–70	n.m.	$3.87{\cdot}10^{-4}$	2.80	6.64	$4.30{\cdot}10^{-4}$	16.4	–0.44	±	0.07
		–80	n.m.	$1.14{\cdot}10^{-3}$	2.66	5.55	$5.22{\cdot}10^{-4}$	20.1	–2.27	±	0.05
	October 31, 2018	0	$7.06{\cdot}10^{-3}$	$4.07{\cdot}10^{-3}$	2.61	4.57	$2.04{\cdot}10^{-3}$	4.4	–3.89	±	0.05
		–10	$9.07{\cdot}10^{-3}$	$3.26{\cdot}10^{-3}$	2.53	4.52	$1.94{\cdot}10^{-3}$	3.8	–4.73	±	0.08
		–20	$8.91{\cdot}10^{-3}$	$6.15{\cdot}10^{-4}$	3.36	6.25	$2.78{\cdot}10^{-3}$	4.1	–4.04	±	0.04
		–30	$9.36{\cdot}10^{-3}$	$2.61{\cdot}10^{-2}$	3.47	6.35	$4.24{\cdot}10^{-3}$	37.0	–0.26	±	0.05
		–40	$8.60{\cdot}10^{-3}$	$4.13{\cdot}10^{-3}$	3.11	5.65	$1.56{\cdot}10^{-3}$	89.7	–4.22	±	0.04
		–50	$8.13{\cdot}10^{-3}$	$8.08{\cdot}10^{-5}$	2.67	6.08	$1.53{\cdot}10^{-4}$	36.9	–2.99	±	0.04
		–60	$7.18{\cdot}10^{-3}$	$4.07{\cdot}10^{-5}$	3.61	8.77	$1.89{\cdot}10^{-4}$	14.4	–2.49	±	0.04
		–70	$6.91{\cdot}10^{-3}$	$9.89{\cdot}10^{-3}$	2.24	5.28	$2.29{\cdot}10^{-4}$	52.1	–4.94	±	0.05
		–80	$6.65{\cdot}10^{-3}$	$9.30{\cdot}10^{-4}$	2.54	5.84	$9.41{\cdot}10^{-4}$	15.1	–2.20	±	0.05
Quilotoa	September 20, 2017	0	n.m.	$7.33{\cdot}10^{-3}$	3.37	6.42	$3.05{\cdot}10^{-5}$	19.3	0.58	±	0.03
		–30	n.m.	$3.66{\cdot}10^{-3}$	2.20	5.93	$1.83{\cdot}10^{-4}$	111.8	–1.49	±	0.09
		–60	n.m.	$2.21{\cdot}10^{-3}$	2.39	7.21	$1.47{\cdot}10^{-4}$	174.4	–1.72	±	0.06
		–90	n.m.	$5.67{\cdot}10^{-3}$	2.17	6.60	$2.70{\cdot}10^{-4}$	189.7	–1.03	±	0.09
		–140	n.m.	$4.05{\cdot}10^{-1}$	1.78	5.39	$2.32{\cdot}10^{-4}$	186.9	0.17	±	0.09
	November 06, 2018	0	$5.12{\cdot}10^{-2}$	$4.88{\cdot}10^{-2}$	2.64	5.12	$1.20{\cdot}10^{-4}$	21.9	–0.65	±	0.05
		–20	$4.08{\cdot}10^{-2}$	$7.76{\cdot}10^{-2}$	4.61	9.70	$8.22{\cdot}10^{-5}$	31.5	–2.65	±	0.06
		–40	$3.27{\cdot}10^{-2}$	$9.51{\cdot}10^{-3}$	2.02	5.38	$3.33{\cdot}10^{-5}$	73.5	–0.27	±	0.09
		–60	$4.68{\cdot}10^{-2}$	$4.41{\cdot}10^{-2}$	2.17	7.52	$4.85{\cdot}10^{-5}$	138.7	–1.55	±	0.05
		–80	n.m.	n.m.	n.m.	n.m.	n.m.	n.m.	–2.97	±	0.04
		–100	$5.11{\cdot}10^{-2}$	$2.71{\cdot}10^{-2}$	2.34	8.88	$5.65{\cdot}10^{-5}$	189.4	–3.50	±	0.07
		–120	$2.21{\cdot}10^{-1}$	$5.08{\cdot}10^{-3}$	0.69	4.52	$1.25{\cdot}10^{-5}$	128.9	–3.45	±	0.03

n.m., not measured.

maximum CO_2 emission to the atmosphere occurs (Padrón et al., 2008). This could be the mechanism that explains the maximum emission rate measured in July 2012, values higher than those estimated as background emission. However, since a much lower value was reported in a survey conducted in 2006 (Padrón et al., 2008), a significant increase in the input of magmatic CO_2 cannot be excluded. The magmatic component increased in 2009 as indicated in **Supplementary Table S2** (Supplementary Material), and the CO_2 released from the fresh magmatic melts persisted during 2009–2012. However, the magmatic He was released more quickly as the magmatic component remained at similar values in 2006 and 2012 and experienced an increase in 2009. Such observations are coherent with the expected geochemical behaviors of He and CO_2. It is also worth noting that the CO_2 emission peak detected in 2012 occurred after episodes of high LP seismicity at the end of 2011 and beginning of 2012 (Sierra et al., 2021). LP events are generally low-amplitude signals linked to alterations in the shallow hydrothermal system. Such alterations might be due to injection of magmatic fluids that were observed at the surface several months later. $^3He/^4He$ ratio measured in bubbling gases in the lake showed an increase from 2006 to 2009 (**Figure 4A**), which means an increase in the magmatic fraction of helium (**Supplementary Table S2** in Supplementary Material). Unfortunately, no data are available between 2009 and 2012 to confirm if the increase persisted after 2009. The increase in magmatic helium emission suggests a magmatic intrusion, which likely occurred in 2009 or before, and injected magmatic gases and perturbed the hydrothermal system, stimulating pressure fluctuations and causing fluid-driven cracks in the volcano-hydrothermal system of Cuicocha.

Lake Water Chemistry and Vertical Profiles at Cuicocha Volcanic Lake

Vertical profiles of water temperature, pH, and EC (**Figures 6A–C**) showed that Cuicocha volcanic lake is comprised of discrete water masses. The water temperature shows variations at 30 cm depth, which are attributed to environmental influences (**Figure 6A**). The temperature differences depicted in **Figure 6A** were observed between the surface waters and 20 m depth in both 2017 and 2018 surveys, and hence the thermal stratification. This observation is consistent with the report of a stratification period (September to May) in Cuicocha volcanic lake by Padrón et al. (2008).

The EC of Cuicocha lake (<700 μS·cm^{-1}) is relatively elevated compared to values of the nonactive Ecuadorian Mojanda caldera (35 μS·cm^{-1}), reported by Gunkel et al. (2009). In general, anions and cations content are present with higher concentration in the hypolimnetic waters than in the epilimnion (**Figures 6D–G**).

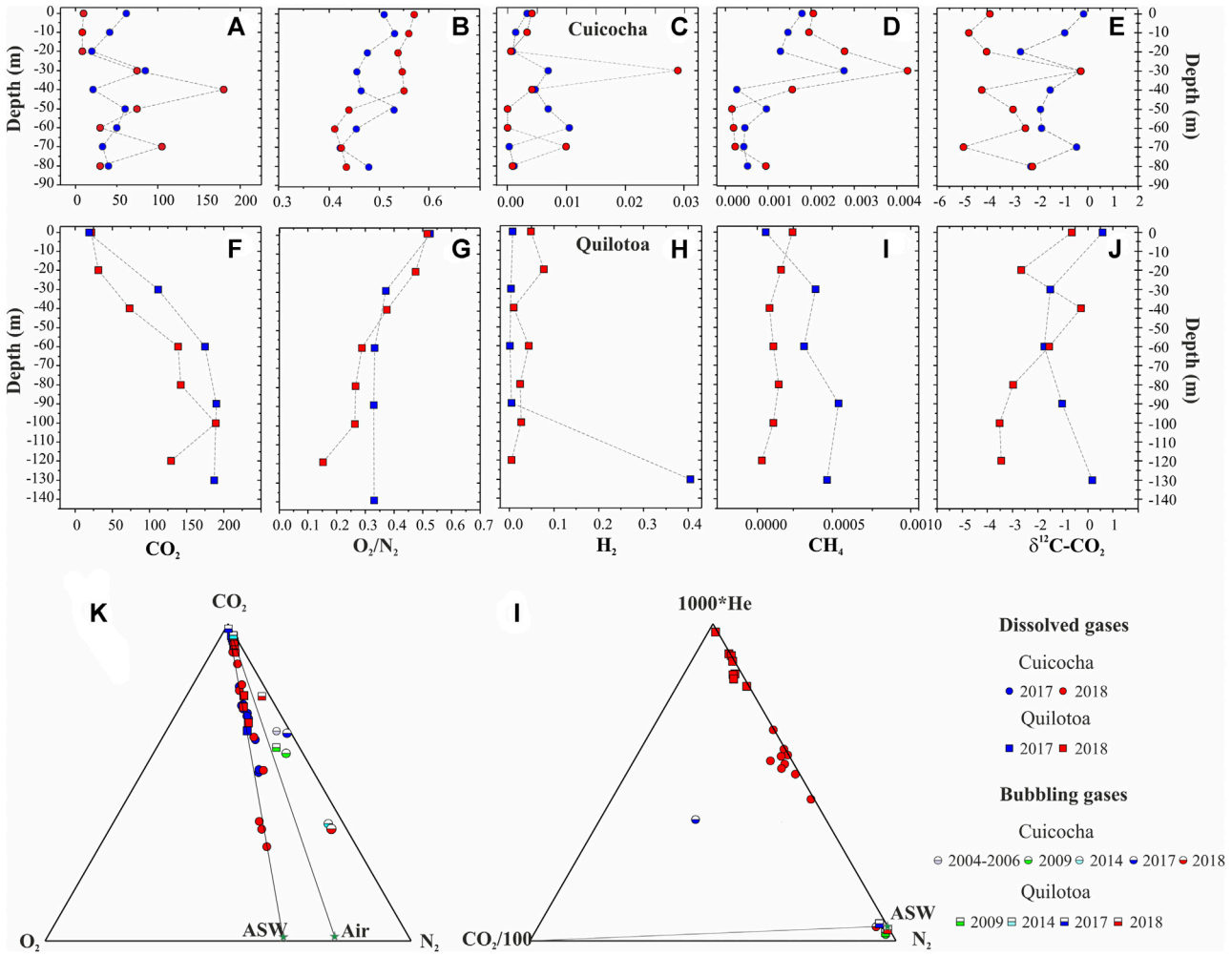

FIGURE 8 | Vertical profiles of dissolved gases from Cuicocha [dots; **(A–E)**] and Quilotoa [square; **(F–J)**] volcanic lake. **(K)** CO_2-N_2-O_2 and **(L)** He-N_2-CO_2 ternary diagram for dissolved gases and for bubbling gases from Cuicocha (dots) and Quilotoa (square) volcanic lake collected during 2014 (cian), 2017 (blue) and 2018 (red) surveys. Data from Gunkel et al. (2009; gray) and Inguaggiato et al. (2010; green) are also shown.

These results are comparable with the data reported by Gunkel et al. (2009). According to the Langelier-Ludwig classification diagram represented in **Figure 10A**, the samples along the water column display a $Ca^{2+}(Mg^{2+})$-HCO_3^- composition typical of worldwide superficial waters and shallow aquifers (Tassi et al., 2009; Inguaggiato et al., 2010). Inguaggiato et al. (2010) report water composition enriched in Cl^- + SO_4^{2-}, probably because the sample was collected in the bubbling zone richest in Cl^- and SO_4^{2} located on the northern shores of Yerovi Island. A similar behavior is observed at a depth of 60 m in one of the profiles reported by Gunkel et al. (2009), where an increase in the concentration of CO_2 was also registered (Gunkel et al., 2009). The samples of Cuicocha present low values of total dissolved solids (TDS = 269 mg·L^{-1}) which could be explained by a weak water-rock interaction due to short residence time and/or low aquifer temperature.

The relative HCO_3^-, SO_4^{2-}, and Cl^- contents in the vertical profiles samples are presented in **Figure 10B** (Giggenbach, 1988) of Cuicocha volcanic lake for the 2017 and 2018 surveys. The samples from the Cuicocha plot close to the HCO_3^- vertex, in the peripheral waters zone, probably due to gas-water interaction processes, CO_2 addition/removal processes in the aquifer (Inguaggiato et al., 2010), and/or addition of organic CO_2 from decomposition of plants and animals (Aguilera et al., 2000). The variation of SO_4^{2-} and Cl^- in water samples relative to the volcanic hydrothermal fluids (VHFs), meteoric water (MW), and seawater (SW) end-members (Hernández et al., 2017) is shown in **Figure 11**. The Cuicocha samples show a low SO_4^{2-} and Cl^- content and plot close to MW, explained by rainfall and input of surface water from the catchment area feed the lake, along with hydrothermal water inflow (Gunkel et al., 2009).

Values for δ^2H_{VSMOW}-H_2O and $\delta^{18}O_{VSMOW}$-H_2O for Cuicocha profiles are presented in **Figure 7**, Local Meteoric Water Line (LMWL; $\delta^2H = 6.3\times\delta^{18}O+8.1$; Inguaggiato et al., 2010), and Global Meteoric Water Line (GMWL; $\delta^2H = 8\times\delta^{18}O+10$; Craig, 1961). To evaluate the evaporation process,

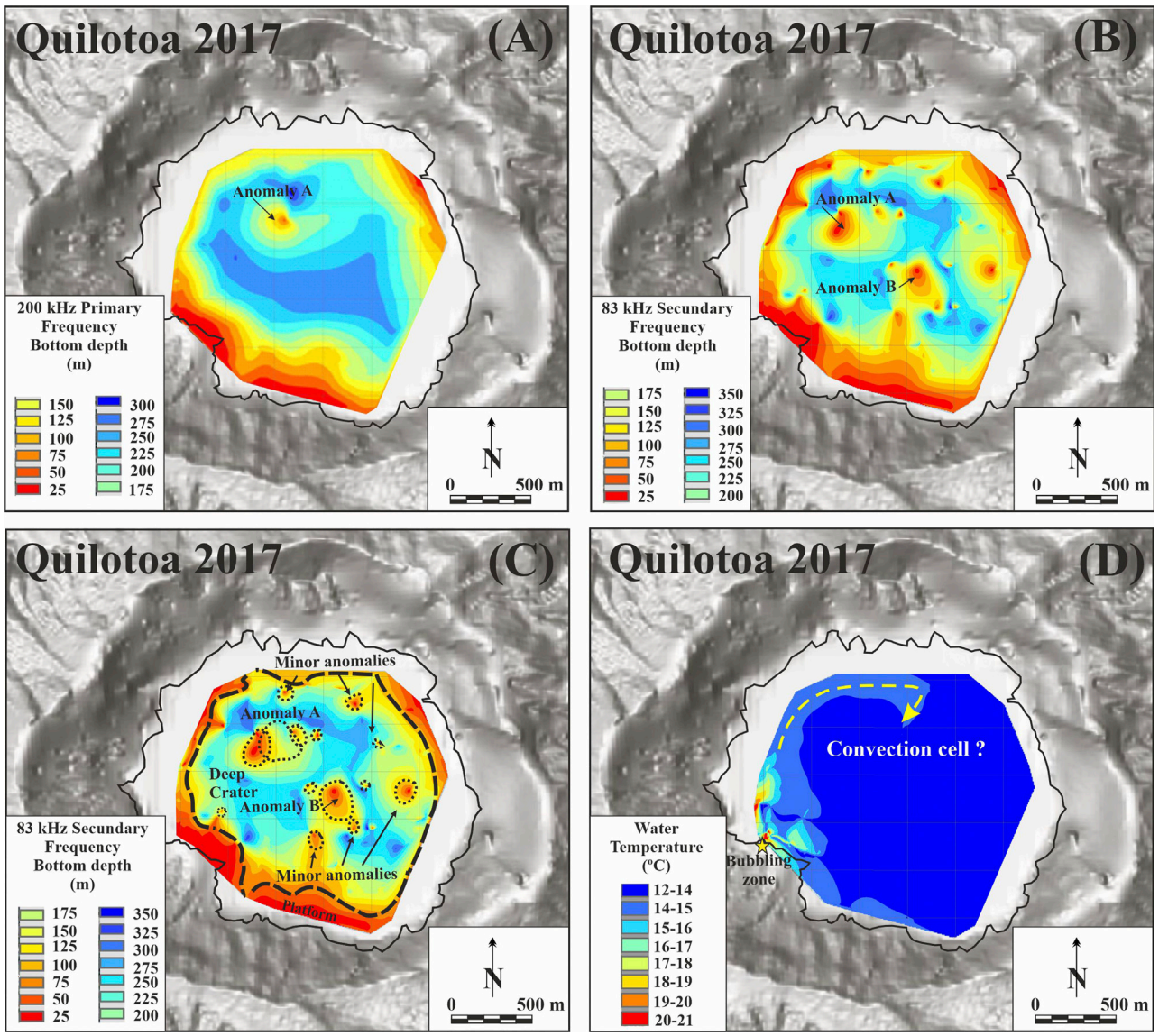

FIGURE 9 | Map of the acoustic data of the Quilotoa volcanic lake derived from the two-frequency echosounder: **(A)** 200 kHz and **(B)** 83 kHz. **(C)** Interpretation of the acoustic anomalies and bathymetric data of the volcanic lake. The positive acoustic anomalies (up to 25 m) are interpreted as false echoes caused by high reflective layers at the top of intense degassing vents **(A,B)**. See the text for further explanation. **(D)** Distribution of surface water temperature of the crater lake obtained from the echosounder sensor.

the isotopic composition of San Vicente, Salinas, and Guapán water from Inguaggiato et al. (2010) is also represented for comparative purposes (**Figure 1A**). The samples of Cuicocha present values of $\delta^{18}O_{VSMOW}$-H_2O and $\delta^{2}H_{VSMOW}$-H_2O very close to the LMWL and/or GMWL, suggesting that the volcanic lake water is mainly recharged by local precipitation that is characterized by a short residence time (Giggenbach, 1991). This result is concordant with the low SO_4^{2-} and Cl^- contents shown in **Figure 11**. There are differences in the $\delta^{2}H_{VSMOW}$-H_2O of Cuicocha between waters collected in 2017 and 2018 (~−6‰). $\delta^{2}H_{VSMOW}$-H_2O changes are related to H_2S exchange from volcanic gases (Karolyte et al., 2017). During 2017, Cuicocha volcanic lake presents values of CO_2 emission and $^3He/^4He$ greater than in 2018 (**Figure 4**), which is consistent with higher values of $\delta^{2}H_{VSMOW}$-H_2O.

Dissolved and Bubbling Gases at Cuicocha Volcanic Lake

Dissolved gases in volcanic lakes are excellent tracers of gas-water interaction, due to their high mobility and different solubilities (Capasso and Inguaggiato, 1998; Capasso et al., 2000). The concentrations of dissolved gases (**Table 3**) in the Cuicocha samples collected during the 2017 and 2018 surveys are higher than expected values for air-saturated water (ASW; Capasso and Inguaggiato, 1998) at the sampling temperature, which suggests an important gas–water interaction. The content of CO_2 in all the

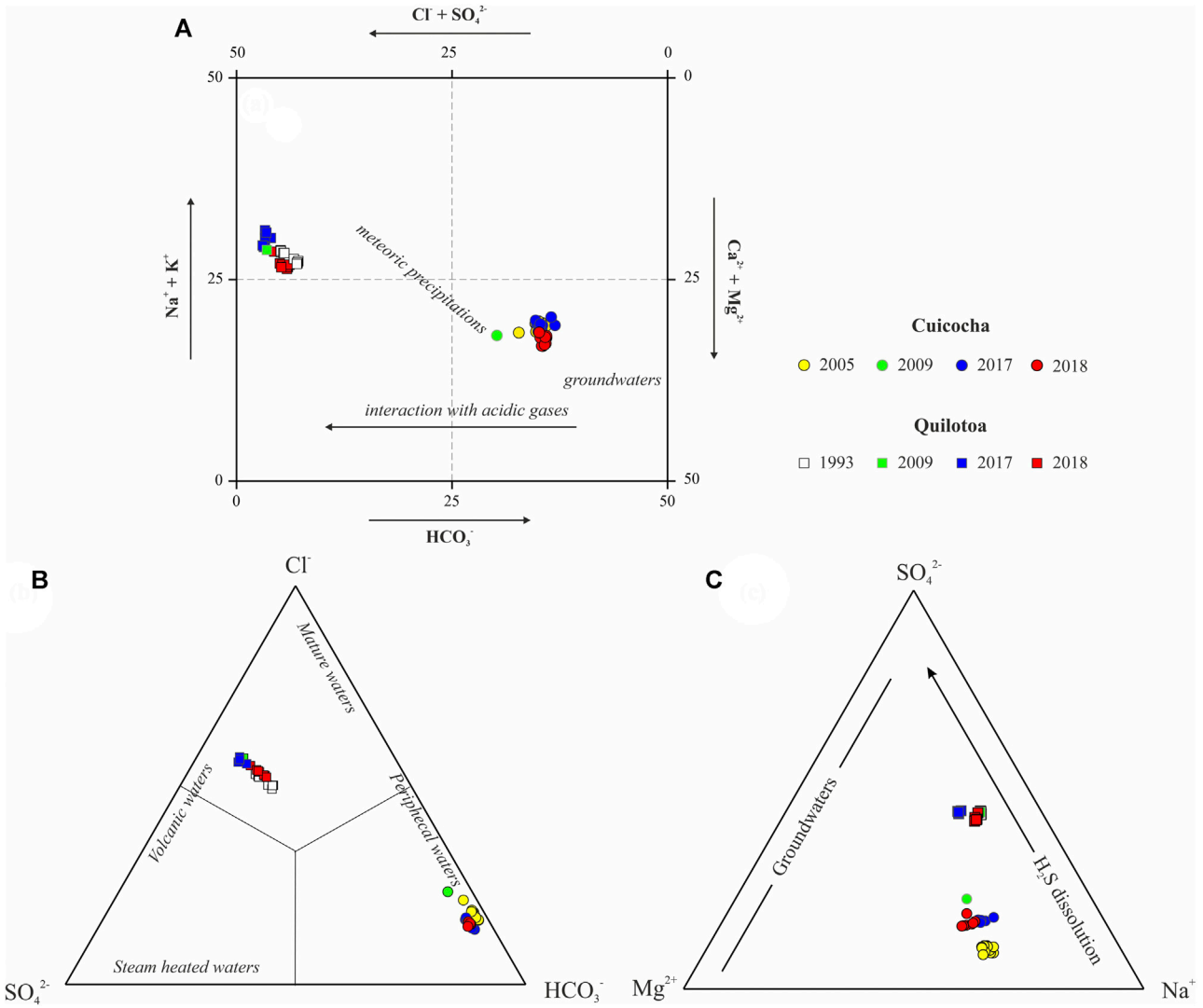

FIGURE 10 | (A) Langelier-Ludwig (1942) diagram for the samples along the water column from Cuicocha (dots) and Quilotoa (squares) lakes for the 2017 (blue) and 2018 (red) surveys. Plot of relative **(B)** HCO_3^-, SO_4^{2-}, and Cl^- and **(C)** Na^+, SO_4^{2-}, and Mg^{2+} contents for the water samples from the Cuicocha (dots) and Quilotoa (square) lakes for the 2017 (blue) and 2018 (red) surveys. Data from Aguilera et al. (2000; white squares), Gunkelet al. (2009; yellow squares), and Inguaggiato et al. (2010; green squares) are also shown.

samples (~26 $cm^3 \cdot STP \cdot L^{-1}$) is much higher than the ASW values (0.32 $cm^3 \cdot STP \cdot L^{-1}$). For the 2018 survey, high concentrations of He (~$8 \cdot 10^{-3}$ $cm^3 \cdot STP \cdot L^{-1}$) were also measured in the water column (ASW = $4.8 \cdot 10^{-5}$ $cm^3 \cdot STP \cdot L^{-1}$). The high concentrations of CO_2 and He measured in dissolved gases suggest a significant contribution of such gases from volatile-rich fluids. No significant variation was observed in the chemical and isotopic composition of water in 2018 compared to 2017.

The thermal stratification observed in Cuicocha volcanic lake (**Figure 6A**) is confirmed by a corresponding stratification of dissolved gases (**Figures 8A–E**). CO_2 concentration in dissolved gases showing a decreasing trend toward the 40 m depth sample (epilimnion zone) could be due to the loss to the atmosphere and photosynthetic utilization, which then increases again to the bottom of the lake (**Figure 8A**). The CH_4 concentrations are lower in the hypolimion with respect to the epilimnion (**Figure 8C**), while high concentrations of dissolved CO_2, H_2, and CH_4 in water have been observed around 20–40 m (**Figures 8A,C,D**), in the metalimnion zone. The carbon isotopic signature (**Figure 8E**) indicates a clear endogenous origin for CO_2, with a greater contribution in the metalimnion zone. These results are congruent with the data observed by Gunkel et al. (2009) who observed emission of gases using sonar from the bottom of the crater lake (see **Figure 1B**).

The relative compositions of both dissolved and bubbling gases are plotted on the CO_2-O_2-N_2 ternary diagram (**Figure 8K**). All samples of dissolved gases of Cuicocha volcanic lake show an alignment with an O_2/N_2 ratio at

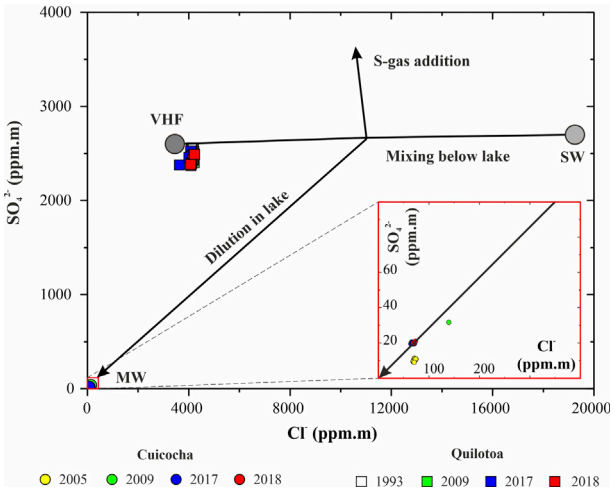

FIGURE 11 | Binary diagram of SO_4^{2-} vs. Cl^- for the Cuicocha and Quilotoa water samples collected during the 2017 (blue) and 2018 (red) surveys. Data from Aguilera et al. (2000; white), Gunkelet al. (2009; yellow), and Inguaggiato et al. (2010; green) are also shown. VHF: volcanic hydrothermal fluid; MW: meteoric water and SW: seawater (Hernández et al., 2017).

around ASW (~0.489; **Figures 8A,K**) and a relative increase of CO_2 with depth was also observed (**Figure 8A**). This result suggests different degrees of interaction between the bubbling gases and the water of Cuicocha volcanic lake. Bubbling gases present an O_2/N_2 ratio lower than that in air (**Figure 8K**), highlighting an excess of non-atmospheric N_2 and/or a consumption of O_2. The O_2 consumption due to reducing redox conditions could be the principal process causing the relative N_2-enrichment. The relative content of He, N_2, and CO_2 in the samples of both dissolved and bubbling gases is represented (**Figure 8L**). All the dissolved gases samples of Cuicocha volcanic lake show very similar He, N_2, and CO_2 content and He/N_2 ratios higher than the atmospheric ratio (~$1.4{\cdot}10^{-3}$). The He/N_2 ratios in dissolved gases were very different from those measured in the bubbling gases, except for Cuicocha in the 2017 survey. All bubbling gases samples plot close to the N_2 vertex, due principally to reducing redox conditions.

Quilotoa volcanic Lake

CO_2 Diffuse Degassing, Temporal Evolution of Diffuse CO_2 Emission, and $^3He/^4He$ Isotopic Composition at Quilotoa volcanic Lake

As in the Cuicocha volcanic lake, two distinct modes were found at Quilotoa volcanic lake (**Figure 2**) suggesting a deep perturbation of the volcanic system for the CO_2 and/or different mechanisms of gas transport (Padrón et al., 2008; Cardellini et al., 2017). Background CO_2 emission values (population I) are predominantly represented by the diffusion of CO_2 through water-air interface during the period 2014–2018. The contribution of CO_2 from population I to the CO_2 emission of Quilotoa lake (3.50 km^2) is estimated as 137 $t{\cdot}d^{-1}$ with a standard deviation as 89 $t{\cdot}d^{-1}$ for −1σ and 212 $t{\cdot}d^{-1}$ for the +1σ. No previous data are described in the literature. Advection might be the responsible transport mechanism to explain the relatively high observed CO_2 efflux values (population III). The isotopic composition of dissolved and bubbling gases (see *Dissolved and Bubbling Gases at Quilotoa volcanic Lake section*) and the observation of acoustic degassing plumes in Quilotoa (see *Acoustic Degassing Plumes and Crater-Lake Bottom Morphology at Quilotoa volcanic Lake section*) evidence the existence of deep-seating degassing from the bottom of the crater lake.

Figure 4B shows the temporal evolution of diffuse CO_2 emission measured at the water surface from Quilotoa volcanic lake (red dots for present work data), plotted together with the $^3He/^4He$ isotopic ratio measured in the bubbling gases (blue dots for present work data and blue diamonds for data from Inguaggiato et al. (2010)). The temporal evolution of diffuse CO_2 emission measured from the water surface of Quilotoa volcanic lake during 2014–2018 period and the $^3He/^4He$ values at the bubbling gases in the period 2009–2018 present maximum values in 2014 and a decreasing trend until the 2018 survey. Unfortunately, geophysical records are not available nor diffuse CO_2 studies prior to 2014. The lack of more records does not allow for the evaluation of the possible origin of this increase; however, it is worth noting that an increase in the magmatic fraction of helium was observed in 2014 (**Supplementary Table S2** in Supplementary Material), so an additional contribution of deep-seated fluids to the volcanic system cannot be ruled out.

The differences observed in the $^3He/^4He$ ratio measured in bubbling gases reported in this work and by other authors between Cuicocha and Quilotoa could be related to the age of the recent volcanism in both systems: Cuicocha has experienced 4 confirmed holocenic volcanic eruptions and Quilotoa only one. In fact, bubbling gases in Quilotoa show a higher percentage of radiogenic (crustal) He (~79%) than that in Cuicocha (~48%), where the magmatic component is higher. It is worth highlighting that the largest magmatic component of Cuicocha bubbling gases was observed in 2009 (Inguaggiato et al., 2010), 2–3 years before the seismic unrest that occurred in the surroundings of Cuicocha. As stated before, a magmatic intrusion, likely occurred in 2009 or before injected magmatic gases, disturbed the hydrothermal system that later originated pressure fluctuations, and caused fluid-driven cracks in the volcano-hydrothermal system of Cuicocha.

Quilotoa presents a relatively low normalized CO_2 emission values by area that was approximately ~94 $t{\cdot}d^{-1}{\cdot}km^{-2}$, which is a typical value for lakes filled with neutral pH waters and comparable to other volcanic lakes as Masaya and Apoyeque (Nicaragua; Pérez et al., 2011) and significantly higher than that of Cuicocha. With a value of normalized CO_2 emission by area of ~27 $t{\cdot}d^{-1}{\cdot}km^{-2}$, excluding the maximum of the 2012 survey where a contribution of magmatic CO_2 cannot be excluded. These values are similar to those estimated in Nejapa (Nicaragua) or Monoun (Cameroon) volcanic lakes (Pérez et al., 2011).

Lake Water Chemistry and Vertical Profiles at Quilotoa volcanic Lake

The water temperatures (**Figure 6A**), pH (**Figure 6B**), and EC (**Figure 6C**) measured during this study in the vertical profiles

indicated that Quilotoa volcanic lake is made up of different water masses. The temperature differences depicted in **Figure 6A** were observed between the surface waters and 30 m depth in both the 2017 and 2018 surveys, and thermal stratification. This observation is consistent with the report by Aguilera et al. (2000). The EC of Quilotoa lake (~12,000 $\mu S \cdot cm^{-1}$) was high, compared with Cuicocha lake (<700 $\mu S \cdot cm^{-1}$) and Mojanda caldera (35 $\mu S \cdot cm^{-1}$; Gunkel et al., 2009). In general, anions and cations content present higher concentration in the hypolimnetic waters than in the epilimnion ones. The Langelier-Ludwig classification diagram (**Figure 10A**) shows that the water samples of the Quilotoa volcanic lake plot in the $Na^+(K^+)$-$Cl^-(SO_4^{2-})$ field, typical of crater lakes in active volcanic systems (Delmelle and Bernard 1994; Tassi et al., 2009; Hernández et al., 2017). These results are in accordance with those reported by other authors who observed similar findings about the chemical composition of Quilotoa volcanic lake (**Figure 10A**; Aguilera et al., 2000; Inguaggiato et al., 2010).

Figure 10B shows the relative HCO_3^-, SO_4^{2-}, and Cl^- contents in the vertical profiles (Giggenbach, 1988) for Quilotoa volcanic lake for the 2017 and 2018 surveys. Data from Aguilera et al. (2000), Gunkel et al. (2009), and Inguaggiato et al. (2010) are also shown. The water from Quilotoa shows an intermediate composition with a trend observed in the Na^+ and SO_4^{2-} contents (**Figure 10C**) that suggests the addition of S-rich gases to the lake water. The relatively higher Cl^-/SO_4^{2-} ratios (**Figure 11**) of Quilotoa samples are probably due to 1) the removal of S (precipitation of SO_4^{2-} minerals and elementary S and/or bacterial reduction of SO_4^{2-} to S^{2-} and precipitation of sulfide minerals); 2) the addition of Cl^- related to inflow of neutral Na-Cl^- geothermal waters or brines; or 3) both (Aguilera et al., 2000). Quilotoa water samples present a typical composition of VHF, a fact that is also endorsed by the δ^2H_{VSMOW}-H_2O and $\delta^{18}O_{VSMOW}$-H_2O values (see **Figure 7**).

The Quilotoa water samples are all enriched in both δ^2H_{VSMOW}-H_2O and $\delta^{18}O_{VSMOW}$-H_2O relative to the GMWL indicating a different origin and/or that waters have modified their isotopic composition (**Figure 7**). A very moderate isotopic shift of oxygen can be observed relative to GMWL values by up to +3.5‰ (**Figure 7**), suggesting the occurrence of enhanced water–rock interactions, mixing with VHF or andesitic water, or/and evaporation processes. There are marked differences in the isotopic composition between the Quilotoa volcanic lake waters collected in 2009 by Inguaggiato et al. (2010) and the samples collected in the present study. Inguaggiato et al. (2010) reported for Quilotoa water samples collected in bubbling gases values of -2.8‰ for $\delta^{18}O_{VSMOW}$-H_2O and -39‰ for δ^2H_{VSMOW}-H_2O. However, in this study, we obtained values for $\delta^{18}O_{VSMOW}$-H_2O of ~ −1.5‰ and δ^2H_{VSMOW}-H_2O of ~ −29‰. Different hypotheses could explain the observed changes of δ^2H_{VSMOW}-H_2O values between the samples collected during 2009 and 2017–2018: 1) changes in evaporation because of an increase in water temperature; 2) increased rainfall (displacement of the data toward the LMWL); 3) incorporation of andesitic water due to an increase in hydrothermal volcanic fluids; and 4) hydrogen exchange between H_2S and H_2O (Hernández et al., 2017). The concentration of Cl^-, SO_4^{2-} and most cations were similar in Quilotoa for 2009 and this study (2017 and 2018 surveys); therefore, isotopic changes cannot be explained as a consequence of variations in concentration. The water temperature of Quilotoa lake in 2009 (22°C; Inguaggiato et al., 2010) was significantly higher than in 2017 and 2018 (~13.5°C), so the evaporation process could explain the changes observed in the isotopic composition of water for the different surveys. For Quilotoa volcanic lake, the values reported by Inguaggiato et al. (2010) for the 2009 survey present lighter values with respect to the 2017 and 2018 surveys, indicating an increase in the isotopic exchange of endogenous CO_2 with water. A similar behavior was observed for δ^2H_{VSMOW}-H_2O, showing a shift toward lighter δ^2H_{VSMOW}-H_2O values, which can be explained in terms of more abundant H_2S and associated isotopic exchange (Aguilera et al., 2000). These variations were agreed with the emission CO_2 and $^3He/^4He$ data observed in 2009 and 2017–2018 from Quilotoa volcanic lake.

Dissolved and Bubbling Gases at Quilotoa volcanic Lake

The concentrations of dissolved gases (**Table 3** and **Figure 7**) in the Quilotoa samples of vertical profiles collected during the 2017 and 2018 surveys are higher than the expected values for ASW (Capasso and Inguaggiato, 1998) at the sampling temperature, which suggests an important gas–water interaction. The content of CO_2 in all the samples (~115 $cm^3 \cdot STP \cdot L^{-1}$) is much higher than the ASW values (0.32 $cm^3 \cdot STP \cdot L^{-1}$; Capasso and Inguaggiato, 1998). For the 2018 survey, high concentrations of He (~$7.0 \cdot 10^{-2}$ $cm^3 \cdot STP \cdot L^{-1}$) were also measured in the water column (ASW = $4.8 \cdot 10^{-5}$ $cm^3 \cdot STP \cdot L^{-1}$; Capasso and Inguaggiato, 1998). The high concentrations of CO_2 and He measured in dissolved gases suggest a significant contribution of such gases from volatile-rich fluids.

The relative composition of both dissolved and bubbling gases is plotted on a CO_2-O_2-N_2 ternary diagram (**Figure 7K**). All samples of dissolved gases at Quilotoa show an alignment with an O_2/N_2 ratio at around ASW (~0.529) and an increase of CO_2 with depth was also observed (**Figure 7K**). This result suggests different degrees of interaction between the bubbling gases and the water of Quilotoa volcanic lakes. Bubbling gases present an O_2/N_2 ratio lower than that in air (**Figure 7J**) with CO_2 content and O_2/N_2 ratio higher than Cuicocha, suggesting a reducing redox condition in Quilotoa volcanic lake.

The relative content of He, N_2, and CO_2 in the samples of both dissolved and bubbling gases are represented (**Figure 7**). All the dissolved gases samples of Quilotoa volcanic lake show very similar He, N_2, and CO_2 content with He/N_2 ratios (~$1.35 \cdot 10^{-2}$) higher than the atmospheric and very different from those measured in the bubbling gases. The physicochemical conditions of the Quilotoa volcanic lake (pH, temperature, and salinity) control the behavior of CO_2 in water due to the different solubility and reactivity between He and CO_2 (Capasso et al., 2000).

The distribution of dissolved H_2 and CH_4 and CO_2, together with the O_2/N_2 ratios along the Quilotoa vertical profile, are shown in **Figure 7L**. For Quilotoa volcanic lake, a stratification of the dissolved gases was observed at ~30 m depth. CO_2 and CH_4

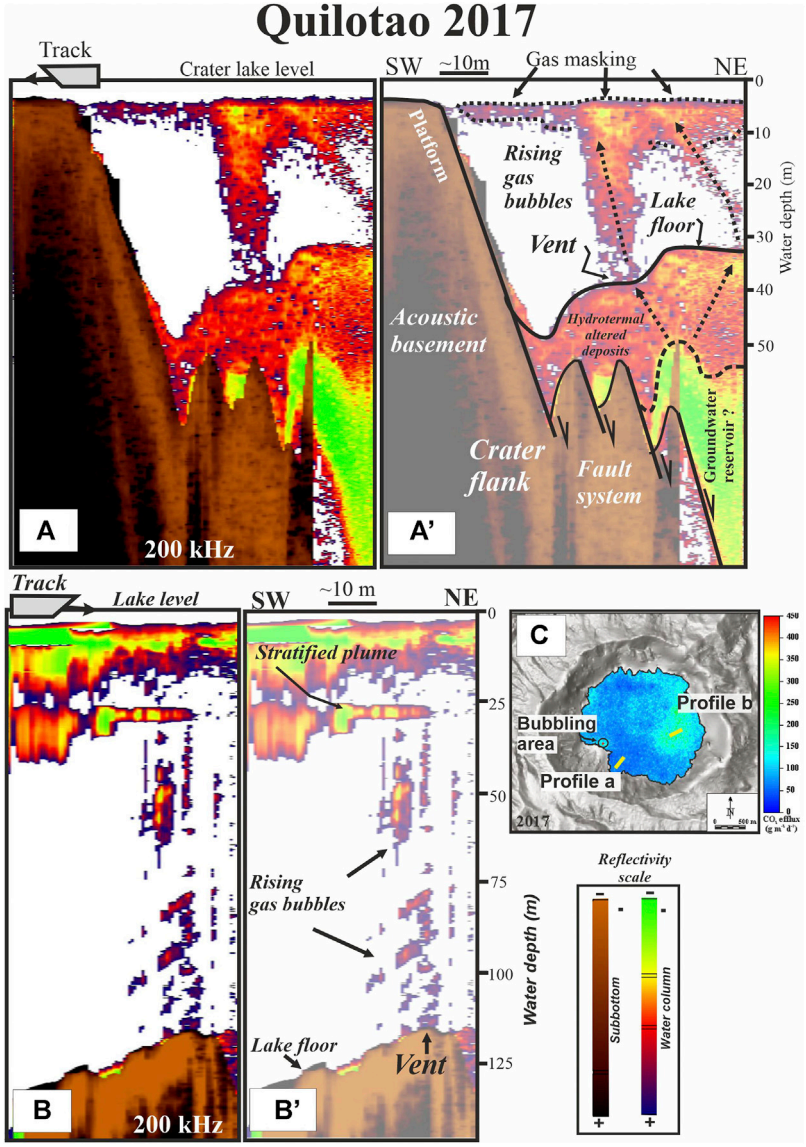

FIGURE 12 | Images of the degassing plumes sourced from the Quilotoa crater floor; **(A,A')** Shallow-water degassing vents (35 m water depths) on the western flank of the crater lake. Degassing takes place through low-backscatter sediments. **(B,B')**. Deep-water degassing vent (120 m) located on the eastern flanks and associated with high CO_2 flux. **(C)** Spatial distribution of CO_2 efflux at Quilotoa volcanic lake for 2017.

concentrations in dissolved gases show an increasing trend toward 120–140 m depth (**Figures 7F,H**). High concentrations of H_2 at depth stand out in the 2017 survey (**Figure 7G**), suggesting a reducing redox condition in Quilotoa volcanic lake. The isotopic signature of carbon (**Figure 7J**) also indicates a clear endogenous origin for CO_2 consistent with the occurrence of significant CO_2 sources rising from the bottom of the lake through fumarolic discharges.

Acoustic Degassing Plumes and Crater-Lake Bottom Morphology at Quilotoa volcanic Lake

Based on both frequencies studied (200 and 83 kHz), it can be interpreted that the acoustic data are composed of true and false bathymetric echoes (**Figures 6A–C**). False echoes forming acoustic positive anomalies are interpreted as zones of intense degassing generating false acoustic domes that mask the real lake floor as reported in other active acid crater lakes and verified in the Taal crater lake 2 years before the explosion of the crater lake, where intense degassing partially masked the lake floor (Hernández et al., 2017). Thus, two main positive anomalies (labeled as A and B in **Figures 6A,B**) are located in the center of ~ 330 m crater floor. Aguilera et al. (2000) described that the deepest lake floor was located at 200 m water depths within an elongated deep basin surrounded by steep flanks, with a morphology and depth very different from those obtained in this work. The northern anomaly A is identified on both 200 and 83 kHz, whereas the southern

anomaly B is only identified with the lowest frequency of 83 kHz (**Figure 6B**). Both anomalies are NW-SE oriented, suggesting they are related to deep vents sourced from the deepest crater lake. Otherwise, minor positive anomalies identified within the flanks are interpreted as minor degassing vents sourced from the flanks of crater (**Figure 6C**). These minor degassing vents do not mask the water column fully, which allows the possibility to image the degassing sourced from the lake's bottom. Thus, two main vertical acoustic degassing plumes have been imaged by the echosounder in both the western and eastern sectors of the crater lake (**Figure 12**). The acoustic plume identified at a depth of 35 m along the western flank of the crater lake (**Figure 12A**) corresponds to a flare-like type interpreted as being related to a focused active continuous degassing vent according to the classification by Melián et al. (2017). The fluid of the vent is sourced from a system of normal faults (brown colors in **Figure 12A**) that constitute the basement of the western flank of the crater lake and migrates upward through a layer of bottom-lake deposits ~20 m in thickness of (orange colors in **Figure 12A**). We interpret this layer beneath the lake bottom as hydrothermal-altered deposits embedded by fluids, since their impedance is very similar to the vertical acoustic plume rising throughout the water column. Therefore, the implication of hot water involved into this type of plume might be related to the occurrence of a groundwater reservoir below the bottom of the crater lake. This degassing vent seems to be related to an active zone of bubbling detected along the western shore of the crater lake (**Figure 12D**). Vents on the southwestern sector of the crater lake were highly active in 2014 when peaks of diffuse CO_2 efflux were measured on the lake surface at this sector (**Figure 4A**).

Otherwise, on the eastern side of the crater lake, another degasification plume was identified sourcing from the bottom at 120 m water depths (**Figure 12B**). The shape of this acoustic plume corresponds to a puffing-like flare caused by intermittent burst of a focused degassing according to the classification mentioned above. In this type of acoustic plumes, frequency of degassing may vary between 1 and 30 s (Melián et al., 2017). Contrary to the observations in the western sector, the degassing is sourced directly from the substrate of the lake bottom. This degassing vent at the bottom of the lake is related to a maximum in the measured CO_2 efflux measured on the lake surface in 2017 (**Figure 4B**, **Figure 12C**). Above the vertical plume, a highly reflective stratified layer is located at 30 m below the surface of the lake (**Figure 12B**). We suggest that this stratified acoustic boundary might represent the abrupt increase in the CO_2 pressure identified at ~ 25 m below the surface of the lake by Aguilera et al. (2000). Another explanation for occurrence of this stratified plume is that they might be created by the formation of particles of calcite precipitated as a result of CO_2 loss, remaining in suspension in epilimnetic waters for long periods of time, perhaps several months or more, as proposed by Aguilera et al. (2000).

Surface Water Temperature Anomalies at *Quilotoa volcanic Lake*

Surface water temperature has also been obtained from the echosounder sensor (**Figure 6D**). The intense anomaly detected along the western side (up to 21°C) is related to a bubbling zone identified in the shallow water (**Figure 6D**). The distribution of the surface temperatures suggests a clockwise convective gyre around the crater lake. Aguilera et al. (2000) calculated the expected changes in density of the Quilotoa crater lake waters at different depths, according to the variations in the temperature. Thus, at 8 m below the surface and a temperature of 20°C, the density is 1.0075 $g{\cdot}cm^{-3}$, increasing exponentially to 1.0090 $g{\cdot}cm^{-3}$ as the temperatures drop to values of 10–12°C. Thus, the rapid cooling of these warm water gyre might lead to the sinking of water as it is cooling. This process could trigger the renewal of stratified waters of the crater lake by opening "holes" within the sub-stratified layer of CO_2.

CONCLUSION

This work presents the results of a complete geochemical study of the Ecuadorian volcanic lakes Cuicocha and Quilotoa during the period 2006–2018 (diffuse CO_2 emission data of 2006 from Padrón et al. (2008)). Vertical profiles of water temperature, pH, and EC showed that these lakes are made up of different water masses. The water samples from Cuicocha have a $Ca^{2+}(Mg^{2+})$–HCO_3^- composition typical of worldwide shallow waters and aquifers, while those from Quilotoa showed a $Na^+(K^+)$–$Cl^-(SO_4^{2-})$ composition typical of crater lakes in active volcanic systems. These observations are complemented by the δ^2H_{VSMOW}-H_2O and $\delta^{18}O_{VSMOW}$-H_2O values and the observation of acoustic degassing plumes in Quilotoa during the 2017 survey. The high concentrations of CO_2 and He measured in dissolved and bubbling gases suggest a significant contribution of such gases from volatile-rich fluids. The thermal stratification observed in Cuicocha volcanic lake is confirmed by a corresponding stratification of dissolved gases. The temporal evolution of diffuse CO_2 emission measured from the water surface of Cuicocha and Quilotoa volcanic lakes and the $^3He/^4He$ ratio measured at the bubbling gases present maximum values in 2012 and 2014, respectively. The maximum values of diffuse CO_2 emission of Cuicocha volcanic lake occurred before high LP seismicity; therefore, an input of magmatic CO_2 cannot be excluded. Unfortunately, geophysical records are not available for Quilotoa volcanic lake. The estimated normalized diffuse CO_2 emissions from Cuicocha and Quilotoa volcanic lakes were ~27 $t{\cdot}d^{-1}{\cdot}km^{-2}$ (excluding the maximum of the 2012 survey) and ~94 $t{\cdot}d^{-1}{\cdot}km^{-2}$, respectively. These values are of the same order of magnitude as those obtained in other volcanic-hydrothermal systems of the world.

The combination of CO_2 efflux, hydrogeochemical (temperature, chemical and isotopic composition of water in vertical profiles, dissolved gases in the water column and bubbling gases) and hydroacoustic (in the case of Quilotoa) studies has been demonstrated to be a powerful tool for monitoring the volcanic activity and to infer the behavior and dynamics of both systems (fluid injections, movement of water masses, origin of dissolved gases, etc).

Cuicocha and Quilota volcanic lakes are potentially dangerous due to the possible accumulation of CO_2 (Gunkel et al., 2008).

The results observed in this work show the existence of different water masses in both lakes, with an increase in the concentration of dissolved gases with depth. However, no significant temporal variations are observed during the investigated period. The study of diffuse CO_2 emissions and possible gas stratifications through ES and vertical profiles of dissolved gases is important for monitoring changes in the volcanic activity and its hazards at these potentially dangerous lakes.

Both lakes present a limited program of volcanic monitoring to date. The presence in Ecuador of volcanoes that present recurrent volcanic events has focused volcanic monitoring efforts on these volcanoes, leaving aside natural hazards associated with volcanic lakes such as Cuicocha and Quilotoa. Their volcanic surveillance should be a priority task, due to the presence of a considerable amount of population living around these lakes. From our point of view, obtaining more complete geophysical data sets (seismic, deformations, etc) to better link temporal variations in lake chemistry, gas flow, temperature, etc. with processes operating at depth within volcanic systems, would be of great scientific and social value. The implementation of a full geophysical program, together with continued monitoring of diffuse CO_2 emissions and an increase in the geochemical sampling period, is required in both lakes to effectively monitor volcanic variations and significantly improve the surveillance of these systems.

There are hundreds of volcanic lakes around the world that represent an important hazard due to the potential occurrence of phreatomagmatic or limnic eruptions. The geophysical and geochemical methods used in this study could be applied to these volcanic lakes to monitor their activity and potential hazards.

DATA AVAILABILITY STATEMENT

The raw data supporting the conclusions of this article will be made available by the authors, without undue reservation.

AUTHOR CONTRIBUTIONS

GM participated in sampling, chemical and isotopic analysis of samples, treatment of data and manuscript writing. TT, NP, PH, LS, EP, and MA-R treatment of data and manuscript writing. TT and EP participated also in the sampling. MC, MA, and CA participated in sampling and contributed chemical and isotopic analysis of samples.

FUNDING

This research was supported by the project "TFassistance" financed by the Program Tenerife INNOVA of the Cabildo Insular de Tenerife, the Centro Panamericano de Estudios e Investigaciones Geográficas (CEPEIGE) and the Universidad de las Fuerzas Armadas ESPE, Ecuador.

ACKNOWLEDGMENTS

Special thanks are given for logistical support from the Reservas Ecológicas Cotocachi-Cayapas and Ilinizas. We would also like to thank Anaí Bustos, Nadia Serrano and all the students at the Universidad de las Fuerzas Armadas ESPE, Ecuador for their participation in the field work. Special thanks to the Brigade of Special Forces Patria of the Ecuadorian Army, for their help during Quilotoa survey in 2014. We would also like to thank Matthew James Pankhurst and Dina Lopez for their revision of written English and constructive comments that greatly improved the quality of paper.

SUPPLEMENTARY MATERIAL

The Supplementary Material for this article can be found online at: https://www.frontiersin.org/articles/10.3389/feart.2021.741528/full#supplementary-material

REFERENCES

Aguilera, E., Chiodini, G., Cioni, R., Guidi, M., Marini, L., and Raco, B. (2000). Water Chemistry of Lake Quilotoa (Ecuador) and Assessment of Natural Hazards. *J. Volcanology Geothermal Res.* 97, 271–285. doi:10.1016/S0377-0273(99)00168-7

Almeida-Vaca, M. A. (2016). *Estudio petrográfico y geoquímico del volcán Cotacachi–provincia de Imbabura. Bachelor's thesis*. Quito, Ecuador: Escuela Politécnica Nacional, 107pp.

Andrade, C., Cruz, J. V., Viveiros, F., Branco, R., and Coutinho, R. (2019). CO_2 Degassing From Pico Island (Azores, Portugal) Volcanic Lakes. *Limnologica.* 76, 72–81. doi:10.1016/j.limno.2019.04.001

Andrade, C., Cruz, J. V., Viveiros, F., and Coutinho, R. (2021). Diffuse CO_2 Emissions From Sete Cidades Volcanic Lake (São Miguel Island, Azores): Influence of Eutrophication Processes. *Environ. Pollut.* 268, 115624. doi:10.1016/j.envpol.2020.115624

Andrade, C., Viveiros, F., Cruz, J. V., Coutinho, R., and Silva, C. (2016). Estimation of the CO2 Flux From Furnas Volcanic Lake (São Miguel, Azores). *J. Volcanology Geothermal Res.* 315, 51–64. doi:10.1016/j.jvolgeores.2016.02.005

Anzidei, M., Carapezza, M. L., Esposito, A., Giordano, G., Lelli, M., and Tarchini, L. (2008). The Albano Maar Lake High Resolution Bathymetry and Dissolved CO2 Budget (Colli Albani Volcano, Italy): Constrains to hazard Evaluation. *J. Volcanology Geothermal Res.* 171, 258–268. doi:10.1016/j.jvolgeores.2007.11.024

Brehme, M., Giese, R., Dokuz, U. E., and Bulut, F. (2021). Fluid Pathways Identified Beneath Narlı Lake (Central Anatolia) Show the Geothermal Potential of Former Volcanoes. *Sci. Rep.* 11, 1–8. doi:10.1038/s41598-021-87743-5

Brehme, M., Giese, R., Suherlina, L., and Kamah, Y. (2019). Geothermal Sweetspots Identified in a Volcanic lake Integrating Bathymetry and Fluid Chemistry. *Sci. Rep.* 9, 1–10. doi:10.1038/s41598-019-52638-z

Bustos-Gordón, E. A., and Serrano-Abarca, N. L. (2014). *Análisis de la distribución espacial de la emisión difusa de CO_2 en las calderas volcánicas Cuicocha y Quilotoa como sustento técnico para la toma de decisiones en la gestión de riesgos. Bachelor's thesis*. Ecuador: Universidad de las Fuerzas Armadas ESPE.Matriz Sangolquí, 118pp.

Capasso, G., Favara, R., and Inguaggiato, S. (2000). Interaction Between Fumarolic Gases and Thermal Groundwaters at Vulcano Island (Italy): Evidences From Chemical Composition of Dissolved Gases in Waters. *J. Volcanology Geothermal Res.* 102, 309–318. doi:10.1016/s0377-0273(00)00193-1

Capasso, G., and Inguaggiato, S. (1998). A Simple Method for the Determination of Dissolved Gases in Natural Waters. An Application to Thermal Waters From Vulcano Island. *Appl. Geochem.* 13, 631–642. doi:10.1016/S0883-2927(97)00109-1

Cardellini, C., Chiodini, G., Frondini, F., Avino, R., Bagnato, E., Caliro, S., et al. (2017). Monitoring Diffuse Volcanic Degassing During Volcanic Unrests: the Case of Campi Flegrei (Italy). *Sci. Rep.* 7, 6757–6815. doi:10.1038/s41598-017-06941-2

Cardellini, C., Chiodini, G., and Frondini, F. (2003). Application of Stochastic Simulation to CO_2flux From Soil: Mapping and Quantification of Gas Release. *J. Geophys. Res.* 108, 2425. doi:10.1029/2002JB002165

Chiodini, G., Cioni, R., Guidi, M., Raco, B., and Marini, L. (1998). Soil CO_2 Flux Measurements in Volcanic and Geothermal Areas. *Appl. Geochem.* 13, 543–552. doi:10.1016/s0883-2927(97)00076-0

Christenson, B. W. (2000). Geochemistry of Fluids Associated With the 1995-1996 Eruption of Mt. Ruapehu, New Zealand: Signatures and Processes in the Magmatic-Hydrothermal System. *J. Volcanology Geothermal Res.* 97, 1–30. doi:10.1016/S0377-0273(99)00167-5

Clarke, W. B., Jenkins, W. J., and Top, Z. (1976). Determination of Tritium by Mass Spectrometric Measurement of 3He. *Int. J. Appl. Radiat. Isotopes.* 27, 515–522. doi:10.1016/0020-708X(76)90082-X

Craig, H. (1961). Isotopic Variations in Meteoric Waters. *Science.* 133, 1702–1703. doi:10.1126/science.133.3465.1702

Craig, H., and Lupton, J. E. (1976). Primordial Neon, Helium, and Hydrogen in Oceanic Basalts. *Earth Planet. Sci. Lett.* 31, 369–385. doi:10.1016/0012-821x(76)90118-7

Delmelle, P., and Bernard, A. (1994). Geochemistry, Mineralogy, and Chemical Modeling of the Acid Crater Lake of Kawah Ijen Volcano, Indonesia. *Geochimica et Cosmochimica Acta.* 58, 2445–2460. doi:10.1016/0016-7037(94)90023-x

Deutsch, C., and Journel, A. (1998). *GSLIB: Geostatistical Software Library and User's Guide*. New York: Oxford University Press.

Di Muro, A., Rosi, M., Aguilera, E., Barbieri, R., Massa, G., Mundula, F., et al. (2008). Transport and Sedimentation Dynamics of Transitional Explosive Eruption Columns: the Example of the 800 BP Quilotoa Plinian Eruption (Ecuador). *J. Volcanology Geothermal Res.* 174 (4), 307–324. doi:10.1016/j.jvolgeores.2008.03.002

Garrison, J. M., and Davidson, J. P. (2003). Dubious Case for Slab Melting in the Northern Volcanic Zone of the Andes. *Geol.* 31 (6), 565–568. doi:10.1130/0091-7613(2003)031<0565:dcfsmi>2.0.co;2

Giggenbach, W. F. (1988). Chemical Techniques in Geothermal Exploration. *In: D'Amore, F(coordinator), Application of geochemistry in geothermal reservoir development*. Rome: UNITAR/UNDP publication, 119–142. doi:10.1016/0016-7037(88)90143-3

Giggenbach, W. F. (1991). *Isotopic Composition of Geothermal Water and Steam Discharges. Application of Geochemistry in Geothermal Reservoir Development*. UNITAR, 253–273. (F. D'Amore coordinator).

Giggenbach, W. F. (1992). Isotopic Shifts in Waters From Geothermal and Volcanic Systems Along Convergent Plate Boundaries and Their Origin. *Earth Planet. Sci. Lett.* 113, 495–510. doi:10.1016/0012-821x(92)90127-h

Goepel, A., Lonschinski, M., Viereck, L., Büchel, G., and Kukowski, N. (2015). Volcano-Tectonic Structures and CO_2-Degassing Patterns in the Laacher See Basin, Germany. *Int. J. Earth Sci. (Geol Rundsch).* 104, 1483–1495. doi:10.1007/s00531-014-1133-3

Gunkel, G., Beulker, C., Grupe, B., and Viteri, F. (2008). Hazards of Volcanic Lakes: Analysis of Lakes Quilotoa and Cuicocha, Ecuador. *Adv. Geosci.* 14, 29–33. doi:10.5194/adgeo-14-29-2008

Gunkel, G., Beulker, C., Grupe, B., and Viteri, F. (2009). Survey and Assessment of post Volcanic Activities of a Young Caldera lake, Lake Cuicocha, Ecuador. *Nat. Hazards Earth Syst. Sci.* 9, 699–712. doi:10.5194/nhess-9-699-2009

Gunkel, G., and Beulker, C. (2009). Limnology of the Crater lake Cuicocha, Ecuador, a Cold Water Tropical lake. *Internat. Rev. Hydrobiol.* 94, 103–125. doi:10.1002/iroh.200811071

Gutscher, M. A., Malavieille, J., Lallemand, S., and Collot, J. Y. (1999). Tectonic Segmentation of the North Andean Margin: Impact of the Carnegie Ridge Collision. *Earth Planet. Sci. Lett.* 168 (3-4), 255–270. doi:10.1016/s0012-821x(99)00060-6

Hall, M. L., and Mothes, P. A. (2008). Quilotoa Volcano - Ecuador: An Overview of Young Dacitic Volcanism in a Lake-Filled Caldera. *J. Volcanology Geothermal Res.* 176, 44–55. doi:10.1016/j.jvolgeores.2008.01.025

Hanuš, V. (1987). Deep Seismically Active Fracture Zones in Ecuador and Northern Peru. *Stud. Geophys. Geod.* 31, 8–25. doi:10.1007/BF01638202

Hernández, P. A., Melián, G. V., Somoza, L., Arpa, M. C., Pérez, N. M., Bariso, E., et al. (2017). The Acid Crater lake of Taal Volcano, Philippines: Hydrogeochemical and Hydroacoustic Data Related to the 2010-11 Volcanic Unrest. *Geol. Soc. Lond. Spec. Publications.* 437, 131–152. doi:10.1144/SP437.17

Hernández, P. A., Mori, T., Padrón, E., Sumino, H., and Pérez, N. (2011). Carbon Dioxide Emission From Katanuma Volcanic Lake, Japan. *Earth Planet. Sp.* 63, 1151–1156. doi:10.5047/eps.2011.06.038

Hillebrant, C. (1989). *Estudio geovolcanológico del Complejo Volcánico Cuicocha Cotacachi y sus aplicaciones. Provincia de Imbabura. Unpubl.* Thesis Escuela Politécnica Nacional. Quito: Ecuador.

Huttunen, J. T., Alm, J., Liikanen, A., Juutinen, S., Larmola, T., Hammar, T., et al. (2003). Fluxes of Methane, Carbon Dioxide and Nitrous Oxide in Boreal Lakes and Potential Anthropogenic Effects on the Aquatic Greenhouse Gas Emissions. *Chemosphere.* 52, 609–621. doi:10.1016/S0045-6535(03)00243-1

IGEPN (2010). *Informe Sísmico para el año 2010*. Quito: Ecuador. www.igepn.edu.ec.

IGEPN (2018). *Informe Anual del Complejo Volcánico Cotacachi y Cuicocha – 2018*. Quito: Ecuador. www.igepn.edu.ec.

IGEPN (2019). *Informe Anual del Complejo Volcánico Cotacachi y Cuicocha – 2019*. Quito: Ecuador. www.igepn.edu.ec.

Inguaggiato, C., Censi, P., Zuddas, P., D'Alessandro, W., Brusca, L., Pecoraino, G., et al. (2016). Zirconium-Hafnium and Rare Earth Element Signatures Discriminating the Effect of Atmospheric Fallout From Hydrothermal Input in Volcanic Lake Water. *Chem. Geology.* 433, 1–11. doi:10.1016/j.chemgeo.2016.04.002

Inguaggiato, S., Hidalgo, S., Beate, B., and Bourquin, J. (2010). Geochemical and Isotopic Characterization of Volcanic and Geothermal Fluids Discharged From the Ecuadorian Volcanic Arc. *Geofluids.* 10, 525–541. doi:10.1111/j.1468-8123.2010.00315.x

Inguaggiato, S., Pecoraino, G., and D'Amore, F. (2000). Chemical and Isotopical Characterisation of Fluid Manifestations of Ischia Island (Italy). *J. Volcanology Geothermal Res.* 99, 151–178. doi:10.1016/s0377-0273(00)00158-x

Jordán, T. E., Isacks, B. L., Allmendinger, R. W., Brewer, J. A., Ramos, V. A., and Ando, C. J. (1983). Andean Tectonics Related to Geometry of Subducted Nazca Plate. *Geol. Soc. America Bull.* 94 (3), 341–361. doi:10.1130/0016-7606(1983)94<341:atrtgo>2.0.co;2

Karolyte, R., Serno, S., Johnson, G., and Gilfillan, S. M. V. (2017). The Influence of Oxygen Isotope Exchange Between CO_2 and H_2O in Natural CO_2-Rich Spring Waters: Implications for Geothermometry. *J. Appl. Geochem.* 84, 173–186.

Lyell, C. (1830). *Principles of Geology*. London: John Murray, 519. doi:10.2307/30058100

Matsuda, J., Matsumoto, T., Sumino, H., Nagao, K., Yamamoto, J., Miura, Y., et al. (2002). The 3He/4He Ratio of the New Internal He Standard of Japan (HESJ). *Geochem. J.* 36, 191–195. doi:10.2343/geochemj.36.191

Mazot, A., Schwandner, F. M., Christenson, B., de Ronde, C. E. J., Inguaggiato, S., Scott, B., et al. (2014). CO_2Discharge From the Bottom of Volcanic Lake Rotomahana, New Zealand. *Geochem. Geophys. Geosyst.* 15, 577–588. doi:10.1002/2013GC004945

Mazot, A., and Taran, Y. (2009). CO_2 Flux From the Volcanic Lake of El Chichón (Mexico). *Geofísica Int.* 48 (1), 73–83. doi:10.22201/igeof.00167169p.2009.48.1.100

Melián, G., Hernández, P. A., Padrón, E., Pérez, N. M., Barrancos, J., Padilla, G., et al. (2014). Spatial and Temporal Variations of Diffuse CO_2 degassing at El Hierro Volcanic System: Relation to the 2011-2012 Submarine Eruption. *J. Geophys. Res. Solid Earth.* 119, 6976–6991. doi:10.1002/2014JB011013

Melián, G., Somoza, L., Padrón, E., Pérez, N. M., Hernández, P. A., Sumino, H., et al. (2017). Surface CO_2 Emission and Rising Bubble Plumes from Degassing of Crater Lakes in São Miguel Island, Azores. *Geol. Soc. Lond. Spec. Publications* 437 (1), 233–252. doi:10.1144/SP437.14

Mothes, P. A., and Hall, M. L. (2008). The Plinian Fallout Associated With Quilotoa's 800 Yr BP Eruption, Ecuadorian Andes. *J. Volcanology Geothermal Res.* 176, 56–69. doi:10.1016/j.jvolgeores.2008.05.018

Padrón, E., Hernández, P. A., Toulkeridis, T., Pérez, N. M., Marrero, R., Melián, G., et al. (2008). Diffuse CO_2 Emission Rate From Pululahua and the Lake-Filled Cuicocha Calderas, Ecuador. *J. Volcanology Geothermal Res.* 176, 163–169. doi:10.1016/j.jvolgeores.2007.11.023

Panchana-Guerra, C. D. (2015). *Estudio de los domos del Volcán Quilotoa y su correlación con la estratigrafía del volcán. Bachelor's thesis*. Quito, Ecuador: Escuela Politécnica Nacional, 178pp.

Parkinson, K. J. (1981). An Improved Method for Measuring Soil Respiration in the Field. *J. Appl. Ecol.* 18, 221–228. doi:10.2307/2402491

Pérez, N. M., Hernández, P. A., Padilla, G., Nolasco, D., Barrancos, J., Melían, G., et al. (2011). Global CO2 Emission From Volcanic Lakes. *Geology.* 39 (3), 235–238. doi:10.1130/G31586.1

Rodriguez, F., Toulkeridis, T., Sandoval, W., Padilla, O., and Mato, F. (2017). Economic Risk Assessment of Cotopaxi Volcano, Ecuador, in Case of a Future Lahar Emplacement. *Nat. Hazards.* 85 (1), 605–618. doi:10.1007/s11069-016-2589-1

Rosi, M., Landi, P., Polacci, M., Di Muro, A., and Zandomeneghi, D. (2004). Role of Conduit Shear on Ascent of the Crystal-Rich Magma Feeding the 800-Year-BP Plinian Eruption of Quilotoa Volcano (Ecuador). *Bull. Volcanology.* 66 (4), 307–321. doi:10.1007/s00445-003-0312-z

Rouwet, D., Christenson, B., Tassi, F., Vandemeulebrouck, J., and Vandemeulebrouck, J. (2015). (Editors). Volcanic Lakes Springer. *Advances in Volcanology*, 533. doi:10.1007/978-3-642-36833-2

Rouwet, D., Mora-Amador, R., Ramírez-Umaña, C. J., González, G., and Inguaggiato, S. (2017). Dynamic Fluid Recycling at Laguna Caliente (Poás, Costa Rica) Before and During the 2006-Ongoing Phreatic Eruption Cycle (2005-10). *Geological Society* 437, 73–96. doi:10.1144/SP437.11

Rouwet, D., Tassi, F., Mora-Amador, R., Sandri, L., and Chiarini, V. (2014). Past, Present and Future of Volcanic lake Monitoring. *J. Volcanology Geothermal Res.* 272, 78–97. doi:10.1016/j.jvolgeores.2013.12.009

Rozanski, K., and Araguás, L. (1995). Spatial and Temporal Variability of Stable Isotope Composition of Precipitation Over the South American continent. *Bulletin de l'Institut francais d'etudes andines* 24 (3), 379–390.

Sano, Y., Urabe, A., WakitaChiba, H. H., Chiba, H., and Sakai, H. (1985). Chemical and Isotopic Compositions of Gases in Geothermal Fluids in Iceland. *Geochem. J.* 19, 135–148. doi:10.2343/geochemj.19.135

Sano, Y., and Wakita, H. (1985). Geographical Distribution of3He/4He Ratios in Japan: Implications for Arc Tectonics and Incipient Magmatism. *J. Geophys. Res.* 90, 8729–8741. doi:10.1029/jb090ib10p08729

Sierra, D., Hidalgo, S., Almeida, M., Vigide, N., Lamberti, M. C., Proaño, A., et al. (2021). Temporal and Spatial Variations of CO_2 Diffuse Volcanic Degassing on Cuicocha Caldera Lake - Ecuador. *J. Volcanology Geothermal Res.* 411, 107145. doi:10.1016/j.jvolgeores.2020.107145

Simkin, T., and Siebert, L. (1994). *Volcanoes of the World*. Tucson: Smithsonian Institution, Geoscience Press, 349.

Tassi, F., Vaselli, O., Fernández, E., Duarte, E., Martínez, M., Delgado, A., et al. (2009). Morphological and Geochemical Features of Crater Lakes in Costa Rica: an Overview. *J. Limnology.* 68, 1–13. doi:10.4081/jlimnol.2009.193

Toulkeridis, T., and Zach, I. (2017). Wind Directions of Volcanic Ash-Charged Clouds in Ecuador - Implications for the Public and Flight Safety. *Geomatics, Nat. Hazards Risk.* 8 (2), 242–256. doi:10.1080/19475705.2016.1199445

Conflict of Interest: The authors declare that the research was conducted in the absence of any commercial or financial relationships that could be construed as a potential conflict of interest.

Publisher's Note: All claims expressed in this article are solely those of the authors and do not necessarily represent those of their affiliated organizations, or those of the publisher, the editors and the reviewers. Any product that may be evaluated in this article, or claim that may be made by its manufacturer, is not guaranteed or endorsed by the publisher.

frontiers in Earth Science

ORIGINAL RESEARCH
published: 17 December 2021
doi: 10.3389/feart.2021.741795

Hydrochemical and Hydroacoustic Investigation of the Yugama Acid Crater Lake, Kusatsu-Shirane, Japan

Pedro A. Hernández[1,2], Kenji Nogami[3], Eleazar Padrón[1,2], Luis Somoza[4], Cecilia Amonte[1,2], Toshiya Mori[5], Gladys V. Melián[1,2], Hirochicka Sumino[6], Yoshikazu Kikawada[7] and Nemesio M. Pérez[1,2]*

[1]Instituto Volcanológico de Canarias (INVOLCAN), Santa Cruz de Tenerife, Spain, [2]Instituto Tecnológico y de Energías Renovables (ITER), Santa Cruz de Tenerife, Spain, [3]Tokyo Institute of Technology, Meguro, Japan, [4]Marine Geology Division, Instituto Geológico y Minero de España (IGME), Madrid, Spain, [5]Geochemical Research Center, Graduate School of Science, The University of Tokyo, Bunkyo, Japan, [6]Department of Basic Science, Graduate School of Arts and Sciences, The University of Tokyo, Bunkyo, Japan, [7]Department of Materials and Life Sciences, Faculty of Science and Technology, Sophia University, Chiyoda, Japan

The gases dissolved in the waters of volcanic lakes can present a serious hazard if the physical-chemical conditions change due to variations in the supply of magmatic gases. The monitoring of gases such as CO_2 and He help us understand the degassing process and their connection with magmatic/hydrothermal system. One of the most acidic volcanic lakes on the planet is the Yugama, on Kusatsu Shirane volcano (Japan). We report the results of an interdisciplinary study carried out in August 2013 at Yugama consisting of the first estimation of rate of diffuse CO_2 emission, the chemical and isotopic analysis of water and dissolved gases in samples from vertical lake profiles, and an echo-sounding survey. The lake water has an average temperature of 24-25°C, pH 1.01, concentrations of SO_4^{2-} between 1,227 and 1,654 mgL^{-1} and Cl^- between 1,506 and 2,562 mgL^{-1}, with gas bubbling at several locations and floating sulfur globules with sulfide inclusions. A total of 66 CO_2 efflux measurements were taken at the lake surface by means of the floating accumulation chamber method to estimate the diffuse CO_2 output from the studied area. CO_2 efflux values ranged from 82 up to 25,800 $g\,m^{-2}\,d^{-1}$. Estimation of the diffuse CO_2 emission at Yaguma Crater Lake was 30 ± 12 $t\,d^{-1}$. Normalized CO_2 emission rate (assuming an area of 0.066 km^2) was 454 $t\,km^{-2}\,d^{-1}$, a value within the range of acid volcanic lakes. Vertical profiles of major ions and dissolved gases showed variations with increases in ion content and dissolved CO_2 and He with depth. Acoustic imaging shows the presence of intense bubbling and provides important information on the bathymetry of the lake. The 50–200 kHz echograms exhibit frequent vertical plumes of rising gas bubbles. Within the crater-lake, three circular submarine vents have been identified showing flares due to a significant activity of sublacustrine emissions. This work shows the first data of diffuse CO_2 degassing, dissolved gases in water and echosounding (ES) from Yugama Crater Lake. Periodic hydrogeochemical and hydroacoustic surveys at Yugama Crater Lakemay thus help to document changes in the state of activity of this high-risk volcanic area.

Keywords: Yugama crater lake, diffuse degassing, echosounding, kusatsu-shirane, hydrochemical

OPEN ACCESS

Edited by:
Dmitri Rouwet,
Istituto Nazionale di Geofisica e Vulcanologia, sezione di Bologna, Italy

Reviewed by:
Tony Hurst,
GNS Science, New Zealand
Johan Varekamp,
Wesleyan University, United States

****Correspondence:***
Pedro A. Hernández
phdez@iter.es

Specialty section:
This article was submitted to Volcanology, a section of the journal Frontiers in Earth Science

Received: *15 July 2021*
Accepted: *15 November 2021*
Published: *17 December 2021*

Citation:
Hernández PA, Nogami K, Padrón E, Somoza L, Amonte C, Mori T, Melián GV, Sumino H, Kikawada Y and Pérez NM (2021) Hydrochemical and Hydroacoustic Investigation of the Yugama Acid Crater Lake, Kusatsu-Shirane, Japan. Front. Earth Sci. 9:741795. doi: 10.3389/feart.2021.741795

INTRODUCTION

Volcanic lakes may have their origin in processes that disturb the watershed: explosion craters, collapse calderas as well as streams and rivers that were cut off by volcanic products like lava flows, lahars, ash flows (Varekamp, 2015). After the gas disasters at lakes Monoun (1984) and Nyos (1986), both in Cameroon (Sigurdsson et al., 1987; Sigvaldason, 1989), the sudden release of CO_2 accumulated in volcanic lakes has become a well-known hazard (Le Guern and Sigvaldason, 1989, 1990; Evans et al., 1994; Kling et al., 2005; Kusakabe et al., 2008). Since a large amount of magmatic gases can be dissolved in water, CO_2 degassing from volcanic lakes should be monitored (Arpa et al., 2013; Burton et al., 2013; Hernández et al., 2011, 2017; Melián et al., 2016:; Padrón et al., 2008; Pérez et al., 2011). Degassing through the lake surface occurs by bubbling (convective/advective degassing) or by diffusion through the water/air interface (Padrón et al., 2008; Mazot and Taran, 2009).

Acidic lakes (pH < 2–3) like Yugama, at Kusatsu-Shirane volcano, Japan, release CO_2 freely into the atmosphere, which makes the lake chemically transparent to CO_2, in contrast to HCl and SO_2-H_2S, which are the cause of acidity. This means that CO_2 represents a transitory phase during its ascent through a lake of pH < 2. In this case, the dissolved gas concentrations are transient and the degassing dynamics is controlled by this "low solubility" of CO_2 throughout the water column. On the other hand, high-pH lakes (pH 6–9) are able to store (or even precipitate) CO_2 depending on the P-T conditions along the vertical profile of a lake. Therefore, in this case CO_2 is not a transient gas and has a long residence time in the lake, especially in the deeper water layers due to hydrostatic loading (Rouwet, 2021).

Chemical and isotopic analysis of lake water samples, as well as fumarolic gases, allow us to assess the importance of magmatic-hydrothermal contributions to crater lakes. Dissolved gases in the lake waters provide a better understanding of the evolution of the crater lakes and their underlying hydrothermal systems (Caudron et al., 2012; Hernández et al., 2017; Jolie, 2019). Finally, hydroacoustic studies provide important information on the characteristics of rising gas bubbles in the water column and the lakebed bathymetry via echo-sounding (ES) surveys (Hernández et al., 2017). Gas bubbles in the water column produce strong ES backscatter signals that allow the detection and quantification of gas fluxes from subaqueous fumaroles (Greinert et al., 2006).

Since diffuse degassing, dissolved gas in water and echosounding (ES) studies had never been performed at Yugama Crater Lake (hereinafter YCL), this work shows the first results that will help to understand degassing dynamics at this active lake. Chemical and isotopic compositions of water samples and dissolved gases are also presented. This report includes a study of the hydroacoustic characteristics of the rising gas bubbles in the water column and a bathymetry of the lakebed by means of echosounder (ES) survey.

Geological Setting

Kusatsu-Shirane volcano (2,165 m a.s.l.) is one of the most active volcanoes in Japan (**Figure 1A**), and thirteen eruptions since 1805 have been recorded. It is located near the meeting point of the Northeast Japan Arc and the Izu-Mariana Arc (Sugimura, 1960), and developed on a Tertiary volcanic basement that dips eastward and southward at 2000 m a.s.l. The summit area of this volcano comprises three young pyroclastic cones, Moto-shirane, Ai-no-mine, and Shirane, aligned north-south. Moto-shirane pyroclastic

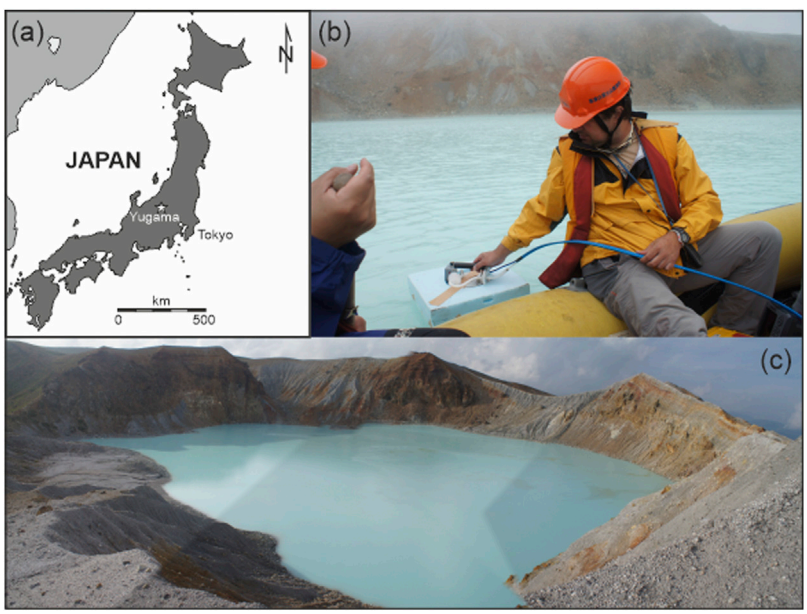

FIGURE 1 | (A) Geographical location of Kusatsu Shirane volcano, Japan. **(B)** Personnel performing diffuse CO_2 efflux measurements at Yugama crater lake. **(C)** Panoramic view of Yugama Crater Lake.

cone, located 2.3 km south of Shirane pyroclastic cone, is the youngest and was formed after effusion of large-scale lava flows 3,000 years ago (Hayakawa and Yui, 1989). The top of this cone is the highest elevation on this mountain. In 2018, a phreatic eruption occurred unexpectedly at the northern extremity of this cone after 1,500 years of dormancy, causing one death and eleven persons injured. Ai-no-mine pyroclastic cone is monogenic and no historical eruptions have occurred. All the historical eruptions at Kusatsu-Shirane volcano were phreatic and occurred intensively at Shirane pyroclastic cone (Hayakawa and Yui, 1989).

At the top of Shirane pyroclastic cone, there are three crater lakes, Mizugama, Yugama, and Karegama aligned in a northeast-southwest direction. Yugama is the main crater lake (**Figure 1B**) with a diameter of 200 m and a depth of 25 m in average, filled with strongly acidic water with a pH of less than 1.2 (Ohba et al., 2008; Terada and Hashimoto, 2017). Volcanic gases with water are discharged ceaselessly from the many vents located at the bottom of the crater lake. Since no thermal activity at Mizugama and Karegama crater lakes is recognized, YCL is currently the focus of volcanic activity because it is the only one that shows thermal anomalies, very acidic waters and gas emission. Since 2008, an area of thermal anomaly with fumaroles has initiated on the northeast shore of the lake, and access to the crater rim without permission has been prohibited due to the risk of sudden eruption. From 2014 to 2017, microearthquake swarms were accompanied by ground deformation, increased water temperature, and changes in the chemical concentrations of the water in YCL (including the detection of Cl and SO_4 ions), but no eruption occurred (Kuwahara et al., 2017; Terada et al., 2018). These signals, together with drastic changes in the chemical composition of fumarolic gases, suggested imminent eruption at the Kusatsu pyroclastic cone, but no eruption occurred.

MATERIALS AND METHODS

In August 2013, a field campaign was carried out at YCL consisting of the measurement of the diffuse CO_2 efflux through the lake surface (**Figure 1C**), an echo-sounding (ES) survey, and water sampling at different depths along three vertical profiles: CW (crater wall), YC (Yugama center) and 83-C (1983 crater; **Figure 2A**). Water samples were collected using a 2.2 L WaterMark horizontal PVC water bottle.

Diffuse CO_2 Efflux Measurements

The CO_2 efflux survey was performed under stable weather conditions (no wind and sunny). A total of 66 sampling sites were selected at the surface of YCL to obtain a homogeneous distribution of the sampling points over an area of 0.066 km^2 (**Figure 2A**). The GPS position of each measurement point was recorded with a resolution ±5 m. The accumulation chamber method (Parkinson 1981) was modified in order to work on the lake surface by using a floating chamber (Mazot and Taran, 2009) (**Figure 1B**). Measurements of CO_2 were performed *in-situ* by means of a portable non-dispersive infrared (NDIR) CO_2 analyzer (LICOR-800 system). The LICOR analyzer was interfaced to a hand size computer that runs data acquisition software. A map of the spatial distribution of diffuse CO_2 emission was constructed using sequential Gaussian simulation (sGs) algorithms provided by GSLIB software (Deutsch and Journel, 1998; Cardellini et al., 2003).

Chemical and Isotopic Analysis of Water and Dissolved Gases

Water samples for laboratory analyses of major and minor elements (Ca^{+2}, Mg^{+2}, K^+, Na^+, NH_4^+, Cl^-, SO_4^{-2} and F^-) and for stable hydrogen and oxygen isotope ratios ($^2H/^1H$ and $^{18}O/^{16}O$) were collected and stored for analysis at ITER lab. Chemical analyses of anions (Cl^-, SO_4^{-2}, F^-) were performed by means of a Dionex DX-500 ion-chromatograph, whereas analyses of cations (Ca^{+2}, Mg^{+2}, K^+, Na^+) were performed with a Metrohm 861 Advanced Compact ion-chromatograph, both in filtered samples (0.45 μm). Accuracy of the analysis was estimated approximately in 2.0–3.5 and 5.0% for the main and minor compounds, respectively. A water sample was collected at Yumiike lake (a rainwater lagoon), located a few hundred meters south of YCL to compare with YCL samples.

Dissolved gases in water were analyzed for 83-C vertical profile samples and stored in 60 ml glass bottles sealed in the field with silicon/rubber septa using special pliers. Before sealing the glass bottle, $CuCl_2$ was added to prevent any biological activity. All the water samples were collected taking care to avoid even the tiniest bubbles to prevent atmospheric contamination (Hernández et al., 2017). Chemical analyses were performed later on the gas phase extracted after the attainment of the equilibrium (at constant temperature) between the water sample and the gaseous phase after the introduction of a host gas (Argon), injected inside the sampling bottle (Sugisaki and Taki, 1987; Capasso and Inguaggiato, 1998; Capasso et al., 2000; Melián et al., 2016; Hernández et al., 2017). A variety of gases dissolved in YCL samples were analyzed (H_2, N_2, O_2, CH_4, CO_2, and He) by means of a Quadrupole Mass Spectrometer (QMS) model Pfeiffer Omnistar 422 (accuracy 0.2%). The detection limit for He was estimated to be about 0.05 ppmv, whereas the analytical accuracy was c. 2.5 and 5% for the main gas components and minor gas compounds, respectively. The QMS was calibrated at the laboratory with bottles containing standards of the measured gases which were used to determine the characteristic fragmentation patterns, sensitivity factors and mass calibration for the dissolved gases in water (Padron et al., 2013).

Hydrogen and oxygen isotopic values of waters were obtained by mass spectrometry (Thermo-Finnigan MAT 253) at ITER laboratory. The results are expressed as δ (‰), defined as:

$$\delta = \left(\frac{Rs - Rp}{Rp}\right) \times 1000‰$$

where δ is the isotopic deviation in ‰, s is the sample, p, the international reference, and R is the isotopic ratio ($^2H/^1H$, $^{18}O/^{16}O$). Accuracies for δD and $\delta^{18}O$ are ±0.5‰ and ±0.1‰ (vs Vienna Standard Mean Ocean Water or V-SMOW), respectively.

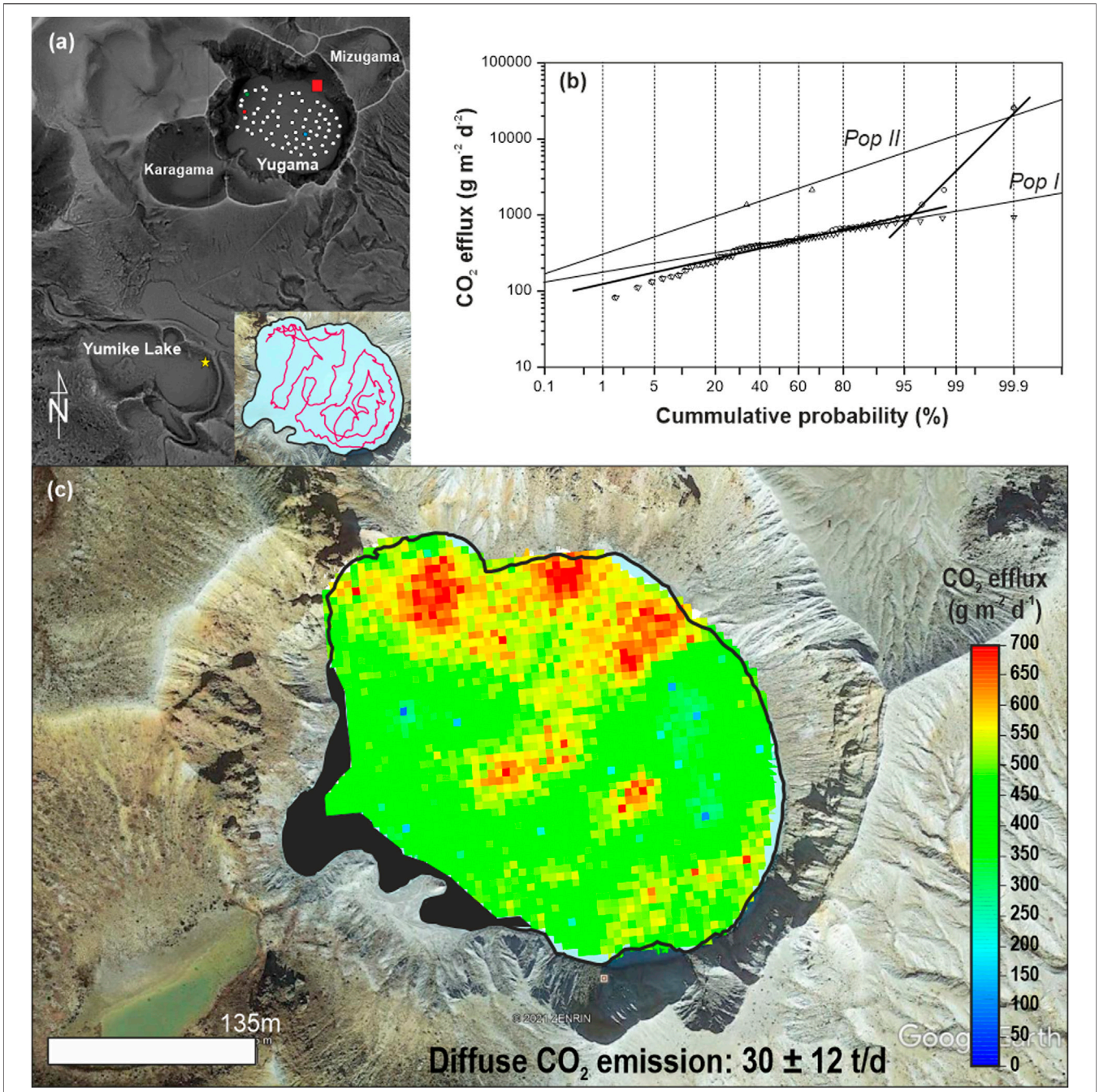

FIGURE 2 | (A) Spatial distribution of diffuse CO_2 efflux measurement points and the three vertical profiles for water sampling. **(B)** Sinclair FCO_2 at Yugama.

Nitrogen isotopic composition of a fumarole sample (YGC) collected during the survey was determined at ITER lab facilities following the method described by Grassa et al. (2010). A Thermo Finnigan MAT253 isotope ratio mass spectrometer, coupled with a Thermo TRACE Gas Chromatograph and a Thermo GC/C III interface were used. $^3He/^4He$ ratios of dissolved gas from YCL were analyzed at the lab facilities of the Geochemical Research Center (GRC) of The University of Tokyo, Japan. Lead-glass sampling bottles with volumes of about 50 cm^3 and with high-vacuum stopcocks at both ends were totally filled with water to sample for dissolved gas. The gas was then extracted by ultrasonic vibration and quantitatively collected into a small volume (10 cm^3) following the method described in Padron et al. (2013). The determination of helium isotopic ratios as well as ^4He and ^{20}Ne concentrations was done following the method described by Sumino et al. (2001). Air standards are measured frequently during analyses to determine sensitivities of the mass spectrometer. The correction factor for helium isotope ratios was

determined by measurement of an inter-laboratory helium standard named HESJ, with recommended $^3He/^4He$ ratio of 20.63 ± 0.10 R_A (Matsuda et al., 2002). Uncertainties associated with reported $^3He/^4He$ ratios are 1 sigma of each measurement, including error in the measured raw $^3He/^4He$ ratio. Errors in concentrations are estimated to be 10% based on reproducibility of noble gas sensitivity of the mass spectrometer after repeated air standard analyses.

Bathymetry and Hydroacoustics

The echo sounder (ES) survey was carried out by means of a Lowrance HDS-5 equipped with a dual frequency (50 and 200 kHz) transducer. The digital ES echograms were processed using Sonar Viewer 2.1.2 software. Extracted bathymetric data were converted from the Lowrance-type Mercator projection to Universal Tranverse Mercator (UTM 54N) using Arc Gis 10.2.1. Bathymetric data from the two frequencies (50 and 200 kHZ) were interpolated using Grapher software and 3-D surface analyses were performed using Fledermaus IVS software. We have followed the same methodology as at Taal crater lake in the Philippines (Hernández et al., 2017), and crater lakes on São Miguel Island in the Azores (Melián et al., 2016). The ES survey was conducted along and crossing the lines shown in **Figure 2A**.

RESULTS

Diffuse CO_2 Degassing From Yugama Crater Lake

The CO_2 efflux values ranged from 82 up to 25,800 g m^{-2} d^{-1} with an average value of 872 g m^{-2} d^{-1}. In order to distinguish different source contributions to the CO_2 efflux, a statistical-graphical analysis (Sinclair, 1974) was done to check whether there were one or more statistical populations. The statistical-graphical analysis method is based on the recognition of inflection points along a curve defined by plotting data cumulatively on a Log-normal probability scale. The resulting probability graph (**Figure 2B**) allowed the separation of two geochemical populations: population I showing a mean of 451 g m^{-2} d^{-1} and represented by 96.2% of the total data; and population II, showing a mean of 1,058 g m^{-2} d^{-1} and represented by 3.8% of the total data. Population I represents those sites where CO_2 emission is low, whereas Population II represents the CO_2 efflux values where vigorous CO_2 emissions occur. One possible mechanism to explain the exsolution of CO_2 is that CO_2 bubbles may have escaped from the hydrothermal fluid during the ascent when the hydrostatic pressure decreases, with a strong deep source of magmatic origin. The advective mechanism represents an important contribution in Population II, with direct transport to the surface and bubble degassing contributing to the dissolved CO_2, increasing the CO_2 gradient between the bottom and the surface of the lake.

A total of 100 simulations were carried out following the variogram model to construct a spatial distribution map for CO_2 efflux. The experimental variogram was fitted with a spherical model. An average map was then constructed using the average of the different values simulated at each cell. Since quantification of the uncertainty of the total CO_2 is an important task, the mean and standard deviation of the 100 simulated values of diffuse CO_2 output were assumed to be characteristic of the CO_2 efflux and its uncertainty (Cardellini et al., 2003). **Figure 2C** shows the diffuse CO_2 efflux distribution map at YCL based on the mean simulated total CO_2 output values. Estimated diffuse CO_2 emission from YCL was 30 ± 12 t d^{-1}.

Physico-Chemical Parameters and Chemical Composition of Yugama Crater Lake Waters

The YCL water is highly acidic, with high concentrations of sulfur, chloride and major cations during the 2013 sampling survey. Physical and chemical parameters are reported in **Table 1**. The average pH of the YCL was 1.1, whereas water temperature was 24.8°C. Total dissolved solids were high at TDS = 4,010–11,387 mg L^{-1}, indicating a high degree of water–rock interaction occurring at deeper levels and/or an enhanced evaporation. All YCL water samples showed high concentrations of Na^+ (22.7–168.4 mg L^{-1}), and moderately high concentrations of K^+ (10.8–89.6 mg L^{-1}), Mg^{2+} (18.8–108.2 mg L^{-1}) and Ca^{2+} (62.3–115.3 mgL^{-1}) and were rich in Cl^- (1,506–2,562 mg L^{-1}) and SO_4^{2-} (1,227–1,654 mg L^{-1}), comparable to data reported in Ohba et al. (2008) and Terada et al. (2018). The water chemistry is presented with a Piper type diagram (**Figure 3A**), where a main group of water is defined: Ca–Cl type water, typical for acidic active volcanic crater lakes. The sample from Yumiike freshwater lake showed low values of both major cations and anions (see **Table 1**). Following Ohba et al. (1994), most of chloride in YCL is derived from thermal waters or vapor from the bottom of the lake. In the Na–SO_4–Mg ternary plot (**Figure 3B**), most samples plot close to the SO_4 end-member, suggesting the dissolution of acidic sulphur gases in the YCL waters.

Stable Isotopes of Water ($\delta^{18}O$ and δD), and Isotopes of Gases ($^3He/^4He$, $\delta^{15}N$).

The stable isotope composition for the YCL waters showed variations in $\delta^{18}O$, ranging from −6.34 to -5.77‰, and in δD from −48 to -46‰ (**Table 1**). The $^3He/^4He$ ratios measured in the water samples collected at the 83-C site ranged from 2.08Ra to 3.43Ra, with $^4He/^{20}Ne$ ratios between 0.30 and 0.38. The $\delta^{15}N$ value of sample collected at the YGC fumarole was 3.4‰ (vs air) with a $N_2/^{36}Ar$ ratio of 72,646.

Dissolved Gases at Yugama Crater Lake

Table 2 shows the chemical composition of dissolved gases sampled at the 83-C site at YCL. Dissolved CO_2 in the YCL waters ranged from 28.5 to 45.4 cm^3 STP L^{-1} (average 34.9 cm^3 STP L^{-1}), two orders of magnitude higher than that of water in equilibrium with the atmosphere (0.32 cm^3 STP L^{-1}, DSR 8.5%). Dissolved H_2, O_2 and CH_4 concentration values ranged from 2.5 × 10^{-3}—2.3 × 10^{-2}, 0.13–2.36 and 1.7410^{-4}—3.3410^{-4} cm^3 STP L^{-1}, respectively. Regarding to the He contents, measured concentrations ranged between 1.72 × 10^{-5} and 7.79 × 10^{-5} cm^3 STP L^{-1}.

TABLE 1 | Chemical composition of the YCL water.

Profile	Sample Code	Depth (m)	pH	T (°C)	Cond (scm^{-1})	Na (mg/L)	K (mg/L)	Mg (mg/L)	Ca (mg/L)	F (mg/L)	Cl (mg/L)	Br (mg/L)	SO_4 (mg/L)	TDS (mg/L)
Crater Wall (CW)	Y1	0	1.14	25.5	4.97	22.78	11.94	19.20	77.09	11.42	2.456	7.38	1.234	4.038.4
Crater Wall (CW)	Y2	5	1.13	24.8	4.97	23.12	11.29	18.32	79.92	11.08	2.501	7.15	1.252	4.099.1
Crater Wall (CW)	Y3	10	1.25	24.8	4.97	79.74	89.65	108.20	62.35	6.54	1.506	4.17	1.654	6.114.0
Yugama Center (YC)	Y4	5	1.14	24.8	4.97	22.96	10.86	18.18	79.76	9.27	2.428	6.72	1.236	4.010.6
Yugama Center (YC)	Y5	10	1.14	25.3	4.97	23.63	11.94	19.28	81.54	12.18	2.499	7.73	1.253	4.109.3
Yugama Center (YC)	Y6	15	1.13	25.3	4.97	23.42	11.75	18.76	79.75	10.35	2.345	6.19	1.227	4.075.8
Yugama Center (YC)	Y7	21	1.12	25.3	4.97	24.43	12.32	18.44	79.94	13.80	2.508	8.10	1.431	4.323.4
83-crater	Y8	5	1.12	24.7	4.97	23.01	11.38	18.28	79.18	12.30	2.529	7.80	1.270	4.148.3
83-crater	Y9	10	1.12	24.4	4.97	23.26	11.76	18.46	78.67	11.12	2.562	8.28	1.382	4.295.7
83-crater	Y10	15	1.26	24.7	4.97	168.43	22.22	87.00	115.30	9.84	1.788	4.92	1.577	11.387.0
Yumike Lake	Y11	0	4.35	nm	nm	0.30	0.61	0.09	0.23	0.03	0.98	nd	3.31	5.9

nd: not detected nm: not measured.

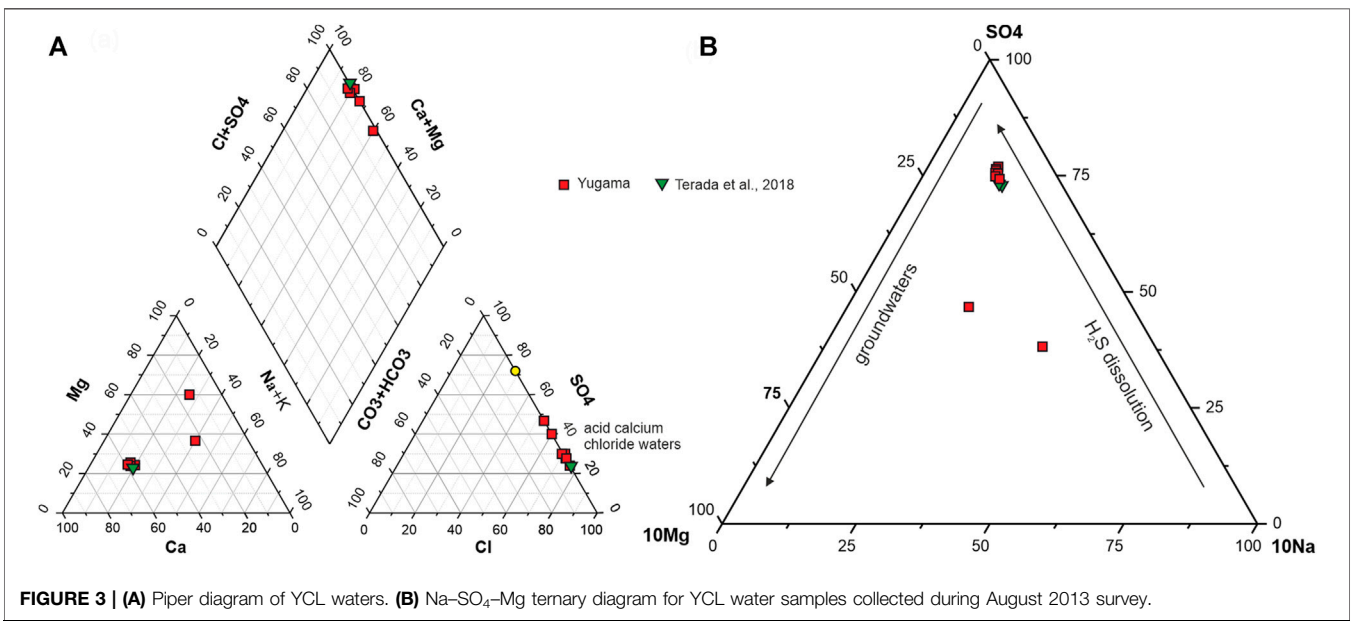

FIGURE 3 | (A) Piper diagram of YCL waters. **(B)** Na–SO_4–Mg ternary diagram for YCL water samples collected during August 2013 survey.

Bathymetry Data

Bathymetry data from the YCL extend over an oval 225 by 170 m, covering a total surface of 38,100 m^2 (**Figure 2A**). The bottom of the YCL is located at 9–11 m water depths showing a NW-SE elongated central depression with slight slope 1-2°. A peripheral minor crater lake is located to the NW of the main crater lake, also with oval shape 70 by 55 m, a surface of 3,500 m^2 and an irregular bottom averaging depth of 12–14 m. (**Figures 4A,B**).

Within the YCL crater lake, two step deep holes (DH1 and DH2) have been identified along the NW-SE central depression at its northern and southern sides (Fig. 54c). The southern hole (DH1) is narrow cone-shape with a diameter of 40 m and maximum depth of 23 m detected with the 200 kHz high-frequency (**Figure 4C**). The depression around DH1 is elliptically shaped with steep slopes up 40° in the north and 20–30° in the south (**Figure 4C**). On the contrary, 50 kHz bathymetry shows a positive anomaly masking this DH1 hole (**Figure 4D**).

The DH2 hole appear as an oval depression 35 m in diameter with a maximum depth of 17 m and steep walls up 40° identified on the 200 kHz frequency bathymetry incising the bottom of the lake located at 9 m (**Figure 4C**). Conversely to DH1, the DH2 hole does not show positive anomalies in the 50 kHz frequency but the same depression hole identified on the 200 kHz frequency (**Figure 4D**).

TABLE 2 | $\delta^{18}O$ vs δD composition of YCL waters and chemical and isotopic composition of dissolved gases in YCL waters.

Profile	Sample Code	Depth (m)	$\delta^{18}O_{SMOW}$	δD_{SMOW}	H_2[a]	O_2[a]	N_2[a]	CH_4[a]	CO_2[a]	He[a]	$^3He/^4He$ (R_A)[b]	$^4He/^{20}Ne$
Crater Wall (CW)	Y1	0	−5.94 ± 0.20	−48 ± 2	na	na	na	na	na	na	na	na
Crater Wall (CW)	Y2	5	−5.77 ± 0.20	−48 ± 1	na	na	na	na	na	na	na	na
Crater Wall (CW)	Y3	10	−6.14 ± 0.17	−48 ± 1	na	na	na	na	na	na	3.43 ± 0.041	0.376
Yugama Center (YC)	Y4	5	na	na	na	na	na	na	na	na	na	na
Yugama Center (YC)	Y5	10	na	na	na	na	na	na	na	na	2.08 ± 0.025	0.339
Yugama Center (YC)	Y6	15	na	na	na	na	na	na	na	na	na	na
Yugama Center (YC)	Y7	21	na	na	na	na	na	na	na	na	na	na
83-crater	Y8	5	−5.96 ± 0.22	−46 ± 2	2,31E-02	0,29	3,50	1,91E-04	28,54	1,72E-5	na	na
83-crater	Y9	10	−6.18 ± 0.18	−48 ± 1	4,35E-03	2,36	11,65	3,34E-04	30,89	5,28E-5	3.15 ± 0.042	0.303
83-crater	Y10	15	−6.34 ± 0.22	−48 ± 1	2,49E-03	0,13	3,22	1,78E-04	45,36	7,78E-5	na	na

[a]*Expressed in cm^3 STP/L.*
[b]*Normalized to atmospheric $^3He/^4He$ ratio = 1.4 × 10^{-6} (Ozima and Podosek, 2002) na: not analyzed.*

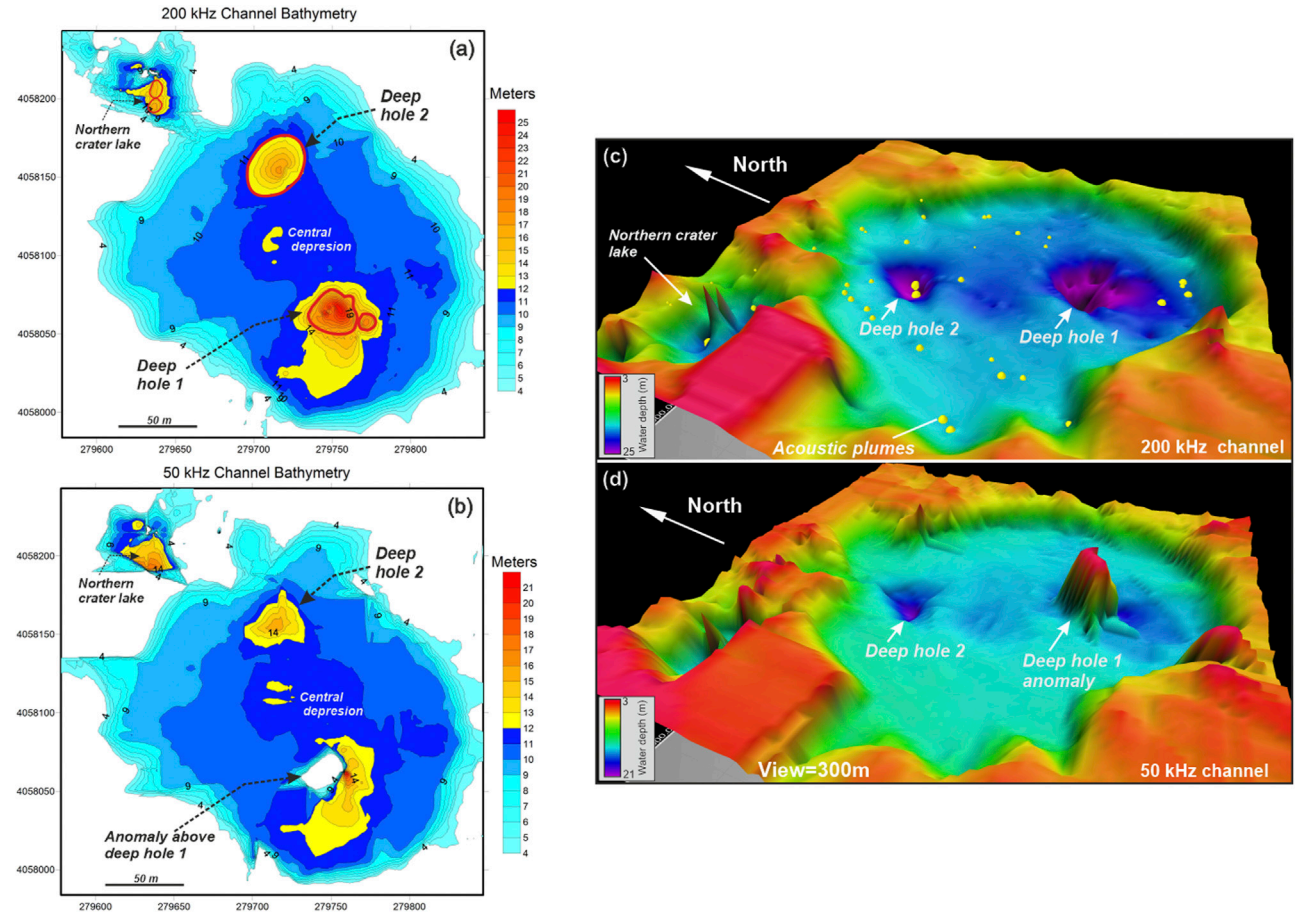

FIGURE 4 | (a) Bathymetry maps of the Yugama crater lake derived from the two frequency channels: **(A)** 200 kHz and **(B)** 50 KHz. The two deep holes (DH1 and DH2) with water depths below 12 m are located along the NW-SE central depression. A minor crater lake is located to the NW of the main lake. **(C)** 3D image obtained with 200 kHz frequency channel of the bathymetry at Yugama crater lake, and **(D)** with 50 kHz frequency channel. Yellow points are the location of acoustic plumes. DH1 and DH2 are clearly identified on 200 kHz bathymetry. The 50 kHz bathymetry shows a peak rising from DH1, interpreted as a dense acoustic plume only observable at low frequencies.

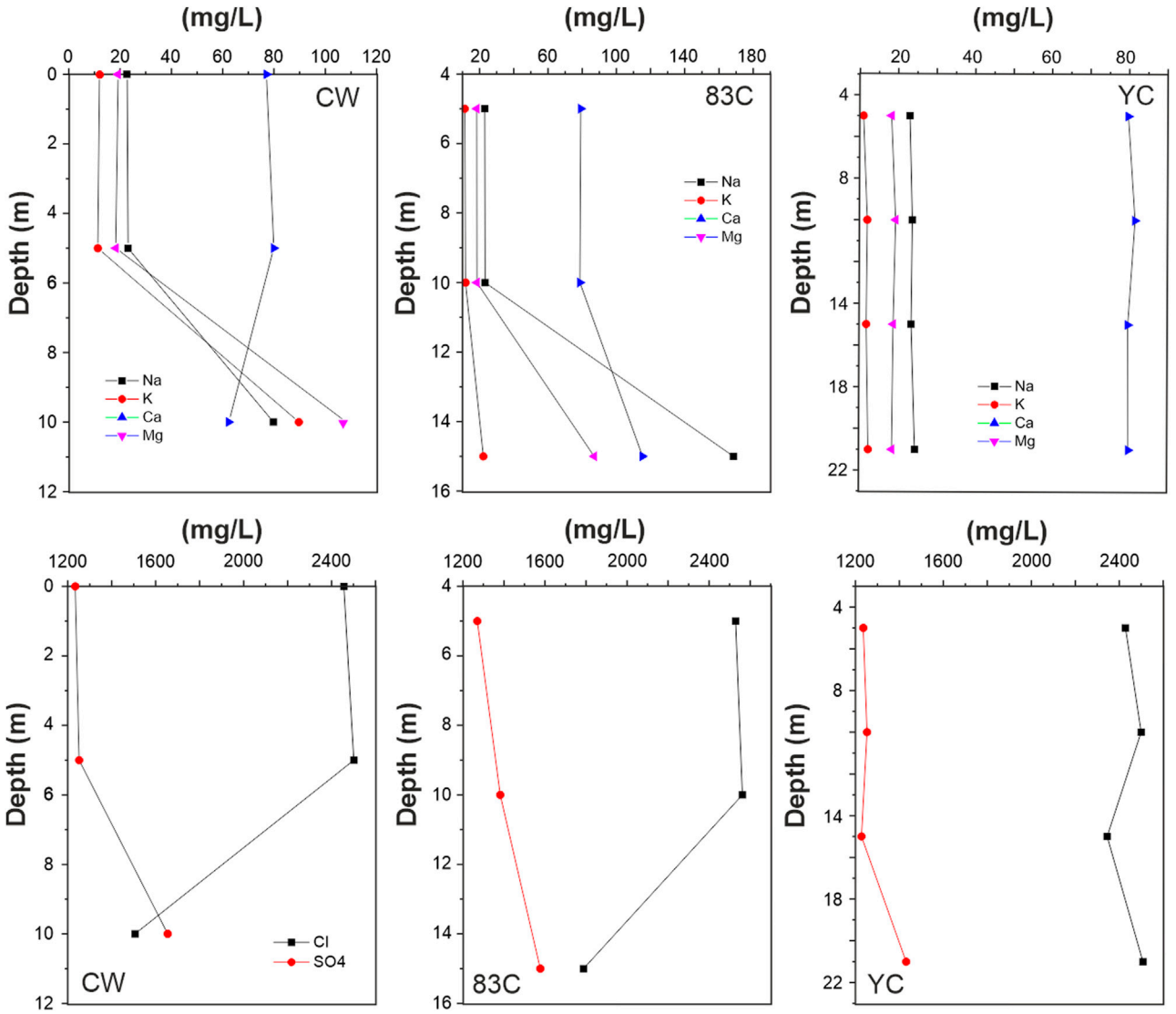

FIGURE 5 | Vertical profiles of major cations and anions at YCL.

A secondary crater lake is located at the NW side of the main crater lake with only 35 m in diameter, steep walls of 20–30°, and a maximum water depth of 15 m which is separated from the main crater lake by a narrow strait of 4 m water depth. The bottom of this minor crater lake shows two acoustic peaks interpreted as degassing plumes.

DISCUSSION

Geochemistry of Yugama Crater Lake Waters

Figure 5 shows the correlation diagrams between the major cations Na^+, Ca^{2+} and Mg^{2+} and the anion SO_4^{2-} versus the Cl^-. Chloride is a conservative element and a good geochemical tracer in volcanic and geothermal fluids when its concentration is compared with that of other ions in solution (Michard, 1990). Hypothetical mixing lines between the sample from Yumiike Lake (representing meteoric water) and YCL data are also shown. Water samples in the Na^+ vs Cl^- diagram **Figure 6A**) suggest strong Cl^- contributions due to the input of magmatic volatiles (Ohba et al., 2000). The Ca-Cl water samples from 2013 (this study) and in 2017 (Terada et al., 2018) show similar trends. However, the Na, K, Ca, Mg and SO_4 contents of two samples (Y3 and Y10) show a different trend, with a different linear correlation versus Cl^- and different slopes. This could be explained in terms of increased hydrothermal activity at the bottom of YCL at the Crater Wall and 83-C vertical profile sampling points, since both samples are close to the bottom of YCH.

Positive correlations are observed between Na^+ vs Cl^- (**Figure 6A**), Ca^{2+} vs Cl^- (**Figure 6B**), Mg^{2+} vs Cl^-

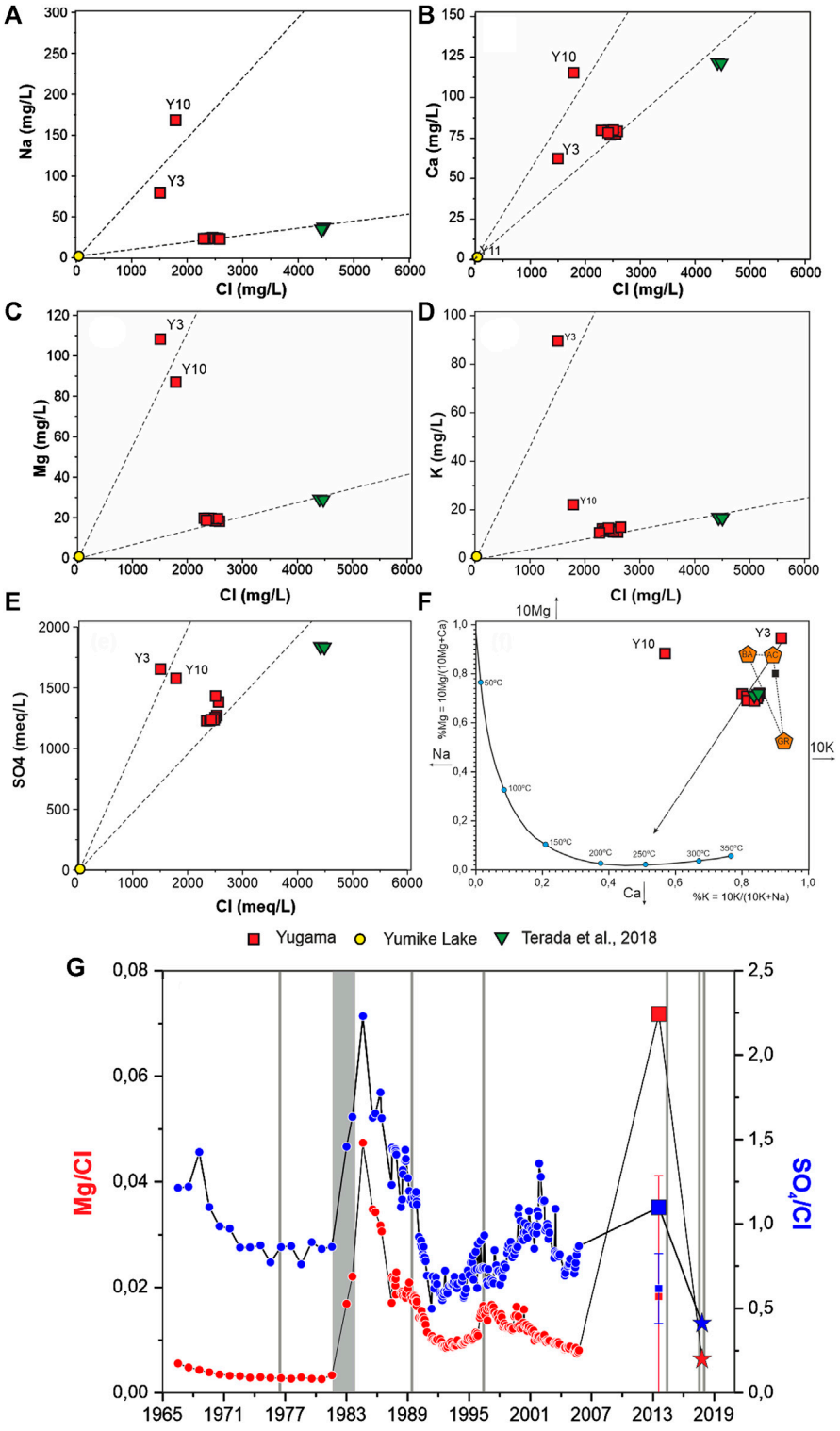

FIGURE 6 | Relationships between Cl and Na **(A)**, Ca **(B)**, Mg **(C)**, K **(D)** and SO_4 **(E)** (in mg/L) for YCL water samples collected during August 2013 survey. Also shown data from Terada et al. (2018). **(F)** Na-K/Mg-Ca diagram for YCL (based on Giggenbach, 1988). **(G)** Temporal evolution of Mg/Cl together with SO_4/Cl at YCL waters since 1966 (data from Minami et al., 1952; Ossaka et al., 1997, Ohba et al., 2008, Terada et al., 2018 and this study).

(**Figure 6C**), K^+ vs Cl^- (**Figure 6D**) and SO_4^{2-} vs Cl^- (Fig. 65e) in all YCL waters may reflect mixing of hydrothermal waters with meteoric waters (Han et al., 2010). However, the observed high Na/Cl ratios may be controlled by water-rock interactions. The relatively high concentrations of Na and Ca in YCL waters suggest strong interaction with Na- and Ca-rich minerals, possibly occurring in the reservoir and/or in the recharge area (Alçiçek et al., 2018). Ca/Na and Ca/Mg ratios also support the existence of ion exchange processes. Finally, the observed low Na/Cl and K/Cl ratios in YCL waters may indicate short and shallow flow paths (Han et al., 2010). The very low Ca/Cl ratios in the YCL waters could be the result of the high Cl contents in YCL water or due to precipitation of $CaSO_4$ depleting the fluids in Ca^{2+}.

Is important to point out that all YCL waters, except sample Y3, show SO_4/Cl ratios >1, which makes Cl the most abundant anion. Following Takano et al. (1997), sulfate within Yugama Lake has two origins: magmatic SO_2 gas and biogenic sulfate (Takano et al., 1997). The biogenic sulfate is produced in the soil around Yugama lake, and is transported to the lake within surface meteoric water. This flux is not affected by volcanic activity, and is therefore expected to be approximately stable over years. We observed a decrease in Cl^- and SO_4^{2-} concentrations at YCL, indicating a decreasing flux in the supply of magmatic volatiles.

Figure 6F shows the Na-K/Mg-Ca diagram of Giggenbach (1988) in terms of the major cations applied to the YCL waters. Data are compared with the composition of waters produced through isochemical dissolution of crustal rocks (BA: Basalts; GR: Granite and AC: average crust) and the composition of waters expected for equilibrium with an isochemically recrustallized, thermodynamically stable average crustal rock (Giggenbach 1984, 1988). This figure shows clearly that there is no equilibrium between reservoir rocks and YCL waters. In addition, all samples have Mg/Ca and K/Na ratios similar to those of volcanic rocks and/or magmas with which they are in contact, suggesting that cationic constituents of YCL waters derive dominantly from dissolution of local volcanic rocks or magmas. This diagram also allows us to infer the reservoir temperatures, which in our case would be close to 240°C. Ohba et al. (2000) proposed a hydrothermal model for Kusatsu Shirane volcano in terms of δD, $\delta^{18}O$ and Cl^- concentrations, in which a high temperature magmatic fluid is mixed with low enthalpy meteoric water, and hydrothermal reservoir separated in vapor and liquid phases, is created at 200°C. This value, also reported in Ohba et al. (2019), is of the same order and close to the value of 240°C previously estimated.

Following Giggenbach (1974) and Ohba et al. (2008), the Mg/Cl ratio is a very valuable geochemical parameter to assess the phreatic activity of Ruapehu, one of New Zealand's most active volcanoes, and Yugama crater lakes. This is partly because the combination of Mg and Cl concentration eliminates the effect of meteoric water dilution, and temporal variations in this relationship may be due to changes in the magmatic-hydrothermal activity of the volcano. SO_4/Cl ratio is also expected to increase before a forthcoming volcanic crisis due to the input of sulphurous magmatic gases into the YCL water. **Figure 5G** shows the temporal evolution of Mg/Cl together with SO_4/Cl since 1966 (data from Minami et al., 1952; Ossaka et al., 1997; , Ohba et al., 2008; Terada et al., 2018). A good temporal correlation between volcanic activity and Mg/Cl ratio is observed. As it was reported by Ohba et al. (2008), the Mg/Cl ratio increased sharply during the eruptive period in 1982–1984. At the activity in 1996, the Mg/Cl ratio showed a synchronized increase. **Figure 6G** shows that the Mg/Cl and SO_4/Cl ratios increase before increases in volcanic activity. In the specific case of the samples taken during the 2013 campaign, a clear increase is observed in both relationships (the squares in **Figure 6G** represent the maximum measured value of both relationships) to later decrease substantially in 2017 (Terada et al., 2018, stars in **Figure 6G**). This increase occurs 1 year before the onset of the unrest period (2014–2017), which was characterized by microearthquake swarms, ground deformation, increased water temperature, and changes in the chemical concentrations of the water (Kuwahara et al., 2017; Terada et al., 2018).

Vertical profiles of T and pH did not show variations with depth, indicating the absence of any significant thermal stratification. **Figure 5** shows the vertical distribution of the major cations and anions at the three vertical profiles, Crater Wall (CW), Crater 1983 (83-C) and Yugama Crater (YC). In relation to the cations, a significant increase can be observed as the depth increases in the vertical profiles CW and 83-C, mainly in Na, K and Mg. In the YC profile, located close to the center of the YCL, no significant variations are observed. Something similar occurs with anions, in which significant variations are observed in Cl and SO_4 but again only in the vertical profiles CW and 83-C. In both, an increase in SO_4 with depth is observed, possibly due to the emission of magmatic gases rich in H_2S and SO_2 and a decrease in Cl. This decrease may be due to greater evaporation in the shallower levels of the YCL, being enriched in conservative ions such as Cl. The small variations observed in the ionic content of the vertical profile YC may be due to the fact that in this area the hydrothermal activity in the bottom of the lake (central depression in **Figure 4**) is very low compared to CW and 83-C.

The stable isotope data from the waters provide an insight into the various water end-members as well as the evaporation processes in the lake (e.g. Varekamp and Kreulen, 2000) and are also representative of the degree of water-rock interaction, and of boiling and mixing processes (Clark and Fritz, 1997). The $\delta^{18}O$-δD water compositions from YCL collected in this study are compared to the samples collected in 2017 (Terada et al., 2018), from 1988 to 1992 (Ohba et al., 2000), Local Meteoric Water Line ($\delta D = 8\delta^{18}O + 16$; Ohba et al., 2000), the Global Meteoric Water Line (GMWL; $\delta D = 8\ \delta^{18}O + 10$; Craig, 1961) as well as data from medium and strong fumaroles and a magmatic water vapor component (Ohba et al., 2000).

The YCL waters are all enriched in both δD and $\delta^{18}O$ (**Table 2**) relative to local meteoric values in a δD vs $\delta^{18}O$ diagram. The YCL waters plot far from the Local Meteoric Line in the δD vs $\delta^{18}O$ diagram (**Figure 7A**). This enrichment in both δD and $\delta^{18}O$ relative to the meteoric values may be the result of mixing with volcanic hydrothermal fluids (VHF) and/or evaporation. Ohba et al. (2000) explained the high isotopic ratio of YCL water as a result of a larger degree of evaporation at elevated temperatures, and also by mixing between local meteoric

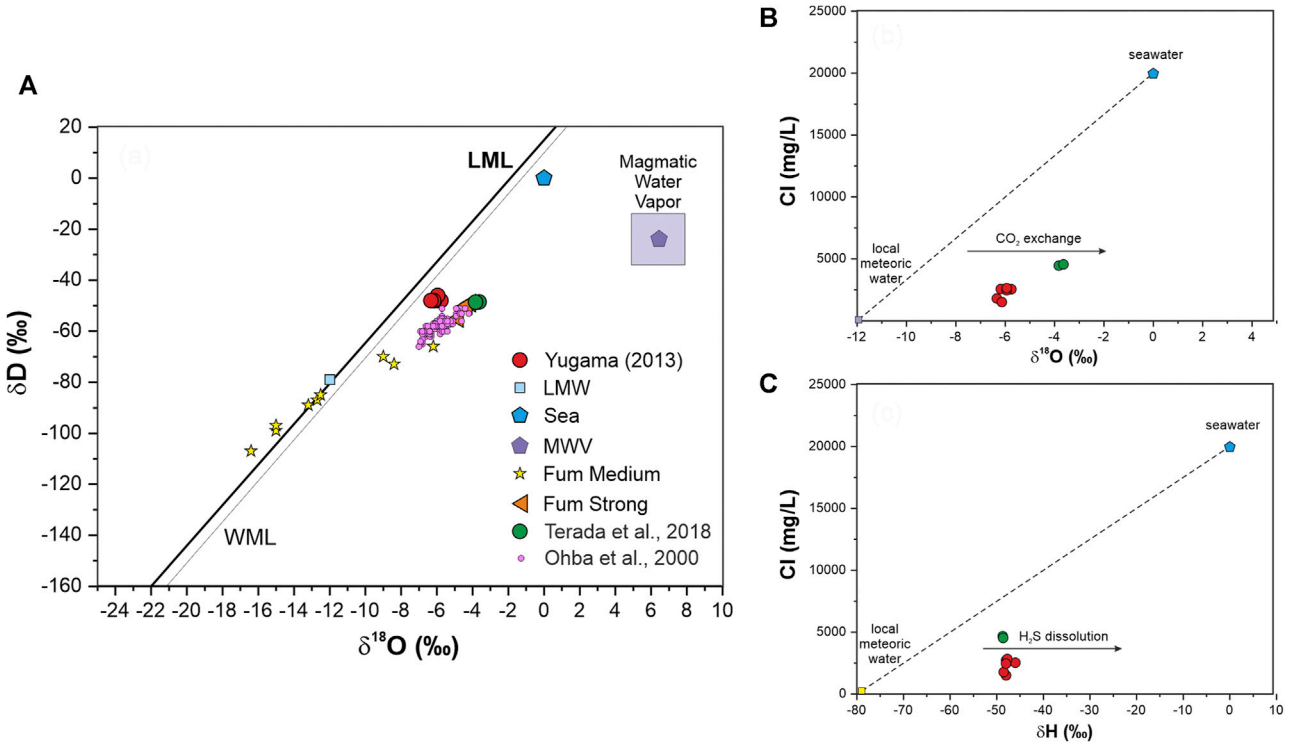

FIGURE 7 | (A) Diagram of $\delta^{18}O$ vs δD in YCL waters. Data from Ohba et al., 2000 and Terada et al., 2018 are also shown. **(B)** $\delta^{18}O$ vs Cl and **(C)** δD vs Cl binary diagrams for the YCL water samples collected during August 2013 survey. Also shown are data from Terada et al., 2018.

water and an isotopically heavy fluid, such as a high-temperature volcanic gas (HTVG), the andesitic water of Giggenbach (1992). Marked differences are observed between YCL waters collected in 2017 by Terada et al. (2018), samples reported by Ohba et al. (2000) between 1988 and 1992, and this study. Samples collected in 2013 show similar δD values to those sampled in 2017, with values ranging from -48.6‰ to -46‰. However, both set of data differ from the samples collected between 1988 and 1992 (between -66‰ and -50‰). Assuming that meteoric waters during the last 20 years have had a similar isotopic composition, the δD values have shown a clear shift to heavier ratios. This shift towards heavier δD values could be explained by increases in the magmatic water vapor component (andesitic water) and/or changes in evaporation rate because of increased water temperature. Hydrogen exchange between H_2S and H_2O could be also an explanation for the observed changes. H_2S and SO_2 have different solubility in water (Symonds et al., 2001), and their relative abundances are mainly controlled by temperature (T), pressure (P) and redox conditions (Giggenbach, 1987). Hydrothermal emissions from the bottom of the crater may have similar H_2S and SO_2 proportions, and under those conditions, most of SO_2 dissolves in water whereas H_2S remains insoluble, having more capability to produce a hydrogen isotopic exchange with water (Hernández et al., 2017). This exchange could be produced by higher dissolution of acid gases rich in H_2S during the 2013–2017 unrest. $\delta^{18}O$ values show significant changes between 2013 and 2017, towards heavier values. This shift (average value of -6.05‰ for 2013 survey and -3.73‰ for 2017 survey) can be explained by an increase in the water-rock interaction processes, again most likely due to the increase in volcanic activity.

Data collected before 2013 align along a mixing line with AW and evaporation processes. The data from this 2013 study present a similar direction, but are aligned with heavier values of δD, most likely due to different evaporation scales. Changes in lake and/or air temperature may be responsible for the observed differences. Hydrothermal fluids are probably a mixture of AW and deep meteoric waters, so the water/rock interaction can cause a change of $\delta^{18}O$ in addition to the mixing of those fluids with shallow MW in the lake environment. Finally, the $\delta^{18}O$ values can be influenced by the rebalancing of CO_2 and the equilibrium of H_2S. Therefore, the final mixture resulting from all these processes will evaporate, creating a trend in $\delta^{18}O$ and δD dependent on local T and H. More detailed analysis of all trends in the Cl—$\delta^{18}O$ and Cl-δD and S—$\delta^{18}O$ and S—δD diagrams will be necessary to derive which processes are the most important determining stable isotope values.

The distribution of YCL water samples in the Cl^- vs δD and Cl^- vs $\delta^{18}O$ binary diagrams (**Figures 7B,C**) diverges from the mixing line between an isotopically light meteoric end-member (Yumiike lake sample) and sea water, suggesting the contribution of different isotopically sources. **Figure 7B** shows a shift in $\delta^{18}O$ from 2013 to 2017 water samples towards lighter values, which may represent an increase on CO_2 exchange between water and a

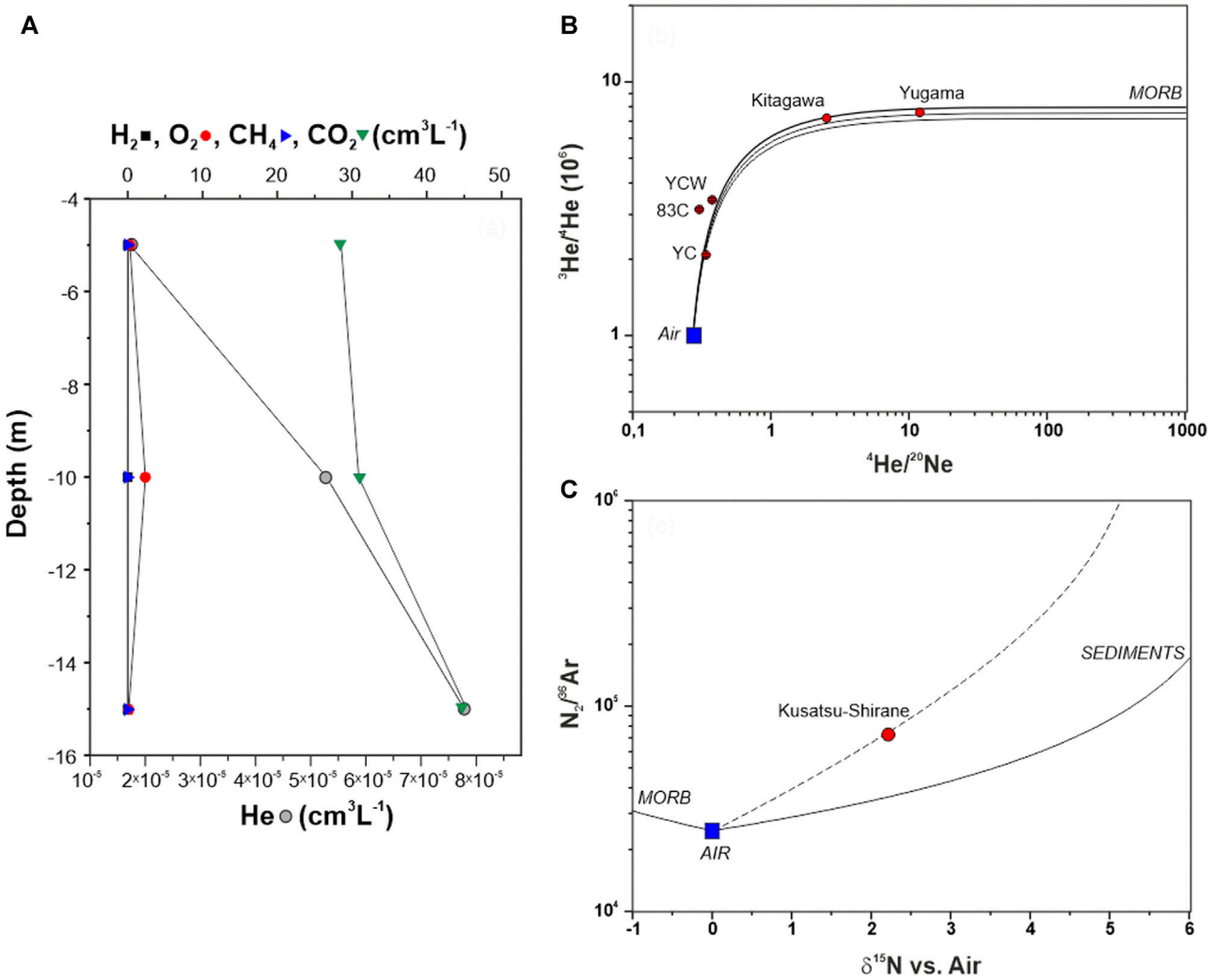

FIGURE 8 | Vertical profile 83-C of dissolved gases in YCL waters. **(B)** Diagram of He isotopes (normalized to the atmosphere) vs $^{4}He/^{20}Ne$ ratios. The samples represent a mixing between the atmosphere and a mantle type end member. The mixing boundary lines have the following end members: atmosphere (as dissolved air) R/Ra = 1 and He/Ne = 0.285; Mantle R/Ra = 6.5 and He/Ne = 1,000; continental crust R/Ra = 0.01 and He/Ne = 1,000. **(C)** $\delta^{15}N$ vs $N^{2}/^{36}Ar$ diagram. Collected fumarole sample is plotted together with the mixing lines relative to MORB, atmosphere and crustal sediments. Theoretical mixing curves between air and the Kusatsu-Shirane volcanic component (dashed line) are also represented along with Kitagawa and Yugama are fumarole data.

rich deep-seated CO_2 end-member. However, not significant changes are observed for δD, which may indicate similar H_2S dissolution rates. Since no data of diffuse CO_2 emission are available for 2017, we cannot rule out that other processes may have affected the $\delta^{18}O$ isotopic composition. Modelling the evaporation of a mixture with variable proportions of endmembers over time is possible (Varekamp and Kreulen, 2000) but such simulations have many degrees of freedom and may not provide truly new insights (Hernández et al., 2017).

The chemical composition of dissolved gases in samples collected during the August 2013 survey at YCL is shown in **Table 2**. **Figure 8A** shows the relative amounts of dissolved H_2, O_2, CH_4, CO_2 and He in YCL waters. No significant trend was observed in the H_2, O_2 and CH_4 vertical profiles. However, a clear increase in the concentrations of dissolved gases CO_2 and He is observed with depth. Diffuse CO_2 emission rate measured at the water surface of YCL (30 ± 12 t d^{-1}) is representative of the observed CO_2 content in the water. Assuming an area of 0.66 km^2, the normalized diffuse CO_2 emission from YCL would be ~454 t km^{-2} d^{-1}. This CO_2 emission rate value is within the range typical of acid volcanic lakes (average 614.2 t km^{-2} d^{-1}, Pérez et al., 2011).

The deepest water sample of 83-C vertical profile also showed discrete enrichments in He (**Figure 8A**). Assuming that the He concentrations in the YCL can be described by the observed concentration profile, it is possible to estimate the He emissions at the water surface by applying a pure diffusive model (Melián et al., 2016). According to Fick's law, the gas flux at the surface of the water is driven by the concentration gradients along the depth and the diffusivity of the gas in water:

$$Fi = -D_{i(w)}\frac{\partial C_{i(w)}}{\partial Z}$$

where *Fi* is the flux of gas i (in kg m^{-2} s^{-1}), *Di(w)* is the diffusion coefficient in water (in m^2 s^{-1}), *Ci(w)* is the concentration of i in water (in kg m^{-3}) and ζ is the depth (in m). For He, we have used a value for *DHe(w)* at the average temperature of YCL waters (~25°C) of c. 2.12×10^{-9} m^2 s^{-1}. This value was calculated as an interpolation of the values between 10°C and 20°C reported by Verhallen et al. (1984). The observed concentrations of He at different depths in 83-C vertical profile were fitted with the following exponential decay function:

$$[He]w = 1 \times 10^{-9}Z - 2 \times 10^{-9}$$

With the derivative respect to depth at ζ = 0 (lake surface), is possible to estimate the He emission through the water surface (0.066 km^2), obtaining a result of 0.012 mg d^{-1}. This value is approximately two orders of magnitude lower that those estimated by Melian et al. (2017), for crater lakes on the island of São Miguel in the Azores. However, this value is subject to uncertainties due to the occurrence of changes in the rate of He input at greater depths. Bubble transfer of He in the CO_2 bubbles, which dissolve during ascent, can change the He concentration independently of diffusion in the water column. The reason for this difference could be due to the fact that in YCL most of the gas (in our case He) is emitted into the atmosphere through bubbles and a small portion of this gas is dissolved in the lake water as He is poorly soluble and hence tends to be liberated in the gas phase, i.e. bubble.

The $^3He/^4He$ ratios measured in dissolved gases at YCL waters along the vertical profile 83-C range from 208.4 to 3.43 R/Ra (where Ra m is the atmospheric $^3He/^4He$ ratio of 1.39×10^{-6}; Mamyrin & Tolstikhin 1984) with $^4He/^{20}Ne$ ratios in the range of 0.30–0.38 (**Table 2**). Sano et al. (1994) reported the chemical compositions, He/Ne ratios, He and C isotopes of 14 gas samples collected from the YCL, fumaroles and hot springs associated with Kusatsu-Shirane volcano. The $^3He/^4He$ and $^4He/^{20}$/Ne ratios vary from 1.51 to 7.21 Ra and from 0.35 to 11.8, respectively. Fluids from mantle degassing show high R/Ra ratios up to 20 or more in hot spot/plume gases, whereas R/Rair ratios for crustal gases are as low as 0.01 (Craig and Lupton, 1976). The measured $^3He/^4He$ values reveal a major contribution from a mantle-type source. **Figure 8B** shows the diagram of uncorrected R/Ra vs $^4He/^{20}Ne$ values. There is a positive correlation between the $^3He/^4He$ and $^4He/^{20}Ne$ ratios suggesting mixing between mantle derived He and atmospheric noble gases. All samples have $^3He/^4He$ values above the ASW, and the measured ratios fall on a mixing line between a local mantle type and an atmosphere-derived end member. Data from Kitagawa fumarole and Yugama Lake bubbling (Sano et al., 1994) show that the $^3He/^4He$ isotopic ratios remain quite constant at ~7.5 Ra, indicating that this ratio is characteristic of mantle contribution at Yugama fumarolic discharges and is not affected by atmospheric contamination. YCL is a high activity volcanic lake affected by the addition of significant amounts of hot hydrothermal-magmatic fluids, and advection seems the main physical process responsible of the observed vertical distribution, as observed for other crater lakes e.g., Taal in Philippines (Hernández et al., 2017).

To investigate the origin of the gases emitted by the Yugama crater, a gas sample was taken from a fumarole located on the northern shore of the lake (red square in **Figure 2A**). In addition to the analysis of the chemical composition of the sample, the isotopic composition of nitrogen was analyzed. **Figure 8C** shows $\delta^{15}N$ vs $N_2/^{36}Ar$ together with the mixing lines relative to MORB, atmosphere (AIR-ASW) and crustal sediments. Correlation between observed $\delta^{15}N$ value and $N_2/^{36}Ar$ ratio (dashed line in **Figure 8C**) might suggests a mixing trend between air ($\delta^{15}N$ = 0‰, $N_2/^{36}Ar = 2.48\times10^4$) and the component of the volcanic gas source at Kusatsu-Shirane volcano, which must be a mixture of magma-derived and crustal components.

Acoustic Plumes

Based on the 200 and 50 kHz echograms, more than 48 vertical acoustic plumes or flares (acoustic signature of bubble plumes) 1.5–22 m in height have been identified sourced from the bottom of the main and secondary crater lakes of Kusatsu-Shirane (**Figure 9**). Acoustic plumes ranging 12–30 m high are located within the deep holes (DH1 and DH2) whereas numerous minor acoustic plumes 8–9 m high are located at the periphery of the YCL and at the northern peripheral crater (**Figure 9**). At the same time, horizontal plumes at 2–5 m water depth were identified.

Deep Hole 1 (DH1)

Two major acoustic plumes 19–20 m in height are identified sourced from the DH1 hole (**Figure 10**). These acoustic plumes are separated by 15 m, and are sourced in deep holes at 24.5 and 23.6 m water depths, excavated to almost 12 m below the bottom of the lake. These acoustic plumes have a funnel shape due to their lateral expansion from the source as they ascend. The plume is linked to a sub-horizontal stratified plume located at two to five and 1.3 m below the lake surface (**Figure 10**) The entire acoustic plume sourced from the DH1 has a mushroom shape, showing a rain of high-backscatter elongated spots detached from the main plumes with descending trajectories, inferred as particles sourced from the deep hole and gravitationally falling to the bottom lake. Low backscatter mounds indicating recent deposits observed on the bottom of the YCL are linked to areas of falling particle material (**Figure 10A**). Aditionally, lighthouse-like plumes, 12 m in height, are also identified on the flanks of the main depression (**Figure 10B**, location in **Figure 2**).

The comparison between the bathymetry of the DH1 obtained with the two frequencies (200 y 50 khZ) allows us to construct a 3D model that relates this deep hole, the acoustic plumes and surrounded bottom deposits (**Figure 11**). The superposition of the bathymetry data obtained with the two frequencies (**Figure 11**) shows a series of lobes sourced from the DH1 which is marked by a pronounced peak observed with the 50 kHz frequency. These lobes are interpreted to be non-consolidated recent sediments expulsed by the plume sourced from the DH1 which are detected with the 200 kHz high frequency data but not for the 50 kHz frequency (**Figure 11**).

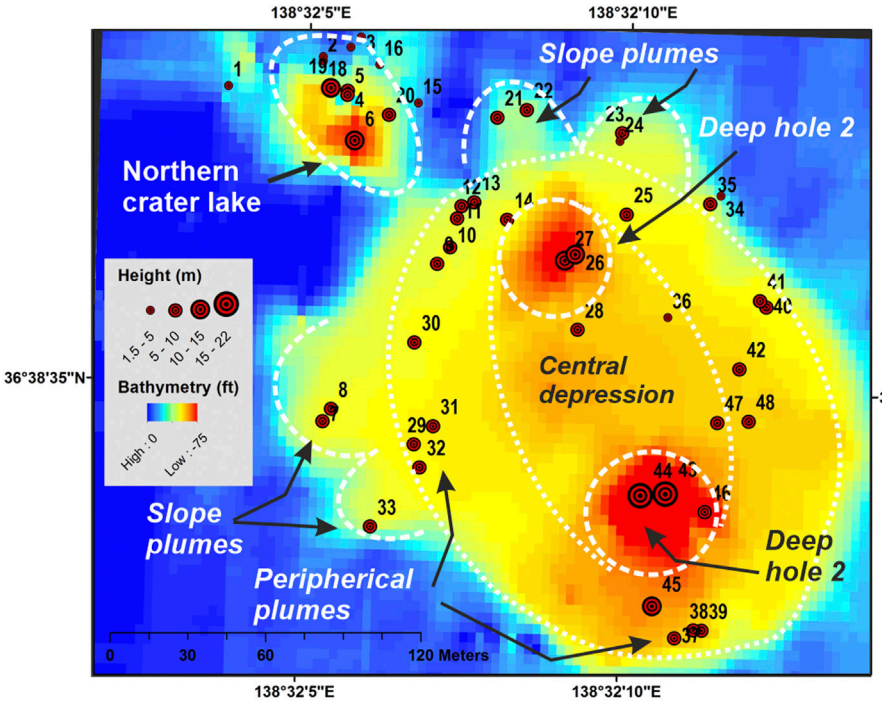

FIGURE 9 | Bathymetric map with location and length of acoustic plumes detected on the echogram. Numbers are the identify the plumes shown in the following figures.

Deep Hole 2 (DH2)

Two giant funnel-shaped acoustic plumes 13–14 m in height and separated by 9 m are identified, with a source at the DH2 hole (**Figure 12A**). Around the hole, numerous flare-like acoustic plumes 6–7 m in height appear sourced from the flat bottom of the YCL (**Figure 11B**). Both funnel-shaped and flares acoustic-type plumes appear linked upwards by a continuous stratified plume located at 0.5 and 3 m below the surface of the lake. As occurred around DH1 hole, numerous elongated high-backscatter hotspots with descending trajectories are identified surrounding the DH2 hole (**Figure 12A**).

Mounded-type deposits along the bottom lake associated to falling solid particles.

Mound-type deposits are identified with the echograms along the bottom of the YCL (**Figure 13**). These mounds are 1–2 m in height and characterized by low-acoustic reflectivity regarding the bottom of the lake. Most of these mounds are located below zones of elongated backscatter hotspots observed within the water column (**Figure 13B**). Such backscatter anomalies showing descending trajectories (following the track of the boat) interpreted as solid particles falling gravitationally to the bottom of the lake, forming mounds.

Hydroacoustic Evidence of Subaqueous Molten Sulfur Pools and Sulfur Spherules

Many active crater lakes contain subaqueous molten sulfur pools at the places of highest thermal activity on their lake floors (e.g., Takano et al., 1994). Volcanic gases discharging through the subaqueous molten sulfur pools convey sulphur spherules of various shapes to the lake surface almost continuously. Occurrence of spherules of solid native sulfur up 4–5 mm in diameter with sulfide inclusions (mainly corroded FeS_2) are commonly reported in acid carter lakes (e.g., Takano et al., 1994) as: Yugama, Kusatsu-Shirane volcano, Japan; Poás volcano Costa Rica, Crater Lake, Ruapehu volcano, New Zealand; and Bannoe lake and Maly Semiachik, Kamchakta, Russia. Sulphur spherules are most likely produced as hot gases (e.g., H_2S or SO_2) released at the bottom of the lake create turbulence in pools of liquid suphur.

In the YCL, the most active zones showing effervescence on the lake surface bring up sulfur slicks of various shapes from the subaqueous vents (Ossaka et al., 1980). Since 1805 more than 10 phreatic eruptions have been recorded (Hayakawa and Yui, 1989), often describing ejection of molten sulfur. Based on morphology and mineralogy of the sulfur slicks sampled in the YCL, Takano et al. (1994) propose four stages (I-IV) for the categorization of thermal state of the crater lakes. Stage I: Weak fumarolic activity is restricted to subaqueous vent discharges of low temperature gases (>119°C); Stage II, Moderate fumarolic activity, when temperature of fumarolic gases exceeding 119°C (melting point of orthorhombic sulfur), is high enough to melt sulfur within sulfur- and pyrite-rich bottom lake sediments. Subaqueous molten sulfur pools (d = 1,500–1800 kg/m^3) are formed on the lake floor and encrusted with the solidified sulfur layer. Two types of floating spherules are sourced from the bottom lake: 1) Black hollow spherules of sulphur are floating from the deeper higher temperature zones;

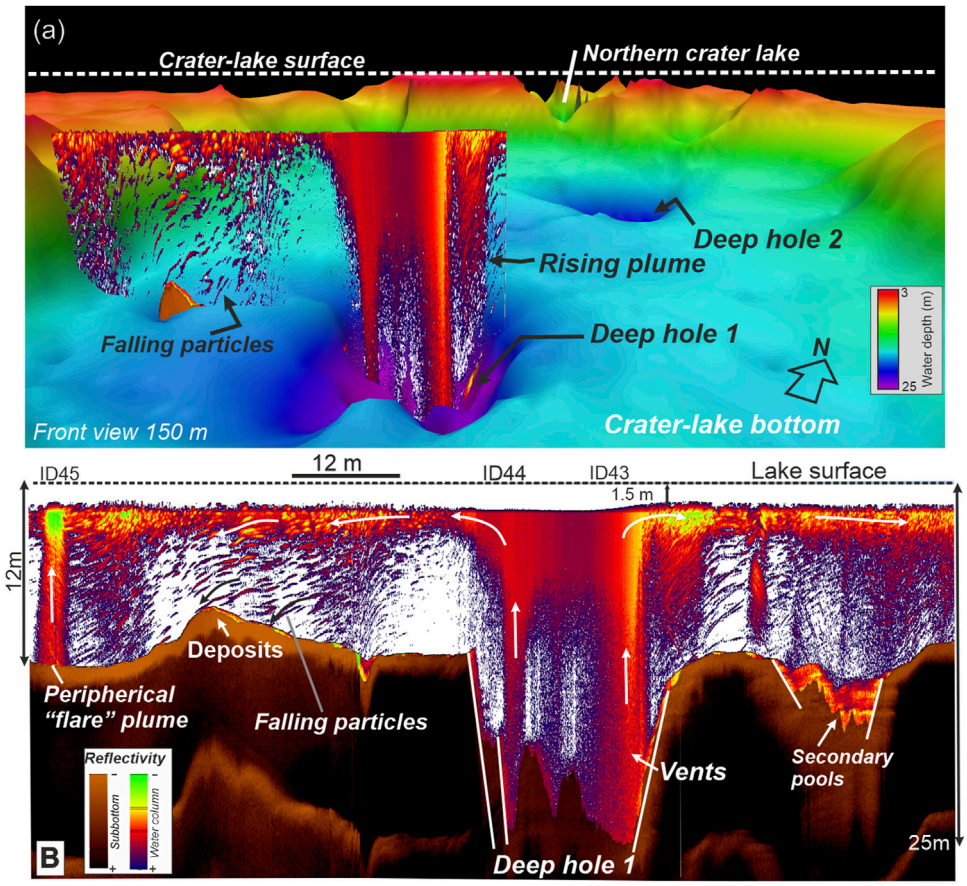

FIGURE 10 | (A) Composition of 3D bathymetry and vertical echogram profile crossing the DH1 hole. **(B)** Echogram crossing the DH1 showing a dense funnel-shaped plume rising from the deep hole DH1. Bright spots sourced from the plumes are falling to the lake bottom. Flare-like plumes are also identified along the flanks of the NW-SE depression. ID location of plumes in **Figure 5**.

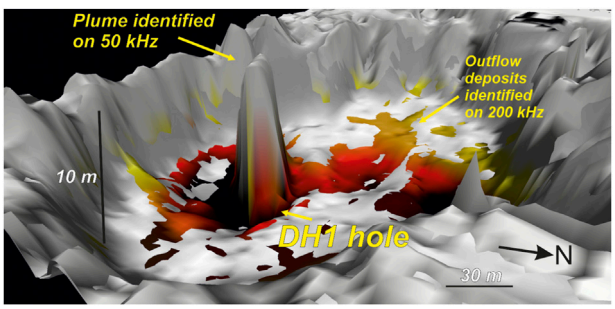

FIGURE 11 | 3D view of the DH1 hole obtained by overlaying the two-frequency bathymetric data: 50 kHz in grey scale and 200 kHz in color scales. The peak identified on 50 kHz within the DH1 is interpreted as dense acoustic plume. The red colors surrounding the deep hole and identified on 200 kHz are interpreted as recent deposits formed on the bottom lake, sourced from the plume.

2) Yellow, plastic sulfur blobs come from the low temperature region, broken to pieces of thin film as they go up to the lake surface. The broken blobs stick together to form a yellow mat on the lake surface. At this stage, the temperature is not enough to maintain vigorous convention within the molten sulfur pools. Stage III; Frequent mud plumes. Intensive gas discharge and much more active convection of the pool due to the low viscosity H_2S, SO_2 dissolving liquid sulfur. Sulfur slicks are composed of yellow mats and black hollow spherules (3–5 mm in diameter) with tails in various lengths (a few cm) 3). Sulfur blobs 4) are accumulated around the vents. Immediately after the mud plume 5) eruption, a sheet of white sulfur bubbles 6) is often observed on the lake surface. Stage IV: Phreatic or geyser like eruptions.

We suggest that our hydroacoustic images display most of subaqueous fumarolic activity described by Takano et al. (1994) within YCL, based on the morphology and mineralogy of sulfur slicks. Based on these descriptions, we interpret hydroacoustic images of the morphology of the deep holes DH1 and DH2 as deep depressions filled by low-reflective sediments and molten sulfur pools formed by venting high T volcanic gases through the main vent conduit. Furthermore, intense gas discharges from DH1 are reflected on the dense acoustic plumes venting from the hole, forming vigorous convention cells in the water column. These convective cells, well identified on acoustic

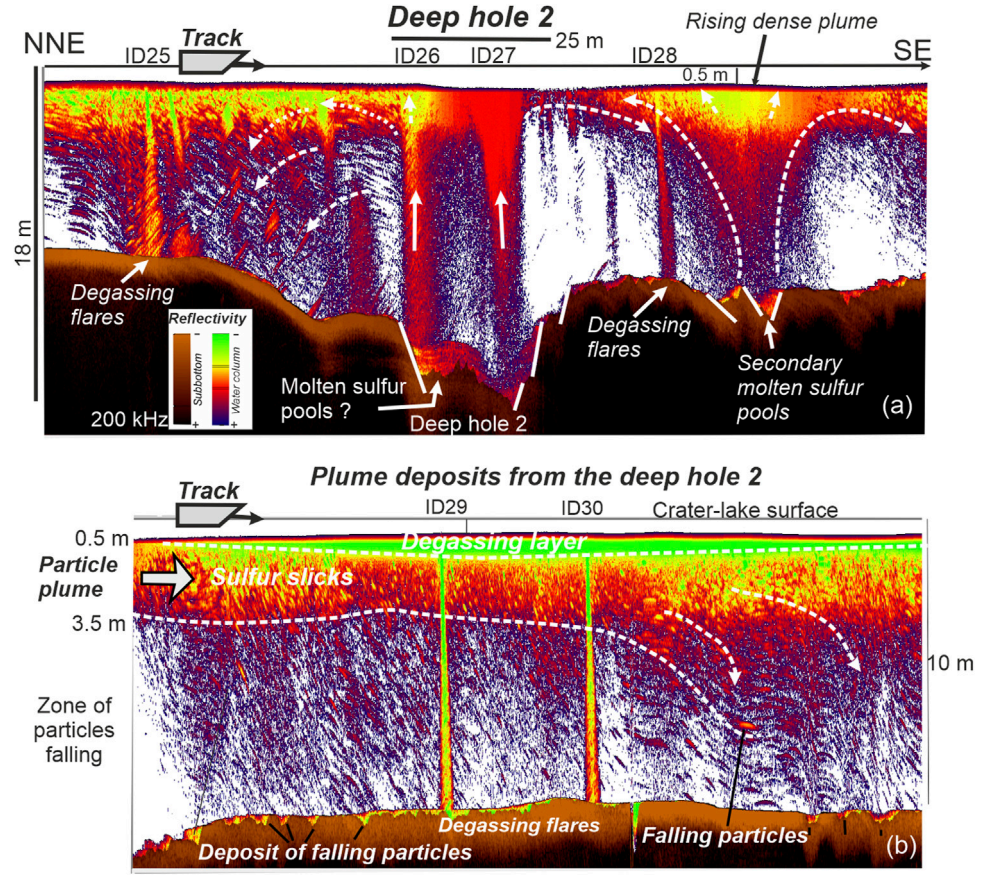

FIGURE 12 | (A) Echogram profile crossing DH2 down to 18 m water depth shows high backscatter "funnel"-like plumes rising from the hole; **(B)** Echogram profile from the central depression (10 m water depth) showing "flare-like" plumes, zones of falling particle material and the stratified sub-horizontal plume.

images, contain reflective particle material inferred to be black hollow sulfur spherules (3–5 mm in diameters) formed within the molten pools, enough to be detected with the 200 kHz echosounder.

Sediments identified around the DH1 are interpreted as sulfur blobs accumulated around the pools by gravitational falling of particle material within the ascending mud plume. These plumes ascend almost to the surface, only ~1 m below, and may cause the effervescence observed at the lake surface.

From our hydroacoustic images, DH1 seems more active, formed by higher temperature fumarolic activity than DH2, with a strong peak anomaly identified only on 50 kHz and attributed to a dense plume of (pyrite-enriched?) sulfur spherules and muds sourced from the molten sulfur pool.

Based on the work of Takano et al. (1994), we agree that the plumes sourced from the two deep holes (DH1 and DH2) are formed by fluids at temperature >150°C due to the presence of gravitationally accumulated sulfur blobs around the vents from strong convection currents. According to the Takano et al. (1994) model, the formation and accumulation of heavy black hollow spherules around the molten sulfur pools take place only during the Stage III. Increase in the pressure of these plumes may cause the black mud plumes with an elevation of up 5 m above the lake surface as identified in the YCL. Otherwise, at this stage, yellow sulfur tail spherules up to a few centimeters form floating sulfur slicks at the lake surface.

Mound Sulfurs Formed From Sinking of Floating Sulfur Spherules

The floating sulfur slicks of spherules progressively lose their buoyancy, and fall to the shallow-water bottom lake. These types of sub-aqueous sulfur mounds have been reported in exhumed zones of the Waiotapu geothermal area, Rotorua, New Zealand (Simmons et al., 1993). Mounds are > 2 m high and composed of small (<0.5 cm) hollow spheres, and occasionally teardrop-shaped globules resulting from rapid deposition of sulfur globules formed when fumarolic gases are discharged through molten sulfur pools. The morphology of these floating teardrops spherules is similar to that of those tailed spherules described in the YCL for the Stage III (Takano et al., 1994). Thus, based on hydroacoustic images, the formation of sulfur mounds takes place in shallow-water areas (3–5 m water depth) of the crater-lake, as a consequence of rapid deposition of sulfur globules detaching from floating sulfur blobs.

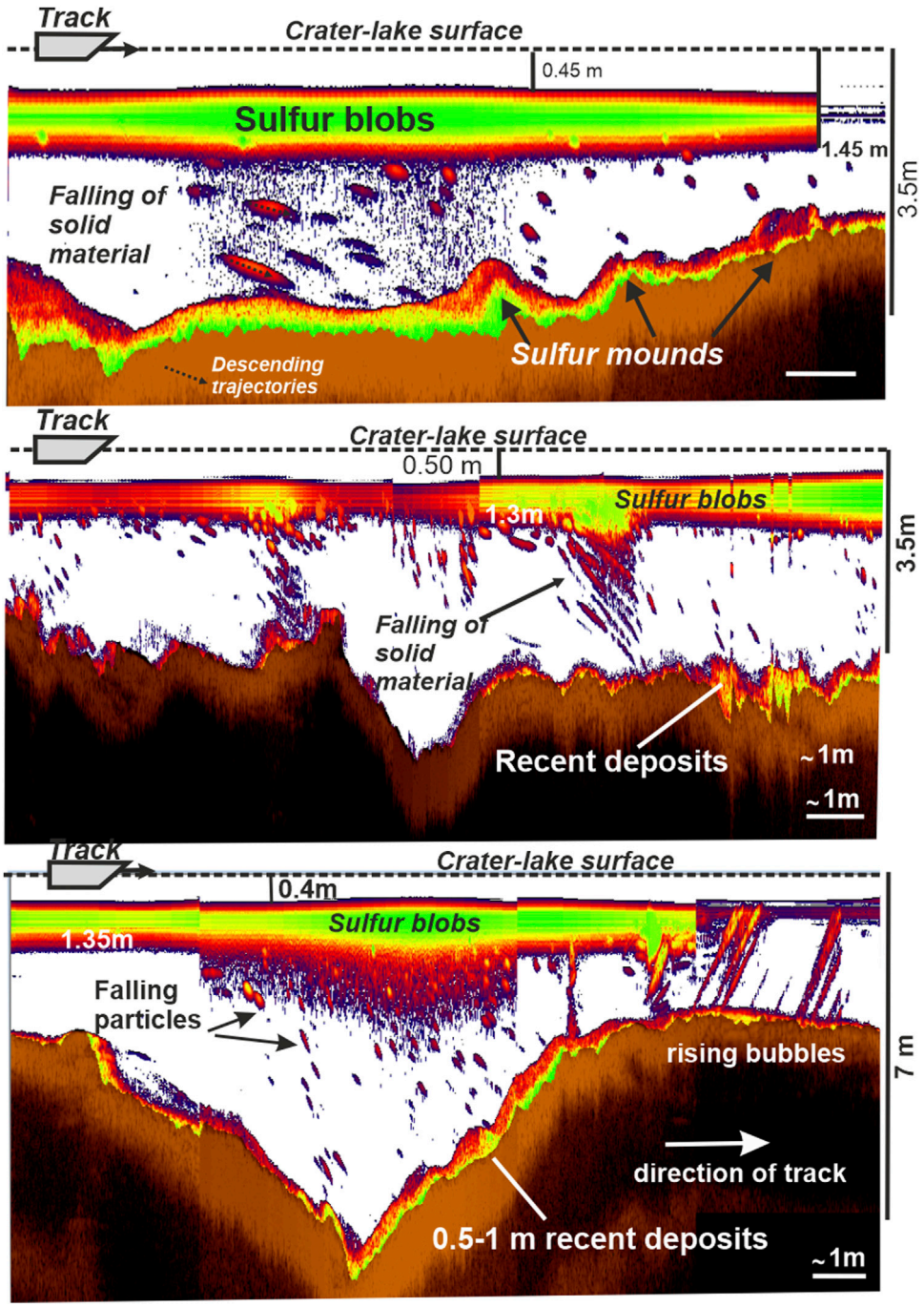

FIGURE 13 | Echogram profiles from shallow water zone (3.5–7 m) located along the flanks of the crater lake show the formation of mounded-type deposits by particle material falling from the floating sub-horizontal plumes. Mounded deposits are characterized by low backscatter, in contrast to the high-backscatter values of the volcanic-derived deposits of the bottom lake.

CONCLUSION

One of the most notable findings in our study is the identification and characterization of the main areas of magmatic-hydrothermal fluid discharges at the bottom of YCL. Our data indicate a strong input of a hot volcanic fluid rich in S and other volatiles. Among them and due to the acidity of the lake waters, most of the CO_2 and He are emitted in a visible form (bubbling). Chemical and isotopic composition of YCL waters showed a potential relationship with changes in volcanic activity, with increases on the Mg/Cl and SO_4/Cl ratios before the 2013–2017 unrest and changes in the $\delta^{18}O$ and dH values to

heavier ones when the 2013 data are compared with the 2017 data, due possibly to an increase in magmatic water vapor component (andesitic water) and/or changes in evaporation rate because of increased water temperature.

Major cations and anions dissolved in YCL water and the distribution of dissolved CO_2 and He gases in the water column show a clear inhomogeneous distribution. The lake water contains contributions of meteoric water and magmatic-hydrothermal fluids. Contents of chemical species in the lake are considerably higher near the lake bottom as a consequence of strong water-rock interaction due to hydrothermal fluid discharges into the lake. The strong emission of magmatic gases also affects the chemistry of the lake. This study allowed us to estimate for the first time the diffuse CO_2 emission from YCL at 30 ± 12 t d^{-1}, with a normalized CO_2 emission rate of 454 t km^{-2} d^{-1}, assuming an area of 0.066 km^2, within the range of acid volcanic lakes.

Intense degassing from the bottom lake of the YCL is observed on hydroacoustic images. Based on a comparison between the geochemical and mineralogical model of Takano et al. (1994) and our hydroacoustic images of subaqueous fumarole activity, we conclude that the deep holes (DH1 and DH2), 35–40 m in diameter and 20–25 m incised into the bottom of the lake, are interpreted as molten sulfur pools formed on the lake floor by high T degassing. Acoustic plumes, 20–25 m in height, are dense plumes including particle material and hollow spherules of solidified molten sulfur formed by volcanic gasses passing through the molten sulfur pools. Rain of these particles around the deep holes is interpreted as falling sulfur blobs rapidly accumulated around the molten sulfur pools. High-density particles enable rapid gravitational deposition around the vents, and are formed of heavy black spherules (pyrite-enriched) formed only at temperatures >150°C of the molten sulfur pools (Takano et al., 1994). Buoyant acoustic plumes identified 0.5–3 m below the lake surface are interpreted as floating yellow sulfur tail spherules, forming visible sulfur slicks at the lake surface.

Mounds, 1–2 m high, identified along the bottom of shallow water parts of the crater lakes and associated with falling particles released from sub-stratified plumes are interpreted as sulfur mounds by rapid deposition of yellow sulfur spherules. These types of sub-aqueous sulfur mounds have never been reported in modern crater lakes by echosounder imaging. In agreement with the model of Takano et al. (1994), we propose that the fumarolic temperature of the deep holes must be > 150°C to enable the formation of a rain of heavy black spherules around the vents the molten sulfur viscosity increases. Finally, the fumarolic activity of the deep holes of the YCL, at the time of the survey, was at Stage III. Otherwise, peripheral shallow-water parts showed only degassing flare-like plumes related to Stage I. The activity of the YCL is mainly focused on the two deep holes identified on hydroacoustic images.

This study greatly contributes to a better understanding of the dynamics of the YCL, identifying the areas of major hydrothermal activity and serving as the basis for future studies that will help to improve the early warning system of the volcano monitoring program for Kusatsu-Shirane volcano.

DATA AVAILABILITY STATEMENTS

The geochemical data supporting this study are stored on servers at ITER and can be made available by reasonable arrangement with the corresponding author.

AUTHOR CONTRIBUTIONS

PH participated in planning of the survey, field work, chemical and isotopic analysis of samples, treatment of data and writing the manuscript. KN participated in planning of the survey, field work, and writing the manuscript. LS participated in treatment of echosounding data and writing the manuscript. EP, TM, and YK participated in the field work. CA, GM, and HS participated in the chemical and isotopic analysis of samples. NP participated in writing the manuscript.

FUNDING

This research was financed by the Japan Society for the Promotion of Science (Fellow's ID No: L13527) and the projects TFvolcano and TFassistance of the Program Tenerife INNOVA, Cabildo Insular de Tenerife.

ACKNOWLEDGMENTS

Thanks to Beverley Coldwell for assistance with the written English.

REFERENCES

Alçiçek, H., Bülbül, A., Brogi, A., Liotta, D., Ruggieri, G., Capezzuoli, E., et al. (2018). Origin, Evolution and Geothermometry of the thermal Waters in the Gölemezli Geothermal Field, Denizli Basin (SW Anatolia, Turkey). *J. Volcanology Geothermal Res.* 349, 1–30. doi:10.1016/j.jvolgeores.2017.07.021

Arpa, M. C., Hernández, P. A., Padrón, E., Reniva, P., Padilla, G. D., Bariso, E., et al. (2013). Geochemical Evidence of Magma Intrusion Inferred from Diffuse CO2 Emissions and Fumarole Plume Chemistry: the 2010-2011 Volcanic Unrest at Taal Volcano, Philippines. *Bull. Volcanol.* 75 (747). doi:10.1007/s00445-013-0747-9

Burton, M. R., Sawyer, G. M., and Granieri, D. (2013). 11. Deep Carbon Emissions from Volcanoes. *Earth. Rev. Min. Geochem.* 75, 323–354. doi:10.1515/9781501508318-013

Capasso, G., Favara, R., and Inguaggiato, S. (2000). Interaction between Fumarolic Gases and thermal Groundwaters at Vulcano Island (Italy): Evidences from Chemical Composition of Dissolved Gases in Waters. *J. Volcanology Geothermal Res.* 102, 309–318. doi:10.1016/s0377-0273(00)00193-1

Capasso, G., and Inguaggiato, S. (1998). A Simple Method for the Determination of Dissolved Gases in Natural Waters. An Application to thermal Waters from Vulcano Island. *Appl. Geochem.* 13, 631–642. doi:10.1016/s0883-2927(97)00109-1

Cardellini, C., Chiodini, G., and Frondini, F. (2003). Application of Stochastic Simulation to CO_2 Flux from Soil: Mapping and Quantification of Gas Release. *J. Geophys. Res.* 108 (B9), 2425. doi:10.1029/2002jb002165

Caudron, C., Mazot, A., and Bernard, A. (2012). Carbon Dioxide Dynamics in Kelud Volcanic lake. *J. Geophys. Res.* 117, a–n. doi:10.1029/2011JB008806

Clark, I. D., and Fritz, P. (1997). *Environmental Isotopes in Hydrogeology*. New York: Lewis Publishers.

Craig, H. (1961). Isotopic Variations in Meteoric Waters. *Science* 133, 1702–1703. doi:10.1126/science.133.3465.1702

Craig, H., and Lupton, J. E. (1976). Primordial Neon, Helium, and Hydrogen in Oceanic Basalts. *Earth Planet. Sci. Lett.* 31, 369–385. doi:10.1016/0012-821x(76)90118-7

Deutsch, C. V., and Journel, A. G. (1998). *GSLIB: Geostatistical Software Library and User Guide*. 2nd ed. New York: Oxford University Press.

Evans, W. C., White, L. D., Tuttle, M. L., Kling, G. W., Tanyileke, G., and Michel, R. L. (1994). Six Years of Change at Lake Nyos, Cameroon, Yield Clues to the Past and Cautions for the Future. *Geochem. J.* 28, 139–162. doi:10.2343/geochemj.28.139

Giggenbach, W. F. (1988). Geothermal Solute Equilibria. Derivation of Na-K-Mg-Ca Geoindicators. *Geochimica et Cosmochimica Acta* 52, 2749–2765. doi:10.1016/0016-7037(88)90143-3

Giggenbach, W. F. (1992). Isotopic Shifts in Waters from Geothermal and Volcanic Systems along Convergent Plate Boundaries and Their Origin. *Earth Planet. Sci. Lett.* 113, 495–510. doi:10.1016/0012-821x(92)90127-h

Giggenbach, W. F. (1984). Mass Transfer in Hydrothermal Alteration Systems-A Conceptual Approach. *Geochimica et Cosmochimica Acta* 48, 2693–2711. doi:10.1016/0016-7037(84)90317-x

Giggenbach, W. F. (1987). Redox Processes Governing the Chemistry of Fumarolic Gas Discharges from White Island, New Zealand. *Appl. Geochem.* 2, 143–161. doi:10.1016/0883-2927(87)90030-8

Giggenbach, W. (1974). The Chemistry of Crater lake, Mt. Ruapehu (New Zealand) during and after the 1971 Active Period. *N. Z. J. Sci.* 17, 33–45.

Grassa, F., Capasso, G., Oliveri, Y., Sollami, A., Carreira, P., Rosário Carvalho, M., et al. (2010). Nitrogen Isotopes Determination in Natural Gas: Analytical Method and First Results on Magmatic, Hydrothermal and Soil Gas Samples. *Isotopes Environ. Health Stud.* 46 (2), 141–155. doi:10.1080/10256016.2010.491914

Greinert, J., Artemov, Y., Egorov, V., Debatist, M., and McGinnis, D. (2006). 1300-m-high Rising Bubbles from Mud Volcanoes at 2080m in the Black Sea: Hydroacoustic Characteristics and Temporal Variability. *Earth Planet. Sci. Lett.* 244, 1–15. doi:10.1016/j.epsl.2006.02.011

Han, D. N., Liang, X., Jin, M. G., Currell, M. J., Song, X. F., and Liu, C. M. (2010). Evolution of Groundwater Hydrochemical Characteristic and Mixing Behavior in the Daying and Qicum Geothermal Systems, Xinzhou Basin. *J. Volcanol. Geotherm. Res.* 189, 99–104. doi:10.1016/j.jvolgeores.2009.10.011

Hayakawa, Y., and Yui, M. (1989). Eruptive History of the Kusatsu Shirane Volcano. *Daiyonki-kenkyu* 28, 1–17. (in Japanese). doi:10.4116/jaqua.28.1

Hernández, P. A., Melián, G. V., Somoza, L., Arpa, M. C., Pérez, N. M., Bariso, E., et al. (2017). The Acid Crater lake of Taal Volcano, Philippines: Hydrogeochemical and Hydroacoustic Data Related to the 2010-11 Volcanic Unrest. *Geol. Soc. Lond. Spec. Publications* 437, 131–152. doi:10.1144/SP437.17

Hernández, P. A., Mori, T., Padrón, E., Sumino, H., and Pérez, N. (2011). Carbon Dioxide Emission from Katanuma Volcanic lake, Japan. *Earth Planet. Sp* 63 (11), 1151–1156. doi:10.5047/eps.2011.06.038

Jolie, E. (2019). Detecting Gas-Rich Hydrothermal Vents in Ngozi Crater Lake Using Integrated Exploration Tools. *Sci. Rep.* 9, 12164. doi:10.1038/s41598-019-48576-5

Kling, G. W., Evans, W. C., Tanyileke, G., Kusakabe, M., Ohba, T., Yoshida, Y., et al. (2005). From the Cover: Degassing Lakes Nyos and Monoun: Defusing Certain Disaster. *Proc. Natl. Acad. Sci.* 102, 14185–14190. doi:10.1073/pnas.0502274102

Kusakabe, M., Ohba, T., Issa, S. A., Yoshida, Y., Satake, H., Ohizumi, T., et al. (2008). Evolution of CO2 in Lakes Monoun and Nyos, Cameroon, before and during Controlled Degassing. *Geochem. J.* 42, 93–118. doi:10.2343/geochemj.42.93

Kuwahara, T., Terada, A., Ohba, T., Yukutake, Y., Kanda, W., and Ogawa, Y. (2017). *Geosci. Union and Ame. Geophys. Union Joint Meet 2017 Abstr: SVC48-02*.A Hydrothermal System of Kusatsu-Shirane Volcano Inferred from Cl Concentrations and Stable Isotope Ratios of Yugama Crater lake Water, Japan

Le Guern, F., and Sigvaldason, G. E. (1989). The Lake Nyos Event and Natural CO_2 Degassing, I. *J. Volcanol. Geotherm. Res.* 39, 95–275.

Le Guern, F., and Sigvaldason, G. E. (1990). The Lake Nyos Event and Natural CO_2 Degassing, II. *J. Volcanol. Geotherm. Res.* 42, 307–404.

Mamyrin, B. A., and Tolstikhin, I. N. (1984). *Helium Isotopes in Nature*. Amsterdam: Elsevier.

Matsuda, J., MatsumotoSumino, T., Sumino, H., Nagao, K., Yamamoto, J., Miura, Y., et al. (2002). The 3He/4He Ratio of the New Internal He Standard of Japan (HESJ). *Geochem. J.* 36, 191–195. doi:10.2343/geochemj.36.191

Mazot, A., and Taran, Y. (2009). CO_2 Flux from the Volcanic lake of El Chichón (Mexico). *Geofísica Int.* 48 (1), 73–83. doi:10.22201/igeof.00167169p.2009.48.1.100

Melián, G., Somoza, L., Padrón, E., Pérez, N. M., Hernández, P. A., Sumino, H., et al. (2016). Surface CO2 Emission and Rising Bubble Plumes from Degassing of Crater Lakes in São Miguel Island, Azores. *Geol. Soc. Lond. Spec. Publications* 437, 233–252. doi:10.1144/SP437.14

Michard, G. (1990). Behaviour of Major Elements and Some Trace Elements (Li, Rb, Cs, Sr, Fe, Mn, W, F) in Deep Hot Waters from Granitic Areas. *Chem. Geology.* 89, 117–134. doi:10.1016/0009-2541(90)90062-c

Minami, E., Yamagata, N., Shima, M., and Saijô, Y. (1952). Crater Lake "Yugama" of Volcano Kusatsu-Shirane. I. *Jpn. J. Limnol.* 16, 1–5. (in Japanese). doi:10.3739/rikusui.16.1

Ohba, T., Hirabayashi, J.-i., and Nogami, K. (2008). Temporal Changes in the Chemistry of lake Water within Yugama Crater, Kusatsu-Shirane Volcano, Japan: Implications for the Evolution of the Magmatic Hydrothermal System. *J. Volcanology Geothermal Res.* 178, 131–144. doi:10.1016/j.jvolgeores.2008.06.015

Ohba, T., Hirabayashi, J.-i., and Nogami, K. (1994). Water, Heat and Chloride Budgets of the Crater lake, Yugama at Kusatsu-Shirane Volcano, Japan. *Geochem. J.* 28, 217–231. doi:10.2343/geochemj.28.217

Ohba, T., Hirabayashi, J., and Nogami, K. (2000). D/H and 18 O/16 O Ratios of Water in the Crater lake at Kusatsu-Shirane Volcano, Japan. *J. Volcanology Geothermal Res.* 97, 329–346. doi:10.1016/s0377-0273(99)00169-9

Ohba, T., Yaguchi, M., Nishino, K., Numanami, N., Tsunogai, U., Ito, M., et al. (2019). Time Variation in the Chemical and Isotopic Composition of Fumarolic Gasses at Kusatsu-Shirane Volcano, Japan. *Front. Earth Sci.* 7, 249. doi:10.3389/feart.2019.00249

Ossaka, J., Ossaka, T., Oi, T., Kikawada, K., Yamano, M., Hukuhara, H., et al. (1997). Volcanic Activity of Kusatsu-Shirane Volcano, Gunma, and Secular Change in Water Quality of Crater lake, Yugama. *Chikyukagaku* 31, 119–128. (in Japanese).

Ossaka, J., Ozawa, T., Nomara, T., Ossaka, T., Hirabayashi, J., Takaesu, A., et al. (1980). Variation of Chemical Compositions in Volcanic Gases and Water at Kusatsu-Shirane Volcano and its Activity in 1976. *Bull. Volcanol.* 43 (1), 207–216. doi:10.1007/bf02597622

Padrón, E., Hernández, P. A., Toulkeridis, T., Pérez, N. M., Marrero, R., Melián, G., et al. (2008). Diffuse CO2 Emission Rate from Pululahua and the lake-filled Cuicocha Calderas, Ecuador. *J. Volcanology Geothermal Res.* 176, 163–169. doi:10.1016/j.jvolgeores.2007.11.023

Padrón, E., Pérez, N. M., Hernández, P. A., Sumino, H., Melián, G. V., Barrancos, J., et al. (2013). Diffusive Helium Emissions as a Precursory Sign of Volcanic Unrest. *Geology* 41, 539–542. doi:10.1130/g34027.1

Parkinson, K. J. (1981). An Improved Method for Measuring Soil Respiration in the Field. *J. Appl. Ecol.* 18, 221–228. doi:10.2307/2402491

Pérez, N. M., Hernández, P. A., Padilla, G., Nolasco, D., Barrancos, J., Melían, G., et al. (2011). Global CO2 Emission from Volcanic Lakes. *Geology* 39 (3), 235–238. doi:10.1130/G3158610.1130/g31586.1

Rouwet, D. (2021). "Volcanic lake Dynamics and Related Hazards," in *Book Chapter in: Volcanic Hazards, Risks and Disasters*. Editor P. Papale (Elsevier). doi:10.1016/b978-0-12-818082-2.00011-1

Sano, Y., Hirabayashi, J.-I., Oba, T., and Gamo, T. (1994). Carbon and Helium Isotopic Ratios at Kusatsu-Shirane Volcano, Japan. *Appl. Geochem.* 9 (4), 371–377. doi:10.1016/0883-2927(94)90059-0

Sigurdsson, H., Devine, J. D., Tchua, F. M., Presser, F. M., Pringle, M. K. W., and Evans, W. C. (1987). Origin of the Lethal Gas Burst from Lake Monoun, Cameroun. *J. Volcanology Geothermal Res.* 31, 1–16. doi:10.1016/0377-0273(87)90002-3

Sigvaldason, G. E. (1989). International Conference on Lake Nyos Disaster, Yaoundé, Cameroon 16-20 March, 1987: Conclusions and

Recommendations. *J. Volcanology Geothermal Res.* 39, 97–107. doi:10.1016/0377-0273(89)90050-4

Simmons, S. F., Keywood, M., Scott, B. J., and Keam, R. F. (1993). Irreversible Change of the Rotomahana-Waimangu Hydrothermal System (New Zealand) as a Consequence of a Volcanic Eruption. *Geol* 21, 643–646. doi:10.1130/0091-7613(1993)021<0643:icotrw>2.3.co;2

Sinclair, A. J. (1974). Selection of Threshold Values in Geochemical Data Using Probability Graphs. *J. Geochemical Exploration* 3, 129–149. doi:10.1016/0375-6742(74)90030-2

Sugimura, A. (1960). Zonal Arrangement of Some Geophysical and Petrological Features in Japan and its Environs. *J. Fac. Sci. Univ. Tokyo Sec.* 12, 133–153.

Sugisaki, R., and Taki, K. (1987). Simplified Analyses of He, Ne, and Ar Dissolved in Natural Waters. *Geochem. J.* 21, 23–27. doi:10.2343/geochemj.21.23

Sumino, H., Nagao, K., and Notsu, K. (2001). Highly Sensitive and Precise Measurement of Helium Isotopes Using a Mass Spectrometer with Double Collector System. *J. Mass. Spectrom. Soc. Jpn.* 49, 61–68. doi:10.5702/massspec.49.61

Takano, B., Koshida, M., Fujiwara, Y., Sugimori, K., and Takayanagi, S. (1997). Influence of Sulfur-Oxidizing Bacteria on the Budget of Sulfate in Yugama Crater lake, Kusatsu-Shirane Volcano, Japan. *Biogeochemistry* 38, 227–253. doi:10.1023/a:1005805100834

Takano, B., Saitoh, H., and Takano, E. (1994). Geochemical Implications of Subaqueous Molten Sulfur at Yugama Crater lake, Kusatsu-Shirane Volcano, Japan. *Geochem. J.* 28, 199–216. doi:10.2343/geochemj.28.199

Terada, A., and Hashimoto, T. (2017). Variety and Sustainability of Volcanic Lakes: Response to Subaqueous thermal Activity Predicted by a Numerical Model. *J. Geophys. Res. Solid Earth* 122, 6108–6130. doi:10.1002/2017JB014387

Terada, A., Morita, Y., Hashimoto, T., Mori, T., Ohba, T., Yaguchi, M., et al. (20182018). Water Sampling Using a Drone at Yugama Crater lake, Kusatsu-Shirane Volcano, Japan. *Earth Planets Space* 70, 64. doi:10.1186/s40623-018-0835-3

Varekamp, J. C., and Kreulen, R. (2000). The Stable Isotope Geochemistry of Volcanic Lakes, with Examples from Indonesia. *J. Volcanology Geothermal Res.* 97, 309–327. doi:10.1016/s0377-0273(99)00175-4

Varekamp, J. C. (2015). "The Chemical Composition and Evolution of Volcanic Lakes," in *Volcanic Lakes. Adv. Volcanol.* Editors D. Rouwet, B. Christenson, F. Tassi, and J. Vandemeulebrouck (Berlin, Heidelberg: Springer), 93–123. doi:10.1007/978-3-642-36833-2_4

Verhallen, P. T. H. M., Oomen, L. J. P., Elsen, A. J. J. M. v. d., Kruger, J., and Fortuin, J. M. H. (1984). The Diffusion Coefficients of Helium, Hydrogen, Oxygen and Nitrogen in Water Determined from the Permeability of a Stagnant Liquid Layer in the Quasi-S. *Chem. Eng. Sci.* 39, 1535–1541. doi:10.1016/0009-2509(84)80082-2

Conflict of Interest: The authors declare that the research was conducted in the absence of any commercial or financial relationships that could be construed as a potential conflict of interest.

Publisher's Note: All claims expressed in this article are solely those of the authors and do not necessarily represent those of their affiliated organizations, or those of the publisher, the editors, and the reviewers. Any product that may be evaluated in this article, or claim that may be made by its manufacturer, is not guaranteed or endorsed by the publisher.

frontiers in Earth Science

ORIGINAL RESEARCH
published: 03 January 2022
doi: 10.3389/feart.2021.716970

Rare Earth Elements Variations in a Hyperacid Crater Lake and Their Relations With Changes in Phreatic Activity, Physico-Chemical Parameters, and Chemical Composition: The Case of Poás Volcano (Costa Rica)

Sabrina Pappaterra[1], Claudio Inguaggiato[2,3], Dmitri Rouwet[3], Raúl Mora-Amador[4], Carlos Ramírez-Umaña[5], Gino González[3,4,6], Lorenzo Brusca[7], Loic Peiffer[2], Gilles Levresse[8] and Sergio Bellomo[7]*

[1]*Posgrado en Ciencias de La Tierra, Centro de Investigación Científica y de Educación Superior de Ensenada, Baja California (CICESE), Ensenada, Mexico,* [2]*Departamento de Geología, Centro de Investigación Científica y de Educación Superior de Ensenada, Baja California (CICESE), Ensenada, Mexico,* [3]*Istituto Nazionale di Geofisica e Vulcanologia, Sezione di Bologna, Bologna, Italy,* [4]*Volcanes Sin Fronteras, San José, Costa Rica,* [5]*Servicio Geológico Ambiental de Costa Rica (SeGeoAm), San José, Costa Rica,* [6]*Dipartimento di Scienze Della Terra e Geoambientali, Università Degli Studi di Bari Aldo Moro, Bari, Italy,* [7]*Istituto Nazionale di Geofisica e Vulcanologia, Sezione di Palermo, Palermo, Italy,* [8]*Centro de Geociencias, UNAM, Querétaro, Mexico*

OPEN ACCESS

Edited by:
Nico Fournier, GNS Science, New Zealand

Reviewed by:
Johan Varekamp, Wesleyan University, United States
Giovanni Vespasiano, University of Calabria, Italy

***Correspondence:**
Claudio Inguaggiato
inguaggiato@cicese.mx

Specialty section:
This article was submitted to Volcanology, a section of the journal Frontiers in Earth Science

Received: *29 May 2021*
Accepted: *08 November 2021*
Published: *03 January 2022*

Citation:
Pappaterra S, Inguaggiato C, Rouwet D, Mora-Amador R, Ramírez-Umaña C, González G, Brusca L, Peiffer L, Levresse G and Bellomo S (2022) Rare Earth Elements Variations in a Hyperacid Crater Lake and Their Relations With Changes in Phreatic Activity, Physico-Chemical Parameters, and Chemical Composition: The Case of Poás Volcano (Costa Rica). Front. Earth Sci. 9:716970. doi: 10.3389/feart.2021.716970

Decades of geochemical monitoring at active crater lakes worldwide have confirmed that variations in major elements and physico-chemical parameters are useful to detect changes in volcanic activity. However, it is still arduous to identify precursors of single phreatic eruptions. During the unrest phase of 2009–2016, at least 679 phreatic eruptions occurred at the hyperacid and hypersaline crater lake Laguna Caliente of Poás volcano (Costa Rica). In this study, we investigate the temporal variations of Rare Earth Elements (REE) dissolved in Laguna Caliente in order to 1) scrutinize if they can be used as a new geochemical tool to monitor changes of phreatic activity at hyperacid crater lakes and 2) identify the geochemical processes responsible for the variations of REE concentrations in the lake. The total concentration of REE varies from 950 to 2,773 μg kg^{-1}. $(La/Pr)_{N\text{-local rock}}$ ratios range from 0.93 to 1.35, and Light REE over Heavy REE $(LREE/HREE)_{N\text{-local rock}}$ ratios vary from 0.71 to 0.95. These same parameters vary in relation to significant changes in phreatic activity; in particular, the $(La/Pr)_{N\text{-local rock}}$ ratio increases as phreatic activity increases, while that of $(LREE/HREE)_{N\text{-local rock}}$ decreases when phreatic activity increases. REE concentrations and their ratios were compared with the variations of major elements and physico-chemical parameters of the lake. Calcium versus $(La/Pr)_{N\text{-local rock}}$ and versus $(LREE/HREE)_{N\text{-local rock}}$ ratios show different trends compared to the other major elements (Na, K, Mg, Al, Fe, SO_4, and Cl). Moreover, a higher loss of Ca (up to 2,835 ppm) in lake water was found with respect to the loss of Al, K, and Na. This loss of Ca is argued to be due to gypsum precipitation, a process corroborated by the mass balance calculation

simulating the precipitation of gypsum and the contemporaneous removal of REE from the lake water. The observed relations between REE, changes in phreatic activity, and the parameters commonly used for the monitoring of hyperacid volcanic lakes encourage investigating more on the temporal and cause-effect relationship between REE dynamics and changes in phreatic activity at crater lake-bearing volcanoes.

Keywords: Rare Earth Elements (REE), Poás volcano, phreatic eruptions, geochemical monitoring, hyperacid volcanic lakes

1 INTRODUCTION

Volcanic areas are often characterized by the presence of lakes that fill the summit crater area (Manville, 2015). The chemical composition of volcanic lakes mainly depends on 1) the fluid input from the underlying magmatic-hydrothermal system, 2) evaporation, meteoric precipitation, and infiltration, 3) dissolution of volcanic rocks, and 4) the precipitation of secondary minerals (Delmelle and Bernard, 1994; van Hinsberg et al., 2010; Varekamp, 2015). The combination of these factors leads to the genesis of fluids that span from dilute meteoric waters to hyperacid and hypersaline waters (Varekamp et al., 2000). Following Pasternack and Varekamp (1997), neutral-dilute volcanic waters are commonly associated with "no activity lakes," while hot hyperacid brines with high Total Dissolved Solids (TDS) are associated with "peak activity lakes".

The major hazards commonly associated with active crater lakes are 1) limnic gas bursts (Rouwet, 2021 and references therein) and 2) phreatic and phreatomagmatic eruptions (Barberi et al., 1992; Christenson, 2000; Christenson et al., 2010; de Moor et al., 2016; Rouwet et al., 2017; Stix and de Moor, 2018); the latter is also often responsible for the explosive ejection of the lake water to create 3) lahars on the volcano flanks (Kilgour et al., 2010; Manville, 2015). Stix and de Moor (2018) investigated the role of the magmatic contribution to phreatic eruptions, analyzing data from six different volcanic hydrothermal systems where phreatic activity is reported. They propose a model that includes two end-member types of phreatic eruptions named "phreato-vulcanian" and "phreato-surtseyan"; their variability is mainly related to the different depths and the different sealing characteristics of the hydrothermal system. The phreato-vulcanian type is more vigorous because of the features of the hydrothermal system, which is deeper and sealed and fed by magmatic gases that generate overpressure. The phreato-surtseyan type, on its turn, is characteristic of systems with open vents and a hydrothermal system close to the surface where the water is vaporized by the magmatic gases. In some conditions, a volcano can exhibit both types of phreatic eruptions, as in the case of Poás (Costa Rica) and Ruapehu (New Zealand) volcanoes (Stix and de Moor, 2018).

Since volcanic lakes represent the intersection of the magmatic-hydrothermal system of a volcano and the surface (Rowe et al., 1992b; Christenson and Tassi, 2015), they offer a "touchable object" and hence a unique opportunity to scrutinize the state of volcanic activity (Rouwet et al., 2017). For various decades, researchers have been looking for a useful tool to identify signals that precede phreatic eruptions at crater lakes; hence, the importance of volcanic lake monitoring is related to the possibility of recognizing short- and long-term signals, likely associated with volcanic hazards, to mitigate the risk (Rymer et al., 2009). The combination of various geophysical and geochemical methods, like microgravity, seismicity, electromagnetism, and gas monitoring, represents a useful approach for the study of sub-surface processes at active volcanoes (Brown et al., 1991; Rymer et al., 2009; Zlotnicki et al., 2009; de Moor et al., 2019). A common monitoring approach tracks the variations over the time of major elements and physico-chemical parameters of crater lake waters (Rowe et al., 1992b; Varekamp et al., 2000; Christenson, 2000; Ohba et al., 2008; Varekamp et al., 2009; Agusto and Varekamp, 2016; Rouwet et al., 2017, 2019). The results obtained investigating the geochemistry of various hyperacid volcanic lakes worldwide are consistent and show that mainly pH, temperature, and some anions and cations concentrations such as SO_4, Cl, and Mg, and their ratios (SO_4/Cl, and Mg/Cl) may be good indicators to monitor chemical changes of crater lake waters likely related to the degree of volcanic unrest (Giggenbach and Glover, 1975; Rowe et al., 1992b; Rouwet et al., 2019).

Since hyperacid volcanic fluids are more aggressive with respect to near-neutral and alkaline fluids during water-rock interaction, a higher amount of rock-derived elements, including Rare Earth Elements (lanthanides + yttrium; REE), is leached and mobilized (Michard, 1989; Lewis et al., 1997; Takano et al., 2004; Varekamp et al., 2009; van Hinsberg et al., 2010; Peiffer et al., 2011; Hikov, 2015; Inguaggiato et al., 2015; Varekamp, 2015; Inguaggiato et al., 2017; van Hinsberg et al., 2017; Woitischek et al., 2017; Inguaggiato et al., 2018; Inguaggiato et al., 2020a; Inguaggiato et al., 2020b). The geochemical and economic importance of REE prompted to study them in a wide variety of environments, among which the fluids associated with volcanic areas, and especially volcanic crater lakes (Kikawada et al., 2004; Takano et al., 2004; Varekamp, 2015; van Hinsberg et al., 2017; Inguaggiato et al., 2018; Inguaggiato et al., 2020a; Inguaggiato et al., 2020b; van Hinsberg et al., 2020). Consequently to the increasing knowledge of the geochemical behavior of REE, it is possible to develop several applications using REE as geochemical tracers of fluid-rock interaction in active volcanic systems.

Inguaggiato et al. (2018) investigated the geochemical processes that affect the pattern of REE at Laguna Caliente (2006–2009), the active hyperacid and hypersaline crater lake of Poás volcano in Costa Rica, the study object of this investigation. Mainly, water-rock interaction processes, congruent dissolution of the andesitic rocks and the precipitation of secondary minerals like gypsum, seem to

control the amount of REE dissolved in crater lake water (Inguaggiato et al., 2018). These processes induce changes in the REE concentrations and control the relative proportion among them over time.

Despite the increasing investigation and the improvement of modern and sophisticated monitoring techniques, it is still difficult to identify precursors for single phreatic eruptions. Moreover, sampling the crater lake of an active volcano is arduous and dangerous, especially during periods of increased activity (i.e., phreatic eruptions). In this study, we had the chance to collect numerous water samples at Poás's Laguna Caliente when hundreds of phreatic eruptions occurred and to experience the potential effectiveness of REE in hyperacid volcanic lakes as a new possible geochemical indicator of changes in phreatic activity. We investigated if the variations of REE in Laguna Caliente could be connected to the main changes of phreatic activity, here represented by the occurrence of 679 phreatic eruptions during the period 2009–2016, and if they could be connected with the temporal variations of the geochemical indicators previously used to monitor Laguna Caliente volcanic activity (Rouwet et al., 2017; Rouwet et al., 2019). Our investigation aims to 1) improve the knowledge on the processes that control the REE variations in hyperacid crater lakes over time and their relations with the changes in volcanic activity, 2) compare the REE variations with the more classic geochemical parameters used to monitor volcanic activity, and 3) prove the usefulness of REE as a possible geochemical tool sensitive to changes in volcanic activity. Laguna Caliente was sampled with an average sampling frequency of 40 days from June 2009 to February 2016. This period is included within the 2006–2016 phreatic eruption cycle but is before the phreatomagmatic activity in 2017 (Mora-Amador et al., 2019a). Here, we compare the variations of REE dissolved in the Laguna Caliente water with the 1) evolution of the volcanic activity of Poás, manifested by 679 phreatic eruptions, 2) variations of physico-chemical parameters, and 3) variations of major elements chemical composition and their ratios in lake water. A key focus will be to describe the REE behavior in the Poás hyperacid crater lake during the phreatic activity and test it as a potential volcanic monitoring tool, in addition to the already proven and well-known geochemical pre-eruption indicators in both Poás lake and other volcanic hydrothermal systems worldwide (i.e., physico-chemical parameters and major elements).

2 BACKGROUND INFORMATION

2.1 Geological Setting

Poás (10°11′26″N 84°13′56″W) is a stratovolcano in Costa Rica that belongs to the Central Volcanic Range (CVR; Ruíz et al., 2019). It is composed of various volcanic structures, such as the composite cones at its top, Von Frantzius, Botos, and the Main Crater, that represents the spot of the historical activity (Prosser and Carr, 1987; Mora-Amador et al., 2019a). The main hydrological features at Poás volcano include 1) a hyperacid crater lake, named Laguna Caliente, that fills the active Main Crater, 2) a freshwater lake hosted at Botos cone, called Laguna Botos, and 3) acid springs and streams at the north-western flank of the volcano, which are part of the Río Agrio drainage basin and that arguably represent the seepage out of Laguna Caliente (Rowe et al., 1995; Sanford et al., 1995).

Poás is one of the most active volcanoes of the Central American Volcanic Arc. Its activity is mostly characterized by phreatic and phreatomagmatic eruption cycles at the Main Crater during the last 200 years (Alvarado, 2009; Ruíz et al., 2010; Mora-Amador et al., 2019a; Rouwet et al., 2019; Vannucchi and Morgan, 2019). The maximum age of the deposits that compose Poás volcano is about 600 ka. The lavas have a geochemical composition resulting from a fractional crystallization that generated products ranging from basalts to dacites; andesites and basaltic andesites are the most common products (Ruíz et al., 2010, 2019).

The chemical composition of Laguna Caliente is typical of "gas-dominated" crater lakes, characterized by an extremely low (hyperacid) pH and very high TDS values, with SO_4, Cl, and F as the most dominant gas-derived anion solutes and Al and Fe as the most abundant cations (Rowe et al., 1992b, 1995; Martínez et al., 2000; Varekamp et al., 2000; Rouwet et al., 2014, 2017, 2019). Lake volume changed dynamically through time and these changes largely result from the input of meteoric precipitation and fluids at the lake bottom and the water loss caused by seepage and evaporation (Brown et al., 1989; Rowe et al., 1992a; Rouwet et al., 2017). Laguna Caliente has dried out various times during the last decades (1989–1994, 2017), inducing subaerial degassing of the fumaroles located at the bottom of the crater (Rowe et al., 1992a; Martínez et al., 2000; Rymer et al., 2009) and peculiar sulfur volcanism (Oppenheimer, 1992; Mora-Amador et al., 2019b).

2.2 Historical Activity at Poás Volcano

At the present day, Poás represents one of the most active volcanoes on Earth. Due to the dense vegetation, very few outcrops exist to reveal the deposits of the eruptions that occurred prior to the 19th century. A recent report about the historical eruptions at Poás volcano is available (Mora-Amador et al., 2019a). von Frantzius (1861) reported intense volcanic activity at Poás volcano in 1828 and in February 1834. Recent studies of the deposits enabled reconstructing the phreatic nature of the 1834 event, which involved blocks and bombs thrown out and pyroclastic flows (Mora-Amador et al., 2019a). The subsequent eruption was reported almost 80 years after, in 1910. It was a phreatomagmatic eruption characterized by fine ashfall. Phreatic activity is reported for the period between 1953 and 1955. In May 1953, a phreatomagmatic eruption, with some strombolian phases, took place, causing the expulsion of the crater lake and the extrusion of a lava dome characterized by fumarolic activity. The eruptive period extended until 1955 (Mora-Amador et al., 2019a) and produced an important change in morphology of the crater area (Brantley et al., 1987; Brown et al., 1989; Vaselli et al., 2003; Hilton et al., 2010; Fischer et al., 2015; Rouwet et al., 2019).

An earthquake swarm in 1986 signaled the start of an unrest phase. A powerful phreatic eruption in 1988 caused a lake level

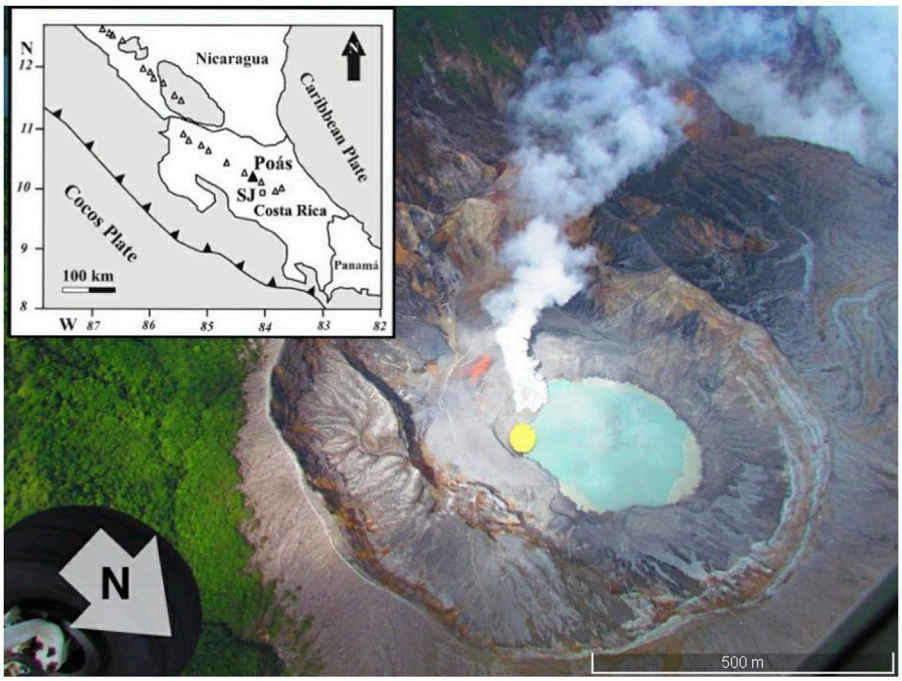

FIGURE 1 | Map of the Cordillera Volcánica Central and location of Poás volcano, Costa Rica (black triangle) (Rouwet et al., 2017). Aerial photograph of Laguna Caliente (Poás volcano) and location of the sampling point "LD" at the dome (yellow dot). The photo was taken by Raúl Mora-Amador on 17/04/2012.

drop and full lake disappearance in 1989 (Rowe et al., 1992a; Oppenheimer, 1993). The phreatic activity continued until 1994, after which a decade of quiescence took over (Mora-Amador et al., 2019a). Since 1998, various changes have been observed in fumarolic activity: new fumarolic vents were formed and fumarolic activity migrated inside the Main Crater; changes in lake level and color were observed (Vaselli et al., 2003, 2019; Rouwet et al., 2017; Mora-Amador et al., 2019a). In December 2005, floating sulfur spherules with tails were present at the lake, an early-warning indicator of oncoming phreatic eruptions (Takano et al., 1994; Mora Amador et al., 2019b).

After more than a decade of quiescence, on March 24, 2006, the first phreatic eruption marked the beginning of 10 years of nearly continuous volcanic activity. During the period 2006–2016 (including the period of observation of the current study), more than 700 phreatic eruptions breached Laguna Caliente, peaking in frequency between 2010 and 2011 (de Moor et al., 2016; Rouwet et al., 2017; Rouwet et al., 2019). Prior to 2009, the activity was less intense; however, the first major phreatic event of the period occurred in September 2009. The frequency of eruptions had declined since 2014 to wane towards 2016 when an apparent stage of quiescence took over. Nevertheless, Poás culminated into explosive phreatomagmatic activity on April 14, 2017, following a few days of intense geysering from new vents southwest outside Laguna Caliente (Mora-Amador et al., 2019a). The April 2017 phreatomagmatic eruption destroyed the 1955 lava dome to enlarge the crater lake basin that filled up after a period of sulfur volcanism at the dried-out lake bottom. On the day of writing (April 2021), Laguna Caliente is in a stage of medium activity (46°C); a new fumarolic field called "planicie de azufre" (sulfur plain) is located at the eastern shore of the lake. However, eruptive activity has not been reported since 2017.

3 SAMPLING AND ANALYTICAL METHODS

3.1 Sampling Methods, Data Provenance, and Their Analysis

Fifty-one aliquots of water were sampled at Laguna Caliente during the period between June 5, 2009, and February 23, 2016 (**Figure 1**). The sampling procedure and physico-chemical parameters are from Rouwet et al. (2017, 2019; **Table 1**). All the samples were filtered *in situ* using 0.45 μm Millipore filters and stored in HDPE bottles. Because of the extremely low pH values (~0), the samples were not acidified.

A comprehensive database of the 679 phreatic eruptions, which took place from June 2008 to June 2016, has been compiled based on data from scientific publications and public sources (Universidad de Costa Rica https://rsn.ucr.ac.cr; Observatorio Vulcanológico y Sismológico de Costa Rica, OVSICORI, 2021; Rouwet et al., 2017, Rouwet et al., 2019).

Phreatic eruptions are subdivided into three categories based on the column height: A) 2–50 m, B) 51–250 m, and C) >250 m (Mora-Amador, 2010; Rouwet et al., 2019). Moreover, a fourth category is here discriminated for all the eruptions without information about the column height ("N.D.": Not Defined).

3.2 Analytical and Laboratory Procedures

Major elements and physico-chemical parameters data are from Rouwet et al. (2017, 2019). REE analyses were carried out at

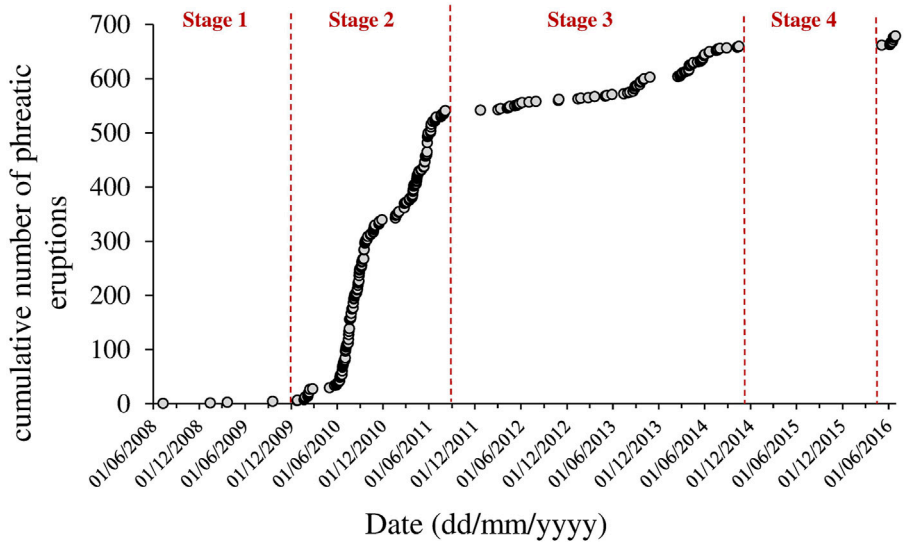

FIGURE 2 | Cumulative number of phreatic eruptions vs. time. Four stages of activity are identified: 1) low frequency of phreatic eruptions, 2) high frequency of phreatic eruptions, 3) decline of phreatic eruptions, and 4) a period of quiescence.

INGV-Palermo using a Q-ICP-MS Agilent 7500 calibrated with a REE multi-element standard solution with 11 calibration points. The sample waters were diluted up to reach salinity around 0.6 g L^{-1}.

The sensitivity variation was monitored by three internal standards (^{103}Rh, ^{115}In, and ^{185}Re) to reach a final concentration of 8 μg L^{-1}.

Memory interferences between consecutive samples were reduced with a 60 s rinse using a 0.5% HCl and 2% HNO_3 solution plus a 60 s rinse using 2% HNO_3 solution. The analyses of three reference materials, SPS-SW1, SPS-SW2, and SLRS-4, were carried out to evaluate data accuracy. Each analysis is obtained by calculating the mean value of five replicates. The accuracy was usually better than 5%, and the average relative standard deviation (RSD) was calculated on five replicates and was mostly better than 7%.

4 RESULTS

4.1. Stages of Phreatic Eruptive Activity

Almost 700 phreatic eruptions were observed and reported at Laguna Caliente between June 2008 and June 2016; however, it is likely that the real number of phreatic eruptions that occurred during this period is even higher. Our database counts 679 phreatic events (**Figure 2**; **Supplementary Table 1**). Approximately about ~62% of the total eruptions are "A" type eruptions, ~ 11% are "B" type eruptions, and only ~ 2% are "C" type eruptions, while the remaining ~ 25% are classified as "not determined" (ND).

Phreatic eruption intensity varies significantly during the time of observation. For the period between June 2008 and June 2016, the phreatic eruption cycle was subdivided into four stages characterized by 1) low phreatic activity, when only three "A" and one "C" type single eruptions occurred (June 2008–December 2009), 2) high frequency of phreatic eruptions (January 2010–August 2011, 535 phreatic eruptions), 3) declining number of phreatic events (September 2011–October 2014), and 4) a period of quiescence (November 2014–May 2016) that finished with the occurrence of 18 phreatic eruptions between May and June 2016. After a quiescent period following June 2016, Poás culminated in phreatomagmatic activity in April 2017 (the eruption is not included in the database of this investigation). These four distinct stages are better marked in **Figure 2**, where the cumulative number of phreatic eruptions is reported versus time. Almost all the multiple-eruptions days, which include at least a B or C eruption type, are between September 2009 and May 2012. After that, multiple eruptions B and C types were absent until mid-2014, when two multiple events, including B-type eruptions, took place and mid-2016, when a multiple event, including a B-type eruption, occurred.

4.2 Temporal Variations of REE

The REE were subdivided into two sub-groups, Light Rare Earth Elements (LREE; from La to Gd) and Heavy Rare Earth Elements (HREE; from Tb to Lu and Y). The concentrations of REE were normalized to the composition of the average local rock to easily compare the REE distribution with the andesitic rocks interacting with the fluids (Carr et al., 2013; **Supplementary Figures 1A,B**) and were subdivided into two groups: 1) samples belonging to stages 2 and 3 characterized by a more intense phreatic activity; 2) samples belonging to stages 1 and 4, characteristic of low phreatic activity. During the intense activity (stages 2 and 3), the patterns of REE are often characterized by different degrees of LREE depletion with respect to the HREE (**Supplementary Figure 1A**).

On the contrary, during low phreatic activity (stages 1 and 4), the patterns of REE do not show a pronounced LREE depletion and almost all the samples have similar trends that only differ for their absolute REE concentrations.

Total REE concentrations (∑REE) dissolved in the lake water change over time from 950 to 2,773 μg kg^{-1} (**Table 2**). ∑REE starts to increase prior to the high-frequency eruptive period starting in December 2009 and progressively increases throughout this high-frequency stage in 2010 and 2011 (**Figure 3**). Towards the end of 2011, the ∑REE started to decrease to reach the lowest values in 2016.

Previous studies have already identified that in the hyperacid crater lakes of Poás (Costa Rica) and Kawah Ijen (Indonesia), gypsum precipitation can be responsible for the fractionation of REE dissolved in waters (Inguaggiato et al., 2018; Inguaggiato et al., 2020a; van Hinsberg et al., 2020). The distribution coefficients of REE, calculated between the REE in gypsum precipitated in the laboratory from the lake water and the REE dissolved in the lake water of Poás and Kawah Ijen crater lakes, demonstrate that LREE are preferentially scavenged by gypsum with respect to the HREE. Cerium, Pr, and Nd show higher distribution coefficients not only with respect to the HREE but also with respect to the other LREE, including the neighboring elements La and Sm. This result shows that REE incorporation in gypsum decreases progressively from Nd to Lu, with La distribution coefficients that are mostly lower with respect to Ce, Pr, and Nd. Praseodymium often has the highest distribution coefficient and hence suggests preferential incorporation in the gypsum crystals during the precipitation process (Inguaggiato et al., 2018). Here, these previous findings $(La/Pr)_{N\text{-local rock}}$ and the $(LREE/HREE)_{N\text{-local rock}}$ ratios were considered to investigate the possible causes of temporal variations of REE in Poás crater lake water. Inguaggiato et al. (2018) suggested that the variations between LREE and HREE in the lake water can be affected by gypsum precipitation; we focused on the possibility that this process could also induce the variation of REE concentrations over time.

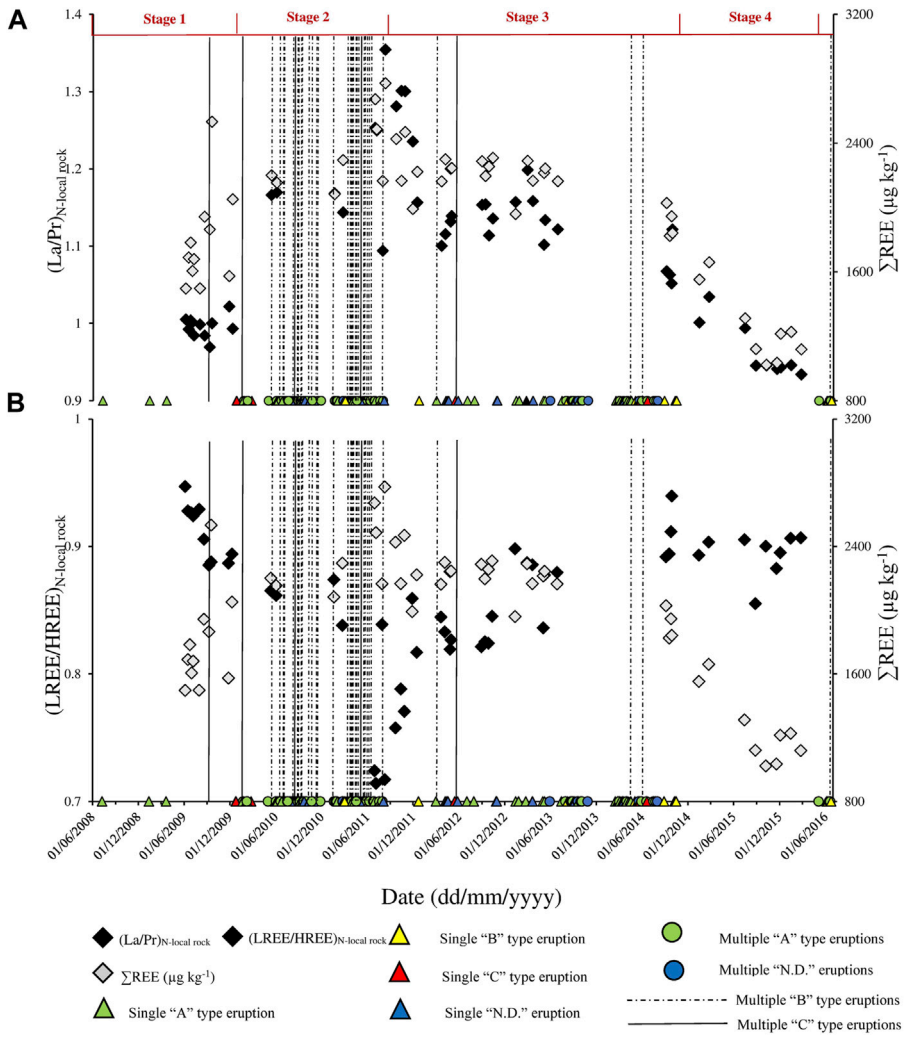

FIGURE 3 | (A) $(La/Pr)_{N\text{-local rock}}$ and ∑ REE vs. time. **(B)** $(LREE/HREE)_{N\text{-local rock}}$ and ∑ REE vs. time.

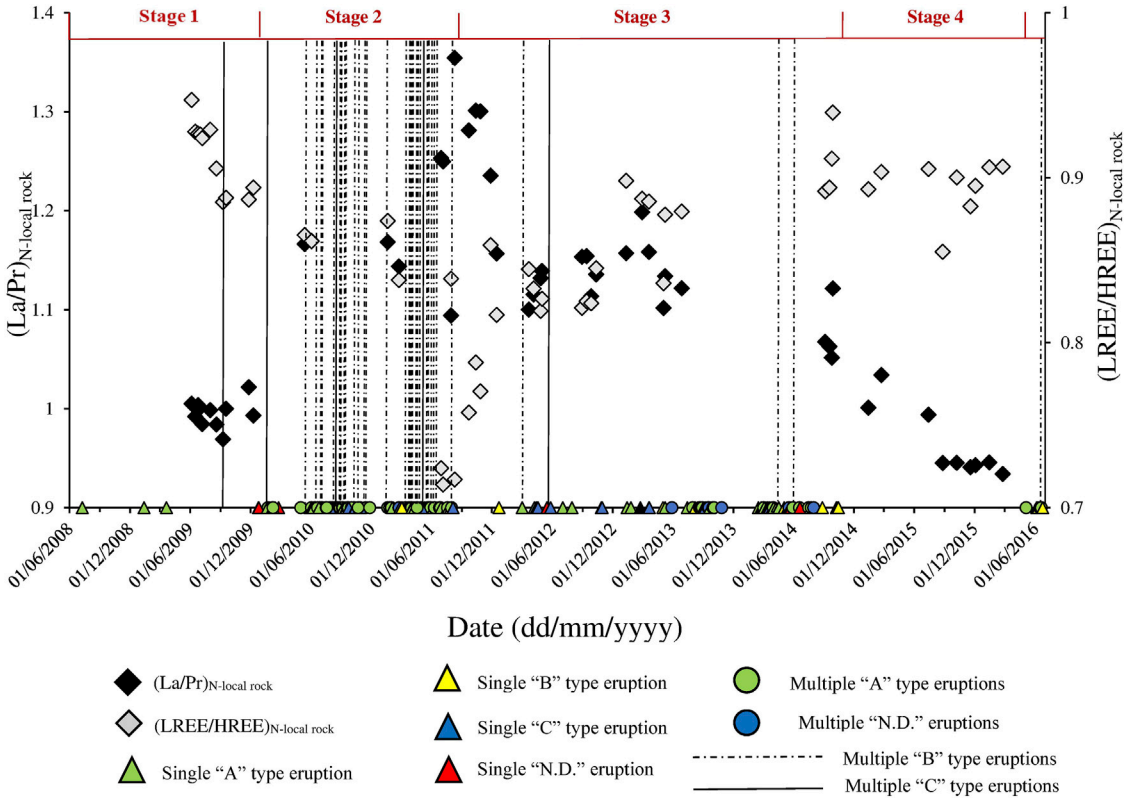

FIGURE 4 | $(La/Pr)_{N\text{-local rock}}$ and $(LREE/HREE)_{N\text{-local rock}}$ vs. time.

During the period of observation, $(La/Pr)_{N\text{-local rock}}$ and $(LREE/HREE)_{N\text{-local rock}}$ showed significant variations from 0.93 to 1.35 and from 0.71 to 0.95, respectively (**Figure 4**). The $(La/Pr)_{N\text{-local rock}}$ ratio was lower in mid-2009, when only a few eruptions have occurred (stage 1), and started to increase in early 2010 when eruptive activity was more intense and of higher frequency, to peak in September 2011 (stage 2). Afterward (early stage 3), $(La/Pr)_{N\text{-local rock}}$ decreased to remain stable between late 2011 and mid-2013 when the number of phreatic eruptions was considerably lower than that in the previous years. After the data gap between mid-2013 and late 2014, the $(La/Pr)_{N\text{-local rock}}$ ratio progressively decreased, starting from mid-2013 ratio values until the end of the time series (2016, stage 4), reaching similarly low values as those during stage 1 (2008–2009).

The $(LREE/HREE)_{N\text{-local rock}}$ ratio shows a trend over time that is nearly opposite to the $(La/Pr)_{N\text{-local rock}}$ trend (**Figure 4**). The decreasing trend in stage 1 (2008–mid-2009) accelerates during the period of high-frequency phreatic activity (stage 2, 2010–2011). From late 2011 until 2013, the $(LREE/HREE)_{N\text{-local rock}}$ ratio progressively increased, concurrently to the decrease in the frequency of phreatic eruptions. The ratio does not vary significantly from 2014 to 2016, with values comparable to the ones of 2009. Moreover, looking at mid-2009, we observed that the $(LREE/HREE)_{N\text{-local rock}}$ ratio started to decrease before the occurrence of the first multiple phreatic eruptions (stage 1, September 2009). The variations of $(La/Pr)_{N\text{-local rock}}$ and $(LREE/HREE)_{N\text{-local rock}}$ ratios are related to the major changes of volcanic activity, reaching the higher and the lower values, respectively, when the activity reaches a climax (stage 2, September 2011).

4.3 REE Versus Physico-Chemical Parameters and Chemical Composition

The $(La/Pr)_{N\text{-local rock}}$, $(LREE/HREE)_{N\text{-local rock}}$ ratios and eruptions data were compared to major element concentrations (Na, K, Mg, Ca, Al, Fe, SO_4, Cl), major element ratios (SO_4/Cl, Mg/Cl), physico-chemical parameters of the lake (pH, T), TDS values (**Table 1**), and the REE total amount (ΣREE; **Table 2**; **Figures 3, 5–9**, **Supplementary Figures 2, 3**).

The graph $(La/Pr)_{N\text{-local rock}}$ and temperature (T) versus time (**Figure 5A**) shows that the temperature of the lake water has a similar, though less marked trend, than the $(La/Pr)_{N\text{-local rock}}$ pattern. Unfortunately, the temperature data are not available for all the water samples. Instead, $(La/Pr)_{N\text{-local rock}}$ and pH versus time (**Figure 6A**) exhibit opposite trends, with pH decreasing when the volcanic activity increases. TDS and $(La/Pr)_{N\text{-local rock}}$ versus time (**Figure 7A**) and ΣREE and $(La/Pr)_{N\text{-local rock}}$ versus time (**Figure 3A**) show similar patterns from stages 1 to 4, with TDS, $(La/Pr)_{N\text{-local rock}}$, and ΣREE increasing with increasing phreatic activity. SO_4 concentrations vary identically to the $(La/Pr)_{N\text{-local rock}}$ pattern (**Figure 8A**). On

TABLE 1 | Major elements concentrations (mg L^{-1}), physico-chemical parameters, TDS (g L^{-1}) and major elements ratios (Rouwet et al., 2017, 2019).

Sample number	Sample ID	Date	T (°C)	pH	Na	K	Ca	Mg	Al	Fe	Cl	SO_4	TDS	SO_4/Cl	Mg/Cl
1	22c	05/06/2009	53.6	−0.07	365	189	1,168	336	990	790	15,400	44,200	63	2.87	0.02
2	23c	16/06/2009	53.2	−0.09	350	154	1,222	340	1,260	630	15,700	46,700	66	2.97	0.02
3	24c	24/06/2009	52.5	−0.10	300	130	1,056	303	1,270	660	15,900	47,200	67	2.97	0.02
4	25c	01/07/2009	55.4	−0.11	314	134	983	316	1,340	700	16,300	48,500	69	2.98	0.02
5	26c	07/07/2009	52.4	−0.09	322	135	1,145	315	1,180	620	15,400	46,600	66	3.03	0.02
6	29c	31/07/2009	52.1	−0.15	321	140	1,134	322	1,270	650	17,000	52,800	74	3.11	0.02
7	30c	19/08/2009	57.0	−0.17	331	144	1,160	327	1,310	680	17,700	56,000	78	3.16	0.02
8	31c	08/09/2009	53.0	−0.15	332	140	1,191	337	1,260	670	17,000	54,100	75	3.18	0.02
9	32c	17/09/2009	57.0	−0.23	372	167	1,205	365	1,470	760	20,700	63,500	89	3.07	0.02
10	33c	25/11/2009	49.2	−0.24	382	172	1,124	373	1,840	1000	20,700	67,100	93	3.24	0.02
11	34c	09/12/2009	48.7	−0.22	397	164	865	399	1,700	950	19,500	63,800	88	3.27	0.02
12	36c	13/05/2010	53.0	−0.28	430	219	715	391	1,730	1,023	22,100	70,900	98	3.21	0.02
13	37c	03/06/2010	48.0	−0.27	454	233	743	415	1,770	1,033	21,600	70,700	97	3.27	0.02
14	38c	19/01/2011	—	−0.39	479	252	834	298	1,649	890	18,700	68,000	91	3.64	0.02
15	39c	22/02/2011	—	−0.40	487	286	687	269	1,428	764	19,000	70,200	93	3.69	0.01
16	41c	30/06/2011	—	−0.52	617	304	650	445	1,806	957	24,300	92,800	122	3.82	0.02
17	42c	06/07/2011	—	−0.52	746	322	569	458	2,286	1,302	24,500	92,900	123	3.79	0.02
18	43c	30/07/2011	—	−0.27	923	192	722	262	1,376	2,079	13,400	56,100	75	4.19	0.02
19	44c	10/08/2011	—	−0.55	642	379	543	435	2,138	1,234	29,900	122,300	158	4.09	0.01
20	45c	22/09/2011	61	−0.55	697	355	595	391	2,643	1,483	28,600	118,000	153	4.13	0.01
21	46c	13/10/2011	53	−0.49	566	307	687	347	2,074	1,103	26,400	106,900	138	4.05	0.01
22	47c	27/10/2011	60	−0.51	597	349	746	419	2,233	1,204	28,800	113,500	148	3.94	0.01
23	48c	27/12/2011	53	−0.34	426	277	920	276	1,704	900	18,800	79,300	103	4.22	0.01
24	49c	15/02/2012	56	−0.36	460	283	817	305	1,679	858	18,700	84,400	108	4.51	0.02
25	50c	21/03/2012	54	−0.35	524	277	706	241	1,680	857	18,700	81,500	104	4.36	0.01
26	51c	05/04/2012	49	−0.40	423	330	748	280	1,717	881	19,800	82,300	106	4.16	0.01
27	52c	26/04/2012	—	−0.36	340	345	884	304	1,920	840	18,800	80,300	104	4.27	0.02
28	53c	30/04/2012	—	−0.37	317	229	781	295	1,900	850	19,300	82,500	106	4.27	0.02
29	54c	29/08/2012	—	−0.37	323	331	765	281	1,840	840	19,000	84,500	108	4.45	0.01
30	55c	12/09/2012	—	−0.37	294	211	779	269	1,710	780	18,400	83,600	106	4.54	0.01
31	56c	26/09/2012	—	−0.37	316	287	726	266	1,760	800	17,900	81,700	104	4.56	0.01
32	57c	11/10/2012	—	−0.36	337	304	760	250	1,700	790	18,400	83,600	106	4.54	0.01
33	58c	10/01/2013	—	−0.24	265	181	785	236	1,450	690	14,300	64,400	82	4.50	0.02
34	59c	27/02/2013	—	−0.27	304	206	888	285	1,500	730	15,000	66,300	85	4.42	0.02
35	60c	20/03/2013	—	−0.27	291	198	854	277	1,520	740	16,600	67,800	88	4.08	0.02
36	61c	03/05/2013	46.1	−0.23	348	184	843	289	1,500	790	15,000	63,800	83	4.25	0.02
37	62c	08/05/2013	44.6	−0.29	318	232	810	286	1,560	780	16,400	70,600	91	4.30	0.02
38	63c	27/06/2013	47.4	−0.28	296	200	818	273	1,370	740	16,900	69,000	90	4.08	0.02
39	64c	04/09/2014	45.1	−0.26	234	149	857	217	1,240	710	25,500	70,500	99	2.76	0.01
40	65c	17/09/2014	47.7	−0.23	240	151	864	217	1,150	640	14,600	86,100	104	5.90	0.01
41	66c	24/09/2014	48.3	−0.22	228	147	966	220	1,130	630	13,700	64,900	82	4.74	0.02
42	67c	27/11/2014	34.6	−0.16	236	114	903	198	1,040	560	12,000	62,600	78	5.22	0.02
43	68c	13/04/2015	—	−0.03	216	89	788	178	890	500	9,200	44,300	56	4.82	0.02
44	69c	21/05/2015	34.6	−0.02	215	87	939	179	900	490	9,400	43,400	56	4.62	0.02
45	70c	14/07/2015	39.5	0.15	226	61	908	174	720	390	6,300	30,000	39	4.76	0.03
46	71c	26/08/2015	—	0.20	214	96	895	133	690	370	5,700	26,800	35	4.70	0.02
47	72c	07/10/2015	—	0.23	140	51	912	120	590	310	5,300	24,300	32	4.58	0.02
48	73c	18/11/2015	—	0.22	143	59	866	117	600	320	5,800	2,4900	33	4.29	0.02
49	74c	03/12/2015	—	0.18	163	57	907	125	650	490	9,900	28,200	40	2.85	0.01
50	75c	14/01/2016	—	0.16	172	54	979	132	630	350	6,400	28,600	37	4.47	0.02
51	76c	23/02/2016	—	0.26	118	35	495	102	530	280	5,100	22,400	29	4.39	0.02

the contrary, Ca concentrations decrease with increasing $(La/Pr)_{N\text{-local rock}}$ and hence increasing phreatic activity (**Figure 9A**) and vice versa. The SO_4/Cl ratio (**Supplementary Figure 2A**) increases from 2008 to 2011, similar to the $(La/Pr)_{N\text{-local rock}}$ ratio. However, SO_4/Cl did not decrease back in 2016 with values similar to 2009, as recognized for all other described parameters. The Mg/Cl ratio (**Supplementary Figure 3A**) varies basically in the opposite way compared to $(La/Pr)_{N\text{-local rock}}$, decreasing during stage 2 of high-frequency activity.

As the $(LREE/HREE)_{N\text{-local rock}}$ ratio essentially behaves in the opposite way with respect to the $(La/Pr)_{N\text{-local rock}}$ ratio (i.e., decreasing when the phreatic activity increases and increasing when the phreatic activity decreases), this implies that the trends obtained comparing $(LREE/HREE)_{N\text{-local rock}}$ ratios with major element concentrations and their ratios, physico-chemical parameters of the waters, TDS and ΣREE values (**Figures 3B**, **5B–9B**, **Supplementary Figures 2B, 3B**) are inverse to the ones obtained for $(La/Pr)_{N\text{-local rock}}$ ratio. The

TABLE 2 | Rare Earth Elements concentrations (μg kg^{-1}). La/Pr and LREE/HREE ratios are normalized to the average volcanic local rock (Carr et al., 2013).

Sample number	Sample ID	Date	La	Ce	Pr	Nd	Sm	Eu	Gd	Tb	Dy	Y	Ho	Er	Tm	Yb	Lu	∑REE	La/Pr	LREE/HREE
1	22c	05/06/2009	242	493	61	248	55	16	55	8	43	215	8	24	3	21	3	1,496	1.01	0.95
2	23c	16/06/2009	272	554	69	279	62	19	61	9	49	246	10	28	4	24	3	1,690	0.99	0.93
3	24c	24/06/2009	287	585	72	294	66	20	66	9	53	258	10	29	4	25	4	1,783	1.00	0.93
4	25c	01/07/2009	259	528	65	265	59	18	58	8	47	233	9	26	4	23	3	1,606	1.00	0.93
5	26c	07/07/2009	266	550	68	279	62	19	62	9	50	246	10	28	4	24	4	1,679	0.98	0.92
6	29c	31/07/2009	241	490	61	249	56	17	57	8	45	212	9	25	3	22	3	1,497	1.00	0.93
7	30c	19/08/2009	309	635	79	322	72	22	73	10	60	278	11	33	5	29	4	1,943	0.98	0.91
8	31c	08/09/2009	290	604	76	311	71	21	71	10	59	271	11	33	4	28	4	1,864	0.97	0.89
9	32c	17/09/2009	403	825	102	415	95	28	98	14	80	366	15	44	6	39	6	2,534	1.00	0.89
10	33c	25/11/2009	257	515	64	255	58	18	59	9	48	224	10	28	4	23	4	1,574	1.02	0.89
11	34c	09/12/2009	327	675	83	337	75	23	78	11	62	290	12	36	5	31	5	2,051	0.99	0.89
12	36c	13/05/2010	383	704	83	332	74	23	75	11	64	358	13	37	5	32	5	2,200	1.17	0.87
13	37c	03/06/2010	375	684	81	332	72	23	74	11	63	347	13	36	5	32	5	2,154	1.17	0.86
14	38c	19/01/2011	367	669	79	320	70	22	72	11	60	326	12	35	5	30	5	2,082	1.17	0.87
15	39c	22/02/2011	398	734	88	359	79	25	82	12	74	341	14	41	6	36	5	2,295	1.14	0.84
16	41c	30/06/2011	477	835	96	379	82	26	94	15	90	446	18	52	7	48	7	2,673	1.25	0.72
17	42c	06/07/2011	438	770	89	354	76	25	87	14	83	425	17	50	7	45	7	2,486	1.25	0.71
18	43c	30/07/2011	361	685	84	341	77	24	80	12	70	337	14	39	5	33	5	2,166	1.09	0.84
19	44c	10/08/2011	513	859	96	374	81	26	94	15	88	490	18	54	8	48	7	2,773	1.35	0.72
20	45c	22/09/2011	437	769	86	345	73	23	82	13	74	413	15	44	6	40	6	2,426	1.28	0.76
21	46c	13/10/2011	402	699	78	308	65	20	70	11	64	353	13	38	5	35	5	2,167	1.30	0.79
22	47c	27/10/2011	455	790	89	346	73	23	82	13	73	411	15	45	6	41	6	2,469	1.30	0.77
23	48c	27/12/2011	367	656	75	297	63	19	64	10	57	300	11	33	5	29	4	1,991	1.24	0.86
24	49c	15/02/2012	383	709	84	343	74	23	79	12	67	349	14	39	6	36	6	2,222	1.16	0.82
25	50c	21/03/2012	363	699	84	343	74	22	76	11	62	334	13	37	5	35	5	2,162	1.10	0.84
26	51c	05/04/2012	391	740	89	359	78	23	80	12	69	357	14	39	6	36	6	2,300	1.12	0.83
27	52c	26/04/2012	384	719	86	348	75	23	77	12	68	349	14	39	5	36	5	2,241	1.13	0.82
28	53c	30/04/2012	388	719	86	349	76	23	78	12	66	349	14	38	6	36	6	2,246	1.14	0.83
29	54c	29/08/2012	396	729	87	357	78	23	79	12	69	356	14	40	6	36	6	2,287	1.15	0.82
30	55c	12/09/2012	384	705	84	340	74	22	75	12	65	338	13	38	5	34	5	2,196	1.15	0.83
31	56c	26/09/2012	384	723	87	353	77	23	81	12	67	348	14	39	6	36	6	2,255	1.11	0.82
32	57c	11/10/2012	399	746	89	360	80	24	81	12	68	351	14	39	6	36	6	2,309	1.14	0.85
33	58c	10/01/2013	351	641	77	312	67	20	66	10	55	281	11	31	4	29	4	1,959	1.16	0.90
34	59c	27/02/2013	420	744	89	361	77	23	77	12	65	327	13	37	5	34	5	2,290	1.20	0.89
35	60c	20/03/2013	385	707	84	345	75	22	74	11	61	311	13	35	5	33	5	2,166	1.16	0.89
36	61c	03/05/2013	374	707	86	351	78	23	78	12	66	341	14	38	5	35	5	2,215	1.10	0.84
37	62c	08/05/2013	390	730	87	358	79	23	77	12	64	328	13	37	5	35	5	2,243	1.13	0.88
38	63c	27/06/2013	376	708	85	349	75	22	73	11	61	312	13	36	5	33	5	2,164	1.12	0.88
39	64c	04/09/2014	340	662	81	331	73	22	71	11	59	295	12	33	5	30	5	2,028	1.07	0.89
40	65c	17/09/2014	305	594	73	299	66	20	64	10	53	264	11	30	4	26	4	1,824	1.06	0.89
41	66c	24/09/2014	324	638	78	322	70	21	68	10	55	280	11	32	4	28	4	1,946	1.05	0.91
42	67c	27/11/2014	326	596	74	302	66	20	64	10	52	259	10	29	4	25	4	1,841	1.12	0.94
43	68c	13/04/2015	249	502	63	260	58	17	56	8	46	229	9	26	4	23	4	1,552	1.00	0.89
44	69c	21/05/2015	275	535	67	278	61	18	59	9	49	240	10	27	4	25	4	1,660	1.03	0.90
45	70c	14/07/2015	209	421	53	223	49	15	47	7	39	192	8	22	3	20	3	1,311	0.99	0.91
46	71c	26/08/2015	167	353	45	191	43	13	43	6	36	174	7	20	3	18	3	1,120	0.95	0.86
47	72c	07/10/2015	146	305	39	164	37	11	35	5	29	141	6	16	2	14	2	951	0.95	0.90
48	73c	18/11/2015	157	330	42	177	40	12	39	6	32	156	6	18	2	16	2	1,034	0.94	0.88
49	74c	03/12/2015	186	392	50	209	47	14	45	7	36	179	7	20	3	18	3	1,215	0.94	0.90
50	75c	14/01/2016	189	398	51	210	47	14	45	7	36	179	7	21	3	18	3	1,227	0.95	0.91
51	76c	23/02/2016	169	359	46	192	44	13	41	6	34	167	7	19	3	16	2	1,118	0.93	0.91

pattern of $(LREE/HREE)_{N\text{-local rock}}$ ratio shows a trend similar to the pH, Ca, and Mg/Cl patterns, while the trend is opposite with respect to the patterns of the remaining parameters and elements considered (T, TDS, ΣREE, SO_4, and SO_4/Cl).

The significance of the relation between all the variables was tested with a correlation matrix (**Table 3**). The result of the correlation coefficient calculated between two variables is a value between +1 and −1, where a correlation of +1 and a correlation of −1 show a perfectly positive and a perfectly negative correlation, respectively, while a correlation equal to 0 means that the relations between the two variables are not linear. The correlation coefficient calculated between $(La/Pr)_{N\text{-local rock}}$ and $(LREE/HREE)_{N\text{-local rock}}$ ratios is equal to −0.64, indicating a moderate negative correlation. The results in **Table 3** show that the values of the correlation coefficient calculated for $(La/Pr)_{N\text{-local rock}}$ are in most cases higher with respect to the values of $(LREE/HREE)_{N\text{-local rock}}$ when they are compared to major elements, their ratios, and physico-chemical parameters.

The pH, TDS, ΣREE, and SO_4 are the variables that are better correlated with $(La/Pr)_{N\text{-local rock}}$ and $(LREE/HREE)_{N\text{-local rock}}$ compared to the other parameters considered and display the highest values of the correlation coefficient, up to |0.90| for $(La/Pr)_{N\text{-local rock}}$. The absolute values of the correlation coefficients calculated between pH and $(La/Pr)_{N\text{-local rock}}$ and between pH and $(LREE/HREE)_{N\text{-local rock}}$ are higher than the correlation coefficients calculated for the temperature; however, the incompleteness of the temperature data set makes it difficult to compare them. For comparison, we also report the correlation coefficients of various major elements that are not presented in the graphs (**Figures 3, 5–9**; Na, K, Mg, Al, Fe, and Cl). All the major elements considered show a positive value of the correlation coefficient when compared to $(La/Pr)_{N\text{-local rock}}$, except Ca, which is the only major element with a negative value of the correlation coefficient. On the contrary, Ca is the only positively correlated to $(LREE/HREE)_{N\text{-local rock}}$. Furthermore, the correlation coefficient of all the major elements (except Ca) with TDS is positive, with values that span from 0.69 to 0.99. Ca is the only major element that exhibits a negative value of the coefficient when compared to TDS, the only one with a correlation value < |0.50|. Mg/Cl ratio displays higher values of the correlation coefficient for both $(La/Pr)_{N\text{-local rock}}$ and $(LREE/HREE)_{N\text{-local rock}}$ relations compared to SO_4/Cl ratio. The latter is also the variable with the lowest correlation coefficients calculated.

5 DISCUSSION

5.1 Temporal Variations in Major Elements, REE, and Physico-Chemical Parameters

The first interesting result from our dataset is that the behavior of REE, especially $(La/Pr)_{N\text{-local rock}}$ and $(LREE/HREE)_{N\text{-local rock}}$ ratios, varies with time following the main variations of volcanic activity, represented by the occurrence of hundreds of phreatic eruptions (679). Despite the impossibility of identifying an unequivocal cause-effect relation between $(La/Pr)_{N\text{-local rock}}$ and $(LREE/HREE)_{N\text{-local rock}}$ ratios variations with the occurrence of a single phreatic eruption, the general trend of both ratios seems to be related to the frequency of phreatic eruptions, here expressed in stages 1 to 4 throughout 2008–2016. Consequently, it is not possible to discern how the different types of eruptions (A, B, and C) affected the trend of $(La/Pr)_{N\text{-local rock}}$ and $(LREE/HREE)_{N\text{-local rock}}$ ratios over time.

Rouwet et al. (2017, 2019) describe in detail how physico-chemical parameters, concentrations of major elements, and major element ratios vary at Laguna Caliente for the period 2005–2010 and 1978–2016, respectively. They suggest that pH is one of the most effective parameters to detect changes in volcanic activity, indicative of the general degassing state of the volcano caused by SO_2, H_2S, HCl, and HF input. They did not deem an increased temperature a strong indicator for enhanced phreatic activity, as, on the contrary, a temperature decrease is often an indication of conduit sealing, causing pressure build-up beneath a lake before phreatic eruptions.

Rouwet et al. (2019) also found that concentrations of SO_4 > 60,000 mg L^{-1} are associated with the most intense eruptive phases (e.g., stage 2, 2010–2011), while SO_4/Cl does not work as a strong indicator, probably because of the loss of HCl by evaporative degassing (Capaccioni et al., 2017; Rouwet et al., 2017). **Supplementary Figures 2A,B** display that the SO_4/Cl ratio steadily increases from 2012 to 2016 despite the number of phreatic eruptions in decline. This trend coincides with the steady lake level drop throughout the entire 2006–2016 phreatic eruption cycle, eventually leading to full lake dry out in 2017. The smaller Laguna Caliente becomes hence more sensitive to HCl degassing through time, imposing inertia on the parameter SO_4/Cl, making it less sensitive and adapted for monitoring purposes (Rouwet et al., 2017).

Since pH and SO_4 seem to represent the most sensitive parameters to monitor the volcanic activity at Laguna Caliente during the eruptive cycle of 2006–2016 (Rouwet et al., 2017; Rouwet et al., 2019), their strong correlation with $(La/Pr)_{N\text{-local rock}}$ and the correlation with $(LREE/HREE)_{N\text{-local rock}}$ (even if lower compared with $(La/Pr)_{N\text{-local rock}}$ ratio) suggest that they are good indicators of changes in volcanic activity, especially the case for $(La/Pr)_{N\text{-local rock}}$ (**Table 3**; **Figures 6**, **8**).

Comparing the variations of Na, K, Mg, Ca, Al, and Fe with the volcanic activity over time, we notice that the concentrations of all the major elements, except Ca, rise when the frequency of the eruptions is higher and decline consequently with a lower frequency of phreatic eruptions. The opposite behavior of Ca compared with the other cations can be explained by secondary processes such as the precipitation of gypsum/anhydrite at the surface of the lake or at depth (Rouwet et al., 2017; Inguaggiato et al., 2018 and references therein). The loss of cations at Laguna Caliente mainly depends, in fact, on minerals precipitation (Rouwet et al., 2019). Since TDS is representative of the variations of all the major elements, except Ca, only the latter was compared with $(La/Pr)_{N\text{-local rock}}$ and $(LREE/HREE)_{N\text{-local rock}}$ ratios (**Figures 9A,B**).

Trends in major elements and physico-chemical parameters suggest that the increase in phreatic activity is related to a higher input of volcanic gases (SO_2, HCl, and HF), in agreement with the gas-driven mechanism of phreatic eruptions (de Moor et al., 2016; Stix and de Moor, 2018). The pH values decrease consequently when gas input is higher. A lower pH renders the water more aggressive during water-rock interaction and hence favors the leaching of rock-forming elements (i.e., cations), resulting in higher TDS values. Despite the greater leaching of rock-derived elements, the opposite trend of Ca is probably due to the gypsum/anhydrite precipitation, a process that mainly affects Ca concentration over time.

Considering the high amount of SO_4 (2–3 orders of magnitude higher with respect to Ca due to massive SO_2 input), the precipitation of gypsum/anhydrite did not induce significant variations in the SO_4 temporal pattern. This could be explained regarding the abundance of SO_4 compared to Ca, which represents, in fact, the limiting reagent for the gypsum/anhydrite precipitation process.

The fact that REE concentrations, as well as changes of $(La/Pr)_{N\text{-local rock}}$ and $(LREE/HREE)_{N\text{-local rock}}$ ratios in the water of Laguna Caliente, are related to the variations of the volcanic activity suggests that REE chemistry could provide additional information on changes in activity and fluid-mineral dynamics to

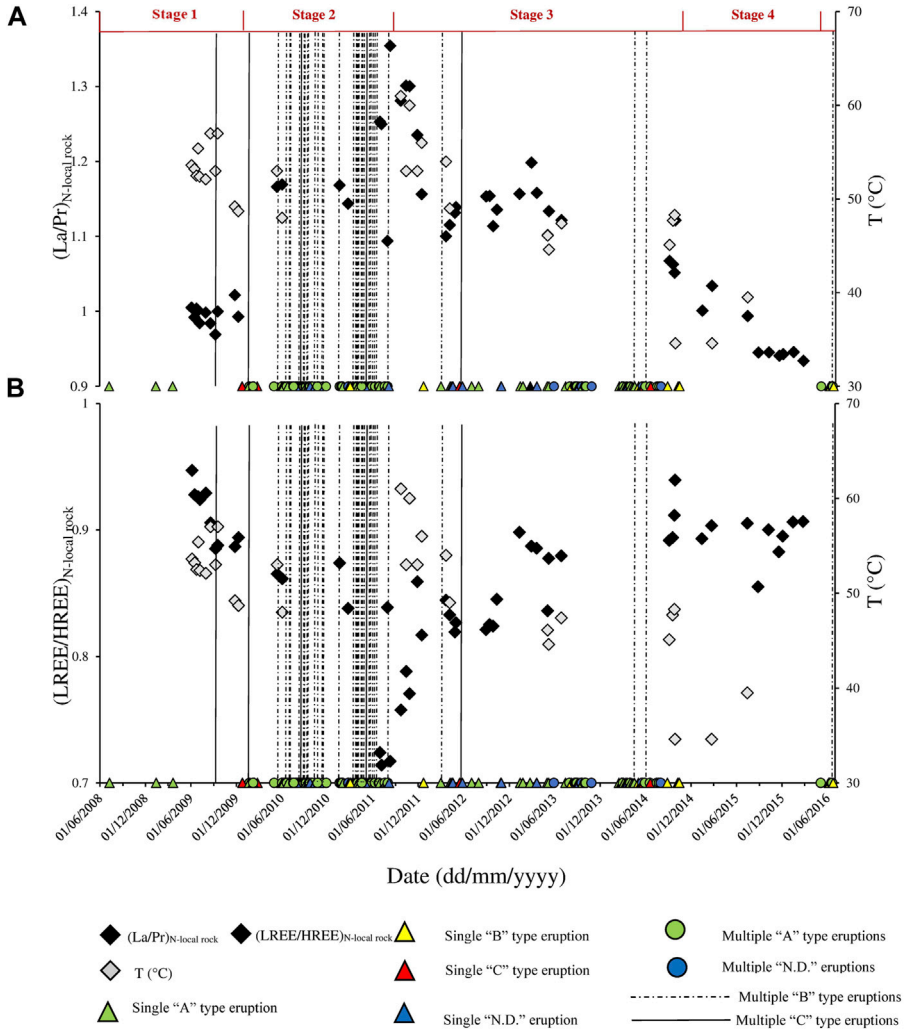

FIGURE 5 | (A) $(La/Pr)_{N\text{-local rock}}$ and T vs. time. **(B)** $(LREE/HREE)_{N\text{-local rock}}$ and T vs. time.

the "classical" monitoring parameters (major elements and their ratios, physico-chemical parameters). Moreover, the variations of $(La/Pr)_{N\text{-local rock}}$ and $(LREE/HREE)_{N\text{-local rock}}$ ratios with varying activity have often revealed a higher sensitivity than, e.g., T and SO_4/Cl ratios.

5.2 Rock Dissolution, Precipitation of Secondary Minerals, and REE Fractionation

Several authors presented that solubility of anhydrite and alunite is retrograde (Bernard et al., 2004; Taran et al., 2008; Colvin et al., 2013; Kalacheva et al., 2015). Rodríguez and van Bergen (2017) ran thermodynamic simulations with PHREEQC to investigate the saturation indexes of representative minerals from lake surface temperature up to 300°C. They show that the solubility of gypsum, anhydrite, and alunite decreases when the temperature increases. In particular, the solubility curve of gypsum is prograde from 0 to ~40°C and retrograde for temperature higher than ~40°C and intercepts the solubility curve of anhydrite at a temperature of ~40°C (Azimi et al., 2010). The increase of the temperature in a volcanic hydrothermal system can hence induce the precipitation of secondary minerals: 1) at the surface when the temperature increases due to the changes of the volcanic activity or 2) in the deeper and hotter part of the system. The processes of precipitation and dissolution of secondary minerals do not only affect the mobility of the main elements that constitute the minerals but also other solutes, including REE. Data from previous studies have demonstrated that minerals such as alunite and gypsum can fractionate the REE in hyperacid fluids (Varekamp, 2015; Inguaggiato et al., 2017; van Hinsberg et al., 2017; Inguaggiato et al., 2018; Inguaggiato et al., 2020a; Inguaggiato et al., 2020b; van Hinsberg et al., 2020).

The isosol plot was used here to calculate the grams of rock dissolved per liter of solution, considering the congruent dissolution of the average local rock (andesite), consequently to the water-rock interaction process (Varekamp, 2015). The average chemical composition of major elements in the local

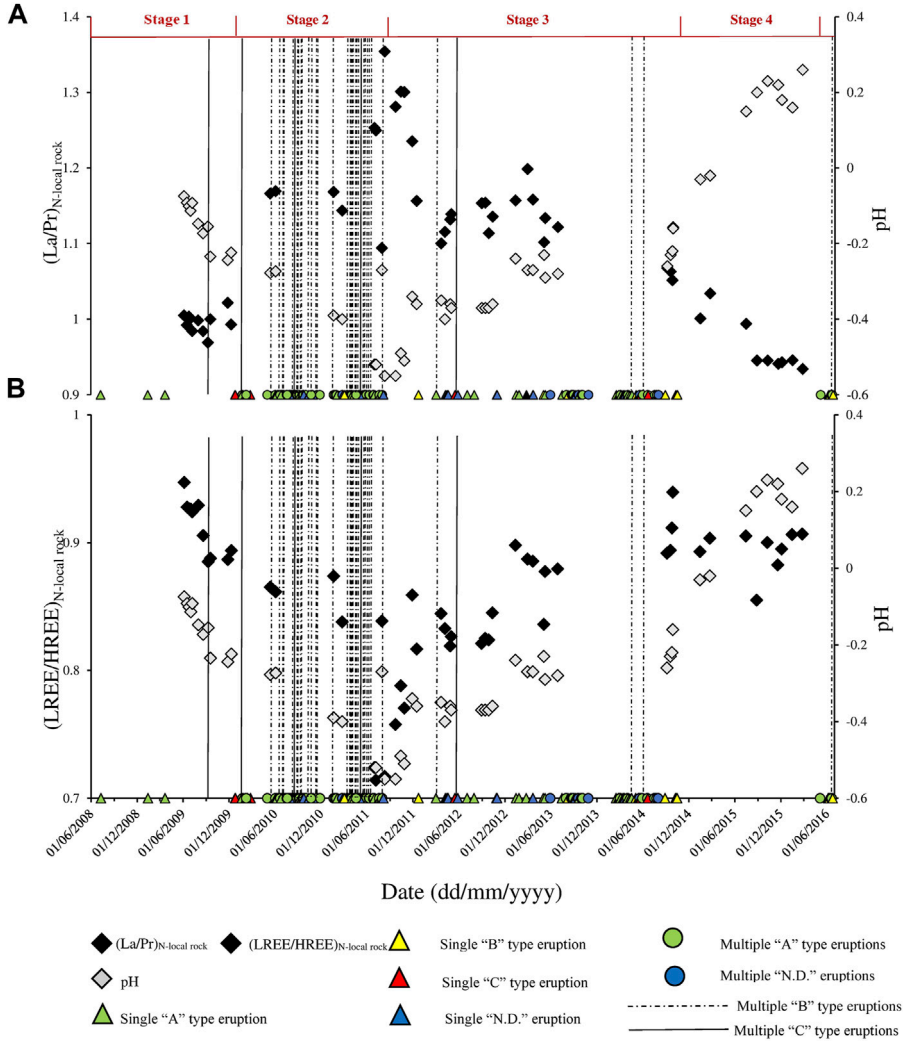

FIGURE 6 | (A) $(La/Pr)_{N\text{-local rock}}$ and pH vs. time. **(B)** $(LREE/HREE)_{N\text{-local rock}}$ and pH vs. time.

andesite for Poás was provided by Cigolini et al. (1991). The amount of local rock dissolved was estimated graphically for all the water samples and varies between ~10 and ~70 g per liter of water; our attention is mainly focused on Ca, Al, K, and Na depletion (constituents of gypsum, anhydrite, and alunite) compared to the hypothetical congruent dissolution of the local rock. Four isosol plots, one for each stage of volcanic activity, were selected as representative of the variation of the dissolution of the local rock and the precipitation of secondary minerals during the activity changes (**Figures 10A–D**). During stage 1 (**Figure 10A**; low phreatic activity), almost all the elements considered lie on the 25 g rock/L line, indicating that gypsum/anhydrite, as well as alunite, could not precipitate in high amounts. At stage 2 (**Figure 10B**; high phreatic activity), the increase of rock dissolution occurs during the increase of temperature and the decrease of the pH of the lake, leading to the highest amount of rock dissolved. Considering the congruent dissolution of the local rock, Ca concentration is strongly depleted with respect to the Ca that should be dissolved in lake water. Aluminum, Na, and K plots on the line are representatives of the congruent dissolution of the rock (50 g rock/L). The precipitation of minerals containing Ca (such as gypsum/anhydrite) is proposed to justify the Ca depletion. During stage 3 (**Figure 10C**; the decline of phreatic activity), the amount of rock dissolved (~35 g rock/L) and the loss of Ca dissolved (gypsum/anhydrite precipitation) are both lower with respect to those of stage 2. Once more, Al, Na, and K are not depleted. Rock dissolution representative of stage 4 (**Figure 10D**; quiescent period) is ~17 g rock/L, with Ca and Al concentrations in lake water comparable to that of the congruent rock dissolution line. These findings confirm that the water-rock interaction processes have varied between 2009 and 2016.

Rock dissolution is favored by more acidic waters, especially evident for the peak activity stages 2 and 3. Contrarily, rock dissolution is less intense during stage 1 (very few phreatic

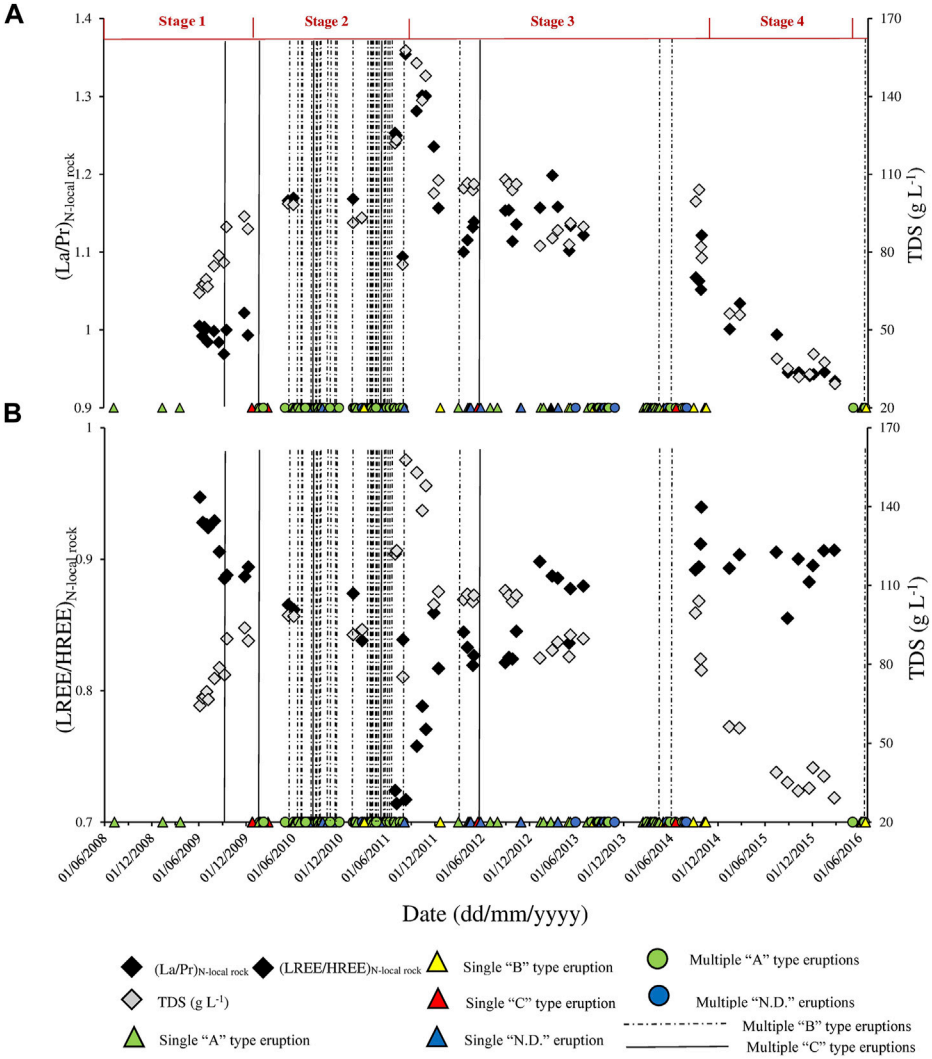

FIGURE 7 | (A) $(La/Pr)_{N\text{-local rock}}$ and TDS vs. time. **(B)** $(LREE/HREE)_{N\text{-local rock}}$ and TDS vs. time.

eruptions) and stage 4 (no evidence of phreatic activity) (**Supplementary Figure 4**).

The estimation of the amount of congruent dissolution of g rock per liter allowed calculating the element loss (element*; ppm) for all the water samples, using the following equation:

$$\text{element}^* = \text{element}_{(\text{isosol})} - \text{element}_{(\text{analyzed})}, \quad (1)$$

where $\text{element}_{(\text{isosol})}$ represents the concentration of the element in the lake water (ppm) resulting from the congruent dissolution of the rock calculated with the isosol plot, while $\text{element}_{(\text{analyzed})}$ is the concentration of the elements (ppm) effectively measured in the lake water. The loss of Ca, Al, K, and Na (Ca*, Al*, K*, Na*) was calculated to consider the potential precipitation of sulfate minerals. The loss of Ca can be the consequence of gypsum ($CaSO_4{\cdot}2H_2O$) and/or anhydrite ($CaSO_4$) precipitation; the loss of Al, Na, and K can be due to the precipitation of alunite minerals [(Na, K) Al_3 $(SO_4)_2$ $(OH)_6$] (Colvin et al., 2013; Varekamp, 2015). The results of Ca*, Al*, K*, and Na* were plotted vs. $(La/Pr)_{N\text{-local rock}}$ and $(LREE/HREE)_{N\text{-local rock}}$ ratios, respectively (**Figures 11A–H**). Near-linear trends can be observed for $(La/Pr)_{N\text{-local rock}}$ vs. Ca* and $(LREE/HREE)_{N\text{-local rock}}$ vs. Ca* (**Figures 11A,B**): increasing the loss of Ca interpreted as gypsum/anhydrite precipitation, the $(La/Pr)_{N\text{-local rock}}$ increases and $(LREE/HREE)_{N\text{-local rock}}$ decreases. These observations corroborate 1) the distribution coefficients calculated during the precipitation of gypsum from the hyperacid and hypersaline waters of Kawah Ijen and Laguna Caliente crater lakes (Inguaggiato et al., 2018; Inguaggiato et al., 2020a), 2) the REE pattern of gypsum collected from the Kawah Ijen terrace, with the seeped-out crater lake water as source fluid (van Hinsberg et al., 2017), and 3) the REE patterns of gypsum precipitated in the laboratory from a synthetic solution (Dutrizac, 2017). The lack of trends of $(La/Pr)_{N\text{-local rock}}$ and $(LREE/HREE)_{N\text{-local rock}}$ each one versus Al*, Na*, and K* (**Figures 11C–H**) allows suggesting that the precipitation of

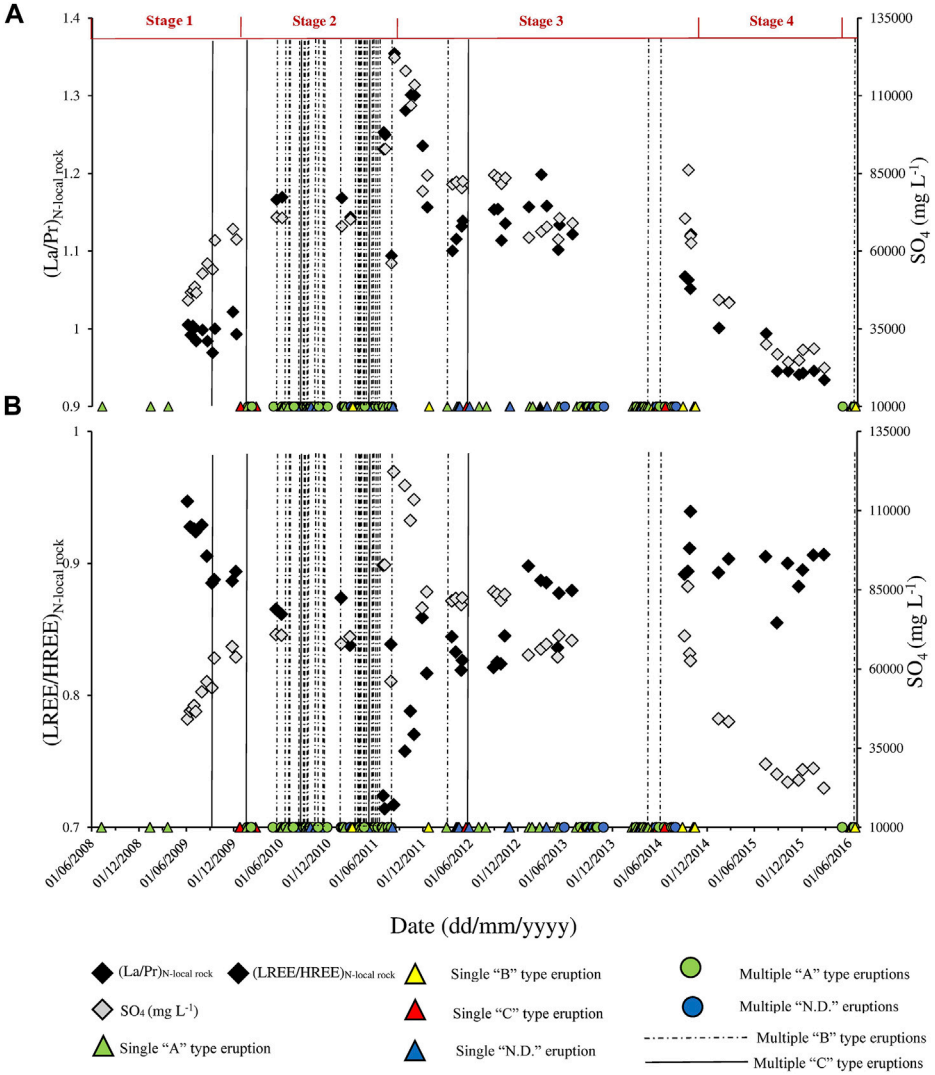

FIGURE 8 | (A) $(La/Pr)_{N\text{-local rock}}$ and SO_4 vs. time. **(B)** $(LREE/HREE)_{N\text{-local rock}}$ and SO_4 vs. time.

alunite, as well as other Al-bearing minerals, is not the main process fractionating the REE over time.

5.3 Processes Affecting REE Fractionation and Their Implications Over Time

Previous studies have already focused on comparing REE variations over time in volcanic fluids and their possible connection with volcanic unrest. Wood (2006) analyzed the patterns of REE in the crater lake of Mount Ruapehu (New Zealand) between 1993 and 1998, a period including the 1995–1996 phreatomagmatic eruption. The REE chondrite normalized patterns vary over time, specifically before and after the eruption occurred in September 1995. The author suggests that the concentrations of REE in the crater lake could probably be correlated with the variation of the volcanic activity. Varekamp (2015), comparing the REE concentrations in the thermal spring fluids of Copahue volcano (Argentina-Chile), found that the La/Sm ratio varied over time (1997–2005), with a minimum in 2000, concomitant with an eruption. REE patterns in the hyperacidic crater lake water of Santa Ana volcano (El Salvador) during 2017 show changes in the LREE/HREE normalized ratios (Colvin et al., 2013). The depletion of LREE was considered as the effect of alunite precipitation (Varekamp, 2015). Morton-Bermea et al. (2010) did not notice an important correlation between REE variations and volcanic activity at El Chichón volcano (Mexico), probably due to the relative stability of the volcanic activity during the period of observation and the less extreme pH (H_2S dominated degassing) and salinity of its crater lake (Rouwet et al., 2008).

Inguaggiato et al. (2018) investigated the REE fractionation during the in-lab precipitation of gypsum from the Laguna Caliente lake waters and proposed that the pattern of REE in water is also controlled by the precipitation of gypsum, a process

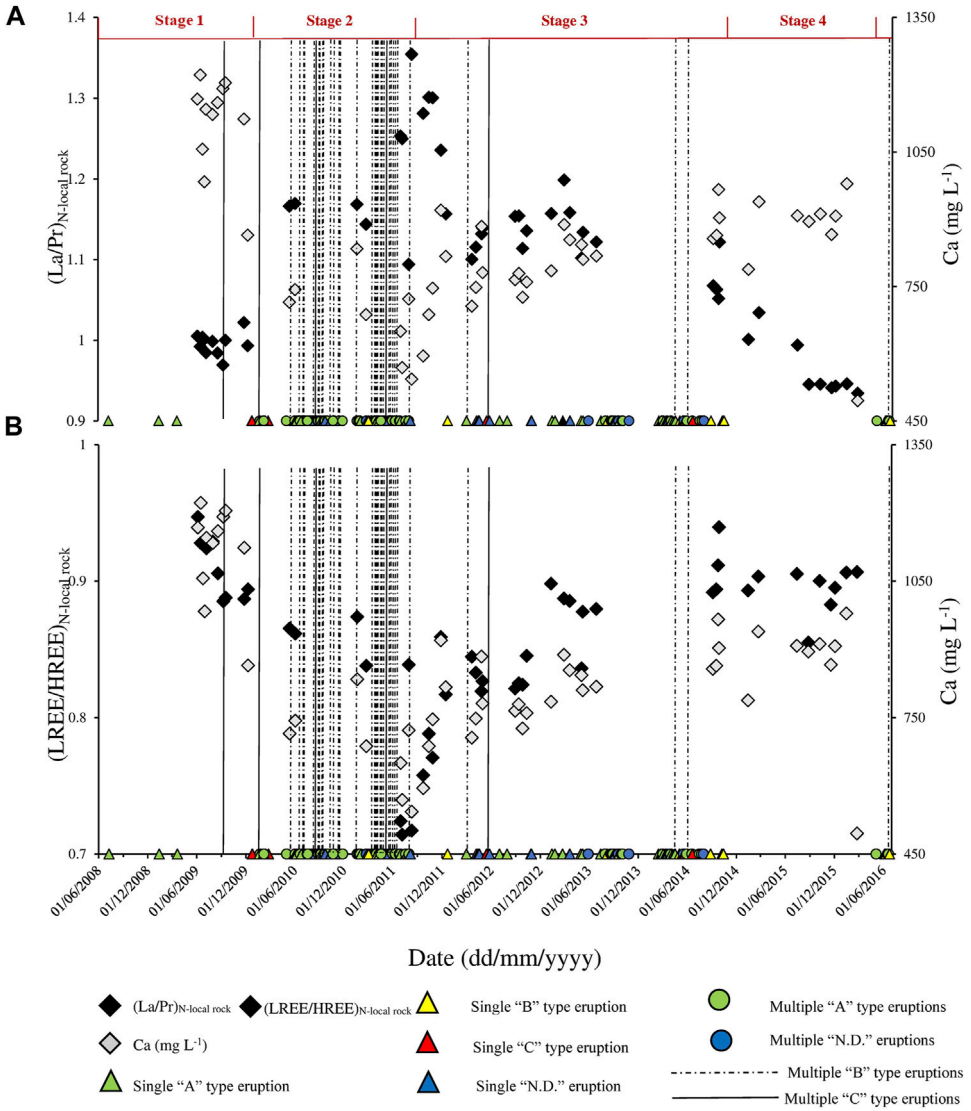

FIGURE 9 | (A) $(La/Pr)_{N\text{-local rock}}$ and Ca vs. time. **(B)** $(LREE/HREE)_{N\text{-local rock}}$ and Ca vs. time.

that naturally occurs at the crater lake (Brantley et al., 1987). They pointed out that gypsum preferentially incorporates LREE with respect to HREE, affecting the relative proportion between the two sub-groups, as also described in detail in **Section 4.2**. Moreover, Ce, Pr, and Nd distribution coefficients, calculated between gypsum and the lake waters of Poás and Kawah Ijen volcanoes, are higher compared with the other REE, including La that is part of the LREE (Inguaggiato et al., 2018; Inguaggiato et al., 2020a). Hence, the preferential incorporation of LREE in gypsum, particularly Pr, is also corroborated by 1) the opposite trend of Ca concentration with respect to $(La/Pr)_{N\text{-local rock}}$ ratio and 2) the same trend of Ca with respect to $(LREE/HREE)_{N\text{-local rock}}$ ratio in this study.

The maximum value of Ca* calculated (2,835 ppm) corresponds to the precipitation of 12 g of gypsum per kg of water. Higher loss of Ca was calculated in lake waters of stages 2 and 3 (periods of high volcanic activity), interpreted as a higher amount of gypsum/anhydrite precipitated than that in stages 1 and 4. A mass balance was simulated to remove REE from lake water during the precipitation of gypsum in a range from 2 to 12 g of gypsum per kg of water. The average REE concentrations of the water samples belonging to stage 1 (low volcanic activity), with $(La/Pr)_{N\text{-local rock}}$ and $(LREE/HREE)_{N\text{-local rock}}$ values close to 1, were considered as the initial point when the REE ratios are not affected by strong fractionation processes. The concentration of each REE in gypsum ($[REE_i]_{gypsum}$) precipitated from the lake was calculated using the concentration of each REE in the water before considered as initial point $[REE_i]_{water}$, and the average distribution coefficients of each REE (K_D) in the gypsum precipitated in the laboratory from Laguna Caliente lake water (Inguaggiato et al., 2018):

$$[REE_i]_{gypsum} = [REE_i]_{water} * K_D. \quad (2)$$

TABLE 3 | Correlation matrix.

	La/Pr	LREE/HREE	T	pH	TDS	ΣREE	Na	K	Mg	Al	Fe	Ca	SO_4	Cl	SO_4/Cl	Mg/Cl
La/Pr	1															
LREE/HREE	−0.64	1														
T	0.21	−0.48	1													
pH	−0.87	0.54	−0.49	1												
TDS	0.88	−0.62	0.49	−0.96	1											
ΣREE	0.81	−0.52	0.37	−0.94	0.88	1										
Na	0.67	−0.70	0.68	−0.73	0.69	0.67	1									
K	0.86	−0.67	0.54	−0.92	0.91	0.85	0.71	1								
Mg	0.59	−0.47	0.70	−0.75	0.73	0.71	0.71	0.67	1							
Al	0.83	−0.62	0.59	−0.93	0.94	0.85	0.73	0.91	0.81	1						
Fe	0.66	−0.58	0.58	−0.73	0.70	0.68	0.93	0.68	0.67	0.76	1					
Ca	−0.62	0.67	0.06	0.40	−0.45	−0.41	−0.40	−0.49	−0.05	−0.40	−0.38	1				
SO_4	0.90	−0.62	0.42	0.95	0.99	0.87	0.66	0.91	0.68	0.92	0.68	−0.49	1			
Cl	0.76	−0.55	0.64	−0.90	0.93	0.83	0.69	0.82	0.85	0.90	0.70	−0.28	0.89	1		
SO_4/Cl	0.18	−0.07	−0.45	0.01	0.02	−0.01	−0.16	0.03	−0.46	−0.10	−0.14	−0.43	0.12	−0.33	1	
Mg/Cl	−0.53	0.23	−0.19	0.62	−0.65	−0.54	−0.23	−0.56	−0.14	−0.51	−0.32	0.38	−0.66	−0.59	−0.03	1

Once the REE concentrations in the gypsum were known, REE concentrations for different amounts of gypsum precipitated per kg of water (six steps: 2, 4, 6, 8, 10, and 12 g of gypsum) were calculated and then subtracted from the REE concentrations of the initial lake water considered $[REE_i]_{water}$. The results mainly show an increase of the $(La/Pr)_{N\text{-local rock}}$ ratio (1–1.12) and a decrease of the $(LREE/HREE)_{N\text{-local rock}}$ ratio (0.92–0.77). The REE ratios of the lake water, calculated during the simulation of gypsum precipitation, are in the range of values found in the lake water over time; $(La/Pr)_{N\text{-local rock}}$

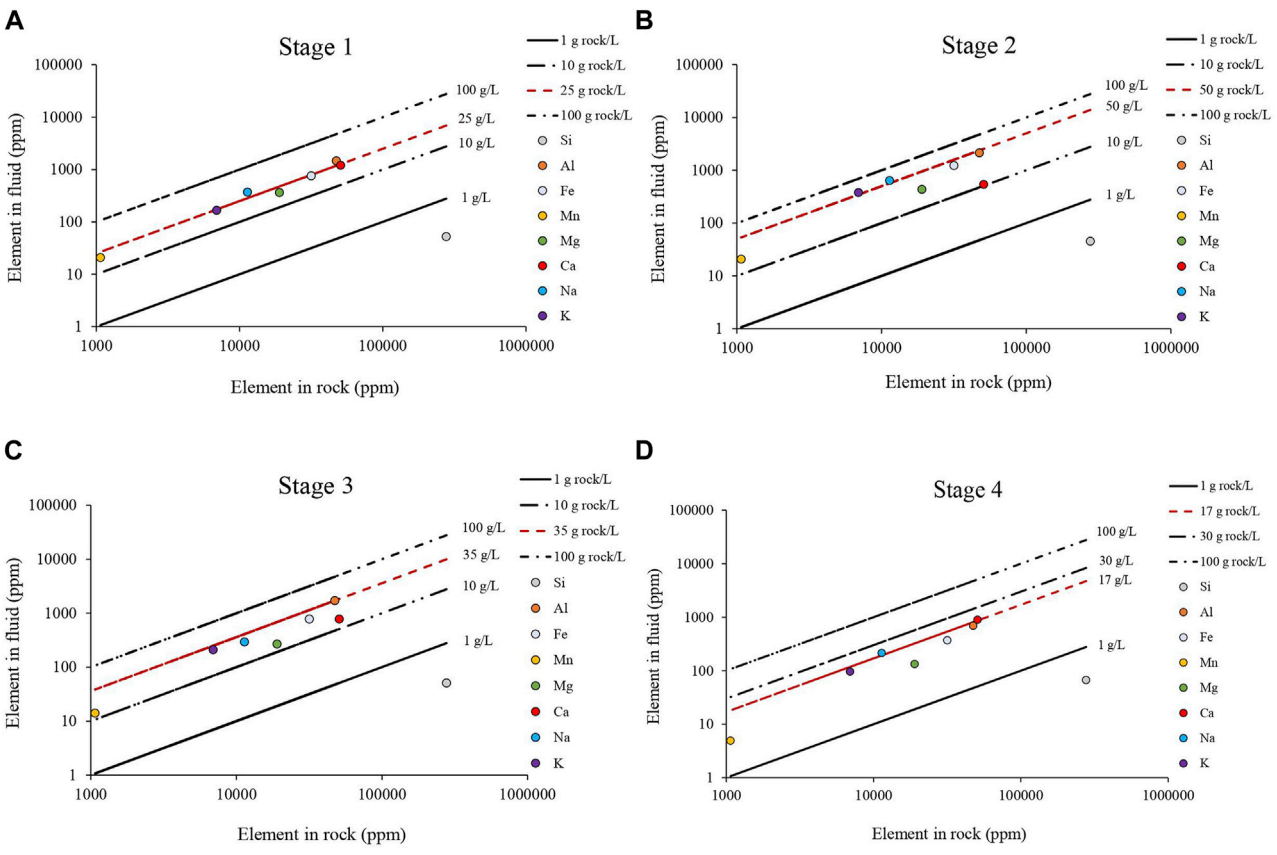

FIGURE 10 | Isosol plots show that the amount of rock dissolved per liter of lake water and the loss of elements in water, especially Ca loss, is considered the effect of the gypsum/anhydrite precipitation. The four isosol plots are representative of the dissolution of the rock and the Ca loss during **(A)** stage 1, **(B)** stage 2, **(C)** stage 3, and **(D)** stage 4.

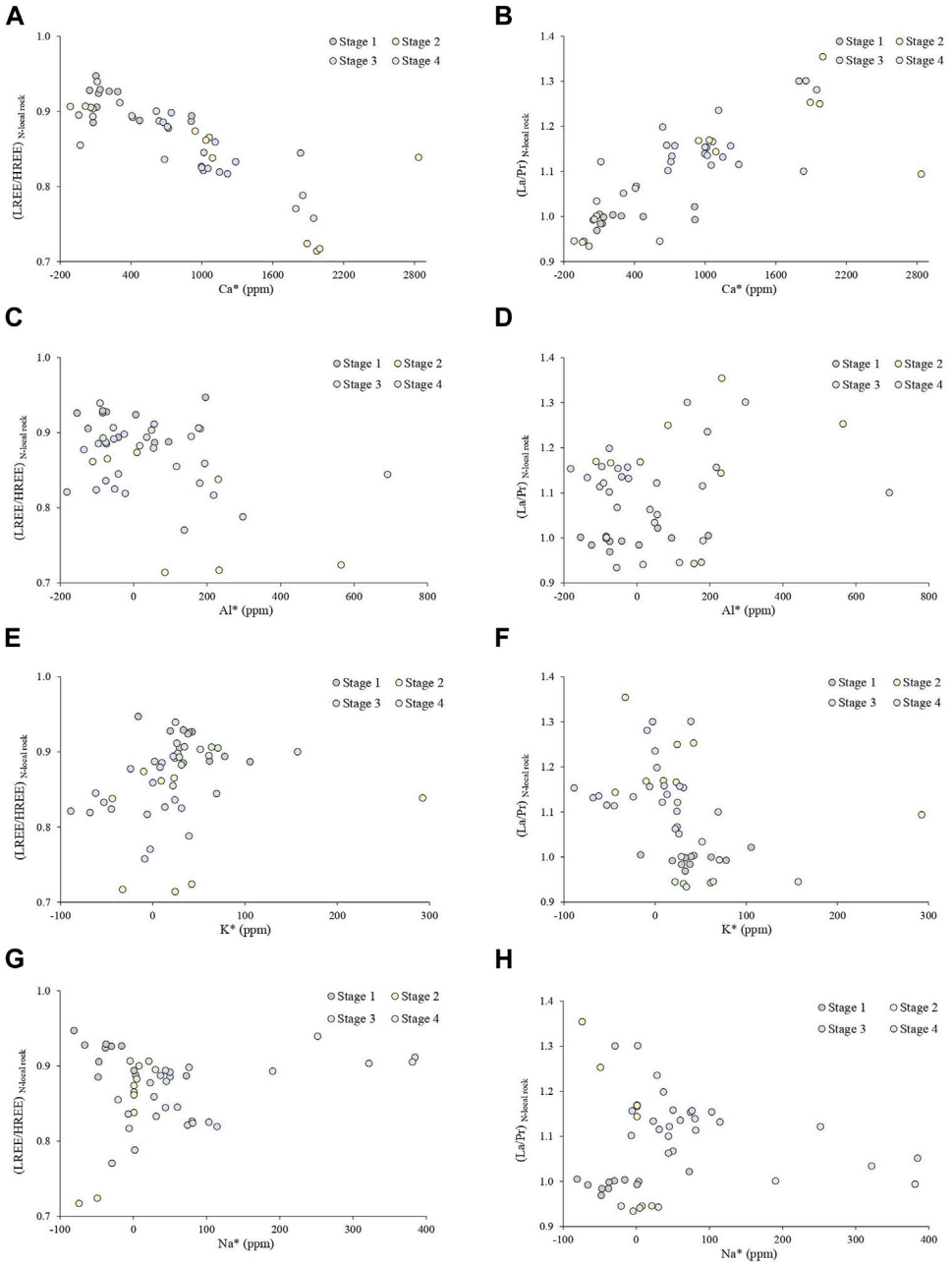

FIGURE 11 | (A) Ca* in lake water vs. $(LREE/HREE)_{N\text{-local rock}}$. **(B)** Ca* in lake water vs. $(La/Pr)_{N\text{-local rock}}$. **(C)** Al* in lake water vs. $(LREE/HREE)_{N\text{-local rock}}$. **(D)** Al* in lake water vs. $(La/Pr)_{N\text{-local rock}}$. **(E)** K* in lake water vs. $(LREE/HREE)_{N\text{-local rock}}$. **(F)** K* in lake water vs. $(La/Pr)_{N\text{-local rock}}$. **(G)** Na* in lake water vs. $(LREE/HREE)_{N\text{-local rock}}$. **(H)** Na* in lake water vs. $(La/Pr)_{N\text{-local rock}}$.

ratio ranges from 0.93 to 1.35 and $(LREE/HREE)_{N\text{-local rock}}$ ratio ranges 0.71–0.95. The highest depletion of LREE is associated with the precipitation of 12 g of gypsum per kg of water (**Figure 12**), corresponding to the loss of Ca estimated in one of the water samples belonging to stage 2. These results allow proposing that the amount of gypsum precipitated is adequate to justify the changes of $(LREE/HREE)_{N\text{-local rock}}$ ratios over time.

Martínez (2008) studied the variations of REE at the crater lake and thermal springs at Poás volcano during the period 1978–2007 and found that the concentrations of REE vary over time; specifically, some REE patterns show a depletion of LREE, as also shown in this investigation. The author suggests that the depleted LREE patterns could result from 1) fluid interaction with altered rocks that were already depleted in LREE or 2) LREE incorporation in alunite. Taking into consideration that REE patterns of alunite group minerals in other volcanic hydrothermal systems (Kikawada et al., 2004) are also enriched in LREE, it is likely that the

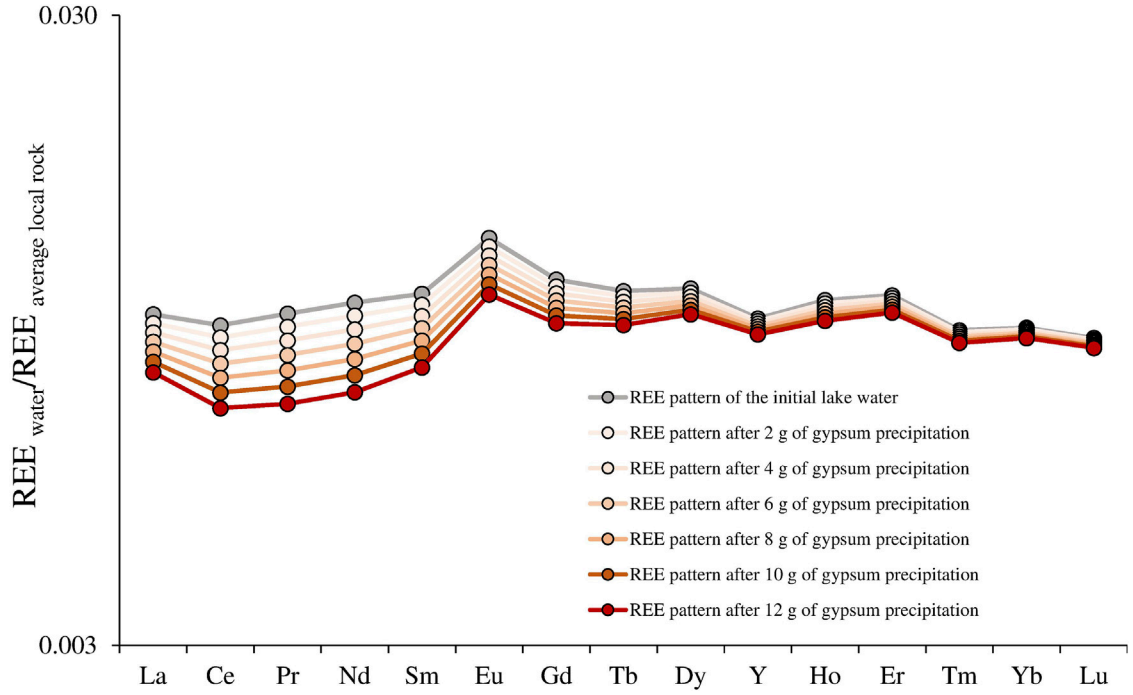

FIGURE 12 | REE concentrations in lake water normalized to the average local rock (Carr et al., 2013) after 2, 4, 6, 8, 10, and 12 g of gypsum precipitation. The average REE concentration [REEi]water was used as the initial point and calculated considering the samples of stage 1 characterized by $(La/Pr)_{N\text{-local rock}}$ and $(LREE/HREE)_{N\text{-local rock}}$ ratios close to 1. REE concentrations removed from the gypsum precipitation were subtracted to the [REEi] water and plotted.

precipitation of alunite in Laguna Caliente crater lake could also favor the decrease of $(LREE/HREE)_{N\text{-local rock}}$ in the water. However, both $(La/Pr)_{N\text{-local rock}}$ and $(LREE/HREE)_{N\text{-local rock}}$ ratios show trends only with Ca*, in contrast to Al*, K*, and Na*. Furthermore, the higher loss of Ca (Ca*) with respect to the loss of Al (Al*) indicates that the amount of gypsum/anhydrite precipitated is greater than the quantity of alunite precipitated. These findings confirm that gypsum and/or anhydrite precipitation play an important role in fractionating the REE in the hyperacid crater lake of Laguna Caliente over time. Moreover, Martinez (2008) also identified gypsum in lake bottom sediments and suspended particulate in the lake water column. The findings of gypsum in lake water corroborate that the Ca loss can be justified by gypsum or anhydrite precipitation. We cannot exclude the precipitation of alunite in the Poás volcanic hydrothermal system and the participation of the alunite in the REE fractionation in water.

The low pH values of the lake waters registered from 2008 to 2016, during the increase of the volcanic activity, reflect an enhanced input of acidic gases (such as SO_2, HCl, and HF), causing highly effective leaching of REE and major elements from "fresh" volcanic rock, probably also accentuated by continuous lake evaporation. This is consistent with the increasing concentrations of ΣREE over time concurrently to an enhanced gas input and the related pH drop. The rise of $(La/Pr)_{N\text{-local rock}}$ ratio and the decrease of $(LREE/HREE)_{N\text{-local rock}}$ ratio, when phreatic activity is more intense, are consistent with the possible gypsum/anhydrite precipitation that affects the concentrations of REE incorporating LREE preferentially with respect to HREE and Pr with respect to La.

Based on the highest Mg/Cl ratios before the 2006–2016 phreatic eruption cycle, Rouwet et al. (2017) argued that the resumed phreatic unrest was caused by the intrusion of a new magma batch in 2005 or before, also supported by geophysical (gravity, Rymer et al., 2009) and gas geochemical surveys (Vaselli et al., 2003; Fischer et al., 2015). These findings highlight that the variations of REE at Laguna Caliente during the period 2009–2016, as well as the common parameters used in volcano monitoring here reported for comparison, are connected to the occurrence of volcanic activity changes observable at the surface as multiple eruptions.

6 CONCLUSION

The crater lake of Poás volcano, Laguna Caliente, was sampled between June 2009 and February 2016, the period concerning the phreatic eruption cycle before the April 2017 phreatomagmatic eruption. The occurrence of hundreds of phreatic eruptions at Laguna Caliente during our sampling period provided a unique occasion to study the role of REE as

possible indicators for volcano monitoring at active hyperacid crater lakes.

The concentrations of REE dissolved in the lake water vary from 950 to 2,773 μg kg^{-1}, increasing as the phreatic activity increases. The temporal evolution of $(La/Pr)_{N\text{-local rock}}$ and $(LREE/HREE)_{N\text{-local rock}}$ ratios shows a clear relation with changes in volcanic activity, i.e., increasing and decreasing, respectively, when the frequency of phreatic eruptions is higher. The similarities observed comparing the patterns of $(La/Pr)_{N\text{-local rock}}$ and $(LREE/HREE)_{N\text{-local rock}}$ ratios with those of physico-chemical parameters, major elements concentrations, and major elements ratios, "classically" used for volcanic lakes surveillance suggest that their variations seem to occur concurrently. The isosol plot, used to calculate the g of rock per liter of lake water dissolved during the congruent dissolution over time (10–70 g/L), shows that the highest values were found in stage 2. The opposite behavior of Ca with respect to the other major elements suggests an important depletion of this element in the water caused by Ca-bearing mineral precipitation, like gypsum and/or anhydrite. The different amount of Ca loss in the water during the four stages of volcanic activity indicates that the precipitation process is greater during the stages of high phreatic activity. Mass balance calculation confirms that the gypsum precipitation, estimated during the period of observation, is a good candidate to justify the depletion of LREE observed in the REE patterns in lake water. Our observations on REE changes over time and their relations with the changes of major elements, physico-chemical parameters, and the major changes of the volcanic activity between 2009 and 2016 at Laguna Caliente demonstrate that REE chemistry is an interesting tool in order to study water-rock interaction processes at Poás volcano, or elsewhere. However, further studies on the usefulness of REE in Laguna Caliente crater lake and in other hyperacid crater lakes are required to generalize the findings of this investigation about the connection of REE with volcanic monitoring.

DATA AVAILABILITY STATEMENT

The original contributions presented in the study are included in the article/**Supplementary Material**; further inquiries can be directed to the corresponding author.

AUTHOR CONTRIBUTIONS

SP wrote the original draft of the manuscript and elaborated the dataset. CI and SP formulated the scientific question, designed the study, and the scientific approach. CI and DR edited the first draft of the manuscript by writing part of the sections. RM-A, CR-U, GG, and DR organized and performed the field sampling. LP and GL revised and edited a version of the manuscript and added new ideas. LB and SB performed the analysis in laboratory. All authors contributed to the final version of the manuscript.

FUNDING

This work was partially supported by the Istituto Nazionale di Geofisica e Vulcanologia (INGV; Italy), Centro de Investigación Científica y de Educación Superior de Ensenada, Baja California (CICESE; Mexico), under internal project no. 644170.

ACKNOWLEDGMENTS

This article is part of the doctoral project thesis of SP and the authors thank CONACYT for funding the doctoral fellowship (1086975).

SUPPLEMENTARY MATERIAL

The Supplementary Material for this article can be found online at: https://www.frontiersin.org/articles/10.3389/feart.2021.716970/full#supplementary-material

REFERENCES

Agusto, M., and Varekamp, J. (2016). "The Copahue Volcanic-Hydrothermal System and Applications for Volcanic Surveillance," in *Copahue Volcano, Active Volcanoes of the World*. Editors F. Tassi, O. Vaselli, and A. T. Caselli (Berlin Heidelberg: Springer), 199–238. doi:10.1007/978-3-662-48005-2_9

Alvarado, G. E. (2009). Los volcanes de Costa Rica: Geología, historia, riqueza natural y su gente. *Univ. Estatal A Distancia* Vol. 32 (3). Costa Rica.

Azimi, G., and Papangelakis, V. G. (2010). The Solubility of gypsum and Anhydrite in Simulated Laterite Pressure Acid Leach Solutions up to 250°C. *Hydrometallurgy* 102 (1-4), 1–13. doi:10.1016/j.hydromet.2009.12.009

Barberi, F., Bertagnini, A., Landi, P., and Principe, C. (1992). A Review on Phreatic Eruptions and Their Precursors. *Hydrometallurgy* 102, 231–246. doi:10.1016/0377-0273(92)90046-G(

Bernard, A., Escobar, C. D., Mazot, A., and Gutierrez, R. E. (2004). "The Acid Volcanic lake of Santa Ana Volcano, El Salvador," in *Natural Hazards in El Salvador*. Editors W. I. Rose, J. J. Bommer, D. L. López, M. J. Carr, and J. J. Major (Geological Society of America), Special paper, Vol. 375, 121–134. doi:10.1130/0-8137-2375-2.121

Brantley, S. L., Borgiatt, A., Rowe, G., Fernández, J. F., and Reynolds, J. R. (1987). Poás Volcano Crater lake Acts as a Condenser for Acid Metal-Rich Brine. *Nature* 330, 470–472. doi:10.1038/330470a0

Brown, G. C., Rymer, H., and Stevenson, D. (1991). Volcano Monitoring by Microgravity and Energy Budget Analysis. *J. Geol. Soc.* 148, 585–593. doi:10.1144/gsjgs.148.3.0585

Brown, G., Rymer, H., Dowden, J., Kapadia, P., Stevenson, D., Barquero, J., et al. (1989). Energy Budget Analysis for Poás Crater lake: Implications for Predicting Volcanic Activity. *Nature* 339, 370–373. doi:10.1038/339370a0

Capaccioni, B., Rouwet, D., and Tassi, F. (2017). HCl Degassing from Extremely Acidic Crater Lakes: Preliminary Results from Experimental Determinations and Implications for Geochemical Monitoring. *Geol. Soc. Lond. Spec. Publications* 437, 97–106. doi:10.1144/SP437.12

Carr, M. J., Feigenson, M. D., Bolge, L. L., Walker, J. A., and Gazel, E. (2013). RU_CAGeochem, a Database and Sample Repository for Central American Volcanic Rocks at Rutgers University. *Earth Chem. Libr.* 1 (1), 43–48. doi:10.1594/IEDA/100403

Christenson, B., and Tassi, F. (2015). "Gases in Volcanic lake Environments," in *Volcanic Lakes*. Editors D. Rouwet, B. W. Christenson, F. Tassi, and

J. Vandemeulebrouck (Heidelberg: Springer), 125–153. doi:10.1007/978-3-642-36833-2_5

Christenson, B. W. (2000). Geochemistry of Fluids Associated with the 1995-1996 Eruption of Mt. Ruapehu, New Zealand: Signatures and Processes in the Magmatic-Hydrothermal System. *J. Volcanology Geothermal Res.* 97, 1–30. doi:10.1016/S0377-0273(99)00167-5

Christenson, B. W., Reyes, A. G., Young, R., Moebis, A., Sherburn, S., Cole-Baker, J., et al. (2010). Cyclic Processes and Factors Leading to Phreatic Eruption Events: Insights from the 25 September 2007 Eruption through Ruapehu Crater Lake, New Zealand. *J. Volcanology Geothermal Res.* 191, 15–32. doi:10.1016/j.volgeores.2010.01.00810.1016/j.jvolgeores.2010.01.008

Cigolini, C., Kudo, A. M., Brookins, D. G., and Ward, D. (1991). The Petrology of Poás Volcano Lavas: basalt-andesite Relationship and Their Petrogenesis within the Magmatic Arc of Costa Rica. *J. Volcanology Geothermal Res.* 48, 367–384. doi:10.1016/0377-0273(91)90052-2

Colvin, A., Rose, W. I., Varekamp, J. C., Palma, J. L., Escobar, D., Gutierrez, E., et al. (2013). "Crater Lake Evolution at Santa Ana Volcano (El Salvador) Following the 2005 Eruption," in *Understanding Open-Vent Volcanism and Related Hazards*. Editors W. I. Rose, J. L. Palma, H. D. Granados, and N. Varley (Boulder, CO: Geological Society of America), 23–43. doi:10.1130/2013.2498(02

de Moor, J. M., Aiuppa, A., Pacheco, J., Avard, G., Kern, C., Liuzzo, M., et al. (2016). Short-period Volcanic Gas Precursors to Phreatic Eruptions: Insights from Poás Volcano, Costa Rica. *Earth Planet. Sci. Lett.* 442, 218–227. doi:10.1016/j.epsl.2016.02.056

Delmelle, P., and Bernard, A. (1994). Geochemistry, Mineralogy, and Chemical Modeling of the Acid Crater lake of Kawah Ijen Volcano, Indonesia. *Geochimica et Cosmochimica Acta* 58, 2445–2460. doi:10.1016/0016-7037(94)90023-X

Dutrizac, J. E. (2017). The Behaviour of the Rare Earth Elements during gypsum (CaSO 4 ·2H 2 O) Precipitation. *Hydrometallurgy* 174, 38–46. doi:10.1016/j.hydromet.2017.09.013

Fischer, T. P., Ramírez, C., Mora-Amador, R. A., Hilton, D. R., Barnes, J. D., Sharp, Z. D., et al. (2015). Temporal Variations in Fumarole Gas Chemistry at Poás Volcano, Costa Rica. *J. Volcanology Geothermal Res.* 294, 56–70. doi:10.1016/j.jvolgeores.2015.02.002

Giggenbach, W. F., and Glover, R. B. (1975). The Use of Chemical Indicators in the Surveillance of Volcanic Activity Affecting the Crater Lake on Mt Ruapehu, New Zealand. *Bull. Volcanol* 39, 70–81. doi:10.1007/BF02596947

Hikov, A. (20152015). "Behaviour of Inert (Immobile) Elements in Extremely Acid Leaching: an Example from Asarel Porphyry Copper deposit," in GEOSCIENCES 2015, Proceedings of Jubilee national Conference (Sofia, 65–66. 10-11.12

Hilton, D. R., Ram‍Iacute;Rez, C. J., Mora-Amador, R., Fischer, T. P., F‍Uuml;Ri, E., Barry, P. H., et al. (2010). Monitoring of Temporal and Spatial Variations in Fumarole Helium and Carbon Dioxide Characteristics at Po‍aacute;s and Turrialba Volcanoes, Costa Rica (2001-2009). *Geochem. J.* 44, 431–440. doi:10.2343/geochemj.1.0085

Inguaggiato, C., Burbano, V., Rouwet, D., and Garzón, G. (2017). Geochemical Processes Assessed by Rare Earth Elements Fractionation at "Laguna Verde" Acidic-Sulphate Crater lake (Azufral Volcano, Colombia). *Appl. Geochem.* 79, 65–74. doi:10.1016/j.apgeochem.2017.02.013

Inguaggiato, C., Censi, P., Zuddas, P., Londoño, J. M., Chacón, Z., Alzate, D., et al. (2015). Geochemistry of REE, Zr and Hf in a wide range of pH and water composition: The Nevado del Ruiz volcano-hydrothermal system (Colombia). *Chem. Geology.* 417, 125–133. doi:10.1016/j.chemgeo.2015.09.025

Inguaggiato, C., Iñiguez, E., Peiffer, L., Kretzschmar, T., Brusca, L., Mora-Amador, R., et al. (2018). REE Fractionation during the gypsum Crystallization in Hyperacid Sulphate-Rich Brine: The Poás Volcano Crater lake (Costa Rica) Exploited as Laboratory. *Gondwana Res.* 59, 87–96. doi:10.1016/j.gr.2018.02.022

Inguaggiato, C., Pappaterra, S., Peiffer, L., Apollaro, C., Brusca, L., De Rosa, R., et al. (2020a). Mobility of REE from a Hyperacid Brine to Secondary Minerals Precipitated in a Volcanic Hydrothermal System: Kawah Ijen Crater lake (Java, Indonesia). *Sci. Total Environ.* 740, 140133–140214. doi:10.1016/j.scitotenv.2020.140133

Inguaggiato, C., Pérez García, M. Á., Meza Maldonado, L. F., Peiffer, L., Pappaterra, S., and Brusca, L. (2020b). Precipitation of Secondary Minerals in Acid Sulphate-Chloride Waters Traced by Major, Minor and Rare Earth Elements in Waters: The Case of Puracé Volcano (Colombia). *J. Volcanology Geothermal Res.* 407, 107106–107110. doi:10.1016/j.jvolgeores.2020.107106

Kalacheva, E., Taran, Y., Kotenko, T.Y., Oi, T., Honda, T., et al. (20151993). Geochemistry and Solute Fluxes of Volcano-Hydrothermal Systems of Shiashkotan, Kuril IslandsLanthanoid Abundances of Acidic Hot spring and Crater lake Waters in the Kusatsu-Shirane Volcano Region, Japan. *J. Volcanology Geothermal ResearchGeochem. J.* 29627, 4019–5433. doi:10.1016/j.jvolgeores.2015.03.010Kikawada10.2343/geochemj.27.19

Kikawada, Y., Uruga, M., Oi, T., and Honda, T. (2004). Mobility of Lanthanides Accompanying the Formation of Alunite Group Minerals. *J. Radioanal. Nucl. Chem.* 261 (3), 651–659. doi:10.1023/B:JRNC.0000037109.34238.cc

Kilgour, G., V. Manville, V., Pasqua, F. D., A. Graettinger, A., Hodgson, K. A., and Jolly, G. E. (2010). The 25 September 2007 Eruption of Mount Ruapehu, New Zealand: Directed Ballistics, Surtseyan Jets, and Ice-Slurry Lahars. *J. Volcanology Geothermal Res.* 191 (12), 1–14. doi:10.1016/j.jvolgeores.2009.10.015

Lewis, A. J., Palmer, M. R., Sturchio, N. C., and Kemp, A. J. (1997). The Rare Earth Element Geochemistry of Acid-Sulphate and Acid-Sulphate-Chloride Geothermal Systems from Yellowstone National Park, Wyoming, USA. *Geochimica et Cosmochimica Acta* 61, 695–706. doi:10.1016/S0016-7037(96)00384-5

Manville, V. (2015). "Volcano-hydrologic Hazards from Volcanic Lakes," in *Volcanic Lakes*. Editors D. Rouwet, B. W. Christenson, F. Tassi, and J. Vandemeulebrouck (Heidelberg: Springer), 21–71. doi:10.1007/978-3-642-36833-2_2

Martínez, M., Fernández, E., Valdés, J., Barboza, V., Van der Laat, R., Duarte, E., et al. (2000). Chemical Evolution and Volcanic Activity of the Active Crater lake of Poás Volcano, Costa Rica, 1993–1997. *J. Volcanol. Geochem. Res.* 97, 127–141. doi:10.1016/S0377-0273(99)00165-1

Martinez, M. (2008). *Geochemical Evolution of the Acidic Crater lake of Poás Volcano (Costa Rica): Insight into Volcanic-Hydrothermal Processes*. Thesis, Universiteit Utrecht: Ph.D., 162p.

Michard, A. (1989). Rare Earth Element Systematics in Hydrothermal Fluids. *Geochimica et Cosmochimica Acta* 53, 745–750. doi:10.1016/0016-7037(89)90017-3

Moor, J. M., Stix, J., Avard, G., Muller, C., Corrales, E., Diaz, J. A., et al. (2019). Insights on Hydrothermal-Magmatic Interactions and Eruptive Processes at Poás Volcano (Costa Rica) from High-Frequency Gas Monitoring and Drone Measurements. *Geophys. Res. Lett.* 46, 1293–1302. doi:10.1029/2018GL080301

Mora Amador, R. A., Rouwet, D., Vargas, P., and Oppenheimer, C. (2019b). "The Extraordinary Sulfur Volcanism of Poás from 1828 to 2018," in *Poás Volcano (Costa Rica): The Pulsing Heart of Central America Volcanic Zone.* Editors F. Tassi, R. Mora-Amador, and O. Vaselli (Heidelberg): Springer), 45–78. doi:10.1007/978-3-319-02156-010.1007/978-3-319-02156-0_3

Mora-Amador, R. A. (2010). *Peligrosidad volcánica del Poás (Costa Rica), basado en las principales erupciones históricas de 1834, 1910 y 1953–1955*. M.Sc. Thesis, Universidad de Costa Rica, 115.

Mora-Amador, R. A., Rouwet, D., González, G., Vargas, P., and Ramírez, C. (2019a). "Poás Volcano," in *Poás Volcano (Costa Rica): The Pulsing Heart of Central America Volcanic Zone.* Editors F. Tassi, R. Mora-Amador, and O. Vaselli (Heidelberg): Springer), 45–78. doi:10.1007/978-3-319-02156-0

Morton-Bermea, O., Aurora Armienta1, M., and Ramos, S. (2010). Rare-earth Element Distribution in Water from El Chichón Volcano Crater Lake, Chiapas Mexico. *GeofInt* 49 (1), 43–54. doi:10.22201/igeof.00167169p.2010.49.1.1474

Ohba, T., Hirabayashi, J.-i., and Nogami, K. (2008). Temporal Changes in the Chemistry of lake Water within Yugama Crater, Kusatsu-Shirane Volcano, Japan: Implications for the Evolution of the Magmatic Hydrothermal System. *J. Volcanology Geothermal Res.* 178, 131–144. doi:10.1016/j.jvolgeores.2008.06.015

Oppenheimer, C. (1992). Sulphur Eruptions at Volcán Poás, Costa Rica. *J. Volcanology Geothermal Res.* 49, 1–21. doi:10.1016/0377-0273(92)90002-U

Oppenheimer, C. (1993). Thermal Distributions of Hot Volcanic Surfaces Constrained Using Three Infrared Bands of Remote Sensing Data. *Geophys. Res. Lett.* 20, 431–434. doi:10.1029/93GL00500

OVSICORI (2021). Open Reports OVSICORI-UNA, Costa Rica. http://www.ovsicori.una.ac.cr.

Pasternack, G. B., and Varekamp, J. C. (1997). Volcanic lake Systematics I. Physical Constraints. *Bull. Volcanology* 58, 528–538. doi:10.1007/s004450050160

Peiffer, L., Taran, Y. A., Lounejeva, E., Solís-Pichardo, G., Rouwet, D., and Bernard-Romero, R. A. (2011). Tracing thermal Aquifers of El Chichón Volcano-Hydrothermal System (México) with 87Sr/86Sr, Ca/Sr and REE. *J. Volcanology Geothermal Res.* 205, 55–66. doi:10.1016/j.jvolgeores.2011.06.004

Prosser, J. T., and Carr, M. J. (1987). Poás Volcano, Costa Rica: Geology of the summit Region and Spatial and Temporal Variations Among the Most Recent Lavas. *J. Volcanology Geothermal Res.* 33, 131–146. doi:10.1016/0377-0273(87)90057-6

Rodríguez, A., and van Bergen, M. J. (2017). Superficial Alteration Mineralogy in Active Volcanic Systems: An Example of Poás Volcano, Costa Rica. *J. Volcanology Geothermal Res.* 346, 54–80. doi:10.1016/j.jvolgeores.2017.04.006

Rouwet, D. (2021). "Forecasting and Planning for Volcanic Hazards, Risks, and Disasters,". Editor P. Papale, 439, 471. Hazard and Disasters 2. doi:10.1016/C2018-0-02632-8

Rouwet, D., Mora Amador, R. A., Sandri, L., Ramírez-Umaña, C., González, G., Pecoraino, G., et al. (2019). "39 Years of Geochemical Monitoring of Laguna Caliente Crater Lake, Poás: Patterns from the Past as Keys for the Future," in *Poás Volcano (Costa Rica): The Pulsing Heart of Central America Volcanic Zone*. Editors F. Tassi, R. Mora-Amador, and O. Vaselli (Heidelberg): Springer), 213–233. doi:10.1007/978-3-319-02156-0_9

Rouwet, D., Mora-Amador, R., Ramírez-Umaña, C. J., González, G., and Inguaggiato, S. (2017). "Dynamic Fluid Recycling at Laguna Caliente (Poás, Costa Rica) before and during the 2006-ongoing Phreatic Eruption Cycle (2005-10)," in *Geochemistry and Geophysics of Active Volcanic Lakes*. Editors T. Ohba, B. Capaccioni, and C. Caudron (Geological Society of London, Special Publications), 437, 73–96. doi:10.1144/SP437.11

Rouwet, D., Taran, Y., Inguaggiato, S., Varley, N., and Santiago Santiago, J. A. (2008). Hydrochemical Dynamics of the "lake-spring" System in the Crater of El Chichón Volcano (Chiapas, Mexico). *J. Volcanology Geothermal Res.* 178, 237–248. doi:10.1016/j.jvolgeores.2008.06.026

Rouwet, D., Tassi, F., Mora-Amador, R., Sandri, L., and Chiarini, V. (2014). Past, Present and Future of Volcanic lake Monitoring. *J. Volcanology Geothermal Res.* 272, 78–97. doi:10.1016/j.jvolgeores.2013.12.009

Rowe, G. L., Brantley, S. L., Fernandez, J. F., and Borgia, A. (1995). The Chemical and Hydrologic Structure of Poa´s Volcano, Costa Rica. *J. Volcanology Geothermal Res.* 64, 233–267. doi:10.1016/0377-0273(94)00079-V

Rowe, G. L., Brantley, S. L., Fernández, M., Fernández, J. F., Borgia, A., and Barquero, J. (1992a). Fluid-volcano Interaction in an Active Stratovolcano: the Crater lake System of Poás Volcano, Costa Rica. *J. Volcanology Geothermal Res.* 64, 233–267. doi:10.1016/0377-0273(92)90003-V

Rowe, G. L., Ohsawa, S., Takano, B., Brantley, S. L., Fernández, J. F., and Barquero, J. (1992b). Using Crater Lake Chemistry to Predict Volcanic Activity at Poás Volcano, Costa Rica. *Bull. Volcanol* 54, 494–503. doi:10.1007/BF00301395

Ruíz, P., Gazel, E., Alvarado, G. E., Carr, M. J., and Soto, G. J. (2010). Caracterización geoquímica y petrográfica de las unidades geológicas del macizo del volcán Poás, Costa Rica. *Rev. Geol. Amér. Cent.* 43, 37–66. doi:10.15517/RGAC.V0I43.3457

Ruíz, P., Mana, S., Gazel, E., Soto, G. J., Carr, M. J., and Alvarado, G. E. (2019). "Geochemical and Geochronological Characterisation of the Poas Stratovolcano Stratigraphy," in *Poás Volcano (Costa Rica): The Pulsing Heart of Central America Volcanic Zone*. Editors F. Tassi, R. Mora-Amador, and O. Vaselli (Heidelberg): Springer), 13–43. doi:10.1007/978-3-319-02156-0_2

Rymer, H., Locke, C. A., Borgia, A., Martínez, M., Brenes, J., Van der Laat, R., et al. (2009). Long-term Fluctuations in Volcanic Activity: Implications for Future Environmental Impact. *Terra Nova* 21, 304–309. doi:10.1111/j.1365-3121.2009.00885.x

Sanford, W. E., Konikow, L. F., Rowe, G. L., and Brantley, S. L. (1995). Groundwater Transport of Crater-lake Brine at Poa´s Volcano, Costa Rica. *J. Volcanology Geothermal Res.* 64, 269–293. doi:10.1016/0377-0273(94)00080-Z

Stix, J., and de Moor, J. M. (2018). Understanding and Forecasting Phreatic Eruptions Driven by Magmatic Degassing. *Earth Planets Space* 70, 83. doi:10.1186/s40623-018-0855-z

Takano, B., Saitoh, H., and Takano, E. (1994). Geochemical Implications of Subaqueous Molten Sulfur at Yugama Crater lake, Kusatsu-Shirane Volcano, Japan. *Geochem. J.* 28, 199–216. doi:10.2343/geochemj.28.199

Takano, B., Suzuki, K., Sugimori, K., Ohba, T., Fazlullin, S. M., Bernard, A., et al. (2004). Bathymetric and Geochemical Investigation of Kawah Ijen Crater Lake, East Java, Indonesia. *J. Volcanology Geothermal Res.* 135, 299–329. doi:10.1016/j.jvolgeores.2004.03.008

Taran, Y., Rouwet, D., Inguaggiato, S., and Aiuppa, A. (2008). Major and Trace Element Geochemistry of Neutral and Acidic thermal Springs at El Chichón Volcano, Mexico. *J. Volcanology Geothermal Res.* 178, 224–236. doi:10.1016/j.jvolgeores.2008.06.030

Universidad de Costa Rica (2021). Reportes Volcanicos. Available at: https://rsn.ucr.ac.cr.

van Hinsberg, V., Berlo, K., and Lowenstern, J. (2020). An Experimental Investigation of Interaction between Andesite and Hyperacidic Volcanic Lake Water. *Minerals* 10, 96–21. doi:10.3390/min10020096

van Hinsberg, V., Berlo, K., Sumarti, S., Van Bergen, M., and Williams-Jones, A. (2010). Extreme Alteration by Hyperacidic Brines at Kawah Ijen Volcano, East Java, Indonesia: II. *J. Volcanology Geothermal Res.* 196, 169–184. doi:10.1016/j.jvolgeores.2010.07.004

van Hinsberg, V., Vigouroux, N., Palmer, S., Berlo, K., Mauri, G., Williams-Jones, A., et al. (2017). "Element Flux to the Environment of the Passively Degassing Crater lake-hosting Kawah Ijen Volcano, Indonesia, and Implications for Estimates of the Global Volcanic Flux for Estimates of the Global Volcanic Flux," in *Geochemistry and Geophysics of Active Volcanic Lakes*. Editors T. Ohba, B. Capaccioni, and C. Caudron (London: Geological Society, Special Publications), 437, 9–34. doi:10.1144/SP437.21

Vannucchi, P., and Morgan, J. P. (2019). "Overview of the Tectonics and Geodynamics of Costa Rica," in *Poás Volcano (Costa Rica): The Pulsing Heart of Central America Volcanic Zone*. Editors F. Tassi, R. Mora-Amador, and O. Vaselli (Heidelberg: Springer), 1–12. doi:10.1007/978-3-319-02156-0_1

Varekamp, J. C., Ouimette, A. P., Herman, S. W., Flynn, K. S., Bermudez, A., and Delpino, D. (2009). Naturally Acid Waters from Copahue Volcano, Argentina. *Appl. Geochem.* 24 (2), 208–220. doi:10.1016/j.apgeochem.2008.11.018

Varekamp, J. C., Pasternack, G. B., and Rowe, G. L. (2000). Volcanic lake Systematics II. Chemical Constraints. *J. Volcanology Geothermal Res.* 97, 161–179. doi:10.1016/S0377-0273(99)00182-1

Varekamp, J. C. (2015). "The Chemical Composition and Evolution of Volcanic Lakes," in *Volcanic Lakes*. Editors D. Rouwet, B. W. Christenson, F. Tassi, and J. Vandemeulebrouck (Heidelberg: Springer), 93–123. doi:10.1007/978-3-642-36833-2_

Vaselli, O., Tassi, F., Fischer, T. P., Tardani, D., Fernández, E., del Mar Martínez, M., et al. (2019). "The Last Eighteen Years (1998-2014) of Fumarolic Degassing at the Poás Volcano (Costa Rica) and Renewal Activity," in *Poás Volcano (Costa Rica): The Pulsing Heart of Central America Volcanic Zone*. Editors F. Tassi, R. Mora-Amador, and O. Vaselli (Heidelberg): Springer), 235–260. doi:10.1007/978-3-319-02156-010.1007/978-3-319-02156-0_10

Vaselli, O., Tassi, F., Minissale, A., Montegrossi, G., Duarte, E., Fernández, E., et al. (2003). "Fumarole Migration and Fluid Geochemistry at Poás Volcano (Costa Rica) from 1998 to 2001," in *Volcanic Degassing. Special Publications*. Editors C. Oppenheimer, D. M. Pyle, and J. Barkley, 213, 247–262. doi:10.1144/GSL.SP.2003.213.01.15*Geol. Soc. Lond. Spec. Publications*

von Frantzius, A. (1861). "Aporte al Conocimiento de los Volcanes de Costa Rica, Escalamiento al Volcán Poás, marzo 1860–1979," in *Volcán Poás*. Editor C. Vargas (San Jose: UNED), 11–34.

Woitischek, J., Dietzel, M., Inguaggiato, C., Böttcher, M. E., Leis, A., Cruz, J. V., et al. (2017). Characterisation and Origin of Hydrothermal Waters at São Miguel (Azores) Inferred by Chemical and Isotopic Composition.

J. Volcanology Geothermal Res. 346, 104–117. doi:10.1016/j.jvolgeores.2017.03.020

Wood, S. A. (2006). Rare Earth Element Systematics of Acidic Geothermal Waters from the Taupo Volcanic Zone, New Zealand. *J. Geochemical Exploration* 89, 424–427. doi:10.1016/j.gexplo.2005.11.023

Zlotnicki, J., Sasai, Y., Toutain, J. P., Villacorte, E. U., Bernard, A., Sabit, J. P., et al. (2009). Combined Electromagnetic, Geochemical and thermal Surveys of Taal Volcano (Philippines) during the Period 2005-2006. *Bull. Volcanol.* 71, 29–47. doi:10.1007/s00445-008-0205-2

Conflict of Interest: The authors declare that the research was conducted in the absence of any commercial or financial relationships that could be construed as a potential conflict of interest.

Publisher's Note: All claims expressed in this article are solely those of the authors and do not necessarily represent those of their affiliated organizations, or those of the publisher, the editors and the reviewers. Any product that may be evaluated in this article, or claim that may be made by its manufacturer, is not guaranteed or endorsed by the publisher.

frontiers in Earth Science

ORIGINAL RESEARCH
published: 03 January 2022
doi: 10.3389/feart.2021.751216

Selected Crater and Small Caldera Lakes in Alaska: Characteristics and Hazards

*Christopher F. Waythomas**

US Geological Survey, Alaska Volcano Observatory, Anchorage, AK, United States

This study addresses the characteristics, potential hazards, and both eruptive and non-eruptive role of water at selected volcanic crater lakes in Alaska. Crater lakes are an important feature of some stratovolcanoes in Alaska. Of the volcanoes in the state with known Holocene eruptive activity, about one third have summit crater lakes. Also included are two volcanoes with small caldera lakes (Katmai, Kaguyak). The lakes play an important but not well studied role in influencing eruptive behavior and pose some significant hydrologic hazards. Floods from crater lakes in Alaska are evaluated by estimating maximum potential crater lake water volumes and peak outflow discharge with a dam-break model. Some recent eruptions and hydrologic events that involved crater lakes also are reviewed. The large volumes of water potentially hosted by crater lakes in Alaska indicate that significant flowage hazards resulting from catastrophic breaching of crater rims are possible. Estimates of maximum peak flood discharge associated with breaching of lake-filled craters derived from dam-break modeling indicate that flood magnitudes could be as large as 10^3–10^6 m^3/s if summit crater lakes drain rapidly when at maximum volume. Many of the Alaska crater lakes discussed are situated in hydrothermally altered craters characterized by complex assemblages of stratified unconsolidated volcaniclastic deposits, in a region known for large magnitude (>M7) earthquakes. Although there are only a few historical examples of eruptions involving crater lakes in Alaska, these provide noteworthy examples of the role of external water in cooling pyroclastic deposits, acidic crater-lake drainage, and water-related hazards such as lahars and base surge.

Keywords: Alaska, crater lakes, hazards, floods, eruptions

OPEN ACCESS

Edited by:
Dmitri Rouwet,
Istituto Nazionale di Geofisica e Vulcanologia, Italy

Reviewed by:
Vern Manville,
University of Leeds, United Kingdom
Valerio Acocella,
Roma Tre University, Italy

****Correspondence:***
Christopher F. Waythomas
cwaythomas@usgs.gov

Specialty section:
This article was submitted to Volcanology, a section of the journal Frontiers in Earth Science

Received: *31 July 2021*
Accepted: *11 October 2021*
Published: *03 January 2022*

Citation:
Waythomas CF (2022) Selected Crater and Small Caldera Lakes in Alaska: Characteristics and Hazards. Front. Earth Sci. 9:751216. doi: 10.3389/feart.2021.751216

1 INTRODUCTION

Volcanic crater lakes are distinguishing features of many active stratovolcanoes in Alaska and elsewhere (Christenson et al., 2015). Crater lakes commonly form after crater-forming eruptions where local volcanic and hydrologic conditions permit the development of confined lakes within the crater itself. Eruptions through crater lakes pose a special type of hazard because of the potential for explosivity associated with magma-water interaction and the possibility for voluminous water-rich mass flows that can develop if lake water is explosively expelled from its host crater or produced by catastrophic breaching of the crater wall (Mastin and Witter, 2000; Manville et al., 2007). The hazards associated with volcanic crater lakes beyond Alaska have received some study especially in locations where people and infrastructure are at risk (Mastin and Witter, 2000; Manville, 2010; Manville, 2015, and references therein). In New Zealand, partial failure of the rim of Crater Lake at Mount Ruapehu in 1953 caused a significant flood and lahar that resulted in 151 fatalities (Manville et al., 2007)

FIGURE 1 | Location of crater and small caldera lakes in Alaska discussed in this study. The Alaska Peninsula is abbreviated AK Pen.

highlighting the importance of catastrophic crater lake drainage. These works and others (Neall, 1996; Strehlow et al., 2017; Rouwet, 2021) have noted the hazard implications of large volumes of water within the craters of active volcanoes and this is in part the motivation to evaluate hydrologic hazards at crater lakes in Alaska.

In Alaska, volcanic craters that contain lakes are present at several locations throughout the Aleutian Arc (**Figure 1**). However, the hydrologic hazards and consequences of eruptions involving these lakes have received little study. The volume of water present in existing crater lakes in Alaska (**Table 1**) indicates that there could be significant hydrologic consequences associated with eruptive activity through water, or failure of crater rims. To address potential hazards and lake water eruption interactions, existing information about a representative sampling of crater and small caldera lakes in Alaska is synthesized and the potential hydrologic hazards associated with failure of crater walls leading to large dam-break type floods is evaluated. Not all crater and caldera lakes in the Aleutian arc are included here. The sampling of study locations provides examples of the main types of crater or potential crater lake settings found in Alaska. Maar craters are also not evaluated because they are uncommon in Alaska, although a maar crater lake drainage event did occur in Aniakchak caldera (McGimsey et al., 2014). Information about some plausible hydrologic hazards associated with drainage of lakes at Okmok and Aniakchak can be found in Larsen et al. (2015) and Neal et al. (2001). Several recent Alaska examples of eruptions and hydrologic events that involved crater lakes also are reviewed to illustrate the role of lake water in influencing eruptive processes and hazardous hydrologic phenomena.

To date, there has been no systematic examination of crater lakes in the Aleutian Arc and thus the potential consequences of water bodies situated at the summit of active high-relief stratovolcanoes are not specifically known. The goal of this work is to establish some of the physical parameters involved with catastrophic release of water from crater lakes and to present examples of recent unrest where crater lakes had or were suspected of playing an important role during unrest. The first part of the study will address breaching of crater rims and associated water floods using a dam-break modeling approach. The second part of the study will focus on lake water involvement in the eruption process and associated hazards. Recent unrest at Kasatochi, Korovin, Makushin, and the north crater of Cerberus volcano, in Alaska (**Figure 1**) have raised numerous questions about the role and fate of external water in augmenting potential hazards during explosive eruptive activity and provide further motivation for this study. Although many of the drainages downstream from crater lakes described here are uninhabited with little infrastructure, these areas are visited seasonally and some contain significant biological resources (fish, wildlife, and habitat) that could be adversely affected by floods originating at crater lakes (Schaefer et al., 2008).

The volcanic craters discussed here are <1 km in diameter which roughly differentiates them from calderas which are larger (Francis, 1976). In Alaska, crater lakes are somewhat uncommon among the historically active volcanoes in the Aleutian Arc and of the volcanoes active during the Holocene, roughly one-third have summit crater lakes (**Table 1**), including two which are small caldera lakes (Katmai, Kaguyak). Kaguyak volcano has a summit caldera that is slightly larger than 1 km in diameter but is included here because it contains a large lake whose surface is close to a pronounced low point along the caldera rim (**Figure 2**). The volcano also has a documented history of explosive dome-forming eruptions of Holocene age (Fierstein and Hildreth, 2008); should similar eruptions occur in the future, they likely would be capable of displacing lake water that could overtop the caldera rim.

Previous studies of Holocene calderas in the Aleutian Arc have identified evidence for large caldera lake floods associated with catastrophic breaching of caldera rims at Aniakchak, Okmok and Fisher calderas (Waythomas et al., 1996; Wolfe, 2001; Stelling et al., 2005). These examples and other large calderas in Alaska will not be discussed further here as the focus of this study is on crater lakes and small caldera lakes that

TABLE 1 | Characteristics of volcanic crater lakes in Alaska. Volume estimates made from IfSAR digital elevation data; * indicates volume estimate based on crater depth multiplied by crater area at the spillover elevation.[#] Indicates volume estimate based on formula for a truncated cone, $V = {}^{1}/_{3}\,\pi d\,[(r^2 + r)(R + R^2)]$ where V is volume, r is bottom radius, R is top radius at the spillover elevation and d is depth. [@] Indicates volume estimate derived from DEM raster volume calculation in Qgis. These estimates do not include the volume of modern lakes. Maximum potential crater lake volume in bold indicates value used in peak discharge calculation.

Volcano and timing of last known eruptive activity	Coordinates	Crater/ caldera area (m^2)	Maximum Crater/ caldera depth (m)	Modern lake area (m^2)	Maximum potential crater lake volume* (m^3)	Maximum potential crater lake volume[#] (m^3)	Maximum potential crater lake volume[@] (m^3)	Comments
Mount Spurr summit 5–6 ka	−152.251° W, 62.300° N	9×10^4	140	1.1×10^4	9.7×10^6	**8.6×10^6**	5.5×10^6	Crater lake is an ephemeral feature; present 2004–2006. Crater depth estimated from IfSar DEM.
Crater Peak 1992	−152.239° W, 61.265° N	3.6×10^5	40	5×10^4	1.4×10^7	1.3×10^7	**1.8×10^6**	Crater lake is an ephemeral feature; present 1978–1992. Crater depth estimated from IfSar DEM and is the minimum depth for lake spillover at the low point on the crater rim
Douglas Holocene?	−153.535° W,58.859° N	1.3×10^5	10	6.1×10^4	9.8×10^5	**1×10^6**	1.6×10^5	Area of crater at low point on crater rim = 97,672 m^2. Lake area is the average of four lake areas measured from satellite images obtained in 2012, 2014, 2019, and 2020
Kaguyak Holocene	−154.0245° W,58.6113° N	6.1×10^6	150	3.6×10^6	9×10^8	**8.3×10^8**	1.3×10^8	The modern lake has a volume of about 5×10^8 m^3
Katmai 1912	−155.2544° W 58.1946° N	9.4×10^6	470	5.4×10^6	3.5×10^9	**1.5×10^9**	2.1×10^8	The modern lake has a volume of at least 1×10^9 m^3
Mageik Holocene	−155.2544° W,58.1946° N	8.5×10^4	35	8.6×10^3	9×10^5	2.2×10^6	**3.1×10^5**	Area of crater at low point on crater rim = 25,710 m^2
Martin Holocene	−155.3566° W 58.1692° N	1.2×10^5	50	9.7×10^3	3.1×10^6	5.1×10^6	**1×10^6**	Area of crater at low point on crater rim = 62,019 m^2
Chiginagak Holocene	−156.9915° W,57.13348° N	2.1×10^5	40	9.4×10^4	2.9×10^6	**3.8×10^6**	1.3×10^6	Crater and lake area from 2009 satellite image.Area of crater at low point on crater rim = 73,400 m^2
Dana Holocene?	−161.2155° W 55.64205° N	2.7×10^6	40	5.8×10^5	2.3×10^7	**2.6×10^7**	3.6×10^5	The depth of the modern lake was estimated in the field
Hague Holocene	−161.9778° W 55.373074° N	1.6×10^5	90	1.3×10^4	1×10^7	1.3×10^7	**4.6×10^6**	Modern crater lake is ephemeral
Makushin 1995	−166.9320° W 53.88707° N	3.5×10^5	100	2.4×10^4	3.5×10^7	**1.9×10^6**	4.2×10^5	Dimensions from August 1, 2020, satellite image. Volume of modern lake unknown
Tana Holocene	−169.758° W 52.839° N	7.7×10^5	10	2.1×10^5	2.4×10^6	**3.4×10^6**	5.4×10^5	The volume of the modern lake is unknown
Herbert Holocene	−170.113° W 52.741° N	3.5×10^6	220	5.7×10^5	4.2×10^8	**3.5×10^8**	1.8×10^8	The volume of the modern lake is unknown
Korovin 1998	−174.1548° W 52.37934° N	3.7×10^5	140	1.6×10^4	3.6×10^7	9.4×10^6	**2.3×10^7**	Modern crater lake is ephemeral
Kasatochi 2008	−175.5113° W 52.1693° N	1.5×10^6	180	8.4×10^5	2.2×10^8	**2×10^8**	4.7×10^7	Dimensions based on November 22, 2020, satellite image
North crater, Cerberus 2021	−179.5856° W 51.935,588° N	1.5×10^7	120	$6–8 \times 10^3$	1.3×10^7	**7.4×10^6**	6.3×10^6	Modern crater lake is ephemeral

have no known catastrophic drainage events except for Chiginagak volcano which experiences repeated episodes of crater lake drainage (Schaefer et al., 2008).

2 METHODS

Crater and small caldera lakes in Alaska were evaluated using several approaches including consultation of photographic records, GIS analysis of digital elevation data, geologic maps, and previously published reports and articles. The methods and approaches used in this study are described briefly below and more fully in *Crater Stability and Susceptibility to Failure* and *Crater Rim Overtopping, Breach Formation, and Peak Flood Discharge*.

2.1 Historical Photographs of Crater Lakes in Alaska

The Alaska Volcano Observatory (AVO) has an extensive collection of photographs and satellite images of volcanoes throughout Alaska contributed by AVO scientists and other observers. This database (Cameron and Snedigar, 2016) was consulted for representative photographs of the crater and caldera lakes described in this paper. Most of the photographs are relatively recent images of the lakes and thus show the near

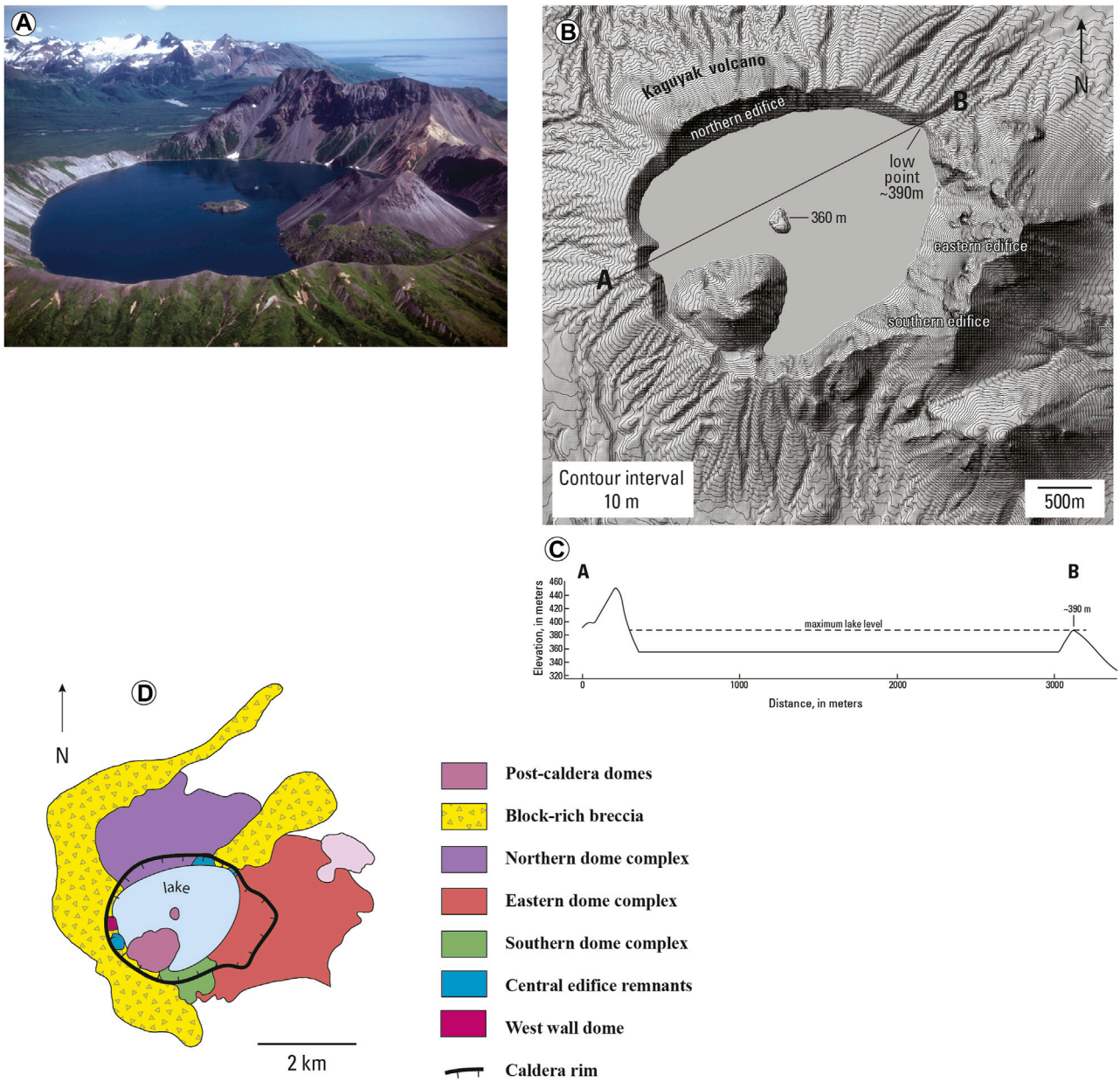

FIGURE 2 | Photograph, ifSAR derived topographic map, cross section, and generalized geologic map of Kaguyak caldera. **(A)**. Photograph of lake-filled caldera, August 1982. Photo by C.J. Nye, AVO. **(B)**. IfSAR derived topographic map of lake-filled caldera of Kaguyak volcano. **(C)**. Topographic profile from southwest to northeast across Kaguyak caldera. **(D)**. Generalized geologic map of Kaguyak volcano. Modified from Fierstein and Hildreth, 2008.

present configurations of the water bodies. Most of these photographs are shown in the **Supplementary Figures** that accompany this paper.

2.2 GIS Analysis and Volume Estimates of Crater Lakes

Spatial information about Alaska crater lakes is presented in the form of topographic maps and cross sections generated from 5 m-resolution ifSAR elevation data acquired 2012–2019 (Carswell, 2013). Digital elevation data for each crater lake was processed in Qgis where hillshade renderings and contour maps were constructed. The digital elevation data was used to identify the lowest point along the crater rim where spillover of lake water would likely occur, if the crater were filled to capacity. Topographic cross sections also were generated in Qgis through each crater rim low point; the cross sections provide a two-dimensional representation of each crater and are shown in the **Supplementary Figures** that accompany this paper. The maximum crater lake area was taken as the elevation contour

corresponding to the lowest point on the crater rim. The maximum potential lake depth was approximated as the elevation difference between the crater rim low point and the crater floor elevation including the lake depth if known or estimated. The maximum crater lake area multiplied by the depth gives a maximum theoretical lake volume estimate (**Table 1**) which is considered an upper bound on lake volume as this estimate does not explicitly account for crater geometry. A second volume estimate was made by assuming a truncated cone for crater shape and using the formula, $V = \frac{1}{3}\pi d[(r^2 + r)(R + R^2)]$ to calculate maximum water volume (V), where r is bottom radius, R is top radius at the spillover elevation, and d is depth. In many instances the volume estimates are about the same (**Table 1**) but in a few cases (Douglas, Makushin) the values differ by more than a factor of 10. Photographs of these two crater lakes indicate that the crater shapes are better approximated by a truncated cone so the volume estimates resulting from application of the truncated cone formula are used for these two volcanoes in subsequent calculations described below. A third maximum potential lake volume estimate was made using the ifSAR digital elevation data and the raster surface volume algorithm in Qgis. This method does not include the present lake volume, but where known gives volume estimates roughly comparable to the estimates made by the other two methods (**Table 1**). In most cases, application of the formula for a truncated cone, where the lake bottom elevation is known or reasonably approximated, gives the plausible estimates for maximum potential lake volume because qualitatively, many of the craters look like truncated cones. In cases where modern lakes are absent or small in volume, the Qgis raster volume estimates of maximum potential lake volume were used for subsequent calculations of maximum peak discharge because these estimates are based on actual ifSAR derived topography. The values used for peak discharge estimates are shown in bold in **Table 1**.

2.3 Previous Studies of Crater Geology

Published geologic information was consulted to make first-order evaluations of crater rim conditions to provide insight into crater wall geology, stability and susceptibility to erosion or failure. At many of the locations discussed, geologic information is limited or nonexistent. The specific reports and articles consulted are given as references throughout *Crater Lakes in Alaska*.

2.4 Assessment of Crater Rim Stability and Crater Lake Hydrology

Volcanic crater rim stability and susceptibility to failure are discussed in *Crater Stability and Susceptibility to Failure* of this paper. To date, there have been no rigorous evaluations of the strength of lake-filled craters using any of the standard approaches for determining rock-mass strength and slope stability (Watters et al., 2000). A first-order attempt to evaluate the seismic effects on crater wall stability is presented in *Seismic Effects on Volcanic Crater Lakes*. To date there have been no systematic studies of Alaska crater lake hydrology although some general conclusions about the hydrologic characteristics of the lakes are possible. These are described further in *Volcanic Crater Lake Hydrology*.

2.5 Dam-Break Modeling of Floods From Lake-Filled Volcanic Craters

The approach used to estimate maximum peak discharge associated with floods from lake-filled craters in Alaska is described in *Crater Rim Overtopping, Breach Formation, and Peak Flood Discharge*. This was done to benefit from the context established by the review of lake-filled volcanic craters in Alaska presented in *Crater Lakes in Alaska* and the analysis of crater rim stability and hydrology presented in *Crater Stability and Susceptibility to Failure*. The basic approach to dam-break analysis is described in Waythomas et al. (1996) but modified here for application to crater lakes.

3 SELECTED CRATER LAKES IN ALASKA

3.1 Mount Spurr Volcano

Mount Spurr volcano is in the Cook Inlet region of south-central Alaska (**Figure 1**). The volcano consists of a stratified assemblage of andesite lava flows and lahar, pyroclastic-flow, and debris-avalanche deposits of late Quaternary age (Nye and Turner, 1990). These rock units are truncated by a horseshoe-shaped avalanche caldera of Holocene age that is open to the southeast (**Supplementary Figure S1**). The summit cone of Mount Spurr is heavily glaciated and rock outcrops on the upper flanks of the volcano are largely obscured by snow and ice. The volume of ice and perennial snow on Mount Spurr when measured in 1981 was 67 ± 17 km^3 (March et al., 1997). A period of elevated heat flow at the summit in 2004–2006 resulted in partial exhumation of a crater on the summit edifice and formation of a small lake within the crater with an interior volume (**Supplementary Figure S1**; Coombs et al., 2006). By the end of this event, a crater about 9.7×10^6 m^3 was visible at the summit of the volcano. A small lake developed on the floor of the crater (first observed in 2004), covering an area of about 11,540 m^2 by 2006 (**Supplementary Figure S1**). The maximum volume of a hypothetical lake in the summit crater is $5.5–9.7 \times 10^6$ m^3 (**Table 1**). The thermal excursion of 2004–2006 is the only known period associated with the exhumation and formation of a crater lake at the Mount Spurr summit. Previous thermal events did occur that partially exposed the summit crater (Coombs et al., 2006) but no lakes were reported.

Crater Peak is a basaltic–andesite satellite cone on the south flank of Mount Spurr volcano (**Supplementary Figure S2**). Crater Peak has been the active vent of Mount Spurr volcano for about the past 5–6 ka (Riehle 1985) and was the site of the two documented historical eruptions in 1953 and 1992 (Keith, 1995). The first known historical eruption occurred on July 9, 1953 (Juhle and Coulter, 1955; Miller et al., 1998). It is unknown if a lake occupied the floor of Crater Peak prior to the 1953 eruption, but for several decades prior to the eruption, plumes of whitish steam commonly were observed

rising from the summit of Crater Peak and pilots reported an increase in the vigor of steaming in late spring 1953 (Juhle and Coulter, 1955). The 1953 eruption was a single explosive burst lasting about 1 hour, and it generated an ash cloud that rose more than 10 km above sea level (Juhle and Coulter, 1955).

Aerial photographs taken in 1952, 1954, and 1957 show no lake on the floor of Crater Peak (**Supplementary Figure S2**). A 1970 visit to Crater Peak indicated a hot lake was present in the crater (Keith et al., 1995). A Landsat satellite image acquired on July 27, 1974, also shows no lake on the crater floor. An aerial photograph taken on August 8, 1978, shows a lake present on the crater floor (**Supplementary Figure S2d**) and opportunistic photographs in the AVO photo database show a lake present from 1982 until the first Crater Peak eruption in 1992 on June 27. Intermittent observations of Crater Peak from 1992 to the present have indicated that a lake has not reformed after the 1992 eruption.

The low point on the crater rim is about 1940 m above sea level and the depth from the low point to the crater floor is about 40 m. The area of the crater is about 360,450 m^2 and the maximum volume of a crater-filling lake is about 1.8–14 × 10^6 m^3 (**Table 1**). Observations and photographic evidence indicate that at no time was the lake ever much more than a shallow feature on the floor of Crater Peak covering an area of about 50,000 m^2.

3.2 Mount Douglas

Mount Douglas is located on the west side of the marine entrance to Cook Inlet (**Figure 1**). Douglas is an ice- and snow-covered stratovolcano (summit altitude 2,140 m) with a summit crater that contains a small lake (**Supplementary Figure S3**). Little is known about the geologic history of Douglas volcano, and it is uncertain when the last eruption of the volcano occurred and when the summit crater developed. Measurements made in 1991 indicated that the lake had a temperature of 25°C and a pH of ~1 (Motyka et al., 1993). The summit crater has an area of about 134,000 m^2 and the crater lake covers an area of about 61,470 m^2 (average of four measurements made from satellite images, **Table 1**). The low point on the crater rim is about 10 m above lake level, and the maximum crater volume at this level is about 9.8–10 × 10^5 m^3 (**Table 1**).

3.3 Mount Chiginagak

Mount Chiginagak is an ice and snow-clad stratovolcano on the Alaska Peninsula near Mother Goose Lake (**Figure 1**). The volcano is about 8 km in diameter and its summit has an elevation of 2,135 m above sea level. The summit crater contains a lake (**Supplementary Figure S4**) that episodically drains through a glaciated breach on the crater rim (Schaefer et al., 2008). The volcano has had no known historical eruptive activity, although fumaroles on the upper flanks of the edifice are occasionally quite vigorous. The volcano developed during the late Quaternary and lava flows, lahar, pyroclastic, tephra and debris-avalanche deposits of Holocene and Pleistocene age characterize the edifice (Schaefer et al., 2017). Rocks in the summit area are hydrothermally altered although the type and extent are not known (**Supplementary Figure S4**; Schaefer et al., 2017).

The summit crater of Chiginagak volcano has an area of about 215,610 m^2 although a pronounced glacial notch in the rim (**Supplementary Figure S4**) precludes the entire crater becoming filled with water. The crater lake is an ephemeral feature that periodically develops when the heat flux through the upper edifice increases to melt snow and ice in the crater. As the lake level rises, the water encounters a glacier-occupied saddle (**Supplementary Figure S4**) that is the low point on the crater rim. At this elevation the maximum area a crater lake could attain is about 73,400 m^2 and the hypothetical lake volume is 1.3–3.8 × 10^6 m^3 (**Table 1**). Erosion of the ice dam allows, acidic lake water to flow from the crater and enter the Indecision Creek drainage on the west-northwest flank of the volcano (Schaefer et al., 2008). Acidic water floods are temporarily destructive to the riparian ecosystem of the Indecision Creek drainage including Mother Goose Lake (Schaefer et al., 2008).

3.4 Kaguyak Volcano

Kaguyak volcano and its defining caldera lake is a silicic volcanic center consisting of numerous nested lava domes and flows. The volcano is in Katmai National Park on the northeastern Alaska Peninsula (**Figure 1**). Kaguyak experienced a caldera-forming eruption about 5.8 ka (Fierstein, and Hildreth, 2008) and a lake formed in the small 2.5 × 3 km diameter caldera after the eruption. The lake is estimated to be about 150 m deep, has a surface area of 3.6 × 10^6 m^2 and an approximate volume of 5 × 10^8 m^3 (Fierstein and Hildreth, 2008). The caldera rim has a distinct low point where the lake spillover should occur if the water level increased by about 30 m (**Figure 2**). The maximum water volume the caldera could hold is 1.3–9 x 10^8 m^3 (**Table 1**). Information about modern lake level fluctuations is not known.

Kaguyak has had no known historical activity and the exposed walls of the caldera do not appear significantly altered. At least three nested dome complexes were identified by Fierstein and Hildreth (2008) that make up the bulk of the volcano (**Figure 2**). There are no outward signs of caldera rim instability although areas of edifice overlap could be somewhat less structurally robust than other parts of the caldera rim. The low point on the caldera rim (**Figure 2B**) is underlain by a block-rich breccia emplaced about 6–6.5 ka, that was associated with a debris-avalanche produced by dome disruption that preceded caldera collapse (Fierstein, and Hildreth, 2008). The "Big Breccia" deposit fills preexisting drainages and low areas and is one of the main deposits that holds in the lake (Fierstein, and Hildreth, 2008). The deposit is massive, unstratified, about 25 m thick, and contains numerous blocks 2–4 m in diameter. The deposit matrix consists of coarse sandy material that is iron-stained and somewhat indurated possibly as a result of iron cementation (Fierstein and Hildreth, 2008).

3.5 Mount Katmai

Mount Katmai is a compound stratovolcano, about 10 km in diameter, that is also located in Katmai National Park on the northeastern Alaska Peninsula (**Figure 1**). Mount

Katmai experienced catastrophic caldera collapse during the June 1912 Katmai-Novarupta eruption (Hildreth and Fierstein, 2012a). The caldera has an area of 9.4×10^6 m^2 and is partially occupied by a lake of about 5.4×10^6 m^2 in area. The low point on the caldera rim is at an elevation of 1,470 m and the lake surface has an elevation of about 1,285 m (**Supplementary Figure S5**). The estimated elevation of the caldera floor is about 995 m, indicating that the lake has a depth of 290 m (Hildreth and Fierstein, 2012a). The maximum depth of a crater-filling lake is about 470 m and the maximum volume of water the crater could hold is $1.5–3.5 \times 10^9$ m^3 (**Table 1**). Upwelling associated with hydrothermal activity on the floor of the lake was reported by Motyka (1978).

Multiple glaciers that resided on the Mount Katmai edifice were truncated by caldera collapse in 1912 (Hildreth and Fierstein, 2012a). Several of these glaciers persist today and occupy shallow glacial troughs on the edifice flanks. Runoff from snow and ice melt and precipitation probably controls the water balance of the lake as there are no perennial streams that flow into the caldera.

The rocks exposed in the walls of the caldera consist of bedded lavas of basalt to rhyodacite composition and a variety of phreatomagmatic fragmental deposits (Hildreth and Fierstein, 2012b). Alteration is common on parts of the caldera wall (**Supplementary Figure S5**) and the extent of alteration is locally intense enough to obscure primary depositional features such as along the east wall of the caldera where the caldera rim is at its lowest elevation (**Figure 6** of Hildreth and Fierstein, 2012b). A possible zone of weakness on the northeast wall of the caldera is indicated by numerous dikes oriented roughly northeast-southwest (Hildreth and Fierstein, 2003; Hildreth and Fierstein, 2012b).

3.6 Mount Mageik

Mount Mageik is one of the Katmai group volcanoes located in Katmai National Park in the northeastern part of the Alaska Peninsula (**Figure 1**). The volcano consists of a 2,165-m-high compound andesite-dacite stratovolcano that includes four overlapping cones that make up a broad edifice that covers about 80 km^2 (Hildreth et al., 2000). A small, elongated crater about 350 m in length on the northeast side of the central peak contains a shallow crater lake that is also the source of vigorous fumarolic activity (**Supplementary Figure S6**). The crater lake covers an area of about 8,600 m^2 and the crater is roughly 8.5×10^4 m^2 in area. The low point on the south crater rim is about 1925 m above sea level (**Supplementary Figure S6**). At this point the maximum potential depth of a crater-filling lake is about 35 m and the corresponding lake volume would be about $3–22 \times 10^5$ m^3 (**Table 1**). The crater resides in andesite-dacite lava flows of late Pleistocene–Holocene age (Hildreth and Fierstein, 2003). Photographs of the crater indicate extensive areas of hydrothermal alteration (**Supplementary Figure S6**) indicating that the crater walls could be susceptible to failure or erosion by water.

3.7 Mount Martin

Mount Martin is a small volcanic cone of Holocene age that consists of numerous overlapping lava flows of blocky dacite (Hildreth and Fierstein, 2003). The volcanic pile rests on a high ridge of Jurassic rocks that provides much of the relief of the volcano. Martin has an active hydrothermal system and numerous jetting fumaroles along the floor of its crater just beyond the margin of a small crater lake (**Supplementary Figure S7**). The Martin crater has an area of about 1.2×10^5 m^2, and the lake covers about 9,700 m^2. The maximum lake volume the crater could hold is about $1–5 \times 10^5$ m^3 (**Table 1**). The cone of Mount Martin consists primarily of andesite ejecta including scoria, agglutinate, and phreatomagmatic breccia (Hildreth and Fierstein, 2003). These deposits are exposed in the crater walls and exhibit variable alteration.

3.8 Mount Dana

Mount Dana is a small volcanic center with a central crater about 2 km in diameter, located northeast of Pavlof Bay on the southwestern Alaska Peninsula (**Figure 1**). Little is known about the geology of the volcano and its eruptive history. Pyroclastic-flow deposits emplaced about 3.8 ka and presumably associated with a large explosive eruption that could have formed the crater are exposed on the west flank of the edifice (Wilson et al., 1995).

The summit crater of Dana volcano has an area of about 2.7×10^6 m^2, and the crater lake covers about 5.8×10^5 m^2. Because the crater is breached on the southwest flank and there is an outlet stream that exiting the lake (**Supplementary Figure S8**), it is unlikely that the lake could get much larger unless the outlet became blocked by a landslide. The depth of the lake is unknown, but is probably on the order of 30–40 m based on visual estimates made during a field visit by the author in 2005. For a lake 40 m deep, the lake volume would be $2.3–2.6 \times 10^7$ m^3 (**Table 1**).

3.9 Mount Hague

Mount Hague is a prominent stratocone within Emmons Lake caldera on the southwestern Alaska Peninsula (**Figure 1**). Mount Hague consists of a twin-peaked basaltic-andesite to dacite stratovolcano about 5 km wide at the base and about 750 m high (**Supplementary Figure S9**). The flanks are largely snow- and ice-covered and scalloped by glacial erosion. The summit area is marked by two over-lapping circular craters, each about 400 m in diameter (**Supplementary Figure S9**). The rim of the northern crater reaches an elevation of 1,540 m above sea level but is cut by the southern crater, indicating the latter is younger. The southern crater is about 250 m deep, and a fumarole field is visible when the crater floor is exposed; however, by mid-summer the bottom of the crater is commonly covered by an ephemeral lake (**Supplementary Figure S9**). The low point on the crater rim is about 1,350 m and the crater floor is about 1,260 m, indicating a maximum potential lake depth of about 90 m. For a lake of this depth, the maximum volume is about $4.6–13 \times 10^6$ m^3 (**Table 1**).

3.10 Makushin Volcano

Makushin Volcano is a 2,036-m-high stratovolcano on Unalaska Island located 8 km west of Dutch Harbor and Unalaska, Alaska (**Figure 1**). The volcano has had at least 17 eruptive episodes since the 1700 s and erupted most recently in 1995 (McGimsey and Neal, 1995; Miller et al., 1998). The summit crater has an area of about 350,000 m^2 and is roughly 217 by 250 m in diameter (**Supplementary Figure S10**). The lake on the floor of the crater has an area of about 24,500 m^2 (**Supplementary Figure S10**). The crater was the source of minor eruptive activity in 1995 when a single eruptive burst generated an ash cloud that reached about 2,400 m above sea level and produced trace ash fallout on the upper part of the edifice (McGimsey and Neal, 1996).

The summit crater is surrounded by an extensive snow and ice field and there are multiple active fumaroles on the crater floor (Werner et al., 2020). The hydrothermal system at Makushin is active and likely driven by shallow magma beneath the summit region (Motyka, et al., 1988). Rock and pyroclastic deposits exposed in the walls of the crater are hydrothermally altered, indicating that the rock mass strength of the crater is likely compromised and could be susceptible to erosion or failure should a larger lake develop in the crater. The crater has a depth of about 100 m and thus the maximum volume of water the crater could hold is 4.2–19 × 10^5 m^3 (**Table 1**).

3.11 Tana Volcano

Tana volcano forms the eastern part of Chuginadak Island and is located east of Cleveland volcano (**Figure 1**). Little is known about the geology and eruptive history of the volcano. Photographs of the crater (**Supplementary Figure S11**) and studies of surficial deposits on the flanks of Tana (Persico et al., 2019) indicate that parts of the edifice are hydrothermally altered. Hot springs and active fumaroles on the flanks of the volcano are described in Werner et al. (2020). The crater on Tana has an area of about 7.7 × 10^5 m^2, and the crater lake covers about 2.1 × 10^5 m^2. The low point on the crater rim is about 780 m, only about 10 m above the modern lake level. The maximum possible volume of a crater lake is about 0.5–3.4 × 10^6 m^3 (**Table 1**).

3.12 Herbert Volcano

Herbert volcano on Herbert Island, is in the Islands of the Four Mountains area of the Aleutian Islands and is the western most volcano of this group of volcanic islands (**Figure 1**). Little is known about the geology and eruptive history of Herbert. The summit of the volcano is characterized by a circular 2.1 km diameter crater (or small caldera) that hosts a small lake that is about 5.7 × 10^5 m^2 in area (**Supplementary Figure S12**). The low point on the crater rim is about 840 m and this corresponds to a maximum potential lake area of about 1.9 × 10^6 m^2. The depth of the largest lake the crater could hold is about 220 m and the volume 1.8–4.2 × 10^8 m^3 (**Table 1**).

3.13 Korovin Volcano

Korovin is one of several stratovolcanoes on the northern part of Atka Island in the central Aleutian Islands (**Figure 1**). The village of Atka is 21 km south of the volcano. The Korovin summit edifice includes two craters, and the southern crater hosts the active vent and contains a small warm lake. Korovin has had minor episodes of phreatomagmatic eruptive activity in 2005, 1998, 1996, 1987, 1986, 1976, 1973, 1954, 1951, and 1907. Some of these eruptions generated small amounts of ash and lava flows of limited extent (Miller et al., 1998; McGimsey et al., 2003). The 1998 eruption produced an ash cloud that reached about 9 km above sea level. Fumaroles and warm mud springs are plentiful on the western and southern flanks of the volcano and overall the level of hydrothermal activity on and around the Korovin edifice is relatively high.

The south crater of the Korovin edifice has an area of about 3.7 × 10^7 m^2 and is partially occupied by a lake with an area of 1.6 × 10^4 m^2 (**Supplementary Figure S13**). The maximum depth of a crater filling lake is about 140 m and the maximum volume 2.3–3.6 × 10^7 m^3 (**Table 1**). The walls of the south crater consist of interbedded lava flows and pyroclastic deposits that do not appear significantly altered except at the base of the crater around the crater lake (**Supplementary Figure S13**).

3.14 Kasatochi Volcano

Kasatochi is a small, isolated island volcano in the east-central part of the Aleutian Arc (**Figure 1**). The volcano makes up all of Kasatochi Island and consists of a circular cone about 3 km in diameter with a lake-filled central crater (**Supplementary Figure S14**) that exhibited minor fumarolic activity in 2005 (McGimsey et al., 2008). Kasatochi experienced a 21-hour-long VEI 4 eruption on August 7–8, 2008 that was the only known historical eruption of the volcano (Waythomas et al., 2010a). As a result of the 2008 eruption, the summit crater was widened by several tens of meters and Kasatochi Island was covered with many tens of meters of pyroclastic debris and fine ash (Nye et al., 2017; Scott et al., 2010; Waythomas et al., 2010b). The Kasatochi summit crater has an area of about 1.5 × 10^6 m^2, and the crater lake has an area of 8 × 10^5 m^2 as determined from a November 22, 2020 WorldView-3, satellite image (**Table 1**). The crater lake had a depth of about 20 m when estimated in 2009 (Nye et al., 2017). The low point on the crater rim is about 160 m above sea level indicating that the maximum depth of the largest possible crater lake is roughly 180 m (**Supplementary Figure S14**). The area of the largest possible lake in the crater is about 1.3 × 10^6 m^2 and the volume about 2.2 × 10^8 m^3.

Geologic studies of Kasatochi following its 2008 eruption indicate that the walls of the crater consist of variable assemblages of bedded lavas and pyroclastic deposits (**Figure 7**, **Supplementary Figure S14**). The pyroclastic deposits on the west and south rims of the crater are loose and not well consolidated and are likely susceptible to erosion by water. The lava flows exposed beneath the low point on the crater rim are thin bedded with rubbly margins (Nye et al., 2017) and could be susceptible to piping should the crater lake increase in volume and approach the low point on the crater rim. Conduit-like, focused flow of water into the crater after the 2008 eruption (Waythomas et al., 2010a) indicates that parts of the crater walls could allow piping style drainage.

3.15 North Crater of Cerberus Volcano

The north crater of Cerberus volcano on Semisopochnoi Island (**Figure 1**) contains an ephemeral lake that was observed during recent periods of unrest in 2020-2021 at north crater. The crater is about 400 m in diameter and has an area of 1.5 × 10^7 m^2. Intermittent satellite observations since 2014, indicate that a small ephemeral lake is

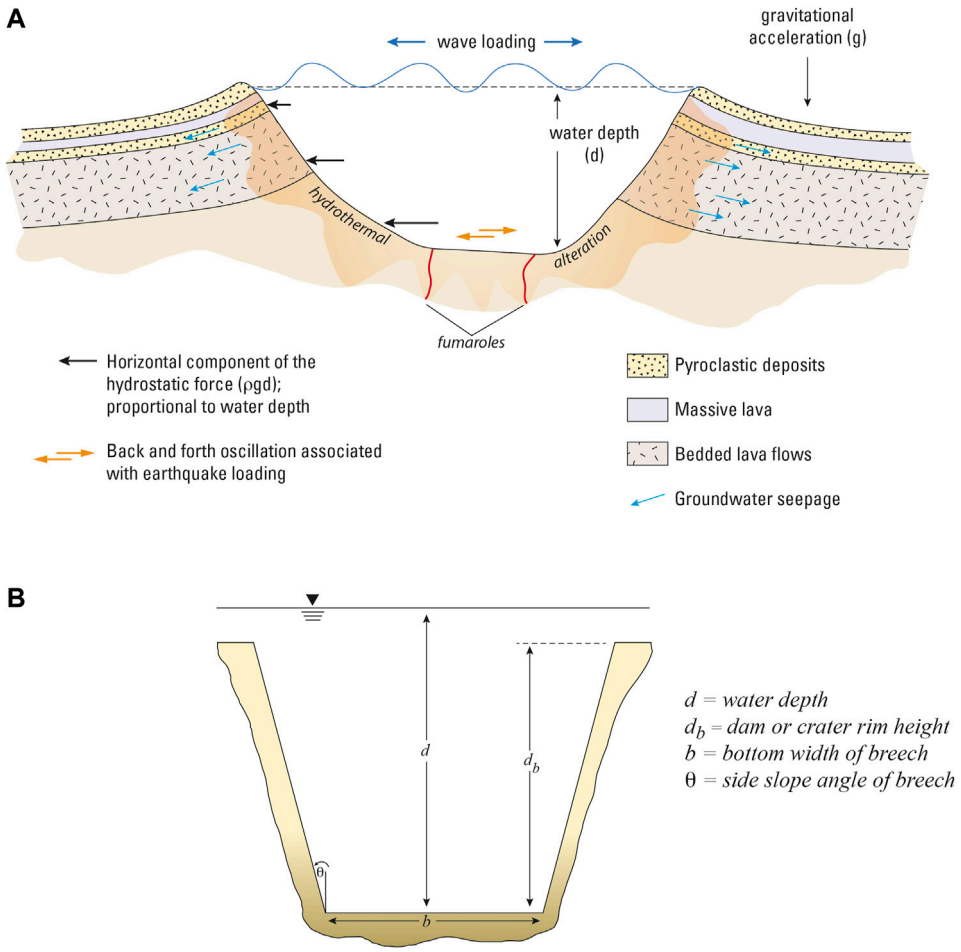

FIGURE 3 | Summary of forces and nomenclature for lake-filled volcanic craters at a typical stratocone. **(A)**. Generic cross section through a lake filled volcanic crater showing idealized stratigraphic elements, zone of hydrothermal alteration, and basic forces acting on crater walls. Fumaroles can occur on the crater walls as well as crater floors. The symbol ρ is water density. **(B)**. Trapezoidal breach and relevant geometric parameters.

sometimes present on the crater floor and likely develops in response to snowmelt runoff sometimes induced by unrest related geothermal heat flow and fumarolic activity within the upper edifice of the north cone. Although its size varies, the crater lake has an area of 6–9 × 10^3 m^3. The low point on the crater rim is about 750 m above sea level, and at this elevation the maximum area of a crater lake is 1 × 10^5 m^2. The maximum depth is about 120 m and thus the greatest volume of water the crater could hold is about 6–7 × 10^6 m^3 (**Table 1**).

The north cone is a basaltic-andesite edifice that consists of lava flows and pyroclastic deposits which are exposed in the walls of the crater (Coombs et al., 2018). None of these deposits appear altered, and the crater itself is steep and little modified (**Supplementary Figure S15**).

4 CRATER STABILITY AND SUSCEPTIBILITY TO FAILURE

The stability of lake-filled volcanic craters in Alaska is a key unknown in the assessment of plausible crater wall failures leading to water floods and associated water-saturated mass flows. The rocks and volcaniclastic deposits that make up many volcanic edifices may be structurally weak as a result of hydrothermal alteration (**Figure 3A**). The inconsistent nature of edifice stratigraphy, where loose, weak, pyroclastic deposits are interbedded with stronger materials such as lava flows also contributes to potential crater wall instability. Localized degradation of crater walls is indicated by accumulations of rockfall talus common on crater floors that is related to the structural integrity of the rocks and deposits that make up the crater. Many of the lake-filled volcanic craters in Alaska have steep internal slopes, include active hydrothermal systems, and exhibit at least surficial evidence of hydrothermal alteration. Some volcanic craters include thick deposits of tephra and pyroclastic density current deposits that are more susceptible to erosion than lava flows or welded spatter. This suggests that volcanic crater walls in Alaska possess some inherent instability.

From a hazard assessment perspective, volcanic craters and calderas are likely to be most susceptible to failure when the lakes they host are at or near capacity. In this state, crater rims are

TABLE 2 | Maximum volcanic crater slope angles, extent of surface alteration, and plausible mode of rim failure.

Volcano	Maximum inner crater wall slope angle, degrees	Hydrothermal alteration of crater walls	Active hydrothermal system present or not	Likely failure mode	Comments
Spurr summit	50–60	Yes. Type and extent not known	Ephemeral	Overtopping	Glacier ice and snow on crater rim. Abundant ice and snow on flanks of summit cone. Lack of obvious melting since about 2010 indicates hydrothermal activity greatly diminished or stopped
Crater Peak	50–60	None apparent	Ephemeral	Overtopping	Crater Peak cone consists primarily of stacks of lava flows with only minor layers of pyroclastic debris
Douglas	40–50	Yes. Type and extent not known	Active	Overtopping	Glacier ice and snow on crater rim. Abundant ice and snow on flanks of summit cone
Kaguyak	30–50	Minor. Type and extent not known	Inactive	Overtopping Piping?	Loose, unconsolidated material occupies lowest terrain on crater rim
Katmai	40–60	Yes. Type and extent not known	Inactive	Overtopping	Some bubbling observed but no robust hydrothermal activity reported. Local slope failures could displace water possibly resulting in overtopping
Mageik	30–45	Yes. Type and extent not known	Active	Overtopping	Crater walls consist primarily of altered lava flows and minor pyroclastic and tephra deposits
Martin	40–60	Yes. Type and extent not known	Active	Overtopping	
Chiginagak	30–50	Yes. Type and extent not known	Ephemeral	Subglacial tunnel	Low point on crater rim mantled by glacier ice forming an ice dam
Dana	30–50	None apparent	Inactive	Overtopping	Outlet stream drains crater lake; a landslide would have to block the channel for a larger lake to form
Hague	30–50	Yes. Type and extent not known	Ephemeral	Overtopping	
Makushin	40–60	Yes. Type and extent not known	Active	Overtopping	Glacier ice and snow on crater rim. Abundant ice and snow on flanks of summit cone
Tana	30–50	Yes. Type and extent not known	Inactive	Overtopping	
Herbert	30–50	Minor. Type and extent not known	Inactive	Overtopping	Little known about the geology of the crater
Korovin	40–60	Yes. Type and extent not known	Active	Overtopping	
Kasatochi	40–60	Yes. Type and extent not known	Generally inactive	Overtopping	Hydrothermal activity increased prior to the 2008 eruption but observations were sporadic
North crater, Cerberus	40–60	None apparent	Ephemeral	Overtopping	Satellite observations indicate that the lake is ephemeral

analogous to other types of natural or constructed dams (such as landslide dams, moraine dams, earth-fill dams, concrete dams, or embankment dams) and can be evaluated as such. The most common mechanism for failure of natural and constructed dams is by overtopping and roughly 90% of landslide dams fail by this process (Costa and Schuster, 1988). Constructed dams of various types also fail predominantly by overtopping but also by piping, seepage, and as a result of foundation defects (Costa, 1985; Foster et al., 2000). Overtopping failures develop from water flowing over the dam crest and subsequent erosion of the dam face. Commonly, water flow over the dam crest results in headward erosion of the dam face until the dam crest is breached, allowing more water to escape resulting in further erosion of the breach. Water seepage through the dam may accelerate the process, especially if groundwater piping develops and some natural dams fail primarily as a result of piping (Costa and Schuster, 1988). For a static condition, with no external stresses applied to the crater wall or lake, the hydrostatic pressure associated with the crater lake can result in the development of saturated conditions within all or part of the crater wall materials. If the crater wall materials are saturated, they should exhibit a decrease in shear strength such that the factor of safety (F_s) is reduced.

Eruptive activity from underwater vents could lead to forceable ejection of water or waves sufficient to overtop crater rim dams. The combined effects of eruptive activity and associated water displacement may enhance erosion of the dam and lead to breaching. In contrast, slow spillover of water associated with hydrologic changes of the lake basin such as rapid snow or ice melt or extreme rainfall (Yang et al., 2005) could also lead to eventual dam breach.

Preliminary stability information for the 16 lake-filled craters evaluated in this study is given in **Table 2**. The steepest parts of the crater walls are in the range of 30–60° and all but Crater Peak and Dana exhibit some outward evidence for hydrothermal alteration. Five of the craters have active hydrothermal systems, six have ephemeral hydrothermal systems, and five have no apparent modern hydrothermal activity (**Table 2**). Hydrothermally altered volcanic edifices have an increased susceptibility to gravitational failure because of the general loss of rock mass strength associated with alteration (Watters, et al.,

2000; Reid et al., 2001; Finn et al., 2018). Crater wall collapse resulting from hydrothermal alteration could be triggered by intense seismic shaking, eruptive activity, or increases in hydrostatic pressure and wall loading associated with the crater lakes if they were at or near full crater capacity (**Figure 3A**).

4.1 Seismic Effects on Volcanic Crater Lakes

Assuming that it is possible for the crater lakes to increase in volume and approach spillover, an important stability concern are the hydrodynamic pressures on the crater walls induced by seismic shaking of the crater lake. Large-magnitude earthquakes (>M7) are common in the Aleutian Arc with one or more occurring almost annually (Sykes et al., 1981) and intense seismic shaking is a well-known mechanism for inducing failure of natural dams (Costa and Schuster, 1988). The magnitude of hydrodynamic pressure depends on the frequency-magnitude characteristics of the seismic load and the material properties of the crater walls. In addition, the seismic shaking of a lake-filled volcanic crater can induce changes in pore-fluid pressure within the crater walls and an associated reduction in shear strength. Volcanic craters that are hydrothermally altered or contain layers that transmit groundwater could be particularly susceptible to failure under seismic loading. In a study of the seismic response of earth-fill dams, Gazetas (1987) showed that ground accelerations are higher near the crest of the dam, suggesting that for lake-filled volcanic craters filled to near capacity, seismic accelerations may be sufficient to cause overtopping and water spillover.

The maximum hydrodynamic pressure ($p_{\max}$) occurs at the base of the crater wall dam and can be expressed as:

$$p_{max} = 0.7 a_c \gamma_w h \quad (1)$$

where a_c is the acceleration coefficient ($a_c = \frac{a_0}{g}$ where a_0 is the maximum value of the horizontal acceleration and g is gravitational acceleration), γ_w is the unit weight of water, and h is the depth of the lake at the crater wall (Pelecanos et al., 2013). This expression is valid for a dam with a vertical lake-side profile. If the internal crater wall is inclined, the hydrodynamic pressure $p_{(y)}$ is expressed as:

$$p_{(y)} = C_p a_c \gamma_w h \quad (2)$$

where C_p is a pressure coefficient (determined analytically, Chwang and Housner, 1978; Chwang, 1978), a_c is the acceleration coefficient, γ_w is the unit weight of water, and h is the depth of the lake (Pelecanos et al., 2013).

Earthquake induced forces on the reservoir-dam system were evaluated by Chwang and Housner (1978). Their analysis concluded that for dams with lake side facing slopes of 0–90°, the total horizontal force on the dam (F_x) is:

$$F_x = C_x \rho a_0 h^2 \quad (3)$$

where C_x is a force coefficient (~0.5), ρ is water density, and a_0 and h^2 are as defined above. Peak ground accelerations in the central-western Aleutian Arc associated with large megathrust earthquakes are roughly in the range of 4–8 m/s^2 (Wesson et al., 2007). Using these values for a_0 in the above expression and 1,000 kg/m^3 for ρ, the estimated maximum force on the crater wall dam for a lake 50 m deep is 1–2 × 10^5 N. For a lake 100 m deep, F_x is 2–4 × 10^5 N. If it is assumed that peak ground acceleration occurs in a largely bidirectional, back and forth manner, only those parts of the crater wall in the domain of motion would be subject to the maximum forces. Using a 200 m long sector of a generic crater and crater lake depths of 50 and 100 m, the above estimated forces would generate maximum crater wall pressures of only 10–40 Pa which are very low and probably not significant enough to cause failure of the crater wall by this mechanism alone.

Seismic shaking of lake-filled volcanic craters could result in liquefaction of strata within the crater walls which could be sufficient to cause crater rim failure. Several tailings dams have failed by this process (Lyu et al., 2019) and where significant portions of volcanic crater walls are composed of relatively loose, unconsolidated or hydrothermally altered material, seismically induced liquefaction could be a concern. The duration and peak ground accelerations associated with large earthquakes also can result in back-and-forth water oscillations known as seiches (McGarr and Vorhis, 1968). Seismic seiches at volcanic lakes are not widely known, but the few examples described in the literature indicate that seiches can be hazardous (Moore et al., 1966; Newhall and Dzurisin, 1988) and could be large enough to overtop crater rims which may lead to water erosion and possible dam failure.

4.2 Volcanic Crater Lake Hydrology

Although it is beyond the scope of this paper to make a quantitative assessment of crater lake hydrology at each location discussed, some general commentary on the hydrologic setting of the Alaska crater lakes is warranted and provides some insight on the potential for changes in the water balance of the lakes. The primary hydrologic inputs are precipitation (snow, meltwater, rainfall; W_p), groundwater (W_g), and water from shallow magmatic sources (W_v). These inputs are affected by evaporation (W_e) and water outflow, either as direct open-channel flow (W_o), groundwater seepage (W_{gw}), or both, such that $W_p + W_g + W_v = W_e + W_o + W_{gw}$ which is a general statement for the water balance of the lake (Pasternack and Varekamp, 1997; Rouwet et al., 2004). None of these variables are known with any degree of certainty for the Alaska crater lake examples discussed here. The Alaska volcanic craters are situated at the summit of their respective volcanic edifices and the crater itself defines the hydrologic catchment. Of the 16 volcanic craters examined in this study, nine are on volcanoes with significant amounts of glacier ice (>1 km^2; GLIMS Consortium, 2005) and the remaining six craters are in areas that receive seasonal snow (typically September–April) that can exceed several meters depth (Brown et al., 2003; https://www.weather.gov/aprfc/Snow_Depth). The volume of glacier ice on volcanoes in Alaska has been measured only at a few locations. At Mount Spurr, about 67 km^3 of glacier ice and perennial snow was present on the edifice when measured in 1981 (March et al., 1997) indicating ice

volumes at similar glaciated stratovolcanoes in Alaska are significant (Waythomas, 2015). Thus, a main hydrologic input, snow and glacier ice, is present at all locations in ample amounts. An example discussed in *Lahars* below, shows that an increase in the thermal output at an ice and snow-clad volcanic crater (Mount Spurr) could be sufficient to cause melting and increase the water input to the crater lake. An increase in heat flux at Chiginagak volcano also led to significant melting and an increase in the volume of the crater lake eventually resulting in catastrophic lake drainage (Schaefer et al., 2008).

All volcanic crater locations receive significant precipitation and annual amounts of >1 m (water equivalent) are not uncommon (Stafford et al., 2000) although long-term weather records in the study region are available only at a few localities at sea level. If a generic volcanic crater with an area of 1×10^5 m^2 receives 1 m of snow accumulation, the approximate snow-water equivalent (SWE) is about 5×10^4 m^3 of water if the SWE of 1 m of snow is about 50 cm water (Sturm et al., 2010). Thus, snowfall could represent a significant input to the Alaska crater lakes although some of this water will be lost to evaporation and groundwater seepage. These components of the water balance are difficult to estimate and although various springs have been observed (Motyka et al., 1993; Evans et al., 2015), little is known about water flux or the state of groundwater at any of the volcanic craters discussed here.

Systematic measurements of water levels in the Alaska crater lakes have not been accomplished, although opportunistic observations, photographs, and satellite data have provided a general sense of the presence and extent of lakes in some locations as described in *Crater Lakes in Alaska* above. Evidence of significant changes in water levels have been noted at Mount Spurr, Crater Peak, Chiginagak, Korovin, and north crater on Cerberus volcano. The summit craters at Mount Spurr and Chiginagak, and possibly Korovin and north crater have been affected by changes in the thermal output of the volcano. A lake was present at Crater Peak prior to the eruptive activity in 1992 and has not reappeared since suggesting that it too may have been a result of an increase in heat flow resulting in local snow and ice melt. Water level observations of Katmai Lake were made in the 1970s and from July 5, 1975, to August 20, 1977, the water level increased by about 6.5 m or an average rate of 3 m/yr (Motyka, 1978). Apparently, Katmai Lake drained sometime between 1919 and 1923 (Fenner, 1930). None of the other cater lakes exhibit any obvious evidence for fluctuations in lake level but it is clear from the few available observations that significant changes in water volume can occur.

5 CRATER RIM OVERTOPPING, BREACH FORMATION, AND PEAK FLOOD DISCHARGE

Assuming that sufficient water can be made to flow over the crater rim to initiate breach formation at the locations considered here, the maximum discharge at the breach can be evaluated using the same techniques for evaluation of breach formation at generic earth-fill dams (Fread, 1996; Walder and O'Connor, 1997; Froehlich, 2008). Given that it would be difficult to specify all the conditions of breaching at the lake-filled craters described here, the goal is to provide first order estimates of the maximum possible peak discharge at the breach from a worst-case scenario perspective. To accomplish this, the method for predicting peak discharge by dam breaching described in Walder and O'Connor (1997) is used.

The physically based model of dam-breach formation described in Walder and O'Connor (1997) makes use of the well-known kinematics of breach formation and the hydraulics of flow through a breach of known shape (typically trapezoidal, **Figure 3B**; Henderson, 1966). This approach provides estimates of peak discharge at the breach that are dependent on the volume of impounded water, breach erosion rate and shape, and lake hypsometry. The discharge estimation technique makes use of a functional relationship between dimensionless peak discharge (Q_p^*) and a dimensionless parameter η ($\eta = kV_0/g^{1/2}d^{7/2}$), where k is the breach erosion rate, V_0 is the initial volume of the lake, g is gravitational acceleration, and d is the drop in lake level. The dimensionless peak discharge is expressed as

$$Q_p^* = \alpha\eta^\beta \tag{4}$$

where α and β are dimensionless coefficients that depend on the width-depth ratio of the breach, the side slope angles of the breach, and crater-lake hypsometry (Walder and O'Connor, 1997).

Assuming that a crater-rim breach forms rapidly to the full depth of the lake and the shape remains relatively fixed throughout the event (MacDonald and Langridge-Monopolis, 1984; Singh et al., 1988; Walder and O'Connor, 1997), the analysis of peak outflow can be simplified such that maximum peak discharge at the breach (Q_p) can be estimated as follows:

$$Q_p = 1.94 g^{1/2} d^{5/2} \left(\frac{D_c}{d}\right)^{3/4} \tag{5}$$

where D_c is the height of the dam crest relative to the dam base. For a worst-case scenario where the breach develops to the full depth of the lake at the breach (d), $d = D_c$. This reduces the expression for Q_p to:

$$Q_p = 1.94 g^{1/2} d^{5/2} \tag{6}$$

and is applicable in situations of rapid breach formation where $\eta \gg 1$. For cases where breach development occurs slowly, and $\eta < 1$, the maximum peak discharge is expressed as:

$$Q_p = 1.51\left(g^{\frac{1}{2}} d^{\frac{5}{2}}\right) \cdot 0.06\left(kV_0/d\right)^{0.94} \tag{7}$$

Breach formation is assumed to occur at a constant rate k through the full depth of the lake at the breach. Values of $k = 1$, 10, and 100 m/h provide estimates of slow to fast breach formation. Studies of breach development during dam failures indicate that the final breach shape is almost always trapezoidal (MacDonald and Langridge-Monopolis, 1984; Singh et al., 1988). Assuming that crater lake breaches are

TABLE 3 | Peak discharge estimates for hypothetical crater-lake dam failure floods at selected Alaska volcanoes assuming maximum initial crater lake volume. 1) calculated from: $Q_p = (c_1 r + c_2 cot\theta) g^{0.5} d^{2.5}$ 2) calculated from: $Q_p = 1.94 g^{1/2} d^{5/2}$ (3, 4, 5) calculated from: $Q_p = 1.51 (g^{\frac{1}{2}} d^{\frac{5}{2}})^{0.06} (kV_0/d)^{0.94}$ where k = 1, 10, and 100 m/h.

Volcano	Maximum crater lake volume V_o, in m^3	(1) Maximum peak discharge, Q_p in m^3/s (trapezoidal breach)	(2) Maximum peak discharge, Q_p in m^3/s ($\eta \gg 1$)	(3) Maximum peak discharge, Q_p in m^3/s (k = 1 m/h)	(4) Maximum peak discharge, Q_p in m^3/s (k = 10 m/h)	(5) Maximum peak discharge, Q_p in m^3/s (k = 100 m/h)
Mt. Spurr summit	9.7×10^6	5.16×10^5	1.41×10^6	47	4.1×10^2	3.6×10^3
Crater Peak	1.4×10^7	2.25×10^4	6.15×10^4	29	2.6×10^2	2.2×10^4
Douglas	1×10^6	2.25×10^4	6.15×10^4	17	1.5×10^2	1.3×10^3
Kaguyak	9×10^8	6.13×10^5	1.67×10^6	3.3×10^3	2.8×10^4	2.5×10^5
Katmai	3.5×10^9	3.19×10^6	8.7×10^6	$3.4\ 10^3$	2.9×10^4	2.6×10^5
Mageik	2.2×10^6	1.61×10^4	4.4×10^4	6	54	4.7×10^2
Martin	5.1×10^6	3.93×10^4	1.07×10^5	14	1.2×10^2	1×10^3
Chiginagak	3.8×10^6	2.25×10^4	6.15×10^4	59	5.1×10^2	4.5×10^3
Dana	2.6×10^7	2.25×10^4	6.15×10^4	3.6×10^2	3.1×10^3	2.7×10^4
Hague	1.3×10^7	1.71×10^5	4.67×10^5	37	3.2×10^2	2.8×10^3
Makushin	3.5×10^7	2.23×10^5	6.07×10^5	15	1.3×10^2	1.1×10^4
Tana	3.4×10^6	3.98×10^3	1.09×10^4	92	8×10^2	7×10^3
Herbert	4.2×10^8	1.6×10^6	4.36×10^6	1×10^3	9.4×10^3	8.2×10^4
Korovin	3.6×10^7	5.16×10^5	1.41×10^6	1.2×10^2	1×10^3	9.1×10^3
Kasatochi	2.2×10^8	9.67×10^5	2.64×10^6	7.5×10^2	6.5×10^3	5.7×10^4
N. crater, Cerberus	1.3×10^7	3.51×10^5	9.58×10^5	47	4×10^2	3.5×10^3

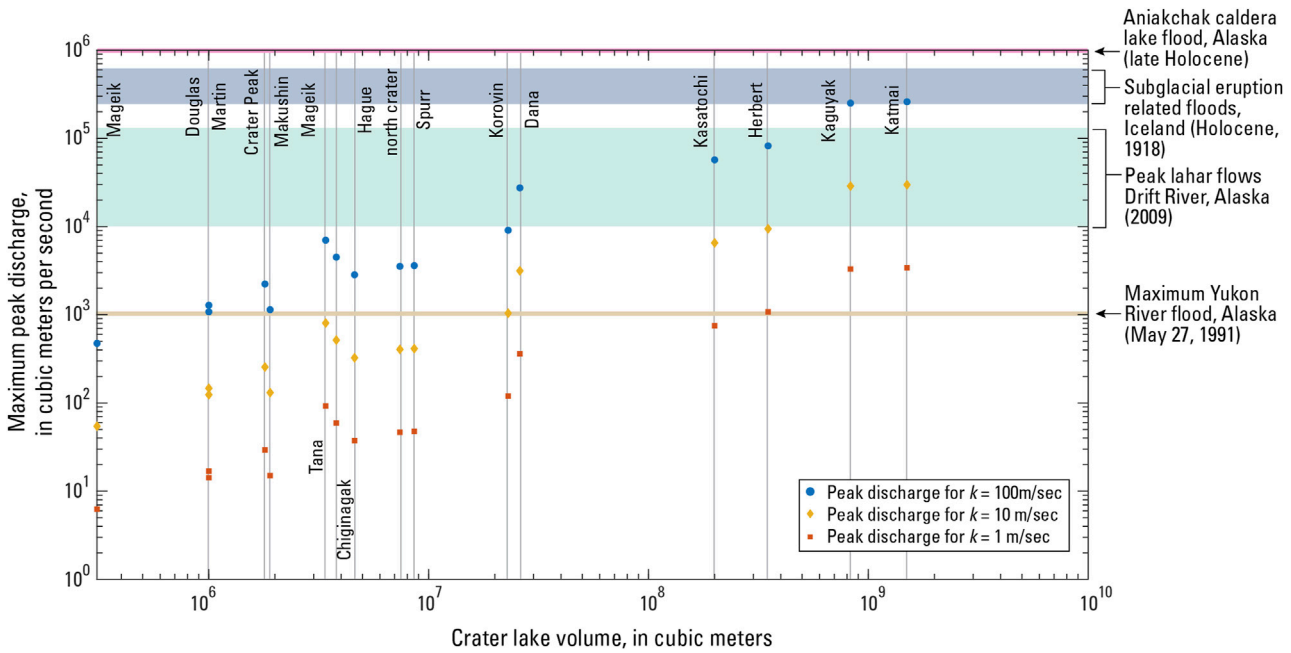

FIGURE 4 | Comparison of maximum peak discharge from hypothetical crater-lake floods in Alaska to other large flows. Peak discharge of Alaska crater-lake floods for breach erosion rates of 1, 10, and 100 m/s estimated with **Eq. 7**. Aniakchak peak discharge estimate from Waythomas et al., 1996; subglacial eruption related flood and Yukon River discharge estimates from O'Connor and Costa, 2004; Drift River lahar discharge estimates from Waythomas et al., 2013.

also trapezoidal in shape, the maximum peak discharge at the breach can be expressed as a relation among Q_p, breach shape and water depth:

$$Q_p = (c_1 b + c_2 H cot\theta) g^{0.5} H^{1.5} \quad (8)$$

where b is the bottom width of the breach, θ is the angle of the breach side slope, c_1 and c_2 are geometric constants ($c_1 = 0.544, c_2 = 0.405$), and H is the water depth of the lake above the base of the breach (Waythomas et al., 1996). If the breach shape remains geometrically similar throughout its formation, the geometric variables c_1, c_2, b, and θ are constants. When the time of breach formation (t) is $\geq d/k$, $b = rd$ where the b/d ratio is ~2.5 (Singh et al., 1988; Waythomas et al., 1996).

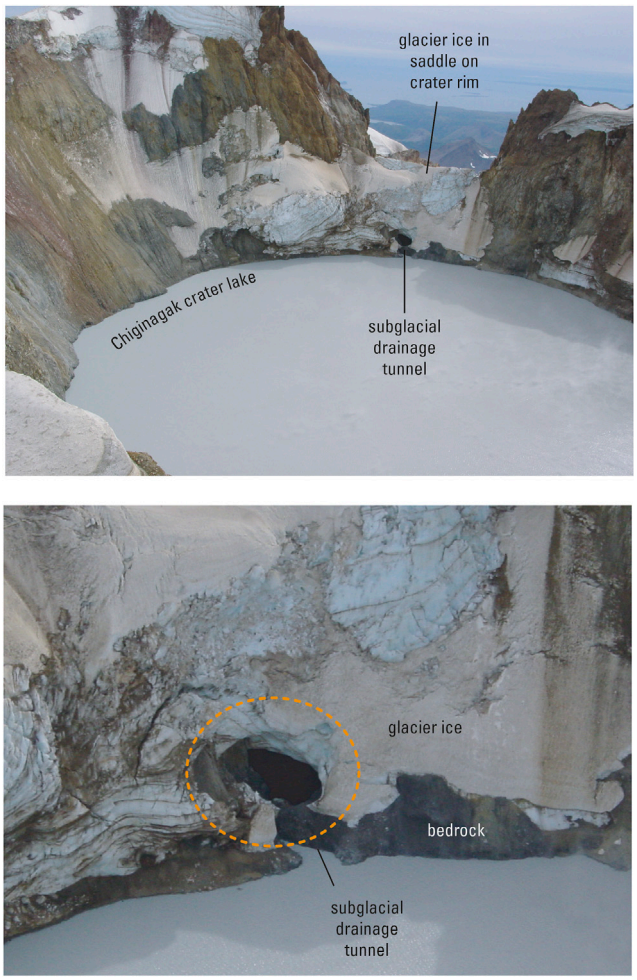

FIGURE 5 | Photographs of subglacial tunnel and site of May 2005 lake drainage event on the rim of the Chiginagak crater. Photographs by R.G. McGimsey, AVO, August 21, 2006.

Lake depth is related to lake volume by the following hypsometric relation:

$$\left(\frac{V}{V_0}\right) = \left(\frac{h_l}{h_0}\right)^p \tag{9}$$

where h_l is the water depth at lake volume V, and V_0 and h_0 are initial values of lake volume and water depth ($h_0 = d$). The exponent p is specific to each lake basin; for long, narrow basins $p \sim 1$ and for circular basins, $p \sim 3$, thus for the crater lakes and calderas examined here, $p = 3$ is used.

The change in water depth at the breach (H) with time (t) is:

$$\frac{dH}{dt} = -\left(\frac{D^p}{pV_0}\right) g^{0.5} H^{2.5-p} (c_1 r D + c_2 H cot\theta) \tag{10}$$

and the maximum theoretical peak discharge for an instantaneously formed breach to the maximum depth of the lake at the breach is:

$$Q_p = (c_1 r + c_2 cot\theta) g^{0.5} d^{2.5} \tag{11}$$

5.1 Discussion of Peak Discharge Estimates

The results of peak discharge estimates for water floods produced by crater wall collapse are given in **Table 3**. The estimates are based on maximum peak discharge associated with a fully formed trapezoidal breach calculated with **Eq. 11**, maximum peak discharge for rapid breach formation calculated with **Eq. 6**, and maximum peak discharge calculated with **Eq. 7** where breach erosion rate k is set to 1, 10, and 100 m/h.

The largest peak discharge values result from application of **Eq. 6** where breach formation is essentially instantaneous. These values are an upper bound on peak discharge and thus may be taken as representing the worst-case condition. The peak discharge values obtained from **Eq. 6** are similar to those resulting from **Eq. 11** where a trapezoidal-shaped breach is assumed throughout each crater rim failure flood event.

Values for maximum peak discharge determined from **Eq. 7** are shown in **Figure 4**. Also shown in **Figure 4** are the maximum peak discharges for other large outburst floods and lahars in Alaska and Iceland. Flood magnitudes associated with water-filled volcanic craters in Alaska are comparable to these volcanogenic flows and river floods and this highlights the potential significance of the Alaska examples.

Variable breach erosion rates in **Eq. 7** yield much smaller values for maximum peak discharge compared to estimates based on nearly instantaneous breach formation (**Table 3**). Although it is difficult to accurately determine the erosion rate of a crater rim a priori, the discharge estimates in **Table 3** indicate the strong dependence between erosion rate and peak discharge. There may be situations where it is possible to reasonably estimate the breach erosion rate and thus application of **Eq. 7** in these situations would be warranted.

6 CRATER LAKE FLOODS ASSOCIATED WITH GLACIER ICE DAMS

Most of the crater lakes evaluated here do not involve glacier ice as a component of the natural dam. The three exceptions are Mount Spurr, Douglas volcano and Mount Chiginagak (**Supplementary Figures S1,3** and **Figure 5**). In these two cases, glacier ice covers a significant part of the crater wall and is either known (Chiginagak) or suspected (Spurr, Douglas) to play a role in the development of floods from the associated lake-filled crater.

At Douglas volcano, a significant portion of the crater wall is covered by glacier ice of unknown geometry. It may be that glacier ice simply drapes the crater rim, although photographs of the crater indicate that glacier ice fills several of the low areas along the rim (**Supplementary Figure S3**). If the crater lake were to increase in volume, the ice may melt, exposing the crater wall, or the ice could lend stability to the rim and make it less susceptible to erosion or failure if the ice cover is thick (>100 m). If the glacier ice is a part of the crater rim, rising lake levels could destabilize the ice when the impounded water became deep enough to float or

TABLE 4 | Expected eruption characteristics in relation to crater lake water supply assuming sustained eruption through lake (Modified from Wohletz et al., 2009).

Water supply	Eruption characteristics	Volcanic cloud height	Main eruptive products
Unlimited	• Surtseyan jets • Base surges • Wet fallout	0.3–1.5 km	• Fine-grained surge deposits • Ballistic particles • Fine-coarse ash and lapilli
Available but not unlimited	• Violent magma-water interactions • Phreatoplinian eruption columns • Column collapse pyroclastic density currents	20–50 km	• Abundant fine ash • Pyroclastic mass-flow deposits • Extensive ash fallout

thermally erode the glacier dam (Björnsson, 1974; Nye, 1976). In this case, flow under the ice could eventually lead to the formation of a subglacial channel that would increase in size roughly proportional to the volume and duration of exiting lake water (Clarke, 1982). If glacier ice makes up a significant part of the crater wall, wholesale failure of the ice would be analogous to rapid breach formation as discussed in the previous section.

Lakes impounded by glaciers pose a well-known flood hazard and are often described as glacier outburst floods or jökulhlaups (Björnsson, 1974; Clague and O'Connor, 2021). For situations where water drainage occurs through a subglacial tunnel, peak discharge (Q_p) can be estimated using an empirical relation between Q_p and lake volume (V) (Walder and Costa, 1996):

$$Q_p = 46V^{0.66} \quad (12)$$

This equation provides first-order estimates of peak discharge for subglacial tunnel drainage but is less analytical than the method described in Clarke (1982) where lake temperature and rate of tunnel closure are incorporated into numerical expressions for Q_p. For the May 2005 crater lake flood at Chiginagak, the lake volume (V) drained was estimated at 3.8×10^6 m^3 (Schaefer et al., 2008). Application of **equation 12** yields $Q_p = 111$ m^3/s. At Chiginagak, elevated water surface temperatures of about 40°C were measured in the crater lake with a Forward Looking Infrared camera (FLIR) about 4 months after the May 2005 crater lake flood (Schaefer et al., 2008). This indicates that lake water temperature could have been of this magnitude when the flood occurred and suggests that the thermal energy of the lake likely influenced tunnel drainage at the base of the ice dam (**Figure 5**) and the Q_p estimate based on **Eq. 12** is likely a minimum value.

7 HAZARDS AND CONSEQUENCES OF ERUPTIONS THROUGH CRATER LAKES IN ALASKA

Of the sixteen volcanoes evaluated here, only six of them have had documented eruptive activity in the past 200-300 years (**Table 1**). However, all sixteen volcanoes have been active during mid–late Holocene time. Thus, it is not unreasonable to consider likely eruptive styles and hazards that are a consequence of future eruptions involving lake-filled craters and calderas addressed in this study. In addition to catastrophic crater rim failure floods described above that could occur during eruptive activity or not, other important hazards are a direct consequence of magma-water interaction influenced by significant volumes of water positioned above potentially active vents. Estimates of the maximum crater lake water depth at the point of spillover range from 10 to 470 m (**Table 1**). These water depths are generally considered shallow and would not exert significant hydrostatic pressure on rising magma to effect volatile exsolution such that explosive activity would be inhibited (Cas and Giordano, 2014). Thus, depending on the volatile content of the erupting magma, the lakes should have no significant effect on the explosiveness of potential eruptions assuming no direct magma-water interaction.

Magma-water interaction in the context of crater lakes can include a range of eruptive styles (**Table 4**), from non-explosive lava effusion to violent explosions associated with magma-water mixing (Kokelaar, 1986; Wohletz et al., 2009). Mafic eruptions involving crater lakes where the supply of water is essentially unlimited are typically Surtseyan style eruptions (Kokelaar, 1983; Németh et al., 2006). In cases where the eruptive conditions promote dynamic interaction of water and magma such that a significant vapor-phase component results, very violent phreatoplinian activity can occur. Both Surtseyan and phreatoplinian activity could generate hazardous phenomena (**Table 4**; Mastin and Witter, 2000; Manville, 2015) that would be significant to areas within 5–10 km of the erupting volcano and ash fallout could affect areas well beyond this range. Among the main outcomes of eruptive activity at the crater and caldera lakes evaluated here are explosive displacement of water, lahars, and base surges. These outcomes are discussed briefly below.

7.1 Explosive Displacement of Water

Expulsion of water beyond crater rims could occur during larger eruptions involving substantial amounts of volatile-rich magma, generally VEI 3 or larger, but possible for eruptions as small as VEI 1 (Mastin and Witter, 2000; Rouwet and Morrissey, 2015). Explosive displacement of water from crater lakes can take on several forms from small seiche-like or splash displacements that may or may not overtop the crater rim such as those that occurred during the initial unrest at Karymskoye Lake, Kamchatka in 1996 (Belousov and Belousova, 2009) and at Ruapehu volcano, New Zealand in 1995 (Lecointre et al., 2004; Kilgour et al., 2010) to wholesale evacuation of the entire crater lake. A numerical modeling study by Morrissey et al. (2010) indicated that if crater lake water depth is > 90 m and eruption pressures are <10 MPa, subaqueous jetting capable of breaching the water surface is unlikely to occur, whereas in situations where the eruption pressure is > 10 MPa, explosive jetting through the

FIGURE 6 | Photographs of Kasatochi crater lake, before **(A)** and after **(B,C)** the August 7, 2008, VEI 4 eruption. **(A)**. View across Kasatochi crater lake to the north, August 6, 2008. Photo by C. Ford, US Fish and Wildlife Service. **(B)**. Interior of Kasatochi crater and small, shallow lake on the crater floor, August 22, 2008, about 2 weeks after the 2008 eruption. View is toward the east. Photo by R. Buchheit, US Fish and Wildlife Service. **(C)**. Panorama of northern, eastern, and southern part of Kasatochi crater, taken from crater rim, August 10, 2010. Photo by J. Williams, US Fish and Wildlife Service.

water column and displacement of water can occur. Given these approximate constraints, physical disruption of crater lakes in Alaska should be expected during future eruptions should they occur at the volcanoes discussed.

7.1.1 Alaska Examples

Complete evacuation of a crater lake occurred during the 2008 eruption of Kasatochi volcano (**Figure 6**) and resulted in some interesting and possibly diagnostic deposits (**Figure 7**). Kasatochi as described previously has a summit-defining crater that hosts a lake that today is about 8.4×10^5 m^2 and has a volume of about 1.7×10^7 m^3. Although the pre-2008 lake was slightly smaller, the volume was likely on the order of 10^7 m^3 (**Figure 6**). This volume of water was explosively discharged from the crater during the early phase of the 2008 Kasatochi eruption (Waythomas et al., 2010a; Scott et al., 2010). Although not widespread on Kasatochi Island, the first of the 2008 eruptive deposits to accumulate were massive grey muddy tephra deposits and multiple beds of pumice rich coarse ash and mud that collectively are up to 50 cm thick. When freshly exposed by shovel, these deposits oxidize rapidly and take on a yellow-brown-gray color indicating that the muddy components were probably chemically reduced when deposited (Scott et al., 2010). The pH of

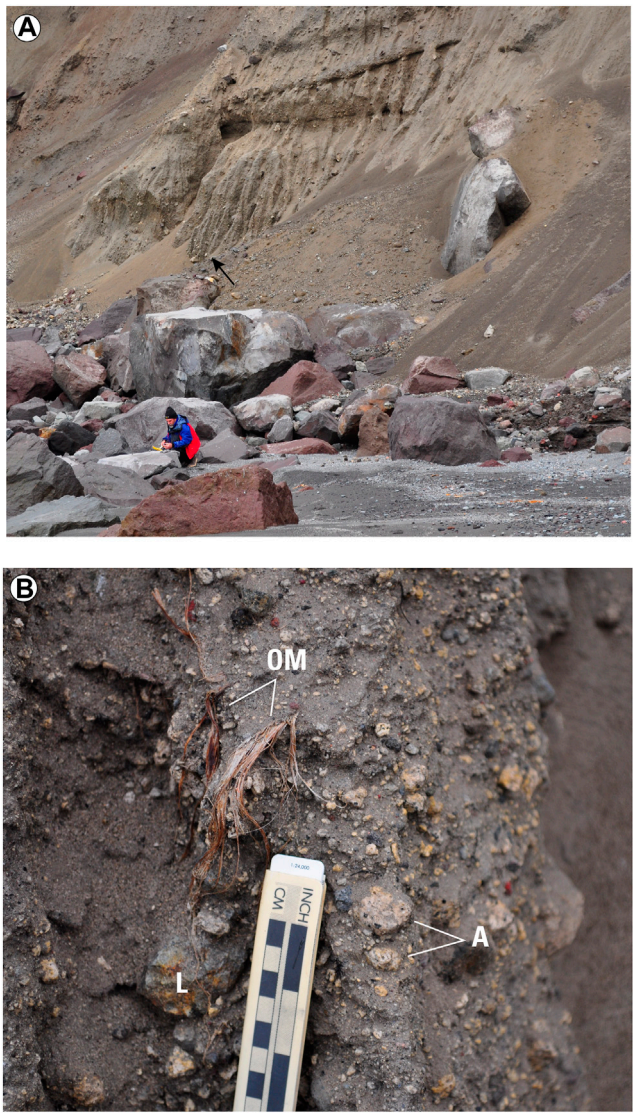

FIGURE 7 | Basal pyroclastic-flow deposits of the 2008 Kasatochi eruption, June 14, 2009. Both photos by C. Waythomas, AVO. **(A)**. Typical outcrop of lithic-rich pyroclastic-flow deposits on west side of Kasatochi Island. These deposits make up the first sequence of pyroclastic-flow deposits emplaced during the early part of the 2008 Kasatochi eruption. Arrow locates area of photo shown in **(B)**. Note person for scale in lower left. **(B)**. Close up view of pyroclastic-flow deposits containing unburned organic matter (OM), juvenile andesite (A) and lithic clasts (L). Organic matter like this is dispersed throughout the lower 1–2 m of the pyroclastic-flow deposits.

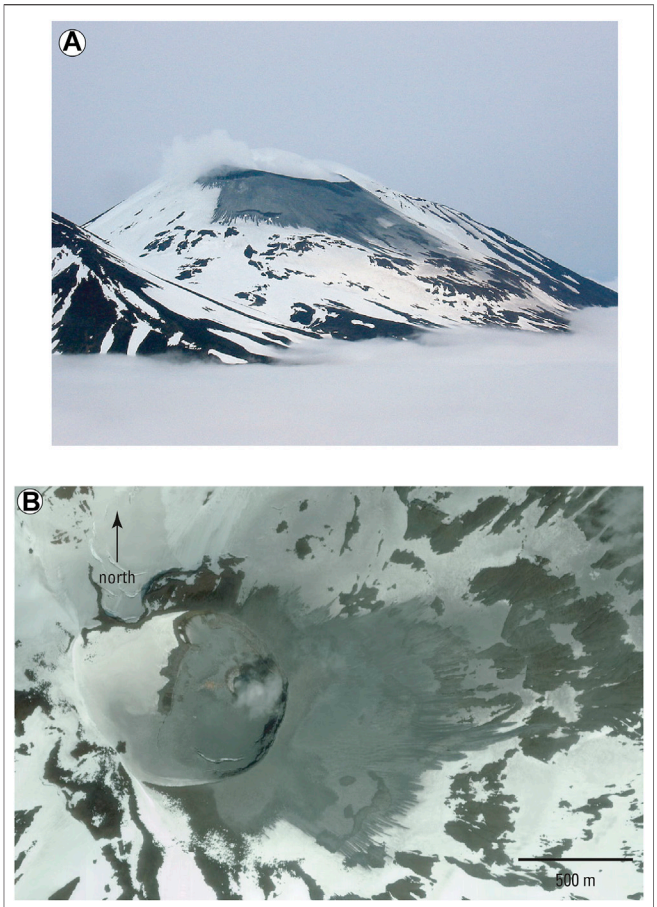

FIGURE 8 | Views of wet eruptive deposits on upper east flank of the south crater at Korovin volcano. **(A)**. Oblique photograph of Korovin south crater, July 1, 2004. Photo by T. Plucinski, AVO. **(B)**. True color Ikonos satellite image of the summit crater of Korovin volcano, July 4, 2004. Grey-colored ash and mass-flow deposit extends about 1 km beyond crater rim. A small lake that is typically present in the inner crater is absent in this image and was likely removed by the small eruption that produced the deposits evident on the east flank of the crater.

these deposits was 3–4.5, lower than all other 2008 eruptive deposits (Wang et al., 2010). A plausible explanation for these deposits is that they represent erupted lacustrine sediment from the floor of the crater lake. The muddy fall deposits are overlain by massive pyroclastic-flow deposits at least 10 m thick, that contain juvenile pyroclasts of light grey andesite and lithic debris (**Figure 7**). Various types of unburned organic matter (twigs, stems, moss, and grass) are dispersed throughout the lower 1–2 m of the pyroclastic-flow unit in several locations (**Figure 7**). This material represents the vegetated surface on the flanks of the volcano that was overrun and eroded by pyroclastic flows. Wave erosion of the Kasatochi coastline exhumed areas where wooden observation structures had been constructed by biologists working on the island; lumber remains in these areas is also unburned or charred. The presence of unburned organic matter and wood in the basal part of the pyroclastic-flow sequence indicates that these deposits were at low temperature (<300 °C) when emplaced. It is reasonable to conclude that water, water vapor, or both were components of the initial erupting mass and present in significant quantities to cool the eruptive mixture including pyroclastic flows emplaced during the early part of the eruption. As the eruption began to subside and water began reentering the crater, ejection of ballistic particles was noted (Waythomas et al., 2010a). This may have been a result of a greater degree of magma-water interaction as the supply of water increased.

Eruptive removal of the crater lake within the south crater of Korovin volcano was suspected in 2002 and 2004 (McGimsey et al., 2008). The south crater typically hosts a small crater lake

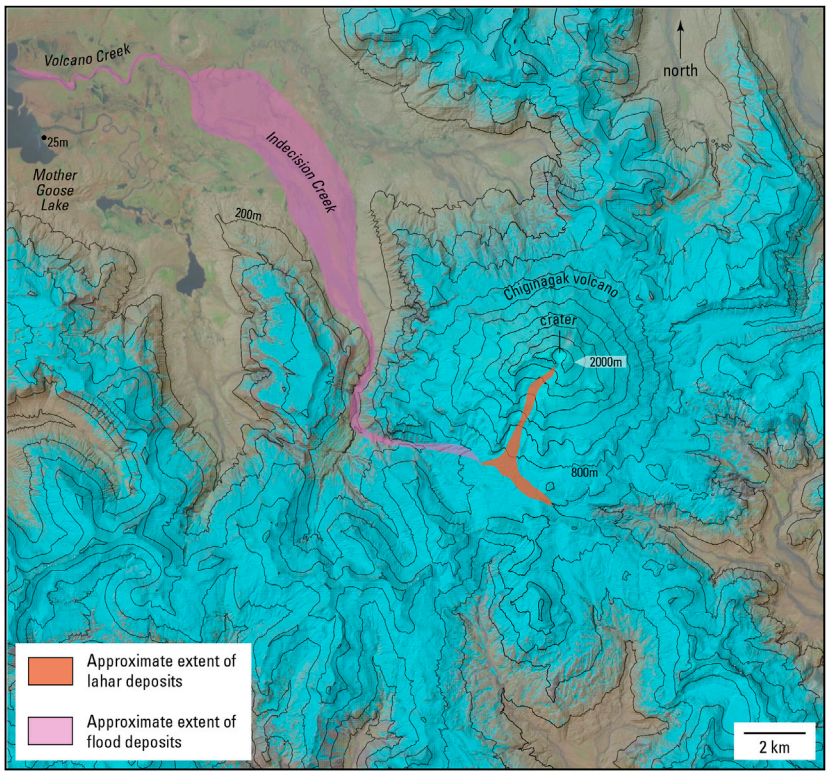

FIGURE 9 | Extent of lahar and flood deposits associated with May 2005 crater lake drainage event at Chiginagak volcano. Modified from Schaefer et al., 2008. Base is Sentinel-2 SWIR image of Chiginagak volcano, May 18, 2021.

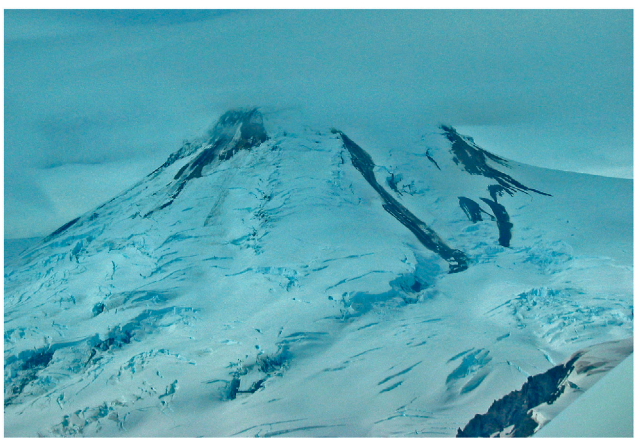

FIGURE 10 | Photograph of the Mount Spurr summit cone, July 15, 2004, view is toward the north. The dark streaks on the upper right (east) side of the cone are small debris flows that emerged through the ice and snow mantling the cone. The largest flow as about 1 km in length. It is unclear if there was a hydrologic connection between these flows and the crater lake that developed within the summit crater (see **Supplementary Figure S1**). Photo by C.A. Neal, AVO.

with an area of about 1.6×10^4 m^2 (**Table 1**; **Supplementary Figure S13**). Images of south crater in 2002 and 2004 show grey, apparently fine-grained deposits on the upper east flank of the cone and these deposits exhibit flowage features (digitate lobes, levees, and shallow channels; **Figure 8**) indicative of water-saturated flow. Brief eruptive bursts at Korovin's south crater are somewhat common historically and are likely phreatic or phreatomagmatic in origin (McGimsey et al., 2008). During these bursts, it is inferred that wet mixtures of ash and debris are emplaced on the upper part of the cone just beyond the crater rim. Although yet unconfirmed with before and after observations, the crater lake is also likely partially or entirely removed during these types of events.

7.2 Lahars

Discharge of water from crater lakes that led to the development of lahars has only been documented a few times in Alaska. The most noteworthy example is at Chiginagak volcano where acidic water drained via an ice dam and produced a lahar and water flood downstream from the crater (**Figure 9**; Schaefer et al., 2008; Schaefer et al., 2013). The volume of water released was about 3.8×10^6 m^3 (Schaefer et al., 2008). Because the fluid component of the flow was acidic (pH at least as low as 2.9) and it liberated acidic aerosols along its flow path, considerable impacts to the riparian ecosystem and to Mother Goose Lake occurred (Schaefer et al., 2008; Schaefer et al., 2013). Apparently, release of acidic water from Chiginagak crater is a recurring event as lake sediment cores from Mother Goose Lake reveal multiple layers

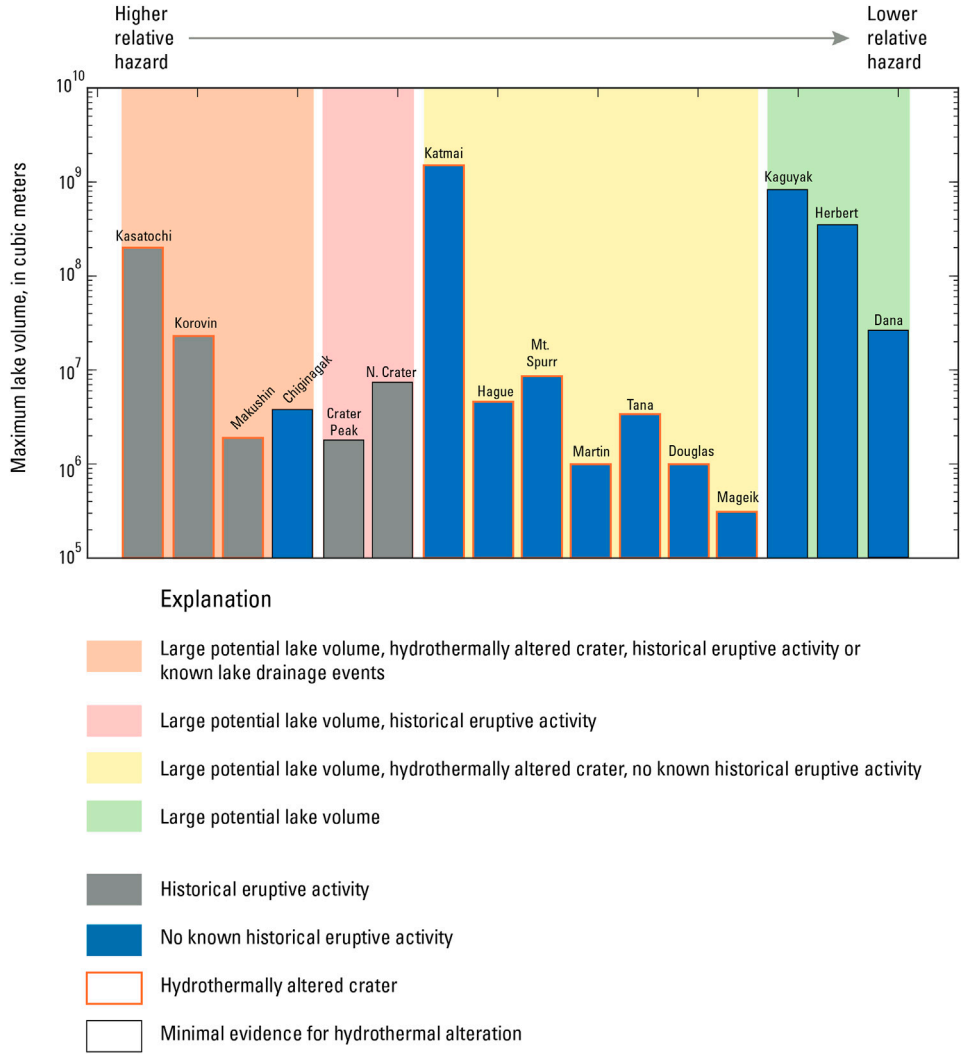

FIGURE 11 | Relative ranking scheme for hydrologic hazards at lake-filled volcanic craters and small calderas in Alaska. Those locations that have hydrothermally altered craters and a record of historical eruptive activity or lake drainage events are more likely to pose greater hydrologic hazards in the future than those locations with minimal evidence for hydrothermal alteration and no known historical eruptive activity.

of orange-colored sediment interpreted as acidic flood deposits (Kassel, 2009).

Watery debris flows were observed on the upper part of the Mount Spurr cone in July 2004 (**Figure 10**). The flows coincided with a period of elevated heat flow at the summit of Mount Spurr that melted a substantial amount of ice and snow at the summit to reveal a summit crater (Coombs et al., 2006). As described in an earlier section of this paper, a small lake developed in the crater. A hydrologic connection between the crater lake and the debris flows observed in July 2004 has not been determined. A plausible explanation for the flows is that they formed by outflow of ponded subglacial water stored on the Mount Spurr edifice that was produced by the elevated heat flow and if so, do not record drainage from the crater lake. Coombs et al. (2006) proposed forceable ejection of water from the crater lake resulting from rapid ice collapse into the water body. For this to occur, a subglacial channel network able to convey the debris-laden water would have to develop either prior to or coincident with ice collapse. Such networks are inferred at the base of thick glaciers (>100 m) but in these situations water release is related to the glacier reaching a flotation condition because of subglacial ponding of water to roughly 0.9 times the ice thickness (Björnsson, 1974; Nye, 1976). The prolonged period of elevated heat flow at the summit of Mount Spurr could have changed the permeability conditions of the snow and ice cover on the edifice such that forceable ejection of water produced the debris flows; however, the hydrologic connection between the crater lake and the flows remains unclear.

7.3 Base Surges

Explosive eruptions through water commonly produce ring-shaped, radially spreading, turbulent clouds known as base surges (Moore, 1967; Waters and Fisher, 1971; Rouwet and Morrissey, 2015). Base

surges move along the surface at speeds on the order of tens of meters per second and can flow as much as 10 km from the eruption site (Mastin and Witter, 2000). Although base surges were observed during the 2016–2017 eruption of Bogoslof volcano (Waythomas et al., 2020) and during the 1977 eruption at Ukinrek Maars (Self et al., 1980), they have not been documented during historical eruptive activity at any of the crater lakes discussed here. It is possible that base surges developed during the 2008 Kasatochi eruption as surge deposits are a component of the sequence of eruptive deposits (Waythomas et al., 2010a; Scott et al., 2010).

8 DISCUSSION AND CONCLUSIONS

Summit craters that contain lakes at stratovolcanoes in Alaska are somewhat uncommon relative to the number of active volcanoes. Of the volcanoes active during the Holocene, only about one-third have summit crater lakes and two of these are small caldera lakes (Katmai, Kaguyak). However, significant amounts of water situated over potentially active vents at the top of volcanic summits with substantial relief augments some of the hazards that are possible at these locations. Although the analysis of floods resulting from failure of the crater rim presented here is based on a worse-case scenario (crater lake at maximum possible volume), excessive volumes of water are not necessary for external water to have a role in affecting eruptive style (Cas and Simmons, 2018). Hydrovolcanic explosions are notoriously violent and when magma-water ratios approach about 5:1 the explosive energy of the mixture reaches a maximum (Wohletz, 1986; Mastin, 1995). Thus, even though a crater lake is shallow, it could supply enough external water to the upper edifice such that water-saturated conditions exist which could promote magma-water interaction possibly increasing the likelihood of explosive phreatomagmatic activity.

Available water in crater lakes in combination with active hydrothermal systems is also a well-known mechanism for enhancing alteration of volcanic edifices (Reid et al., 2001; Heap et al., 2021) which may lead to slope failures and catastrophic crater lake drainage. Several volcanic craters examined here exhibit some degree of hydrothermal alteration, but the extent and type of alteration and strength of the crater walls is not known.

The estimates of maximum peak discharge associated with rapid breach formation through the crater rims indicates that significant water floods could be generated. The flood magnitudes are comparable to the flood peaks associated with large volcanigenic floods in other settings, indicating that Alaskan crater lakes could pose significant hydrologic hazards should the craters become water filled.

The Alaska crater lakes discussed here can be grouped according to the relative hazard posed by each lake (**Figure 11**). The estimated maximum lake volumes for all craters and small calderas indicate that large floods could occur as all locations have large potential lake volumes (**Table 1**). Kasatochi, Korovin, Chiginagak, and Makushin also have hydrothermally altered craters and a record of historical eruptive activity or lake drainage events suggesting that they have a higher relative likelihood of experiencing hydrologic hazards related to their crater lakes. Crater Peak, and north crater on Cerberus volcano have been historically active, which suggests that if lakes develop at these locations, future eruptive activity can have a hydrologic component. Craters and associated lakes at Katmai, Hague, Mount Spurr, Martin, Tana, Douglas, and Mageik have hydrothermally altered craters but no known or limited historical eruptive activity. At these locations non-eruptive mechanisms for crater rim collapse, such as seismically induced liquefaction or seiching, could be important. That these locations have experienced several large historical earthquakes, including the M 9.2 1964 Alaska earthquake without associated crater wall collapse, suggests that the crater walls possess some inherent stability and thus a lower relative hazard potential. Qualitatively, the craters at Kaguyak, Herbert, and Dana appear to be the most stable and thus have the lowest relative crater wall failure hazard.

In comparison to crater lakes elsewhere, there are only a few documented cases of large floods associated with partial degradation of crater rim dams (Yang et al., 2005; Manville, 2015) with Crater Lake at Mt. Ruapehu, New Zealand being the most noteworthy (Massey et al., 2010). Water floods from lakes impounded by calderas have received more study but these are considerably larger than those associated with crater lakes (Waythomas et al., 1996; Manville, 2010). Given the relatively large number of crater lakes in Alaska, additional analysis of crater wall stability, crater hydrology and water balance, and an appropriate monitoring scheme for detecting lake level changes would provide much useful information for improving our understanding of the potential hazards associated with lake-filled volcanic craters.

DATA AVAILABILITY STATEMENT

The original contributions presented in the study are included in the article/**Supplementary Material**, further inquiries can be directed to the corresponding author.

AUTHOR CONTRIBUTIONS

The author confirms being the sole contributor of this work and has approved it for publication.

ACKNOWLEDGMENTS

The author wishes to thank the journal editor, D. Rouwet, two reviewers, C. A. Neal and J. Schaefer for their thoughtful reviews and comments which helped clarify several important points and better focus the manuscript.

SUPPLEMENTARY MATERIAL

The Supplementary Material for this article can be found online at: https://www.frontiersin.org/articles/10.3389/feart.2021.751216/full#supplementary-material

REFERENCES

Belousov, A., and Belousova, M. (2009). Eruptive Process, Effects and Deposits of the 1996 and the Ancient Basaltic Phreatomagmatic Eruptions in Karymskoye Lake, Kamchatka, Russia. *Volcaniclastic Sedimentation in Lacustrine Settings*, 35–60. doi:10.1002/9781444304251.ch3

Björnsson, H. (1974). Explanations of jökulhlaups from Grímsvötn, Vatnajökull, Iceland. *Jökull* 24, 1–26.

Brown, R. D., Brasnett, B., and Robinson, D. (2003). Gridded North American monthly snow depth and snow water equivalent for GCM evaluation. *Atmosphere-Ocean* 41 (1), 1–14. doi:10.3137/ao.410101

Cameron, C. E., and Snedigar, S. F. (2016). Alaska Volcano Observatory image database: *Alaska Div. Geol. Geophys. Surv. Digital Data Ser.* 13. doi:10.14509/29689. https://www.avo.alaska.edu/images/.

Carswell, W. J., Jr. (2013). The 3D Elevation Program: Summary for Alaska. US Geological Survey Fact Sheet FS 2013-3083.

Cas, R. A. F., and Giordano, G. (2014). Submarine volcanism: A review of the constraints, processes and products, and relevance to the Cabo de Gata volcanic succession. *Ijg* 133 (3), 362–377. doi:10.3301/IJG.2014.46

Cas, R. A. F., and Simmons, J. M. (2018). Why deep-water eruptions are so different from subaerial eruptions. *Front. Earth Sci.* 6, 1–21. doi:10.3389/feart.2018.00198

Christenson, B., Németh, K., Rouwet, D., Tassi, F., Vandemeulebrouck, J., and Varekamp, J. C. (2015). "Volcanic Lakes," in *Advances In Volcanology*. Editors D. Rouwet, B. Christenson, F. Tassi, and J. Vandemeulebrouck (Barcelona, Spain: IAVCEI), 1–20. doi:10.1007/978-3-642-36833-2_1

Chwang, A. T., and Housner, G. W. (1978). Hydrodynamic pressures on sloping dams during earthquakes. Part 1. Momentum method. *J. Fluid Mech.* 87 (2), 335–341. doi:10.1017/s0022112078001639

Chwang, A. T. (1978). Hydrodynamic pressures on sloping dams during earthquakes. Part 2. Exact theory. *J. Fluid Mech.* 87 (2), 343–348. doi:10.1017/s0022112078001640

Clague, J. J., and O'Connor, J. E. (2021). "Glacier-related outburst floods," in *Snow and ice-related hazards, risks, and disasters*. Editors W. Haeberli and C. Whiteman (Amsterdam, Netherlands: Elsevier), 467–499. doi:10.1016/b978-0-12-817129-5.00019-6

Clarke, G. K. C. (1982). Glacier Outburst Floods from "Hazard Lake", Yukon Territory, and the Problem of Flood Magnitude Prediction. *J. Glaciol.* 28, 3–21. doi:10.1017/s0022143000011746

Coombs, M. L., Larsen, J. F., and Neal, C. A. (2018). Postglacial Eruptive History and Geochemistry of Semisopochnoi Volcano, Western Aleutian Islands. *US Geol. Surv. Sci. Inv. Rep.*, 2017–5150.

Coombs, M. L., Neal, C. A., Wessels, R. L., and McGimsey, R. G. (2006). Geothermal disruption of summit glaciers at Mount Spurr volcano, 2004-6: An unusual manifestation of volcanic unrest. *US Geol. Surv. Prof. Paper* 1732, 1–33.

Costa, J. E. (1985). Floods from dam failures. *US Geol. Surv. Open-file Rep.* 85–560, 54p. doi:10.3133/ofr85560

Costa, J. E., and Schuster, R. L. (1988). The formation and failure of natural dams. *Geol. Soc. Amer. Bull.* 100 (7), 1054–1068. doi:10.1130/0016-7606(1988)100<1054:tfafon>2.3.co;2

Evans, B. W. C., Bergfeld, D., Neal, C. A., McGimsey, R. G., Werner, C. A., Waythomas, C. F., et al. (2015). Aleutian Arc Geothermal Fluids: Chemical Analyses of Waters and Gases Sampled in Association with the Alaska Volcano Observatory. US Geol. Survey Data Release. doi:10.5066/F78G8HR1

Fenner, C. N. (1930). Mount Katmai and Mount Mageik. *Zeit. F Vulkanol* 13 (1), 1–24.

Fierstein, J., and Hildreth, W. (2008). Kaguyak dome field and its Holocene caldera, Alaska Peninsula. *J. Volcanology Geothermal Res.* 177 (2), 340–366. doi:10.1016/j.jvolgeores.2008.05.016

Finn, C. A., Deszcz-Pan, M., Ball, J. L., Bloss, B. J., and Minsley, B. J. (2018). Three-dimensional geophysical mapping of shallow water saturated altered rocks at Mount Baker, Washington: Implications for slope stability. *J. Volcanology Geothermal Res.* 357, 261–275. doi:10.1016/j.jvolgeores.2018.04.013

Foster, M., Fell, R., and Spannagle, M. (2000). The statistics of embankment dam failures and accidents. *Can. Geotech. J.* 37 (5), 1000–1024. doi:10.1139/t00-030

Francis, P. (1976). *Volcanoes*. Middlesex, England: Penguin, 368 p.

Fread, D. L. (1996). "Dam-Breach Floods," in *Hydrology of Disasters*. Editor V. P. Singh (Dordrecht, Netherlands: Springer), 85–126. doi:10.1007/978-94-015-8680-1_5

Froehlich, D. C. (2008). Embankment dam breach parameters and their uncertainties. *J. Hydraul. Eng.* 134 (12), 1708–1721. doi:10.1061/(asce)0733-9429(2008)134:12(1708)

Gazetas, G. (1987). Seismic response of earth dams: some recent developments. *Soil Dynam. Earthquake Eng.* 6 (1), 3–47. doi:10.1016/0267-7261(87)90008-x

GLIMS Consortium (2005). *GLIMS Glacier Database, Version 1*. Boulder, Colorado USA: NASA National Snow and Ice Data Center Distributed Active Archive Center. doi:10.7265/N5V98602

Heap, M. J., Baumann, T., Gilg, H. A., Kolzenburg, S., Ryan, A. G., Villeneuve, M., et al. (2021). Hydrothermal alteration can result in pore pressurization and volcano instability. *Geology* 49. doi:10.1130/G49063.1

Henderson, F. M. (1966). *Open Channel Flow*. New York: Macmillan, 522 p.

Hildreth, W., and Fierstein, J. (2012b). Eruptive history of Mount Katmai, Alaska. *Geosphere* 8 (6), 1527–1567. doi:10.1130/GES00817.1

Hildreth, W., and Fierstein, J. (2003). Geologic Map of the Katmai Volcanic Cluster, Katmai National Park, Alaska. *US Geol. Surv. Geol. Inv.*, 2778, *Map* I-.

Hildreth, W., Fierstein, J., Lamphere, M. A., and Siems, D. F. (2000). Mount Mageik: A compound stratovolcano in Katmai National Park. *US Geol. Surv. Prof. Paper*, 1912–1615, 23–41.

Hildreth, W., and Fierstein, J. (2012a). The Novarupta-Katmai eruption of 1912 - largest eruption of the twentieth century; centennial perspectives. *US Geol. Surv. Prof.*, 1–278. Paper 1791. doi:10.3133/pp1791

Juhle, W., and Coulter, H. (1955). The Mt. Spurr eruption, July 9, 1953. *Trans. AGU* 36 (2), 199–202. doi:10.1029/tr036i002p00199

Kassel, C. M. (2009). *Lacustrine evidence from Mother Goose Lake of Holocene geothermal activity at Mount Chiginagak, Alaska Peninsula: Flagstaff, Arizona*. Arizona: Northern Arizona University, 138. unpublished M.S. thesis.

Keith, T. E. C. (Editor) (1995). "The 1992 Eruptions of Crater Peak Vent, Mount Spurr Volcano, Alaska." *US Geol. Surv. Bull.*, 2139, 220.

Keith, T. E. C., Thompson, J. M., and McGimsey, R. G. (1995). Chemistry of Crater Lake waters prior to the 1992 eruptions of Crater Peak, Mount Spurr volcano, Alaska. US Geol. Surv. Bull., 2139, 59–63.

Kilgour, G., Manville, V., Della Pasqua, F., Graettinger, A., Hodgson, K. A., and Jolly, G. E. (2010). The 25 September 2007 eruption of Mount Ruapehu, New Zealand: directed ballistics, surtseyan jets, and ice-slurry lahars. *J. Volcanol. Geotherm. Res.* 191 (1-2), 1–14. doi:10.1016/j.jvolgeores.2009.10.015

Kokelaar, B. P. (1983). The mechanism of Surtseyan volcanism. *J. Geol. Soc.* 140 (6), 939–944. doi:10.1144/gsjgs.140.6.0939

Kokelaar, P. (1986). Magma-water interactions in subaqueous and emergent basaltic. *Bull. Volcanol.* 48 (5), 275–289. doi:10.1007/BF01081756

Larsen, J. F., Neal, C. A., Schaefer, J. R., Kaufman, A. M., and Lu, Z. (2015). The 2008 phreatomagmatic eruption of Okmok volcano, Aleutian Islands, Alaska: Chronology, deposits, and landform changes. State of Alaska, Division of Geological and Geophysical Surveys Report of Investigations 2015-2, 52.

Lecointre, J., Hodgson, K., Neall, V., and Cronin, S. (2004). Lahar-triggering mechanisms and hazard at Ruapehu volcano, New Zealand. *Nat. Hazards* 31 (1), 85–109. doi:10.1023/B:NHAZ.0000020256.16645.eb

Lyu, Z., Chai, J., Xu, Z., Qin, Y., and Cao, J. (2019). A Comprehensive Review on Reasons for Tailings Dam Failures Based on Case History. *Adv. Civil Eng.* 2019, 1–18. doi:10.1155/2019/4159306

MacDonald, T. C., and Langridge-Monopolis, J. (1984). Breaching Charateristics of Dam Failures. *J. Hydraulic Eng.* 110 (5), 567–586. doi:10.1061/(asce)0733-9429(1984)110:5(567)

Manville, V. (2010). An overview of break-out floods from intracaldera lakes. *Glob. Planet. Change* 70 (1–4), 14–23. doi:10.1016/j.gloplacha.2009.11.004

Manville, V., Hodgson, K. A., and Nairn, I. A. (2007). A review of break-out floods from volcanogenic lakes in New Zealand. *New Zealand J. Geology Geophys.* 50 (2), 131–150. doi:10.1080/00288300709509826

Manville, V. (2015). "Volcano-Hydrologic Hazards from Volcanic Lakes," in *Volcanic Lakes*. Editors D. Rouwet, B. Christenson B., F. Tassi, and J. Vandemeulebrouck (Berlin, Heidelberg: Springer), 21–71. Advances in Volcanology. doi:10.1007/978-3-642-36833-2_2

March, R., Mayo, L. R., and Trabant, D. (1997). Snow and ice volume on Mount Spurr Volcano, Alaska, 1981. *US Geol. Surv. Water-res. Inv. Rep. WRI* 97-4142, 362. plates, scale 1:50,000. doi:10.3133/wri974142

Massey, C. I., Manville, V., Hancox, G. H., Keys, H. J., Lawrence, C., and McSaveney, M. (2010). Out-burst flood (lahar) triggered by retrogressive landsliding, 18 March 2007 at Mt Ruapehu, New Zealand-a successful early warning. *Landslides* 7 (3), 303–315. doi:10.1007/s10346-009-0180-5

Mastin, L. G. (1995). Thermodynamics of gas and steam-blast eruptions. *Bull. Volcanol.* 57 (2), 85–98. doi:10.1007/bf00301399

Mastin, L. G., and Witter, J. B. (2000). The hazards of eruptions through lakes and seawater. *J. Volcanology Geothermal Res.* 97, 195–214. doi:10.1016/s0377-0273(99)00174-2

McGarr, A., and Vorhis, R. C. (1968). Seismic seiches from the March 1964 Alaska earthquake. *US Geol. Surv. Prof.* Paper 544–E, 43 p., 1 sheet, scale 1:5,000,000. doi:10.3133/pp544e

McGimsey, R. G., and Neal, C. A. (1996). 1995 volcanic activity in Alaska and Kamchatka: summary of events and response of the Alaska Volcano Observatory: U.S. *Geol. Surv. Open-File Rep.* 96-0738, 22.

McGimsey, R. G., Neal, C. A., Dixon, J. P., and Ushakov, S. (2008). Volcanic activity in Alaska, Kamchatka, and the Kurile Islands: Summary of events and response of the Alaska Volcano Observatory. *US Geol. Surv. Sci. Inv. Rep*. 2007-5269, 94.

McGimsey, R. G., Neal, C. A., and Girina, O. (2003). 1998 volcanic activity in Alaska and Kamchatka: Summary of events and response of the Alaska Volcano Observatory. *US Geol. Surv. Open-file Rep. 03* 423, 35.

McGimsey, R. G., Maharrey, J. Z., and Neal, C. A. (2014). 2011 volcanic activity in Alaska: Summary of events and response of the Alaska Volcano Observatory. US Geol. Surv. Sci. Inv. Report 2014-5159, 49.

Miller, T. P., McGimsey, R. G., Richter, D. H., Riehle, J. R., Nye, C. J., Yount, M. E., et al. (1998). Catalog of the historically active volcanoes of Alaska. *US Geol. Surv. Open-file Rep*. 98-0582, 104. doi:10.3133/ofr98582

Moore, J. G. (1967). Base surge in recent volcanic eruptions. *Bull. Volcanol.* 30 (1), 337–363. doi:10.1007/bf02597678

Moore, J. G., Nakamura, K., and Alcaraz, A. (1966). The 1965 eruption of Taal Volcano. *Science* 151, 955–960. doi:10.1126/science.151.3713.955

Morrissey, M., Gisler, G., Weaver, R., and Gittings, M. (2010). Numerical model of crater lake eruptions. *Bull. Volcanol.* 72 (10), 1169–1178. doi:10.1007/s00445-010-0392-5

Motyka, R. I., Queen, L. D., Janik, C. J., Sheppard, D. S., Poreda, R. J., and Liss, S. A. (1988). Fluid geochemistry and fluid mineral equilibria in test wells and thermal gradient holes at the Makushin geothermal area, Unalaska Island, Alaska. *Alsk. Div. Geol. Geophys. Surv. Rep. Inv.* 88-14, 90.

Motyka, R. I. (1978). *Surveillance of Katmai caldera and crater lake, Alaska*. US: Unpub. Report to U.S. Park Service, University of Alaska Fairbanks Geophysical Institute Report UAG-R, 19. PX9100-7-1009.

Motyka, R. J., Liss, S. A., Nye, C. J., and Moorman, M. A. (1993). Geothermal resources of the Aleutian Arc. *Alsk. Div. Geol. Geophys. Surv. Prof. Rep. PR* 0114, 17, p., 4 sheets, scale 1:1,000,000.

Neal, C. A., McGimsey, R. G., Miller, T. P., Riehle, J. R., and Waythomas, C. F. (2001). Preliminary volcano-hazard assessment for Aniakchak Volcano, Alaska. US Geol. Surv. Open-File Report 00-0519, 35.

Neall, V. E. (1996). "Hydrological disasters associated with volcanoes," in *Hydrology of disasters*. Editor V. P. Singh (Dordrecht: Springer), 395–425.

Németh, K., Cronin, S. J., Charley, D., Harrison, M., and Garae, E. (2006). Exploding lakes in Vanuatu - "Surtseyan-style" eruptions witnessed on Ambae Island. *Episodes* 29 (2), 87–92. doi:10.18814/epiiugs/2006/v29i2/002

Newhall, C. G., and Dzurisin, D. (1988). Historical unrest at large calderas of the world. *US Geol. Surv. Bull.* 1855, 1108. doi:10.3133/b1855

Nye, C. J., Scott, W. E., Neill, O. K., Waythomas, C. F., Cameron, C. E., and Calvert, A. T. (2017). Geology of Kasatochi volcano, Aleutian Islands, Alaska. *Alsk. Div. Geol. Geophys. Surv. Prof. Rep.* 123, 127, p., 1 sheet, scale 1:5000. doi:10.14509/29718

Nye, C. J., and Turner, D. L. (1990). Petrology, geochemistry, and age of the Spurr volcanic complex, eastern Aleutian Arc. *Bull. Volcanol.* 52 (3), 205–226. doi:10.1007/bf00334805

Nye, J. F. (1976). Water Flow in Glaciers: Jökulhlaups, Tunnels and Veins. *J. Glaciol.* 17 (76), 181–207. doi:10.1017/s002214300001354x

O'Connor, J. E., and Costa, J. E. (2004). The world's largest floods, past and present: their causes and magnitudes. *US Geol. Surv. Circ.* 1254, 13p. doi:10.3133/cir1254

Pasternack, G. B., and Varekamp, J. C. (1997). Volcanic lake systematics I. Physical constraints. *Bull. Volcanology* 58 (7), 528–538. doi:10.1007/s004450050160

Pelecanos, L., Kontoe, S., and Zdravković, L. (2013). Numerical modelling of hydrodynamic pressures on dams. *Comput. Geotechnics* 53, 68–82. doi:10.1016/j.compgeo.2013.04.003

Persico, L., Lanman, H., Loopesko, L., Bruner, K., and Nicolaysen, K. (2019). Geomorphic processes influence human settlement on two islands in the Islands of Four Mountains, Alaska. *Quat. Res.* 91 (3), 953–971. doi:10.1017/qua.2018.112

Reid, M. E., Sisson, T. W., and Brien, D. L. (2001). Volcano collapse promoted by hydrothermal alteration and edifice shape, Mount Rainier, Washington. *Geol.* 29 (9), 779–782. doi:10.1130/0091-7613(2001)029<0779:vcpbha>2.0.co;2

Riehle, J. R. (1985). A reconnaissance of the major Holocene tephra deposits in the upper Cook Inlet region, Alaska. *J. Volcanol. Geotherm. Res.* 26 (1-2), 37–74. doi:10.1016/0377-0273(85)90046-0

Rouwet, D., and Morrissey, M. M. (2015). "Mechanisms of Crater Lake Breaching Eruptions," in *Volcanic Lakes*. Editors D. Rouwet, B. Christenson B., F. Tassi, and J. Vandemeulebrouck (Berlin, Heidelberg: Springer), 73–91. Advances in Volcanology. doi:10.1007/978-3-642-36833-2_210.1007/978-3-642-36833-2_3

Rouwet, D., Taran, Y. A., and Varley, N. R. (2004). Dynamics and mass balance of El Chichón crater lake, Mexico. *Geofisica Internacional* 43 (3), 427–434.

Rouwet, D. (2021). "Volcanic lake dynamics and related hazards," in *Hazards and Disasters, Forecasting and Planning for Volcanic Hazards, Risks, and Disasters*. Editor P. Papale (Amsterdam: Elsevier), v. 2, 439–471. doi:10.1016/b978-0-12-818082-2.00011-1

Schaefer, J. R., Scott, W. E., Evans, W. C., Wang, B., and McGimsey, R. G. (2013). Summit crater lake observations, and the location, chemistry, and pH of water samples near Mount Chiginagak volcano, Alaska: 2004-2012. *Alsk. Div. Geol. Geophys. Surv. Rep. Inv.* 6 (2), 25. doi:10.14509/25602

Schaefer, J. R., Scott, W. E., and Layer, P. W. (2017). Geologic map of Mount Chiginagak volcano, Alaska. *Alsk. Div. Geol. Geophys. Surv. Rep. Inv* 10, 32, p., 1 sheet, scale 1:25,000. doi:10.14509/29769

Schaefer, J. R., Scott, W. E., Evans, W. C., Jorgenson, J., McGimsey, R. G., and Wang, B. (2008). The 2005 catastrophic acid crater lake drainage, lahar, and acidic aerosol formation at Mount Chiginagak volcano, Alaska, USA: Field observations and preliminary water and vegetation chemistry results. *Geochem. Geophys. Geosyst.,* 9(7), a, n p., doi:10.1029/2007GC001900

Scott, W. E., Nye, C. J., Waythomas, C. F., and Neal, C. A. (2010). August 2008 Eruption of Kasatochi Volcano, Aleutian Islands, Alaska-Resetting an Island Landscape. *Arctic, Antarctic, Alpine Res.* 42 (3), 250–259. doi:10.1657/1938-4246-42.3.250

Self, S., Kienle, J., and Huot, J. P. (1980). Ukinrek Maars, Alaska: II, Deposits and formation of the 1977 craters. *J. Volcanol. Geotherm. Res.* 7 (1-2), 39–65. doi:10.1016/0377-0273(80)90019-0

Singh, V. P., Scarlatos, P. D., Collins, J. G., and Jourdan, M. R. (1988). Breach erosion of earthfill dams (BEED) model. *Nat. Hazards* 1 (2), 161–180. doi:10.1007/bf00126613

Stafford, J. M., Wendler, G., and Curtis, J. (2000). Temperature and precipitation of Alaska: 50 year trend analysis. *Theor. Appl. Climatology* 67 (1–2), 33–44. doi:10.1007/s007040070014

Stelling, P., Gardner, J. E., and Begét, J. (2005). Eruptive history of Fisher Caldera, Alaska, USA. *J. Volcanology Geothermal Res.* 139 (3–4), 163–183. doi:10.1016/j.jvolgeores.2004.08.006

Strehlow, K., Sandri, L., Gottsmann, J. H., Kilgour, G., Rust, A. C., and Tonini, R. (2017). Phreatic eruptions at crater lakes: occurrence statistics and probabilistic hazard forecast. *J. Appl. Volcanol.* 6, 4. doi:10.1186/s13617-016-0053-2

Sturm, M., Taras, B., Liston, G. E., Derksen, C., Jonas, T., and Lea, J. (2010). Estimating snow water equivalent using snow depth data and climate classes. *J. Hydromet.* 11 (6), 1380–1394. doi:10.1175/2010JHM1202.1

Sykes, L. R., Kisslinger, J. B., House, L., Davies, J. N., and Jacob, K. H. (1981). Rupture zones and repeat times of great earthquakes along the Alaska-Aleutian Arc, 1784–1980. *Earthquake Prediction: Int. Rev.* 4, 73–80.

Walder, J. S., and O'Connor, J. E. (1997). Methods for predicting peak discharge of floods caused by failure of natural and constructed earthen dams. *Water Resour. Res.* 33 (10), 2337–2348. doi:10.1029/97wr01616

Wang, B., Michaelson, G., Ping, C.-L., Plumlee, G., and Hageman, P. (2010). Characterization of Pyroclastic Deposits and Pre-eruptive Soils following the 2008 Eruption of Kasatochi Island Volcano, Alaska. *Arctic, Antarctic, Alpine Res.* 42, 276–284. doi:10.1657/1938-4246-42.3.276

Waters, A. C., and Fisher, R. V. (1971). Base surges and their deposits: Capelinhos and Taal Volcanoes. *J. Geophys. Res.* 76 (23), 5596–5614. doi:10.1029/JB076i023p05596

Watters, R. J., Zimbelman, D. R., Bowman, S. D., and Crowley, J. K. (2000). Rock mass strength assessment and significance to edifice stability, Mount Rainier and Mount Hood, Cascade Range volcanoes. *Pure Appl. Geophys.* 157 (6), 957–976. doi:10.1007/s000240050012

Waythomas, C. F., Angeli, K., and Wessels, R. L. (2020). Evolution of the submarine–subaerial edifice of Bogoslof volcano, Alaska, during its 2016–2017 eruption based on analysis of satellite imagery. *Bull. Volc.* 82 (2), 1–26. doi:10.1007/s00445-020-1363-0

Waythomas, C. F. (2015). Geomorphic consequences of volcanic eruptions in Alaska: A review. *Geomorphology* 246, 123–145. doi:10.1016/j.geomorph.2015.06.004

Waythomas, C. F., Pierson, T. C., Major, J. J., and Scott, W. E. (2013). Voluminous ice-rich and water-rich lahars generated during the 2009 eruption of Redoubt Volcano, Alaska. *J. Volcanology Geothermal Res.* 259, 389–413. doi:10.1016/j.jvolgeores.2012.05.012

Waythomas, C. F., Scott, W. E., and Nye, C. J. (2010b). The geomorphology of an Aleutian volcano following a major eruption: the 7-8 August 2008 eruption of Kasatochi Volcano, Alaska, and its aftermath. *Arctic, Antarctic, Alpine Res.* 42 (3), 260–275. doi:10.1657/1938-4246-42.3.260

Waythomas, C. F., Scott, W. E., Prejean, S. G., Schneider, D. J., Izbekov, P., and Nye, C. J. (2010a). The 7–8 August 2008 eruption of Kasatochi Volcano, central Aleutian Islands, Alaska. *J. Geophys. Res. Solid Earth* 115, B12. doi:10.1029/2010jb007437

Waythomas, C. F., Walder, J. S., McGimsey, R. G., and Neal, C. A. (1996). A catastrophic flood caused by drainage of a caldera lake at Aniakchak Volcano, Alaska, and implications for volcanic hazards assessment. *Geol. Soc. Am. Bull.* 108 (7), 861–871. doi:10.1130/0016-7606(1996)108<0861:ACFCBD>2.3.CO;2

Werner, C. A., Kern, C., and Kelly, P. J. (2020). Chemical Evaluation of Water and Gases Collected from Hydrothermal Systems Located in the Central Aleutian Arc. *US Geol. Surv. Sci. Inv. Rep.* 5043, 35.

Wesson, R. L., Boyd, O. S., Mueller, C. S., Bufe, C. G., Frankel, A. D., and Petersen, M. D. (2007). Revision of time-independent probabilistic seismic hazard maps for Alaska. *US Geol. Surv. Open-file Rep.* 1043, 33 p. doi:10.3133/ofr20071043

Wilson, F. H., Detterman, R. L., Miller, J. W., and Case, J. E. (1995). Geologic map of the Port Moller, Stepovak Bay, and Simeonof Island quadrangles, Alaska Peninsula, Alaska. *US Geol. Surv. Misc. Invest. Ser. Map* 2272, 2, sheets, scale 1: 250,000.

Wohletz, K. H. (1986). Explosive magma-water interactions: Thermodynamics, explosion mechanisms, and field studies. *Bull. Volcanol.* 48, 245–264. doi:10.1007/bf01081754

Wohletz, K., Zimanowski, B., Büttner, R., and Fagents, S. A. (2009). "Magma-water interactions," in *Modeling Volcanic Processes: The Physics and Mathematics of Volcanism*. Editors S. A. Fagents, T. K. P. Gregg, and R. M. C. Lopes (Cambridge, United Kingdom: Cambridge Univ. Press), 230–257. doi:10.1017/CBO9781139021562.011

Wolfe, B. A. (2001). *Paleohydrology of a catastrophic flood release from Okmok caldera and post-flood eruption history at Okmok volcano, Umnak Island*. Alaska: University of Alaska-Fairbanks, Ph.D. Dissertation, 100 p.

Yang, P., Yokoyama, N., Inoue, K., and Amino, K. (2005). Preliminary Investigation of the Crater Lake Breach at Mt. Pinatubo, Philippines. *J. Jpn. Soc. Eng. Geology* 46 (5), 287–292. doi:10.5110/jjseg.46.287

Conflict of Interest: The author declares that the research was conducted in the absence of any commercial or financial relationships that could be construed as a potential conflict of interest.

frontiers in Earth Science

ORIGINAL RESEARCH
published: 07 January 2022
doi: 10.3389/feart.2021.740671

Quantitative Assessment of Temporal Changes in Subaqueous Hydrothermal Activity in Active Crater Lakes During Unrest Based on a Time-Series of Lake Water Chemistry

Akihiko Terada[1]*, *Muga Yaguchi*[2] *and Takeshi Ohba*[3]

[1]Volcanic Fluid Research Center, School of Science, Tokyo Institute of Technology, Meguro, Japan, [2]Meteorological Research Institute, Japan Meteorological Agency, Tsukuba, Japan, [3]Department of Chemistry, School of Science, Tokai University, Hiratsuka, Japan

OPEN ACCESS

Edited by:
Dmitri Rouwet, Istituto Nazionale di Geofisica e Vulcanologia, Italy

Reviewed by:
Jacob B. Lowenstern, Cascades Volcano Observatory, United States
Ben Matthew Kennedy, University of Canterbury, New Zealand

***Correspondence:**
Akihiko Terada
terada@ksvo.titech.ac.jp

Specialty section:
This article was submitted to Volcanology, a section of the journal Frontiers in Earth Science

Received: *13 July 2021*
Accepted: *18 November 2021*
Published: *07 January 2022*

Citation:
Terada A, Yaguchi M and Ohba T (2022) Quantitative Assessment of Temporal Changes in Subaqueous Hydrothermal Activity in Active Crater Lakes During Unrest Based on a Time-Series of Lake Water Chemistry. Front. Earth Sci. 9:740671. doi: 10.3389/feart.2021.740671

Regular sampling of lake water has been performed at many volcanoes to assess the state of volcanic activity. However, it is not clear whether the absolute concentrations or, instead, rate of changes in concentrations are more suitable for such assessments. In this study, we show that temporal changes in concentrations of an element in lake water are described by a simple differential equation, assuming changes in lake volume and chemical processes are negligible. The time constants (63% response time for changes in the chemical concentration in lake water) have a wide range varying between 20 and 1,000 days for the studied volcanoes in Japan, meaning it takes a long time to assess volcanic activity based on the absolute concentration of an element. In order to assess the volcanic activity in a shorter time period, based on a time-series of lake element concentration data, we developed a numerical model to calculate temporal changes in the steady-state concentration, which is proportional to the elemental concentrations of the bulk hydrothermal fluid injected from subaqueous fumaroles and hot springs. We applied our method to Yugama crater lake at Kusatsu–Shirane volcano, Japan, and quantitatively evaluated temporal changes in the hydrothermal input from 1964 to 2020. As a result, we detected changes in the Cl concentrations of the bulk hydrothermal input that were associated with unrest including the phreatic eruption in 1976 and earthquake swarms in 1989–1992 and 2014–2020. The future concentration in the lake water can be predicted from the most recent steady-state concentrations. Comparing the predicted concentration curve with the concentration obtained from lake water samples, it is possible to quickly assess whether the concentration of the bulk hydrothermal input has increased/decreased or remained constant.

Keywords: active crater lake, volcanic lake, chloride, volcanic unrest, monitoring, Kusatsu-Shirane Volcano, Aso volcano

1 INTRODUCTION

Volcanic lakes can cause a variety of hazards, such as phreatic eruptions, mud eruptions, tsunamis, base surges, and lahars (Morrissey et al., 2010; Manville, 2015; Edwards et al., 2017). These can be hazards near the volcanic lake, and also near rivers that drain the lake. Therefore, assessing activity of a volcanic lake is a critical issue for society. In addition, volcanic lakes can act as condensers of heat and materials released from hydrothermal systems. To understand material circulation in hydrothermal systems, measurements of lake water levels, temperatures, and concentrations of elements have been undertaken at crater lakes worldwide (e.g., Pasternack and Varekamp, 1997).

Prior to an eruption, increases/decreases in lake volume have occurred (Barberi et al., 1992; Werner et al., 2008; Fournier et al., 2009, 2011; Christenson et al., 2017), which have been interpreted to reflect changes in the mass flux and enthalpy of fluid emitted from the lake bottom (Terada and Hashimoto, 2017). Monitoring the surface water temperature of volcanic lakes, which is a simple remote measurement by infrared thermometry, is a key observation for monitoring volcanic activity (Oppenheimer, 1997; Lewicki et al., 2016; Cigolini et al., 2018; Candela-Becerra et al., 2020). In addition, regular sampling of lake water has been performed at many volcanoes, including Ruapehu (Giggenbach and Glover, 1975; Hurst et al., 1991; Christenson, 2000), Kusatsu–Shirane (Ohba et al., 1994, 2008), Poás (Rowe et al., 1992; Martínez et al., 2000; Rouwet et al., 2017), Kawah Ijen (van Hinsberg et al., 2017), Copahue (Agusto et al., 2017), and crater lakes in Mexico (Armienta et al., 2000; Rouwet et al., 2008; Peiffer and Taran, 2013; Peiffer et al., 2015).

Yugama crater lake of Kusatsu–Shirane volcano has repeatedly experienced gradual increases/decreases in concentrations of chemical components, although water temperatures and levels have not changed significantly (Ohba et al., 2008). Such changes in concentrations are accompanied by earthquake swarms, ground deformation, and thermal demagnetization beneath the crater lake (Takahashi and Fujii, 2014), corresponding to a volcano with slow unrest (Stix, 2018).

Although phreatic eruptions have occurred repeatedly at Yugama crater lake since the 1880s, the lake is a popular tourist attraction. In the assessment of volcanic activity at Kusatsu–Shirane volcano, the Japan Meteorological Agency (JMA) considers changes in concentrations of elements to be a key parameter, in addition to geophysical observations. However, it is unclear whether the absolute concentrations or rate of changes in concentrations are more suitable for such assessments. Concentrations of lake water are adjusted according to the mass balance of the lake system (Pasternack and Varekamp, 1997; Rouwet and Tassi, 2011). Furthermore, the absolute lake concentration depends on the history of the lake concentration because the current concentration is a result of integrating the past inputs and outputs of the element. The rate of changes in concentrations can occur slowly in large-volume crater lakes (Varekamp, 2002, 2015; Rouwet et al., 2014), and thus it takes a long time to assess changes in volcanic activity based on absolute concentrations. To assess changes in volcanic activity, monitoring changes in the concentration of the hydrothermal fluid injected from the lake bottom is more suitable rather than tracking element concentrations in lake water.

In this study, we developed a simple numerical model to calculate temporal changes in concentrations of the bulk hydrothermal fluid injected from the lake bottom, by assuming the water volume remains largely constant during each analytical period. If pH of lake water is not extremely low (pH > 0), this model can be applied to elements such as chloride (Cl) for which chemical reactions and evaporation from the lake surface are negligible (Rouwet and Ohba 2015; Capaccioni et al., 2017). In addition, we propose a method for predicting future lake concentrations based on a time-series of recent concentrations of water samples taken from crater lakes. Our model is applied to active crater lakes in Japan, particularly Yugama crater lake at Kusatsu–Shirane volcano, in order to test the validity of our assessment of volcanic activity.

2 MODELING

Volcanic lakes, particularly active hot crater lakes, exhibit variable chemical characteristics from lake to lake (e.g., Rouwet et al., 2014). Such lakes with diameters greater than several tens of meters in Japan are Yugama crater lake at Kusatsu–Shirane volcano (Kusakabe et al., 2000; Ohba et al., 2008), Yudamari cater lake at Aso volcano (Terada et al., 2012), Oyunuma crater lake at Noboribetsu volcano (Murozumi et al., 1966; Fukutomi et al., 1968; Inoue and Aoki, 2000), and Okama crater lake at Zao volcano (Anzai, 1961; Miura et al., 2012) (**Figure 1**). In such crater lakes, the annual water level is largely maintained throughout periods of volcanic quiescence, although there are seasonal fluctuations due to meteorological factors. Our model does not take into account chemical reactions.

2.1 General Mass Balance of a Chemical Component of Interest

We assumed that fumaroles and hot-water fountains exist on the bottom of the crater lakes. All mass injected from the lake bottom is absorbed by the lake water. For simplicity, it was assumed that the lake water is well mixed, and thus the element concentration in the lake water is homogeneous. We considered a closed lake without surface runoff outlets and inlets, which is the case for Yugama, Yudamari, and Okama crater lakes (**Figures 1A–C**). Oyunuma crater lake (**Figure 1D**) is affected by surface runoff inlets and outlets, and is discussed further in *Notes on the Analysis*.

The lake water is supplied by fluid injected from the hydrothermal system beneath the lake bottom (m_{in} in kg/s) and by precipitation (rainfall) inflow (m_{pr} in kg/s). Lake water is lost by evaporation from the lake surface (m_{ev} in kg/s) and seepage through the lake bottom (m_{sp} in kg/s) (e.g., Hurst et al., 1991; Rowe et al., 1992; Pasternack and Varekamp, 1997). If $V(t)$ (in m^3) is the lake volume as a function of time (t in s) and the density of lake water (ρ in 1,000 kg/ m^3) (**Table 1**), the mass

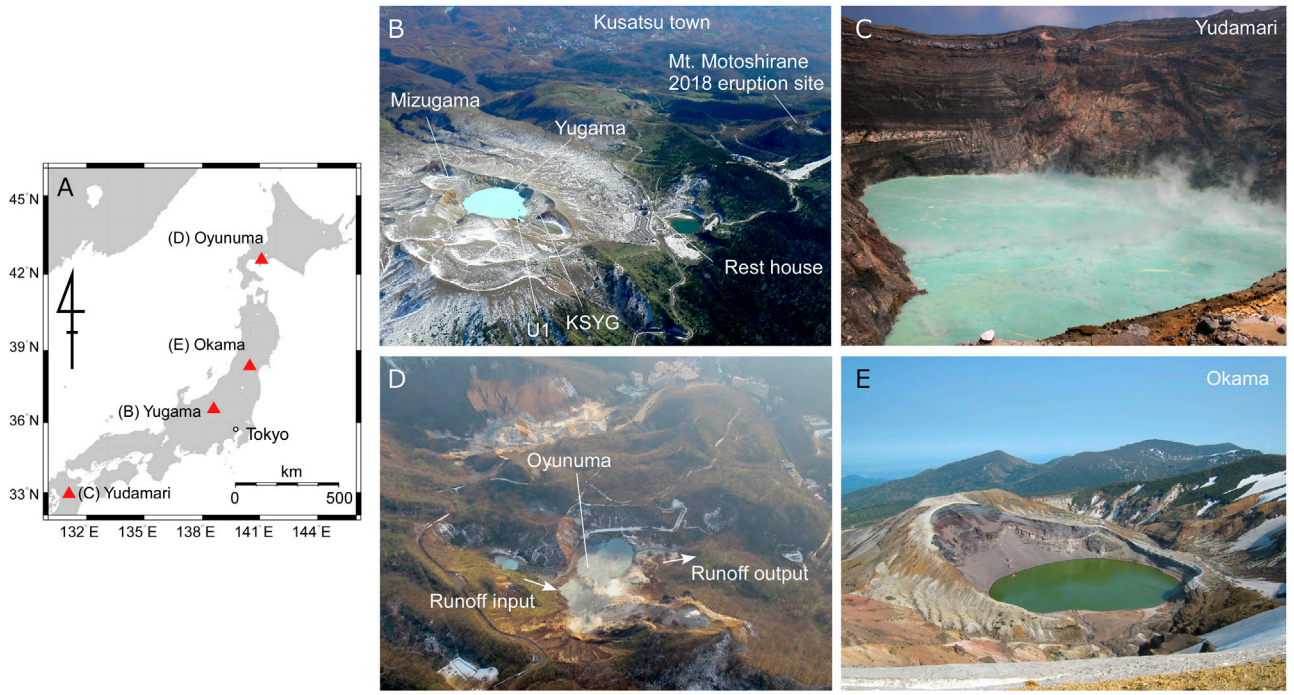

FIGURE 1 | (A) Location map of active crater lakes in Japan. Photographs of **(B)** Yugama crater lake at Kusatsu–Shirane volcano taken on November 6, 2017, **(C)** Yudamari crater lake at Aso volcano taken by Shin Yoshikawa on July 27, 2007, **(D)** Oyunuma crater lake at Noboribetsu volcano taken by Hiroshi Aoyama on December 7, 2020 with the cooperation of the Hokkaido Regional Development Bureau, and **(E)** Okama crater lake at Zao volcano taken by Mare Yamamoto on May 29, 2017.

TABLE 1 | Definitions of abbreviations.

t Time, s
a Time constant, s
ρ Water density, 1,000 kg/m^3
τ Dimensionless time, t/a
V Lake volume, m^3
(Mass flux, kg/s)
m_{in} Sum of the hydrothermal fluid injected from subaqueous fumaroles and hot springs.
m_{sp} Seepage through the lake bottom.
m_{pr} Rain water inflow.
m_{ev} Evaporating water from the lake surface.
m_{ri} Surface runoff input containing the element of interest.
m_{ro} Surface runoff output containing the element of interest.
(Chemical concentration, mg/kg)
C The lake water.
C_0 The lake water at t = 0.
C_{in} The concentration of the bulk hydrothermal fluid injected from subaqueous fumaroles and hot springs.
C_{pr} Rain water.
C_{ev} Evaporating water.
C_{ri} Surface runoff input.
C_{eq} Steady-state lake water defined by the **Eq. 3**.
C'_{eq} Steady-state lake water defined by the **Eq. 16**, which m_{ri} and m_{ro} are considered.

conservation for an element in the lake water (Taran and Rouwet, 2008; Rouwet and Tassi, 2011) is:

$$\rho \frac{d}{dt}[V(t)C(t)] = m_{in}C_{in} - m_{sp}C(t) + m_{pr}C_{pr} - m_{ev}C_{ev} \quad (1)$$

where $C(t)$ is the concentration of the element (mg/kg) as a function of t. Parameters C_{in}, C_{pr}, and C_{ev} are the concentrations of the bulk hydrothermal fluid injected from the lake bottom, rain water, and evaporated water, respectively.

2.2 Steady-State Condition

We assumed that evaporation loss of elements from the lake surface is negligible. This assumption can be applied to elements such as Cl (Simonson and Palmer, 1993) as long as pH of lake water is not extremely low to evaporate HCl (Rouwet and Ohba 2015; Capaccioni et al., 2017). Assuming conservative elements such as Cl or Mg as the chemical tracers in our model, C_{pr} and C_{ev} are negligible compared to $C(t)$ and C_{in}. **Eq. 1** is rewritten

$$\rho \frac{d}{dt}[V(t)C(t)] = m_{in}C_{in} - m_{sp}C(t) \quad (2)$$

If $V(t)$ and $C(t)$ are approximately maintained, i.e., the mass equilibrium of the lake system is achieved, the steady-state concentration of the element, C_{eq} mg/kg, is defined as

$$C_{eq} = \frac{m_{in}}{m_{sp}}C_{in} \quad (3)$$

Equation 3 corresponds to the expression for the steady-state lake by Varekamp (2002). In the lake system represented by **Eq. 1**, C_{eq} is not equal to C_{in} in the steady-state because the water mass is balanced between m_{pr} and m_{ev},

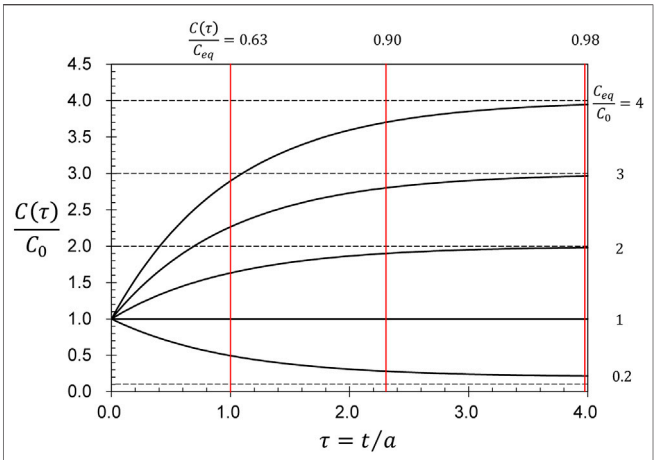

FIGURE 2 | The dimensionless concentration $C(\tau)/C_0$ as a function of dimensionless time $\tau = t/a$, assuming C_{eq}/C_0 = 0.2, 1.0, 2.0, 3.0, and 4.0. Red bars show the 63, 90, and 98% response for $C(\tau)/C_0$.

which do not contain the element of interest, as well as m_{in} and m_{sp}.

2.3 Non-steady State Conditions

In a lake system where a fluid with a constant concentration of an element enters at a constant rate and the lake water leaves at a constant rate, the temporal change in the concentration can be represented by a response of a first-order system (Albarède, 1995; Varekamp, 2002, 2015). In this section, we represent the time constant of the system, assuming the water volume is constant.

If the temporal change in water volume is negligible, **Eq. 3** can be rewritten with C_{eq} as:

$$\frac{dC(t)}{dt} = \frac{m_{sp}}{\rho V}\left(C_{eq} - C(t)\right) \tag{4}$$

A nearly constant water volume suggests that temporal changes in m_{in} and m_{sp} are negligible. Assuming constant m_{in} and m_{sp}, the change in $C(t)$ in response to the constant C_{in} is obtained by integrating **Eq. 4**:

$$C(t) = C_{eq} + \left(C_0 - C_{eq}\right)e^{-\frac{t}{a}} \tag{5}$$

where C_0 is the concentration of the element in lake water at t = 0. Here, a is a time constant, corresponding to the residence time (Taran and Rouwet, 2008):

$$a = \frac{\rho V}{m_{sp}} \tag{6}$$

The time constant a increases with increasing V, whereas it decreases with increasing m_{sp}. **Figure 2** shows calculations for the dimensionless concentration $(C(\tau)/C_0)$ as a function of dimensionless time $\tau = t/a$. For a given C_0 and a, which are proportional to V/m_{sp}, the rate of change in concentration $C(t)$ increases with C_{eq}, which is proportional to C_{in}. Response times at 63, 90, and 98% were calculated to be $2a$, $2.2a$, and $3.8a$, respectively.

2.4 Estimations of the Time Constant

The seepage flux (m_{sp}) is required to estimate the time constant a. For Yugama crater lake (**Figure 1B**), daily seepage flux ($m_{sp} \times 86,400$) is estimated to be $V/1000$, based on temporal changes in ^{134}Cs and ^{136}Cs activity (Hirayama et al., 2021). Therefore, the time constant a was estimated to be 8.6×10^7 s (1,000 days) from **Eq. 6** (**Table 2**).

In the case of Yudamari crater lake (**Figure 1C**), V and m_{sp} during calm periods (2006/10/21–12/21, 2007/9/20–11/7, and 2008/3/12–5/31) were estimated by Terada et al. (2012) using a numerical model, which takes into account mass and energy balance and meteorological conditions. Therefore, the time constant a was estimated to be 2.0–2.2 $\times 10^7$ s (230–250 days) (**Table 2**).

For Okama crater lake (**Figure 1D**), the m_{sp} has not yet been estimated. In such a situation, the empirical relationship $m_{sp} = 0.2 \times V_e^{0.39}$ (V_e is the equivalent water volume of the lake, which is the product of lake area and mean depth; **Figure 6** in Terada et al., 2012) can be applied. Using a surface area of 8.3×10^4 m^2 and mean depth of 18.1 m (Kato, 1960), m_{sp} is calculated to be 48 kg/ s and, therefore, the time constant was estimated to be 3.1×10^7 s (360 days) (**Table 2**).

3 EVALUATION OF CHANGES IN THE STEADY STATE CONCENTRATION

In this section, we calculate temporal changes in C_{eq} (steady-state concentration of an element of interest in the lake water) based on two or three analyses of the lake composition. If m_{in}/m_{sp} (mass flux ratio of the bottom input fluid to seepage through the lake bottom) is known, temporal changes in the concentration of the bulk hydrothermal fluid injected from the subaqueous fumaroles and hot springs C_{in} can be estimated from **Eq. 3**.

3.1 Estimation of the Temporal Changes in the Steady-State Concentration C_{eq}

We define C^i as the concentration of an element in the lake water at time t^i. The time interval between t^i and t^{i-1} is referred to as Δt_i. During each analytical period ($t^{i-1} < t < t^i$), we assumed the concentration of the bulk hydrothermal input C_{in}^i and time constant a^i were constant. In such a case, the relationship between C^i and C^{i-1} in each period is expressed using **Eq. 5** as follows:

$$C^{i-1} = C_{eq}^i + \left(C^i - C_{eq}^i\right)\cdot e^{\frac{\Delta t^i}{a^i}} \tag{7}$$

Here we define F^i as:

$$F^i \equiv e^{-\frac{\Delta t^i}{a^i}} \tag{8}$$

Combining **Eqs 7**, **8**, the lake concentration C^i at time t_i can be rewritten as:

$$C^i = \left(1 - F^i\right)C_{eq}^i + F^i C^{i-1} \tag{9}$$

TABLE 2 | Summary of the seepage flux m_{sp}, water volume V, and time constant a for each volcano. Numbers refer to the following references: [1] Hirayama et al. (2020), [2] Terada et al. (2012), [3] Kato (1960), and [4] Fukutomi et al. (1968).

Crater lake	Term	m_{sp} kg/s	V m^3	a day
Yugama, Kusatsu–Shirane[1]	2012			1,000
Yudamari, Aso[2]	2006/10/21–12/21	27.4	5.5×10^5	230
	2007/9/20–11/7	30.2	6.5×10^5	250
	2008/3/12–5/31	22.2	4.5×10^5	240
Okama, Zao[3]	–	48[a]	1.5×10^6	360
Oyunuma, Noboribetu[4]	1966–1967	46[b]	9×10^4	23

[a]*Calculated by the empirical relation of* $m_{sp} = 0.2 \times V_e^{0.39}$ *(V_e is the equivalent water volume of the lake;* ***Figure 6*** *in Terada et al., 2012).*
[b]*Surface runoff output (Fukutomi et al., 1968).*

This equation corresponds to the form of a recursive filter (Smith, 1997; Robert et al., 2014). The time-series of C^i_{eq} at time t_i was calculated sequentially by **Eq. 9** using data, C^{i-1} and C^i, as a two data calculation:

$$C^i_{eq} = \frac{C^i - F^i C^{i-1}}{1 - F^i} \tag{10}$$

The concentration of the lake water can fluctuate due to meteorological factors and analytical uncertainties. To reduce the effects of such fluctuations, we used C^{i-2} in addition to C^{i-1} and C^i. We define G^i as:

$$G^i \equiv e^{-\frac{\Delta t^{i-1}}{a^{i-1}}} \tag{11}$$

where $\Delta t_{i-1} = t_{i-1} - t_{i-2}$. Like **Eq. 9**, C^i is expressed by the following equation:

$$C^i = \left(1 - F^i G^i\right) C^i_{eq} + F^i G^i C^{i-2} \tag{12}$$

Summing **Eqs 9**, **12**, C^i_{eq} at a time t_i can be calculated by the following equation as a three data calculation:

$$C^i_{eq} = \frac{2C^i - F^i C^{i-1} - F^i G^i C^{i-2}}{2 - F^i - F^i G^i} \tag{13}$$

Assuming C^i_{eq} does not change during each period of $t^{i-2} < t < t^i$, we sequentially calculated temporal changes in C^i_{eq}. If C_{in} and m_{in}/m_{sp} do not change during each period, then temporal changes in C^i_{in} were calculated by **Eq. 3** with an assumed $(m_{in}/m_{sp})^i_{in}$.

3.2 Computational Test of C^i_{eq}

Figure 3 shows the time-series computational test for the C^i_{eq} estimations described in *Estimation of the Temporal Changes in the Steady-State Concentration* C_{eq}. The time-series of the test C_i data in response to step-like changes in C^{set}_{eq} (2,300, 11,500, 23,000, 2,300, and 17,000 mg/ kg) were calculated using **Eq. 5** at intervals of 30 days, assuming $a = 8.6 \times 10^7$ s (1,000 days), which corresponds to Yugama crater lake (**Table 2**). Here the chemical concentration of the lake water at $t = 0$, C_0, was set to 2,300 mg/ kg (**Figure 3A**). The results for C^i_{eq} calculated with the two data calculation (**Figure 3B**) are in good agreement with the temporal changes in C^{set}_{eq}. For the results of the three data calculation (**Figure 3C**), transitional responses in calculated C^i_{eq} occur when C^{set}_{eq} has step-like changes.

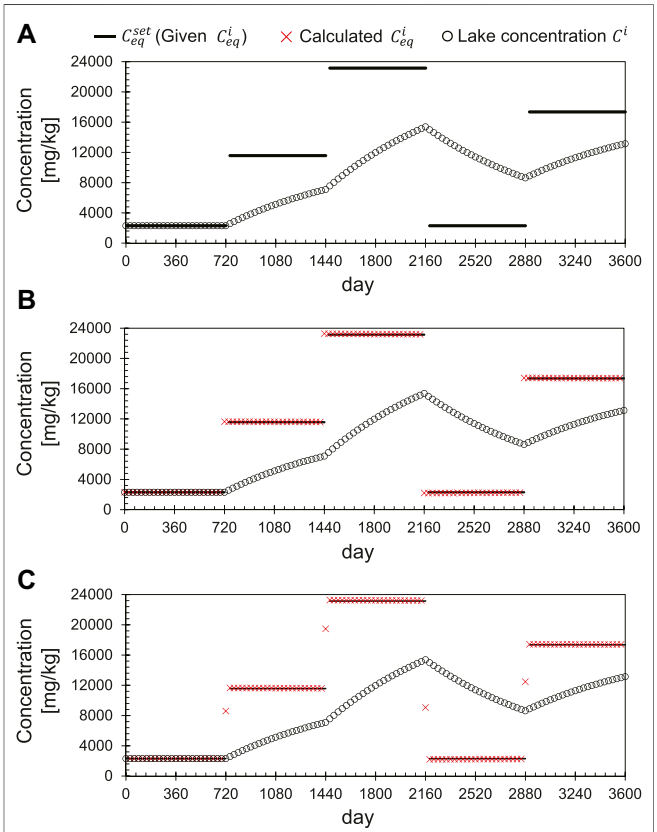

FIGURE 3 | Time-series computational test of the C^i_{eq} estimation described in *Estimation of the Temporal Changes in the Steady-State Concentration* C_{eq}, assuming a = 1,000 days, corresponds to the case of Yugama crater lake (**Table 2**). **(A)** Time-series of C^i (at intervals of 30 days) in response to step-like changes in C_{eq} defined as C^{set}_{eq} = 2,300, 11,500, 23,000, 2,300, and 17,000 mg/ kg, as calculated by **Eq. 5**. **(B)** Two data (**Eq. 10**) and **(C)** three data (**Eq. 13**) calculation of C^i_{eq} from C^i.

4 ANALYSIS OF YUGAMA CRATER LAKE AT KUSATSU–SHIRANE VOLCANO

In this section we apply the model introduced in *Evaluation of Changes in the Steady State Concentration* to Kusatsu-Shirane volcano, as a representative case for which long-term time series of lake element concentration data have been obtained. Kusatsu–Shirane volcano has a hot crater lake, called Yugama,

with a pH ~ 1.0. Phreatic eruptions have occurred repeatedly at the volcano, including from the Mizugama Crater in 1976 (Ossaka et al., 1980) (**Figure 1B**) and from the Yugama Crater in 1982–1983 (Ohba et al., 2008) and 1989 (Ida et al., 1989). In 2018, a phreatic eruption occurred at the Motoshirane pyroclastic cone group, which is located 1.2 km south of Yugama crater lake (Kametani et al., 2021; Terada et al., 2021; Yamada et al., 2021). In 1989–1993 and 2014–2020, earthquake swarms were observed around Yugama crater lake. In this section, we analyze temporal changes in Cl concentrations. We assumed a time constant a^i of 8.6×10^7 s (1,000 days) (**Table 2**) throughout the analysis, because the lake water volume has not been recorded accurately but the lake level has remained largely unchanged over the long term as seen in photographs.

4.1 Chloride Concentrations of Yugama Crater Lake

The earliest Cl concentration data are from 1949 (Minami et al., 1952). After 1967, regular sampling of the lake water has been carried out at site U1 located on its southern shore (**Figure 1B**) (Ohba et al., 2008). We used the data of Ossaka et al. (1997) from 1967/7/4–1985/7/26 and Ohba et al. (2008) from 1985/10/22–2005/10/3. Lake waters sampled by us from 2005/11/4 to 2005/11/4 were analyzed by ion chromatography at the Meteorological Research Institute, JMA (Yaguchi et al., 2021).

Figure 4A shows the temporal changes in Cl concentrations. Sampling prior to 1984 was undertaken once a year in summer and, since April 1985, monthly sampling has been carried out except in winter. Snow cover hinders fieldwork during winter, but from 1990 to the early 2000s, helicopters allowed sampling at site U1. Apart from the period prior to 1984 and 2010–2014, the mean sampling interval was 44 days. We labeled the periods (a)–(d), based on the trend of temporal changes in Cl concentrations. **Figure 4B** shows the monthly numbers of earthquakes around Yugama crater lake. Earthquake swarms in periods (b) and (d) were accompanied by an increase in Cl concentrations (arrows in **Figure 4A**). During a series of phreatic eruptions in 1982–1983 (**Figure 4A**) earthquake swarms occurred, but Cl concentrations remained unchanged (Ohba et al., 2008). The annual precipitation (**Figure 4C**) observed at Kusatsu town, which is located 6 km east of the Yugama Crater, is almost constant at ~1,700 mm and does not affect the temporal changes in Cl concentrations over the long term.

4.2 Estimations of C^i_{eq}

A moving average of ±60 days at intervals of 60 days was applied to smooth the raw data (**Figure 4A**), because Cl concentrations can fluctuate due to atmospheric conditions, such as heavy rain, snow melt, and drought, leading to changes in lake water volume. The moving average also reduces uncertainties related to the analyses and potential concentration heterogeneities around the sampling site.

Computational results for C^i_{eq} (steady-state concentration of an element of interest in the lake water for each period i) are shown in **Figures 5A,B** using the two and three data calculations, respectively. The results of the three data calculation show less fluctuation than those of the two data calculation throughout the entire period. Both moving averages of C^i_{eq} are similar, and thus we discuss the results from the three data calculation for each period.

4.2.1 Period (a), 1966–1986

Prior to the eruptions in 1982–1983, calculated C^i_{eq} values gradually decreased from 3,500 to 2,000 mg/ kg at a rate of 70 mg kg^{-1} yr^{-1} (**Figure 6A**). Although water level fluctuated annually by 1–2 m before the start of the eruptions in 1982–1983, there was no long-term increase/decrease in lake water level, suggesting no long-term changes in m_{in} (mass flux of the bottom input fluid) during the period (a) (Terada and Hashimoto, 2017). Therefore, our results indicate that the Cl concentrations of the bulk hydrothermal input decreased gradually preceding the eruptions.

However, calculated C_{eq} values were temporarily constant at 3,500 mg/kg in 1976–78 (A yellow hatch in **Figure 6A**). The hiatus in the decrease in C_{eq} values was probably caused by a transient increase in subaqueous hydrothermal activity, which may have been associated with the phreatic eruption that occurred at the Mizugama Crater (**Figure 1B**) in 1976.

During the series of eruptions in 1982–1983, Cl concentrations of the lake water showed no eruption-related changes, resulting in no eruption-related changes in C_{eq} values. After the eruptions, calculated C_{eq} values fluctuated around 1,900 mg/kg.

Our calculation results show that the concentration of the bulk hydrothermal input gradually decreased over the long term, except for 1976–1978 after the Mizugama eruption. The lowest value of C_{eq} (130 mg/kg), in spring in 1986, was probably caused by localized, temporary dilution around the sampling site U1 due to enhanced snow melting in spring.

4.2.2 Period (b), 1987–1993

This period includes unrest in terms of an earthquake swarm and increase in Cl concentrations from 1989 to 1992. After the temporary increase in C_{eq} values in 1987, C_{eq} values fluctuated around 1,400 mg/ kg (**Figure 6B**). The small eruption at Yugama crater lake (Ida et al., 1989) occurred at a time when C_{eq} values were low. From 1990, C_{eq} values increased markedly (3,000–6,000 mg/kg, yellow hatches in **Figure 6B**), which was accompanied by the earthquake swarm (**Figure 5C**) and thermal demagnetization around the Yugama Crater (Takahashi and Fujii, 2014). In 1993, the C_{eq} values decreased to values of 1,000–2,000 mg/ kg, which correspond to concentrations prior to the earthquake swarm.

After the earthquake swarm from 1989 to 1992, the annual mean water temperature increased by 5°C (Ohba et al., 2008), suggesting that evaporative loss from the lake surface increased. The water level did not decrease at this time, which means that the mass flux of the hydrothermal fluid injected from the subaqueous fumaroles and hot springs (m_{in}) increased after the earthquake swarms (Terada and Hashimoto, 2017).

Our calculations reveal that the small eruption in 1989 occurred when C_{eq} fluctuated at a relatively low value. The marked increase in C_{eq} values corresponds to an increase in magmatic fluid supply suggested by geophysical observations. At

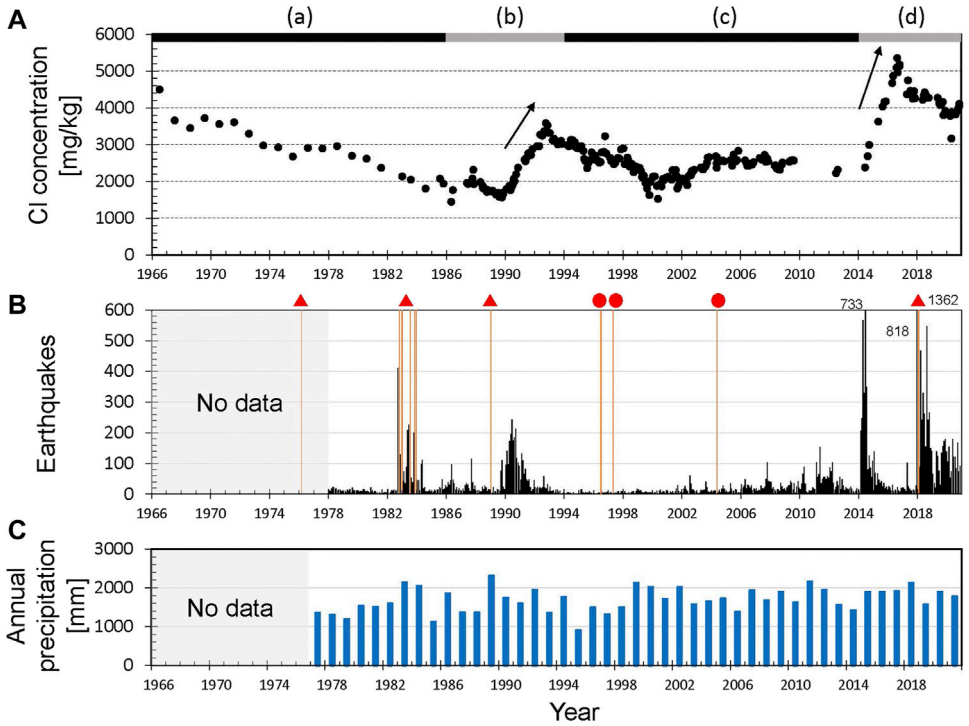

FIGURE 4 | (A) Cl concentrations of Yugama crater lake. (a–d) represent the periods defined in *estimations of* C^{i}_{eq}. **(B)** Monthly numbers of earthquakes with maximum amplitudes of >0.05 μm and S–P times of <2 s measured by the UD component at a seismic station that is 1 km northeast of Yugama crater lake. Triangles indicate the eruption at Kusatsu–Shirane volcano, and circles show lake water turbulence at Yugama crater lake, such as the appearance of a water dome. **(C)** Annual rainfall at Kusatsu town, which is 6 km east of Yugama crater lake. The data in **(B)** and **(C)** were provided by the JMA.

the end of the earthquake swarm period, our calculation results indicate that the increase in C_{in} stopped before the Cl concentration achieved a steady-state condition.

4.2.3 Period (c), 1994–2013

Chloride concentrations decreased slowly, albeit with large fluctuations, from 1993 to 2000, and increased slowly in the early 2000s (**Figure 6C**). This period is characterized by significant short-term fluctuations in calculated C_{eq} values, especially in the 1990s. It is notable that water domes and jetting, which may be related to the earthquake swarm and thermal demagnetization in 1989–1992, were observed on the lake surface during the short-term fluctuations. Since 2005, these significant short-term fluctuations have subsided.

Such significant short-term fluctuations in C_{eq} can be caused by an unstable C_{in} (the concentration of the bulk hydrothermal input), however, the significant short-term fluctuations in C_{eq} can also be attributed to an unstable m_{in} (mass flux of the bottom input fluid) causing temporary changes in water volume V.

It is difficult to identify the reason for the significant short-term fluctuations in C_{eq} during this period. If non-negligible changes in m_{in} (mass flux of the bottom input fluid) occurred, changes in the values of C_{eq} would not represent actual changes in C_{in} (the concentration of the bulk hydrothermal input). Furthermore, snowmelt and heavy rains may have caused local and temporary dilution around sampling site U1, resulting in extremely low and negative C_{eq} values. Water level needs to be monitored in order to evaluate the possible changes in m_{in} (mass flux of the bottom input fluid), and to correct for the effects of meteoric factors based on an accurate time constant value a calculated by the lake volume V.

4.2.4 Period (d), 2014–2020

This period corresponds to a phase of unrest and unusual volcanic activity. A marked increase in Cl concentrations from 2014 to 2016 (**Figure 6D**) was followed by a slight decrease in Cl concentrations from 2017 to 2020 while calculated C_{eq} values indicate three events of an increase in the Cl concentrations of the bulk hydrothermal input occurred in 2014–2016, 2018, and 2020.

During the first event in 2014–2016, calculated C_{eq} values were constant at ~7,000 mg/ kg (A yellow hatch 1 in **Figure 6D**), which was three times higher than the value before the onset of the earthquake swarm. A high CO_2 concentration in nearby subaerial fumaroles was observed in 2014 (Ohba et al., 2019). From 2014 to 2016, a tiltmeter network revealed that volume inflation of 1.2×10^5 m^3 at a depth of 1,000 m beneath Yugama crater lake was observed from 2014 to 2016 (Terada et al., 2021). Moreover, Munekane (2021) also detected a significant increase in pressure at 6.4 km beneath the volcano. These geodetic studies suggest an increase in the supply of magmatic fluid from depth to the

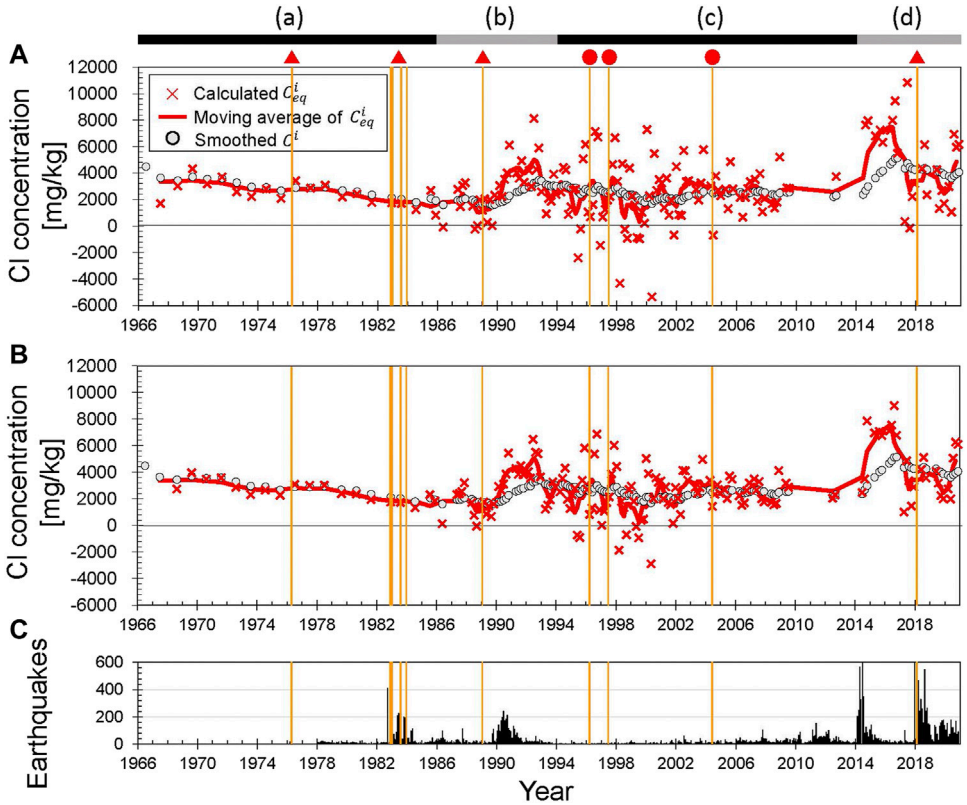

FIGURE 5 | Computational results for C_{eq}^{i} using **(A)** the two and **(B)** the three data calculation (red crosses) of Yugama crater lake at Kusatsu-Shirane volcano. Smoothed Cl concentrations are shown as gray circles. (a–d) represent the periods defined in *estimations of* C_{eq}^{i}. **(C)** Monthly numbers of earthquakes, which is the same as **Figure 4B**.

hydrothermal reservoir, which is consistent with the increase in C_{eq}.

Since 2017, Cl concentrations of Yugama crater lake have decreased slowly, but fluctuated. In 2017, calculated C_{eq} values fluctuated around 2,300 mg/kg, similar to the values prior to the earthquake swarm. No earthquake swarm and ground deformation were observed in 2017, indicating that the supply of magmatic fluid from depth has not increased. The marked decrease in C_{eq} values in the spring of 2017 were probably caused by a localized, temporary dilution of the lake water around the sampling site U1 due to melting of snow.

In 2018, during the second event, calculated C_{eq} values increased to 4,000 mg/kg (A yellow hatch 2 in **Figure 6D**) and this was accompanied by a re-activated earthquake swarm and ground deformation (Munekane, 2021). Prior to the second event, a phreatic eruption occurred at Mt. Motoshirane (**Figure 1B**). In 2019, calculated C_{eq} values decreased, similar as observed in 2017. However, ground deformation and an earthquake swarm became more intense in the latter half of 2019 preceding the third event in 2020 (A yellow hatch 3 in **Figure 6D**). The calculated C_{eq} value increased markedly from 2,300 to 6,000 mg/kg in 2020. Moderate ground deformation and an earthquake swarm continued throughout 2020, indicating repeated increases in the supply of magmatic fluid from depth to the hydrothermal reservoir.

During this period, we have detected changes in C_{eq} values which are consistent with geophysical observations and changes in gas composition nearby subaerial fumaroles. Since the water temperature and level did not change significantly, the changes in C_{eq} values can be attributed to the changes in C_{in} (the concentration of the bulk hydrothermal input) as changes in magmatic fluid supply altered chemical composition of the hydrothermal reservoir. The phreatic eruption in 2018 occurred when C_{eq} fluctuated at a relatively low value, similar to the small eruption in 1989 (*Period (b), 1987–1993*). Therefore, we consider that C_{eq} is a good indicator to evaluate subaqueous hydrothermal activity.

5 DISCUSSION

In order to assess changes in volcanic activity, based on a time-series of concentrations of an element in lake water, such as Cl, we developed a numerical model to calculate temporal changes in C_{eq} (steady-state concentration of an element of interest in the lake water, which changes depending on the concentration of the bulk hydrothermal input C_{in}). Our assumption can be applied during unrest or quiescent periods if there are no significant changes in water level and temperature, meaning that m_{in} (mass flux of the bottom input fluid) remains constant. In the case of

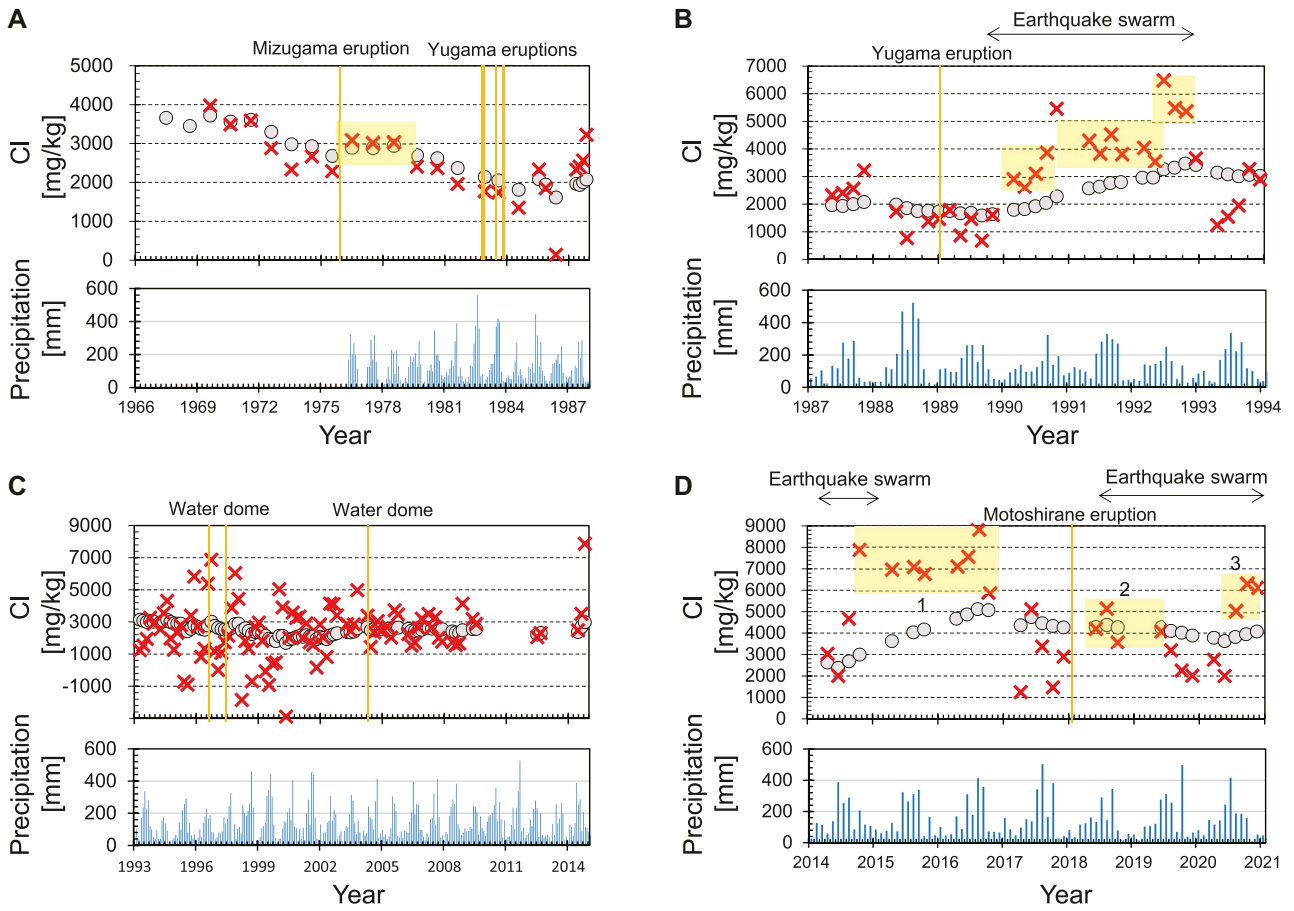

FIGURE 6 | Smoothed C^i values (gray circles) and computational results for C^i_{eq} (red crosses) using the three data calculation (**Eq. 13**) and monthly precipitation at Kusatsu town, which is 6 km east of Yugama crater lake, as measured by the JMA for each time period. The yellow vertical lines represent eruptions at Kusatsu–Shirane volcano or unusual turbulence events on the surface of Yugama crater lake. **(A)** Period a, 1966–1986, **(B)** period b, 1987–1993, **(C)** period c, 1994–2013 and **(D)** period d, 2014–2020.

Yugama crater lake, temporal changes in Cl concentrations can occur over a long time (e.g., >1,000 days; **Table 2**), whereas our model uses two or three recent concentration measurements to estimate changes in C_{eq}. In our analysis for Yugama crater lake during the unrest in 2014–2020 (**Figure 6D**), by the end of 2014, the gradual increase in Cl concentration from June 2014 could be identified as a step-like increase in C_{eq}, without the need for gradual increase in C_{in}. Our calculation results for Yugama crater lake suggest that C_{eq} is a good indicator to evaluate subaqueous hydrothermal activity of a volcanic lake. In this section, we consider different situations where the model is appropriate or needs adjustment to account for various conditions. Prediction of temporal changes in the lake concentration will also be discussed.

5.1 Estimation of the Concentration of the Bulk Hydrothermal Input C_{in}

For some volcanic lakes, m_{in} (mass flux of the bottom input fluid) and m_{sp} (seepage flux through the lake bottom) have been estimated using a box model. If $(m_{sp}/m_{in})^i$ is known, we can calculate a time-series for C^i_{in} based on the estimated C^i_{eq}.

For Yugama crater lake of Kusatsu-Shirane volcano, m_{in} and m_{sp} were calculated by Ohba et al. (1994) for 1988–1993. In the period of the earthquake swarm from 1990 to 1993 (**Figure 5**), the average m_{in} and m_{sp} were 22 and 30 kg/ s, respectively, meaning that m_{sp}/m_{in} = 1.4. In this period, C^i_{eq} varied between 3,000 and 4,500 mg/kg (**Figure 6B**). Assuming $(m_{sp}/m_{in})^i$ = 1.4, C^i_{in} can be calculated to be 4,100–6,100 mg/ kg (**Table 3**). This value is almost the same as the average of 6,600 mg/ kg estimated for the same period (1990–1993) by a box model (Ohba et al., 1994). On the other hand, m_{sp} for 2012–2014 was estimated to be 6.8 kg/ s (Hirayama et al., 2021), which is one-third of the estimate for 1990–1993 by Ohba et al. (1994). To estimate the recent C_{in} value of Yugama crater lake, it is necessary to examine the recent mass balance of the lake.

At Yudamari crater lake of Aso volcano, regular water samplings have not been performed due to steep topography, but a few water samples have revealed that the Cl concentrations of Yudamari crater lake during quiescent period were 20,000–38,000 mg/ kg (Miyabuchi and Terada, 2009; Shinohara et al., 2015). During this period, m_{sp}/m_{in} has been estimated to be ~0.3, without significant changes in lake volume (Terada et al.,

TABLE 3 | Summary of the Cl concentrations of the bulk hydrothermal fluid injected from subaqueous fumaroles and hot springs C^i_{in} in the period of interest *i*. In the cases of Yugama and Yudamari crater lakes, C^i_{in} were calculated from **Eq. 3**, based on m_{in}, m_{sp}, and C^i_{eq}. For Oyunuma crater lake, C^i_{in} was calculated from **Eq. 16**, using m_{rv} and C^i_{rv}, in addition to m_{in}, m_{sp}, and C^i_{eq}. The C^i_{eq} for Yugama crater lake was obtained from this study. C^i_{eq} for Yudamari and Oyunuma crater lakes are the Cl concentrations of the lake water assuming steady-state conditions. Numbers refer to the following references: [1] Ohba et al. (1994), [2] Terada et al. (2012), [3] Miyabuchi and Terada (2009), [4] Shinohara et al. (2015), [5] Murozumi et al. (1966), [6] Fukutomi et al. (1968), and [7] Kato (1960).

Crater lake	Period i	m_{in} kg/s	m_{ri} kg/s	m_{sp} kg/s	m_{ro} kg/s	C^i_{eq} (Cl) mg/kg	C^i_{rv} (Cl) mg/kg	C^i_{in} (Cl) mg/kg	Reference
Yugama, Kusatsu–Shirane	1990–1993	22[a]	0	30[a]	0	–	–	6,600	[1]
						3,000–4,500	–	4,100–6,100	This study
Yudamari, Aso	2006/10/21–12/21	98	0	27.4	0	20,000[b] (2007/3/28)	–	5,592	[2][3]
	2007/9/20–11/7	104	0	30.2	0	21,400[b] (2007/7/26)	–	6,214	[2][4]
	2008/3/12–5/31	81	0	22.2	0	38,000[b] (2008/7/8)	–	10,415	[2][4]
Oyunuma, Noboribetsu	1966–97	26	11	?	46	361	183	565	[5][6]
Okama, Zao	–	?	0	48[c]	0	<10	–	?	[7]

[a]*Average for 1990–1993.*
[b]*Cl concentration of lake water collected close to the time of interest.*
[c]*Refere to* ***Table 2****.*

2012). Assuming that the Cl concentrations of the lake water correspond to C_{eq} (i.e., a steady-state condition was achieved, $C(t) = C_{eq}$, the Cl concentrations of the bulk hydrothermal input C_{in} can be calculated to be 5,600–10,000 mg/kg, which correspond to the values during the recent unrest from 2014 to 2020 at Yugama crater lake of Kusatsu-Shirane volcano **(Table 3)**. It should be noted that pH of Yudamari crater lake was less than 0.4 (Shinohara et al., 2015). Considering HCl degassing from the lake surface, the calculated C_{in} of 5,600–10,000 mg/ kg is a minimum estimate.

5.2 Effects of Surface Runoff Input and Output

If the surface runoff output and input contain the element of interest, the mass balance in **Eq. 2** is modified as follows:

$$\rho \frac{d}{dt}\left[V(t)C(t)\right] = m_{in}C_{in} + m_{ri}C_{ri} - \left(m_{sp} + m_{ro}\right)C(t) \qquad (14)$$

where m_{ri} and C_{ri} are the mass flux (kg/s) and concentration (mg/kg) of the element of interest of the runoff input, respectively. We define m_{ro} as the surface runoff output (kg/s). Assuming that the lake volume V is approximately constant, **Eq. 14** can be rewritten as:

$$\frac{dC(t)}{dt} = \frac{m_{sp} + m_{ro}}{\rho V}\left(C'_{eq} - C(t)\right) \qquad (15)$$

where C'_{eq} is the concentration at the steady-state. $C(t) = C'_{eq}$ can be expressed by the following equation:

$$C'_{eq} = \frac{m_{in}C_{in} + m_{rv}C_{rv}}{m_{sp} + m_{ro}} \qquad (16)$$

Oyunuma crater lake at Noboribetsu volcano has both surface runoff inputs and outputs relevant to the element of interest (Murozumi et al., 1966; Fukutomi et al., 1968; Inoue and Aoki, 2000) (**Figure 1D**). The seepage through the lake bottom is unconstrained, and thus we assumed the surface runoff output is dominant compared with the seepage through the lake bottom ($m_{sp} \ll m_{ro}$).

In this case, a is estimated to be 2.0×10^6 s (23 days) from **Eq. 6**, based m_{ro} instead of m_{sp} (**Table 2**). **Table 3** lists m_{in}, m_{rv}, and m_{ro} values, which are averages for 1966–1967 estimated by Fukutomi et al. (1968). The Cl concentration of the surface runoff input C_{rv} in 1964 was 361 mg/ kg (Murozumi et al., 1966). Assuming that the Cl concentrations correspond to C_{eq} (i.e., steady-state conditions), C_{in} is estimated to be 565 mg/ kg from **Eq. 16** (**Table 3**).

5.3 Notes on the Analysis

Our model is based on a simple mass balance model represented in **Eq. 2**. This model has been applied to other volcanoes including El Chichón in Mexico (Taran and Rouwet, 2008) and Maly Semyachik in Kamchatka (Taran et al., 2021). This model can be applied to non-reactive elements (e.g. Cl and Mg) in various volcanic lakes if the evaporation losses of the elements from the lake surface are negligible. However, in the case of extremely low pH crater lakes (less than ~0) (Rouwet and Ohba 2015; Capaccioni et al., 2017) such as Poás during eruption period (Martínez et al., 2000), Kawah Ijen (van Hinsberg et al., 2017), White Island (Christenson et al., 2017) and Yudamari crater lake at Aso volcano (Shinohara et al., 2015), the application of this model requires the evaluation of evaporation loss of HCl.

One of the factors that create uncertainty in C_{eq} estimation is the analytical error of the elements. The error of the chemical analysis used in this study is 0.15% for Cl (Yaguchi et al., 2021). In the case of two data calculation (**Eq. (10)**), assuming Kusatsu-Shirane [time constant a = 1,000 days, time interval of samplings Δt = 60 days, and Cl concentration of 3,000 mg/ kg), the error of calculated C_{eq} is estimated to be 110 mg/ kg, based on the law of propagation of errors (63 mg/ kg error for three data calculation, **Eq. 13**)]. The analytical error is small enough to discuss the changes in C_{eq} associated with changes in volcanic activity.

Our model yields a time-series for C_{eq} values, by assuming that changes in the water volume V are negligible during each analysis period i [$t^{i-1} < t < t^i$ or $t^{i-2} < t < t^i$, **Eqs 10**, **13**].

However, V would vary due to changes in m_{in} (mass flux of the bottom input fluid), m_{sp} (seepage flux through the lake bottom) and meteorological factors such as snow melting, heavy rainfalls and drought. In such cases, calculated C_{eq} not always represents actual changes in C_{in}. In the case where the water volume changes with time, the time constant a^i must be specified for each analysis period (Δt^i). Therefore, monitoring of the water level or volume using photographs is essential for a hyper-acidic hot crater lake (Rouwet, 2011; Terada et al., 2008). If temporal changes in m_{in} are not negligible, as suggested by changes in lake volume and temperature (Terada and Hashimoto, 2017), it is necessary to evaluate changes in (m_{sp}/m_{in}) using the box model (e.g., Pasternack and Varekamp, 1997) to calculate changes in C_{in}.

An element concentration in lake water can fluctuate due to meteorological factors and local heterogeneity around the water sampling site. In such a situation, a low-path filter including the moving average is effective in smoothing out the short-term fluctuations. When a moving average of ±60 days at intervals of 60 days was applied to the time-series of Cl concentrations in Yugama crater lake, temporal changes in C_{eq} are detected (**Figure 6**), whereas short-term changes in C_{eq} can be obscured. The moving average parameters should be selected on a case-by-case basis for each crater lake. Moreover, Inoue and Aoki (2000) identified spatial heterogeneity in element concentrations in Oyunuma crater lake at Noboribetsu volcano. In this case, use of the spatial mean concentration is desirable to estimate C_{eq}.

The time constant (a) is a critical parameter for calculating C_{eq}; however, it is difficult to estimate m_{sp} without precise field surveys and a box model. We applied the empirical relationship presented in *Estimations of the Time Constant* (**Table 2**), while Varekamp (2015) proposed that both C_{eq} and a can be obtained simultaneously by fitting to a time-series of concentration data using the following equation:

$$\log\left[C(t) - C_{eq}\right] = -\frac{t}{a}\log\left[C_0 - C_{eq}\right] \quad (17)$$

This equation is obtained by taking the logarithm of **Eq. 5**. Although the time range for fitting **Eq. 17** to the data is somewhat arbitrary, time constant a estimated from **Eq. 17** can be used to calculate m_{sp} from **Eq. 6**. This allows m_{sp} to be estimated when Cl concentrations change gradually and the water volume is broadly constant.

5.4 Prediction and Monitoring of Lake Water

Provided V (lake volume) and m_{sp} (mass flux of seepage through the lake bottom) do not change significantly during the period of interest, the future concentration in the lake water can be predicted from **Eq. 5**, based on the latest C^i_{eq} value calculated from two or three analyses of the recent chemical concentration C_i values. By comparing the predicted and observed concentration, it is possible to assess whether the concentration of the bulk hydrothermal input has increased/decreased or remained constant.

In this section, we predict temporal changes in Cl concentration of Yugama crater lake at Kusatsu-Shirane volcano, as a representative case for which a long-term time series has been obtained. We believe that the crystallizing magma, surrounded with a self-sealing zone (Fournier, 1999), is underlain in a shallow depth beneath Yugama crater lake (Ohba et al., 2008; Tseng et al., 2020; Yaguchi et al., 2021). When the overpressure of the crystallizing magma causes fractures in the self-sealing zone, the supply of magma fluid such as HCl from within the self-sealing zone is expected to increase. Therefore, measurements of temporal changes in Cl concentration are essential to monitor the volcanic activity of Kusatsu-Shirane volcano.

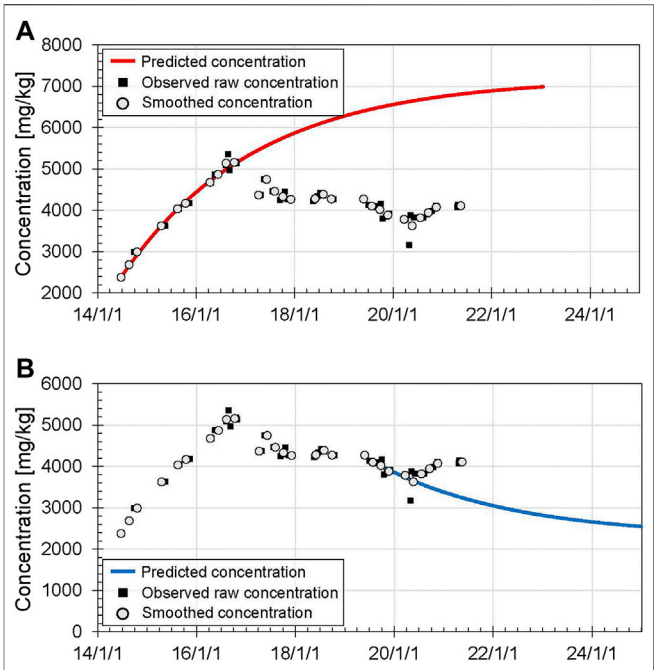

FIGURE 7 | Predicted Cl concentrations of Yugama crater lake calculated with **Eq. 5**, assuming V and m_{sp} do not change during the period of interest. Black squares and gray circles represent raw and smoothed C^i values, respectively. **(A)** Predicted concentration curve after June 2014. The initial concentration C_0 was set to 2,380 mg/ kg. This is the smoothed Cl concentration of the lake on June 22, 2014, which was the average observed concentration over ± 60 days. C_{eq} was set to 7,200 mg/ kg as estimated by **Figure 5B**. **(B)** Predicted concentration curve after September 2019. The initial concentration C_0 was set to 4,020 mg/kg. This is the smoothed Cl concentration of the lake on September 24, 2019, which was the average observed concentration over ±60 days. C_{eq} was set to 2,300 mg/ kg as estimated by **Figure 5B**.

Figure 7A shows the predicted Cl concentrations of Yugama crater lake after June 2014, as a representative period when the concentration increased steadily. Here, the initial concentration C_0 was set to 2,380 mg/ kg, corresponding to the smoothed measured concentration in the lake water in June 2014 (average observed concentration over ±60 days). We used C_{eq} = 7,200 mg/ kg estimated from **Figure 6D**.

The predicted Cl concentration increases with time because $C_0 < C_{eq}$. The curve of the predicted Cl concentration is in good agreement with the observed concentrations obtained until 2016, meaning that the gradual increase from 2014 to 2016 was caused

by an initial change in C_{eq}, without the need for further increase in the concentration of the bulk hydrothermal input. Since 2017, the observed Cl concentrations have deviated significantly from the predicted curve. The water level and temperature did not change significantly, suggesting m_{in} (the hydrothermal input from the lake bottom) is not expected to decrease (Terada and Hashimoto, 2017). Therefore, the deviation from the predicted curve in 2017 is interpreted as a decrease in the Cl concentrations of the bulk hydrothermal input in 2017 as compared with 2014–2016, although Cl concentrations in the lake water remained high values of >4,000 mg/ kg.

Figure 7B shows the predicted Cl concentrations after September 2019, as a representative period when the concentration decreased steadily. Here, the initial concentration C_0 was set to 4,020 mg/ kg, corresponding to the smoothed measured concentration in the lake water in September 2019 (average observed concentration over ± 60 days). We use C_{eq} = 2,300 mg/ kg calculated from the smoothed C^i values (27 May, 26 July, and September 24, 2019) obtained from **Eq. 13** (**Figure 6D**). The predicted Cl concentration curve shows decrease in the concentration with time because $C_0 > C_{eq}$, which is in good agreement with the observed concentrations until May 2020. Therefore, in 2019, we can see that C_{in} (the concentrations of the bulk hydrothermal input) returned to the value observed before the start of the earthquake swarm in 2014.

The curve predicts that chloride concentrations of the lake water will decrease from 4,020 mg/ kg in September 2019 to 2,470 mg/ kg in January 2026 as the 90% response, or 2,335 mg/ kg in May 2030 as the 98% response. Thus, it takes a long time if absolute concentrations are to be used as the basis for assessing the end of unrest. However, by the end of 2019, our model indicates the decreases in the Cl concentrations of the bulk hydrothermal input using the three recent concentration data. Furthermore, the predicted curve also clearly reveals an increase Cl concentration in the bulk hydrothermal input (C_{in}) in the latter half of 2020. For Kusatsu-Shirane volcano, our model using time-series of lake concentration for the past 6 months can be used to quickly assess the state of volcanic activity.

6 CONCLUSIONS

Temporal changes in the concentrations in the lake can take a long time to be evident (e.g., >1,000 days). In order to assess volcanic activity based on a time-series of concentrations of an element in crater lake waters, we developed a numerical model to calculate temporal changes in the steady-state concentration C_{eq}, assuming the water volume in the lake V is almost constant. The C_{eq} values are proportional to the values of C_{in} (the concentrations of the bulk hydrothermal fluid injected from subaqueous fumaroles and hot springs) and, therefore, can be used to assess volcanic activity. Our analyses for Yugama crater lake suggest that C_{eq} is a good indicator to evaluate subaqueous hydrothermal activity. Future concentrations in the lake water at a given time can be predicted based on the recent steady state concentration C_{eq}. The values of C_{eq} can be easily calculated using time series of lake water concentrations, time interval of water samplings and lake water volume. Temporal changes in the concentrations of the bulk hydrothermal input C_{in} were calculated based on C_{eq} when the ratio of seepage flux to fluid emitted from the lake bottom (m_{sp}/m_{in}) remains constant. Therefore, we conclude that steady-state concentration C_{eq} is the key parameter in assessing volcanic activity. For Kusatsu-Shirane volcano, our model using time-series of Cl concentration for the past 6 months can be used to quickly assess the state of volcanic activity.

DATA AVAILABILITY STATEMENT

Chemical concentration data for Yugama crater lake were published in Ossaka et al. (1997), Ohba et al. (2008), and Yaguchi et al. (2021).

AUTHOR CONTRIBUTIONS

AT constructed the numerical model, analyzed the time-series of the lake data, and drafted the manuscript. MY and TO analyzed the water chemistry and helped interpret the data. All authors read and approved the final manuscript.

FUNDING

This research was supported by the Ministry of Education, Culture, Sports, Science, and Technology (MEXT) of Japan through its Second Earthquake and Volcano Hazards Observation and Research Program (Earthquake and Volcano Hazard Reduction Research) and Integrated Program for Next Generation Volcano Research and Human Resource Development.

ACKNOWLEDGMENTS

Officials of Kusatsu town and the Ministry of Agriculture, Forestry, and Fisheries provided approval for our research observations. We also thank Jun'ichi Hirabayashi and the staff at the Volcanic Fluid Research Center, School of Science, Tokyo Institute of Technology, for their valuable comments. Hiroshi Aoyama, Mare Yamamoto, and Shin Yoshikawa kindly allowed us to use their photographs. The Japan Meteorological Agency provided the number of earthquakes at Kusatsu–Shirane volcano. We used Generic Mapping Tools (Wessel and Smith, 1998) to generate the maps. We thank Dmitri Rouwet and the reviewers for their constructive revision.

REFERENCES

Agusto, M. R., Caselli, A., Daga, R., Varekamp, J., Trinelli, A., Dos Santos Afonso, M., et al. (2016). The Crater Lake of Copahue Volcano (Argentina): Geochemical and Thermal Changes between 1995 and 2015. *Geol. Soc. Lond. Spec. Publications* 437, 107–130. doi:10.1144/SP437.16

Albarède, F. (1995). *Introduction to Geochemical Modeling*. Cambridge: Cambridge University Press. doi:10.1017/CBO9780511622960

Anzai, T. (1961). *The Mysterious Crater Lake Okama, Zao Volcano*. Yamagata, Japan: Yamagata Geological Institute, 224 p.

Armienta, M. A., De la Cruz-Reyna, S., and Macías, J. L. (2000). Chemical Characteristics of the Crater Lakes of Popocatetetl, El Chichon, and Nevado de Toluca Volcanoes, Mexico. *J. Volcanol. Geotherm. Res.* 97, 105–125. doi:10.1016/S0377-0273(99)00157-2

Barberi, F., Bertagnini, A., Landi, P., and Principe, C. (1992). A Review on Phreatic Eruptions and Their Precursors. *J. Volcanol. Geotherm. Res.* 52, 231–246. doi:10.1016/0377-0273(92)90046-G

Candela-Becerra, L. J., Toyos, G., Suárez-Herrera, C. A., Castro-Godoy, S., and Agusto, M. (2020). Thermal Evolution of the Crater Lake of Copahue Volcano with ASTER during the Last Quiescence Period between 2000 and 2012 Eruptions. *J. Volcanol. Geotherm. Res.* 392, 106752. doi:10.1016/j.jvolgeores.2019.106752

Capaccioni, B., Rouwet, D., and Tassi, F. (2017). HCl Degassing from Extremely Acidic Crater Lakes: Preliminary Results from Experimental Determinations and Implications for Geochemical Monitoring. *Geol. Soc. Lond. Spec. Publications* 437, 97–106. doi:10.1144/SP437.12

Christenson, B. W. (2000). Geochemistry of Fluids Associated with the 1995-1996 Eruption of Mt. Ruapehu, New Zealand: Signatures and Processes in the Magmatic-Hydrothermal System. *J. Volcanol. Geotherm. Res.* 97, 1–30. doi:10.1016/S0377-0273(99)00167-5

Christenson, B. W., White, S., Britten, K., and Scott, B. J. (2017). Hydrological Evolution and Chemical Structure of a Hyper-Acidic spring-Lake System on Whakaari/White Island, NZ. *J. Volcanol. Geotherm. Res.* 346, 180–211. doi:10.1016/j.jvolgeores.2017.06.017

Cigolini, C., Coppola, D., Yokoo, A., and Laiolo, M. (2018). The Thermal Signature of Aso Volcano during Unrest Episodes Detected from Space and Ground-Based Measurements. *Earth Planets Space* 70, 67. doi:10.1186/s40623-018-0831-7

Edwards, M. J., Kennedy, B. M., Jolly, A. D., Scheu, B., and Jousset, P. (2017). Evolution of a Small Hydrothermal Eruption Episode through a Mud Pool of Varying Depth and Rheology, White Island, NZ. *Bull. Volcanol.* 79, 16. doi:10.1007/s00445-017-1100-5

Fournier, N., Moreau, M., and Robertson, R. (2011). Disappearance of a Crater Lake: Implications for Potential Explosivity at Soufrière Volcano, St Vincent, Lesser Antilles. *Bull. Volcanol.* 73, 543–555. doi:10.1007/s00445-010-0422-3

Fournier, N., Witham, F., Moreau-Fournier, M., and Bardou, L. (2009). Boiling Lake of Dominica, West Indies: High-Temperature Volcanic Crater Lake Dynamics. *J. Geophys. Res.* 114, B02203. doi:10.1029/2008jb005773

Fournier, R. O. (1999). Hydrothermal Processes Related to Movement of Fluid from Plastic into Brittle Rock in the Magmatic-Epithermal Environment. *Econ. Geol.* 94, 1193–1211. doi:10.2113/gsecongeo.94.8.1193

Fukutomi, T., Nakao, K., Miyoshi, H., and Tanoue, R. (1968). Studies of Water Balance and Heat Budget at Ōyunuma Hot Lake in Noboribetsu, Hokkaido. *Geophys. Bull. Hokkaido Univ.* 19, 1–19. doi:10.14943/gbhu.19.1

Giggenbach, W. F., and Glover, R. B. (1975). The Use of Chemical Indicators in the Surveillance of Volcanic Activity Affecting the Crater Lake on Mt Ruapehu, New Zealand. *Bull. Volcanol.* 39, 70–81. doi:10.1007/BF02596947

Hirayama, Y., Okawa, A., Nakamachi, K., Aoyama, T., Okada, Y., Oi, T., et al. (2020). Estimation of Water Seepage Rate in the Active Crater Lake System of Kusatsu-Shirane Volcano, Japan, Using FDNPP-Derived Radioactive Cesium as a Hydrological Tracer. *J. Environ. Radioactivity* 218, 106257. doi:10.1016/j.jenvrad.2020.106257

Hurst, A. W., Bibby, H. M., Scott, B. J., and McGuinness, M. J. (1991). The Heat Source of Ruapehu Crater Lake; Deductions from the Energy and Mass Balances. *J. Volcanol. Geotherm. Res.* 46, 1–20. doi:10.1016/0377-0273(91)90072-8

Ida, Y., Osada, N., Sawada, M., Koyama, E., and Kagiyama, T. (1989). Seismological Study Based on Recently Installed Permanent Stations and a Small Eruptive Event on January 6, 1989 at Kusatsu-Shirane Volcano. *Bull. Earth. Res. Ins.* 64, 325–345. (in Japanese with English abstract). doi:10.15083/0000032805

Inoue, A., and Aoki, M. (2000). Mineralogy of Ohyunuma Explosion Crater Lake, Hokkaido, Japan Part 1: Geochemistry, Hydrology, and Bulk Mineralogy. *Clay Sci.* 11, 147–168. doi:10.11362/jcssjclayscience1960.11.147

Kametani, N., Ishizaki, Y., Yoshimoto, M., Maeno, F., Terada, A., Furukawa, R., et al. (2021). Total Mass Estimate of the January 23, 2018 Phreatic Eruption of the Kusatsu-Shirane Volcano, Central Japan. *Earth Planets Space* 73, 141. doi:10.1186/s40623-021-01468-3

Kato, T. (1960). Some Limnological Remarks on the Crater Lake, "Okama". *Jpn. J. Limnol.* 21, 141–150. doi:10.3739/rikusui.21.141

Kusakabe, M., Komoda, Y., Takano, B., and Abiko, T. (2000). Sulfur Isotopic Effects in the Disproportionation Reaction of Sulfur Dioxide in Hydrothermal Fluids: Implications for the δ34S Variations of Dissolved Bisulfate and Elemental Sulfur from Active Crater Lakes. *J. Volcanol. Geotherm. Res.* 97, 287–307. doi:10.1016/S0377-0273(99)00161-4

Lewicki, J. L., Caudron, C., van Hinsberg, V. J., and Hilley, G. E. (2016). High Spatio-Temporal Resolution Observations of Crater Lake Temperatures at Kawah Ijen Volcano, East Java, Indonesia. *Bull. Volcanol.* 78, 53. doi:10.1007/s00445-016-1049-9

Manville, V. (2015). "Volcano-Hydrologic Hazards from Volcanic Lakes," in *Volcanic Lakes. Advances in Volcanology*. Editors D. Rouwet, B. Christenson, F. Tassi, and J. Vandemeulebrouck (Berlin, Heidelberg: Springer), 21–71. doi:10.1007/978-3-642-36833-2_2

Martínez, M., Fernández, E., Valdés, J., Barboza, V., Van der Laat, R., Duarte, E., et al. (2000). Chemical Evolution and Volcanic Activity of the Active Crater Lake of Poás Volcano, Costa Rica, 1993–1997. *J. Volcanol. Geotherm. Res.* 97, 127–141. doi:10.1016/S0377-0273(99)00165-1

Minami, E., Yamagata, N., Shima, M., and Saijô, Y. (1952). Crater Lake "Yugama" of Volcano Kusatsu-Shirane. I. *Jpn. J. Limnol.* 16, 1–5. (in Japanese). doi:10.3739/rikusui.16.1

Miura, K., Ban, M., Ohba, T., and Fujinawa, A. (2012). Sequence of the 1895 Eruption of the Zao Volcano, Tohoku Japan. *J. Volcanol. Geotherm. Res.* 247-248, 139–157. doi:10.1016/j.jvolgeores.2012.08.005

Miyabuchi, Y., and Terada, A. (2009). Subaqueous Geothermal Activity Revealed by Lacustrine Sediments of the Acidic Nakadake Crater Lake, Aso Volcano, Japan. *J. Volcanol. Geotherm. Res.* 187, 140–145. doi:10.1016/j.jvolgeores.2009.08.001

Morrissey, M., Gisler, G., Weaver, R., and Gittings, M. (2010). Numerical Model of Crater Lake Eruptions. *Bull. Volcanol.* 72, 1169–1178. doi:10.1007/s00445-010-0392-5

Munekane, H. (2021). Modeling Long-Term Volcanic Deformations at the Kusatsu-Shirane and Asama Volcanoes, Japan Using the GNSS Coordinate Time Series. *Earth Planets Space* 73, 192. doi:10.1186/s40623-021-01512-2

Murozumi, M., Abiko, T., and Nakamura, S. (1966). Geochemical Investigation of the Noboribetsu Oyunuma Explosion Crater Lake. *J. Volcanol. Soc. Jpn.* 11, 1–16. doi:10.18940/kazanc.11.1_1

Ohba, T., Hirabayashi, J., and Nogami, K. (2008). Temporal Changes in the Chemistry of Lake Water within Yugama Crater, Kusatsu-Shirane Volcano, Japan: Implications for the Evolution of the Magmatic Hydrothermal System. *J. Volcanol. Geotherm. Res.* 178, 131–144. doi:10.1016/j.jvolgeores.2008.06.015

Ohba, T., Hirabayashi, J., and Nogami, K. (1994). Water, Heat and Chloride Budgets of the Crater Lake, Yugama at Kusatsu-Shirane Volcano, Japan. *Geochem. J.* 28, 217–231. doi:10.2343/geochemj.28.217

Ohba, T., Yaguchi, M., Nishino, K., Numanami, N., Tsunogai, U., Ito, M., et al. (2019). Time Variation in the Chemical and Isotopic Composition of Fumarolic Gasses at Kusatsu-Shirane Volcano, Japan. *Front. Earth Sci.* 7, 249. doi:10.3389/feart.2019.00249

Oppenheimer, C. (1997). Ramifications of the Skin Effect for Crater Lake Heat Budget Analysis. *J. Volcanol. Geotherm. Res.* 75, 159–165. doi:10.1016/S0377-0273(96)00037-6

Ossaka, J., Ossaka, T., Oi, T., Kikawada, K., Yamano, M., Hukuhara, H., et al. (1997). Volcanic Activity of Kusatsu-Shirane Volcano, Gunma, and Secular Change in Water Quality of Crater Lake, Yugama. *Chikyukagaku* 31, 119–128. (in Japanese).

Ossaka, J., Ozawa, T., Nomara, T., Ossaka, T., Hirabayashi, J., Takaesu, A., et al. (1980). Variation of Chemical Compositions in Volcanic Gases and Water at Kusatsu-Shirane Volcano and its Activity in 1976. *Bull. Volcanol.* 43, 207–216. doi:10.1007/BF02597622

Pasternack, G. B., and Varekamp, J. C. (1997). Volcanic Lake Systematics I. Physical Constraints. *Bull. Volcanol.* 58, 528–538. doi:10.1007/s004450050160

Peiffer, L., Rouwet, D., and Taran, Y. (2015). "Fluid Geochemistry of El Chichón Volcano-Hydrothermal System," in *Active Volcanoes of Chiapas (Mexico): El Chichón and Tacaná. Active Volcanoes of the World*. Editors T. Scolamacchia and J. Macías (Berlin, Heidelberg: Springer), 77–95. doi:10.1007/978-3-642-25890-9_4

Peiffer, L., and Taran, Y. (2013). Heat and Mass Fluxes Monitoring of El Chichon Crater Lake. *Rev. Mex. Cienc. Geol.* 30, 500–511.

Roberts, T. J., Saffell, J. R., Oppenheimer, C., and Lurton, T. (2014). Electrochemical Sensors Applied to Pollution Monitoring: Measurement Error and Gas Ratio Bias - A Volcano Plume Case Study. *J. Volcanol. Geotherm. Res.* 281, 85–96. doi:10.1016/j.jvolgeores.2014.02.023

Rouwet, D. (2011). A Photographic Method for Detailing the Morphology of the Floor of a Dynamic Crater Lake: the El Chichón Case (Chiapas, Mexico). *Limnology* 12, 225–233. doi:10.1007/s10201-011-0343-7

Rouwet, D., Mora-Amador, R., Ramírez-Umaña, C. J., González, G., and Inguaggiato, S. (2017). Dynamic Fluid Recycling at Laguna Caliente (Poás, Costa Rica) before and during the 2006-ongoing Phreatic Eruption Cycle (2005-10). *Geol. Soc. Lond. Spec. Publications* 437, 73–96. doi:10.1144/SP437.11

Rouwet, D., and Ohba, T. (2015). "Isotope Fractionation and HCl Partitioning during Evaporative Degassing from Active Crater Lakes," in *Volcanic Lakes. Advances in Volcanology*. Editors D. Rouwet, B. Christenson, F. Tassi, and J. Vandemeulebrouck (Berlin, Heidelberg: Springer), 179–200. doi:10.1007/978-3-642-36833-2_7

Rouwet, D., Taran, Y., Inguaggiato, S., Varley, N., and Santiago Santiago, J. A. (2008). Hydrochemical Dynamics of the "Lake-spring" System in the Crater of El Chichón Volcano (Chiapas, Mexico). *J. Volcanol. Geotherm. Res.* 178, 237–248. doi:10.1016/j.jvolgeores.2008.06.026

Rouwet, D., and Tassi, F. (2011). Geochemical Monitoring of Volcanic Lakes. A Generalized Box Model for Active Crater Lakes. *Annal. Geophys.* 54. doi:10.4401/ag-50310.4401/ag-5035

Rouwet, D., Tassi, F., Mora-Amador Sandri, R. L., Sandri, L., and Chiarini, V. (2014). Past, Present and Future of Volcanic Lake Monitoring. *J. Volcanol. Geotherm. Res.* 272, 78–97. doi:10.1016/j.jvolgeores.2013.12.009

Rowe, G. L., Brantley, S. L., Fernandez, M., Fernandez, J. F., Borgia, A., and Barquero, J. (1992). Fluid-volcano Interaction in an Active Stratovolcano: the Crater Lake System of Poás Volcano, Costa Rica. *J. Volcanol. Geotherm. Res.* 49, 23–51. doi:10.1016/0377-0273(92)90003-V

Shinohara, H., Yoshikawa, S., and Miyabuchi, Y. (2015). "Degassing Activity of a Volcanic Crater Lake: Volcanic Plume Measurements at the Yudamari Crater Lake, Aso Volcano, Japan," in *Volcanic Lakes. Advances in Volcanology*. Editors D. Rouwet, B. Christenson, F. Tassi, and J. Vandemeulebrouck (Berlin, Heidelberg: Springer), 201–217. doi:10.1007/978-3-642-36833-2_8

Simonson, J. M., and Palmer, D. A. (1993). Liquid-vapor Partitioning of HCl(aq) to 350°C. *Geochimica et Cosmochimica Acta* 57, 1–7. doi:10.1016/0016-7037(93)90462-6

Smith, S. W. (1997). *The Scientist and Engineer's Guide to Digital Signal Processing*. San Diego, California, USA: California Technical Publishing, 626. Chapter 19.

Stix, J. (2018). Understanding Fast and Slow Unrest at Volcanoes and Implications for Eruption Forecasting. *Front. Earth Sci.* 6, 56. doi:10.3389/feart.2018.00056

Takahashi, K., and Fujii, I. (2014). Long-term Thermal Activity Revealed by Magnetic Measurements at Kusatsu-Shirane Volcano, Japan. *J. Volcanol. Geotherm. Res.* 285, 180–194. doi:10.1016/j.jvolgeores.2014.08.014

Taran, Y., Kalacheva, E., Dvigalo, V., Melnikov, D., and Voloshina, E. (2021). Evolution of the Crater Lake of Maly Semyachik Volcano, Kamchatka (1965-2020). *J. Volcanol. Geotherm. Res.* 418, 107351. doi:10.1016/j.jvolgeores.2021.107351

Taran, Y., and Rouwet, D. (2008). Estimating Thermal Inflow to El Chichón Crater Lake Using the Energy-Budget, Chemical and Isotope Balance Approaches. *J. Volcanol. Geotherm. Res.* 175, 472–481. doi:10.1016/j.jvolgeores.2008.02.019

Terada, A., Hashimoto, T., and Kagiyama, T. (2012). A Water Flow Model of the Active Crater Lake at Aso Volcano, Japan: Fluctuations of Magmatic Gas and Groundwater Fluxes from the Underlying Hydrothermal System. *Bull. Volcanol.* 74, 641–655. doi:10.1007/s00445-011-0550-4

Terada, A., Hashimoto, T., Kagiyama, T., and Sasaki, H. (2008). Precise Remote-Monitoring Technique of Water Volume and Temperature of a Crater Lake in Aso Volcano, Japan: Implications for a Sensitive Window of a Volcanic Hydrothermal System. *Earth Planet. Space* 60, 705–710. doi:10.1186/BF03353134

Terada, A., and Hashimoto, T. (2017). Variety and Sustainability of Volcanic Lakes: Response to Subaqueous Thermal Activity Predicted by a Numerical Model. *J. Geophys. Res. Solid Earth* 122, 6108–6130. doi:10.1002/2017JB014387

Terada, A., Kanda, W., Ogawa, Y., Yamada, T., Yamamoto, M., Ohkura, T., et al. (2021). The 2018 Phreatic Eruption at Mt. Motoshirane of Kusatsu–Shirane Volcano, Japan: Eruption and Intrusion of Hydrothermal Fluid Observed by a Borehole Tiltmeter Network. *Earth Planets Space* 73, 157. doi:10.1186/s40623-021-01475-4

Tseng, K. H., Ogawa, Y., Nurhasan, Tank, S. B., Ujihara, N., Honkura, Y., et al. (2020). Anatomy of Active Volcanic Edifice at the Kusatsu-Shirane Volcano, Japan, by Magnetotellurics: Hydrothermal Implications for Volcanic Unrests. *Earth Planets Space* 72, 161. doi:10.1186/s40623-020-01283-2

van Hinsberg, V., Vigouroux, N., Palmer, S., Berlo, K., Mauri, G., Williams-Jones, A., et al. (2017). Element Flux to the Environment of the Passively Degassing Crater Lake-hosting Kawah Ijen Volcano, Indonesia, and Implications for Estimates of the Global Volcanic Flux. *Geol. Soc. Lond. Spec. Publications* 437, 9–34. doi:10.1144/SP437.2

Varekamp, J. C. (2002). Lake Contamination Models for Evolution towards Steady State. *J. Limnol.* 62, 67–72. doi:10.4081/jlimnol.2003.s1.67

Varekamp, J. C. (2015). "The Chemical Composition and Evolution of Volcanic Lakes," in *Volcanic Lakes. Advances in Volcanology*. Editors D. Rouwet, B. Christenson, F. Tassi, and J. Vandemeulebrouck (Berlin, Heidelberg: Springer), 93–123. doi:10.1007/978-3-642-36833-2_4

Werner, C., Hurst, T., Scott, B., Sherburn, S., Christenson, B. W., Britten, K., et al. (2008). Variability of Passive Gas Emissions, Seismicity, and Deformation during Crater Lake Growth at White Island Volcano, New Zealand, 2002-2006. *J. Geophys. Res.* 113, B01204. doi:10.1029/2007JB005094

Wessel, P., and Smith, W. H. F. (1998). New, Improved Version of Generic Mapping Tools Released. *EOS Trans. AGU* 79, 579. doi:10.1029/98EO00426

Yaguchi, M., Ohba, T., and Terada, A. (2021). Groundwater Interacting at Depth with Hot Plastic Magma Triggers Phreatic Eruptions at Yugama Crater Lake of Kusatsu-Shirane Volcano (Japan). *Front. Earth Sci.* 9, 741742. doi:10.3389/feart.2021.741742

Yamada, T., Kurokawa, A. K., Terada, A., Kanda, W., Ueda, H., Aoyama, H., et al. (2021). Locating Hydrothermal Fluid Injection of the 2018 Phreatic Eruption at Kusatsu-Shirane Volcano with Volcanic Tremor Amplitude. *Earth Planets Space* 73, 14. doi:10.1186/s40623-020-01349-1

Conflict of Interest: The authors declare that the research was conducted in the absence of any commercial or financial relationships that could be construed as a potential conflict of interest.

frontiers | Frontiers in Earth Science

ORIGINAL RESEARCH
published: 25 May 2022
doi: 10.3389/feart.2022.766791

A Depression Containing CO_2-Enriched Water at the Bottom of Lake Monoun, Cameroon, and Implications for the 1984 Limnic Eruption

Takeshi Ohba[1]*, *Yu Oginuma*[1], *Kazuto Saiki*[2], *Minoru Kusakabe*[3], *Issa*[4], *Takounjou A. Fouepe*[5], *Romaric Ntchantcho*[5], *Gregory Tanyileke*[5] and *Joseph V. Hell*[5]

[1]Department of Chemistry, School of Science, Tokai University, Hiratsuka, Japan, [2]Graduate School of Science, Osaka University, Suita, Japan, [3]Department of Environmental Biology and Chemistry, Faculty of Science, University of Toyama, Toyama, Japan, [4]Water Resources Manager, Flood Emergency Project, Yagoua, Cameroon, [5]Institute for Geological and Mining Research, Yaounde, Cameroon

In 1984, a limnic eruption occurred in Lake Monoun, Cameroon, and the CO_2 gas released from the lake surface resulted in casualties in the neighboring communities. Subsequent scientific research revealed that the CO_2 gas released from the lake surface was CO_2 of magmatic origin dissolved in the lake water; however, the mechanism of that limnic eruption remains unclear. In this study, we analyzed in detail the lake-bottom bathymetry of the eastern basin, i.e., one of the three basins in Lake Monoun, to understand the mechanism of the 1984 limnic eruption. We discovered two significant depressions at the lake bottom near the scarp and obtained vertical profiles of several parameters of the lake water at the depression locations. The northeastern depression (D1) was ~ 1.2 m deeper than the lake bottom and contained water with higher temperature and electrical conductivity and lower pH relative to the lake water. Conversely, the southern depression (D2) was ~ 2.2 m deeper than the lake bottom, and there were no anomalies regarding its water parameters. Although the warm water discharged from the bottom of D1 was not saturated with dissolved CO_2, bubbles likely existed at the bottom of D1, influenced by the partial pressure of dissolved CH_4 in the lake water. Our results suggest that just before the 1984 limnic eruption, water containing high concentrations of dissolved CO_2 was discharged from D1; this water would have reached the lake surface with bubbles. According to earlier numerical simulations of the limnic eruption, rising bubbles could have induced the limnic eruption. The rising bubbles entrained the surrounding lake water containing high concentrations of dissolved CO_2, which amplified the flow rate of CO_2 degassing from the lake water and resulted in a limnic eruption. The limnic eruption that occurred just above D1 displaced lake water on the eastern shore. It is estimated that the impact of the displaced water eroded the scarp and deposited sediment as a mound near D1. A similar mound also exists near D2, suggesting that D2 is a trace of another limnic eruption that occurred earlier than 1984. Of the three basins that make up Lake Monoun, the two smaller basins to the west have high concentrations of dissolved CO_2 in their deep waters. This dissolved CO_2 was not supplied from the bottom of the basins but is likely a remnant of the dissolved CO_2 that existed in 2003 before the start of artificial CO_2

OPEN ACCESS

Edited by:
Corentin Caudron,
Université Libre de Bruxelles, Belgium

Reviewed by:
John Stix,
McGill University, Canada
Alain Bernard,
Université Libre de Bruxelles, Belgium

***Correspondence:**
Takeshi Ohba
takeshi_ohba@tokai-u.jp

Specialty section:
This article was submitted to Volcanology, a section of the journal Frontiers in Earth Science

Received: *30 August 2021*
Accepted: *07 March 2022*
Published: *25 May 2022*

Citation:
Ohba T, Oginuma Y, Saiki K, Kusakabe M, Issa, Fouepe TA, Ntchantcho R, Tanyileke G and Hell JV (2022) A Depression Containing CO_2-Enriched Water at the Bottom of Lake Monoun, Cameroon, and Implications for the 1984 Limnic Eruption. Front. Earth Sci. 10:766791. doi: 10.3389/feart.2022.766791

degassing. Our results suggest that another limnic eruption occurred before 1984. Lake Monoun may have experienced several limnic eruptions in the past. If the artificial degassing of CO_2 is not continued, the water released from D1, containing high concentrations of dissolved CO_2, will increase the concentration of dissolved CO_2 in the lake water, and the bubbles rising from D1 will cause another limnic eruption. In the future, the flux of CO_2 supplied from D1 may increase and exceed the flux of CO_2 removed by the artificial degassing, potentially increasing the amount of CO_2 accumulated in the lake water. The regular monitoring of the CO_2 amount in lake water should be also continued.

Keywords: Lake Monoun, limnic eruption, CO_2, bathymetry, lake basin, hypolimnion

INTRODUCTION

Two maars in Cameroon, i.e., lakes Monoun and Nyos, caused natural disasters in 1984 and 1986, respectively, when CO_2 was explosively released from the lake waters and resulted in casualties in the nearby communities (Tanyileke et al., 2019). Such explosive CO_2 releases are known as *limnic eruptions*; the term was first used by J. C. Sabroux at the conference regarding the Lake Nyos disaster, which was organized by UNESCO and the Cameroon government at Yaoundé, Cameroon, in March 1987 (Sigvaldason, 1989; Halbwachs et al., 2004).

A limnic eruption is an extremely rare geological phenomenon; other than the two cases at lakes Monoun and Nyos, no other limnic eruptions have been reported. In addition, it is not known whether limnic eruptions occurred in lakes Monoun and Nyos before the 1980s. In general, magmatic eruptions are driven by the degassing of H_2O dissolved in magma; conversely, limnic eruptions are driven by degassing of CO_2 dissolved in lake water. During limnic eruptions, the entire lake body corresponds to the magma chamber during a magmatic eruption. Magmatic eruptions can be initiated by the depressurization of the upper part of the magma chamber; conversely, the initiation of limnic eruptions is not clear. During the limnic eruptions, lake water was blown up from the lake surface by the explosive degassing of CO_2, and CO_2 dissolved in the lake water mixed with the ambient air and formed an air mass with low oxygen concentration. This air mass diffused from the lake to the surrounding area (Costa and Chiodini, 2015) and suffocated the people (Baxter and Kapila, 1989). Magmatic eruptions cannot be artificially suppressed; conversely, limnic eruptions can be suppressed by artificially removing dissolved CO_2 from the lake water (Halbwachs et al., 2020). Research on limnic eruptions has focused on the triggering mechanism and history of limnic eruptions in lakes Monoun and Nyos before the 1980s.

The Cameroon Volcanic Line (CVL) consists of alkaline volcanoes extending from Annobon Island in the Atlantic Ocean to the interior of the African continent (Fitton and Dunlop, 1985) and has branches within Cameroon. One of the branches extends to the east, reaching the Ngaoundéré Plateau; another branch goes to the north, reaching the Biu Plateau in Nigeria. Lake Monoun (5.579,784 °N, 10.587,654 °E) and Lake Nyos (6.438,545 °N, 10.298,798 °E) are located in the central part of the CVL.

Many maars are located on the CVL, of which 39 have been investigated by Kling (1988). Except for lakes Monoun and Nyos, no other lakes have high concentrations of dissolved CO_2 in their water, thereby causing limnic eruptions (Kling, 1988). Geologically, Lake Nyos is a young maar; it formed approximately 9 ka before present (BP) according to $^{226}Ra/^{230}Th$ of the lava (Aka and Yokoyama, 2013). CO_2 in lakes Monoun and Nyos is accompanied by He with a high $^3He/^4He$ ratio and MORB-type Ne (Nagao et al., 2010), suggesting the existence of mantle-derived degassing magmas beneath both lakes. Nagao et al. (2010) discovered also that magmatic He-laden water was discharged into Lake Nyos at −190 m depth, i.e., 20 m higher than the lake bottom; they suggested that the magmatic He-laden water traveled along the ring fault of a potential diatreme structure (Lockwood and Rubin, 1989). The consensus is that the driving force of the limnic eruptions was CO_2 dissolved in the lake water (Kling et al., 1987; Sigurdsson et al., 1987).

To prevent the recurrence of limnic eruptions in lakes Monoun and Nyos, degassing pipes were installed in both lakes; these pipes transport deep lake water safely to the lake surface (Halbwachs et al., 2004, 2020). CO_2 is separated from the lake water and diffused into ambient air. The amount of CO_2 dissolved in the water of Lake Nyos was 14.8 Gmol in 2001 (Kusakabe et al., 2008), when degassing started; by 2015, the amount had been reduced to 3.9 Gmol (Ohba et al., 2015). In Lake Monoun, the amount of dissolved CO_2 was 0.61 Gmol in 2003 (Kusakabe et al., 2008), when degassing started; by 2007, the amount had been reduced to 0.25 Gmol. The force transporting lake water through degassing pipes is the buoyancy of the CO_2 bubbles that are separated from the lake water. When the concentration of dissolved CO_2 decreases below a certain threshold, the transportation of lake water stops. Water flowing through the degassing pipe at Lake Monoun decreased significantly in 2010 (Yoshida et al., 2015), at which point the operation of the degassing pipe stopped; however, the water in Lake Monoun would inevitably become again saturated with CO_2, likely resulting in limnic eruptions. A mechanical device consisting of an electric rotary pump powered by a solar panel was installed to restore the water flow in the degassing pipe at Lake Monoun, thereby successfully resuming the degassing (Yoshida et al., 2015).

By 1987, when the conference on the Lake Nyos disaster took place, there was a consensus that limnic eruptions are caused by

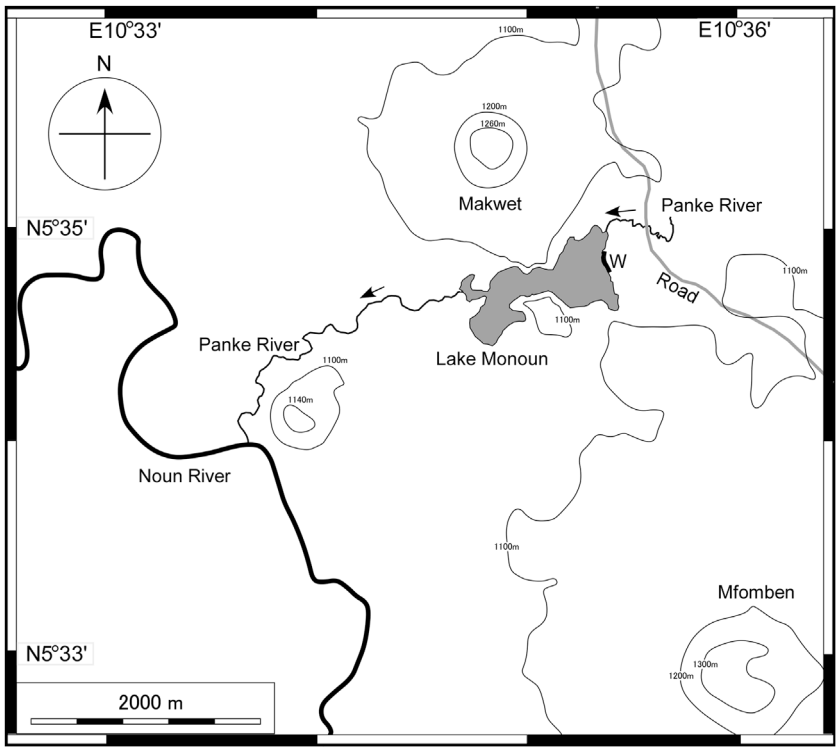

FIGURE 1 | Location of Lake Monoun in Cameroon. The shaded region indicates lake water. Arrows indicate the direction of river flow. W is the area affected by the waves generated during the limnic eruption in 1984 (Sigurdsson et al., 1987).

the CO_2 gas dissolved in the lake water; however, the mechanism of their early eruptive stages remained unknown, and several hypotheses were proposed. Sigurdsson et al. (1987) suggested that the limnic eruption in Lake Monoun was caused by sediment that fell to the bottom of the lake because of a landslide on the scarp of the lake and disturbed the lake water saturated with CO_2. Giggenbach (1990) suggested that the limnic eruption in Lake Nyos was caused by the inflow of cold rainwater into the deeper layers of the lake, thereby lifting the CO_2-saturated lake water. Kusakabe et al. (2008) proposed that limnic eruptions at Lake Monoun occurred spontaneously without any triggering events.

Woods and Phillips (1999) conducted laboratory experiments and numerical analyses regarding Lake Nyos, when its lake water contained high concentrations of CO_2; they found that the upwelling of a small amount of CO_2 bubbles at the bottom of the lake could be magnified 10^4–10^5 times at the lake surface, thereby resulting in a limnic eruption. Kozono et al. (2016) estimated numerically that the upwelling of small CO_2 bubbles in the middle depths of Lake Monoun could be amplified, thereby leading to a limnic eruption. Elucidating the mechanism of limnic eruptions is important for forecasting potentially catastrophic future limnic eruptions. In this study, we attempted to elucidate the limnic eruption process at Lake Monoun based on the detailed lake-bottom bathymetry obtained by Alain et al. (2019) and the original observations of CO_2-enriched lake water.

MATERIALS AND METHODS

The most important material in this study was a detailed bathymetric map of the bottom of Lake Monoun. The following information is necessary for interpreting the lake-bottom bathymetry. According to Sigurdsson et al. (1987), lava flowing from the Mfomben Crater dammed the Panke River and formed Lake Monoun (**Figure 1**); after the formation of Lake Monoun, the Makwet scoria cone adjacent to Lake Monoun was deposited. Although the radioactive formation age of Lake Monoun has not been obtained, the age of the last eruptive activity in the area surrounding Lake Monoun may have been a few centuries ago, considering the young volcanic topography of the Makwet scoria cone (Sigurdsson et al., 1987). Lake Monoun is a part of the Panke River; the river water enters the lake through the northeast inlet, and the lake water exits the lake through the west outlet. According to Sigurdsson et al. (1987), the 1984 limnic eruption caused waves of 5 m higher than the surface, which crashed onto the eastern shore of Lake Monoun (W in **Figure 1**). These large waves destroyed the vegetation within 100 m from the shore.

The bathymetric map of the lake bottom shown in **Figure 2** was obtained through a multibeam sonar survey conducted in November 2014 (Alain et al., 2019). An image of the basin with resolution higher than that of **Figure 2** is provided as the supplementary figure. The high-resolution image was analyzed

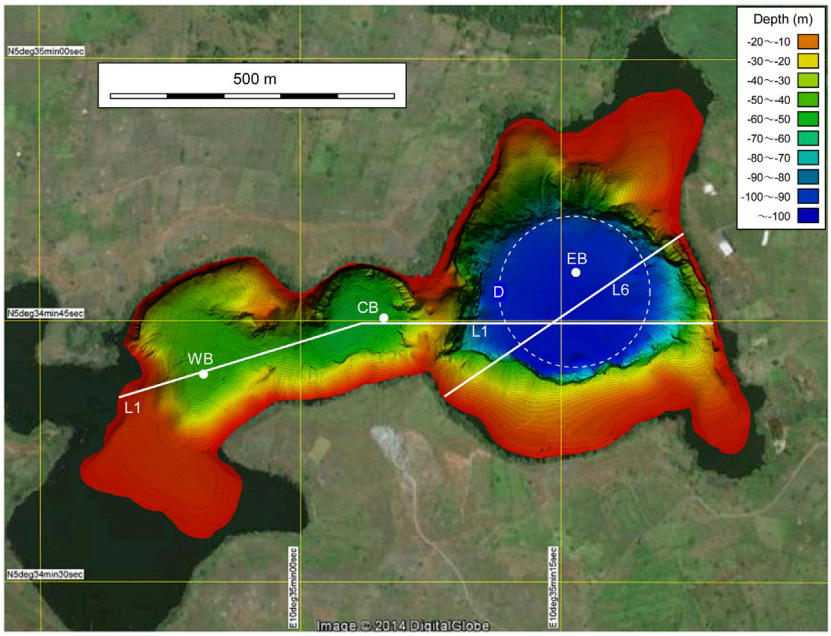

FIGURE 2 | Bathymetries of the three basins WB, CB, and EB in Lake Monoun. Dots indicate the location of CTD measurements. The vertical cross sections along lines L1 and L6 are shown in **Figure 3A**, **Figure 9**, respectively. D is a potential diatreme ring fault, assuming that the shape of the fault is a true circle, and the fault includes D1, D2, and D3.

for extracting features that seemed to be related to the 1984 limnic eruption.

We obtained vertical profiles of temperature, electrical conductivity, and pH using a CTD probe (Ocean Seven Model 316, IDRONAUT) at several points in the lake in 2015. After submerging the probe in the lake water, temperature, electrical conductivity, and pH were measured every second. *In situ* lake-water sampling revealed the total concentration of carbonate species. Owing to the high concentration of dissolved CO_2, effervescence from deep water reaching the surface would result in loss of most of dissolved CO_2; to address this problem, a plastic syringe containing 10 ml of 5 M KOH solution was used (Kusakabe et al., 2000). This method is known as the "MK method." The syringe was attached to a mechanical device and would be sent to the desired depth, where approximately 30 ml lake water would be obtained by the syringe. The amount of sampled lake water would be determined more accurately based on the weight difference of the syringe before and after sampling. Each sample was analyzed in the laboratory for the total carbonate content (i.e., $CO_{2aq} + HCO_3^- + CO_3^{2-}$) using the microdiffusion–titration method (Conway, 1950). This total concentration of carbonate species is denoted as Ct. In this study, CO_2 dissolved in lake water is expressed as "CO_{2aq}" and was the driving force behind the limnic eruption; however, the CO_{2aq} concentration cannot be measured directly and was theoretically estimated from the Ct and pH values of lake water. The advantage of the MK method is its high accuracy in determining Ct values. The analytical error of the method is approximately ±2.5 mmol/L. The data from the CTD probe were combined with the analytical results of the MK method to estimate the CO_{2aq} concentration profile.

RESULTS

Based on the high-resolution images obtained from the multibeam sonar survey (Alain et al., 2019), three basins were recognized within Lake Monoun (**Figure 2**). The maximum depths in the eastern basin (EB), central basin (CB), and western basin (WB) were −100, −56, and −44 m, respectively (**Figure 2**). To define the water exchange between basins, the depth profile, as shown in **Figure 3A**, was obtained along line L1 (**Figure 2**), which passed through the saddles on the ridges separating WB, CB, and EB. The depth of the ridge separating WB and CB was −42 m, i.e., 2 m higher than the bottom of WB. Below −22 m depth, the waters in WB and CB mixed laterally (**Figure 3A**). The depth of the ridge separating CB and EB was −22 m, i.e., 34 m higher than the bottom of CB. Below −22 m depth, the waters in CB and EB could not be laterally mixed (**Figure 3A**).

The bathymetric features of EB were extracted (**Figure 4**) by visual inspection of the supplementary high-resolution images. Three major depressions (i.e., D1, D2, and D3) were found in the area near the basin scarp. The depths at points p1 and p1o were −98.3 and −97.1 m, respectively. The depth ranging from −98.3 to −97.1 m corresponds to the interior of D1. The depth of D1 relative to the surrounding lake bottom was 1.2 m. The depths at points p2 and p2o were −102.1 and −99.9 m, respectively. The depth ranging from −102.1 to −99.9 m corresponds to the interior

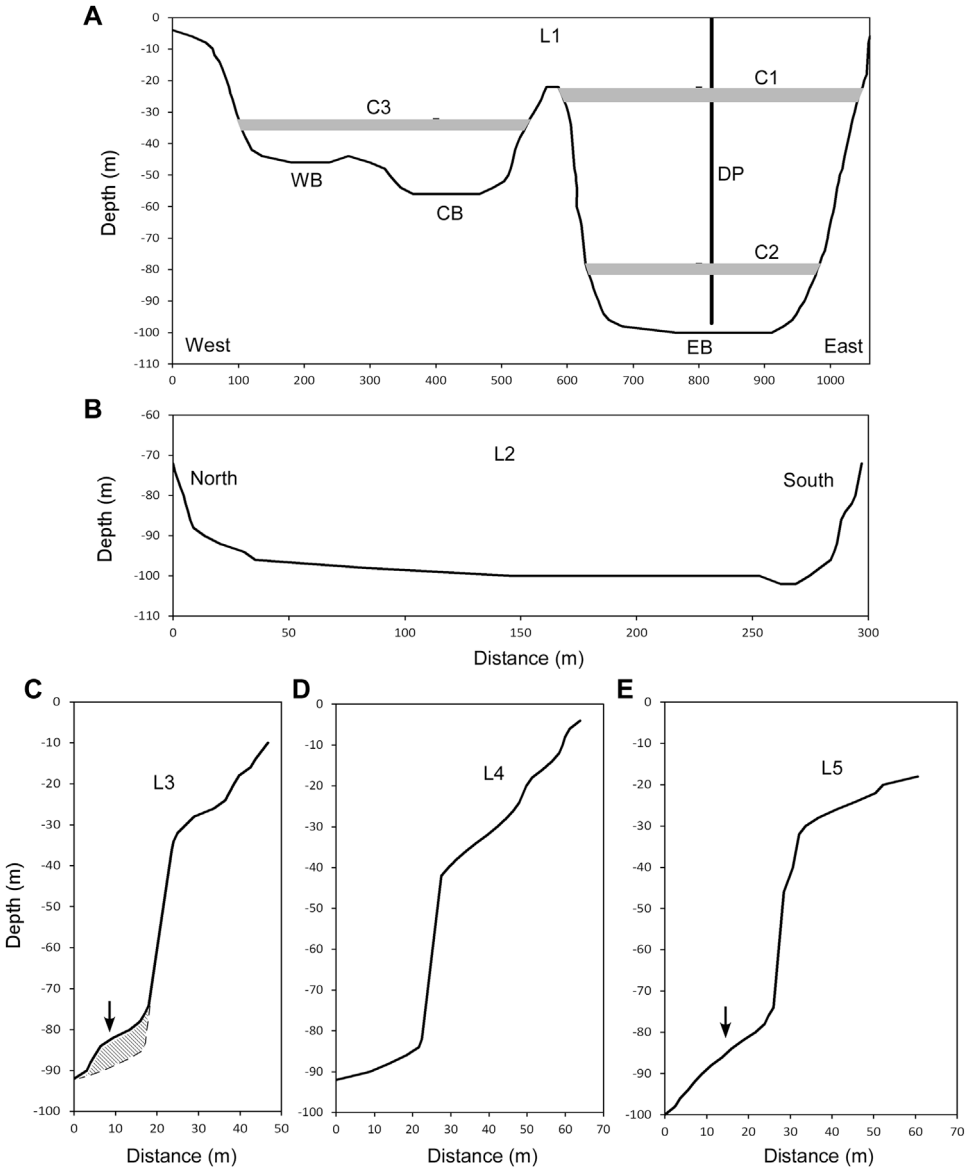

FIGURE 3 | Cross sections in Lake Monoun. **(A)** Cross section along L1 in **Figure 2**. C1 is the shallow chemocline in 2003. C2 and C3 are the chemoclines in 2015. DP is an artificial degassing pipe with 97 m length. **(B)** Cross section along L2 in **Figure 4**. **(C)** Cross section along L3 in **Figure 4**. The arrow indicates the position of M1. The shaded area indicates the body of M1. **(D)** Cross section along L4 in **Figure 4**. **(E)** Cross section along L5 in **Figure 4**. The arrow indicates the position of M2.

of D2. The depth of D2 relative to the surrounding lake bottom was 2.2 m. The depth of D3 relative to the surrounding lake bottom was not precisely determined but appeared to be approximately 1 m or less. Besides the aforementioned major depressions, small depressions were also evident (blue spots in **Figure 4**). Four major mounds (i.e., M1, M2, M3, and M4) were found near the scarp of the basin. Besides the aforementioned major mounds, smaller mounds were also evident (red spots in **Figure 4**). Many grooves (green curves in **Figure 4**) were evident on the scarp of the basin. Most of the grooves were located in the northern half of the scarp. An area free of grooves was found on the northern wall of the basin (F in **Figure 4**). This area is adjacent to a small ridge (R in **Figure 4**).

Figure 3B shows the depth profile along line L2 in **Figure 4**. The EB was gently inclined from north to south. The cross sections along lines L3, L4, and L5 in **Figure 4** are shown in **Figures 3C–E**, respectively. Lines L3 and L5 straddle mounds M1 and M2, respectively. The depth profiles along lines L3 and L5 revealed a raised section in the corresponding mound section (**Figures 3C,E**).

The temperature, electrical conductivity (C_{25}), and pH of the lake water were measured along the depth of each basin

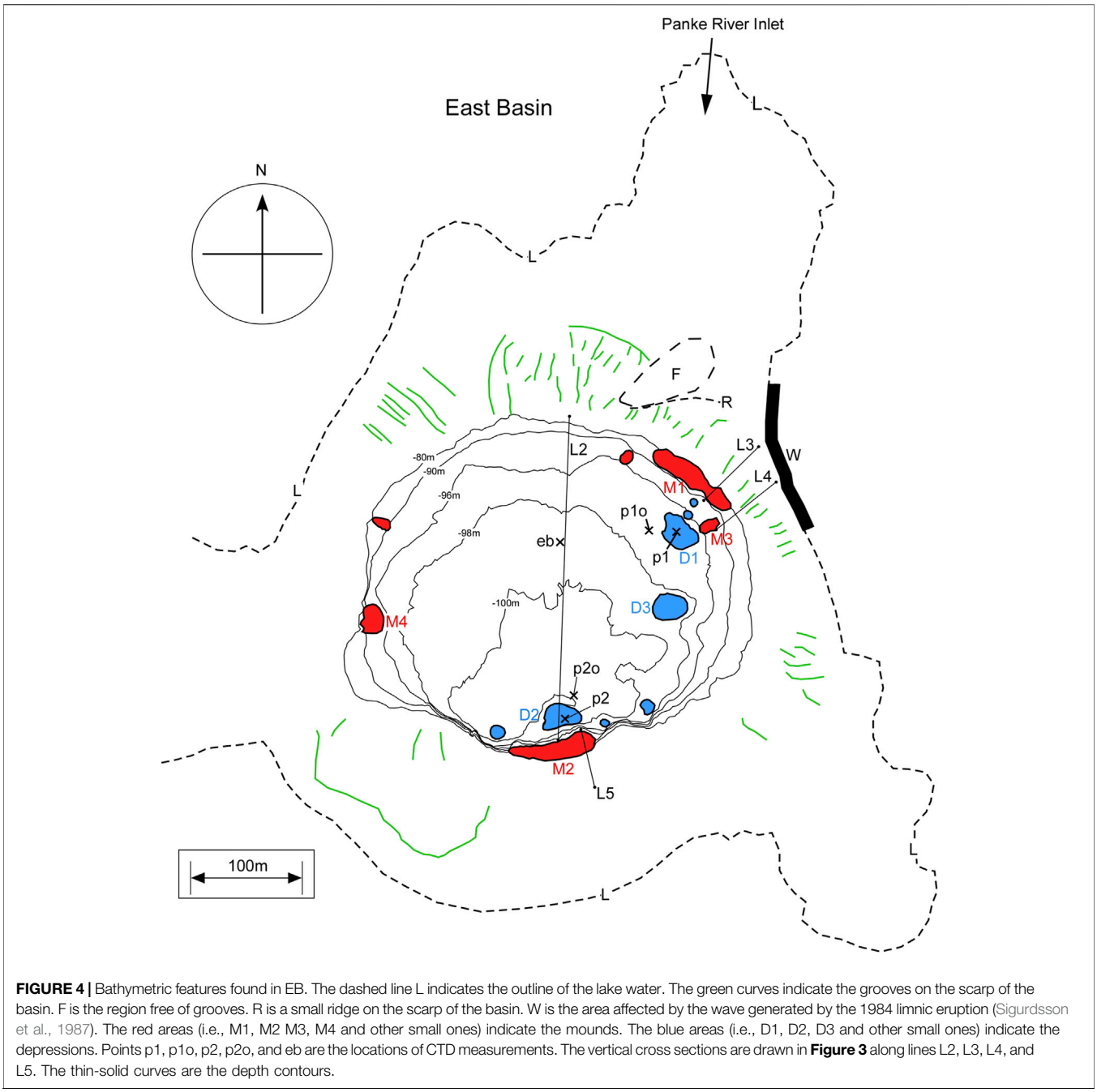

FIGURE 4 | Bathymetric features found in EB. The dashed line L indicates the outline of the lake water. The green curves indicate the grooves on the scarp of the basin. F is the region free of grooves. R is a small ridge on the scarp of the basin. W is the area affected by the wave generated by the 1984 limnic eruption (Sigurdsson et al., 1987). The red areas (i.e., M1, M2 M3, M4 and other small ones) indicate the mounds. The blue areas (i.e., D1, D2, D3 and other small ones) indicate the depressions. Points p1, p1o, p2, p2o, and eb are the locations of CTD measurements. The vertical cross sections are drawn in **Figure 3** along lines L2, L3, L4, and L5. The thin-solid curves are the depth contours.

using a CTD probe, in which C_{25} is the electrical conductivity normalized at 25°C using the following equation:

$$C_{25} = C\{1 + 0.02\,(t_c - 25)\}^{-1}, \quad (1)$$

where C is the raw electrical conductivity measured at Tc (°C). On 28 February 2015, CTD observations were conducted at points p1, p1o, p2, p2o, and eb (**Figure 4**). On 1 March 2015, CTD observations were conducted at the points of the closed circles in WB and CB (**Figure 2**). The closed circle for EB in **Figure 2** is identical to point eb in **Figure 4**. The measured temperature, C_{25}, and pH values are shown in **Figures 5A–C**, respectively.

The temperature profile of Lake Monoun has features that are not found in ordinary lakes (**Figure 5A**). In EB, the temperature at the surface was high, while it reached a minimum at approximately −30 m depth. Further below, the temperature increased as the depth increased, and a thermocline appeared at approximately −80 m depth. Under the thermocline, a mixed layer of approximately 10 m thick was developed. Under the mixed layer, the water temperature increased further toward the

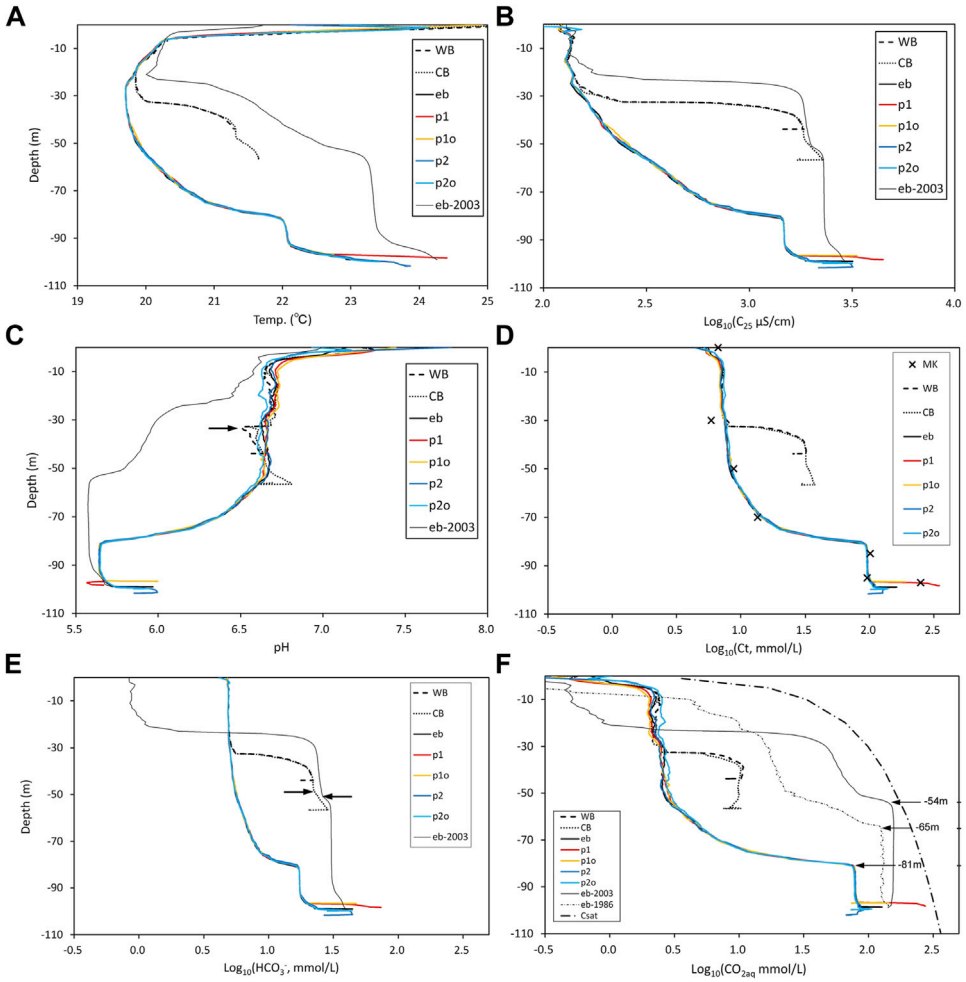

FIGURE 5 | Vertical profiles in Lake Monoun. **(A)** Temperature profiles measured in 2015 at point eb in **Figure 4** along with the profile in 2003 (Kusakabe et al., 2008).**(B)** C_{25} profiles in 2015 at point eb in **Figure 4** along with the 2003 profile (Kusakabe et al., 2008). The *x*-axis is the logarithm of C_{25} (µS/cm).**(C)** pH profiles in 2015 at point eb in **Figure 4** along with the 2003 profile (Kusakabe et al., 2008).**(D)** Estimated Ct profiles in 2015 along with the Ct ("x") measured using the MK method. The *x*-axis is the logarithm of Ct (mmol/L).**(E)** Estimated [HCO_3^-] profiles along with the 2003 profile measured at point eb in **Figure 4**. The *x*-axis is the logarithm of [HCO_3^-] (mmol/L). **(F)** Estimated [CO_{2aq}] profiles at point eb in **Figure 4** along with the 1986 and 2003 profiles (Kusakabe et al., 2008). The bold dashed and dotted line indicates the saturated [CO_{2aq}]. The *x*-axis is the logarithm of [CO_{2aq}] (mmol/L). The depths of the [CO_{2aq}] chemocline in 1986, 2003, and 2015 were −65, −54, and −81 m, respectively, as indicated by arrows.

bottom of the lake. In WB and CB, the thermocline appeared at approximately −33 m depth. Below the thermocline, the temperature increased slightly toward the bottom of WB and CB. Toward the bottom of WB, the temperature profile in CB was almost identical to that in WB. Over the entire depth range, excluding the surface, the temperature in EB significantly decreased relative to the temperature in 2003 (Kusakabe et al., 2008).

C_{25} in EB was low and approximately constant from the surface to approximately −30 m depth (**Figure 5B**); further below, it increased with depth, and a chemocline appeared at approximately −80 m (the term "chemocline" used here refers to the boundary in which the chemical properties of lake water change rapidly). Below the chemocline, a mixed layer of approximately 10 m thick was developed. Under the mixed layer, C_{25} increased toward the bottom of EB. The C_{25} profiles in WB and CB revealed chemoclines at approximately −33 m depth (**Figure 5B**). C_{25} in CB increased in the layer below the chemocline toward the bottom. The highest C_{25} value in the CB profile was close to the C_{25} value observed in 2003 at EB. Over the entire depth range, except for the surface and near the bottom, C_{25} in EB decreased significantly relative to C_{25} in 2003.

The pH of the lake water in WB, CB, and EB was weakly alkaline near the surface (**Figure 5C**). In EB, the lake water was close to neutral, and the pH was almost constant from −10 to −50 m depth. Further below, the pH fell with increasing depth, and a chemocline appeared at approximately −80 m depth. Below the chemocline, a mixed layer of approximately 10 m thick was developed. Below the mixed layer, the pH rose toward the lake bottom. The pH profiles in WB and CB were different from those

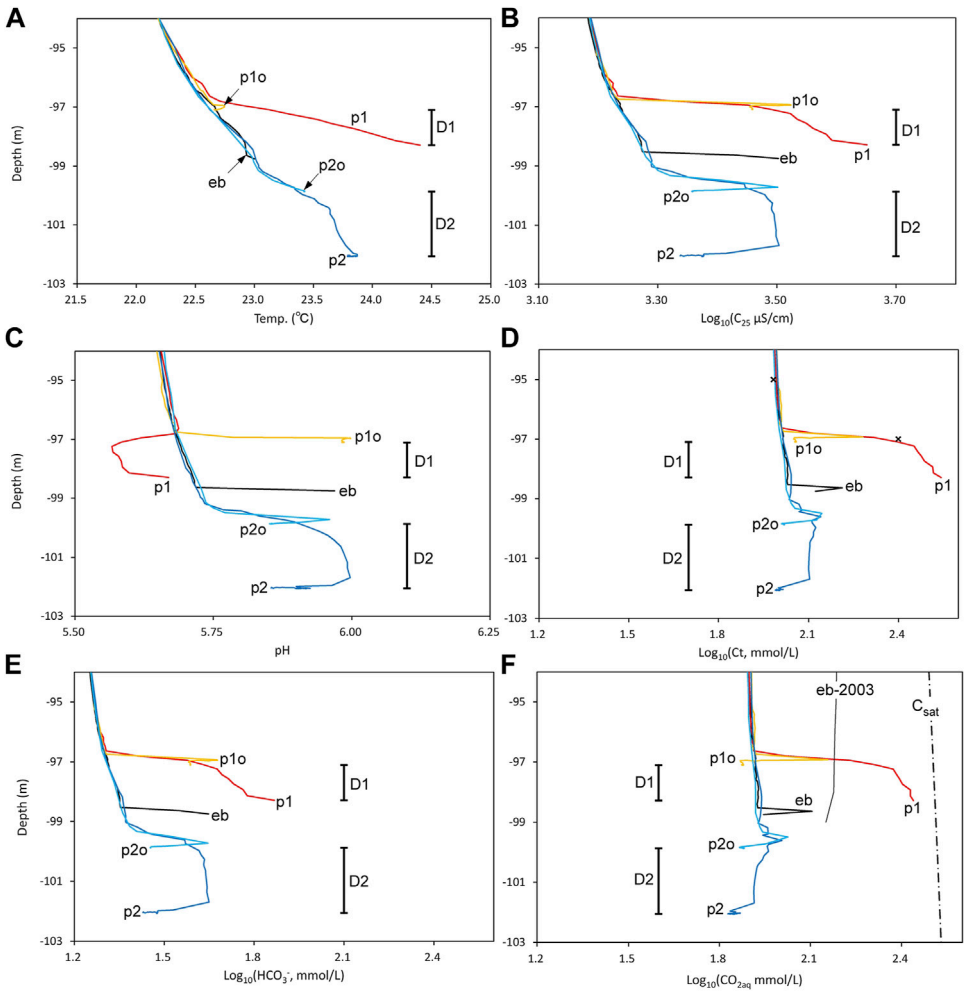

FIGURE 6 | Profiles below −94 m depth in EB. **(A)** Temperature, **(B)** Log (C_{25} µS/cm), **(C)** pH, **(D)** Log (Ct mmol/L), **(E)** Log ([HCO_3^-] mmol/L), and **(F)** Log ([CO_{2aq}] mmol/L). Vertical bars indicate the ranges of depth inside D1 and D2. In **(F)**, the CO_{2aq} saturation curves and the profile in 2003 (Kusakabe et al., 2008) measured at point eb in **Figure 4** are indicated.

in EB, exhibiting left-pointing "projections" locally falling pH at the chemocline at around −33 m depth (right arrow in **Figure 5C**). Over the entire depth range, except for the surface and near the bottom, the pH in EB significantly rose relative to the pH in 2003.

Figure 6 shows the profiles in **Figure 5** enhanced near the bottom of EB. At all points, temperature increased toward the lake bottom (**Figure 6A**). Except for the profile at point p1, the thermal gradient (i.e., −dT/dz; T: temperature; z: depth) was common and almost constant, suggesting an established stable thermal gradient in the lake water near the bottom. Inside D1, the thermal gradient was high, suggesting discharged hot water at the bottom of D1. However, the thermal gradient inside D2 was similar to that at points other than p1. At point p1, C_{25} increased toward the bottom, where the highest C_{25} value was recorded (**Figure 6B**), suggesting discharged high C_{25} water at the bottom of D1. At points eb and p1o, C_{25} sharply increased at the lake bottom. At point p2o, C_{25} peaked before reaching the lake bottom. The interior of D2 was filled with high C_{25} water, with values close to the maximum value at point p2o. At point p2, C_{25} decreased toward the bottom, suggesting no discharge of water with high C_{25} within D2. At point p1, the pH started to fall at the upper limit of D1 and then turned to rise toward the bottom (**Figure 6C**). At points p1, p1o, and eb, pH rose at the lake bottom. At point p2o, the pH peaked before the bottom. The interior of D2 was filled with high-pH water; the value was close to the maximum value at point p2o. At point p2, the pH fell at the bottom, suggesting no discharge of water with high pH at the bottom of D2.

On 2 March 2015, lake water was collected at point p1 using the MK method. **Supplementary Table S1** lists the Ct values determined by the MK method. The Ct values are plotted in **Figure 5D**, **Figure 6D**. **Supplementary Table S1** also presents the theoretically estimated [CO_{2aq}] and [HCO_3^-] based on the chemical equilibrium among CO_{2aq}, HCO_3^-, and CO_3^{2-} (in this study, brackets, i.e., [ ] indicate the concentration of

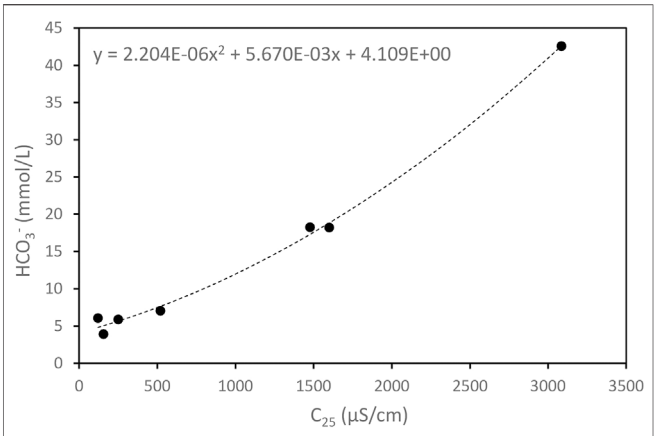

FIGURE 7 | Correlation between the HCO_3^- concentration and electrical conductivity. The correlation was approximated by the quadratic equation as shown in the figure.

chemical species in mmol/L). The theoretical relationship between $[HCO_3^-]$ and Ct is given by the following equation (Stumm and Morgan, 1996):

$$[HCO_3^-] = C_t\left(\frac{a_H\,\gamma_{HCO3}}{K_{a1}} + 1 + \frac{K_{a2}\,\gamma_{HCO3}}{a_H\,\gamma_{CO3}}\right)^{-1}. \quad (2)$$

Here, a_H is the activity of H^+ ion given by,

$$a_H = 10^{-pH}. \quad (3)$$

K_{a1} and K_{a2} in **Equation 2** denote the acidity constants of CO_{2aq} and HCO_3^-, respectively. K_{a1} and K_{a2} are functions of temperature, and the concrete formula is given by Ohba et al. (2015). γ_{HCO3} and γ_{CO3} in **Equation 2** are the activity coefficients of HCO_3^- and CO_3^{2-}, respectively, given by the Davies equation (Butler, 1991):

$$\log\gamma = -0.5z^2\left(\frac{I^{0.5}}{1+I^{0.5}} - 0.2I\right)\left(\frac{298}{T}\right)^{\frac{2}{3}}, \quad (4)$$

where z, I, and T denote the charge of the species, ionic strength, and temperature in Kelvin, respectively. Based on the cationic composition of the water at −96.5 m depth in Lake Monoun in 2006 (Kusakabe et al., 2008), I can be estimated as follows:

$$I = 1.463\,[HCO_3^-]/1000. \quad (5)$$

$[HCO_3^-]$ was calculated from Ct using the following procedure:

Step 1. γ_{HCO3} and γ_{CO3} were initially set equal to 1.

Step 2. K_{a1} and K_{a2} were calculated from the temperature of the lake water.

Step 3. a_H was calculated from the pH of the lake water.

Step 4. Substituting the above values into **Equation 2**, the initial $[HCO_3^-]$ was calculated from Ct obtained using the MK method.

Step 5. Substituting the initial $[HCO_3^-]$ into **Equation 5**, I was obtained.

Step 6. Substituting the ionic strength, ion charge, and lake water temperature into **Equation 4**, γ_{HCO3} and γ_{CO3} were obtained.

Step 7. Finally, steps 2, 3, and 4 were repeated.

In general, the electrical conductivity (C_{25}) of lake water is proportional to the concentration of the dissolved ions. According to Kusakabe et al. (2008), the main anion contained in the lake water of Lake Monoun was HCO_3^-. The concentrations of anions other than HCO_3^-, such as Cl^- and SO_4^{2-}, were negligibly lower than $[HCO_3^-]$. Therefore, a positive correlation is expected between C_{25} and $[HCO_3^-]$. **Figure 7** depicts C_{25} versus $[HCO_3^-]$ (**Supplementary Table S1**), in which the correlation is approximated by the following quadratic equation in terms of C_{25}:

$$y = 2.204\times10^{-6}x^2 + 5.670\times10^{-3}x + 4.109, \quad (6)$$

where x and y denote C_{25} and $[HCO_3^-]$, respectively. Based on **Equation 6**, the C_{25} profiles were converted to continuous profiles of $[HCO_3^-]$, as shown in **Figures 5E**, **6E**. The Ct profiles can be calculated from the $[HCO_3^-]$ profile using **Equations 2–5**. The Ct profiles are shown in **Figures 5D**, **6D** and are consistent with the discrete Ct values obtained using the MK method. $[CO_{2aq}]$ is obtained from $[HCO_3^-]$ using the following equation:

$$[CO_{2aq}] = \gamma_{HCO3}[HCO_3^-]10^{-pH}K_{a1}^{-1}. \quad (7)$$

Since $[CO_3^{2-}]$ is less than one-thousandth of $[HCO_3^-]$ at a pH of 7.3 or lower, $[CO_3^{2-}]$ can be safely neglected in the case of Lake Monoun, while $[CO_{2aq}]$ can be simply expressed as the difference between Ct and $[HCO_3^-]$ as follows:

$$[CO_{2\,aq}] = C_t - [HCO_3^-]. \quad (8)$$

The obtained $[CO_{2aq}]$ profiles are shown in **Figures 5F**, **6F**.

The Ct profiles at all points exhibited almost constant values from the surface to approximately −33 m depth (**Figure 5D**). At points in WB and CB, a chemocline appeared at −33 m depth; at points outside WB and CB, a chemocline appeared at around −80 m depth, while a mixed layer of approximately 10 m thick was developed below. The characteristics of the Ct profile (**Figure 5D**) are similar to those of the C_{25} profile (**Figure 5B**); nevertheless, they exhibit the following differences: the C_{25} value at the bottom of CB was close to the C_{25} value at the bottom of points eb, p2, and p2o (**Figure 5D**), whereas the Ct value at the bottom of CB was only one-tenth of the Ct value at the bottom of points eb, p2, and p2o (**Figure 5D**). At point p1, Ct continued to rise toward the lake bottom within D1 (**Figure 6D**), suggesting the discharge of high-Ct water at the bottom. At point p1o, adjacent to point p1, Ct peaked near the

bottom (**Figure 6D**). Point p2, in the interior of D2, was filled with water; the value of Ct at point p2 was slightly higher than that of the ambient lake water represented by the water at point eb, except for near the bottom. The Ct value at point p2 decreased at the lake bottom, suggesting that no high-Ct water was discharged at the bottom of D2. The Ct values at points eb and p2o peaked near the lake bottom (**Figure 6D**). The [HCO_3^-] profiles (**Figure 6E**) were similar to the Ct profiles (**Figure 6D**), except for points p1o and eb, in which [HCO_3^-] did not decrease at the lake bottom. The [CO_{2aq}] profiles (**Figure 6F**) were similar to the Ct profiles (**Figure 6D**). Allowing equilibrium between CO_{2aq} and HCO_3^-, the [HCO_3^-]/[CO_{2aq}] ratio was 0.19 and 0.43, respectively, when the pH was 5.65 and 6.00, which was the pH range of lake water below −95 m depth (**Figure 6C**). The similarity between the [CO_{2aq}] and Ct profiles is reasonable, considering the dominance of CO_{2aq} over HCO_3^-. At point p1, [CO_{2aq}] increased toward the lake bottom, suggesting the discharge of high-[CO_{2aq}] water at the bottom of D1. Inside D1, [CO_{2aq}] exceeded the value observed at point eb in 2003 (**Figure 6F**), suggesting that the high-[CO_{2aq}] water at the bottom of D1 could be the source of the high-[CO_{2aq}]-mixed layer developed below the chemocline at approximately −81 m depth. The [CO_{2aq}] profile at point p1 did not reach the saturation concentration of CO_{2aq} estimated using Henry's constant of CO_2 (Fernandez-Prini et al., 2003).

DISCUSSION

Three large depressions, i.e., D1, D2, and D3, were found at the bottom of EB, and hot water rich in CO_{2aq} and HCO_3^- was discharged at the bottom of D1. However, within D2, [CO_{2aq}] and [HCO_3^-] decreased toward the bottom, indicating no discharge of water rich in CO_{2aq} and HCO_3^-. At points p1o, eb, and p2o, [CO_{2aq}] peaked above the lake bottom (**Figure 6F**). The [CO_{2aq}] peak height was the highest at p1o, followed by eb and p2o, while it decreased with distance from D1 (**Figure 4**). The above observations suggest the wide horizontal distribution of high-[CO_{2aq}] hot water along the bottom of EB.

At points p1o and eb, pH rose sharply at the lake bottom (**Figure 6C**). The pH behavior indicated that the [HCO_3^-]/[CO_{2aq}] ratio increased near the lake bottom. The [HCO_3^-]/[CO_{2aq}] ratio and pH are related through the following formula:

$$pH = log\left(\gamma_{HCO3}\frac{[HCO_3^-]}{[CO_{2aq}]}\right) - logK_{a1}. \quad (9)$$

$FeCO_3$ siderites were present in the bottom sediments of Lake Monoun, and the lake water near the bottom was supersaturated with respect to $FeCO_3$ (Sigurdsson et al., 1987). Fine $FeCO_3$ particles could be suspended in the lake water near the bottom. The pH increase, i.e., the [HCO_3^-]/[CO_{2aq}] ratio increase, near the bottom of the lake is indicative of the reaction between CO_{2aq} and $FeCO_3$ particles as follows:

$$FeCO_3 + CO_{2aq} + H_2O = Fe^{2+} + 2HCO_3^-. \quad (10)$$

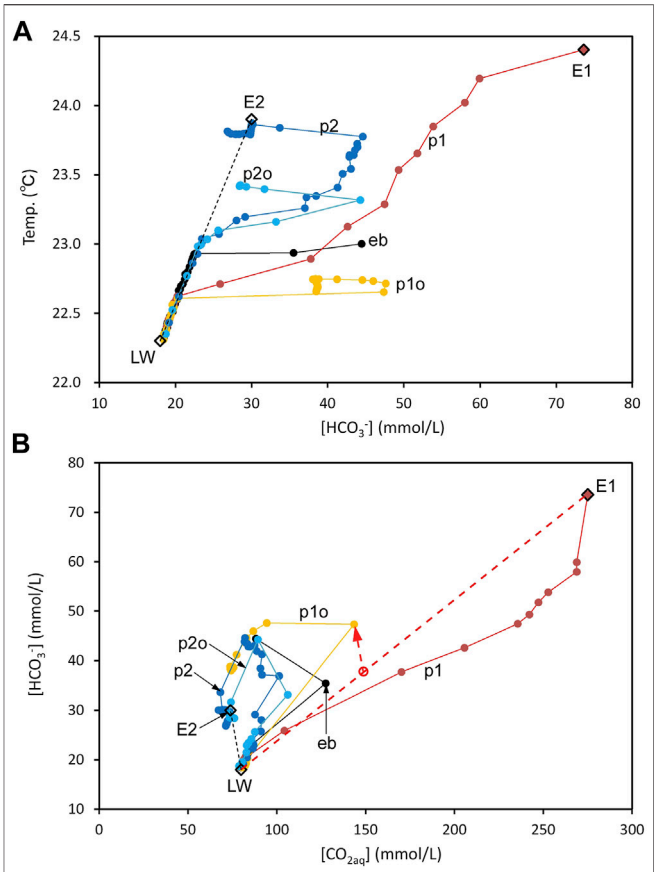

FIGURE 8 | Correlations among the temperature, [HCO_3^-], and [CO_{2aq}] in lake water below −95 m depth. **(A)** Correlation between temperature and [HCO_3^-]. LW is the end-member representing lake water. E2 is the end-member representing lake water reacted with postulated $FeCO_3$ particles. E1 is the end-member representing lake water at the bottom of D1. **(B)** Correlation between [HCO_3^-] and [CO_{2aq}]. The red dashed line and arrow indicate the formation process of water located above the line connecting LW and E1, namely, a simple mixture between LW and E1, followed by the reaction with postulated $FeCO_3$ particles suspended in the lake water.

In the above reaction, 1 mol CO_{2aq} is consumed, and 2 mol HCO_3^- is generated; when it occurs, the [HCO_3^-]/[CO_{2aq}] ratio as well as the pH rises. **Figure 8A** shows the relationship between water temperature and [HCO_3^-] below −95 m depth. As shown, LW is an end-member representing the lake water. The water temperature, [CO_{2aq}], and [HCO_3^-] of LW were assumed to be 22.3°C, 80 mmol/L, and 18 mmol/L, respectively. End-member E2 represents lake water after reaction with $FeCO_3$. The temperature, [CO_{2aq}], and [HCO_3^-] of E2 were assumed to be 23.9°C, 74 mmol/L, and 30 mmol/L, respectively. Through the reaction, the [CO_{2aq}] decrease of LW was 6 mmol/L, and the [HCO_3^-] increase was 12 mmol/L. The data points distributed on the line connecting LW and E2 (**Figure 8A**) indicate a linear relationship between temperature and [HCO_3^-] near the lake bottom, especially in the range of low [HCO_3^-]. The hot water at the bottom of D1 is assumed to be end-member E1. As shown in **Figure 8A**, the lake water located in the area to the right of the line connecting LW and E2 can be a mixture of LW and E1. **Figure 8B**

shows the relationship between [CO_{2aq}] and [HCO_3^-] below −95 m depth. The bottom-water compositions at points p2 and p2o were close to E2, suggesting that the bottom water at p2 and p2o was lake water reacting with $FeCO_3$. The other points cannot be easily explained by a simple mixture of LW and E1. As shown by the red dashed line and arrow, if mixing between LW and E1 is followed by the reaction with $FeCO_3$, the observed relationship between [CO_{2aq}] and [HCO_3^-] can be explained because [HCO_3^-] increases and [CO_{2aq}] decreases, as indicated by the red arrow.

In the numerical simulation of limnic eruptions by Kozono et al. (2016), the following initial conditions were adopted: the lake water was saturated with CO_2 at approximately −50 m depth. The [CO_{2aq}] of the lake water below −50 m depth was equal to [CO_{2aq}] at −50 m depth. Below −50 m depth, the lake water was unsaturated with CO_2. The conditions described previously were based on the CO_{2aq} profile (eb-2003 in **Figure 5F**) observed by Kusakabe et al. (2008). Sigurdsson et al. (1987) supposed that the lake water was supersaturated with respect to CO_{2aq} before the 1984 limnic eruption, which was triggered by the disturbance of the lake water by a landslide. However, in the initial condition by numerical simulation, the lake water below −50 m depth is unsaturated with CO_2. Actually, in 1986, when 2 years later of limnic eruption, the [CO_{2aq}] of lake water deeper than −65 m was unsaturated with respect to CO_{2aq} (**Figure 5F**). The falling sediment displaced lake water from near the chemocline to the deep layer. Because the difference between the CO_2 partial pressure of the displaced lake water and the surrounding pressure increases, degassing of CO_2 from the displaced lake water is not likely to occur. Therefore, it is unlikely that any falling sediment triggered the limnic eruption.

In this study, [CO_{2aq}] at the bottom of D1 was estimated to be 275 mmol/L. From Henry's constant of CO_2 (Fernandez-Prini et al., 2003), the equilibrium gas pressure of CO_2 was estimated to be 8.2×10^5 Pa, which was lower than the hydrostatic pressure at the lake bottom (i.e., 1.0×10^6 Pa). At the bottom of D1, CO_{2aq} was unsaturated. According to Issa et al. (2013), CO_2 dissolved in the water of Lake Monoun was accompanied by CH_4; they found that the contributions of CO_2 and CH_4 to the total pressure of the gas phase equilibrated with water near the lake bottom were 63 and 37%, respectively. This suggests that the total gas pressure in equilibrium with the lake water could be 1.3×10^6 Pa, thereby exceeding the hydrostatic pressure, and the bubbles consisting of CO_2 and CH_4 were always present at the bottom of D1.

Sigurdsson et al. (1987) discovered a trace of a landslide in W, as shown in **Figure 4**. Mound M1 is located close to W, and it has likely formed by the sediment slumped from W. All mounds at the bottom of the EB were located along the scarp of the basin. The volume of M1 can be estimated by comparing the cross section along L3, which straddles M1, and the cross section along L4 (**Figures 3C,D**). The shaded area in **Figure 3C** corresponds to the body of M1 by comparing the cross sections and assuming that the terrain below M1 is equal to the cross section along L4. The cross-sectional area, length, and volume of M1 were 73 m^2, 83 m, and 6×10^3 m^3, respectively. The horizontal cross-sectional area of the EB at −50 m depth was 1.02×10^5 m^2. If the entire mass of M1 slumped from W, then the mass pushed the chemocline at −50 m depth upward by approximately 0.06 m.

According to the limnic eruption scenario of Sigurdsson et al. (1987), a landslide occurred at W, and the collapsed sediment agitated the lake water near the bottom, thereby triggering the limnic eruption. What role does D1 play in the limnic eruption scenario described by Sigurdsson et al. (1987)? D1 was an outlet for hot water supplying CO_{2aq}, which was the driving force of limnic eruption. In the limnic eruption scenario of Sigurdsson et al. (1987), D1 can play its role regardless of its location at the bottom of the lake. Because M1 is located directly under W, M1 is considered to be sediment deposited by a landslide. D1 does not necessarily need to be adjacent to M1. In the limnic eruption scenario of Sigurdsson et al. (1987), the coupling of M1 and D1 was considered to be a coincidence; however, in our limnic eruption model, the coupling of M1 and D1 is not a coincidence but an inevitable consequence.

As shown in **Figure 5F**, [CO_{2aq}] near the bottom of the lake in 1986, 2003, and 2015 was similar and approximately equal to 160 mmol/L, suggesting that the hot water with high [CO_{2aq}] discharging at D1 was diluted by the lake water with low [CO_{2aq}]. The mixing ratio between the two waters was probably constant throughout the period between 1986–2015. It is likely that the sustained discharge of hot water with high [CO_{2aq}] at D1 occurred even before the 1984 limnic eruption.

Woods and Phillips (1999) reproduced the limnic eruption in Lake Nyos at −210 m depth through laboratory experiments and numerical analysis. They found that a small amount of CO_2 bubble flow at the lake bottom entrained CO_{2aq}-saturated lake water, and the rising flow was strengthened by CO_2 degassing. The CO_2 flux at the lake surface could reach 10^5 times that at the bottom of the lake. Under the initial conditions in the numerical simulation by Kozono et al. (2016) for Lake Monoun, the lake water is only saturated with CO_{2aq} at −50 m depth, and a slow upward flow of lake water (i.e., >0.01 m/s) near −50 m depth is necessary for initiating the first degassing of CO_2 (**Figure 9A**). Kozono et al. (2016) suggested a perturbation of the layer boundary caused by double-diffusive convection and a seiche induced by external forcings, such as strong wind causing the slow updrift of lake water. In this study, we propose that bubbles rising from D1 cause a slow upward flow of lake water. The first degassing of CO_2 generates buoyancy in the lake water, and a parcel of lake water containing CO_2 bubbles starts to rise. The rising parcel of lake water entrains lake water enriched in CO_{2aq} below −50 m depth (**Figure 9B**). The degassing of the entrained lake water increases the rising speed. The increased velocity of lake water results in explosive degassing (i.e., limnic eruption). Considering the chemocline of [CO_{2aq}] in 1986 (**Figure 5F**), the layer above −65 m depth suffered degassing. The slow upward flow of lake water around −50 m depth was the "seed" of the limnic eruption. The hot water discharged from D1 was accompanied by bubbles. The bubbles rising from D1 and reaching −50 m depth probably produced a slow upward flow of lake water (**Figure 9A**). As shown in **Figure 9B**, the 1984 limnic eruption was likely initiated above D1. The lake-water wave generated by the limnic eruption impacted the lake shoreline at W, thus causing a landslide and resulting in the

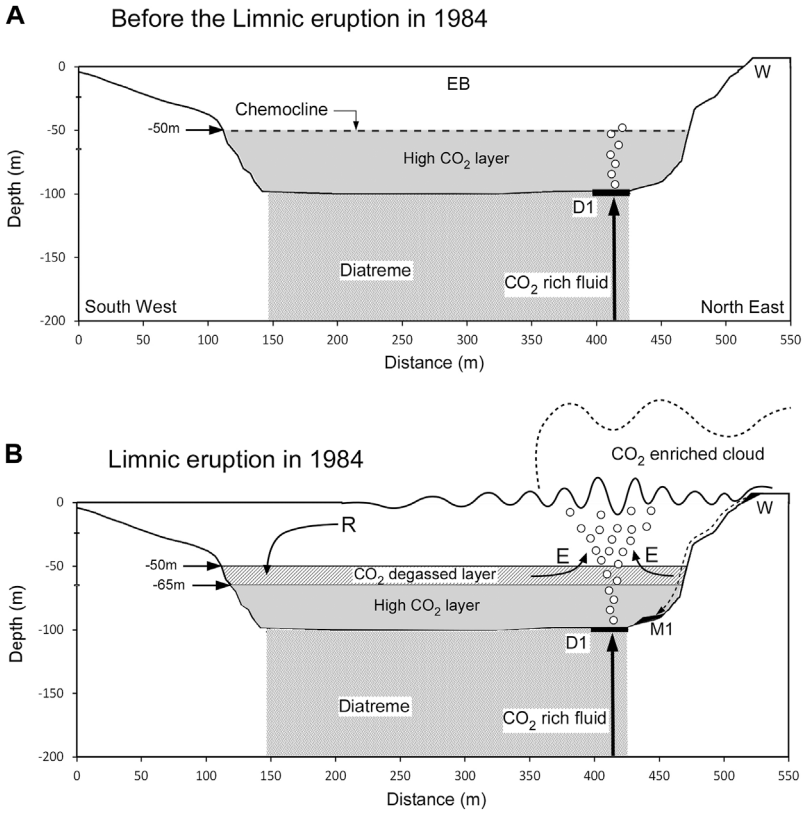

FIGURE 9 | Estimated structure beneath Lake Monoun and the situation of limnic eruption.**(A)** Presumed situation in EB of Lake Monoun before the 1984 limnic eruption. The shape of the basin corresponds to the cross section along line L6 in **Figure 2**. The lake water at –50 m depth was assumed to be saturated with respect to CO_{2aq}, based on the CO_{2aq} profile in 2003 (Kusakabe et al., 2008). The layer below –50 m depth was undersaturated with respect to CO_{2aq}. A CO_2-rich fluid was transported along the diatreme ring fault and discharged at the bottom of D1. The discharged water at the bottom of D1 was accompanied by bubbles. The bubbles would rise to the chemocline developed at –50 m depth. **(B)** Presumed situation of the 1984 limnic eruption. E: entrainment of high-CO_{2aq} lake water into the ascending turbulent flow of CO_2 bubbles, which amplified the CO_2 flux at the lake surface. W: east shore of Lake Monoun impacted by the waves generated by the limnic eruption. A landslide started at W, and the mound M1 was deposited beside D1. R: return flow depleted in CO_{2aq}, which invaded the high-CO_{2aq} layer above –65 m depth, which was the depth of the [CO_{2aq}] chemocline in 1986 **(Figure 5F)**.

M1 deposits. In this model, the coupling between D1 and M1 was not a coincidence but an inevitable consequence.

The coupling of D2 and M2 may be the trace of another limnic eruption before 1984, strongly implying the probability of future recurrence of limnic eruptions at Lake Monoun if the artificial CO_2 degassing stops. Shanklin (1992) collected oral testimonies by several traditional ethnic groups in the area near Lake Monoun from 1981 to 1986. Several oral testimonies showed that the lake exploded, and subsequently the ethnic groups left the lake area. The oral testimonies suggest that limnic eruptions have occurred in the past at Lake Monoun or another lake, which is consistent with the idea that the coupling of D2 and M2 is likely the trace of a limnic eruption that occurred before 1984.

Many grooves were observed on the scarps of EB (**Figure 4**). It is likely that the waves generated by the limnic eruption collided with the scarp, thereby destabilizing the surface layer while part of the surface layer collapsed to form grooves. The distribution of grooves was limited to the slopes of the northern half, suggesting that the waves arriving at the southern shore were weak. These probabilities are consistent with the estimation that the starting point of the limnic eruption was directly above D1 and far from the southern shore. Near the inlet of the Panke River, there was an area free of grooves (F in **Figure 4**). As shown in **Figure 3B**, EB gently inclined from north to south. It is likely that the gentle inclination was caused by the sedimentation of suspended materials carried by the Panke River, which flowed into EB from the north side. The grooves in area F may have been filled with a suspended material carried by river water, thereby erasing the grooves.

A diatreme structure generally develops beneath a maar (Lorenz, 1973). Nagao et al. (2010) suggested that CO_2-rich fluid rose along the ring fault of the potential diatreme structure developed beneath Lake Nyos. In Lake Monoun, D1, D2, D3, and other small depressions are distributed on the bottom of EB along its scarp. This distribution suggests that a diatreme structure also exists beneath Lake Monoun (**Figure 2**), while the CO_2-containing fluid rose along the ring fault of the diatreme and was discharged on D1. However, D2 seems to be a trace of the outlet, in which CO_2-enriched water was discharged before 1984.

The $[HCO_3^-]$ profile near the bottom of CB in 2015 was similar to that of EB in 2003 (**Figure 5E**). For example, in 2003, the $[HCO_3^-]$ value near the bottom of CB was close to the $[HCO_3^-]$ value at the same depth in EB. Furthermore, the $[HCO_3^-]$ profile in CB had a bending point near −49 m depth (right arrow in **Figure 5E**). The $[HCO_3^-]$ profile in EB in 2003 also had a bending point at −50 m depth (left arrow in **Figure 5E**). This suggests that the estimated profiles in WB and CB in 2003 were identical to those in EB in 2003, and the $[HCO_3^-]$ profiles in WB and CB in 2015 were remnants of the profile established in 2003. As shown in **Figure 3A**, the depth of the EB chemocline in 2003 was close to the depth of the saddle between CB and EB. By 2003, the dense lake water that had accumulated in the hypolimnion of EB may have flowed into CB and WB beyond the saddle. Here, the hypolimnion is the region beneath the chemocline where mass transfer is restricted to and from the shallow layer of lake water. Since 2003, when artificial degassing began, the EB chemocline has deepened rapidly; however, the dense lake water that flowed into CB and WB could not return to the EB beyond the saddle and was left behind as of 2015.

The $[CO_{2aq}]$ profiles in WB and CB in 2015 were almost vertical toward the lake bottom (**Figure 5F**), suggesting no discharge of high-$[CO_{2aq}]$ water at the bottoms of WB and CB. In 2015, the highest $[CO_{2aq}]$ value in WB and CB was 10.8 mmol/L at −39 m depth, which was much lower than the $[CO_{2aq}]$ value of 58.7 mmol/L in EB in 2003 at the same depth. Considering the above difference in $[CO_{2aq}]$ and the similar $[HCO_3^-]$ profiles, CO_{2aq} in the hypolimnion of WB and CB was preferentially lost. The difference between the properties of CO_{2aq} and HCO_3^- is that the former has no electrical charge, whereas the latter has an electrical charge. Therefore, CO_{2aq} escapes as it can diffuse into the atmosphere as gas through the lake surface while HCO_3^- does not.

The flux of CO_2 gas released from the surface of a crater lake can be interpreted as a sign of volcanic activity (e.g., Mazot and Bernard, 2015). It would be interesting to see how much CO_{2aq} stored in the hypolimnion of Lake Monoun contributed to the CO_2 gas released from the lake surface. According to Issa et al. (2014), CO_2 gas was released from the entire lake surface of Lake Monoun to the ambient atmosphere at a rate of 21.8 ton/day in 2013. The volume of WB and CB below −22 m depth is 1.5×10^6 m^3. The total amount of CO_{2aq} was estimated at 8.4 Mmol by integrating the $[CO_{2aq}]$ value in 2015. Assuming that the $[CO_{2aq}]$ profiles in WB and CB are the same as those in EB in 2003, the total amount of CO_{2aq} stored in lake water below −22 m depth was 74 Mmol. Therefore, 74 Mmol of CO_{2aq} dissolved in the lake water in WB and CB in 2003 was estimated to have decreased to 8.4 Mmol in 2015. Assuming a constant rate of the CO_{2aq} decrease, the rate is estimated at 14.7 kmol/day (or 0.647 ton/day). This amount of flux is only approximately 3% of the flux observed by Issa et al. (2014), which was 21.8 ton/day. Among the CO_2 gases emitted from the entire lake surface of Lake Monoun, CO_2 originating from the hypolimnion of WB and CB is expected to be negligible.

CONCLUSION

Near the lake bottom in EB of Lake Monoun, a stratified structure developed in which the temperature and $[HCO_3^-]$ increased toward the bottom while maintaining a linear relationship between temperature and $[HCO_3^-]$. The $[HCO_3^-]$ increase could be due to the reaction between CO_{2aq} in the lake water and possible $FeCO_3$ particles suspended in lake water. The reacted CO_{2aq} is converted to HCO_3^-. In addition to the stratified structure, hot water enriched in CO_{2aq} and HCO_3^- was diffused horizontally along the lake bottom. Hot water was discharged from D1. At the bottom of D1, the temperature, pH, $[CO_{2aq}]$, and $[HCO_3^-]$ were 24.4°C, 5.67, 275 mmol/L, and 73.6 mmol/L, respectively.

In WB and CB of Lake Monoun, a hypolimnion was sustained below −30 m depth. In 2015, the hypolimnion seemed to keep CO_{2aq} and HCO_3^- dissolved in the lake water in 2003. The total amount of CO_{2aq} stored in the hypolimnion in 2015 and 2003 was estimated to be 8.4 and 74 Mmol, respectively. If CO_{2aq} in the hypolimnion diffused out through the lake surface, a 14-kmol/day flux would be expected, corresponding to 3% of the CO_2 flux through the entire lake surface in 2013. The CO_2 flux through the lake surface in 2003 seemed to be dominated by the CO_2 originating from EB, and the contributions of CO_{2aq} stored in the hypolimnion of WB and CB were limited.

The hot water discharged from the bottom of D1 could have been accompanied by bubbles affected by the partial pressure of CH_4 dissolved in the lake water. The bubbles rising from D1 reached the chemocline at −50 m depth and formed a weak upward flow of lake water. The upward flow of lake water at −50 m depth was the "seed" of the limnic eruption (Kozono et al., 2016). The upward flow of lake water induced the initial degassing of CO_2. The initial degassing of CO_2 was amplified by the entrainment of CO_2-enriched lake water below −50 m depth, resulting in the 1984 limnic eruption. The wave generated by the limnic eruption impacted the east shore, causing a landslide and forming mound M1 beside D1. The coupling of D1 and M1 was regarded as a trace of the limnic eruption in 1984. Another coupling, i.e., that of D2 and M2, is likely the trace of another limnic eruption that occurred earlier than 1984. Lake Monoun may have experienced several limnic eruptions in the past. If the artificial degassing of CO_2 is not continued in Lake Manoun, the water containing high concentrations of CO_{2aq} released from D1 will increase the CO_{2aq} concentration in the lake water, and the bubbles rising from D1 will cause a limnic eruption. In the future, the flux of CO_{2aq} supplied from D1 may increase and exceed the flux of CO_{2aq} removed by the artificial degassing, potentially increasing the amount of CO_{2aq} accumulated in the lake water. The regular monitoring of the CO_{2aq} amount in lake water should also be continued.

DATA AVAILABILITY STATEMENT

The original contributions presented in the study are included in the article/**Supplementary Material**, further inquiries can be directed to the corresponding author.

AUTHOR CONTRIBUTIONS

TO drafted the manuscript. TO, YO, KS, MK, Issa, TF, RN and GT conducted the lake observations. All authors participated in the discussion of the content of the manuscript and read and approved its final version.

FUNDING

This study was funded by the Japan Science and Technology Agency (JST) and Japan International Cooperation Agency (JICA).

ACKNOWLEDGMENTS

This study was part of the project "Magmatic Fluid Supply into Lakes Nyos and Monoun, and Mitigation of Natural Disasters through Capacity Building in Cameroon" under the program "Science and Technology Research Partnership for Sustainable development (SATREPS)." We also thank the researchers and engineers at IRGM and the local people around Lake Monoun who supported our research expedition. We express our sincere gratitude to the two reviewers. Their careful review and constructive suggestions have improved the initial draft. We also thank Dr. Corentin Caudron and Dr. Valerio Acocella for the editorial handling of the manuscript. We would like to thank Editage (www.editage.com) for English language editing.

SUPPLEMENTARY MATERIAL

The Supplementary Material for this article can be found online at: https://www.frontiersin.org/articles/10.3389/feart.2022.766791/full#supplementary-material

REFERENCES

Aka, F. T., and Yokoyama, T. (2013). Current Status of the Debate about the Age of Lake Nyos Dam (Cameroon) and its Bearing on Potential Flood Hazards. *Nat. Hazards* 65, 875–885. doi:10.1007/s11069-012-0401-4

Alain, F. T., Romaric, N., Kazuto, S., Takeshi, O., Brice, K., Gregory, T., et al. (2019). New Insights into Volume Estimates and Gas Contents from the Acoustic Investigation at Lake Monoun, Cameroon. *J. Afr. Earth Sci.* 160. doi:10.1016/j.jafrearsci.2019.103604

Baxter, P. J., and Kapila, M. (1989). Acute Health Impact of the Gas Release at Lake Nyos, Cameroon, 1986. *J. Volcanology Geothermal Res.* 39, 265–275. doi:10.1016/0377-0273(89)90064-4

Butler, J. N. (1991). *Carbon Dioxide Equilibria and Their Applications*. Michigan, United State: Lewis pub.

Conway, E. J. (1950). *Microdiffusion Analysis and Volumetric Error*. 3rd edn. London: Crosby-Lockwood.

Costa, A., and Chiodini, G. (2015). "Modeling Air Dispersion of CO2 from Limnic Eruptions. Volcanic Lakes," in *Advances in Volcanology*. (Berlin Heidelberg: Springer-Verlag).

Fernández-Prini, R., Alvarez, J. L., and Harvey, A. H. (2003). Henry's Constants and Vapor-Liquid Distribution Constants for Gaseous Solutes in H2O and D2O at High Temperatures. *J. Phys. Chem. Reference Data* 32, 903–916. doi:10.1063/1.1564818

Fitton, J. G., and Dunlop, H. M. (1985). The Cameroon Line, West Africa, and its Bearing on the Origin of Oceanic and continental Alkali basalt. *Earth Planet. Sci. Lett.* 72, 23–38. doi:10.1016/0012-821x(85)90114-1

Giggenbach, W. F. (1990). Water and Gas Chemistry of Lake Nyos and its Bearing on the Eruptive Process. *J. Volcanology Geothermal Res.* 42, 337–362. doi:10.1016/0377-0273(90)90031-a

Halbwachs, M., Sabroux, J.-C., Grangeon, J., Kayser, G., Tochon-Danguy, J.-C., Felix, A., et al. (2004). Degassing the "Killer Lakes" Nyos and Monoun, Cameroon. *Eos Trans. AGU* 85, 281–288. doi:10.1029/2004eo300001

Halbwachs, M., Sabroux, J. C., and Kayser, G. (2020). Final Step of the 32-year Lake Nyos Degassing Adventure: Natural CO_2 Recharge Is to Be Balanced by Discharge through the Degassing Pipes. *J. Afr. Earth Sci.* 167. doi:10.1016/j.jafrearsci.2019.103575

Issa, T., Ohba, T., Chako Tchamabé, B., Padrón, E., Hernández, P., Eneke Takem, E. G., et al. (2014). Gas Emission from Diffuse Degassing Structures (DDS) of the Cameroon Volcanic Line (CVL): Implications for the Prevention of CO2-related Hazards. *J. Volcanology Geothermal Res.* 283, 82–93. doi:10.1016/j.jvolgeores.2014.07.001

Issa, T., Ohba, T., Fantong, W., Fouepe, A., Tchamabe, B. C., Yoshida, Y., et al. (2013). Contribution of Methane to Total Gas Pressure in Deep Waters at Lakes Nyos and Monoun (Cameroon, West Africa). *Geochem. J.* 47, 349–362. doi:10.2343/geochemj.2.0250

Kling, G. W., Clark, M. A., Wagner, G. N., Compton, H. R., Humphrey, A. M., Devine, J. D., et al. (1987). The 1986 Lake Nyos Gas Disaster in Cameroon, West Africa. *Science* 236, 169–175. doi:10.1126/science.236.4798.169

Kling, G. W. (1988). Comparative Transparency, Depth of Mixing, and Stability of Stratification in Lakes of Cameroon, West Africa1. *Limnol. Oceanogr.* 33, 27–40. doi:10.4319/lo.1988.33.1.0027

Kozono, T., Kusakabe, M., Yoshida, Y., Ntchantcho, R., Ohba, T., Tanyileke, G., et al. (2016). "Numerical Assessment of the Potential for Future Limniceruptions at Lakes Nyos and Monoun, Cameroon, Based on Regular Monitoring Data," in *Geochemistry and Geophysics of Active Volcanic Lakes* (London: Geological SocietySpecial. Publications), 437. doi:10.1144/sp437.8

Kusakabe, M., Ohba, T., IssaYoshida, Y., Yoshida, Y., Satake, H., Ohizumi, T., et al. (2008). Evolution of CO2 in Lakes Monoun and Nyos, Cameroon, before and during Controlled Degassing. *Geochem. J.* 42, 93–118. doi:10.2343/geochemj.42.93

Kusakabe, M., Tanyileke, G. Z., McCord, S. A., and Schladow, S. G. (2000). Recent pH and CO 2 Profiles at Lakes Nyos and Monoun, Cameroon: Implications for the Degassing Strategy and its Numerical Simulation. *J. Volcanology Geothermal Res.* 97, 241–260. doi:10.1016/s0377-0273(99)00170-5

Lockwood, J. P., and Rubin, M. (1989). Origin and Age of the Lake Nyos Maar, Cameroon. *J. Volcanology Geothermal Res.* 39, 117–124. doi:10.1016/0377-0273(89)90052-8

Lorenz, V. (1973). On the Formation of Maars. *Bull. Volcanol.* 37, 183–204. doi:10.1007/bf02597130

Mazot, A., and Bernard, A. (2015). "CO_2 Degassing from Volcanic Lakes. Volcanic Lakes," in *Advances in Volcanology*. (Berlin Heidelberg: Springer-Verlag).

Nagao, K., Kusakabe, M., Yoshida, Y., and Tanyileke, G. (2010). Noble Gases in Lakes Nyos and Monoun, Cameroon. *Geochem. J.* 44, 519–543. doi:10.2343/geochemj.1.0101

Ohba, T., Ooki, S., Oginuma, Y., Kusakabe, M., Yoshida, Y., Ueda, A., et al. (2015). "Decreasing Removal Rate of the Dissolved CO_2 in Lake Nyos, Cameroon, after the Installation of Additional Degassing Pipes," in *Geochemsitry and Geophysics of Active Volcanic Lakes*. Editors T. Ohba, B. Capaccioni, and C. Caudron (Bath, United Kingdom: The Geological Society of London, special publication), 437. doi:10.1144/sp437.6

Shanklin, E. (1992). "Natural Disasters in the Oral History of West Cameroon," in *Natural Hazards in West and Central Africa*. Editor S. J. Freeth (Vieweg Pub). doi:10.1007/978-3-663-05239-5_7

Sigurdsson, H., Devine, J. D., Tchua, F. M., Presser, F. M., Pringle, M. K. W., and Evans, W. C. (1987). Origin of the Lethal Gas Burst from Lake Monoun, Cameroun. *J. Volcanology Geothermal Res.* 31, 1–16. doi:10.1016/0377-0273(87)90002-3

Sigvaldason, G. E. (1989). International Conference on Lake Nyos Disaster, Yaoundé, Cameroon 16-20 March, 1987: Conclusions and Recommendations. *J. Volcanology Geothermal Res.* 39, 97–107. doi:10.1016/0377-0273(89)90050-4

Stumm, W., and Morgan, J. J. (1996). *Aquatic Chemistry*. 3rd. Ed. Jhon Wiley & Sons.

Tanyileke, G., Ntchantcho, R., Fantong, W. Y., Aka, F. T., and Hell, J. V. (2019). 30 Years of the Lakes Nyos and Monoun Gas Disasters: A Scientific, Technological, Institutional and Social Adventure. *J. Afr. Earth Sci.* 150, 415–424. doi:10.1016/j.jafrearsci.2018.11.022

Woods, A. W., and Phillips, J. C. (1999). Turbulent Bubble Plumes and CO2-driven lake Eruptions. *J. Volcanology Geothermal Res.* 92, 259–270. doi:10.1016/s0377-0273(99)00028-1

Yoshida, Y., Kusakabe, M., Issa, O., T., Tanyileke, G., and Hell, J., V. (2015). "Decreasing Capability of the Degassing Systems at Lakes Nyos and Monoun (Cameroon): A New Gas Removal System Applied to Lake Monoun to Prevent a Future Limnic Eruption," in *Geochemistry and Geophysics of Active Volcanic Lakes*. Editors T. Ohba, B. Capaccioni, and C. Caudron (London: Geological SocietySpecial Publications), 437.

Conflict of Interest: The authors declare that the research was conducted in the absence of any commercial or financial relationships that could be construed as a potential conflict of interest.

Advantages of publishing in Frontiers

OPEN ACCESS
Articles are free to read for greatest visibility and readership

FAST PUBLICATION
Around 90 days from submission to decision

HIGH QUALITY PEER-REVIEW
Rigorous, collaborative, and constructive peer-review

TRANSPARENT PEER-REVIEW
Editors and reviewers acknowledged by name on published articles

Frontiers
Avenue du Tribunal-Fédéral 34
1005 Lausanne | Switzerland

Visit us: www.frontiersin.org
Contact us: frontiersin.org/about/contact

REPRODUCIBILITY OF RESEARCH
Support open data and methods to enhance research reproducibility

DIGITAL PUBLISHING
Articles designed for optimal readership across devices

FOLLOW US
@frontiersin

IMPACT METRICS
Advanced article metrics track visibility across digital media

EXTENSIVE PROMOTION
Marketing and promotion of impactful research

LOOP RESEARCH NETWORK
Our network increases your article's readership